

F. N. Lin  
Assoc. Research Scientist,  
Lockheed Missiles and Space Co.,  
Huntsville, Ala.

B. T. Chao  
Professor,  
University of Illinois at Urbana-Champaign,  
Urbana, Ill.  
Fellow ASME

# Laminar Free Convection Over Two-Dimensional and Axisymmetric Bodies of Arbitrary Contour

*A rapid computation procedure is described for the prediction of heat transfer in laminar free convection boundary layers, either two-dimensional or axisymmetrical, over isothermal smooth objects with fairly arbitrary shape. The analysis employs suitable coordinate transformation which makes it possible to express the solutions of the governing conservation equations in terms of a sequence of universal functions that depend on the fluid Prandtl number and a configuration function. The latter is completely determined by the body contour and its orientation relative to the body force that generates the motion. Several of the leading universal functions have been evaluated and tabulated. The theory was applied to a number of body configurations and the results compared well with published analytical and/or experimental information. Some new results are also obtained for the local Nusselt number over horizontal elliptical cylinders and ellipsoids of revolution.*

## Introduction

At the present time, adequate information is available for laminar free convection in boundary layers over isothermal objects of simple shapes, such as a vertical plate or cone, for which the flow is similar. Only a few studies have dealt with bodies of arbitrary shape, although their asymptotic behavior for large and for small Prandtl numbers is well known. The series expansion method of Chiang, et al. [1, 2],<sup>1</sup> as extended by Fox [3], is purported to treat arbitrary body contours. The method is patterned after the Blasius-Frössling procedure for forced convection and makes use of "universal" functions. As in the case of the Blasius series, it is useful for blunt objects but becomes impractical for slender bodies due to the excessive number of terms required of the series. Recognizing the need for a procedure to account for the effects of body shape in a general manner, Saville and Churchill [4] proposed the use of a Görtler-type series. The solution is also expressible in universal functions. When applied to horizontal, circular cylinders or spheres, the series converge faster than the corresponding Blasius type expansion. The computed temperature and velocity fields at 90° and 150° from the front stagnation point showed reasonable agreement with experimental data even if only one term of the series were used. However, the authors were uncertain whether equal success could be expected of other body configurations. Unfortunately, this crucial question cannot be readily answered due to the lack of information of the universal functions as-

sociated with the method. In the present study, an alternative approach has been investigated. It is based on the simple notion that the body force which sustains the motion can be viewed as an equivalent pressure gradient effect in the corresponding forced flow. This viewpoint has been used by Acrivos [5] in his examination of the asymptotic behavior of mass transfer rates in laminar boundary layer at large interfacial velocities. The results obtained to date are very encouraging.

## Problem Statement and Governing Conservation Equations

Consideration is hereby given to the steady, laminar, free convection boundary layer flow over two-dimensional or rotationally symmetrical bodies of uniform surface temperature  $T_w$  situated in an infinite ambient fluid of undisturbed temperature  $T_\infty$  as illustrated in Fig. 1. The coordinate  $x$  is the distance measured along the surface from the stagnation point  $S$  in the direction of main flow,  $y$  being normal to it. The corresponding velocity components are  $u$  and  $v$ . For rotationally symmetrical bodies, we also introduce  $r$  which is the radial distance from a surface element to the axis of symmetry.

The conservation equations governing the boundary layer flow are well known. They are

$$\frac{\partial(\bar{r}u)}{\partial x} + \frac{\partial(\bar{r}v)}{\partial y} = 0 \quad (1)$$

$$u \frac{\partial u}{\partial x} + v \frac{\partial u}{\partial y} = -\alpha_x \beta (T - T_\infty) + \nu \frac{\partial^2 u}{\partial y^2} \quad (2)$$

$$\bar{u} \frac{\partial T}{\partial x} + \bar{v} \frac{\partial T}{\partial y} = \kappa \frac{\partial^2 T}{\partial y^2} \quad (3)$$

<sup>1</sup> Numbers in brackets designate References at end of paper.

Contributed by the Heat Transfer Division for publication in the JOURNAL OF HEAT TRANSFER. Manuscript received by the Heat Transfer Division May 6, 1974. Paper No. 75-HT-K.

wherein  $\beta$ ,  $\nu$ ,  $\kappa$ , and  $T$  are, respectively, the thermal expansion coefficient, kinematic viscosity, thermal diffusivity, and temperature of the fluid, and  $a_{\bar{x}}$  is the  $\bar{x}$ -component of the local acceleration vector in the direction of increasing  $\bar{x}$ . It may be gravitational or centrifugal in origin. For convenience of further discussion, we write

$$a_{\bar{x}} = \mp a\phi(\bar{x}) \begin{cases} -\text{for } T_w > T_\infty \\ +\text{for } T_w < T_\infty \end{cases} \quad (4)$$

where  $a$  is a positive constant having the dimension of acceleration and  $\phi$  is a nondimensional function of  $\bar{x}$ . In the gravitational field,  $a = g$  and  $\phi = \sin \alpha$ ,  $\alpha$  being the angle between the gravitational acceleration vector and the outdrawn normal to the body surface. In writing (2) and (3), it has been assumed that  $\beta|T_w - T_\infty| \ll 1$ . As has been ably demonstrated by Ostrach [6], the consequence of this assumption is that the dissipative effects and the compression work are negligible and that all fluid properties can be taken as constants except for the density changes which give rise to the motion. The appropriate boundary conditions are

$$\bar{u}(\bar{x}, 0) = \bar{v}(\bar{x}, 0) = 0, \quad T(\bar{x}, 0) = T_w \quad (5a, b, c)$$

$$\bar{u}(\bar{x}, \infty) \rightarrow 0, \quad T(\bar{x}, \infty) \rightarrow T_\infty. \quad (6a, b)$$

The conservation equations can be recast into dimensionless form by introducing a reference length  $L$ , the appropriate stretched coordinates, and the normalizing velocities and temperatures as defined below.

$$x = \bar{x}/L, \quad r = \bar{r}/L, \quad y = \text{Gr}^{1/4} \bar{y}/L, \quad (7a, b, c)$$

$$u = \frac{\bar{u}}{(\nu/L)\text{Gr}^{1/2}}, \quad v = \frac{\bar{v}}{(\nu/L)\text{Gr}^{1/4}}, \quad (8a, b)$$

$$\theta = (T - T_\infty)/(T_w - T_\infty), \quad (9)$$

where the Grashof number  $\text{Gr} = a\beta|T_w - T_\infty|L^3/\nu^2$ . Accordingly, (1), (2), and (3) become

$$\frac{\partial(ru)}{\partial x} + \frac{\partial(rv)}{\partial y} = 0 \quad (10)$$

$$u \frac{\partial u}{\partial x} + v \frac{\partial u}{\partial y} = \phi(x)\theta + \frac{\partial^2 u}{\partial y^2} \quad (11)$$

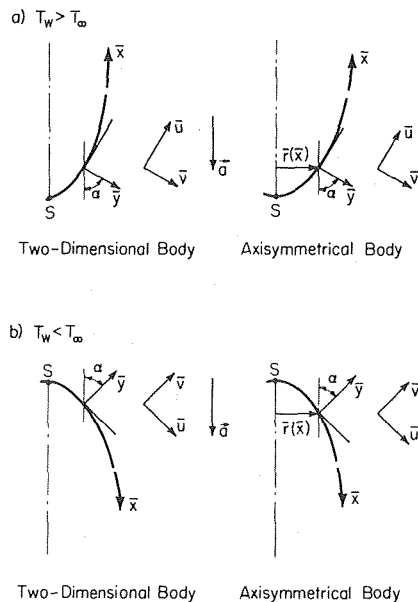


Fig. 1 Physical model and coordinate system

$$u \frac{\partial \theta}{\partial x} + v \frac{\partial \theta}{\partial y} = \text{Pr}^{-1} \frac{\partial^2 \theta}{\partial y^2} \quad (12)$$

with

$$u(x, 0) = v(x, 0) = 0, \quad \theta(x, 0) = 1 \quad (13a, b, c)$$

$$u(x, \infty) \rightarrow 0, \quad \theta(x, \infty) \rightarrow 0. \quad (14a, b)$$

In (12),  $\text{Pr}$  denotes the Prandtl number,  $\nu/\kappa$ . It may be noted that (11) is valid for either  $T_w > T_\infty$  or  $T_w < T_\infty$ . For two-dimensional bodies, one needs only to set  $r = 1$ .

In forced flows, the streamwise pressure gradient in the momentum boundary layer equation assumes the role of the buoyancy in (2). This observation suggests that one may define a hypothetical or "equivalent" outer stream velocity function  $\bar{U}(\bar{x})$  in such a way that

$$a\beta|T_w - T_\infty|\phi = \bar{U} \frac{d\bar{U}}{d\bar{x}}. \quad (15a)$$

Or, in dimensionless form,

$$\phi = U \frac{dU}{dx} \quad (15b)$$

where  $U = \bar{U}/(\nu \text{Gr}^{1/2}/L)$  and  $x = \bar{x}/L$  as previously defined. Upon integration, (15b) gives

$$U = (2 \int_0^x \phi dx)^{1/2}. \quad (15c)$$

The continuity equation (10) is identically satisfied by introducing a stream function  $\psi(x, y)$  defined by

$$ru = \frac{\partial \psi}{\partial y}, \quad rv = -\frac{\partial \psi}{\partial x}. \quad (16a, b)$$

The  $(x, y)$  coordinate system is transformed into the Görtler-Meksyn system  $(\xi, \eta)$  according to

$$\xi = \int_0^x r^2 U dx, \quad \eta = \frac{rU}{(2\xi)^{1/2}} y \quad (17a, b)$$

and the corresponding dimensionless stream function  $f(\xi, \eta)$  defined by

$$\psi(x, y) = (2\xi)^{1/2} f(\xi, \eta) \quad (18)$$

is introduced. It follows then

$$u = \bar{u}/(\nu \text{Gr}^{1/2}/L) = Uf' \quad (19a)$$

$$v = \bar{v}/(\nu \text{Gr}^{1/4}/L) = -\frac{rU}{(2\xi)^{1/2}} \left[ f + 2\xi \frac{\partial f}{\partial \xi} + \left( \Lambda + 2 \frac{\xi}{r} \frac{dr}{d\xi} - 1 \right) \eta f' \right] \quad (19b)$$

where

$$\Lambda = 2 \frac{\xi}{U} \frac{dU}{d\xi} = 2 \frac{\phi \xi}{r^2 U^3}. \quad (20)$$

In (19a, b) and other equations which follow, the prime denotes  $\partial/\partial \eta$ . It should be noted that  $\Lambda$  is a function of  $x$  only. It is called the *configuration function* since it is determined completely by the body shape and its orientation relative to the body force vector. It is analogous to the "wedge" variable in forced flows. The outcome of the foregoing transformation is that the momentum equation (11) and the energy equation (12) become, respectively,

$$f''' + ff'' + \Lambda[\theta - (f')^2] = 2\xi \frac{\partial(f', f)}{\partial(\xi, \eta)} \quad (21)$$

and

$$\text{Pr}^{-1}\theta'' + f\theta' = 2\xi \frac{\partial(\theta, f)}{\partial(\xi, \eta)} \quad (22)$$

with

$$f(\xi, 0) = f'(\xi, 0) = 0, \quad \theta(\xi, 0) = 1 \quad (23a, b, c)$$

$$f'(\xi, \infty) \rightarrow 0, \quad \theta(\xi, \infty) \rightarrow 0. \quad (24a, b)$$

In (21) and (22),  $\partial(\cdot, \cdot)/\partial(\xi, \eta)$  denotes the Jacobian. The equation pair bears a striking resemblance to that given by Merk [7] in his study of boundary layer transfer in forced flows. In fact, if one sets  $\theta = 1$  in (21), the pair becomes formally identical to equations (14) and (17) in [7]. Needless to say, in these equations of Merk,  $f$ ,  $\xi$ , and  $\eta$  have different meanings.

For a vertical plate,  $\alpha = \pi/2$ ,  $\phi = 1$ , and, accordingly,  $U = (2x)^{1/2}$ ,  $\xi = (1/3)(2x)^{3/2}$  and hence  $\Lambda = 2/3$ , a constant. Consequently, both  $f$  and  $\theta$  depend only on  $\eta$  and the Jacobian in (21) and (22) vanish. As is well known, the free convection flow is similar. While the resulting simplified equations appear different from those given by Ostrach [6], it can be demonstrated that the solutions, when expressed in terms of physical variables, are identical.<sup>2</sup> For inclined flat plates,  $\phi = \sin \alpha$  which is a constant and  $\Lambda$  remains to be  $2/3$ . For vertical, circular cones,  $\Lambda = 2/7$ . It can be readily shown that at the front stagnation point of two-dimensional and rotationally symmetrical bodies,  $\Lambda = 1$  and  $1/2$ , respectively, as the wedge variable is in forced flows.

Braun, Ostrach, and Heighway [8] examined families of bodies which gave rise to similar free convection flows. They have shown that for two-dimensional, isothermal objects, the body contour satisfies the relation:

$$\frac{dr}{dx} = [1 - (\frac{m+1}{m}x)^{2(m-3)/(m+1)}]^{1/2} \quad (25a)$$

where  $m$  is any constant except for values in the range  $-1 \leq m \leq 3$ . Since  $dr/dx = (1 - \phi^2)^{1/2}$ , it follows that

$$\phi = (\frac{m+1}{m}x)^{(m-3)/(m+1)} \quad (25b)$$

Clearly  $\phi \geq 0$  for the permissible values of  $m$ . Using (15c), (17a), and (20), one obtains

$$\Lambda = (m-1)/m \quad (25c)$$

which is constant and, hence, the flow is similar. Braun, et al., further noted that for a flat plate  $m = 3$  and, accordingly,  $\Lambda = 2/3$  which agrees with our result.

### Series Solution

The recent investigation of Chao and Fagbenle [9] for the prediction of forced convection boundary layer transfer suggests that the appropriate series solutions for (21) and (22) satisfying (23a,b,c) and (24a,b) are:

$$f(\xi, \eta) = f_0(\Lambda, \eta) + \xi \frac{d\Lambda}{d\xi} f_1(\Lambda, \eta) + \xi^2 \frac{d^2\Lambda}{d\xi^2} f_2(\Lambda, \eta) + (\xi \frac{d\Lambda}{d\xi})^2 f_3(\Lambda, \eta) + \dots \quad (26)$$

$$\theta(\xi, \eta) = \theta_0(\Lambda, \eta) + \xi \frac{d\Lambda}{d\xi} \theta_1(\Lambda, \eta) + \xi^2 \frac{d^2\Lambda}{d\xi^2} \theta_2(\Lambda, \eta) + (\xi \frac{d\Lambda}{d\xi})^2 \theta_3(\Lambda, \eta) + \dots \quad (27)$$

<sup>2</sup> A second coordinate transformation has been found which leads to momentum and energy boundary layer equations identical to those given by Ostrach [6] if they are specialized for the vertical plate. However, their solutions in series form are not as satisfactory as those reported herein when used for nonsimilar flows.

Upon substituting (26) and (27) into (21) and (22), followed by first collecting terms free of derivatives of  $\Lambda$  and then terms common to  $\xi(d\Lambda/d\xi)$ ,  $\xi^2(d^2\Lambda/d\xi^2)$ , etc., we obtain a sequence of coupled sets of differential equations. The first set is

$$f_0''' + f_0 f_0'' + \Lambda[\theta_0 - (f_0')^2] = 0 \quad (28)$$

$$\text{Pr}^{-1}\theta_0'' + f_0\theta_0' = 0 \quad (29)$$

with

$$f_0(\Lambda, 0) = f_0'(\Lambda, 0) = 0, \quad \theta_0(\Lambda, 0) = 1 \quad (30a, b, c)$$

$$f_0'(\Lambda, \infty) \rightarrow 0, \quad \theta_0(\Lambda, \infty) \rightarrow 0. \quad (31a, b)$$

At a given streamwise location,  $\Lambda$  is fixed. Hence, (28) and (29) can be integrated as if they were ordinary differential equations. It should be noted that  $f_0$  and  $\theta_0$  are universal in the sense that, for a given  $\Lambda$  and  $\text{Pr}$ , they may be evaluated once and for all.

The second and third sets of equations are

$$f_1''' + f_0 f_1'' - 2(1 + \Lambda)f_0' f_1' + 3f_0'' f_1 + \Lambda\theta_1 = 2 \frac{\partial(f_0', f_0)}{\partial(\Lambda, \eta)} \quad (32)$$

$$\text{Pr}^{-1}\theta_1'' + f_0\theta_1' - 2f_0'\theta_1 + 3f_1\theta_0' = 2 \frac{\partial(\theta_0, f_0)}{\partial(\Lambda, \eta)} \quad (33)$$

and

$$f_2''' + f_0 f_2'' - 2(2 + \Lambda)f_0' f_2' + 5f_0'' f_2 + \Lambda\theta_2 = 2(f_0' f_1' - f_0'' f_1) \quad (34)$$

$$\text{Pr}^{-1}\theta_2'' + f_0\theta_2' - 4f_0'\theta_2 + 5f_2\theta_0' = 2(f_0'\theta_1 - f_1\theta_0') \quad (35)$$

with

$$f_i(\Lambda, 0) = f_i'(\Lambda, 0) = 0, \quad \theta_i(\Lambda, 0) = 0 \quad (36a, b, c)$$

$$f_i'(\Lambda, \infty) \rightarrow 0, \quad \theta_i(\Lambda, \infty) \rightarrow 0 \quad (37a, b)$$

where  $i = 1$  or  $2$ . Like  $f_0$  and  $\theta_0$ ,  $f_i$ 's and  $\theta_i$ 's are also universal. The foregoing three sets of coupled differential equations have been numerically integrated for  $\text{Pr} = 0.72, 2, 5, 10$ , and  $100$  and for  $26$  values of  $\Lambda$  ranging from  $1.4$  to  $2/7$ . A tabulation of the appropriate wall derivatives of these universal functions for  $\text{Pr} = 0.72$  and  $100$  is given in the Appendix. Others may be obtained from the authors. With these, the local heat transfer rate and wall shear can be readily computed by using formulas given in the following section. Computer compiled tabulations of the universal functions are deposited in the Heat Transfer Laboratory of the University of Illinois. With the availability of such information, the velocity fields can be evaluated from (19a,b) and the temperature field from (27). Details of the numerical procedure, including integration step size, methods of iteration, satisfaction of the asymptotic boundary conditions, estimation of the numerical accuracy, etc., are given by Lin [10].

### Surface Heat Flux And Shear Stress

In technological applications, it is often the surface heat flux  $q_w$  that is of the greatest interest. In terms of the local Nusselt number, it is given by

$$\frac{\text{Nu}}{\text{Gr}^{1/4}} = \frac{q_w L}{\text{Gr}^{1/4} k (T_w - T_\infty)} = rU(2\xi)^{-1/2} [-\frac{\partial\theta}{\partial\eta}(\xi, 0)] \quad (38a)$$

where

$$\frac{\partial\theta}{\partial\eta}(\xi, 0) = \theta_0'(\Lambda, 0) + \xi \frac{d\Lambda}{d\xi} \theta_1'(\Lambda, 0) + \xi^2 \frac{d^2\Lambda}{d\xi^2} \theta_2'(\Lambda, 0) + \dots \quad (38b)$$

and  $k$  denotes the thermal conductivity. Although the wall shear  $\tau_w$  in free convection is usually of secondary concern, some infor-

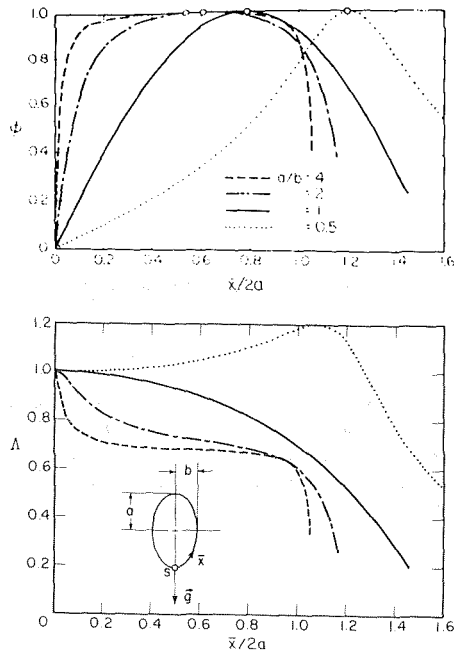


Fig. 2 Variations of  $\phi$  and  $\Lambda$  over horizontal, circular and elliptical cylinders

mation has been reported in the literature. It can be easily obtained from the following expression

$$\frac{\bar{\tau}_w}{\rho(\nu/L)^2 Gr^{3/4}} = r^{-1/3} \phi^{2/3} \xi^{1/4} \frac{\partial^2 f}{\partial \eta^2}(\xi, 0) \quad (39a)$$

where

$$\begin{aligned} \frac{\partial^2 f}{\partial \eta^2}(\xi, 0) = & f_0''(\Lambda, 0) + \xi \frac{d\Lambda}{d\xi} f_1''(\Lambda, 0) \\ & + \xi^2 \frac{d^2 \Lambda}{d\xi^2} f_2''(\Lambda, 0) + \dots \quad (39b) \end{aligned}$$

and  $\rho$  is the density.

It is fitting to reiterate that when  $\Lambda$  is a constant, the free convection flow is similar and the series expansions (26) and (27) have only the first term. For nonsimilar flows, the two first terms,  $f_0$  and  $\theta_0$  constitute the so-called local similarity solution and the remaining terms in each series, taken collectively, may be regarded as "corrections." It is important to recognize that the local similarity solution is *not* unique; it depends on the configuration function associated with it. Therefore, it is meaningful only to speak of a local similarity solution *with respect to* a parameter which, in the present instance, is  $\Lambda$ . The series solution referred to in Footnote 2 also leads to a local similarity solution but it is with respect to a different configuration function. For similar flows, the two solutions when reflected in terms of physical quantities are necessarily identical. This has indeed been found to be the case. On the other hand, the two local similarity solutions are *not* equal for nonsimilar flows. Obviously, the corrections just referred to are also different. Since, in practice, only a very limited number of terms in the series is available, the solution which requires a smaller correction is clearly preferred and that is the one described herein.

### Applications

To examine the usefulness and limitations of the present analysis, the results have been applied to a variety of body shapes. They include vertical or inclined flat plates, vertical circular cones, a flat plate rotating about its leading edge, long horizontal circular and elliptical cylinders, spheres, and ellipsoids of revolution. In the case of the vertical plate, the computed data for local Nusselt

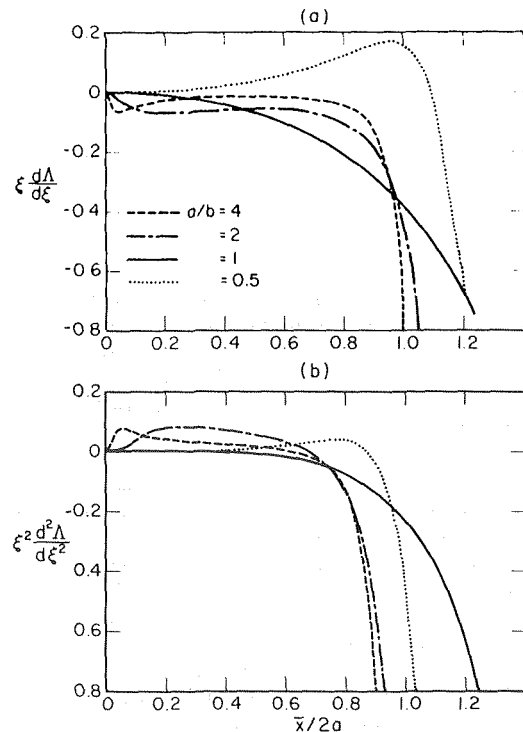


Fig. 3 Variations of  $\xi d\Lambda/d\xi$  and  $\xi^2 d^2\Lambda/d\xi^2$  over horizontal, circular and elliptical cylinders

number, wall shear distribution, temperature, and velocity fields agree with those reported by Ostrach [6] to a very high degree of precision for all Prandtl numbers investigated. Satisfactory results are also obtained for the cone, the rotating flat plate, the horizontal cylinder, and the sphere, based on comparisons made with either known solutions or experiments or both. The results for horizontal elliptical cylinders and ellipsoids of revolution are, to our knowledge, new. A portion of our findings is briefly presented in the following sections. The more complete information is available from [10].

**Long, Horizontal Elliptical Cylinders.** Under consideration are elliptical cylinders of semidiameters  $a$  and  $b$  oriented with respect to the local gravitational acceleration vector  $\bar{g}$  as illustrated in the insert of Fig. 2. Upon selecting  $2a$  as the reference length  $L$ , the following geometric relationships can be readily established:

$$x = \bar{x}/2a = \frac{1}{2} \int_0^\vartheta (1 - e^2 \cos^2 \vartheta)^{1/2} d\vartheta \quad (40)$$

and

$$\phi = [1 + (\frac{b}{a})^2 \cot^2 \vartheta]^{-1/2} \quad (41)$$

where  $\vartheta$  is the eccentric angle and  $e$  is the eccentricity given by  $e^2 = 1 - (b/a)^2$ . The variations of  $\phi$  with  $x$  for  $a/b = 0.5, 1$  (circular cylinder), 2, and 4, are displayed in the upper half of Fig. 2. They hold also for ellipsoids of revolution to be considered later. In order to apply the present method of analysis, we identify

$$U = (2 \int_0^x \phi dx)^{1/2} = (1 - \cos \vartheta)^{1/2}, \quad (42)$$

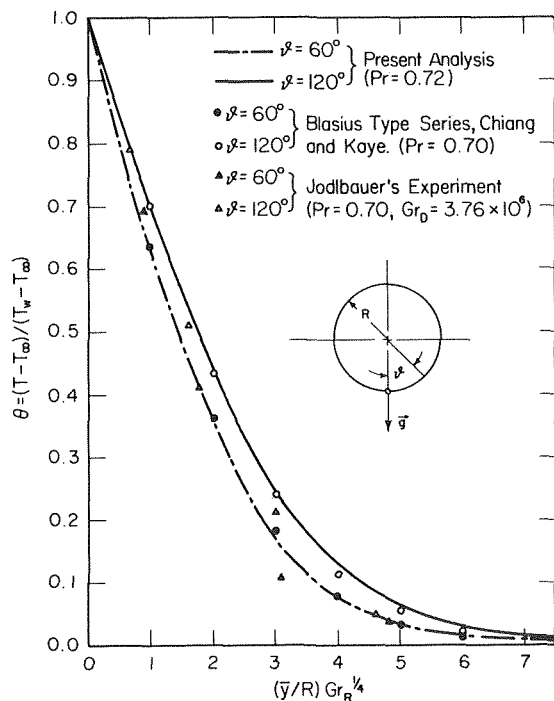
$$\xi = \int_0^x U dx = \frac{1}{2} \int_0^\vartheta (1 - \cos \vartheta)^{1/2} (1 - e^2 \cos^2 \vartheta)^{1/2} d\vartheta, \quad (43)$$

$$\eta = \frac{U}{(2\xi)^{1/2}} y = \frac{U}{(2\xi)^{1/2}} Gr^{1/4} \frac{\bar{y}}{2a}, \quad (44)$$

**Table 1 Local heat transfer parameter;  $Nu/Gr^{1/4}$ , for isothermal, horizontal, circular cylinder—a comparison of different predictive methods;  $Pr = 0.70$**

$\vartheta$ , deg.	Present Analysis				Blasius-Type Series [1]			Görtler-Type Series [4]		
	1st Term	2nd Term	3rd Term	Sum*	1st Term	2nd Term	Sum	1st Term	2nd Term	Sum
0	0.4402	0.0000	0.0000	0.4402	0.4402	0.0000	0.4402	0.4402	0.0000	0.4402
10	0.4393	0.0000	0.0000	0.4393	0.4402	-0.0006	0.4396	0.4396	0.0000	0.4396
20	0.4376	-0.0001	0.0000	0.4375	0.4402	-0.0023	0.4379	0.4376	-0.0001	0.4375
30	0.4347	-0.0001	0.0000	0.4346	0.4402	-0.0052	0.4350	0.4343	-0.0003	0.4340
40	0.4306	-0.0002	0.0000	0.4304	0.4402	-0.0093	0.4309	0.4295	-0.0005	0.4290
50	0.4255	-0.0003	0.0000	0.4252	0.4402	-0.0146	0.4256	0.4234	-0.0007	0.4227
60	0.4191	-0.0005	0.0001	0.4186	0.4402	-0.0210	0.4192	0.4158	-0.0010	0.4148
70	0.4116	-0.0007	0.0001	0.4109	0.4402	-0.0286	0.4116	0.4068	-0.0013	0.4055
80	0.4027	-0.0009	0.0002	0.4018	0.4402	-0.0373	0.4029	0.3963	-0.0017	0.3946
90	0.3925	-0.0012	0.0004	0.3913	0.4402	-0.0472	0.3930	0.3842	-0.0020	0.3822
100	0.3808	-0.0014	0.0006	0.3794	0.4402	-0.0583	0.3819	0.3703	-0.0023	0.3680
110	0.3676	-0.0017	0.0010	0.3659	0.4402	-0.0705	0.3697	0.3546	-0.0026	0.3520
120	0.3527	-0.0019	0.0015	0.3508	0.4402	-0.0839	0.3563	0.3367	-0.0029	0.3338
130	0.3358	-0.0020	0.0024	0.3338	0.4402	-0.0985	0.3417	0.3163	-0.0031	0.3132
140	0.3161	-0.0016	0.0038	0.3145	0.4402	-0.1142	0.3260	0.2928	-0.0032	0.2896
150	0.2924	-0.0001	0.0060	0.2923	0.4402	-0.1311	0.3091	0.2649	-0.0032	0.2617
159	0.2661	0.0039	0.0092	0.2700	0.4402	-0.1474	0.2928	---	---	---
160	---	---	---	---	0.4402	-0.1492	0.2910	0.2301	-0.0031	0.2270

\*Sum is based on the first two terms.  $\vartheta$  is measured from the forward stagnation point; the reference length in  $Nu$  and  $Gr$  is cylinder diameter.



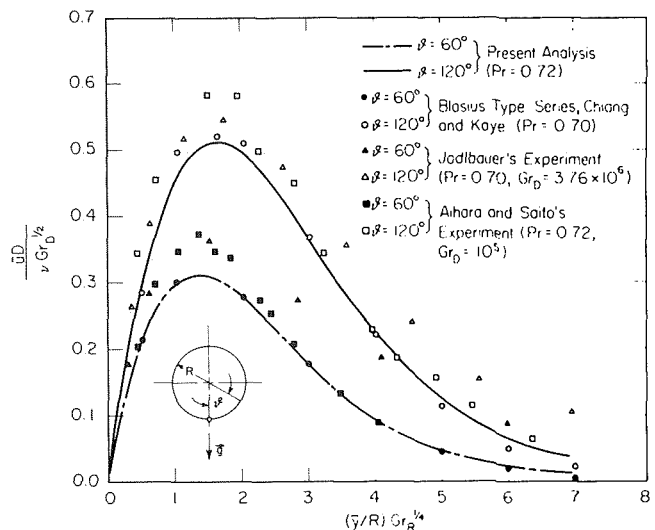
**Fig. 4 Temperature distribution in boundary layers around a heated, isothermal, horizontal circular cylinder**

and

$$\Lambda = 2\phi\xi/U^3. \quad (45)$$

The lower half of Fig 2 shows the variations of  $\Lambda$  with  $x$ . With the availability of the foregoing information,  $\xi(d\Lambda/d\xi)$  and  $\xi^2(d^2\Lambda/d\xi^2)$  can be evaluated and the results are plotted in Fig. 3. Generally speaking, when the magnitude of  $\xi(d\Lambda/d\xi)$  and  $\xi^2(d^2\Lambda/d\xi^2)$  are small, the series solution converges rapidly and is overwhelmingly dominated by the first term.

We begin by presenting some results obtained from the present analysis for a circular cylinder since experimental data and results from other methods are available for comparison. The local heat transfer coefficients, expressed in terms of  $Nu/Gr^{1/4}$ , are summarized in Table 1 for  $Pr = 0.70$ . While three terms of the series in (38b) have been evaluated, the sum given in the table is based on two terms only in order to effect a direct comparison with results obtained from the Blasius- and Görtler-type series for which only



**Fig. 5  $\bar{u}$ -velocity distribution in boundary layers around a heated, isothermal, horizontal circular cylinder**

two terms are available. It may be noted that, at the forward stagnation point, the flow is similar and all three methods lead to identical results. As  $\vartheta$  increases from zero, minor discrepancies appear and they increase with  $\vartheta$ . At  $\vartheta = 150$  deg, notable differences exist among the three methods. Of interest is the fact that the results of the present analysis lie between the high value of the Blasius series and the low value of the Görtler series.

The temperature distribution in the boundary layer can be calculated in a straightforward manner from (27) using either the available tabulated functions or the computer program developed in this study. The results for  $\vartheta = 60$  and  $120$  deg are shown in Fig. 4. The series was found to be overwhelmingly dominated by the first term. Included in the figure are the theoretical results based on the two-term Blasius-type series reported in [1] and the measured data of Jodlbauer [11]. Computation was also made for  $\vartheta = 90$  deg and the results agreed well with the predictions of Saville and Churchill [4]. The results of the  $u$ -velocity distribution for  $\vartheta = 60$  and  $120$  deg are displayed in Fig. 5, along with the experimental data of Jodlbauer and of Aihara and Sato [12] as well as those computed according to Chiang and Kaye [1]. While the experimental results lie above both theoretical predictions, obvious discrepancies exist between the two sets of measured data. The abscissa in both Figs. 4 and 5 is the dimensionless transverse coordinate used

in [1] and  $Gr_R$  denotes the Grashof number based on the cylinder radius. Several  $v$ -velocity distributions have also been computed and they agree well with those obtained from the two-term Blasius series for  $\vartheta = 0$  and  $\vartheta = 60$  deg. However, considerable discrepancy is noted for  $\vartheta = 120$  deg. Unfortunately, we were unable to find any measured data for comparison. Readers are referred to [10] for details.

The variations of the local Nusselt number over the periphery of elliptical cylinders of aspect ratio  $a/b = 0.5, 1, 2,$  and  $4$  are shown in Fig. 6 for  $Pr = 0.72$ . The case of  $a/b = 0.5$  depicts an ellipse with a horizontal major diameter and represents a "blunt" configuration with respect to the gravity driven free convection flow. In contrast, ellipses of  $a/b = 2$  and  $4$  represent "slender" configurations. For the circular cylinder and the slender ellipses, the reduction in heat transfer as one moves away from the stagnation point is due to the increase in the boundary layer thickness. For the blunt ellipse, the local heat transfer coefficient first increases with distance from the stagnation point  $S$ , reaches a maximum at the location labeled  $M$  in Fig. 6 which corresponds to an eccentric angle  $\vartheta$  of approximately 86 deg. In the region between  $S$  and  $M$ , the relative changes in the local streamwise buoyancy force and the viscous force are such that they result in a decrease of the thermal boundary layer thickness. The phenomenon is not unlike that of laminar film condensation over a cooled horizontal flat surface. We are not aware of any experimental or analytical information which may be available for comparison. The combined influence of Prandtl number and aspect ratio on the variation of the local Nusselt number is summarily displayed in Figs. 7(a) and 7(b). Of interest is the fact that, for the slender ellipses, the dimensionless group  $Nu/(Gr \cdot Pr)^{1/4}$  is almost independent of the aspect ratio for  $\bar{x}/2a > 0.2$ .

As  $Pr \rightarrow \infty$ , the free convection flows are similar regardless of the body shape. In this case, the governing conservation equations become greatly simplified. It can be demonstrated that the local Nusselt number is given by:

$$\frac{Nu}{(Gr \cdot Pr)^{1/4}} = 0.50275 \frac{(r\phi)^{1/3}}{[\int_0^x (r^4 \phi)^{1/3} dx]^{1/4}} \quad (46)$$

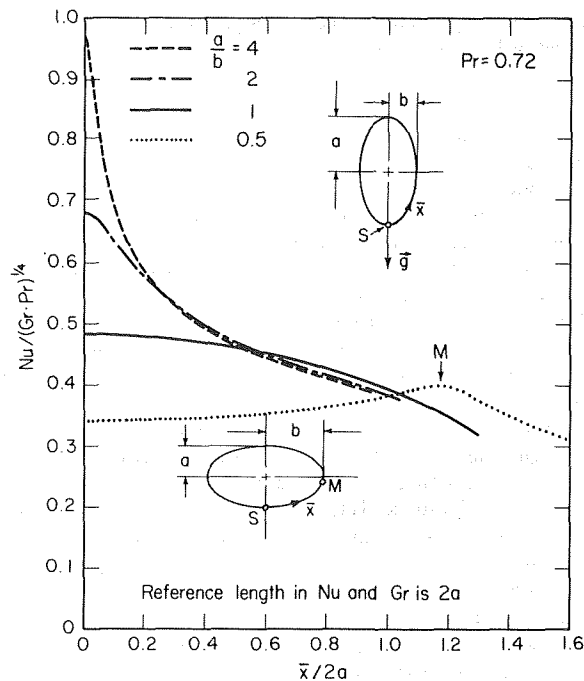


Fig. 6 Heat transfer over isothermal, horizontal circular and elliptical cylinders;  $Pr = 0.72$

For two-dimensional bodies,  $r = 1$ , as has previously been stated.

**Sphere and Ellipsoids of Revolution.** Computation has been carried out for the local heat transfer coefficient as well as the temperature and velocity fields in boundary layers over a sphere and other ellipsoids of revolution. The results are qualitatively similar to those for the horizontal circular and elliptical cylinders.

We consider a body of revolution whose meridian plane is an ellipse as illustrated in Fig. 2. If one selects  $2a$  as the reference length, then equations (40), (41), and (42) remain unaltered. Since, in the present case,

$$r = \bar{r}/2a = \frac{1}{2} \frac{b}{a} \sin \vartheta, \quad (47)$$

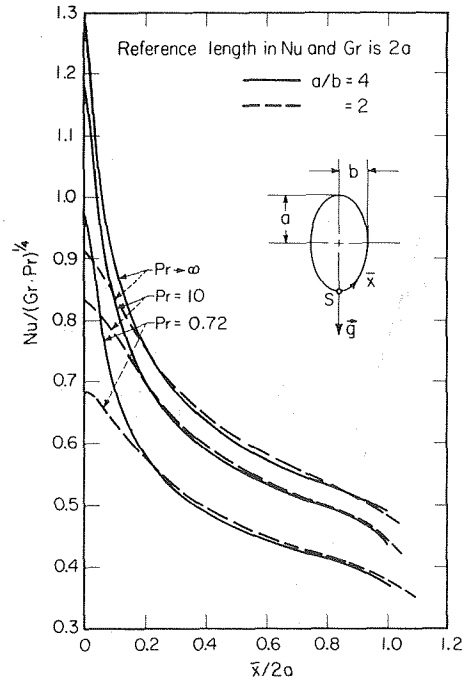


Fig. 7(a) Heat transfer over isothermal, horizontal slender elliptical cylinders for a range of Prandtl numbers

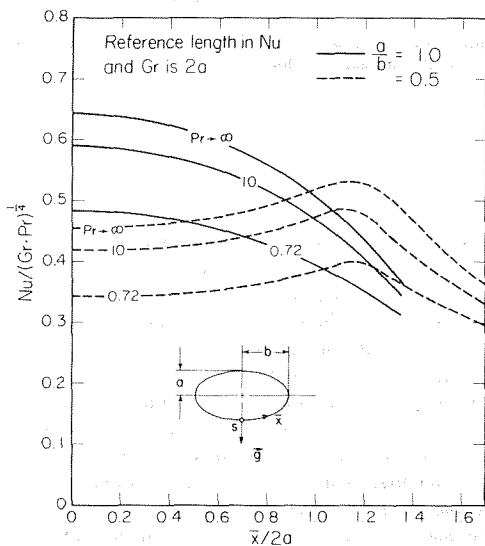


Fig. 7(b) Heat transfer over isothermal, horizontal circular and blunt elliptical cylinders for a range of Prandtl numbers

it follows that

$$\xi = \int_0^x r^2 U dx = \frac{1}{8} \left(\frac{b^*}{a}\right)^2 \int_0^\vartheta \sin^2 \vartheta (1 - \cos \vartheta)^{1/2} \times (1 - e^2 \cos^2 \vartheta)^{1/2} d\vartheta, \quad (48)$$

$$\eta = \frac{rU}{(2\xi)^{1/2} y} = \frac{1}{2} \frac{b}{a} \frac{U \sin \vartheta}{(2\xi)^{1/2}} Gr^{1/4} \frac{\bar{y}}{2a} \quad (49)$$

and

$$\Lambda = 2\phi \xi / r^2 U^3. \quad (50)$$

With these,  $\xi(d\Lambda/d\xi)$  and  $\xi^2(d^2\Lambda/d\xi^2)$  can be evaluated. We shall refrain from presenting the details. Instead, we merely note that at the forward stagnation point,  $\Lambda = 0.5$  and the variations of  $\Lambda$ ,  $\xi(d\Lambda/d\xi)$  and  $\xi^2(d^2\Lambda/d\xi^2)$  with  $\bar{x}/2a$  behave like the mirror image of the corresponding curves shown in Figs. 2 and 3. For instance, for the circular cylinder  $\Lambda$  decreases with increasing distance from the stagnation point, slowly at the beginning and at an increasingly rapid pace for larger values of  $\bar{x}/2a$ . For the sphere, on the other hand,  $\Lambda$  increases with distance from the stagnation point, slowly at small values of  $\bar{x}/2a$  and the graph exhibits a relatively sharp upturn when  $\bar{x}/2a$  exceeds 1.2. Details are given in [10]. In Fig. 8, the computed local Nusselt numbers are plotted in solid lines for a sphere over a wide span of Prandtl numbers. Included for comparison are the experimental results for air and benzene reported by Cremers and Finley [13] and by Kranse and Schenk [14], respectively. Cremers and Finley's experiments involved relatively large temperature differences. The data shown in Fig. 8 were read from Fig. 4 of [13] for which the authors evaluated all properties at a reference temperature proposed by Sparrow and Gregg [15] with the exception of the thermal expansion coefficient. The data for benzene shown in open triangles are the mean of three sets of results obtained by Kranse and Schenk using a solid copper sphere of 5.15 cm dia. The filled triangles represent the mean of two sets of data reported by the same authors using a slightly larger diameter copper sphere. All factors considered, it seems reasonable to conclude that the agreement is probably as good as one may hope for.

If the curve shown in Fig. 6 for the variation of the local Nusselt number ( $Pr = 0.72$ ) over the periphery of the circular cylinder is replotted in Fig. 8, one finds that it intersects with the curve for the same  $Pr$  at  $\vartheta \approx 115$  deg. Over the forward half of the body, the sphere has a higher heat transfer coefficient mainly due to the more rapid divergence of the streamlines which result in a thinner boundary layer when compared with the circular cylinder at the same angular location. For the rear half of the sphere or the cylinder, the streamlines converge so long as the flow does not separate and the  $v$ -velocity component continues to entrain fluid at the edge of the boundary layer. Again, due to the difference between the axisymmetric and two-dimensional geometry, the streamlines for the sphere converge faster and, hence, the thickening of the boundary layer takes place at a more rapid pace. Therefore, the local heat transfer diminishes at a faster rate and eventually drops below that for the circular cylinder.

Nusselt number results for ellipsoids of revolution of several aspect ratios and for a range of Prandtl numbers have also been calculated. They are qualitatively similar to those displayed in Figs. 7(a) and 7(b) for the elliptical cylinders. In the interest of conserving journal space, we shall refrain from presenting the details which are available in [10].

### Acknowledgments

The authors are indebted to the Graduate College of the University of Illinois at Urbana-Champaign for granting the computer

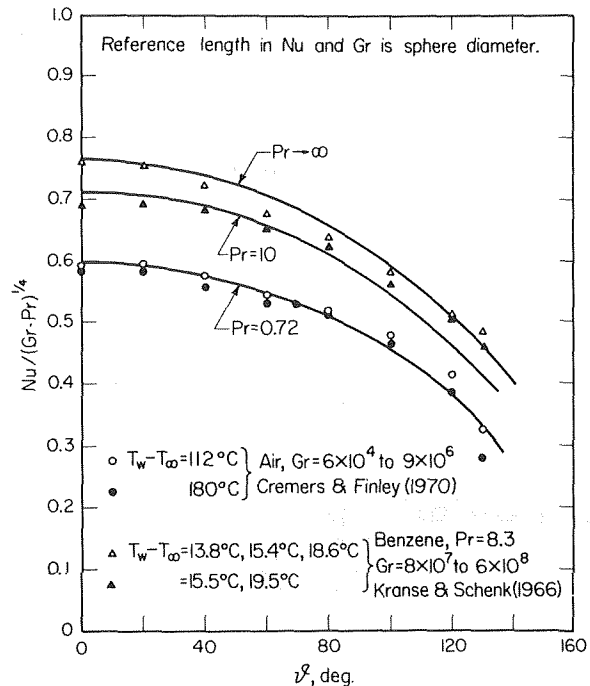


Fig. 8 Local Nusselt number over isothermal spheres

time. Thanks are due to the staff of the Mechanical Engineering Publications Office for their skillful preparation of the manuscript.

### References

- Chiang, T., and Kaye, J., "On Laminar Free Convection From a Horizontal Cylinder," *Proceedings 4th National Congress of Applied Mechanics*, 1962, pp. 1213-1219.
- Chiang, T., Ossin, A., and Tien, C. L., "Laminar Free Convection From a Sphere," *JOURNAL OF HEAT TRANSFER*, TRANS. ASME, Series C, Vol. 86, 1964, pp. 537-542.
- Fox, J., Discussion of reference [2].
- Saville, D. A., and Churchill, S. W., "Laminar Free Convection in Boundary Layers Near Horizontal Cylinders and Vertical Axisymmetric Bodies," *Journal of Fluid Mechanics*, Vol. 29, 1967, pp. 391-399.
- Acrivos, A., "The Asymptotic Form of the Laminar Boundary-Layer Mass-Transfer Rate for Large Interfacial Velocities," *Journal of Fluid Mechanics*, Vol. 12, 1962, pp. 337-357.
- Ostrach, S., "An Analysis of Laminar Free-Convection Flow and Heat Transfer About a Flat Plate Parallel to the Direction of the Generating Body Force," NACA Report No. 1111, 1953.
- Merk, H. J., "Rapid Calculations for Boundary-Layer Transfer Using Wedge Solutions and Asymptotic Expansions," *Journal of Fluid Mechanics*, Vol. 5, 1959, pp. 460-480.
- Braun, W. H., Ostrach, S., and Heighway, J. E., "Free Convection Similarity Flows About Two-Dimensional and Axisymmetric Bodies With Closed Lower Ends," *International Journal of Heat and Mass Transfer*, Vol. 2, 1961, pp. 121-135.
- Chao, B. T., and Fagbenle, R. O., "On Merk's Method of Calculating Boundary Layer Transfer," *International Journal of Heat and Mass Transfer*, Vol. 17, 1974, pp. 223-240.
- Lin, F. N., "Free Convection Heat Transfer in Laminar Boundary Layers," PhD thesis, Department of Mechanical and Industrial Engineering, University of Illinois at Urbana-Champaign, 1974.
- Jodlbauer, K., "Das Temperatur- und Geschwindigkeitsfeld um ein geheiztes Rohr bei freier Konvektion," *Forschung auf dem Gebiete des Ingenieurwesens*, Band 4, 1933, pp. 157-172.
- Aihara, T., and Saito, E., "Measurements of Free Convection Velocity Field Around the Periphery of a Horizontal Torus," *JOURNAL OF HEAT TRANSFER*, TRANS. ASME, Series C, Vol. 94, 1972, pp. 95-98.
- Cremers, C. J., and Finley, D., "Natural Convection About Isothermal Spheres," Fourth International Heat Transfer Conference, Paris-Ver-sailles, Vol. IV, 1970, pp. 1-11.
- Kranse, A. A., and Schenk, J., "Thermal Free Convection From a Solid Sphere," *Applied Scientific Research*, Vol. A15, 1966, pp. 397-403.
- Sparrow, E. M., and Gregg, J. L., "The Variable Fluid-Property Problem in Free Convection," *Recent Advances in Heat and Mass Transfer*, J. P. Hartnett, ed., McGraw-Hill, New York, 1961.

# APPENDIX

**Tables of wall derivatives of universal functions  
for Pr = 0.72 and Pr = 100**

(A) Pr = 0.72						
$A$	$F''_0(A,0)$	$\theta''_0(A,0)$	$F''_1(A,0)$	$\theta''_1(A,0)$	$F''_2(A,0)$	$\theta''_2(A,0)$
1.40	0.10592761D 01	-0.39648696D 00	-0.42618D-01	-0.62770D-02	0.9949D-02	0.3674D-02
1.20	0.96158345D 00	-0.38632730D 00	-0.49941D-01	-0.62118D-02	0.1200D-01	0.3995D-02
1.00	0.85604510D 00	-0.37410582D 00	-0.59568D-01	-0.59194D-02	0.1477D-01	0.4362D-02
0.99	0.85052770D 00	-0.37342695D 00	-0.60127D-01	-0.58958D-02	0.1493D-01	0.4382D-02
0.98	0.84498525D 00	-0.37274072D 00	-0.60696D-01	-0.58712D-02	0.1510D-01	0.4402D-02
0.97	0.83941742D 00	-0.37204698D 00	-0.61273D-01	-0.58455D-02	0.1527D-01	0.4422D-02
0.95	0.82820426D 00	-0.37063641D 00	-0.62455D-01	-0.57906D-02	0.1561D-01	0.4462D-02
0.93	0.81688546D 00	-0.36919400D 00	-0.63675D-01	-0.57308D-02	0.1597D-01	0.4503D-02
0.90	0.79970278D 00	-0.36696784D 00	-0.65579D-01	-0.56312D-02	0.1653D-01	0.4566D-02
0.85	0.77049361D 00	-0.36307873D 00	-0.68969D-01	-0.54355D-02	0.1753D-01	0.4673D-02
0.80	0.74052387D 00	-0.35894411D 00	-0.72657D-01	-0.51964D-02	0.1862D-01	0.4785D-02
0.75	0.70973371D 00	-0.35453459D 00	-0.76684D-01	-0.49049D-02	0.1983D-01	0.4901D-02
0.70	0.67805493D 00	-0.34981517D 00	-0.81098D-01	-0.45498D-02	0.2115D-01	0.5022D-02
2/3	0.65640334D 00	-0.34647631D 00	-0.84282D-01	-0.42709D-02	0.2211D-01	0.5105D-02
0.65	0.64540313D 00	-0.34474379D 00	-0.85955D-01	-0.41169D-02	0.2282D-01	0.5148D-02
0.60	0.61170534D 00	-0.33926915D 00	-0.91326D-01	-0.35873D-02	0.2425D-01	0.5280D-02
0.57	0.59093158D 00	-0.33576504D 00	-0.94831D-01	-0.32131D-02	0.2532D-01	0.5362D-02
0.55	0.57683676D 00	-0.33332783D 00	-0.97299D-01	-0.29362D-02	0.2607D-01	0.5418D-02
0.54	0.56971251D 00	-0.33207689D 00	-0.98575D-01	-0.27886D-02	0.2646D-01	0.5447D-02
0.52	0.56253554D 00	-0.33080342D 00	-0.99880D-01	-0.26345D-02	0.2686D-01	0.5476D-02
0.53	0.55530468D 00	-0.32950665D 00	-0.10122D 00	-0.24736D-02	0.2727D-01	0.5505D-02
0.51	0.54801871D 00	-0.32818578D 00	-0.10258D 00	-0.23054D-02	0.2769D-01	0.5535D-02
0.50	0.54067636D 00	-0.32683995D 00	-0.10398D 00	-0.21297D-02	0.2812D-01	0.5565D-02
0.40	0.46583008D 00	-0.31178105D 00	-0.12013D 00	0.15930D-03	0.3311D-01	0.5889D-02
0.30	0.37941598D 00	-0.29277041D 00	-0.14169D 00	0.40046D-02	0.3982D-01	0.6289D-02
2/7	0.36658772D 00	-0.28960330D 00	-0.14540D 00	0.47643D-02	0.4098D-01	0.6352D-02

(B) Pr = 100						
$A$	$F''_0(A,0)$	$\theta''_0(A,0)$	$F''_1(A,0)$	$\theta''_1(A,0)$	$F''_2(A,0)$	$\theta''_2(A,0)$
1.40	0.42244894D 00	-0.17994412D 01	-0.15257D-01	-0.61018D-01	0.5310D-02	0.2382D-01
1.20	0.37719855D 00	-0.17342794D 01	-0.16142D-01	-0.67955D-01	0.5616D-02	0.2662D-01
1.00	0.32979466D 00	-0.16598892D 01	-0.17230D-01	-0.77187D-01	0.5992D-02	0.3034D-01
0.99	0.32735919D 00	-0.16558719D 01	-0.17291D-01	-0.77731D-01	0.6013D-02	0.3056D-01
0.98	0.32491696D 00	-0.16518226D 01	-0.17353D-01	-0.78285D-01	0.6035D-02	0.3079D-01
0.97	0.32246787D 00	-0.16477407D 01	-0.17416D-01	-0.78848D-01	0.6056D-02	0.3101D-01
0.95	0.31754881D 00	-0.16394768D 01	-0.17544D-01	-0.80006D-01	0.6101D-02	0.3148D-01
0.93	0.31260130D 00	-0.16310752D 01	-0.17675D-01	-0.81205D-01	0.6146D-02	0.3197D-01
0.90	0.30512503D 00	-0.16182031D 01	-0.17879D-01	-0.83090D-01	0.6217D-02	0.3273D-01
0.85	0.29251116D 00	-0.15959821D 01	-0.18237D-01	-0.86483D-01	0.6341D-02	0.3410D-01
0.80	0.27969348D 00	-0.15727157D 01	-0.18621D-01	-0.90235D-01	0.6475D-02	0.3561D-01
0.75	0.26665631D 00	-0.15482798D 01	-0.19036D-01	-0.94414D-01	0.6619D-02	0.3730D-01
0.70	0.25338165D 00	-0.15225403D 01	-0.19485D-01	-0.99100D-01	0.6775D-02	0.3920D-01
2/3	0.24438977D 00	-0.15045736D 01	-0.19807D-01	-0.10256D 00	0.6886D-02	0.4059D-01
0.65	0.23984862D 00	-0.14953269D 01	-0.19975D-01	-0.10440D 00	0.6954D-02	0.4134D-01
0.60	0.22603269D 00	-0.14664344D 01	-0.20511D-01	-0.11046D 00	0.7131D-02	0.4379D-01
0.57	0.21759546D 00	-0.14481897D 01	-0.20859D-01	-0.11453D 00	0.7253D-02	0.4543D-01
0.55	0.21190476D 00	-0.14356088D 01	-0.21103D-01	-0.11745D 00	0.7338D-02	0.4661D-01
0.54	0.20903877D 00	-0.14291850D 01	-0.21229D-01	-0.11898D 00	0.7382D-02	0.4725D-01
0.53	0.20615861D 00	-0.14226685D 01	-0.21358D-01	-0.12057D 00	0.7427D-02	0.4787D-01
0.52	0.20326395D 00	-0.14160561D 01	-0.21489D-01	-0.12220D 00	0.7472D-02	0.4853D-01
0.51	0.20035444D 00	-0.14093447D 01	-0.21624D-01	-0.12389D 00	0.7519D-02	0.4922D-01
0.50	0.19742974D 00	-0.14025307D 01	-0.21762D-01	-0.12564D 00	0.7568D-02	0.4992D-01
0.40	0.16725548D 00	-0.13278401D 01	-0.23550D-01	-0.14722D 00	0.8122D-02	0.5865D-01
0.30	0.13500561D 00	-0.12370560D 01	-0.25491D-01	-0.18085D 00	0.8870D-02	0.7224D-01
2/7	0.13018428D 00	-0.12222552D 01	-0.25864D-01	-0.18730D 00	0.9000D-02	0.7484D-01



J. R. Lloyd  
Assoc. Professor,  
University of Notre Dame,  
Notre Dame, Ind.  
Assoc. Mem. ASME

W. R. Moran<sup>1</sup>  
Graduate Assistant,  
University of Notre Dame,  
Notre Dame, Ind.

# Natural Convection Adjacent to Horizontal Surface of Various Planforms

*Natural convection adjacent to horizontal surfaces of circular, square, rectangular, and right triangular planforms has been studied experimentally. Electrochemical techniques were employed involving a fluid with a Schmidt number of about 2200. The results encompass a wide range of Rayleigh numbers thus providing information on both the laminar and the turbulent regimes. The data for all planforms are reduced to a single correlation in the laminar and turbulent regimes using the characteristic length, as recommended by Goldstein, Sparrow, and Jones,  $L^* = A/p$ , where  $A$  is the surface area and  $p$  is the surface perimeter. The laminar data for all planforms are correlated by the expression*

$$Sh = 0.54 Ra^{1/4} (2.2 \times 10^4 \leq Ra \leq 8 \times 10^6)$$

*and the data for the turbulent regime are correlated by the expression*

$$Sh = 0.15 Ra^{1/3} (8 \times 10^6 \leq Ra \leq 1.6 \times 10^9)$$

*Transition is found to occur at about  $Ra = 8 \times 10^6$ . The present work thus significantly extends the Rayleigh number range of validity for the use of  $L^*$  through the  $1/4$  power laminar regime into the turbulent  $1/3$  power regime. It also demonstrates the validity of the use of  $L^*$  to correlate natural convection transfer coefficients for highly unsymmetrical planforms, which heretofore had not been demonstrated. Comparisons to analytical solutions and other experimental heat and mass transfer data are presented.*

## Introduction

This paper presents an experimental investigation of natural convection adjacent to horizontal surfaces of various planforms. The results encompass a wide range of Rayleigh numbers, including the laminar and turbulent flow regimes, for circular, square, rectangular, and right triangular planforms. An electrochemical technique was employed to obtain the natural convection mass transfer measurements. This technique has been used by many investigators in recent years to study mass transfer, as evidenced by the recently published review by Mizushima [1].<sup>2</sup> The electrolyte employed in the present investigation was an aqueous solution of cupric sulphate and sulphuric acid, wherein the  $Cu^{++}$  ions were the transferred ions and the sulphuric acid served as the supporting electrolyte. The boundary condition for these experiments was uniform concentration at the test surface, which is the counterpart of uniform surface temperature in the corresponding heat transfer problem. The Schmidt numbers were on the order of 2200 so that these results apply to the analogous high Prandtl number heat transfer problem. One of the advantages of using the present mass transfer technique over heat transfer experiments

for high Prandtl number fluids is the fact that the property variations for the mass transfer experiments are essentially zero, whereas the corresponding heat transfer experiments exhibit large variation in properties. The present results apply to either the heated upward facing heat transfer surface or the cooled downward facing heat transfer surface.

A review of the literature reveals both analytical and experimental investigations of horizontal surfaces of various planforms. Analyses of the natural convection [2, 3, 4, 5] generally employ a boundary layer model applied to the two-dimensional problem of long thin rectangles. Suriano and Yang [6] solved the problem numerically for small and moderate Grashof numbers. It should be noted that the analyses give a  $1/5$ -power dependence of the dimensionless transfer coefficients on the Rayleigh number for the laminar regime.

Experimentally, both heat and mass transfer investigations have been presented for horizontal surfaces e.g., [7-16]. The correlation between Nusselt number and Rayleigh number for the heat transfer problem which is the most widely accepted is that of Fishenden and Saunders [7]. Their experiments involved square planforms situated in air. The temperature differences involved were as high as 1000°F indicating extreme property variations and radiation corrections. Bosworth [8] provides very little information on his experiments, and Mikheyev [9] apparently used rectangular planforms, although this is not certain. Fujii and Imura [10] and Hassan and Mohamed [11] considered the horizontal upward facing surface as part of larger studies of heat transfer to inclined surfaces.

<sup>1</sup> Present address: Pratt and Whitney Aircraft, East Hartford, Conn.

<sup>2</sup> Numbers in brackets designate References at end of paper.

Contributed by the Heat Transfer Division and presented at the Winter Annual Meeting, New York, N. Y., November 17-22, 1974, of THE AMERICAN SOCIETY OF MECHANICAL ENGINEERS. Manuscript received by the Heat Transfer Division April 8, 1974. Paper No. 74-WA/HT-66.

Mass transfer natural convection experiments are provided by Fenech and Tobias [12], Wragg [13], Wragg and Loomba [14], Tobias and Boeffard [15], and Goldstein, Sparrow, and Jones [16]. References [12-15] used the same electrochemical technique employed herein. Fenech and Tobias [12] used electrodes embedded in the floor of the test cell. The electrodes had various widths and the length of each electrode stretched from one wall of the test cell to the other. Due to experimental difficulties only their wider test strips were used in their correlation and thus their results were only for the turbulent regime. Wragg [13] and Wragg and Loomba [14] used circular disks, but again embedded them flush in a surrounding collar. Tobias and Boeffard [15] studied both circular and rectangular horizontal electrodes surrounded by side walls. The side walls were both vertical and coplanar in nature. The object of this study was to determine the effect of the side walls and to determine the effect of electrode size on the mass transfer.

The work by Goldstein, Sparrow, and Jones [16] deserve special attention. They performed their experiments using naphthalene vapor sublimation. They investigated unshrouded circles, squares, and equilateral triangles, and proposed a characteristic length so that the results from these planforms could be correlated by a common expression. Heretofore this had not been possible. Unfortunately, their results did not span the full Rayleigh number range of the laminar flow regime, and did not contain any irregular or nonsymmetrical planforms.

The present results, to the best of the authors' knowledge, provide the only electrochemical mass transfer data for any free-standing, unshrouded planform. The results of the investigation are also the first for any mode of transfer involving the nonsymmetrical right triangle planforms. The Rayleigh numbers based on Goldstein, Sparrow, and Jones characteristic length range from  $2.6 \times 10^4$  to  $1.55 \times 10^9$ , thus providing laminar, transition, and turbulent mass transfer information. By analogy, the results also apply to the corresponding isothermal horizontal surface heat transfer problem.

### Data Analysis

In the present electrochemical mass transfer experiments, the total mass transfer rate of copper ions to the test surface was a result of three basic transfer mechanisms [21]: migration, convection, and diffusion

$$\dot{N} = \dot{N}_m + \dot{N}_c + \dot{N}_d \quad (1)$$

The three fluxes can be defined by the following relations which are all evaluated at the test surface

$$\dot{N}_m = U c \frac{\partial \phi}{\partial y} \quad (2)$$

$$\dot{N}_c = v c \quad (3)$$

$$\dot{N}_d = - D \frac{\partial c}{\partial y} \quad (4)$$

The relative importance of each mechanism is revealed by exam-

ining their magnitudes under limiting current conditions. As explained in reference [1], under certain operating conditions, termed limiting current conditions, the concentration of the transferred species is essentially zero at the test surface.

Considering first the migration term, it is seen that  $\dot{N}_m$  contains the transferred species concentration. Since this concentration is essentially zero at the surface, the entire term is, while in the presence of the supporting electrolyte where  $\partial \phi / \partial y$  is small, negligibly small.

Next, consider the convection and diffusion terms together. Modeling the electrolyte solution as a binary mixture of copper ions as one component and the rest as the other component, reference [30] shows that  $v = D / (1 - c/\rho) \partial(c/\rho) / \partial y$ . Realizing that the concentration of the transferred species is approximately zero, the following is obtained

$$\dot{N}_c + \dot{N}_d = - \left( \frac{c/\rho}{1 - c/\rho} + 1 \right) D \frac{\partial c}{\partial y} \cong - D \frac{\partial c}{\partial y} \quad (5)$$

Thus

$$\dot{N} \cong \dot{N}_d = - D \frac{\partial c}{\partial y} \quad (6)$$

The total rate of ion transfer is given in reference [21] as

$$\dot{N} = \frac{i}{nF} \quad (7)$$

It is thus clear that the surface mass transfer is diffusive in nature which establishes the analogy between the present mass transfer experiments and the corresponding heat transfer problem.

It is possible now to define the mass transfer coefficient  $k$  in the same manner as is done in the analogous heat transfer problem

$$k = \frac{i}{nF(c_\infty - c)} \cong \frac{i}{nF c_\infty} \quad (8)$$

The dimensionless mass transfer number (analogous to the Nusselt number for the corresponding heat transfer problem) is given by the Sherwood number

$$\text{Sh} = \frac{kL^*}{D} \quad (9)$$

Here  $D$  is the diffusion coefficient of the transferred species and  $L^*$  is the characteristic length. The characteristic length defined by Goldstein, Sparrow, and Jones [16] is

$$L^* = \frac{A}{P} \quad (10)$$

where  $A$  is the transfer area of the test surface and  $P$  is the perimeter. The Rayleigh number is

$$\text{Ra} = \left[ \frac{\xi g (\xi_\infty - \xi_w) L^{*3}}{\mu^2} \right] \text{Sc} \quad (11)$$

where  $\text{Sc}$  is the Schmidt number (analogous to the Prandtl num-

### Nomenclature

$A$  = surface area of transfer surface  
 $c$  = transferred species concentration  
 $D$  = diffusion coefficient of transferred species  
 $F$  = Faraday number  
 $g$  = gravitational acceleration  
 $i$  = current density  
 $k$  = mass transfer coefficient  
 $L^*$  = characteristic length  $L^* = A/P$   
 $n$  = valence of transferred species

$\dot{N}$  = rate of mass transfer  
 $p$  = perimeter of transfer surface  
 $\text{Pr}$  = Prandtl number  
 $\text{Ra}$  = Rayleigh number  
 $\text{Sc}$  = Schmidt number  
 $\text{Sh}$  = Sherwood number  
 $t$  = transference number  
 $U$  = ion mobility  
 $v$  = convection velocity normal to test surface  
 $y$  = distance normal to test surface

$\mu$  = viscosity  
 $\zeta$  = density  
 $\phi$  = electric field potential

### Subscripts

$c$  = due to convection  
 $d$  = due to diffusion  
 $m$  = due to migration  
 $w$  = surface conditions  
 $\infty$  = bulk conditions

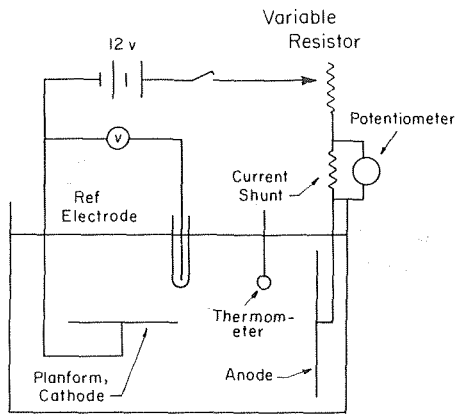


Fig. 1 Schematic of experimental apparatus

Table 1 Characteristic dimensions of various planforms

PLANFORM	CHARACTERISTIC DIMENSIONS, cm
CIRCLE (Diameter)	0.316
	0.597
	1.27
	5.08
	10.16
SQUARES (Length x Width)	0.635 x 0.635
	1.27 x 1.27
	12.7 x 12.7
RECTANGLES (Length x Width)	0.635 x 1.27
	2.54 x 1.27
	3.81 x 1.27
	6.35 x 1.27
	12.7 x 1.27
	12.7 x 2.54
RIGHT TRIANGLES (Base x Height x Hypotenuse)	1.91 x 2.54 x 3.18
	1.27 x 1.91 x 2.29
	7.62 x 10.17 x 12.7
	15.25 x 20.3 x 25.4

ber)  $\mu/\zeta D$ ;  $\mu$ ,  $\zeta$ , and  $D$  are viscosity, density, and diffusion coefficient, respectively, at the average concentrations; and  $\zeta_w$  and  $\zeta_w$  are the fluid densities in the bulk and at the test surface, respectively. The properties were evaluated using the data of references [22-28], as described in reference [17]. As noted previously, property variations were practically nonexistent being 3 percent maximum. This is where this electrochemical technique has its major advantage over high Prandtl number heat transfer experiments.

### Experimental Apparatus and Measurement Technique

A schematic of the experimental apparatus is presented in Fig. 1. A 30 gal polyethylene tank 61 cm x 45.6 cm x 45.6 cm (length x width x depth) served as the test chamber. The tank contained the electrolyte which was made up using reagent grade chemicals. The electrolyte solution was approximately 0.035 M  $\text{CuSO}_4$  as the transferred species and 1.5 M  $\text{H}_2\text{SO}_4$  as the supporting electrolyte.

The test surface was the cathode in the circuit. Table 1 provides a listing of the planforms tested and their characteristic di-

mensions. Each cathode was constructed of 0.635 cm thick copper. To the back side of each of the surfaces was attached a lead wire which connected to the main electrical circuit. The back and sides of the test pieces were carefully insulated with epoxy and Glyptal (an insulating paint). The test surface was held in position by a plexiglass holder. The lead wire was connected to a 12V automotive storage battery to provide the electric power. The potential of the cathode was measured relative to a reference electrode which consisted of a bare copper wire inserted into a glass tube. The glass tube had a small hole in the bottom to provide electrical contact between the reference electrode and the electrolyte solution. The potential was controlled with a series of precision variable resistors. The current flowing in the circuit, which is directly proportional to the mass transfer rate, was obtained by measuring the potential drop across a calibrated precision resistor, called a current shunt, with a Leeds and Northrup 8686 potentiometer. The anode was a large thin copper sheet 50 cm x 50 cm (length by width). It was purposely larger than the cathode so that the reaction would be totally controlled by conditions at the cathode.

To obtain a datum point the following procedure was followed. Prior to each test run the anode and cathode were carefully resurfaced and cleaned, essentially as described in reference [17], and then placed in the tank. The cathode was carefully leveled to provide a horizontal surface located about 15 cm off the bottom of the tank, and time was allowed for the system to come to complete equilibrium. Limiting currents, where the concentration of the transferred species is zero at the test surface [21], were determined in each run by noting the characteristic plateau in the current-potential curves in the voltage range between 0.40V and 0.50V as will be discussed further in a later section. The copper ion and sulphuric acid concentrations of the bulk solution were determined for each run by standard spectrometric and titration methods [18, 19]. Vertical bulk concentration gradients at the time of data acquisition were determined for each run to insure that all data would not be influenced by stratification. Finally, it should be noted that the length of each run was critical since it was necessary to operate long enough to insure steady operating conditions, but not so long as to generate any recirculation effects on the transfer at the surface. All data were taken so as to insure steady operating conditions without recirculation effects.

### Results and Discussion

Before discussing the results of the experiments, a short discussion of the characteristic length is presented. The characteristic length employed in this investigation is that proposed by Goldstein, Sparrow, and Jones [16]. It was their "expectation" that this particular characteristic length would enable all horizontal planforms to exhibit a common correlation. Unfortunately, they investigated a more limited number of planforms and smaller Rayleigh numbers than in the present investigation. The present investigation should serve to prove or disprove their expectations.

As discussed earlier, limiting current-voltage curves as shown in Fig. 2 were generated in each run. Plotted in the figure on rectangular coordinates is the current density at the cathode versus the cathode voltage. As indicated in the figure, the plateau, signifying limiting current conditions, was reached in several steps. At each step, the system was allowed to reach steady conditions. All data were taken at cathode voltages of 0.40V to 0.50V to insure that limiting conditions had been reached. Current shunt signals for the laminar flow regime were very steady and could be read directly. In the turbulent regime the shunt signals fluctuated making it necessary to time average the data over a period of approximately two minutes, which was determined in the present investigation to be sufficient to obtain accurate time averages without encountering stratification effects. This time averaging was accomplished by recording the data digitally on the tape unit of a Hewlett Packard 2019A Data Acquisition System and then statistically averaging them on a computer.

Fig. 3 presents the data for the laminar flow regime. The Sher-

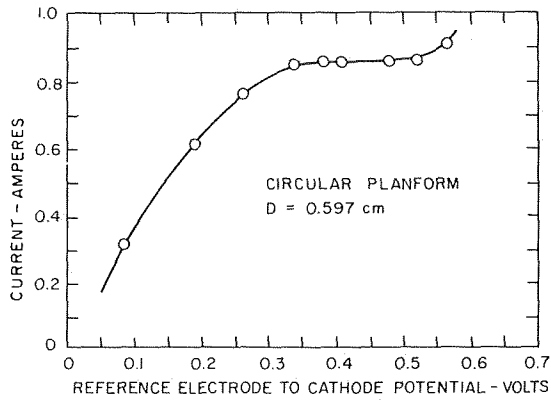


Fig. 2 Limiting current plateau

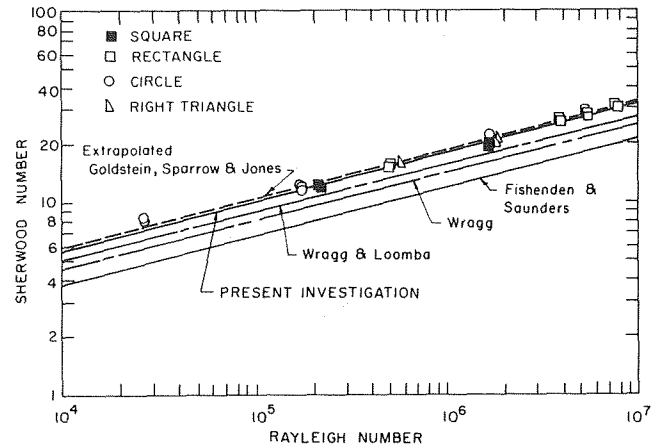


Fig. 3 Laminar mass transfer results

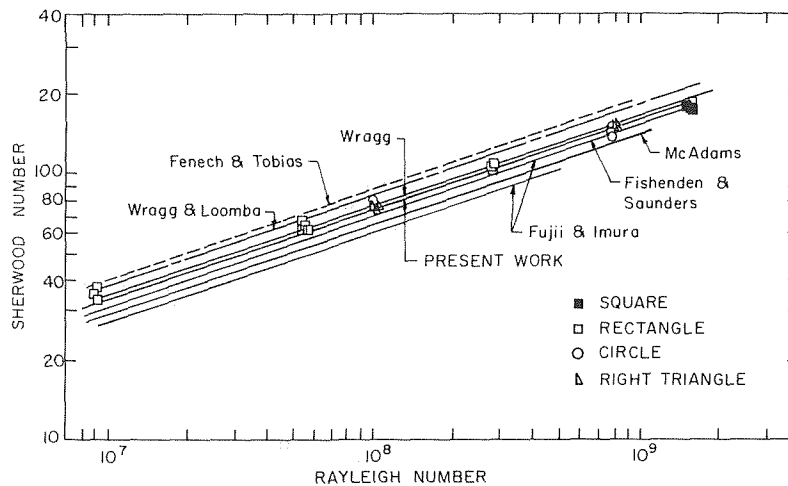


Fig. 4 Turbulent mass transfer results

wood number is plotted as a function of the Rayleigh number on logarithmic coordinates. The shape of the symbols reflect the planforms of the various surfaces as indicated in the upper left corner of the figure. It is immediately obvious that within the scatter of the data, approximately  $\pm 5$  percent, the data from all planforms are correlated through the use of  $L^*$ , including the nonsymmetric right triangle planform. This confirms the expectations of Goldstein, Sparrow, and Jones. A least squares fit through the data yields the relation

$$Sh = 0.50 Ra^{0.255}$$

Forcing a slope of  $\frac{1}{4}$ , as has been reported in the literature for the heat transfer experiments, one finds the relation

$$Sh = 0.54 Ra^{1/4}$$

for the data in the Rayleigh number range from  $2.6 \times 10^4$  to  $8 \times 10^6$ .

Since  $L^*$  appears to correlate all the horizontal planforms, other published experimental results can be appropriately modified and compared to the present work. The data of Wragg and Loomba [14] and Wragg [13] can be compared directly to the present work since the same electrochemical technique was employed. Wragg and Loomba, it should be noted, is a revision of Wragg. They concerned themselves with circular surfaces which had a flush fitting collar surrounding their free-standing test surface. The revised data of Wragg and Loomba fall 10 percent below the present results. This difference could be a result, at least in part, from the presence of the surrounding collar.

The prediction of Goldstein, Sparrow, and Jones also involved mass transfer but at a much lower Schmidt number, approximately 2.5. Although their data only extended up to a Rayleigh number of  $7 \times 10^3$ , it is interesting that extension of their prediction into the Rayleigh number range covered in the present investigation falls very close to the present result. This would indicate that the Rayleigh number may be sufficient to account for Schmidt or Prandtl number variations.

Fig. 4 presents data for the turbulent flow regime. The Sherwood number is plotted as a function of the Rayleigh number on logarithmic coordinates. As in Fig. 3 the symbols reflect the planforms of the various surfaces. There does not appear to be any difference in the data for the various planforms. A least squares fit through the data for Rayleigh numbers greater than  $8 \times 10^6$  provide the following correlation

$$Sh = 0.169 Ra^{0.327}$$

If a  $\frac{1}{3}$  slope is enforced the best fit expression becomes

$$Sh = 0.15 Ra^{1/3}$$

With the exception of two data points, the data scatter  $\pm 7$  percent about this correlation.

The results of other investigators are also presented. The heat transfer correlations of Fishinden and Saunders [7] and McAdams [29] are seen to fall 4 to 12 percent lower than the present investigation. The data of Fujii and Imura [10] using water as the working fluid are perhaps the most interesting heat transfer data for comparison to the present work. They present two Nusselt num-

ber expressions, for the turbulent regime. Both have the form  $Nu = C Ra^{1/3}$ , but the value for  $C$  is 0.13 for  $Ra$  less than  $5 \times 10^8$  and 0.16 for  $Ra$  greater than  $2 \times 10^8$ . The difference, they state, is due to edge effects on the surface. These experimental results using water as the surrounding medium have, within experimental scatter, essentially the same correlation as the present work when their edge effects are minimal. This would indicate again that the use of the Rayleigh number may be sufficient to account for Prandtl or Schmidt number effects.

The data of Fenech and Tobias [12], Wragg [13], and Wragg and Loomba [14] employed the same electrochemical techniques but with the previously discussed differences in the experimental setup. The data of Fenech and Tobias fall about 12 percent higher than the present data. This difference is in all probability due to the differences in the experimental setup as have been discussed earlier. The data of Wragg and Loomba are about 8 percent higher than the present work. It is important to note, however, that the correlation of Wragg and Loomba is a revised version of Wragg, due to the use of different physical properties, and that the correlation of Wragg, which uses almost the same values for properties as the present work, falls within the scatter of the present data. In this regime, the effect of the surrounding collar appears to be negligible, based on comparisons of Wragg's data to the present investigation.

Finally, the work of Tobias and Boeffard [15] deserves special mention. They considered the effect of both vertical and coplanar surrounding walls on the mass transfer to horizontal surfaces using the same experimental techniques. They found that the surrounding walls had no effect on the mass transfer correlation if the surfaces were large enough. For smaller electrodes their correlation underpredicts and it must be multiplied by a factor  $d_n$ , a number which is larger than one. When one considers their data in the light of the present investigation it appears that their size effect is related to the transition noted in the present work from the turbulent range to the laminar range. Indeed, if one takes Schmidt and Grashof numbers characteristic of the present data and use their expression to predict the Sherwood number for the turbulent regime, it is found that their prediction falls within the scatter of the present turbulent data. If one considers the small electrodes found in the laminar regime of the present work and applies the  $d_n$  correction discussed in their work, their Sherwood number prediction falls approximately within the scatter of the present work. Thus, it appears to be possible that their size effects, even with the surrounding walls, may be related to the difference between the laminar and turbulent flow regimes discussed in the present work.

### Concluding Remarks

The present data are the first electrochemical mass transfer investigations of truly free-standing unshrouded horizontal surfaces. They also present the only data available for any mode of transfer involving right triangular planforms. The characteristic length as proposed by Goldstein, Sparrow, and Jones appears to bring all the data into a common correlation, even the nonsymmetrical surfaces such as the right triangles, for all Rayleigh numbers investigated. Special note should be made that the experimentally determined laminar correlation involves the  $1/4$  power of the Rayleigh number whereas the laminar boundary layer analyses indicate a  $1/2$  power dependence. This is probably the result of using a boundary layer approach in the analyses.

It is highly encouraging to see data from circular, square, rectangular, and right triangular planforms exhibit a common correlation through the use of the characteristic length proposed by Goldstein, Sparrow, and Jones. There are indications that the use of the Rayleigh number in the mass or heat transfer relations is sufficient to account for Schmidt or Prandtl number variations. These observations, based on the experimental data, will enable calculation of transfer rates involving any shaped upward facing horizontal surface provided the transfer surface area and perimeter are known.

### Acknowledgment

The authors gratefully acknowledge the support for this work provided by the National Science Foundation under Grant Number GK 32658.

### References

- Mizushima, T., "The Electrochemical Method in Transport Phenomena," *Advances in Heat Transfer*, Vol. 7, J. P. Hartnett and T. F. Irvine, eds., Academic Press, New York, 1971.
- Levy, S., "Integral Methods in Natural Convection Flow," *Journal of Applied Mechanics*, Vol. 77, No. 5, May 1955, pp. 515-525.
- Stewartson, K., "On the Free Convection From a Horizontal Plate," *Z. Angew. Math. Phys.*, Vol. 9a, 1958, p. 276.
- Gill, W. N., Zeh, D. W., and del Casal, E., "Free Convection on a Horizontal Plate," *Z. Angew. Math. Phys.*, Vol. 15, 1965, p. 539.
- Roten, Z., and Classen, L., "Natural Convection Above Unconfined Horizontal Surfaces," *Journal of Fluid Mechanics*, Vol. 39, Part I, Oct. 23, 1969, pp. 173-192.
- Suriano, F. J., and Yang, K. T., "Laminar Free Convection About Vertical and Horizontal Plates at Small and Moderate Grashof Numbers," *International Journal of Heat and Mass Transfer*, Vol. 11, No. 3, Mar. 1968, pp. 473-490.
- Fishenden, M., and Saunders, O. A., *An Introduction to Heat Transfer*, Oxford University Press, London, 1950.
- Bosworth, R. L. C., *Heat Transfer Phenomena*, Wiley, New York, 1952.
- Mikheyev, M., *Fundamentals of Heat Transfer*, Peace Publishers, Moscow, 1968.
- Fuji, T., and Imura, H., "Natural Convection Heat Transfer From a Plate With Arbitrary Inclination," *International Journal of Heat and Mass Transfer*, Vol. 15, No. 4, Apr. 1972, pp. 755-767.
- Hassan, K., and Mohamed, S. A., "Natural Convection From Isothermal Flat Surfaces," *International Journal of Heat and Mass Transfer*, Vol. 13, No. 12, Dec. 1970, pp. 1866-1873.
- Fenech, E. S., and Tobias, C. W., "Mass Transfer by Free Convection at Horizontal Electrodes," *Electrochem. Acta*, Vol. 2, No. 3, Mar. 1960, pp. 311-321.
- Wragg, A. A., "Free Convection Mass Transfer at Horizontal Electrodes," *Electrochem. Acta*, Vol. 13, No. 12, Dec. 1968, pp. 2159-2165.
- Wragg, A. A., and Loomba, R. P., "Free Convection Flow Patterns at Horizontal Surfaces With Ionic Mass Transfer," *International Journal of Heat and Mass Transfer*, Vol. 13, No. 2, Feb. 1970, pp. 439-442.
- Tobias, C. W., and Boeffard, A. L., "Ionic Mass Transport by Free Convection at Horizontal Electrodes," 17th General Meeting of CITCE, Sept. 5-9, 1966, Tokyo, Japan, pp. 23-24.
- Goldstein, R. J., Sparrow, E. M., and Jones, D. C., "Natural Convection Mass Transfer Adjacent to Horizontal Plates," *International Journal of Heat and Mass Transfer*, Vol. 16, No. 5, May 1973, pp. 1025-1034.
- Lloyd, J. R., Sparrow, E. M., and Eckert, E. R. G., "Local Natural Convection Mass Transfer Measurements," *J. Electrochem. Soc.*, Vol. 119, No. 6, June, 1972, pp. 702-707.
- Sandell, E. B., *Colorimetric Determination of Traces of Metal*, Interscience Publishers, New York, 1950.
- Kolthoff, I. M., and Sandell, E. B., *Textbook of Quantitative Inorganic Analysis*, Macmillan, New York, 1965.
- Lloyd, J. R., Sparrow, E. M., and Eckert, E. R. G., "Laminar Transition and Turbulent Natural Convection Adjacent to Inclined and Vertical Surfaces," *International Journal of Heat and Mass Transfer*, Vol. 15, No. 3, Mar. 1972, pp. 457-473.
- Wilke, C. R., Eisenberg, M., and Tobias, C. W., "Correlation of Limiting Currents Under Free Convection Conditions," *J. Electrochem. Soc.*, Vol. 100, No. 11, Nov. 1953, pp. 513-523.
- Eisenberg, M., Tobias, C. W., and Wilke, C. R., "Selected Physical Properties of Ternary Electrolytes Employed in Ionic Mass Transfer Studies," *J. Electrochem. Soc.*, Vol. 103, No. 7, July 1956, pp. 413-416.
- Vinal, G. W., and Craig, D. N., *J. Res. Nat. Bur. Std.*, Vol. 10, 1933, p. 781.
- Cole, A. F. W., and Gordon, A. R., "The Diffusion of Copper Sulphate in Aqueous Solutions of Sulphuric Acid," *J. Phys. Chem.*, Vol. 40, No. 9, Sept. 1935, pp. 773-775.
- James, W. A., Hollingshead, E. A., and Gordon, A. R., "The Differential Diffusion Constants of Hydrochloric and Sulphuric Acids," *J. Chem. Phys.*, Vol. 7, No. 2, Feb. 1939, pp. 89-92.
- Hollingshead, E. A., and Gordon, A. R., "The Variation of the Differential Diffusion Constant of Sulphuric Acid With Temperature," *J. Chem. Phys.*, Vol. 8, No. 5, May, 1940, pp. 423-425.
- Landolt-Bornstein, "Physikalisch-Chemische Tabellen," 5. Auflage, Vol. 1, 1936, pp. 248-397.
- Dorsey, E. N., *Properties of Ordinary Water Substance in All Its Phases: Water Vapor, Water, and All the Ices*, Hafner Publishing Co., 1968.
- McAdams, W. H., *Heat Transmission*, McGraw-Hill, New York, 1954.
- Eckert, E. R. G., and Drake, Jr., R. M., *Heat and Mass Transfer*, McGraw-Hill, New York, 1959.

R. G. Colwell

Assoc. Professor and Chairman,  
Department of Mechanical Engineering,  
California State University, Chico,  
Chico, Calif. Mem. ASME

J. R. Welty

Professor and Head,  
Department of Mechanical Engineering,  
Oregon State University,  
Corvallis, Oregon. Mem. ASME

# An Experimental Investigation of Natural Convection With a Low Prandtl Number Fluid in a Vertical Channel With Uniform Wall Heat Flux

*An experimental program was conducted to study the heat transfer characteristics of mercury in laminar natural convection flow within a vertical open-ended channel over a range of channel widths. Two sets of boundary conditions were investigated separately: (1) uniform heat flux at one wall with the other insulated, and (2) both walls symmetrically and uniformly heated.*

*A decrease in channel width caused a decrease in channel wall temperature in the developing portion of the flow. This unexpected phenomenon persisted until the channel height-to-width ratio,  $Ar$ , reached a value greater than 18. Hence, the buoyancy induced flow of a low Prandtl number fluid in a channel is more thermally efficient than a single heated plate.*

*Temperature data have been correlated into local Nusselt versus modified Grashof number plots, based on streamwise position, for several aspect ratios. The effect of aspect ratio on channel temperature is displayed on  $\bar{Nu}_L$  versus  $Ar$  curves for several  $Gr_1^*$ . The infinite spacing limit is compared to previous work with temperature profiles and local heat transfer results. Expressions for local and average heat transfer correlations are presented, with suggested limits on their application. The effect of flow in from the sides of the channel was investigated by affixing plastic side plates to the channel.*

## Introduction

Predictions of natural convection heat transfer to liquid metals had their origin with Saunder's [11]<sup>1</sup> experiments in mercury. His temperature measurements next to a nearly uniform heat flux surface and his approximate theoretical treatment agreed to a fair degree and are still quite well accepted.

A technical review of liquid metal heat transfer work by Kutateladze, et al. [8] describes natural convection experiments performed by Fedynskii in several liquid metals. Vertical surfaces and horizontal cylinders were investigated.

Julian [7] measured temperature at and near a vertical constant flux heated plate immersed in mercury.

Experiments performed in liquid metals flowing naturally in a narrow open-ended channel are almost nonexistent. This is surprising as analysis is very difficult. Heinisch [6] measured tem-

peratures within a vertical uniform heat flux channel of fixed geometry of  $Ar = 10$ . The heat transfer fluid was mercury, but his main concern was the transient response to a step change in wall heat flux. He presented steady-state data but did not report a correlation equation for the points. A least squares fit of these data, converted to the coordinates used here is

$$\bar{Nu}_D = 0.353 (Gr_D^* \frac{D}{L})^{0.184}$$

This equation provides the only known experimental result which can be compared to the present study.

The early channel literature is due to Elenbaas [5], who performed experiments with a variable geometry isothermal channel in air. He discussed the condition for maximum heat transfer from an isothermal surface with isothermal fins or plates (each pair forming a channel) attached to it. The heat transfer from the heated surface will increase with the addition of fins only until the increase in total surface area is overcome by the ever decreasing heat transfer from each fin.

Bodoia and Osterle [2] performed a numerical integration to solve the channel natural convection problem in air. Inspection of their results shows good agreement with Elenbaas' heat transfer prediction and fair agreement with the optimum width criterion.

<sup>1</sup> Numbers in brackets designate References at end of paper.

Contributed by the Heat Transfer Division of THE AMERICAN SOCIETY OF MECHANICAL ENGINEERS and presented at the ASME-AIChE Conference, Atlanta, Ga., August 5-8, 1973. Journal manuscript received by the Heat Transfer Division, January 25, 1974. Paper No. 73-HT-52.

Aung, et al. [1], using Nusselt and Grashof numbers based on the maximum wall temperature increase, obtained a similar kind of channel spacing optimum for constant heat flux plates. They used numerical methods and experiments to obtain heat transfer information in air.

Levy [9] has recently reported on channel width optimization using a different criterion than maximized heat transfer from the surface to which the channel walls are attached. He points out that one may wish to know the spacing of a pair of isothermal plates for which the heat transfer begins to decrease. This optimum condition is met when the boundary layers from each plate meet at the top of the channel. A fundamentally unique optimum spacing condition is found in low, Pr fluids. This will be discussed in this paper.

The only analytical prediction of natural convection heat transfer to a low Pr fluid in a channel was presented by Quintiere and Mueller [10]. Their approximate solution agrees well with previous investigators' results for Prandtl numbers on the order of one, but the discrepancy between existing data from this work and their solution is striking. This will be discussed in the results section.

None of the literature reviewed contains complete, workable relationships for the laminar, natural convection heat transfer in a liquid metal within a vertical channel, taking account of channel width. There is no indication of the anomalous increase in streamwise Nusselt number as the channel is made narrower; this apparently is a unique feature of liquid metal flow in which conduction effects are much greater than viscous effects. Both of these areas will be discussed in this paper.

### Experimental Equipment

The heart of the experimental apparatus used for this investigation was a 12 in. × 12 in. × 16 in. deep stainless steel vessel for mercury containment. An isothermal water bath surrounded the mercury vessel for the purpose of maintaining the mercury pool at a constant temperature. The water temperature was held constant with a proportional controller, which used a 1 kW heater. Water circulation was accomplished by two stirrers and the controller pump. Fig. 1 depicts the mercury bath and related equipment. Energy was removed from the bath by tap water flow through two immersed coils of 3/8 in. copper tubing. The temperature variation of the mercury bath far below the channel during a run was typically 0.05 deg F.

A significant vertical temperature gradient at a  $y$  position far from the heated surface would indicate that the mercury containment vessel was too small. With one surface heated and the channel made as wide as possible (2.5 in.) the temperature stratification 2 in. away from the surface was measured. The total temperature range from entrance to exit of the channel was less than 5 percent of the total temperature variation of the heated surface. This is not negligible but it is partly related to a small

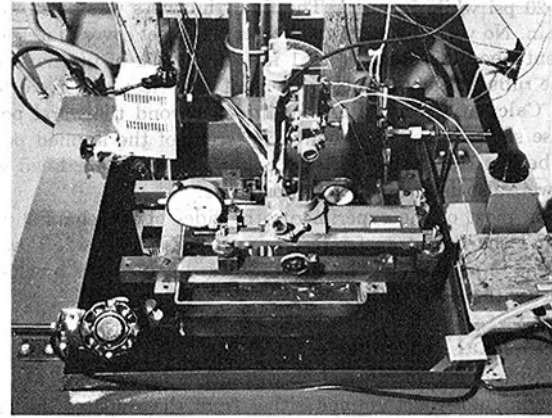


Fig. 1 Experimental apparatus

channel effect. The heat transfer surface area of the channel was about 4 percent of the wetted perimeter area of the containment vessel. The channel flow area was also 4-5 percent of the flow area for circulation outside the channel. It thus seemed reasonable to assume the mercury bath behaved as an infinite medium and that closed circuit effects were negligible.

The temperature sensor was an iron-constantan couple with 0.01 in. dia, type 304 stainless steel sheath, with the junction grounded to the sheath. An ice-bath reference was used. Each thermocouple used was calibrated against a platinum resistance thermometer.

The thermocouple was positioned manually with a vernier x-y traverse mechanism, which allowed  $\pm 0.001$  in. positioning accuracy.

One of the channel walls was stationary, while the other was movable using a dovetail slide driven by a manually operated rack and pinion. Positioning for narrow channels ( $Ar \leq 6$ ) was accurate to  $\pm 0.001$  in. using a dial indicator. Wide channel configurations were positioned by visual alignment of scribe marks on the dovetail slide.

The heated channel walls were constructed from a 5 in. square, patch heater. The heater element was 0.001 in. thick nichrome foil, chemically etched to yield quite uniform heat flux. The leading edge was trimmed to give a sharp boundary condition at the channel entrance.

The foil heater was sandwiched between 0.026 in. thick silicone rubber/glass cloth layers. The heater sandwich was completed by cementing 0.015 in. spring steel cover plates to both sides of the heater with silicone rubber. Fig. 2 is a schematic of the channel and its construction. A fixture was built that insured the silicone rubber to be uniformly thick and held in alignment during curing. A hydraulic press was used to compress the heater assembly to

### Nomenclature

$$Ar = \frac{L}{D}, \text{ aspect ratio}$$

$$D = \text{channel width}$$

$$Gr_x = \text{Grashof number, } \frac{g\beta x^3(T_s - T_\infty)}{\nu^2}$$

$$Gr_x^* = \text{modified Grashof number, } \frac{g\beta q'' x^4}{\nu^2 k}$$

$$h = \text{film conductance, Btu/hr ft}^2 \text{ }^\circ\text{F}$$

$$k = \text{fluid thermal conductivity, Btu/hr ft }^\circ\text{F}$$

$$L = \text{channel height}$$

$$Nu_x = \text{Nusselt number, } \frac{hx}{k} = \frac{q'' x}{k(T_s - T)}$$

$$\overline{Nu}_L = \frac{hL}{k}$$

$$\overline{Nu}_D = \frac{hD}{k}$$

$$Pr = \text{Prandtl number, } \frac{\nu}{\alpha}$$

$$q'' = \text{heat flux, Btu/hr ft}^2$$

$$T = \text{temperature, }^\circ\text{F}$$

$$u = x\text{-component velocity}$$

$$x = \text{streamwise coordinate}$$

$$y = \text{wall normal coordinate}$$

$$\eta = \text{similarity variable, } \frac{y}{x} \left( \frac{Gr_x^*}{5} \right)^{1/5},$$

dimensionless position

$$\theta = \text{similarity variable, } \frac{(T - T_\infty) Gr_x^*}{q'' x \left( \frac{Gr_x^*}{5} \right)^{1/5}},$$

dimensionless temperature

### Subscripts

$s$  = surface

$\infty$  = ambient

$f$  = film

$x$  = local condition measured from channel entrance

$D$  = based on channel width

$L$  = based on channel height

about 20 psi while it cured. The final thickness was 0.082 in.  $\pm$  0.0025 in. No voids between the heater and steel cover plates were apparent upon disassembly. A 1 in. thick block of urethane was silicone rubber cemented to the back of each heater to avoid heat losses. Calculations made for conditions beyond the worst possible case showed that less than 0.5 percent of the applied power could be lost from the back side of the channel wall. Lead wire losses were also determined to be negligible.

During most of the experiments the sides of the channel were open and the heat transfer results were subject to side flow effects. The importance of the side flow was investigated by closing the sides with plastic plates.

### Experimental Procedure

The Nusselt number based on distance from the entrance can be experimentally determined either from the slope of the temperature profile at the heated surface or from the calculated heat flux. A very slight error in the reading of the wall temperature can lead to a large error in the gradient determination. Both methods require  $(T_w - T_\infty)$  but the same error in measuring  $T_w$  does not lead to a large error in  $Nu_x$ . The heat flux determination error is mostly related to error in the calculation of the active plate area. Contact X-ray photographs allowed quite accurate determination of a proper area for average flux density evaluation. Hence, it was decided to use the measured heat flux calculation of  $Nu_x$ . Data acquisition was thereby made simpler since only surface temperatures were required.

Data were acquired only after very stable thermal conditions were observed in the apparatus; approximately 2 hr were required from the time the system was energized. Only about 5 min were required for new equilibrium to be reached upon change of aspect ratio or heat flux.

Data were collected for several values of  $x$  position, and at three power settings for each integer aspect ratio from 2 to 10 plus 13, 15, and 19. Two sets of boundary conditions were involved; thus, approximately 450 data points were obtained for the heat transfer correlations.

### Data Reduction

Local Nusselt modulus  $Nu_x$  was based on distance from the channel entrance  $x$ , and the temperature difference between the ambient entering fluid and the wall at  $x$ . This is defined in the nomenclature section. For this definition,  $k$  is the thermal conductivity of mercury at the wall temperature. Local modified Grashof modulus  $Gr_x^*$  is defined in the nomenclature section. All of the thermal properties are determined at a weighted "film" temperature calculated as

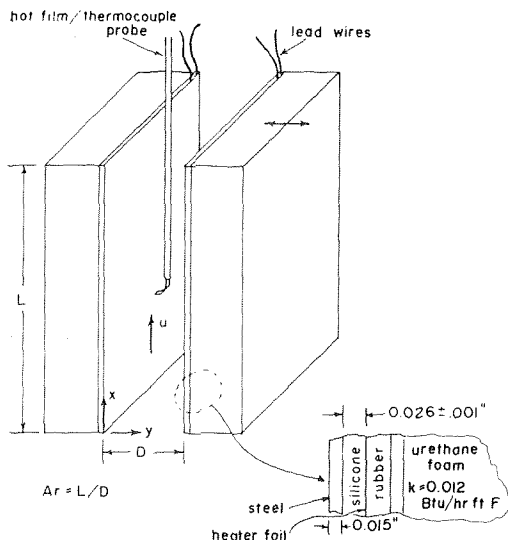


Fig. 2 Schematic diagram of vertical channel

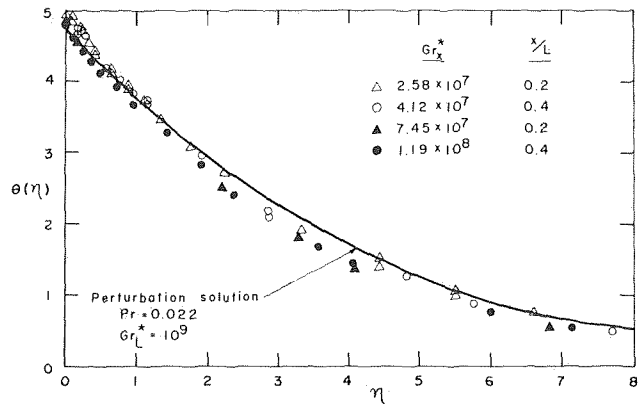


Fig. 3 Dimensionless temperature profiles, data and perturbation solution, single vertical plate

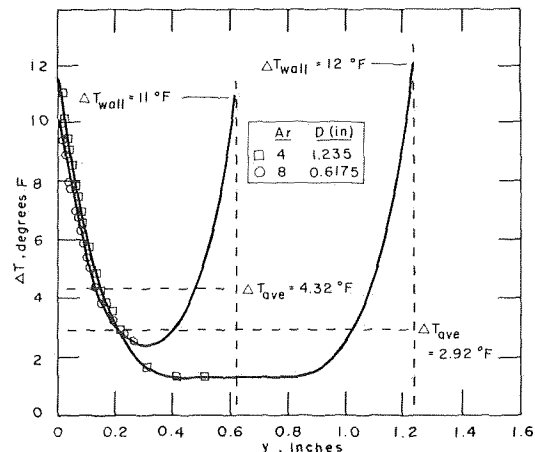


Fig. 4 Comparison of wall and mean temperature at different  $Ar$ , symmetrically heated channel

$$T_f = 0.7T_s + 0.3T_\infty,$$

as recommended by Sparrow and Gregg [13]. For both sets of boundary conditions,  $\dot{q}''$  is the heat flux from one wall.

The average correlations, based on channel height, were obtained by integration of the local correlations, using a space-averaged convection coefficient.

### Results and Discussion

Experimental temperature profiles for two wide channel cases have been nondimensionalized using the similarity variables employed by Sparrow and Gregg [12]. These are defined in the Nomenclature section. These profiles have been compared in Fig. 3 to the perturbation solution of Chang, et al. [3] which pertains to a uniform heat flux vertical surface in an infinite expanse of fluid. The two are remarkably similar and indicate the data are accurate.

The influence of channel width on wall temperature is clarified in Figs. 4 and 5. Fig. 4 illustrates that, at a particular position, the wall temperature decreases while the average fluid temperature increases as the flow passage is narrowed. For this graph  $\Delta T = T_w - T_\infty$ , and the same  $x$  position and heat flux applies to each curve. This effect appears to be small but it was easy to measure at the wall by placing a thermocouple there and sequentially changing channel spacing. This phenomenon was always observed until the channel spacing was decreased greatly. Although individual temperature measurements were accurate to within  $\pm 0.5^\circ\text{F}$ , differences in temperature could be obtained with an uncertainty of about  $\pm 0.1^\circ\text{F}$ , when laminar conditions prevailed.

Fig. 5 shows that the average velocity is higher in the narrower



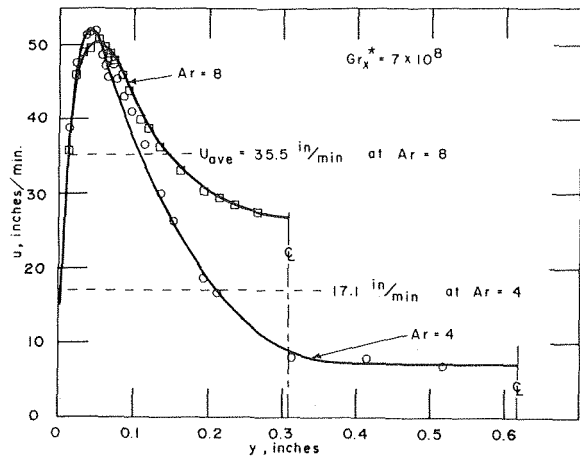


Fig. 5 Influence of aspect ratio on mean velocity

channel. The velocity data were obtained under the same channel conditions as the temperature data in Fig. 4 ( $Gr_x^* = 7 \times 10^8$ ,  $Ar = 4$  and 8). The mass flow rate appears to remain essentially constant, although this has not been concluded to be a general result. Velocity profiles were obtained in the same experiment by using a hot film anemometer. The velocity study and prediction of conditions for transition to turbulent flow will be discussed in subsequent papers.

The rationale for the observed channel behavior follows. The balance of forces in the natural convection boundary layer of a low Prandtl number fluid is unusual in that, since the diffusion of vorticity is far less effective than the diffusion of internal energy, the viscous forces become negligible a short distance out from the velocity peak. The peak in velocity was observed to be around 0.050 in. from the heated wall. So for wide channels buoyant force governs the velocity in most of the boundary layer. If the channel width is decreased, the energy flux from the wall is distributed over a narrower region which leads to an average fluid temperature rise. In the absence of viscous interplay, the increase in buoyant force (or fluid temperature) must cause the velocity to increase. An increase in velocity is related to an increase in the film coefficient of heat transfer and for constant heat flux boundaries, a decrease in wall temperature must result.

It is only when the channel is made narrow enough that influence of the wall friction is felt in a large portion of the stream that wall temperatures begin to rise when aspect ratio is increased.

Following this reasoning, it seems logical that a symmetrically heated channel (for the same  $q''$ ) can be narrower before the wall temperature reversal occurs than the channel with only one heat-

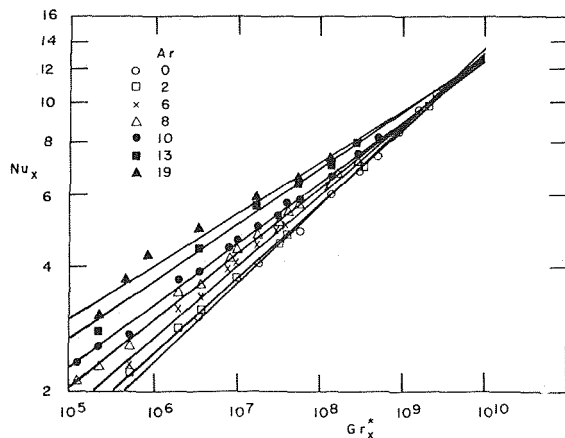


Fig. 6  $Nu_x$  versus  $Gr_x^*$  for various  $Ar$ , one wall insulated

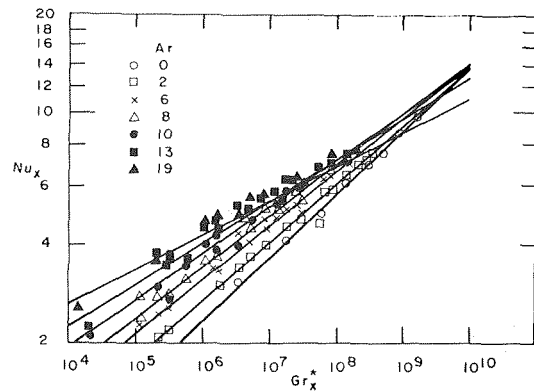


Fig. 7  $Nu_x$  versus  $Gr_x^*$  for various  $Ar$ , symmetrically heated channel

ed side. More buoyant force is available to counteract a slightly increased amount of viscous force. This effect has been demonstrated experimentally.

Correlations for local Nusselt number versus local modified Grashof number at several aspect ratios are presented in Figs. 6 and 7 to illustrate the change in heat transfer characteristics with geometry. The multiple regression coefficients for these correlations ranged from 0.920 in the worst case to 0.999. All of the  $R^2$  values for the one-side heated channel were above 0.990 and 12 of the 13 aspect ratios had local correlations above 0.995. The both-sides heated case was not so consistent. Only 3 of 12 cases had  $R^2 > 0.995$ , but 7 of the 12 had values above 0.985. The cases with increased data scatter were all at the high values of  $Ar$ .

In the first case (Fig. 6) the data indicate a common point of intersection for all aspect ratios, within experimental accuracy. This corresponds to an axial surface location where the temperature remains independent of channel width over a broad range of widths. Above this location the channel walls always increase in temperature with an increased aspect ratio, although it must be realized that a Grashof modulus of this magnitude would correspond to an axial position far up the channel, or perhaps beyond the exit.

A common point is not so apparent in the symmetrically heated case. To the contrary, the correlations above  $Ar = 10$  imply that a large portion of the channel increases in temperature as  $Ar$  is increased. The region of intersection at  $Ar = 10$  is at a slightly higher value of  $Gr_x^*$  than in the previous case, as one would expect. The data for large  $Ar$  are considerably more scattered for the channel with both walls heated. It is believed that this was caused by slight errors in balancing the power supplied to the two plates at the various power settings. Separate trends in the data were noted at the different heat flux levels and a statistical test for the hypothesis of equal slopes could be rejected at the 99 percent level. No such trends were seen in other cases so the heat transfer parameters are still regarded as proper dimensionless groups for establishing dynamic similarity.

All of the data for each set of boundary conditions can be generalized onto one correlation with the parameters  $Nu_x/Ar$  and  $Gr_x^*/Ar^5$ . This is shown in Fig. 8. The least squares regression lines for both cases were plotted on one graph to justify the presentation of one overall correlation for each region of  $Gr_x^*/Ar^5$ . The regression equations for each case, along with the resulting multiple regression coefficients, are given in the following. For the channel heated on one side only:

$$Nu_x/Ar = 0.237 (Gr_x^*/Ar^5)^{0.138} \quad (1)$$

$$10^{-2} \leq Gr_x^*/Ar^5 \leq 10^3$$

$$R^2 = 0.982$$

and

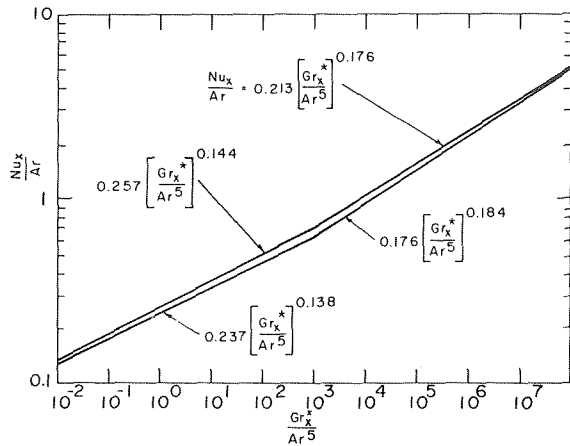


Fig. 8  $Nu_x/Ar$  versus  $Gr_x^*/Ar^5$ , open channel sides

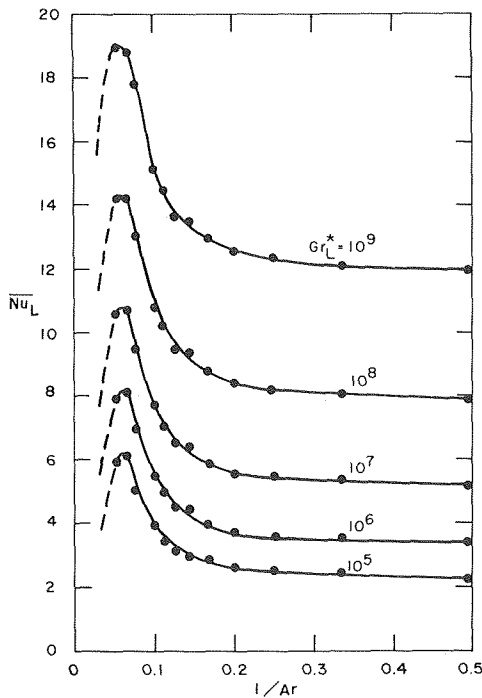


Fig. 9  $\bar{Nu}_L$  versus  $1/Ar$ , one wall insulated

$$Nu_x/Ar = 0.176 (Gr_x^*/Ar^5)^{0.184} \quad (2)$$

$$10^3 \leq Gr_x^*/Ar^5 \leq 10^9$$

$$R^2 = 0.997$$

For the symmetrically heated channel:

$$Nu_x/Ar = 0.257 (Gr_x^*/Ar^5)^{0.144} \quad (3)$$

$$10^{-2} \leq Gr_x^*/Ar^5 \leq 10^3$$

$$R^2 = 0.950$$

and

$$Nu_x/Ar = 0.213 (Gr_x^*/Ar^5)^{0.177} \quad (4)$$

$$10^3 \leq Gr_x^*/Ar^5 \leq 10^9$$

$$R^2 = 0.993$$

Overall correlations of these local data for each region take the form:

$$Nu_x/Ar = 0.247 (Gr_x^*/Ar^5)^{0.141} \quad (5)$$

$$10^{-2} \leq Gr_x^*/Ar^5 \leq 10^3$$

and

$$Nu_x/Ar = 0.194 (Gr_x^*/Ar^5)^{0.180} \quad (6)$$

$$10^3 \leq Gr_x^*/Ar^5 \leq 10^9$$

The upper limit on  $Gr_x^*/Ar^5$  is conservative; the results are likely accurate well into transition; however, experimental data were not obtained above  $Gr_x^*/Ar^5 = 10^9$ .

The slopes of the lines in the upper range on Fig. 8 are approximately 5 percent lower than the  $Ar = 0$ ,  $Nu_x$  versus  $Gr_x^*$  correlation obtained in this experiment. This is a consequence of the slight influence of the curvature of the data on the regression. A scatter diagram of the residual values from the least squares analysis showed a slight lack of fit, but was not considered serious enough to warrant the complexity of a higher-order model. Also the  $Ar = 0$  correlation from the present work had a slope of 0.180, while the evaluation of the limiting slope of  $\ln(Nu_x/Ar)/\ln(Gr_x^*/Ar^5)$  as  $Ar$  approaches zero is 0.2. The increase in accuracy with the use of an exponent on  $Ar$  which would result in the correct limiting slope was not considered worth the associated inconvenience to the user.

The integration of the overall correlations over the channel height gives the average channel expressions

$$\bar{Nu}_D = 0.438 (Gr_D^* \frac{D}{L})^{0.141} \quad (7)$$

$$10^{-2} \leq Gr_D^* \frac{D}{L} \leq 10^3$$

and

$$\bar{Nu}_D = 0.227 + 0.269 (Gr_D^* \frac{D}{L})^{0.180} \quad (8)$$

$$10^3 \leq Gr_D^* \frac{D}{L} \leq 10^9$$

As seen in Fig. 8 the experimental data for two quite different kinds of boundary conditions almost fall on the same line. The lines were shown to be statistically distinct and for accurate work the separate correlations are recommended, but if small error can be tolerated the overall correlation can be used in cases of unsymmetrical but uniform channel heating. The film conductance can be evaluated for each wall, separately.

Eventually, as  $Ar$  is increased, viscous forces must play a significant role in the overall channel momentum balance. When this occurs, the average velocity in the channel must decrease with further decrease in width. The experiments indicate that this turnaround in behavior is encountered very suddenly as  $Ar$  is increased. A small decrease in width, beyond the condition of maximum average velocity, decreases the average drastically and a corresponding large surface temperature increase is inevitable.

Figs. 9 and 10 portray this phenomenon for each channel boundary set studied. In each case several curves of  $\bar{Nu}_L$  versus  $Ar$  at several  $Gr_L^*$  have been plotted from regression equations for  $\bar{Nu}_L$  versus  $Gr_L^*$  at the various  $Ar$ .

The peaks in  $\bar{Nu}_L$  shown in Fig. 9 correspond, for given heat flux, to the channel spacing at which the average wall temperature was minimized. This occurred at approximately  $Ar = 18$  ( $D \approx 0.275$  in.). This minimum was located distinctly and repeatedly in the case where only one wall was heated, but the channel width adjustment precluded making the channel sufficiently narrow to locate the peak when both walls were heated. The dashed lines beyond the data were sketched in to remind the reader that such a peak must exist and do not imply knowledge of their precise location. It is expected that once the channel is made narrow enough that viscous forces have a significant influence (say at the outer inflection points of the curves in Figs. 9 and 10) the flow velocity (temperature) will decrease its rate of increase with in-

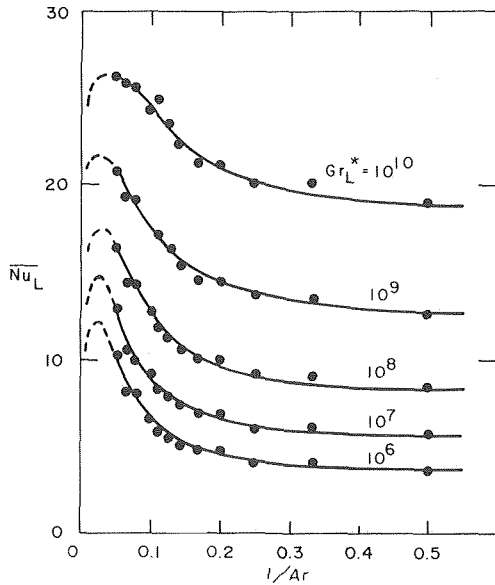


Fig. 10  $\overline{Nu}_L$  versus  $1/Ar$ , symmetrically heated channel

crease in  $Ar$ . When viscous forces become sufficiently strong the velocity must decrease with further decrease in width. The condition of zero channel width corresponds to infinite surface temperature or zero  $\overline{Nu}_L$ .

The peak shown on the  $Gr_{L,*} = 10^{10}$  curve of Fig. 10 is due to the hotter upper portion of the channel at high  $\dot{q}''$ . The lower portion of the channel continued to decrease in temperature with  $Ar$  increase. The symmetrically heated channel exhibited this tendency because of earlier flow development than the other case, and not because of a decrease in average velocity.

It was observed that for the natural convection situation studied, using a low Pr fluid, a narrow channel which has liquid metal flowing in it due to buoyant forces only is a more efficient heat transfer geometry than a wide channel. The channel height-to-width ratio reached a value of nearly 20 before this trend was seen to reverse. When the reversal did occur, a small decrease in width was seen likely to cause a catastrophic increase in surface temperature. Experimentally obtained plots of average Nusselt number versus dimensionless channel width for various exit Grashof numbers show this behavior.

Since the sides of the 5 in.  $\times$  5 in. channel were open, it was expected that the induced side leakage would tend to retard the flow at the channel entrance somewhat and lead to higher surface temperatures than would be observed for a truly two-dimensional channel flow. To approximate a two-dimensional flow, a plastic plate was fastened to each side of the channel and the range of channel conditions were repeated. The results of this experiment are shown as a comparison to the previous data correlations in Fig. 11. At the narrowest channel conditions the Nusselt number is about 20 percent larger than the open-sided channel result. As expected this diminishes toward zero as  $Gr_{x,*}/Ar^5$  gets large.

The tendency for the  $\overline{Nu}_L$  versus  $D/L$  curves to have a peak is observed in the case with side plates, but as expected, it occurs at narrower channels than were obtainable.

The local correlations for this phase of the study were

$$\overline{Nu}_x/Ar = 0.298 (Gr_{x,*}/Ar^5)^{0.141} \quad (9)$$

$$10^{-2} \leq Gr_{x,*}/Ar^5 \leq 10^3$$

and

$$\overline{Nu}_x/Ar = 0.268 (Gr_{x,*}/Ar^5)^{0.165} \quad (10)$$

$$10^3 \leq Gr_{x,*}/Ar^5 \leq 10^9$$

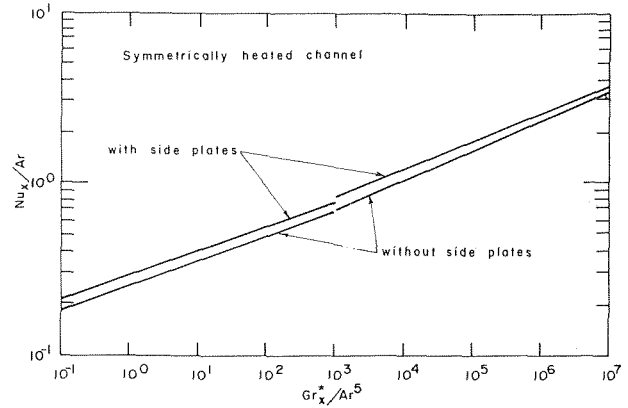


Fig. 11 Comparison of correlation for channel with open and closed sides

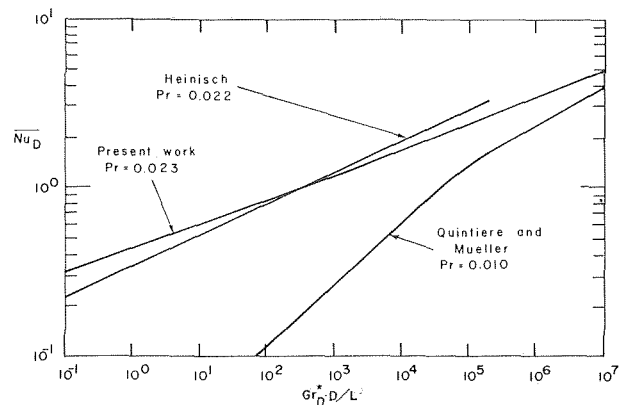


Fig. 12 Comparisons of heat transfer results with previous investigations

The average correlations obtained from this study were compared to the experimentally obtained uniform heat flux correlation of Heinisch [6] and the constant wall temperature analytical result for  $Pr = 0.01$  of Quintiere and Mueller [10]. The Grashof numbers used in each of these reports employed  $(T_s - T_\infty)$ . These were converted to the modified form,  $Gr_D^* D/L$ . The average Nusselt number was based on space-averaged  $h$  in each work. Hence, it seems valid to compare trends from these studies. The comparisons are shown in Fig. 12.

The two lines for mercury data do not disagree substantially over the range explored by Heinisch. However, there is a disturbing lack of agreement in the trends exhibited for the analytical and experimental lines at small values of  $Gr_D^* D/L$ . The analytical solution predicts the same type of behavior at low Pr as has been measured for air. The evidence presented here tends to refute this. The analysis indicates the wall heat flux does not increase (for a constant surface temperature condition) as the channel width decreases.

For additional details (experimental apparatus, velocity measuring techniques, data distributions, flow stability, etc.) the reader is referred to the thesis on which this paper is based [4].

#### Acknowledgment

The work described herein was supported by the Atomic Energy Commission, Contract No. AT (45-1)-2227.

#### References

- 1 Aung, W., Beitin, K. I., and Kessler, T. J., "Natural Convection Cooling of Electronic Cabinets Containing Arrays of Vertical Circuit Cards," ASME Paper No. 72-WA/HT-40.
- 2 Bodoia, J. R., and Osterle, J. F., "The Developments of Free Convection Between Heated Vertical Plates," JOURNAL OF HEAT TRANSFER, TRANS. ASME, Series C, Vol. 84, 1962, pp. 40-44.

- 3 Chang, K. S., Akins, R. G., Burris, L., and Bankoff, S. G., "Free Convection of a Low Prandtl Number Fluid in Contact With a Uniformly Heated Vertical Plate," Argonne National Laboratory Report ANL 6835, 1964.
- 4 Colwell, R. G., "Experimental Investigation of Natural Convection of Mercury in an Open, Uniformly Heated Vertical Channel," PhD thesis, Oregon State University, 1974.
- 5 Elenbaas, W., "Dissipation of Heat by Free Convection (Part II)," N. V. Philips Gloeilampenfabrieken, Eindhoven, Holland, Philips Research Report R 95, 1948, pp. 450-465.
- 6 Heinisch, R. P., "Transient Free-Convection Heat Transfer in Liquid Metals in Vertical Rectangular Channels," Argonne National Laboratory Report ANL 7452, 1968.
- 7 Julian, D. V., and Akins, R. G., "Experimental Investigation of Natural Convection Heat Transfer to Mercury," *Industrial and Engineering Chemistry-Fundamentals*, Vol. 8, No. 4, 1969, pp. 641-646.
- 8 Kutateladze, S. S., Borishanskii, V. M., Novikov, I. I., and Fedynskii, O. S., "Liquid Metal Heat Transfer Media," *Supplement of the Soviet Journal of Atomic Energy*, No. 2, 1958 (Translated by Consultants Bureau, Inc., N. Y., 1959).
- 9 Levy, E. K., "Optimum Plate Spacing for Laminar Natural Convection of Heat Transfer from Parallel Vertical Isothermal Flat Plates," *JOURNAL OF HEAT TRANSFER*, TRANS. ASME, Series C, Vol. 93, 1971, pp. 463-465.
- 10 Quintiere, J., and Mueller, W. K., "An Analysis of Laminar Free and Forced Convection Between Finite Vertical Parallel Plates," ASME Paper No. 72-WA/HT-3.
- 11 Saunders, O. A., "Natural Convection in Liquids," *Proc. Royal Soc. of London*, A172, 1939, pp. 55-71.
- 12 Sparrow, E. M., and Gregg, J. L., "Laminar Free Convection From a Vertical Plate With Uniform Surface Heat Flux," *TRANS. ASME*, Vol. 78, 1956, pp. 435-440.
- 13 Sparrow, E. M., and Gregg, J. L., "The Variable Fluid Property Problem in Free Convection," *TRANS. ASME*, Vol. 80, 1958, pp. 879-886.

L. E. Wiles

Research Assistant.

J. R. Welty

Professor and Head, Mem. ASME

Department of Mechanical Engineering  
Oregon State University  
Corvallis, Ore.

# An Experimental Investigation of Natural Convection With Vertical Cylinders in Mercury

*An experimental investigation of laminar natural convection heat transfer from a uniformly heated vertical cylinder immersed in an effectively infinite pool of mercury is described. A correlation was developed for the local Nusselt number as a function of local modified Grashof number for each cylinder. A single equation incorporating the diameter-to-length ratio was formulated that satisfied the data for all three cylinders. An expression derived by extrapolation of the results to zero curvature (the flat plate condition) was found to agree favorably with others' work, both analytical and experimental. The influence of curvature upon the heat transfer was found to be small but significant. It was established that the effective thermal resistance through the boundary layer is less for a cylinder of finite curvature than for a flat plate. Consequently, local heat transfer coefficients for cylinders are larger than those for flat plates operating under identical conditions.*

## Introduction

The phenomenon of laminar natural convection heat transfer from vertical surfaces to low Prandtl number fluids has received increased interest in recent years. Analytical and experimental investigations have been partially motivated by the necessity for using liquid metals as the coolant medium in the forthcoming Liquid Metal Fast Breeder Reactors.

The boundary condition considered here is that of uniform wall heat flux. This generally approximates the entry region of the reactor core and is also amenable to both analytical and experimental examination.

The geometry that has historically received the greatest consideration is that of the flat plate. Low Prandtl number solutions of the governing equations of continuity, momentum, and energy have been obtained numerically by Sparrow and Gregg [1]<sup>1</sup> using a similarity transformation and by Chang, et al. [2], using a first order perturbation technique. Experimental studies have been performed by Julian and Akins [3], White [4], and Colwell [5], using mercury as the heat transfer medium.

The geometry of primary importance to the design of core elements in the nuclear reactor is the circular cylinder. An analytical study of this geometry subject to a uniform wall heat flux boundary condition was performed by Nagendra, et al. [6] and Fugii and Uehara [7]. Prior to the present study, however, there has been no reported experimental work involving natural con-

vection from a vertical cylinder to a low Prandtl number fluid except for the case of small diameter wires [8].

A priori, one would expect that the heat transfer results for a flat plate will differ from those of a cylinder of some finite diameter due to the effects of curvature. In contrast to a flat plate, heat transferred away from the surface of a cylinder and conducted through the boundary layer is associated with an ever-increasing radial heat transfer area. Therefore, due to the inverse proportionality between heat transfer area and thermal resistance, the overall thermal resistance through the boundary layer should be less for a cylinder than for a flat plate, other conditions being the same. This implies that the local heat transfer coefficient for a cylinder should be larger than that for a flat plate under identical conditions and that it should continue to increase with decreasing diameter to the limiting condition posed by wires. The effect of diameter upon the heat transfer should be most significant when the cylinder radius and boundary layer thickness are of similar magnitude.

## Apparatus

Experiments were conducted using three heated circular cylinders with outside diameters of 0.590, 1.355, and 2.108 in. Each heated section was 3.85 in. high.

The heater design consisted of a chemically etched, printed-circuit-type electrical resistance element sandwiched between layers of silicone rubber reinforced with fiberglass.

Each heater was attached to a machined acrylic core. A 0.010-in. thick mild steel sleeve was then affixed to the heater surface and thus became the outer surface in contact with the mercury. The bottom edge of the cylinder assembly was positioned ten in. below the surface of a 12 in. × 12 in. × 16 in. deep mercury pool.

Temperatures were measured with a grounded, sheathed, iron-

<sup>1</sup> Numbers in brackets designate References at end of paper.

Contributed by the Heat Transfer Division for publication in the Journal of Heat Transfer. Manuscript received by the Heat Transfer Division, November 5, 1973. Paper No. 75-HT-C.

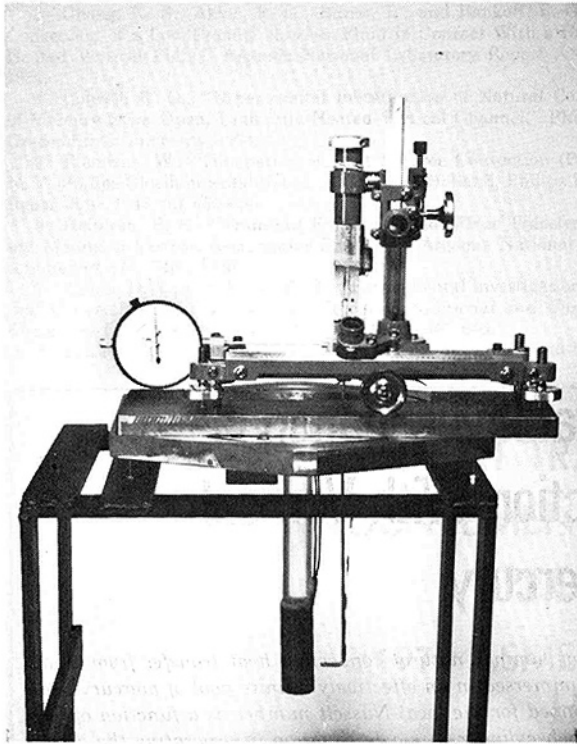


Fig. 1 Basic test apparatus

constantan thermocouple, enclosed in a 0.010 in. OD outer sheath. The thermocouple was attached to a vertical probe shaft which was suspended from a traverse mechanism. The traverse mechanism was mounted such that the probe shaft could be rotated about an axis coincident with the center line of the fixed cylinder. A dial indicator, mounted to the traverse mechanism, assisted in locating the radial position of the thermocouple to within  $\pm 0.00005$  in. A vernier on the vertical rack of the traverse mechanism provided resolution to  $\pm 0.0005$  in. for the determination of axial position. The system allowed the thermocouple to be

rotated through  $180^\circ$  about the surface of the cylinder. Within this circumferential range surface temperatures and radial temperature profiles could be measured at any axial position. The thermocouple probe, cylinder, and traverse mechanism are shown in Fig. 1.

Ambient temperature in the mercury was maintained constant by an isothermal water bath outside the stainless steel tank containing the mercury. The water bath was insulated with vermiculite packed loosely within a rectangular enclosure surrounding the entire apparatus.

Ambient temperature was measured at a position 2 in. radially outward from the heated surface and 2 in. below the leading edge of the cylinder. It was assumed that the mercury tank was large enough that it could be considered an essentially infinite medium. This assumption was validated by the fact that ambient temperature stratification did not occur over the range of axial positions investigated.

### Procedure

Simultaneous determination of surface heat flux,  $q$ , axial position,  $x$ , and the temperature difference between the heated surface and the ambient fluid,  $T_s - T_\infty$  enabled the heat transfer results to be correlated in terms of local Nusselt number and local modified Grashof number. Maximum values of  $T_s - T_\infty$  were about  $15^\circ\text{F}$ . Surface temperatures were recorded with the tip of the thermocouple butted against the heated surface. The midpoint of the thermocouple junction was less than 0.002 in. from the interface.

Temperature profiles were obtained from thermocouple readings taken at the surface and at radial positions of 0.01, 0.02, 0.03, 0.04, 0.05, 0.06, 0.08, 0.10, 0.15, and 0.30 in. from the surface. The similarity parameters of Sparrow and Gregg [1] were used to represent temperature versus radial position in nondimensional fashion as  $\theta(\eta)$ .

Additional details describing the apparatus, instrumentation, and experimental procedure are available in [9].

### Results and Discussion

Prior to the experimental investigation it was anticipated that as the curvature of a heated vertical surface was increased from zero, the flat plate condition, the local Nusselt number would also increase for any prescribed local modified Grashof number. The results show this to be correct within a  $D/L$  range of 0.15 to 0.55

### Nomenclature

cylinder 1 = refers to cylinder of diameter 0.590 in.

cylinder 2 = refers to cylinder of diameter 1.355 in.

cylinder 3 = refers to cylinder of diameter 2.108 in.

$C_p$  = specific heat at constant pressure

$D$  = diameter of cylinder

$g$  = acceleration of gravity

$Gr_x^*$  = local modified Grashof number;  $= \frac{\beta g q x^4}{\nu^2 k}$ ; evaluated at  $T_r$

$k$  = thermal conductivity

$L$  = length of heated surface

$Nu_x$  = local Nusselt number;  $= \frac{qx}{k(T_s - T_\infty)}$ ; evaluated at  $T_s$

$Pr$  = Prandtl number;  $= \frac{\mu C_p}{k}$

$q$  = surface heat flux;  $= \frac{\text{current} \cdot \text{volts}}{\text{heated area}}$

$r$  = radial distance from heated surface

$R$  = radius of cylinder

$Ra_D$  = Rayleigh number;  $=$

$$\frac{\beta g D^3 (T_s - T_\infty)}{\nu^2}$$

$T$  = temperature

$T_r$  = reference temperature;  $= 0.7T_s + 0.3T_\infty$

$\overline{T_s - T_\infty}$  = average of  $T_s - T_\infty$  over length  $L$

$x$  = vertical distance from leading edge of heated surface

$\alpha$  = thermal diffusivity

$\beta$  = coefficient of thermal expansion

$\eta$  = nondimensional coordinate normal to heated surface;

$= \frac{r}{x} (Gr_x^*/5)^{0.20}$ ; evaluated at  $T_r$

$\theta$  = nondimensional temperature;

$= \frac{k}{qx} (T - T_\infty) (Gr_x^*/5)^{0.20}$ ; evaluated at  $T_r$

$\mu$  = viscosity

$\nu$  = kinematic viscosity

### Subscripts

$\infty$  = value at distance far from surface

$D$  = parameter based on diameter

$s$  = parameter based on surface condition

$x$  = parameter evaluated at location  $x$  from leading edge of heated surface

for local modified Grashof numbers between  $10^5$  and  $10^{10}$ , and for a Prandtl number of 0.023 which was constant in this work.

It is of interest to note that for  $Gr_x^*$  as high as  $2 \times 10^{10}$  there was no evidence of the onset of transition from laminar to turbulent flow. For the flat plate in mercury, transition values of  $Gr_x^*$  are reported to be on the order of  $5 \times 10^9$  [5].

Approximately two hundred data points were obtained for each cylinder. Representative data are presented in Figs. 2, 3, and 4 as local Nusselt number versus local modified Grashof number with different symbols denoting data taken at various circumferential positions. Agreement among the data obtained at these positions verifies that the results are valid for the case of axisymmetric heating.

Regression equations of the data, obtained by computer analysis, are as follows

$$\text{Cyl. 1 } Nu_x = 0.216 (Gr_x^*)^{0.195} \quad (1)$$

$$\text{Cyl. 2 } Nu_x = 0.217 (Gr_x^*)^{0.189} \quad (2)$$

$$\text{Cyl. 3 } Nu_x = 0.224 (Gr_x^*)^{0.186} \quad (3)$$

By introducing the geometric parameter,  $D/L$ , the data were made to fit one generalized equation, specifically

$$Nu_x = 0.226 \left(\frac{D}{L}\right)^{0.032} (Gr_x^*)^{0.183} \left(\frac{D}{L}\right)^{-0.032} \quad (4)$$

This equation predicts the results of the individual regressions to within  $\pm 2$  percent; it is valid within the laminar flow regime for the range of  $D/L$  from 0.15 to 0.55. Extrapolation beyond these limits is not advised.

As indicated by the small powers on the  $D/L$  terms in the generalized equation, the effect of curvature upon the heat transfer is small for the range of  $D/L$  considered in this work. Therefore, it may be acceptable to use an expression for local Nusselt number which was obtained by combining the 592 total data points for the three cylinders and regressing the entire group. The result was

$$Nu_x = 0.216 (Gr_x^*)^{0.191} \quad (5)$$

For the Grashof number range of interest the deviations from the individual regressions are less than  $\pm 10$  percent.

Extrapolation of the data to determine the limit at zero curvature provides a basis for comparison of the present results for a cylinder with those of a flat plate. The extrapolation was accomplished by plotting local Nusselt number versus  $L/D$  for various prescribed local modified Grashof numbers. A smooth curve, made to fit through the three available points for each value of  $Gr_x^*$ , was extrapolated to the intercept ( $L/D = 0$ ). The intercepts were determined for each curve and these values of  $Nu_x$  plotted against  $Gr_x^*$ . The equation fitted to these values was

$$Nu_x = 0.232 (Gr_x^*)^{0.181} \quad (6)$$

Colwell [5] performed similar heat transfer experiments in mercury using a 5 in.  $\times$  5 in. vertical flat plate. His correlation for local Nusselt number was

$$Nu_x = 0.230 (Gr_x^*)^{0.180} \quad (7)$$

The agreement between equations (6) and (7) is remarkable, particularly so since equation (6) was obtained by the extrapolation procedure just described. Equation (6) also compares favorably to the experimental results of Julian and Akins [3],

$$Nu_x = 0.196 (Gr_x^*)^{0.188} \quad (8)$$

and to the analytical results of Chang, et al. [2],

$$Nu_x = 0.157 (Gr_x^*)^{0.20} \quad (9)$$

and Sparrow and Gregg [1],

$$Nu_x = 0.161 (Gr_x^*)^{0.20} \quad (10)$$

With the exception of Julian's work for a Prandtl number of

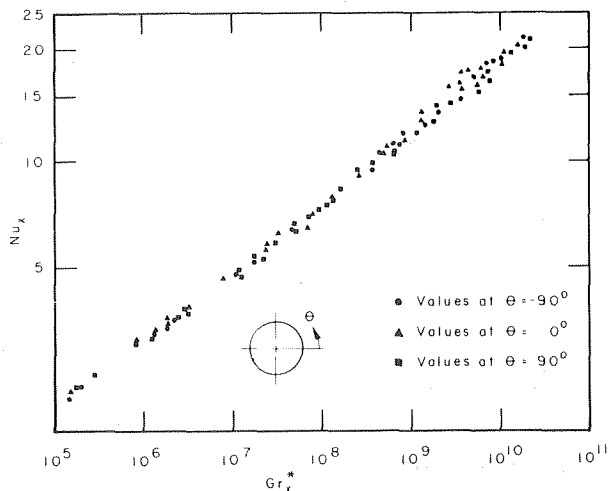


Fig. 2 Local heat transfer data for cylinder 1,  $D/L = 0.153$

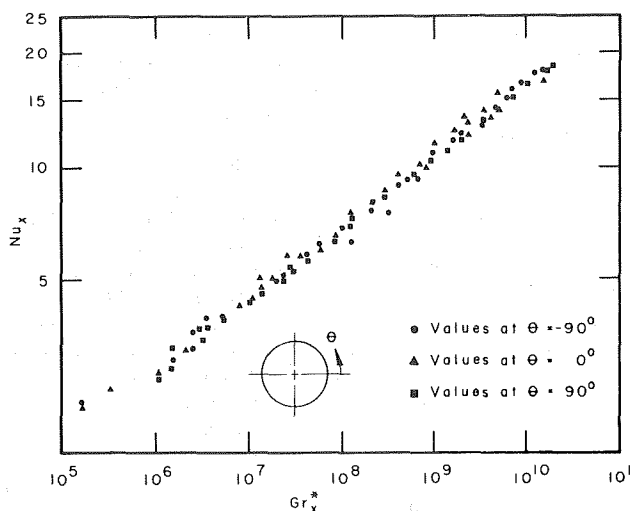


Fig. 3 Local heat transfer data for cylinder 2,  $D/L = 0.352$

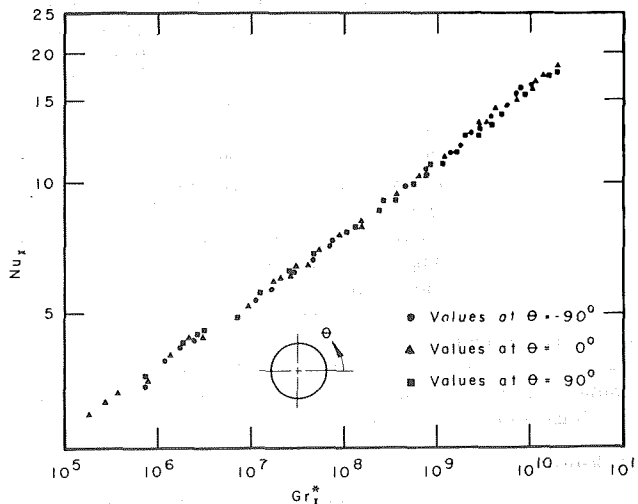


Fig. 4 Local heat transfer data for cylinder 3,  $D/L = 0.548$

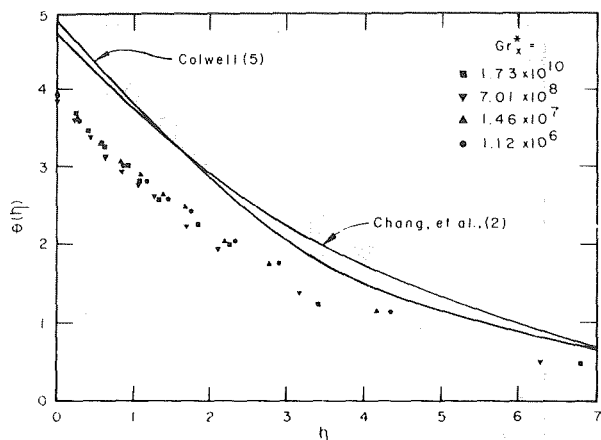


Fig. 5 Dimensionless temperature profiles, cylinder 1,  $D/L = 0.153$

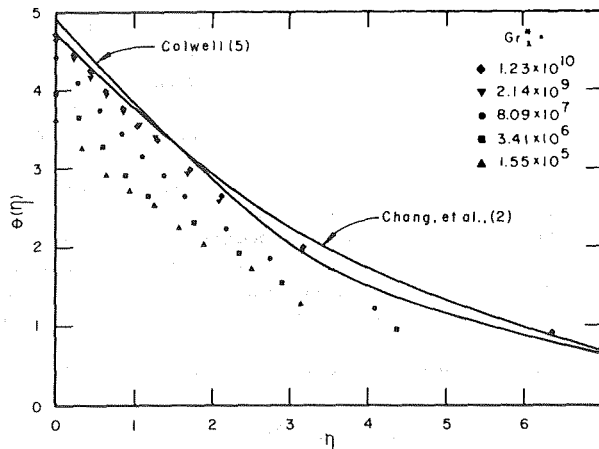


Fig. 6 Dimensionless temperature profiles, cylinder 2,  $D/L = 0.352$

0.022, all other correlations are valid for a Prandtl number of 0.023.

The present results have been compared with the results of others for the cylindrical geometry, as well as for the flat plate. Nagendra, et al. [6], used a numerical iteration technique to solve the governing equations for the case of free convection from a uniformly heated vertical cylinder. Their results predict significantly larger values of local Nusselt number than those obtained in the present work, however. The portion of Nagendra's results supposedly applicable to flat plates also overpredicts local Nusselt number as compared to the results of other authors.

By using a perturbation technique Fujii and Uehara [7] arrived at a correlation for local Nusselt number for a cylinder. Their result predicts Nusselt numbers that are up to 5 percent greater than the experimental values. This comparison is considerably more favorable than the comparison to Nagendra's results.

The nondimensionalized temperature profiles obtained for the three cylinders are shown graphically in Figs. 5, 6, and 7 as  $\theta(\eta)$ . The results are compared to the analytical solution of Chang, et al. [2], and to the experimental results of Colwell [5]. The trends in the results are of some interest.

According to a solution by Sparrow and Gregg [10] for natural convection from an isothermal vertical cylinder, as Grashof number increases the heat transfer results for a cylinder should approach those of a flat plate; i.e., as  $Gr_x^*$  increases, the ratio  $(Nu_{x, cyl})/(Nu_{x, flat plate})$  approaches unity. Likewise, the nondimensional temperature profiles for the cylinder should approach those of the flat plate as Grashof number increases. Such is the trend for cylinders 2 and 3. Also, for similar values of  $Gr_x^*$  the profiles of cylinder 2 are below those of cylinder 3, an effect predictable from the considerations of curvature. However, cylinder 1 does not display these trends.

The reasons for these results are subject to some conjecture. Nagendra, et al. [6], have suggested three separate heat transfer regimes for vertical cylinders, these being wires ( $Ra_D D/L < 0.05$ ), long cylinders ( $0.05 < Ra_D D/L < 10^4$ ), and short cylinders ( $Ra_D D/L > 10^4$ ). According to this classification cylinder 1 was in the category of long cylinders while cylinders 2 and 3 were characteristically in the regime of short cylinders [9]. Significant surface curvature apparently has a disrupting effect on similarity in the regime of short cylinders, while for long cylinders the temperature profiles appear to be more similar. In this case there is indication that Nagendra's classification scheme may indeed be valid.

#### Acknowledgments

The work described herein was supported by the Atomic Energy Commission, Contract No. AT (45-1)-2227.

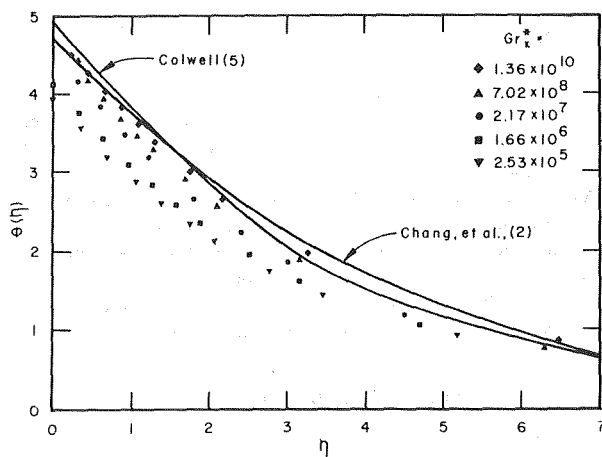


Fig. 7 Dimensionless temperature profiles, cylinder 3,  $D/L = 0.548$

#### References

- 1 Sparrow, E., and Gregg, J., "Laminar Free Convection From a Vertical Plate With Uniform Surface Heat Flux," *TRANS. ASME*, Vol. 78, 1956, pp. 435-440.
- 2 Chang, K., Akins, R., Burris, L., and Bankoff, S., "Free Convection of a Low Prandtl Number Fluid in Contact With a Uniformly Heated Vertical Plate," Argonne National Laboratory—6835, 1964.
- 3 Julian, D., and Akins, R., "Experimental Investigation of Natural Convection Heat Transfer to Mercury," *I. and E.C. Fundamentals*, Vol. 8, Nov., 1969, pp. 641-646.
- 4 White, D., "An Experimental Investigation of Natural Convection Heat Transfer From Vertical Flat Plates in Mercury," PhD thesis, Oregon State University, Corvallis, Ore., 1971.
- 5 Colwell, R., "Experimental Investigation of Natural Convection in Mercury in an Open, Uniformly Heated, Vertical Channel," PhD thesis, Oregon State University, Corvallis, Ore., 1973.
- 6 Nagendra, H., Tirunaryanan, M., and Ramachandran, A., "Laminar Free Convection From Vertical Cylinders With Uniform Surface Heat Flux," *JOURNAL OF HEAT TRANSFER, TRANS. ASME, Series C*, Vol. 92, Feb., 1970, pp. 191-194.
- 7 Fujii, T., and Uehara, H., "Laminar Natural Convective Heat Transfer From the Outer Surface of a Vertical Cylinder," *International Journal of Heat and Mass Transfer*, Vol. 13, 1970, pp. 607-615.
- 8 Hill, J., and Sleicher, C., "Convective Heat Transfer From Small Cylinders to Mercury," *International Journal of Heat and Mass Transfer*, Vol. 12, 1969, pp. 1595-1604.
- 9 Wiles, L., "An Experimental Investigation of Laminar Natural Convection With a Uniformly Heated Vertical Cylinder in Mercury," MS thesis, Oregon State University, Corvallis, Ore., 1973.
- 10 Sparrow, E., and Gregg, J., "Laminar Free Convection Heat Transfer From the Outer Surface of a Vertical Circular Cylinder," *TRANS. ASME*, Vol. 78, 1956, pp. 1823-1829.



Terukazu Ota

Assist. Professor.

Nobuhiko Kon

Technical Assistant.

Department of Mechanical Engineering  
Akita University  
Akita, Japan

# Heat Transfer in the Separated and Reattached Flow on a Blunt Flat Plate

*Heat transfer measurements are made in the separated, reattached, and redeveloped regions of the two-dimensional air flow on a flat plate with blunt leading edge. The flow reattachment occurs at about four plate thicknesses downstream from the leading edge and the heat transfer coefficient becomes maximum at that point and this is independent of the Reynolds number which ranged from 2720 to 17900 in this investigation. The heat transfer coefficient is found to increase sharply near the leading edge. The development of flow is shown through the measurements of the velocity and temperature in the separated, reattached, and redeveloped regions.*

## Introduction

The determination of the heat transfer in the separated, reattached, and redeveloped flow regions has been recognized to be very important in relation to the various engineering aspects, and there have been many papers on the wide variety of flow configurations. Those are the downward or upward surface steps [1, 2, 3, 4, 5],<sup>1</sup> the abrupt circular channel expansions or contractions including the orifice induced separations [6, 7, 8, 9, 10, 11] and the roughness elements attached to the surface [12]. In many of these cases, the flow separation and reattachment may be affected by the boundary layer just upstream of the separation point. However, for many cases in which those effects are expected to be small (for example: blunt bodies, stalled thin wings, and finned surfaces), there appears to be little information except the flat plate attached normal to a wall [13].

From this standpoint, experiments are carried out for heat transfer in the separated, reattached, and redeveloped regions of a two-dimensional air flow over a flat plate with blunt leading edge. Velocity and temperature profiles are also measured in the boundary layer. The flow configuration investigated in this paper and the coordinate system are shown in Fig. 1. The flow separates at the leading edge and reattaches on the plate surface and subsequently redevelops in the downstream direction.

## Experimental Apparatus and Technique

The experiments are worked out in an open-circuit wind tunnel with exhaust. The test section is a rectangle of 100 mm wide and 400 mm high and the nozzle contraction ratio is 3.0 to 1. The air, driven by a centrifugal fan, is exhausted into the room as a free jet, but the exhaust is equipped with side plates of plexiglass to ensure the two-dimensionality of the flow. The turbulence level of uniform flow  $\sqrt{u^2}/U_\infty$  is about 0.8 percent throughout the present investigation. The test plate (20 mm thick, 100 mm wide and 400 mm long) is made from a stainless steel sheet (0.05 mm thick

and 100 mm wide), bakelite, and plywood as shown in Fig. 2. The leading edge of the plate is sharply cut at an angle of 90 deg in order that the flow always separates there. Heating of the plate is done by means of electric current to both sides of the plate because of the axisymmetry of flow and temperature fields involved and heat flux is controlled with sliders. The temperatures on the heating surface are measured with 0.07 mm copper-constantan thermocouples soldered on the back of the stainless steel sheet, 20 in the flow direction at midspan, 12 in the spanwise direction at three cross sections; furthermore 3 are added to the back of the bakelite in order to estimate the heat loss from the test surface to the side walls. The positions of thermocouples are shown in Fig. 2. Electrical measurements are made with precision type instruments and thermocouple voltages are read with a digital potentiometer.

The experiments are carried out under the condition of constant heat flux, and the supplying heat flow rate  $Q_0$  is determined from the measured electric current  $I$  and voltage  $V$  following the equation

$$Q_0 = 0.86 VI. \quad (1)$$

The heat loss  $Q_l$  is estimated from the temperature gradient across the bakelite and is found to be smaller than 1 percent of  $Q_0$  throughout the present investigation. The heat conduction originating from the temperature gradient of the heating surface itself is ignored. The net heat flow rate to air  $Q$  is obtained by subtracting  $Q_l$  from  $Q_0$  and the heat flux and the heat transfer coefficient are respectively determined by the following equations

$$q = Q/A, \quad (2)$$

$$h = q/(T_w - T_\infty). \quad (3)$$

Furthermore Nusselt number is defined as

$$Nu = hH/\lambda, \quad (4)$$

where the thermal conductivity of air is estimated at the upstream temperature. In operating the system, about three hours are required to attain a steady state. The upstream velocity ranges

<sup>1</sup> Numbers in brackets designate References at end of paper.

Contributed by the Heat Transfer Division for publication in the JOURNAL OF HEAT TRANSFER. Manuscript received by the Heat Transfer Division, April 25, 1974. Paper No. 75-HT-D.

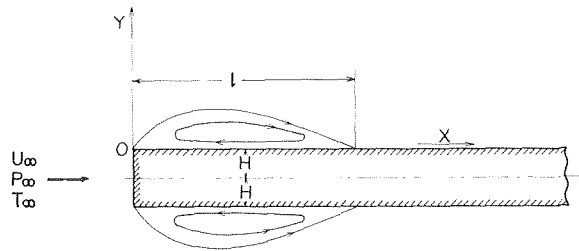
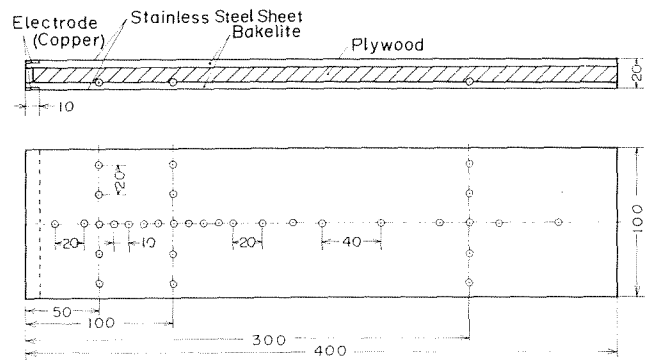


Fig. 1 Flow configuration and coordinate system



Thermocouple

Fig. 2 Test plate and position of thermocouple

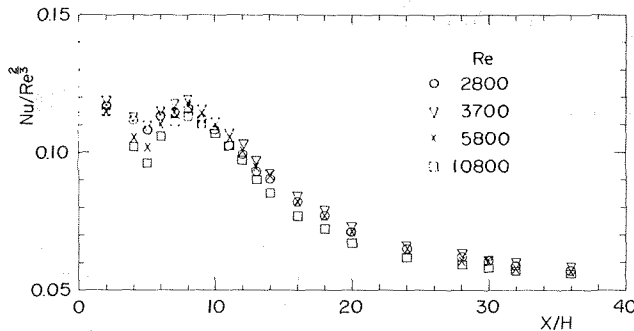


Fig. 3 Local Nusselt number distribution

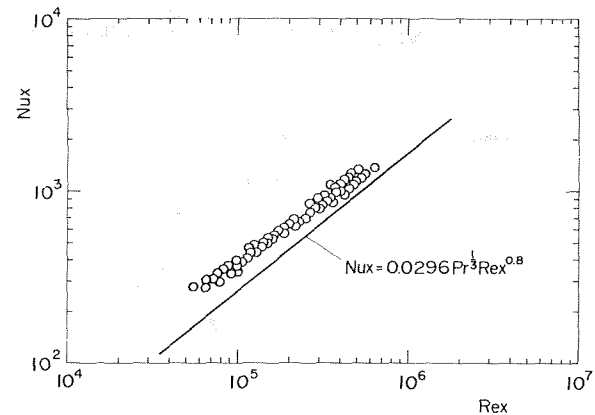


Fig. 4 Local Nusselt number distribution in downstream region ( $x/H \geq 20$ )

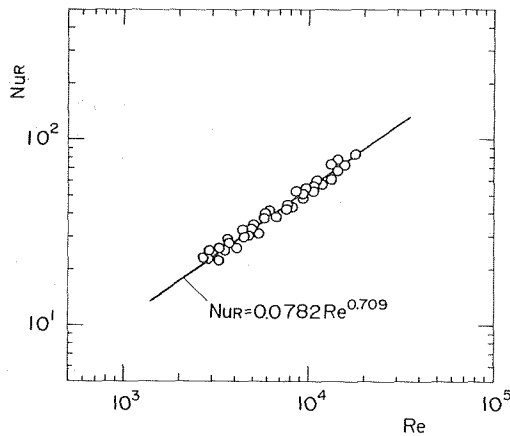


Fig. 5 Correlation of  $Nu_R$  with Reynolds number

from 4 m/s to 27 m/s and the Reynolds number from 2720 to 17900. The Reynolds number is based on the uniform velocity upstream of the plate, half the plate thickness, and the kinematic viscosity at upstream temperature.

The velocity and pressure distributions in the boundary layer are measured with a Pitot tube having an elliptic nose (1.0 mm  $\times$  0.5 mm) and a 1.0 mm static tube and a temperature probe consisting of a 0.07 mm copper-constantan thermocouple attached to the Pitot tube. It is confirmed that the wall temperature and pressure hold the two-dimensionality except in the separated flow region, and similarly, velocity and temperature profiles in the boundary layer behave two-dimensionally except in the reattachment region and those characters are independent of the Reynolds number. However, the recirculating flow in the separated region is found to fluctuate with flow visualization experiments

## Nomenclature

$2H$ = plate thickness	$T_w$ = wall temperature	$l$ = distance from leading edge to reattachment point
$A$ = area of heating surface	$q$ = heat flux per unit area from wall to fluid	$\delta_d$ = displacement thickness
$U$ = $x$ -component of velocity	$h$ = heat transfer coefficient	$\theta$ = momentum thickness
$T$ = temperature	$\lambda$ = thermal conductivity of air	$U_m$ = free stream outside boundary layer
$U_\infty, P_\infty, T_\infty$ = velocity, pressure and temperature at upstream uniform flow	$Nu$ = Nusselt number, $hH/\lambda$	$C_f$ = skin friction coefficient
$Re$ = Reynolds number, $U_\infty H/\nu$	$Nu_x$ = Nusselt number, $hx/\lambda$	$U_*$ = friction velocity
$Re_x$ = local Reynolds number, $U_\infty x/\nu$	$Nu_R$ = maximum Nusselt number at reattachment point	$\nu$ = kinematic viscosity

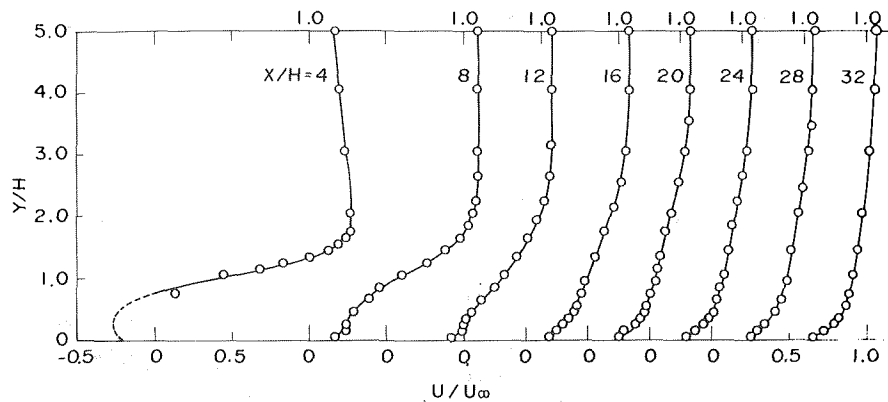


Fig. 6 Velocity profile in boundary layer,  $Re = 11700$ ,  $q = 575 \text{ kcal/m}^2 \text{ hr}$

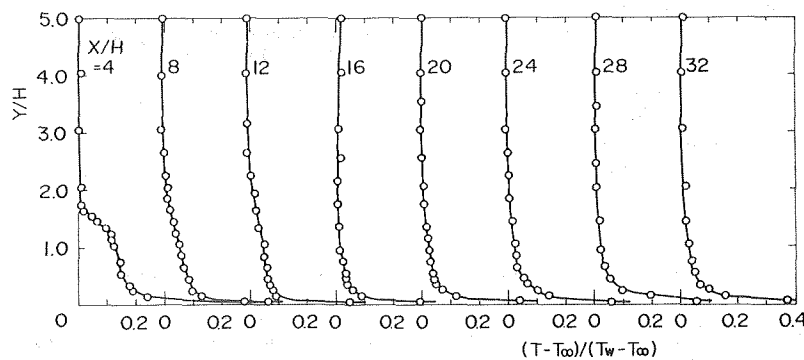


Fig. 7 Temperature profile in boundary layer,  $Re = 11700$ ,  $q = 575 \text{ kcal/m}^2 \text{ hr}$

conducted in a water tunnel floated aluminum powders [14].

## Results and Discussion

Distributions of the heat transfer coefficient are shown in the form of  $Nu/Re^{2/3}$  for various Reynolds numbers in Fig. 3. The heat transfer coefficient is always maximum at  $x/H = 8$  and this position is confirmed to be the reattachment point with the tuft. Hereafter the Nusselt number at  $x/H = 8$  is called as the reattachment Nusselt number,  $Nu_R$ . The heat transfer near the leading edge is due to the strong shear layer there and therefore the heat transfer coefficient is sharply increased as shown in Fig. 3. Similar trends are also detected in the results on the double step by Filetti and Kays [3]. The heat transfer coefficient decreases downstream from the reattachment point and approaches the value for the turbulent boundary layer on the flat plate, and then the conventional specification of  $Nu_x$  and  $Re_x$  is shown in Fig. 4 for the downstream region ( $x/H \geq 20$ ). However, it is clear that the present results are about 30 to 50 percent larger than the Colburn equation for the turbulent boundary layer on the flat plate. It is concluded that the present high heat transfer coefficient may be produced from the high turbulence intensity as compared with the normal boundary layer for the flat plate without separation and reattachment [14]. The correlation of  $Nu_R$  with the Reynolds number is shown in Fig. 5.  $Nu_R$  increases linearly with  $Re$  in logarithmic scale and the following empirical expression is obtained by means of the method of least square,

$$Nu_R = 0.0782 Re^{0.709} \quad (5)$$

The power of Reynolds number is nearly equal to 2/3 used in

many of existing results, and  $Nu/Re^{2/3}$  is independent of the Reynolds number with some scatters and is a function of only the distance from the leading edge as shown in Fig. 3. The velocity and temperature profiles in the separated, reattached, and redeveloped flow regions are shown in Figs. 6 and 7, respectively. A dotted line found in Fig. 6 is a result with a linearized hot-wire anemometer. In the separated region, a large reverse velocity exists and the temperature distribution shows a peculiar deviation from other regions. In the developed flow region, the boundary layer thickness is about two times the plate thickness, while the thermal boundary layer thickness is about the same as the plate thickness. The characteristics of the boundary layer downstream of the reattachment point are shown in Table 1, in which values of the skin friction coefficient are determined from the Ludwig-Tillmann formula [15],

$$C_f = 0.246 \times 10^{-0.6786 u/\nu} \left( \frac{U_m \theta}{\nu} \right)^{-0.268} \quad (6)$$

Furthermore the universal velocity distributions are shown in Fig. 8 in the downstream region. The present results are found to approach the Coles formula [16]. The development of the boundary layer downstream from the reattachment point may be easily understood from these results.

## Concluding Remarks

Heat transfer measurements are carried out in the separated, reattached, and redeveloped regions of the two-dimensional air flow on a blunt flat plate and the velocity and temperature profiles are measured in these flow regions. It is found that the flow reattachment occurs at about four plate thicknesses downstream from the leading edge and is independent of the Reynolds num-

**Table 1 Characteristics of boundary layer downstream of reattachment point**

$x/H$	$\delta_t/H$	$\theta/H$	$C_f \times 10^3$
8	0.974	0.352	0.39
12	0.708	0.420	1.78
16	0.633	0.439	2.58
20	0.569	0.418	2.96
24	0.524	0.404	3.31
28	0.508	0.388	3.28
32	0.471	0.366	3.45

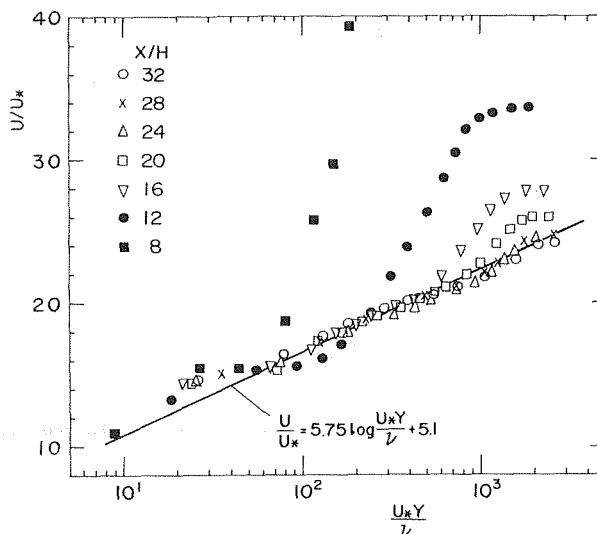
ber, and the Nusselt number reaches its maximum there. The heat transfer near the leading edge is due to the shear layer and subsequently the Nusselt number is sharply increased. An empirical formula is presented for the reattachment Nusselt number. The developments of flow and temperature fields in the boundary layer are explained through the velocity and temperature measurements in the separated, reattached, and redeveloped flow regions. The redevelopment of flow downstream of the reattachment is found to be very slow and a long distance is needed to attain the normal boundary layer on the flat plate.

### Acknowledgment

The authors express their sincere thanks to Lecturer Etsuro Yamada for helpful discussions and to Mr. Mitsugu Kudo and Mr. Toyokazu Takahasi for assistance in the experiments. Significant comments and suggestions of the referees of this paper are gratefully acknowledged.

### References

- Seban, R. A., Emery, A., and Levy, A., "Heat Transfer to Separated and Reattached Subsonic Turbulent Flows Obtained Downstream of a Surface Step," *Journal of AeroSpace Science*, Vol. 26, 1959, pp. 809-814.
- Seban, R. A., "Heat Transfer to the Turbulent Separated Flow of Air Downstream of a Step in the Surface of a Plate," *JOURNAL OF HEAT TRANSFER, TRANS. ASME, Series C*, Vol. 86, 1964, pp. 259-264.
- Filetti, E. G., and Kays, W. M., "Heat Transfer in Separated, Reattached, and Redevelopment Regions Behind a Double Step at Entrance to a Flat Duct," *JOURNAL OF HEAT TRANSFER, TRANS. ASME, Series C*, Vol. 89, 1967, pp. 163-168.
- Aung, W., and Goldstein, R. J., "Temperature Distribution and Heat Transfer in a Transitional Separated Shear Layer," *Heat Transfer 1970*, Vol. 2, Elsevier Publishing Co., Amsterdam, 1970.
- Luzhanskiy, B. Y., and Solntsev, V. P., "Experimental Study of Heat Transfer in the Zone of Turbulent Boundary Layer Separation Ahead of a Step," *Heat Transfer-Soviet Research*, Vol. 3, 1971, pp. 200-206.
- Boelter, L. M. K., Young, G., and Iverson, H. W., "An Investigation of Aircraft Heaters, XXVII—Distribution of Heat Transfer Rate in the Entrance Section of a Circular Tube," NACA TN 1451, 1948.
- Ede, A. J., "Effect of an Abrupt Disturbance of the Flow on the



**Fig. 8 Redevelopment of flow downstream of reattachment point,  $Re = 11700$ ,  $q = 575 \text{ kcal/m}^2 \text{ hr}$**

Local Heat Transfer Coefficient in a Pipe," *Heat 164*, National Engineering Laboratory, 1959.

8 Ede, A. J., Morris, R., and Birch, E. S., "The Effect of Abrupt Changes of Diameter on Heat Transfer in Pipes," NEL Report No. 73, National Engineering Laboratory, 1962.

9 Krall, K. M., and Sparrow, E. M., "Turbulent Heat Transfer in the Separated, Reattached, and Redevelopment Regions of a Circular Tube," *JOURNAL OF HEAT TRANSFER, TRANS. ASME, Series C*, Vol. 88, 1966, pp. 131-136.

10 Zemanick, P. P., and Dougall, R. S., "Local Heat Transfer Downstream of Abrupt Circular Channel Expansion," *JOURNAL OF HEAT TRANSFER, TRANS. ASME, Series C*, Vol. 92, 1970, pp. 53-60.

11 Back, L. H., Massier, P. F., and Roschke, E. J., "Partially Ionized Gas Flow and Heat Transfer in the Separation, Reattachment, and Redevelopment Regions Downstream of an Abrupt Circular Channel Expansion," *JOURNAL OF HEAT TRANSFER, TRANS. ASME, Series C*, Vol. 94, 1972, pp. 119-127.

12 Seban, R. A., and Caldwell, G. L., "The Effect of a Spherical Protuberance on the Local Heat Transfer to a Turbulent Boundary Layer," *JOURNAL OF HEAT TRANSFER, TRANS. ASME, Series C*, Vol. 90, 1968, pp. 408-412.

13 Daigo, Y., Nishiwaki, N., and Tsuchida, A., Preprint presented at Symposium of Heat Transfer Society of Japan, 1972.

14 Ota, T., and Itasaka, M., To be published.

15 Hinze, J. O., *Turbulence*, McGraw-Hill, New York, 1959.

16 Coles, D., "The Law of the Wake of the Turbulent Boundary Layer," *Journal of Fluid Mechanics*, Vol. 1, 1956, pp. 191-226.

B. T. Chao<sup>1</sup>  
R. Greif

University of California,  
Berkeley, Calif.

# Laminar Forced Convection Over Rotating Bodies

*A simple computational procedure is described for ascertaining the heat or mass transfer in laminar forced convection over a rotating body of revolution. The analysis is applicable to nonuniform surface condition and for fluids having a large or a moderate value of the Prandtl (Schmidt) number. Examples are given to illustrate the usefulness of the analysis as well as to expose its limitation.*

## Introduction

The present investigation concerns laminar forced convection over a rotating body of revolution in a fluid of large or moderate value of the Prandtl number. The analysis extends Lighthill's study [1]<sup>2</sup> which used a linear distribution of the streamwise velocity component in the boundary layer. Lighthill's analysis is asymptotically exact as  $Pr \rightarrow \infty$ . For finite values of  $Pr$ , the inaccuracy depends on the departure of the actual profile from the linear approximation in the region where significant heat transfer takes place. In flows induced by rotating bodies, the meridional velocity component,  $u$ , increases from zero at the surface, reaches a maximum and then decreases to zero at a sufficiently large distance away from the surface. This is in contrast to the streamwise velocity distribution in boundary layers produced by forced flow past stationary bodies which increases *monotonically* with distance and eventually tends to the value of the external flow. The need for a better representation of the velocity field is obviously called for in the prediction of the heat or mass transfer associated with rotating surfaces.

The use of a two-term representation of the velocity field in the boundary layer has been recently reported by Chao [2] for forced flows past two-dimensional stationary bodies. The analysis introduces a unique coordinate transformation which makes it possible to express the solution of the energy boundary layer equation in terms of universal functions. In this study, it is shown that the same analysis can be used for a rotating body of revolution with or without axial forced flow. Furthermore, the results can be expressed in terms of the same universal functions already reported and tabulated in [2] when the transformed coordinates are appropriately selected. The analysis may also be used for non-Newtonian flows and for mass transfer in high or moderate Schmidt number fluids, provided that the mass transfer rate is sufficiently low that it does not significantly interfere with the velocity field.

<sup>1</sup> On leave from the University of Illinois at Urbana-Champaign, to serve as Russell Severance Springer Professor of Mechanical Engineering.

<sup>2</sup> Numbers in brackets designate References at end of paper.

Contributed by the Heat Transfer Division and presented at the Winter Annual Meeting, New York, N.Y., November 17-22, 1974, of THE AMERICAN SOCIETY OF MECHANICAL ENGINEERS. Manuscript received by the Heat Transfer Division, November 5, 1973. Paper No. 74-WA/HT-67.

## Analysis and Results

Let  $x$ ,  $y$ , and  $z$  be an orthogonal curvilinear coordinate system with the corresponding velocity components,  $u$ ,  $v$ , and  $w$  as shown in Fig. 1. The flow and heat transfer are axially symmetric. A forward portion of the surface is unheated. Neglecting dissipation, the steady-state energy equation for a viscous incompressible fluid under the usual boundary layer approximations is given by:

$$u \frac{\partial \theta}{\partial x} + w \frac{\partial \theta}{\partial z} = \kappa \frac{\partial^2 \theta}{\partial z^2} \quad (1)$$

where  $\theta = (T - T_w)/(T_w - T_\infty)$  or  $(C - C_w)/(C_w - C_\infty)$ , for heat or mass transfer, respectively. The initial condition is given by  $\theta(x_0, z) = 0$ , and for  $x > x_0$ , the boundary conditions are  $\theta(x, 0) = 1$  and  $\theta(x, \infty) \rightarrow 0$ . The two-term representation for the  $u$ -component of the velocity field may be written as

$$u = \beta_1(x)z - \frac{1}{2}\beta_2(x)z^2 \quad (2)$$

where  $\beta_1(x)$  is determined by the wall shear in the  $x$  direction. In pure forced flows,  $\beta_2(x)$  is related to the streamwise pressure gradient while in flows solely induced by rotation, it is determined by the accompanying centrifugal action. In combined rotation and forced external flows, both effects come into play. In the analysis which follows, they are merely regarded as known functions of  $x$  to be determined either from *analysis* or *experiment*.

Substituting (2) into the continuity equation

$$\frac{\partial(ru)}{\partial x} + \frac{\partial(rw)}{\partial z} = 0 \quad (3)$$

and integrating, yield

$$w = -\frac{z^2}{2r} \frac{d(r\beta_1)}{dx} + \frac{z^3}{6r} \frac{d(r\beta_2)}{dx} \quad (4)$$

since  $w = 0$  at  $z = 0$ . To solve the energy equation, the following transformation is made (Chao [2]):

$$x \Rightarrow \chi = \chi(x) \quad (5a)$$

$$z \Rightarrow \eta = zg(x) \quad (5b)$$

where the functions  $\chi(x)$  and  $g(x)$  are to be determined. Using the velocity components given by (2) and (4) and the transformed coordinates of (5a) and (5b), the energy equation can be expressed as

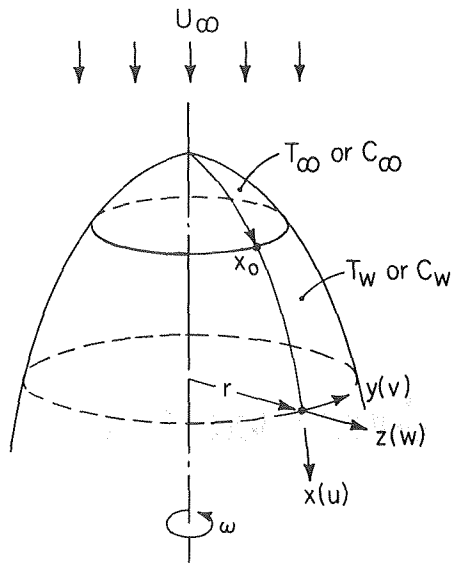


Fig. 1 Curvilinear coordinate system

$$\frac{\partial^2 \theta}{\partial \eta^2} + \frac{1}{2\kappa r g} \frac{d}{dx} \left( \frac{r \beta_1}{g^2} \right) \eta^2 \frac{\partial \theta}{\partial \eta} - \frac{1}{6\kappa r g} \frac{d}{dx} \left( \frac{r \beta_2}{g^3} \right) \eta^3 \frac{\partial \theta}{\partial \eta} = \frac{\beta_1}{\kappa g^3} \frac{d\chi}{dx} \left( 1 - \frac{\beta_2 \eta}{2g\beta_1} \right) \eta \frac{\partial \theta}{\partial \chi} \quad (6)$$

To proceed with the solution we first consider the one term representation for  $u$ , that is, with  $\beta_2 = 0$ . In this case it can be readily demonstrated that a similar solution exists and we need only introduce the transformation (5b), namely,  $\eta = zg(x)$ . By setting the coefficient of  $\eta^2 \partial \theta / \partial \eta$  equal to a constant which is chosen to be 3 for convenience, we find

$$g = \frac{(r\beta_1)^{1/2}}{[9\kappa \int_{x_0}^x r^{3/2} \beta_1^{1/2} dx]^{1/3}} \quad (7)$$

Clearly,  $\eta$  tends to infinity as  $x$  tends to  $x_0$ .

For the more general problem, that is  $\beta_2$  not equal to zero, we make the same specification for  $g$  and, thus, the coefficient of the second term on the left-hand side of (6) is still 3. In order to make possible the direct use of the universal functions tabulated in [2], we set

$$\frac{\beta_1}{\kappa g^3} \frac{d\chi}{dx} = 9 \quad (8)$$

and obtain

$$\chi = \ln \int_{x_0}^x r^{3/2} \beta_1^{1/2} dx \quad (9)$$

Furthermore, we define a dimensionless parameter  $\epsilon$  according to

$$\epsilon = \frac{\beta_2}{2g\beta_1} \quad (10)$$

which is a function of  $x$  only and, hence, may also be regarded as a function of  $\chi$ . From the foregoing relations we find that

$$\frac{1}{6\kappa r g} \frac{d}{dx} \left( \frac{r \beta_2}{g^3} \right) = 2\epsilon + 3 \frac{d\epsilon}{d\chi}$$

and (6) simplifies to:

$$\frac{\partial^2 \theta}{\partial \eta^2} + 3\eta^2 \frac{\partial \theta}{\partial \eta} - (2\epsilon + 3 \frac{d\epsilon}{d\chi}) \eta^3 \frac{\partial \theta}{\partial \eta} = 9(1 - \epsilon\eta) \eta \frac{\partial \theta}{\partial \chi} \quad (11)$$

with the boundary conditions

$$\theta = 1 \text{ for } \eta = 0; \theta = 0 \text{ for } \eta \rightarrow \infty \quad (12a, b)$$

A series solution of (11) satisfying the stated boundary conditions and expressed in terms of universal functions is given in [2]. For the convenience of discussion, we present in the following the expression for the local wall heat flux:

$$q_w = -k \left( \frac{\partial T}{\partial z} \right)_{z=0} = (T_w - T_\infty) k g \left( -\frac{\partial \theta}{\partial \eta} \right)_{\eta=0} \quad (13a)$$

where

$$\begin{aligned} \left( -\frac{\partial \theta}{\partial \eta} \right)_{\eta=0} = & 1.11985 - 0.18868\epsilon - 0.07271\epsilon^2 - 0.05079\epsilon^3 - \dots \\ & - 0.05751 \frac{d\epsilon}{d\chi} - 0.0360\epsilon \frac{d\epsilon}{d\chi} - \dots \\ & + 0.09861 \frac{d^2\epsilon}{d\chi^2} + 0.09161\epsilon \frac{d^2\epsilon}{d\chi^2} + \dots \\ & - 0.11358 \frac{d^3\epsilon}{d\chi^3} - 0.10676\epsilon \frac{d^3\epsilon}{d\chi^3} - \dots \\ & + 0.12004 \frac{d^4\epsilon}{d\chi^4} + 0.10557\epsilon \frac{d^4\epsilon}{d\chi^4} + \dots \end{aligned} \quad (13b)$$

For mass transfer, (13a) provides the local mass flux at the surface when  $(T_w - T_\infty)$  is replaced by  $(C_w - C_\infty)$  and  $k/\kappa^{1/3}$ , which appears in the product  $kg$ , is replaced by  $D^{2/3}$ ,  $D$  being the mass diffusivity.

### Applications

We examine heat transfer to a rotating, isothermal sphere with or without a uniform stream of undisturbed velocity  $U_\infty$  parallel to the axis of rotation. We first present the case of pure rotation, i.e.,  $U_\infty = 0$ . From the solution of the hydrodynamic equations (Banks [3]), we obtain

$$\beta_1 = 0.51023R \left( \frac{\omega^3}{\nu} \right)^{1/2} \phi (1 - 0.43371\phi^2 + 0.04059\phi^4 - 0.00370\phi^6 + \dots) \quad (14a)$$

$$\beta_2 = R \frac{\omega^2}{\nu} \phi \left( 1 - \frac{2}{3}\phi^2 + \frac{2}{15}\phi^4 - \frac{4}{315}\phi^6 + \dots \right) \quad (14b)$$

where  $R$  is the radius of the sphere and  $\phi = x/R$ . In addition, we have

$$r = R \sin \phi = R\phi \left( 1 - \frac{\phi^2}{6} + \frac{\phi^4}{120} - \frac{\phi^6}{5040} + \dots \right) \quad (15)$$

Substituting (14a) and (15) into (7) and carrying out the integration with  $x_0 = 0$  lead to

$$g = 0.55405 \text{Pr}^{1/3} \left( \frac{\omega}{\nu} \right)^{1/2} (1 - 0.2068\phi^2 - 0.0056\phi^4 - 0.0024\phi^6 - \dots) \quad (16)$$

It follows then from (10) that

$$\epsilon = 1.76872 \text{Pr}^{-1/3} (1 - 0.0261\phi^2 - 0.0081\phi^4 - 0.0026\phi^6 - \dots) \quad (17)$$

### Nomenclature

$C$  = concentration, also denotes  $2U_\infty/\pi R$  in the rotating disk problem

$k$  = thermal conductivity

$\text{Pr}$  = Prandtl number

$q$  = heat flux

$r$  = radial distance from a surface element to the axis of rotation

$R$  = radius of disk or sphere

$T$  = temperature

$u$  = velocity component in the  $x$  direction

$w$  = velocity component in the  $z$  direction

$x$  = coordinate measured along the surface and in the meridional direction

$z$  = coordinate normal to the surface

$\theta$  = dimensionless temperature or concentration

$\kappa$  = thermal diffusivity

$\nu$  = kinematic viscosity

$\omega$  = angular speed

### Subscripts

$w$  = wall condition

$\infty$  = freestream condition

Defining a local Nusselt number as  $Nu = 2Rq_w/k(T_w - T_\infty)$ , we find

$$Nu \left(\frac{R^2\omega}{\nu}\right)^{-1/2} Pr^{-1/3} = 1.108(1 - 0.2068\phi^2 - 0.0056\phi^4 - 0.0024\phi^6 - \dots) \cdot \left(-\frac{\partial\theta}{\partial\eta}\right)_{\eta=0} \quad (18a)$$

where

$$\begin{aligned} \left(-\frac{\partial\theta}{\partial\eta}\right)_{\eta=0} = & 1.1199 - 0.3337 Pr^{-1/3}(1 - 0.0286\phi^2 \\ & - 0.0086\phi^4 - 0.0030\phi^6 - \dots) - 0.2275 Pr^{-2/3}(1 - 0.0539\phi^2 \\ & - 0.0138\phi^4 - 0.0007\phi^6 - \dots) \\ & + \text{terms involving } Pr^{-1}, Pr^{-4/3}, \text{ etc.} \end{aligned} \quad (18b)$$

In (18b), the numerical coefficients of  $\phi^2$ ,  $\phi^4$ , etc., are evaluated from the sum of the appropriate series in (13b). Although the sequence is dominated by the first term, it is not always convergent and use has been made of Euler's procedure for finding the sum. The computed results for the local Nusselt number are shown in Fig. 2. The uppermost curve is for the limiting case of  $Pr \rightarrow \infty$ , for which  $(-\partial\theta/\partial\eta)_{\eta=0}$  tends to a constant and  $Nu$  becomes proportional to  $Pr^{1/3}$  as expected. At the stagnation point,  $\phi = 0$ , the foregoing result leads to a wall heat flux which is in excellent agreement with that for a disk in pure rotation considered later in this section.

We now turn to the general case of heat transfer to a rotating sphere situated in a uniform stream of undisturbed velocity  $U_\infty$  parallel to the axis of rotation. Using the results for the velocity field obtained by Hoskin [4],<sup>3</sup> we identify

$$\beta_1 = \left(\frac{3}{2}\right)^{3/2} A_1 \left(\frac{U_\infty^3}{\nu R}\right)^{1/2} \phi \left(1 - \frac{1}{6} \frac{A_3}{A_1} \phi^2 + \frac{1}{120} \frac{A_5}{A_1} \phi^4 - \frac{1}{5040} \frac{A_7}{A_1} \phi^6 + \dots\right) \quad (19a)$$

$$\beta_2 = \frac{9}{4}(\lambda + 1) \frac{U_\infty^2}{\nu R} \phi \left(1 - \frac{2}{3} \phi^2 + \frac{2}{15} \phi^4 - \frac{4}{315} \phi^6 + \dots\right) \quad (19b)$$

where  $\lambda = (2\omega R/3U_\infty)^2$  which characterizes the relative importance of the speed of rotation to that of the forced flow. The numerical coefficients  $A_1, A_3, A_5$ , and  $A_7$  depend on  $\lambda$  and are tabu-

<sup>3</sup>Hoskin assumed that the velocity at the edge of the boundary layer was that of potential flow, i.e.,  $U = (\frac{2}{3})U_\infty \sin\phi$ . Hence, the result is not expected to be valid as  $\phi$  approaches  $\pi/2$ .

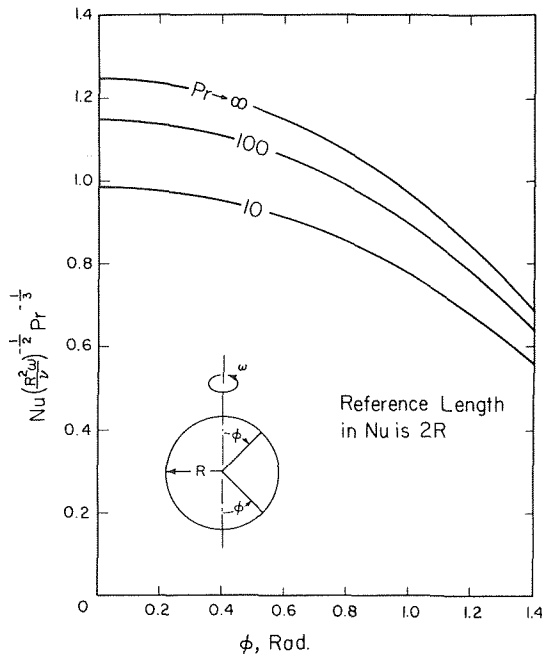


Fig. 2 Local Nusselt number over an isothermal sphere rotating in a quiescent fluid of infinite extent

lated in [4]. Proceeding in the manner previously described, we may again deduce expressions for  $g$ ,  $\epsilon$ , and, finally, the local Nusselt number. We shall refrain from exhibiting the details and merely present the results which are summarily displayed in Fig. 3. The case of  $\lambda = 0$  corresponds to pure forced flow. When  $\lambda = 1$ , the surface speed at the equator due to rotation is 1.5 times  $U_\infty$ . It increases to 4.74  $U_\infty$  for  $\lambda = 10$ . The augmentation of heat transfer due to rotation is clearly seen. We are not aware of any prior publication of such information.

Next we consider heat transfer from a rotating disk in forced flow produced by a uniform free stream  $U_\infty$  impinging normally on its surface. The velocity field in the boundary layer has been calculated by Hannah [5]. From Hannah's work, we readily identify

$$\beta_1 = a(C^2 + \omega^2)^{3/4} r/\nu^{1/2}, \quad \beta_2 = (C^2 + \omega^2)r/\nu \quad (20a,b)$$

where  $C = 2U_\infty/\pi R$  and the numerical constant "a" depends on the ratio  $(\omega/C) (= \pi R\omega/2U_\infty)$  which characterizes the relative importance of the speed of rotation to that of the forced flow. Several values of  $a$  reported by Hannah are listed in Table 1. Using (20a) and (7), we find

$$g = \left(\frac{\alpha Pr}{3}\right)^{1/3} \frac{(C^2 + \omega^2)^{1/4}}{\nu^{1/2}} \left[1 - \left(\frac{r_0}{r}\right)^3\right]^{-1/3} \quad (21)$$

For a disk at a uniform temperature,  $r_0 = 0$ , and hence  $g$  becomes a constant, independent of  $r$ . Accordingly,

$$\epsilon = \frac{\beta_2}{2g\beta_1} = \frac{3^{1/3}}{2} (a^4 Pr)^{-1/3} \quad (22)$$

which is also independent of  $r$ . Thus, the heat flux, or the Nusselt number (in the form defined by Tien and Tsuji [6]) is given by

$$Nu = \frac{q_w \nu^{1/2}}{k(T_w - T_\infty)(C^2 + \omega^2)^{1/4}} = \left(\frac{\alpha Pr}{3}\right)^{1/3} \cdot [1.11985 - 0.18868\epsilon - 0.07271\epsilon^2 - 0.05079\epsilon^3 - \dots] \quad (23)$$

since all the terms involving the derivatives of  $\epsilon$  vanish. The numerical results for  $Pr = 100, 10$ , and  $1$  and for values of  $\omega/C = 0, 1, 2$ , and  $\infty$  are presented in Table 1 using one, two, three, and

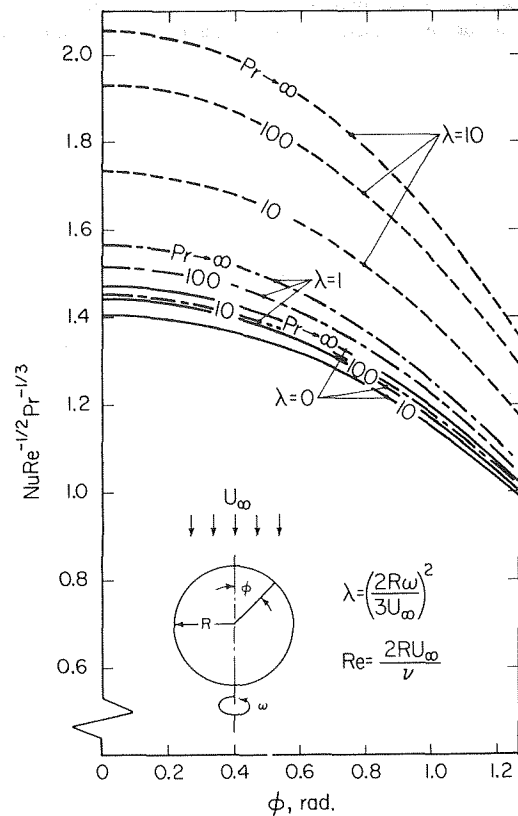


Fig. 3 Local Nusselt number over an isothermal sphere in combined forced and induced flows

**Table 1 Comparison of Nusselt number for forced flow against rotating disks**

$\omega/C$	$a^0$	$\epsilon$	Pr	Equation (23)				Numerical Results	
				1 Term ( $\beta_2 = 0$ )	2 Terms	3 Terms	4 Terms	From [8]	From [7]
0	1.312	0.1082	100	3.945	3.873	3.870	3.870	-	-
1	0.836	0.1637	100	3.525	3.424	3.418	3.417	-	-
2	0.686	0.2568	100	3.178	3.041	3.027	3.025	-	-
$\infty$	0.510	0.3913	100	2.879	2.694	2.684	2.677	2.69	2.6371
								From [8]	
0	1.312	0.2330	10	1.891	1.759	1.753	1.752	1.752	-
1	0.736	0.3656	10	1.636	1.536	1.521	1.518	1.535	-
2	0.605	0.5532	10	1.475	1.338	1.309	1.297	1.340	-
$\infty$	0.510	0.8215	10	1.337	1.152	1.093	1.059	1.134	1.1341
0	1.312	0.5021	1	0.850	0.7781	0.7643	0.7594	0.762	-
1	0.936	0.7876	1	0.760	0.6587	0.6281	0.6113	0.658	-
2	0.685	1.192	1	0.685	0.5473	0.484	0.432	0.557	-
$\infty$	0.510	1.770	1	0.620	0.4354	0.309	Divergent	0.395	0.3963

\*Denoted by  $\alpha_0$  in [5].

four terms of the foregoing series. For Pr = 100, the Nusselt number data have been reported by Sparrow and Gregg [7] and by Hartnett and Deland [8] for  $\omega/C \rightarrow \infty$ . The four-term result of 2.677 is in excellent agreement with the reported values and the one-term result differs by only 7 percent. Of all the values of  $\omega/C$  shown, this is the only case where the radial velocity component,  $u$ , rises to a maximum near the surface and then decreases to zero at a large distance from it [5]. Thus, we anticipate that the maximum error should result for this condition. The same can be observed from the results for Pr = 10 and Pr = 1. For a given Pr, the best agreement is obtained at  $\omega/C = 0$ . The data for Pr = 1 and for  $\omega/C \rightarrow \infty$  are included for the purpose of bringing out the limitations of the present analysis. Under these conditions, the

two-term representation of the velocity field is inadequate.

If the disk has an unheated region extending from  $r = 0$  to  $r = r_0$ , then  $\epsilon = \epsilon_0[1 - (r_0/r)^3]^{1/3}$ ,  $\epsilon_0$  being a constant given by (22). Furthermore, we find

$$\frac{d\epsilon}{d\chi} = \frac{\epsilon_0}{3} \left(\frac{r_0}{r}\right)^3 \left[1 - \left(\frac{r_0}{r}\right)^3\right]^{1/3}, \quad \frac{d^2\epsilon}{d\chi^2} = -\frac{\epsilon_0}{3} \left(\frac{r_0}{r}\right)^3 \left[1 - \left(\frac{r_0}{r}\right)^3\right]^{-2/3} \left[1 - \frac{4}{3} \left(\frac{r_0}{r}\right)^3\right] \text{ etc.}$$

Hence, the wall heat flux distribution may again be evaluated. The local Nusselt number as defined by (23) can be obtained by multiplying its right-hand side by the factor  $[1 - (r_0/r)^3]^{1/3}$  and, in addition, by including terms involving  $d\epsilon/d\chi$ ,  $\epsilon(d\epsilon/d\chi)$ ,  $d^2\epsilon/d\chi^2$ , etc., in series (13b). We therefore obtain the kernel function in the Stieltjes integral for the problem of arbitrary nonuniform surface temperature.

### References

- 1 Lighthill, M. J., "Contributions to the Theory of Heat Transfer Through a Laminar Boundary Layer," *Proceedings of the Royal Society, London*, Vol. 202A, 1950, pp. 359-377.
- 2 Chao, B. T., "An Improved Lighthill's Analysis of Heat Transfer Through Boundary Layers," *International Journal of Heat and Mass Transfer*, Vol. 15, 1972, pp. 907-920.
- 3 Banks, W. H., "The Boundary Layer on a Rotating Sphere," *Quarterly Journal of Mechanics and Applied Mathematics*, Vol. 18, Part 4, 1965, pp. 443-454.
- 4 Hoskin, N. E., "The Laminar Boundary Layer on a Rotating Sphere," *50 Jahre Grenzschichtforschung*, H. Görtler and W. Tollmien, eds., Braunschweig, 1955, pp. 127-131.
- 5 Hannah, D. M., "Forced Flow Against a Rotating Disc," British Aeronautical Research Council Reports and Memoranda No. 2772, 1947.
- 6 Tien, C. L., and Tsuji, J., "Heat Transfer by Laminar Forced Flow Against a Non-Isothermal Rotating Disk," *International Journal of Heat and Mass Transfer*, Vol. 7, 1964, pp. 247-252.
- 7 Sparrow, E. M., and Gregg, J. L., "Heat Transfer From a Rotating Disk to Fluids of any Prandtl Number," *JOURNAL OF HEAT TRANSFER, TRANS. ASME, Series C*, Vol. 81, 1959, pp. 249-251.
- 8 Hartnett, J. P. and Deland, E. C., "The Influence of Prandtl Number on the Heat Transfer from Rotating Nonisothermal Disks and Cones," *JOURNAL OF HEAT TRANSFER, TRANS. ASME, Series C*, Vol. 83, 1961, pp. 95-96.



H. F. Cooper

R & D Associates,  
Santa Monica, Calif.

G. N. Williams

Computer Science Department,  
Texas A&M University,  
College Station, Texas

# Transient Electrical Heating of Toroidal Coils of Rectangular Cross Section

*The exact solution is obtained for the transient thermal response of toroidal coils of rectangular cross section with orthotropic constant thermal conductivity, constant density, and specific heat, and linear boundary conditions. The solution is a rapidly converging doubly infinite eigenfunction expansion whose leading term is generally accurate to within 5 percent. No conclusive results were obtained from our evaluation of the applicability of previously obtained solutions for the infinite rod approximation for the toroidal coils. In some cases, the infinite rod approximation is accurate even for large curvatures, but in other cases it is in substantial error for relatively small curvatures. Hence, the solution presented here is generally recommended to predict the temperature distribution in toroidal coils and a number of design curves are provided for prediction purposes.*

## Introduction

Joule heating of various electrical coils has long been of interest to designers of solenoids, transformers, and other current-carrying apparatus. Early theoretical analyses by Cockroft [1]<sup>1</sup> assumed heat generated by current flow to be constant throughout the cross section. Jakob [2, 3] introduced inhomogeneous heat generation into steady-state one-dimensional (plane, cylindrical, and spherical geometries) analyses, accounting for variations in resistance of a conductor with temperature. Higgins extended Jakob's work to consider steady-state temperature distributions in infinite rectangular rods [4, 5] and toroidal coils [6].

Carslaw and Jaeger [7] considered the transient Joule heating of infinite slabs of finite thickness and observed certain conditions for which no steady-state solution exists. Cooper [8] found similar theoretical conditions for the transient heating of infinite rectangular rods. From a practical point of view, these theoretical predictions of unbounded temperatures are invalid because the constant current driving condition, assumed in references [1-8], would require infinite voltages to produce infinite temperatures. A steady state is always achieved if the coil is driven with constant voltage, a condition which can be treated with a simple extension of the constant current solution when the temperature rise is not too great [9].

With the exception of Higgins' work [6], theoretical analyses of toroidal coils have received little attention. This paper provides the solution for the transient response of toroidal coils of rectangular cross section and evaluates the approximations in previous analyses of infinite rods [8, 9].

## Formulation

Consider an electrical coil of inner radius  $a$ , outer radius  $a + h$ , and length  $l$  (rectangular cross section  $h \times l$ ). The governing equation for the temperature distribution, assuming orthotropic thermal conductivity and cylindrical symmetry is<sup>2</sup>

$$\frac{k_r}{r} \frac{\partial}{\partial r} \left[ r \frac{\partial T}{\partial r} \right] + k_z \frac{\partial^2 T}{\partial z^2} + q''' = \rho c_p \frac{\partial T}{\partial t} \quad (1)$$

For a constant current driving condition,

$$q''' = q_0 [1 + \alpha(T - T_0)] \quad (2)$$

If  $|\alpha(T - T_0)| \ll 1$ , a constant voltage driving condition may also be approximated by equation (2) if  $\alpha$  is interpreted as minus the resistance-temperature coefficient [9]. At the boundaries, we assume that heat is transferred to the adjacent medium according to Newton's law of cooling

$$\begin{aligned} -k_r \partial T / \partial r + U_{r1}(T - T_0) &= 0 \text{ at } r = a, \\ k_r \partial T / \partial r + U_{r2}(T - T_0) &= 0 \text{ at } r = a + h, \\ -k_z \partial T / \partial z + U_{z1}(T - T_0) &= 0 \text{ at } z = 0, \\ k_z \partial T / \partial z + U_{z2}(T - T_0) &= 0 \text{ at } z = l. \end{aligned} \quad (3)$$

The temperature of the medium adjacent to the solenoid is assumed to be uniform. If the spatial variation of the bounding temperatures is important, then procedures applied in reference [8] will provide the more general solution. We further assume that the initial temperature in the solenoid is  $T(r, z, 0) = T_0$  and define:

<sup>1</sup> Numbers in brackets designate References at end of paper.

Contributed by the Heat Transfer Division for publication in the JOURNAL OF HEAT TRANSFER. Manuscript received by the Heat Transfer Division, January 11, 1974. Paper No. 75-HT-B.

<sup>2</sup> See Nomenclature for definition of terms.

$$\xi = r/a, \eta = z/l, \tau = k_r l / \rho c_p h^2, \theta = T - T_0, \\ \kappa = k_z h^2 / k_r l^2, \\ Q_0 = q_0 h^2 / k_r, B_{ri} = U_{ri} h / k_r, B_{zi} = U_{zi} l / k_z, \\ d = a/h, e = d + 1. \quad (4)$$

Then the mathematical problem can be stated as

$$\frac{1}{\xi} \frac{\partial}{\partial \xi} \left[ \xi \frac{\partial \theta}{\partial \xi} \right] + \kappa \frac{\partial^2 \theta}{\partial \eta^2} - \frac{\partial \theta}{\partial \tau} + \alpha Q_0 \theta = -Q_0; \quad (5)$$

$$-\partial \theta / \partial \xi + B_{r1} \theta = 0 \text{ at } \xi = d, \quad (6)$$

$$\partial \theta / \partial \xi + B_{r2} \theta = 0 \text{ at } \xi = e;$$

$$-\partial \theta / \partial \eta + B_{z1} \theta = 0 \text{ at } \eta = 0, \quad (7)$$

$$\partial \theta / \partial \eta + B_{z2} \theta = 0 \text{ at } \eta = 1;$$

$$\theta(\xi, \eta, 0) = 0. \quad (8)$$

### Solution

Consider the Sturm-Liouville system for  $\psi(\eta)$  such that  $d^2\psi/d\eta^2 + \gamma^2\psi = 0$ , with boundary conditions  $-d\psi/d\eta + B_{z1}\psi = 0$  at  $\eta = 0$ , and  $d\psi/d\eta + B_{z2}\psi = 0$  at  $\eta = 1$ . The eigenfunctions ( $\psi_n$ ), eigenvalues ( $\gamma_n$ ), and normalizing factors ( $N_{zn}$ ) for  $n = 1, 2, \dots$  are derived from

$$\psi_n = \cos \gamma_n \eta + (B_{z1}/\gamma_n) \sin \gamma_n \eta,$$

$$(\gamma_n^2 - B_{z1}B_{z2}) \sin \gamma_n - \gamma_n (B_{z1} + B_{z2}) \cos \gamma_n = 0, \quad (9)$$

$$N_{zn} = \int_0^1 \psi_n^2 d\eta = \frac{\gamma_n^2 + B_{z1}^2}{2\gamma_n^2} \\ \times \left\{ 1 + \frac{(B_{z1} + B_{z2})(\gamma_n^2 + B_{z1}B_{z2})}{(\gamma_n^2 + B_{z1}^2)(\gamma_n^2 + B_{z2}^2)} \right\}.$$

Similarly, consider the Sturm-Liouville system for  $\phi(\xi)$  such that  $d^2\phi/d\xi^2 + \xi^{-1}d\phi/d\xi + \lambda^2\phi = 0$ ;  $-d\phi/d\xi + B_{r1}\phi = 0$  at  $\xi = d$ ; and  $d\phi/d\xi + B_{r2}\phi = 0$  at  $\xi = e$ . The eigenfunctions ( $\phi_n$ ), eigenvalues ( $\lambda_n$ ) and the normalizing factors ( $N_{rn}$ ) [10] for  $n = 1, 2, \dots$  are derived from

$$\phi_n = \frac{\pi \lambda_n d}{2} \left\{ W_n(d, \xi) + \frac{B_{z1}}{\lambda_n} X_n(d, \xi) \right\}, \\ \lambda_n^2 U_n(d, e) + \lambda_n [B_{r1} V_n(d, e) + B_{r2} W_n(d, e)] \\ + B_{r1} B_{r2} X_n(d, e) = 0, \quad (10)$$

$$N_{rn} = \int_d^e \phi_n^2 \xi d\xi = \frac{1}{2\lambda_n^2} \left\{ e^2 (B_{r2}^2 + \lambda_n^2) \phi_n^2(\lambda_n e) \right. \\ \left. - d^2 (B_{r1}^2 + \lambda_n^2) \phi_n^2(\lambda_n d) \right\};$$

where

$$U_n(p, q) = Y_1(\lambda_n p) J_1(\lambda_n q) - J_1(\lambda_n p) Y_1(\lambda_n q), \\ V_n(p, q) = Y_0(\lambda_n p) J_1(\lambda_n q) - J_0(\lambda_n p) Y_1(\lambda_n q), \\ W_n(p, q) = J_1(\lambda_n p) Y_0(\lambda_n q) - Y_1(\lambda_n p) J_0(\lambda_n q), \\ X_n(p, q) = J_0(\lambda_n p) Y_0(\lambda_n q) - Y_0(\lambda_n p) J_0(\lambda_n q). \quad (11)$$

Here,  $J_0(\lambda_n \xi)$ ,  $J_1(\lambda_n \xi)$ ,  $Y_0(\lambda_n \xi)$  and  $Y_1(\lambda_n \xi)$  are the usual Bessel functions of the first and second kinds. The eigenfunctions  $\psi_n$  and  $\phi_n$  constitute complete orthogonal sets. Hence

$$\int_0^1 \psi_m \psi_n d\eta = \delta_{mn} N_{zn} \quad \text{and} \quad \int_d^e \phi_m \phi_n \xi d\xi = \delta_{mn} N_{rn} \quad (12)$$

where  $\delta_{mn} = 0$  for  $m \neq n$  and  $\delta_{mn} = 1$  for  $m = n$ .

We now assume an eigenfunction expansion for  $\theta$  in the form

$$\theta = \sum_{m,n=1}^{\infty} T_{mn}(\tau) \phi_m(\lambda_n \xi) \psi_n(\gamma_n \eta) \quad (13)$$

which satisfies the boundary conditions (6) and (7) term by term. Substituting (13) into (5), multiplying by  $\phi_i \psi_j \xi d\xi d\eta$ , integrating from  $\eta = 0$  to  $\eta = 1$  and  $\xi = d$  to  $\xi = e$ , and noting the orthogonality relations, we obtain an ordinary first order differential equation for  $T_{mn}$ . Noting the initial condition (8), we obtain the solution as

$$T_{mn} = F_{mn} [1 - \exp(-\Delta_{mn} \tau)] \quad (14)$$

where

$$F_{mn} = Q_0 \zeta_{rm} \zeta_{zn} / \Delta_{mn}; \quad \Delta_{mn} = \lambda_n^2 + \kappa \gamma_n^2 - \alpha Q_0, \quad (15)$$

$$\zeta_{rm} = N_{rm}^{-1} \int_d^e \phi_m \xi d\xi = N_{rm}^{-1} \lambda_m^{-2} [d B_{r1} \phi_m(\lambda_m d) \\ + e B_{r2} \phi_m(\lambda_m e)] \quad (16)$$

$$\zeta_{zn} = N_{zn}^{-1} \int_0^1 \psi_n d\eta = N_{zn}^{-1} \gamma_n^{-2} [\gamma_n \sin \gamma_n \\ + B_{z1} (1 - \cos \gamma_n)] \quad (17)$$

From (14), the temperature is unbounded for increasing  $\tau$  if

### Nomenclature

$a$  = inside radius of coil, ft  
 $B_{ri}, B_{zi}$  = Biot numbers =  $U_{ri} h / k_r$ ,  
 $U_{zi} l / k_z, i = 1, 2$   
 $c_p$  = constant specific heat,  
 Btu/hr lb-mass °F  
 $d, e$  = nondimensional inner and  
 outer coil radii =  $a/h$ ,  
 $(a+h)/h$   
 $h$  = coil thickness, ft  
 $k_r, k_z$  = thermal conductivities in  
 $r, z$  directions, Btu/hr  
 ft °F  
 $l$  = height of coil, ft  
 $M_{rm}, M_{zn}$  = nondimensional parameters  
 $N_{rm}, N_{zn}$  = normalizing factors in the  
 $r, z$  directions  
 $q'''$  = heat generation, Btu/hr ft<sup>3</sup>  
 $q_0$  = heat generation at ambient  
 temperature, Btu/hr ft<sup>3</sup>

$Q_0 = q_0 h^2 / k_r$   
 $r, z$  = cylindrical coordinates, ft  
 $R$  = dimensionless parameter  
 $T$  = temperature, °F  
 $T_0$  = ambient temperature, °F  
 $T_{mn}$  = generalized temperature co-  
 efficients, °F  
 $t$  = time, hr  
 $t_0$  = thermal time constant, hr  
 $U_{ri}, U_{zi}$  = total heat-transfer coeffi-  
 cients at the boundaries  
 in the  $r, z$  directions,  $i =$   
 $1, 2$ , Btu/hr ft<sup>2</sup> °F  
 $\alpha$  = resistance temperature co-  
 efficient, ohm/ohm °F  
 $\Delta_{mn}$  = parameter =  $\lambda_m^2 + \kappa \gamma_n^2 -$   
 $\alpha Q_0$

$\xi, \eta$  = nondimensional cylindrical  
 coordinates =  $r/h, z/l$   
 $\xi_m, \eta_m$  = location of maximum tem-  
 perature  
 $\lambda_m, \gamma_n$  = eigenvalues in the  $r, z$  direc-  
 tions  
 $\kappa$  = parameter =  $k_z h^2 / k_r l^2$   
 $\rho$  = density, lb-mass/ft<sup>3</sup>  
 $\phi_m, \psi_n$  = eigenfunctions in the  $r, z$  di-  
 rection  
 $\theta$  = temperature rise =  $T - T_0$ ,  
 °F  
 $\theta_A$  = average temperature rise,  
 °F  
 $\theta_M$  = maximum temperature rise,  
 °F  
 $\tau$  = nondimensional time =  
 $k_r t / \rho c_p h^2$   
 $\zeta_{rm}, \zeta_{zn}$  = parameter

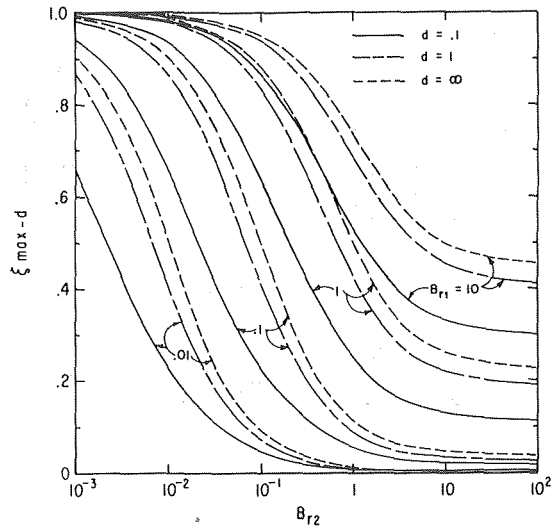


Fig. 1 Location of maximum temperature

$\Delta_{mn} \leq 0$  for any  $m, n$ . Because the eigenvalues are a monotonically increasing set, a necessary and sufficient condition for a steady-state solution is  $\Delta_{11} > 0$ . If  $\alpha > 0$ , possible values of  $Q_0$  associated with some boundary conditions lead to no steady state. For the constant voltage approximation ( $\alpha < 0$ ),  $\Delta_{11}$  is always positive and a steady-state condition always exists [9].

### Approximate Solution

Numerous test cases have shown the solution (13) to be given to within 5 percent for all  $\tau$  and to within 2 percent in the steady state by the leading term

$$\theta \approx A(\tau)\xi_r \xi_z \phi(\xi)\psi(\eta) \quad (18)$$

where  $A = Q_0[1 - \exp(-\Delta\tau)]/\Delta$ . (Here we have dropped the 1 subscripts for convenience.) This simple product form leads to separable design formula for temperature variations in the  $\xi$  and  $\eta$  directions. For example, the maximum temperature is located at the point where  $d\phi/d\xi = d\psi/d\eta = 0$ , or else on the boundary if this condition is not met in the interior. The coordinates ( $d \leq \xi_m \leq e$ ;  $0 \leq \eta_m \leq 1$ ) of the interior hot spot are given by solving  $\lambda U(d, \xi_m) + B_{r1}V(d, \xi_m) = 0$  and  $-\gamma \sin \gamma \eta_m + B_{z1} \cos \gamma \eta_m = 0$ . Fig. 1 locates the maximum radial temperature as a function of  $B_{r1}$ ,  $B_{r2}$  and  $d$ . The case  $d = \infty$  corresponds to an infinite rectangular rod [9] and may be used to determine  $\eta_m$  by using  $B_{z1}$ ,  $B_{z2}$  in place of  $B_{r1}$ ,  $B_{r2}$ .<sup>3</sup> Fig. 1 shows that the hot spot moves toward the center of the solenoid as the inner radius decreases. The maximum temperature rise is approximated by substituting  $\xi_m$  and  $\eta_m$  into (18)

$$\theta_m = A(\tau)\xi_r \xi_z \phi_{\max} \psi_{\max} \quad (19)$$

The average temperature rise is given by

$$\theta_A = \int_d^e \int_0^1 \theta d\xi d\eta \approx A(\tau)\xi_r \xi_z M_r M_z \quad (20)$$

where

$$M_r = \int_d^e \phi d\xi; \quad M_z = \int_0^1 \psi d\eta \quad (21)$$

One other design formula that is easily obtained from the approximate solution is the thermal time constant ( $t_0$ ) at which time  $\Delta\tau = 1$ . Hence,  $t_0 = \rho c_p h^2 / k_r \Delta$ .

From (18), the spatial shape of the temperature distribution is determined by the boundary conditions independently of  $\tau$ ,  $\alpha$ ,

<sup>3</sup>Note that  $\xi \rightarrow \infty$  as  $d \rightarrow \infty$  such that  $|\xi - d| \leq 1$  is the normalized coordinate measured from the inner radius of the coil.

Table 1 Variation of pertinent ratios with coil curvature

d	$\lambda/\gamma$		$(\lambda/\gamma)^2$		$\xi_r \xi_z / \xi_{r,\max} \xi_{z,\max}$		$\xi_r M_r / \xi_{r,\max} M_r$		R		$(\xi_{\max} - d)/\eta_{\max}$	
	Min	Max	Min	Max	Min	Max	Min	Max	Min	Max	Min	Max
0.1	0.42	1.41	0.176	1.98	0.85	1.23	0.99	1.15	0.82	1.11	0.45	1.0
0.2	0.55	1.35	0.30	1.82	0.87	1.19	0.99	1.11	0.86	1.09	0.55	1.0
0.5	0.71	1.23	0.50	1.52	0.91	1.12	0.99	1.06	0.92	1.06	0.65	1.0
1	0.82	1.15	0.67	1.32	0.94	1.07	0.99	1.03	0.95	1.04	0.75	1.0
2	0.90	1.10	0.81	1.21	0.96	1.04	0.99	1.02	0.97	1.05	0.84	1.0
5	0.95	1.04	0.90	1.08	0.98	1.02	0.99	1.01	0.99	1.01	0.92	1.0
10	0.98	1.02	0.96	1.04	0.99	1.01	1.00	1.00	1.00	1.01	0.96	1.0

and  $Q_0$ . For example, a gross measure of the temperature gradient is the ratio of maximum to average temperature given by  $\theta_m/\theta_A \approx [\phi_{\max}/M_r][\psi_{\max}/M_z]$ . (Strictly speaking, the rapid convergence properties of (13) indicate that variations in  $\tau$ ,  $\alpha$ , and  $Q_0$  make less than a 5 percent difference in the temperature distribution.)

### Effect of Curvature on Coil Heating Characteristics

As  $d \rightarrow \infty$  (zero curvature), (18) is asymptotic to the solution for an infinite rectangular rod. We chose the particular form in (10) to assure  $\phi_n \sim (d/\xi)^{(1/2)}[\cos \lambda_n(\xi - d) + (B_{r1}/\lambda_n)\sin \lambda_n(\xi - d)]$  when  $d \gg 1$ . Thus, from (9),  $\phi_n$  is asymptotic to  $\psi_n$  if  $B_{z1}$  and  $B_{z2}$  are set equal to  $B_{r1}$  and  $B_{r2}$ . In this case,  $\lambda_n \rightarrow \gamma_n$ ;  $N_{rn} \rightarrow N_{zn}$ ;  $\xi_{rn} \rightarrow \xi_{zn}$ ; etc. Thus, we can evaluate curvature effects by setting  $B_{z1} = B_{r1}$  and  $B_{z2} = B_{r2}$  and studying the approximate solution for  $\lambda/\gamma$ ,  $\phi_{\max}/\psi_{\max}$ , etc., which should approach unity as the curvature effects become negligible.<sup>4</sup>

Table 1 summarizes the range of some pertinent ratios as a function of  $d = a/h$ . Here  $R = (\phi_{\max}/M_r)/(\psi_{\max}/M_z)$  is useful in determining the ratio of maximum to average temperature rise. Other ratios in Table 1 indicate curvature effects on maximum and average temperature rises (see (19) and (20)). Figs. 2-6 show the main variations as a function of  $B_{r1}$  and  $B_{r2}$  and several values of  $d$ . For  $0.1 \leq d \leq 1$ , most pertinent factors are within 10 to 20 percent of those predicted for infinite rods. However,  $(\lambda/\gamma)^2$  is probably the most critical ratio (particularly if  $\Delta \ll 1$ ) and it can differ from the solution for an infinite rod by much larger factors. Table 1 shows discrepancies in this parameter as large as  $\pm 20$  percent for some cases when  $d$  is as large as 2. Thus, depending on the application, significant errors could result from the infinite rod approximation, even if  $d \geq 2$ .

When the same cooling conditions exist on the inside and outside coil surfaces (i.e., when  $B_{r1} = B_{r2}$ ), average and maximum temperature rises for toroidal coils are very accurately predicted by the infinite rod approximation independent of the curvature. However, the location of maximum temperature rise varies significantly, moving outward with increasing  $B_{r1} = B_{r2}$  and increasing  $d$ . This interesting case, which appears to minimize curvature effects, exists when the ratio of heat transferred across the boundaries (per unit area) to the heat generated (per unit volume) is independent of  $d$ . Because the ratio of surface area to volume for the toroidal coil is constant, the condition  $B_{r1} = B_{r2}$  assures such a heat balance independent of the curvature.

### Design Aids

In essence, Figs. 2-6 provide ratios between radial parameters and analogous parameters for the infinite rectangular rod that can be used with previously published results [8, 9] to determine the solution for toroidal coils. For completeness, previously published plots for  $\gamma$  and  $\xi_z$  are repeated in Figs. 7 and 8, and addi-

<sup>4</sup>This use of boundary conditions is a mathematical artifice (without loss of generality) to reference the solution to the case of zero curvature, and should not be interpreted as representing the boundary conditions for any specific coil.

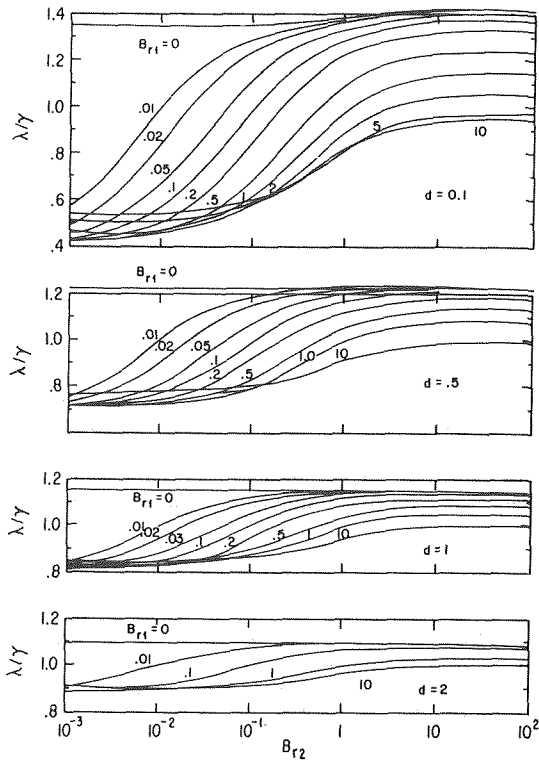


Fig. 2 Variation of  $\lambda/\gamma$  ( $B_{r1} = B_{z1}$ ,  $B_{r2} = B_{z2}$ )

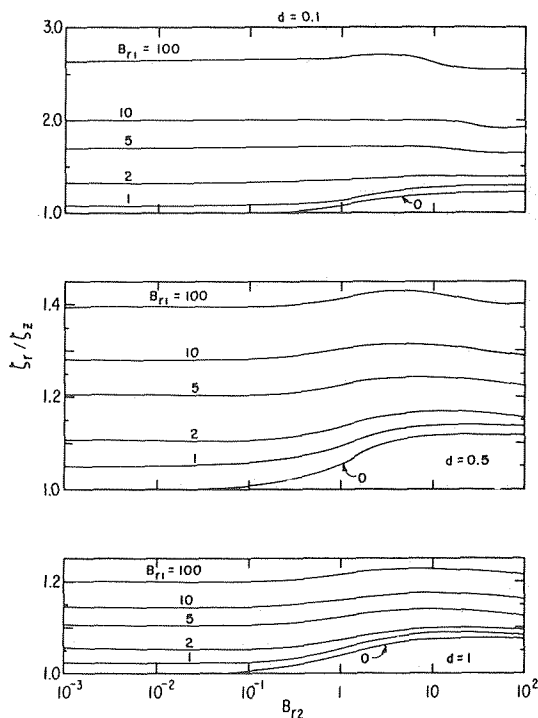


Fig. 3 Variation of  $\zeta_r/\zeta_z$  ( $B_{r1} = B_{z1}$ ,  $B_{r2} = B_{z2}$ )

tional design curves for estimating maximum and average temperature rises are given in Fig. 9. If the ratio of maximum-to-average temperature rise is of interest as a gross measure of the temperature gradient, the designer may obtain a quick estimate of  $\phi_{max}/M_r$  by multiplying  $R$  from Fig. 6 by  $\psi_{max}/M_z$  from Fig. 10 (using  $B_{z1} = B_{r1}$  and  $B_{z2} = B_{r2}$ ).  $\psi_{max}/M_z$  is also determined from Fig. 10 (using  $B_{z1}$  and  $B_{z2}$  for the coil of interest). Then  $\theta_M/\theta_A = (\phi_{max}/M_r)(\psi_{max}/M_z)$ .

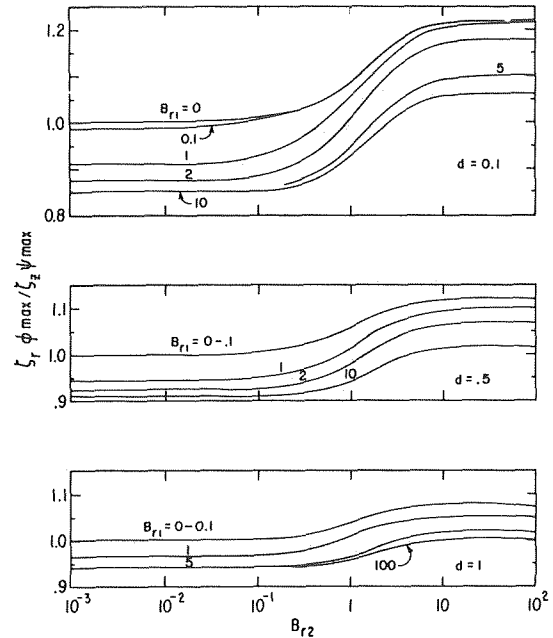


Fig. 4 Maximum temperature parameter ( $B_{r1} = B_{z1}$ ,  $B_{r2} = B_{z2}$ )

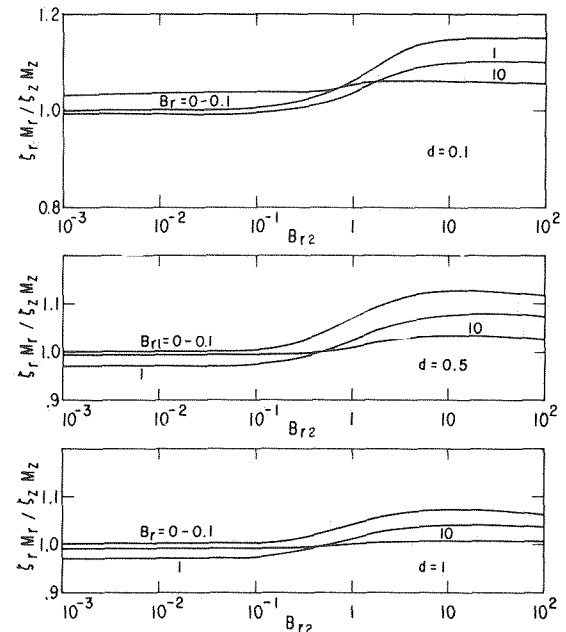


Fig. 5 Average temperature parameter ( $B_{r1} = B_{z1}$ ,  $B_{r2} = B_{z2}$ )

## Examples

Consider the solenoid driven with a constant current condition previously studied in [8, 9]. The input parameters are  $\alpha = 0.0022$  ohm/ohm  $^{\circ}\text{F}$ ,  $q_0 = 318$  Btu/hr ft $^3$ ,  $U_{z1} = U_{z2} = 5$  Btu/hr ft $^2$   $^{\circ}\text{F}$ ,  $U_{r1} = 0$ ,  $U_{r2} = 1$  Btu/hr ft $^2$   $^{\circ}\text{F}$ ,  $l = 4$  ft,  $h = 0.528$  ft,  $k_r = 2$  Btu/hr ft  $^{\circ}\text{F}$ ,  $k_z = 131$  Btu/hr ft  $^{\circ}\text{F}$ ,  $\rho = 166$  lb mass/ft $^3$ , and  $c_p = 0.213$  Btu/hr lb mass  $^{\circ}\text{F}$ . In this case we find that  $B_{r1} = 0$ ,  $B_{r2} = 0.264$ ,  $B_{z1} = B_{z2} = 0.52$ ,  $\kappa = 1.141$ ,  $Q_0 = 44.33$ .

Symmetry in the  $z$  direction and the insulated inner boundary lead to a maximum temperature at  $\eta = 0.5$  and  $\xi = d$ . The steady-state temperature distribution along  $\eta = 0.5$  is within about 5 percent of that for an infinite rod if  $d \geq 5$ . The temperature drops as  $d$  decreases because the ratio of the area across which heat is transferred to the volume of the solenoid (the heat generated is proportional to the volume) increases as the ra-

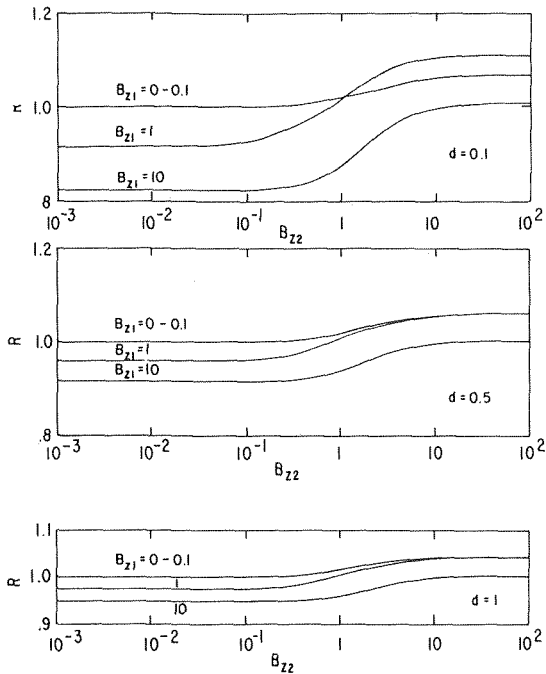


Fig. 6 Variation of  $R$  ( $B_{r1} = B_{z1}$ ,  $B_{r2} = B_{z2}$ )

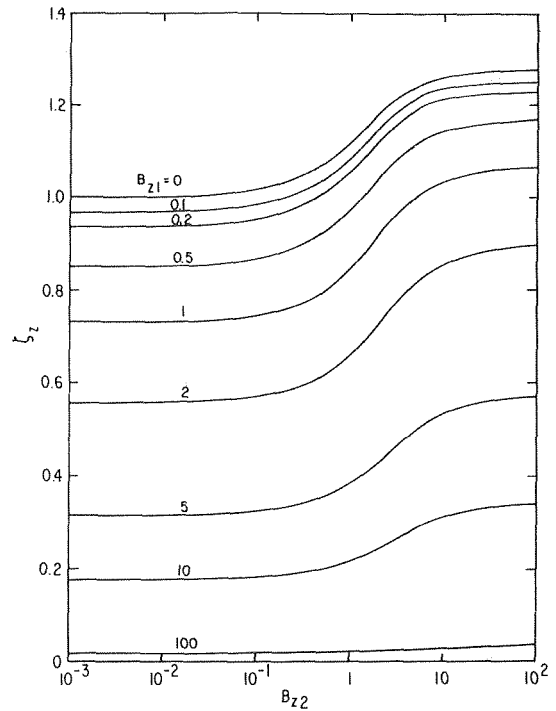


Fig. 8 Variation of  $\zeta_z$

dius of the solenoid decreases. The spatial variation of temperature appears to be independent of  $d$ , and the variation in maximum temperature is almost entirely due to the variation of  $\lambda^2$  as a function of  $d$  (see Fig. 2). Because  $\Delta$  increases with decreasing  $d$ , the thermal time constant decreases with decreasing  $d$  (see Fig. 11).

Suppose that by some means of cooling we can obtain a heat transfer coefficient at the inner boundary of  $U_{r1} = 1$  Btu/hr ft<sup>2</sup> °F ( $B_{r1} = B_{r2} = 0.264$ ). Then the temperature distribution across  $\eta = 0.5$  is given by Fig. 12. Although the spatial variation of temperature varies with  $d$ , details of the infinite rod solution are approximated to within 10 percent for  $d \geq 0.1$ , and the average and peak temperatures are almost independent of  $d$ . As indicated previously, the surface area to volume ratio is a constant in this case; therefore, the heat balance required for a steady state occurs at about the same temperature regardless of the radius of the coil. The thermal time constant is also essentially independent of  $d$  in this case.

### Conclusions

The exact solution for the transient temperature response of a toroidal coil of rectangular cross section has been given in the form of a rapidly convergent doubly infinite eigenfunction expansion.

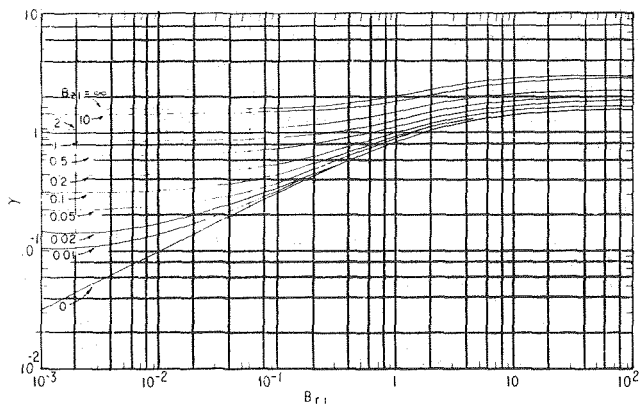


Fig. 7 Variation of  $\gamma$

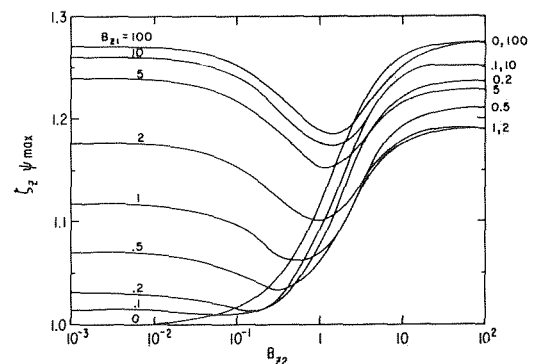


Fig. 9(a)

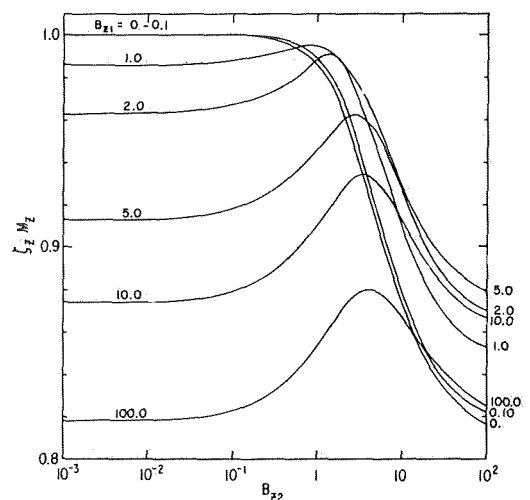


Fig. 9(b)

Fig. 9 Variation of  $\zeta_z \psi_{\max}$  and  $\zeta_z M_z$

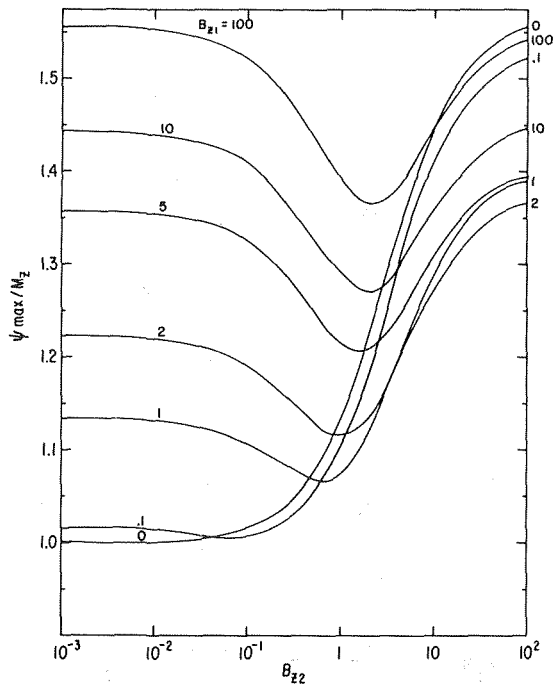


Fig. 10 Ratio of maximum to average temperature rise

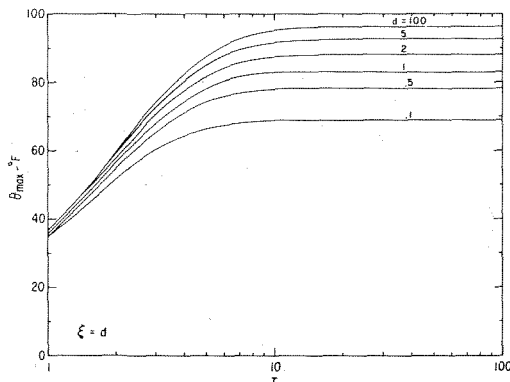


Fig. 11 Temperature rise along  $\eta = 0.5$  for the insulated boundary case

sion. The leading term approximation is generally accurate to within 5 percent, i.e., it is more accurate than one can read the design curves presented.

There is a particular current density for a given solenoid or a coil driven with a constant current condition for which no steady state exists. In reality, no constant current condition can be indefinitely fulfilled because there will be some maximum voltage associated with the particular situation. The temperature is always bounded in the constant voltage case for  $\alpha > 0$ ; and, when  $|\alpha\theta| \ll 1$ , the solution is given approximately by the results presented here with  $\alpha$  replaced by  $-\alpha$ .

The shape of the temperature distribution across a given solenoid is quite insensitive to changes in the resistance-temperature coefficient  $\alpha$ , the normalized heat generation density  $Q_0 = q_0 h^2 / k_r$ , the ratio  $\kappa = k_z h^2 / k_r l^2$  and the normalized time  $\tau = k_r t / c_p h^2$ . The variation in the temperature distribution shape because of changes in these variables is expected to be less than 5 percent. In particular, the ratio of the maximum-to-average temperature rise is determined primarily by the boundary conditions.

One cannot make a meaningful general statement as to the accuracy of the assumption of an infinite rod for a coil because the validity of the assumption depends on the particular boundary conditions as well as the curvature. The assumption is quite good for  $B_{r1} = B_{r2}$  and  $d \geq 0.1$  insofar as average and maximum tem-

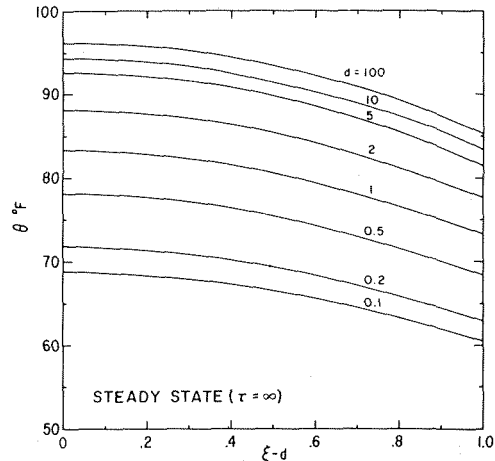


Fig. 12(a)

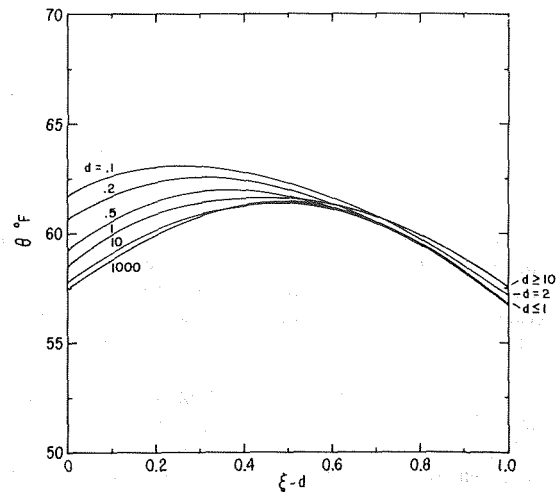


Fig. 12(b)

Fig. 12 Steady-state radial temperature distribution at  $\eta = 0.5$  (same cooling conditions at inner and outer boundaries)

peratures are concerned, but not for the location of the maximum temperature or the precise shape of the temperature distribution. For small Biot numbers, the chief effect of varying the curvature is in changing  $\lambda$ , i.e., the variation of  $\Delta$ . This affects the amplitude of the temperature and the thermal time constant.

The solution for the infinite rod is not necessarily a bound for the true solenoid. In some cases, where it is a bound, it may not be a very good one. Thus, we conclude that the solution for the most realistic case, namely the toroidal coil, should be used by the designer in all cases except  $B_{r1} = B_{r2}$ . Because of the rapid convergence, one need only consider the leading term, and thereby might even write a rather simple computer program to be used by the designer. However, he may apply the design curves presented here and obtain an answer with reasonable speed and accuracy.

## References

- 1 Cockroft, J. D., "The Temperature Distribution in a Transformer or Other Laminated Core of Rectangular Cross-Section in Which Heat is Generated at a Uniform Rate," *Proc. Cambridge Phil. Soc.*, Vol. 22, 1923-1925, pp. 759-772.
- 2 Jakob, M., "Influence of Nonuniform Development of Heat Upon the Temperature Distribution in Electrical Coils and Similar Heat Sources of Simple Form," *TRANS. ASME*, Vol. 65, 1943, pp. 593-605.
- 3 Jakob, M., *Heat Transfer*, Wiley, New York, Vol. I, 1958, pp. 181-192.
- 4 Higgins, T. J., "Formulas for Calculating the Temperature Distribu-

tion in Electrical Coils of General Rectangular Cross Section," TRANS. ASME, Vol. 66, 1944, pp. 665-670.

5 Higgins, T. J., "Formulas for Calculating Temperature Distribution in Transformer Cores and Other Electric Apparatus of Rectangular Cross-Section," TRANS. ASME, Vol. 64, 1945, pp. 190-194.

6 Higgins, T. J., "Temperature Distribution in Toroidal Electrical Coils of Rectangular Cross-Section," *Franklin Institute Journal*, Vol. 240, 1945, pp. 97-112.

7 Carslaw, H. S., and Jaeger, J. C., *Conduction of Heat in Solids*, Second ed., Oxford, New York, 1959, pp. 404-405.

8 Cooper, H. F., "Transient and Steady-State Temperature Distribution in Foil Wound Solenoids and Other Electric Apparatus of Rectangular Cross-Section," *IEEE Trans. on Parts, Materials, and Packaging*, Vol. PMP-2, No. 1/2, Mar.-June 1966, pp. 3-9.

9 Cooper, H. F., "Joule Heating of an Infinite Rectangular Rod With Orthotropic Thermal Properties," JOURNAL OF HEAT TRANSFER, TRANS. ASME, Series C, Vol. 89, No. 1, 1967, pp. 37-43.

10 Abramowitz, M., and Stegun, I. A., *Handbook of Mathematical Functions*, National Bureau of Standards, Applied Math. Series, 55, U.S. Government Printing Office, Washington, 5th Printing, Aug. 1966, p. 485.

G. Ahmadi

School of Engineering,  
Pahlavi University,  
Shiraz, Iran

# Heat Conduction in Solids With Random Initial Conditions

The problem of heat conduction in solids with random initial condition is studied. A general theory is first discussed and several examples are considered. It is observed that the homogeneity of the random initial condition is sufficient for the homogeneity of the temperature field in an unbounded domain. But in bounded domains the random temperature field becomes nonhomogeneous even though the initial condition is homogeneous.

## 1 Introduction

In recent years, there have been increasing applications of probabilistic methods to engineering problems involving random functions. Among the most important in mechanical engineering are the problems of turbulence [1],<sup>1</sup> vibrations and acoustics [2, 3]. It appears, however, that only recently some attention has been given to the problem of heat conduction in solid with random conditions. Samuels [4] stated the possible sources of randomness in a heat conduction problem and solved several one dimensional examples of heat transfer with random boundary conditions and random heat generation. In a recent paper Hung [5] studied the heat transfer of thin fins with stochastic root temperature.

In the present work, the problem of heat conduction in solids with random initial temperature is considered. The general theory in an unbounded domain is discussed and several examples in bounded domains are solved. The correlation functions of the random temperature field are obtained, the variances are calculated and plotted. It is observed that the homogeneity of the random initial condition implies the homogeneity of the random temperature field in an unbounded domain but in bounded regions the stochastic temperature field becomes nonhomogeneous even though the initial field is homogeneous.

## 2 General Theory

Before going to specific problems, we discuss some general features of heat conduction with random initial condition. The basic equation for heat conduction in homogeneous isotropic solids is

$$\frac{\partial T}{\partial t} = k \nabla^2 T. \quad (1)$$

Assuming that the initial condition

$$T|_{t=0} = f(\mathbf{x}) \quad (2)$$

is a random function of space, the temperature distribution be-

comes also a random function. The correlation function of a random field  $f(\mathbf{x})$  with zero mean is defined as

$$R_f(\mathbf{x}_1, \mathbf{x}_2) = \langle f(\mathbf{x}_1)f(\mathbf{x}_2) \rangle, \quad (3)$$

where  $\langle \rangle$  is the expectation operator. The value of the correlation function at  $\mathbf{x}_1 = \mathbf{x}_2 = \mathbf{x}$  is the mean square of the random field at point  $\mathbf{x}$ . The equation governing the dynamics of the temperature correlation is simply obtained by first multiplying equation (1) at  $\mathbf{x}_2$  by  $T(\mathbf{x}_1, t)$ , and furthermore, multiplying equation (1) evaluated at  $\mathbf{x}_1$  by  $T(\mathbf{x}_2, t)$ , and then adding the two resulting equations. The result then becomes

$$\frac{\partial}{\partial t} R_T(\mathbf{x}_1, \mathbf{x}_2, t) = k [(\nabla_1^2 R_T(\mathbf{x}_1, \mathbf{x}_2, t) + \nabla_2^2 R_T(\mathbf{x}_1, \mathbf{x}_2, t))] \quad (4)$$

where  $\nabla_1^2$  and  $\nabla_2^2$  are the Laplacian at  $\mathbf{x}_1$  and  $\mathbf{x}_2$ , respectively. Let

$$\mathbf{x} = \mathbf{x}_2 - \mathbf{x}_1 \quad (5)$$

equation (4) then becomes

$$\frac{\partial R_T}{\partial t}(\mathbf{x}_1, \mathbf{x}_1 + \mathbf{x}, t) = 2k R_T(\mathbf{x}_1, \mathbf{x}_1 + \mathbf{x}, t) \quad (6)$$

which is the basic equation for the dynamics of the correlation function. In an unbounded domain for a homogeneous random field, that is when  $R_T$  is only a function of  $\mathbf{x}$  equation (6) may be easily integrated to give

$$R_T(\mathbf{x}, t) = \frac{kH(t)}{(2k\pi t)^{3/2}} \int \int \int \exp \left\{ -\frac{(x-x')^2 + (y-y')^2 + (z-z')^2}{8kt} \right\} R_f(\mathbf{x}') dx' dy' dz' \quad (7)$$

where  $H(t)$  is the Heaviside unit step function. Equation (7) shows that the correlation function  $R_T(\mathbf{x}, t)$  decays to zero with time.

As an special example let us consider the case of a purely random initial conditions, i.e.,

$$R_f(\mathbf{x}) = S_0 \delta(x) \delta(y) \delta(z) \quad (8)$$

where  $\delta(x)$  is the Dirac delta function.

<sup>1</sup> Numbers in brackets designate References at end of paper.

Contributed by the Heat Transfer Division for publication in the JOURNAL OF HEAT TRANSFER. Manuscript received by the Heat Transfer Division, January 29, 1974. Paper No. 75-HT-E.



The correlation function at time  $t$  then becomes

$$\text{Insert c } R_T(\mathbf{x}, t) = \frac{kS_0H(t)}{(2k\pi l)^{3/2}} \exp\left\{-\frac{x^2 + y^2 + z^2}{8kl}\right\} \quad (9)$$

It is observed that the homogeneity of the initial condition in an unbounded domain implies the homogeneity of the correlation at any later time. Note that the homogeneity of a random variable in space corresponds to the stationarity in time. We now consider some example of heat conduction with random initial conditions which may be of some practical interest.

### 3 One Dimensional Bounded Domain

Consider a thin wire of length  $l$  or an infinite slab of thickness  $l$ , both ends of which are kept at zero temperature. The initial temperature field is assumed to be a random function  $f(x)$  of space with zero mean. In order to find the temperature correlation function we note that the general solution of the one-dimensional heat equation

$$\frac{\partial T}{\partial t} = k \frac{\partial^2 T}{\partial x^2} \quad (10)$$

with boundary conditions

$$T|_{x=0} = T|_{x=l} = 0 \quad (11)$$

and initial condition

$$T|_{t=0} = f(x) \quad (12)$$

is [6]

$$T(x, t) = \frac{2}{l} \sum_{n=1}^{\infty} \sin \frac{n\pi x}{l} \exp\{-kn^2\pi^2 t/l^2\} \int_0^l f(x') \sin \frac{n\pi x'}{l} dx' \quad (13)$$

The correlation function then becomes

$$R_T(x, x_1) = \frac{4}{l^2} \sum_{n=1}^{\infty} \sum_{m=1}^{\infty} \sin \frac{n\pi x}{l} \sin \frac{m\pi x_1}{l} \exp\{-k(n^2 + m^2)\pi^2 t/l^2\} \int_0^l \int_0^l R_f(x', x_1') \sin \frac{n\pi x'}{l} \sin \frac{m\pi x_1'}{l} dx' dx_1' \quad (14)$$

Assuming now that  $f(x)$  is a purely random function i.e.,

$$R_f(x, x_1) = R_f(x - x_1) = S_0 \delta(x - x_1) \quad (15)$$

Employing (15) into equation (14) we find

$$R_T(x, x_1, t) = \frac{2S_0}{l} \sum_{n=1}^{\infty} \sin \frac{n\pi x}{l} \sin \frac{n\pi x_1}{l} \exp\{-2kn^2\pi^2 t/l^2\} \quad (16)$$

which is the expression for the correlation function. Note that although the initial temperature distribution  $f(x)$  is a homogeneous random function the temperature field at time  $t$  is not homogeneous. This is of course due to the effect of the deterministic boundary conditions imposed on the problem.

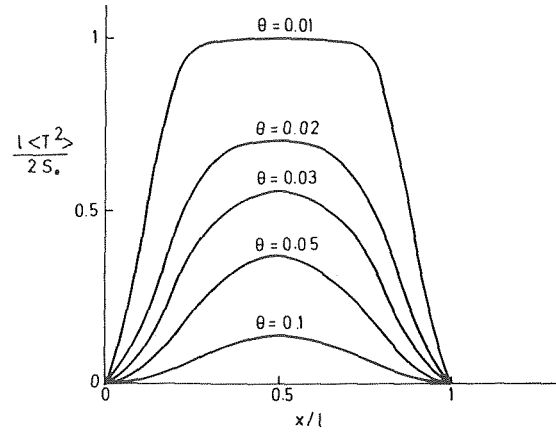


Fig. 1 The variation of the mean square temperature with  $x/l$  and  $\theta = kt/l^2$

The mean square of the temperature distribution is

$$\langle T^2(x, t) \rangle = R_T(x, x, t) = \frac{2S_0}{l} \sum_{n=1}^{\infty} \sin^2 \frac{n\pi x}{l} \exp\{-2kn^2\pi^2 t/l^2\} \quad (17)$$

Fig. 1 shows the variation of the mean square temperature with space and time.

### 4 Semi-Infinite Solid

Consider a semi-infinite solid whose temperature at  $x = 0$  is kept at a constant temperature which is assumed to be zero. The initial temperature field is assumed to be a homogeneous random function  $f(x)$  with given correlation function  $R_f(x_1 - x_2)$ . The general solution for the temperature field is [6]

$$T(x, t) = \frac{1}{2\sqrt{\pi kt}} \int_0^{\infty} f(x') [\exp\{-(x - x')^2/4kt\} - \exp\{-(x + x')^2/4kt\}] dx' \quad (18)$$

The temperature correlation function then becomes

$$R_T(x, x_1, t) = \frac{1}{4\pi kt} \int_0^{\infty} dx' \int_0^{\infty} dx_1' R_f(x', x_1') \times [\exp\{-(x - x')^2/4kt\} - \exp\{-(x + x')^2/4kt\}] \times [\exp\{-(x_1 - x_1')^2/4kt\} - \exp\{-(x_1 + x_1')^2/4kt\}] \quad (19)$$

For purely random initial condition. i.e.,

$$R_f(x, x_1) = S_0 \delta(x - x_1) \quad (20)$$

the correlation function becomes

$$R_T(x, x_1, t) = \frac{S_0}{\sqrt{8\pi kt}} [\exp\{-\frac{(x - x_1)^2}{8kt}\} - \exp\{-\frac{(x + x_1)^2}{8kt}\}] \quad (21)$$

The variance of the temperature field at point  $x$  and at time  $t$  is

### Nomenclature

$G_0$  = constant  
 $H(t)$  = Heaviside unit step function  
 $k$  = thermal diffusivity  
 $l$  = length of the wire  
 $R$  = correlation function

$S_0$  = constant  
 $T$  = temperature  
 $t$  = time  
 $x, y, z$  = space coordinates  
 $\delta(x)$  = Dirac delta function

### Subscripts

$T$  = refers to temperature field  
 $f$  = refers to forcing function

$$\langle T^2(x, t) \rangle = \frac{S_0}{\sqrt{8\pi kt}} [1 - \exp\{-\frac{x^2}{2kt}\}] \quad (22)$$

Fig. 2 shows the variation of the variance with space and time.

For a random initial condition whose correlation function is constant, i.e.,

$$R_f(x, x_1) = G_0 \quad (23)$$

equation (19) after the integration yields

$$R_T(x, x_1, t) = G_0 \operatorname{erf}\left(\frac{x}{\sqrt{4kt}}\right) \operatorname{erf}\left(\frac{x_1}{\sqrt{4kt}}\right) \quad (24)$$

The expression of the variance of the temperature field then becomes

$$\langle T^2(x, t) \rangle = G_0 [\operatorname{erf}\left(\frac{x}{\sqrt{4kt}}\right)]^2 \quad (25)$$

the foregoing is being plotted in Fig. 3.

### 5 Three-Dimensional Solid

Let us consider a three-dimensional half space bounded by the plane  $x = 0$  which is kept at zero temperature. The initial temperature is assumed to be given by a homogeneous random function  $f(x, y, z)$  with correlation function

$$R_f(x - x_1, y - y_1, z - z_1) = \langle f(x, y, z)f(x_1, y_1, z_1) \rangle \quad (26)$$

Equation (1) is the basic equation of heat conduction in a homogeneous isotropic solid. The general solution of this equation satisfying the boundary condition at  $x = 0$  and for arbitrary initial condition  $f(x, y, z)$  is [6]

$$T(x, y, z, t) = \frac{1}{8(\pi kt)^{3/2}} \int_0^\infty dx' \int_{-\infty}^{+\infty} dy' \int_{-\infty}^{+\infty} dz' f(x', y', z') \times [\exp\{-\frac{(x-x')^2}{4kt}\} - \exp\{-\frac{(x+x')^2}{4kt}\}] \times \exp\{-\frac{(y-y')^2 + (z-z')^2}{4kt}\} \quad (27)$$

The correlation function of the temperature field may then be obtained by direct substitution of the foregoing into

$$R_T(x, y, z; x_1, y_1, z_1; t) = \langle T(x, y, z, t)T(x_1, y_1, z_1, t) \rangle \quad (28)$$

Assuming that the initial field is completely random, i.e.,

$$\langle f(x, y, z)f(x_1, y_1, z_1) \rangle = S_0 \delta(x - x_1) \delta(y - y_1) \delta(z - z_1) \quad (29)$$

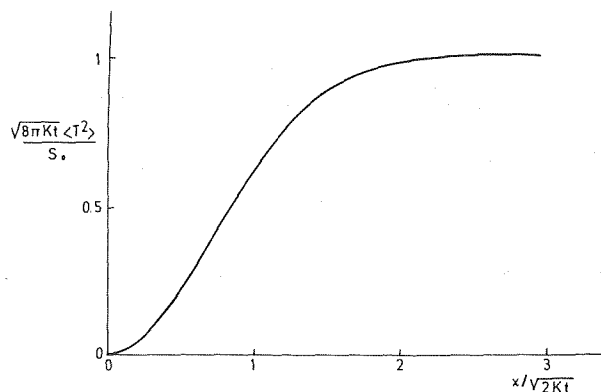


Fig. 2 The variation of the mean square temperature with  $x/\sqrt{2kt}$

The expression for the correlation function of the temperature field becomes

$$R_T(x, y, z; x_1, y_1, z_1, t) = \frac{S_0}{(2\pi kt)^{3/2}} \times \exp\{-\frac{(y-y_1)^2}{8kt}\} (1 + \operatorname{erf}\frac{y+y_1}{\sqrt{8kt}}) \exp\{-\frac{(z-z_1)^2}{8kt}\} \times (1 + \operatorname{erf}\frac{z+z_1}{8kt}) [\exp\{-\frac{(x-x_1)^2}{8kt}\} - \exp\{-\frac{(x+x_1)^2}{8kt}\}] \quad (30)$$

the variance of the temperature field is simply obtained by setting  $x_1, y_1, z_1$  equal to  $x, y, z$ . Then we find

$$\langle T^2(x, y, z, t) \rangle = \frac{S_0}{(2\pi kt)^{3/2}} (1 + \operatorname{erf}\frac{y}{\sqrt{2kt}}) (1 + \operatorname{erf}\frac{z}{\sqrt{2kt}}) \cdot [1 - \exp\{-\frac{x^2}{2kt}\}] \quad (31)$$

For constant  $y$  and  $z$  the foregoing is similar to equation (22) which is the expression for variance in a one-dimensional field.

### 6 Conclusions

In the present work several problems in heat conduction with random initial conditions are solved. The problems considered are an extension of the work carried out by Samuels [4], but they are different from his in a fundamental way. In this paper the case of random initial condition is considered, but in Samuels', the cases of random forcing function and random boundary conditions are discussed. It must be pointed out that heat conduction with random initial condition is of great practical interest, since in most of the practical heat conduction problems, usually, the initial condition is not known, and at best is estimated; it is random in nature.

We conclude the paper by following remarks:

1 Due to the nature of the diffusion equation the effect of the initial condition diminishes gradually with time. For a constant boundary condition the solution of the heat equations approaches that constant independent of the initial condition, even if it is random. Hence as we see from Figs. 1-3 the variance of the temperature field decays to zero asymptotically.

2 The effect of the deterministic boundary conditions is a definite reduction of the variance of the temperature field in the neighborhood of the boundary. This can be clearly seen from Figs. 1-3. The penetration distance of the deterministic boundary conditions as can be seen from Figs. 2 and 3 are approximately  $4\sqrt{kt}$  and  $2\sqrt{kt}$ , respectively. In other words, the effect of the deterministic boundary condition penetrates with a speed proportional to  $1/\sqrt{t}$  into the random field.

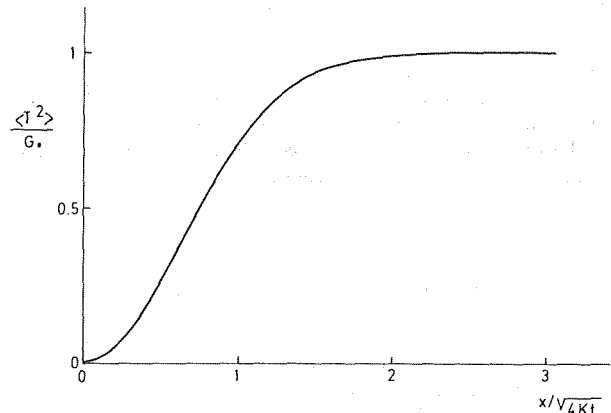


Fig. 3 The variation of the mean square temperature with  $x/\sqrt{4kt}$

## References

- 1 Hinze, J. O., *Turbulence*, McGraw Hill, 1959.
- 2 White, P. H., "Some Useful Approximation for Determining the Vibration of Structures Excited by Random Pressures," *Journal of the Acoustical Society of America*, Vol. 36, 1964.
- 3 Crandall, S. H., and Mark, W. D., *Random Vibration in Mechanical Systems*, Academic Press, New York, 1963.
- 4 Samuels, J. C., "Heat Conduction in Solids With Random External Temperature and/or Random Internal Heat Generation," *International Journal of Heat and Mass Transfer*, Vol. 9, 1966, pp. 301-304.
- 5 Hung, H. M., "Heat Transfer of Thin Fins With Stochastic Root Temperature," *JOURNAL OF HEAT TRANSFER, TRANS. ASME*, 1969, pp. 129-139.
- 6 Carslaw, H. S., and Jaeger, J. C., *Conduction of Heat in Solids*, Oxford University Press, 1959.

## ERRATA

An errata on D. M. France, "Experimental Determination of Sodium Superheat Employing LMFBR Simulation Parameters," published in the Aug., 1974, issue of the JOURNAL OF HEAT TRANSFER, pp. 359-364.

Third paragraph, line three on p. 363, should read:  $P_{L_j}(Z)$  instead of  $P_j(Z)$ .

F. A. Morrison, Jr.

Professor.  
Mem. ASME

L. D. Reed

Research Assistant.

Department of Mechanical and Industrial  
Engineering, University of Illinois at Urbana-  
Champaign, Urbana, Ill.

# Low Knudsen Number Heat Transfer From Two Spheres in Contact

*Heat transfer from an aerosol aggregate composed of two touching spheres is investigated analytically. In the range of interest, the Knudsen number is small and the Peclet number negligible. The Nusselt number of a sphere is found to be reduced by the presence of a neighbor and by temperature jump. Expressions for the Nusselt number are obtained.*

## Introduction

While heat transfer from aerosol particles is a matter of considerable technical interest, there is relatively little analytical work that is directly applicable. The reason appears to be that, unlike the objects of most studies, aerosol particles are characterized by nonvanishing Knudsen numbers and their motion relative to the surrounding gas is characterized by low Reynolds numbers.

Consider, for example, a spherical particle having a radius of 1  $\mu\text{m}$ . This size roughly corresponds to the upper limit of readily respirable particles. These small particulates, when emitted, are difficult to collect and present significant health hazards. The 1- $\mu\text{m}$  radius particle in air at standard conditions has a Knudsen number,  $\text{Kn}$ , of about 0.1. The Knudsen number is the ratio of the molecular mean free path to a characteristic length—the particle radius in this instance. When the Knudsen number is not vanishingly small, continuum analysis does not strictly apply and effects of the finite mean free path become apparent. For small Knudsen number these effects are confined to a region close to the particle surface. Continuum analysis, used with modified boundary conditions to account for gas-surface interactions, is frequently used in this regime to yield expressions valid to the first order in Knudsen number.

A temperature jump at a solid-gas interface results from a normal component of the temperature gradient at the surface. This phenomenon is discussed by Chapman and Cowling [1].<sup>1</sup> The gas temperature near the surface, as elsewhere, is related to the distribution of molecular velocities. The molecules near the surface can be divided into two showers, those approaching and those receding from the surface. For heat transfer calculations the molecules approaching the surface can be considered to originate at an effective distance,  $2\phi'l$ , from the surface.  $\phi'$  is a constant of order unity

while  $l$  is the molecular mean free path. This characteristic length is greater than that associated with momentum transport because of the correlation between a molecule's translational energy and its mean free path.

The molecules receding from the surface may be treated in two groups. In lieu of a detailed examination of gas-solid interaction, the molecules are considered to leave with a fraction,  $a_T$ , having come to thermal equilibrium with the solid and with the remaining fraction thermally unaffected.  $a_T$  is called the thermal accommodation coefficient. Its value depends on the gas-solid combination and on the condition of the surface. Several values are presented by Eckert and Drake [2].

Simply calculating a mean gas temperature at the surface,  $T_g$ , by using the temperatures associated with each of these groups, we find

$$T_g - T_s = 2\phi' \frac{2 - a_T}{a_T} l \frac{dT}{dy} \quad (1)$$

$T_s$  is the surface temperature of the solid and  $dT/dy$  is the normal component of the temperature gradient in the gas. The coefficients are often combined into a single coefficient,  $C_t$ , of order unity and the temperature jump expressed by

$$T_g - T_s = C_t l \frac{dT}{dy} \quad (2)$$

Utilizing this boundary condition in low Knudsen number heat transfer gives a correction of the order of the Knudsen number.

The analysis presented here is not restricted to the particular simple model of the jump coefficient expressed in equation (1). More accurate and sophisticated expressions, e.g., see [3, 4], for the temperature jump coefficient exist and may be directly employed here.

Consider again the 1- $\mu\text{m}$  radius spherical particle. With a density of 1  $\text{g}/\text{cm}^3$ , the particle will settle in still air with a Reynolds number of about  $10^{-5}$ . Since the Prandtl number is of order unity, the Peclet number will also be approximately  $10^{-5}$ . These estimates remain the same for particle motions within most control equipment and sampling devices and for motion in the atmo-

<sup>1</sup>Numbers in brackets designate References at end of paper.

Contributed by the Heat Transfer Division for publication in the JOURNAL OF HEAT TRANSFER. Manuscript received by the Heat Transfer Division February 28, 1974. Paper No. 75-HT-L.

sphere. Because of the very small Peclet numbers, convective contributions to the heat transfer from such particles are normally considered negligible. Convective effects are insignificant when compared with the effects arising from nonzero Knudsen number.

For larger particles possessing larger Peclet numbers and smaller Knudsen numbers, the effects of convection become increasingly important. Acrivos and Taylor [5] analyzed small Peclet number heat transfer from a single sphere in the Stokes flow regime. This analysis was extended by Rimmer [6] to Reynolds numbers near unity by using the Proudman and Pearson [7] expansion for the velocity field.

Taylor [8] extended the analysis of Acrivos and Taylor to the small Knudsen number regime by including the effects of fluid slip and temperature jump at the surface of the sphere. For zero Peclet number, only the temperature jump has any effect. In this limit Taylor's expression for the Nusselt number is equivalent to a result of Kavanau [9]. In our notation the Nusselt number based on particle diameter  $2a$  is

$$\text{Nu} = \frac{2}{1 + C_t l/a} \quad (3)$$

which, to first order in the Knudsen number, is

$$\text{Nu} = 2(1 - C_t l/a) \quad (4)$$

Equation (3), valid for low Knudsen number conduction heat transfer from a sphere, is particularly easy to obtain because the temperature gradient is uniform over the surface.

Here we wish to examine the low Knudsen number conduction heat transfer from a nonspherical aerosol particle. An aggregate of two touching spheres is of interest because of the frequent observations of such agglomerates. These doublets may also be readily produced by atomization of a suspension of spheres in a volatile solvent.

It is instructive to consider first the conduction heat transfer from a pair of spheres to an infinite medium in the absence of a temperature jump. The result may be obtained by analogy from an analysis of Russell [10], who determined the capacitance of two closely spaced spherical conductors. Aside from a brief mention by Cornish [11], this result does not seem to be known in the heat transfer literature. Because we can readily treat spheres of disparate sizes and because the approach is considerably simpler than that of Russell, we prepare the background for the low Knudsen number analysis by briefly considering this case.

### Heat Transfer Without Temperature Jump

A pair of spheres in contact, external to one another, are immersed in an infinite medium. We consider the steady conduction heat transfer from these spheres to the medium. The effect of a temperature jump is not included. We determine the influence of a

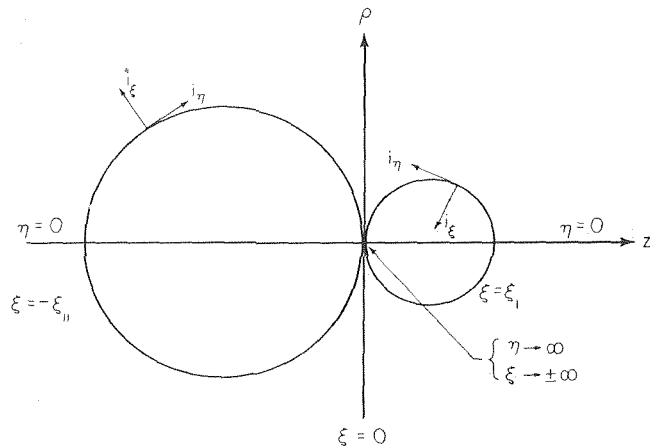


Fig. 1 Tangent sphere coordinates

spherical, touching neighbor on the Nusselt number of a sphere.

The conduction heat transfer through the surrounding medium is governed by Laplace's equation,  $\nabla^2 T = 0$ , with temperature  $T_s$  at the spheres' surfaces and a temperature asymptotically approaching  $T_\infty$  as the distance from the spheres increases without bound.

The shape of the bounding surfaces suggests the use of tangent sphere coordinates. The tangent sphere coordinate system [12]  $(\eta, \xi, \phi)$  is a rotational orthogonal curvilinear coordinate system. The relation to cylindrical coordinates  $(z, \rho, \phi)$  is

$$z = \frac{\xi}{\xi^2 + \eta^2}, \quad \rho = \frac{\eta}{\xi^2 + \eta^2}, \quad \phi = \phi \quad (5)$$

The metric coefficients are

$$h_\eta = h_\xi = \frac{1}{\xi^2 + \eta^2}, \quad h_\phi = \frac{\eta}{\xi^2 + \eta^2} \quad (6)$$

The  $\xi$  coordinate surfaces are spheres of radius  $|2\xi|^{-1}$  with centers on the axis of revolution at  $z = (2\xi)^{-1}$ . Fig. 1 shows the intersection of two such surfaces with a meridian plane.

Laplace's equation is  $R$ -separable in tangent sphere coordinates. A solution of sufficient generality for our purpose is

$$\frac{T - T_\infty}{T_s - T_\infty} = (\xi^2 + \eta^2)^{1/2} \int_0^\infty [c_1(\lambda) \cosh \lambda \xi + c_2(\lambda) \sinh \lambda \xi] J_0(\lambda \eta) d\lambda \quad (7)$$

$J_0(\lambda \eta)$  is a Bessel function of the first kind of order zero.

The coefficients  $c_1$  and  $c_2$  are functions of  $\lambda$  and are found by setting  $T$  equal to  $T_s$  on each spherical surface. The spheres, de-

### Nomenclature

$A$  = sphere surface area  
 $a$  = sphere radius  
 $a_T$  = thermal accommodation coefficient  
 $C_t = 2\phi'(2 - a_T)/a_T$   
 $c_i$  = coefficients defined by equation (7)  
 $c_{i,j}$  = coefficients defined by equations (33) and (34)  
 $F$  = function defined by equation (24)  
 $h$  = heat transfer coefficient  
 $I$  = integral defined by equation (26)  
 $k$  = thermal conductivity  
 $l$  = mean free path  
 $\text{Nu}$  = Nusselt number  
 $\dot{Q}$  = heat transfer rate

$q$  = heat flux  
 $T$  = temperature  
 $x$  = dummy variable  
 $y$  = distance from wall  
 $z$  = axial position in cylindrical coordinates  
 $\gamma$  = Euler's constant  
 $\eta$  = tangent sphere coordinate defined by equation (5)  
 $\lambda$  = dummy variable  
 $\xi$  = tangent sphere coordinate defined by equation (5), having spherical coordinate surface

$\rho$  = radial position in cylindrical coordinates  
 $\phi$  = angular position in cylindrical coordinates  
 $\phi'$  = constant related to temperature jump  
 $\psi$  = psi function

### Subscripts

$g$  = gas at surface  
 $s$  = solid  
 $\infty$  = far from particle  
 $I, II$  = denote spheres

noted by I and II, respectively, are shown in Fig. 1 and are not presumed to have equal size. Their surfaces correspond to  $\xi$  equal to  $\xi_I$  and to  $-\xi_{II}$ .

Using the relation

$$(\xi^2 + \eta^2)^{-1/2} = \int_0^\infty \exp(-\lambda|\xi|) J_0(\lambda\eta) d\lambda \quad (8)$$

and imposing the specified temperature boundary condition on equation (7) at spheres I and II in turn, we find

$$c_1 \cosh \lambda \xi_I + c_2 \sinh \lambda \xi_I = \exp(-\lambda \xi_I) \quad (9)$$

$$c_1 \cosh \lambda \xi_{II} - c_2 \sinh \lambda \xi_{II} = \exp(-\lambda \xi_{II}) \quad (10)$$

Solving,

$$c_1 = \frac{\exp(-\lambda \xi_I) \sinh \lambda \xi_{II} + \exp(-\lambda \xi_{II}) \sinh \lambda \xi_I}{\sinh \lambda (\xi_I + \xi_{II})} \quad (11)$$

and

$$c_2 = \frac{\exp(-\lambda \xi_I) \cosh \lambda \xi_{II} - \exp(-\lambda \xi_{II}) \cosh \lambda \xi_I}{\sinh \lambda (\xi_I + \xi_{II})} \quad (12)$$

The temperature distribution has been determined.

The rate of heat transfer from one of the spheres—say, sphere I—can now be calculated. The heat transfer rate per unit area from sphere I is

$$q = k(\nabla T)_t|_I = \frac{k}{h_t} \frac{\partial T}{\partial \xi} \Big|_I \quad (13)$$

$k$  is the thermal conductivity. The sign results from the direction of the  $\xi$  unit vector at the surface. See Fig. 1. The total heat transfer rate from the sphere is

$$\dot{Q} = \int_{A_I} q dA = 2\pi k \int_0^\infty \frac{\rho h_\eta}{h_t} \frac{\partial T}{\partial \xi} \Big|_I d\eta \quad (14)$$

The integral over the surface is evaluated using equations (5) and (6) and the temperature gradient determined from equation (7). The definite integrals,

$$\int_0^\infty \frac{\eta J_0(\lambda\eta)}{(\xi^2 + \eta^2)^{1/2}} d\eta = \lambda^{-1} \exp(-\lambda\xi) \quad (15)$$

and

$$\int_0^\infty \frac{\eta J_0(\lambda\eta)}{(\xi^2 + \eta^2)^{3/2}} d\eta = |\xi|^{-1} \exp(-\lambda\xi) \quad (16)$$

are also employed. The result is

$$\dot{Q} = 2\pi k (T_s - T_\infty) \int_0^\infty (c_1 + c_2) d\lambda \quad (17)$$

Equating this expression to

$$\dot{Q} = h_I A_I (T_s - T_\infty) = \pi h_I (T_s - T_\infty) / \xi_I^2 \quad (18)$$

where  $h$  is the heat transfer coefficient, and then rearranging, we find the Nusselt number for sphere I. The Nusselt number, based on the diameter of sphere I, is

$$Nu_I = \frac{h_I}{k \xi_I} = 2 \xi_I \int_0^\infty (c_1 + c_2) d\lambda \quad (19)$$

The coefficients are given by equations (11) and (12). The integral can be expressed in terms of a well tabulated function. The result of integration is

$$Nu_I = \frac{-2\xi_I}{\xi_I + \xi_{II}} \left[ \psi\left(\frac{\xi_I}{\xi_I + \xi_{II}}\right) + \gamma \right] \quad (20)$$

$\psi$  is the psi function or digamma function. Its properties are described in [13].  $\gamma$  is Euler's constant,

$$\gamma = 0.5772156649 \dots$$

and is described and given to 25 places in [13]. The final form of the result is expressed in terms of the radii,  $a_I$  and  $a_{II}$ , of spheres I and II. The Nusselt number of sphere I is

$$Nu_I = \frac{-2a_{II}}{a_I + a_{II}} \left[ \psi\left(\frac{a_{II}}{a_I + a_{II}}\right) + \gamma \right] \quad (21)$$

We may now examine a few special cases. A solitary sphere I results from letting  $a_{II}$  approach zero. Since  $\lim_{x \rightarrow 0} x \psi(x) = -1$ , we recover the well known result that the conduction heat transfer Nusselt number of a single sphere is 2. The presence of a neighboring body at the same temperature will, in all cases, result in a lower Nusselt number.

The case of equal spheres, also corresponding to a sphere resting on an insulating plane, yields

$$Nu_I = 2 \ln 2 \quad (22)$$

since  $\psi(1/2)$  is  $-\gamma - 2 \ln 2$ . The effect of temperature jump on this heat transfer is examined in detail in the next section.

Finally,  $\psi(1)$  is  $-\gamma$  so that the Nusselt number of sphere I vanishes as the size of sphere II increases without bound.

The effect, expressed in equation (21), of a neighboring sphere on the conduction heat transfer from a sphere is shown in Fig. 2.

### Heat Transfer With Temperature Jump

The effect of a small Knudsen number on conduction heat transfer through a gas is expressed in terms of a temperature jump at the surface. This boundary condition, equation (2), becomes, using equation (6)

$$T_g - T_s = \mp C_t l (\xi^2 + \eta^2) \frac{\partial T}{\partial \xi} \quad (23)$$

at the sphere surfaces. The upper sign refers to sphere I and the lower sign to sphere II. This convention will be retained throughout. Both spheres are assumed to have the same thermal accommodation coefficient, although this restriction is easily relaxed.

It should be noted that use of the temperature jump boundary condition implicitly presumes that the molecules approaching any element of surface come from an effectively infinite expanse of gas. Each of the spherical surfaces, however, is partially shielded by the other sphere. The effect of this shielding is expected to be small for two reasons. First, we have restricted the analysis to small Knudsen numbers so that molecules impinging on the surface have typically traveled comparatively small distances and the shielding effect is thus limited to the surface near the contact point. Second,

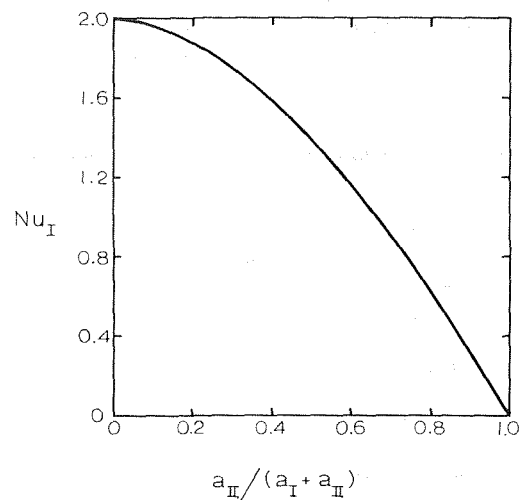


Fig. 2 Effect of a neighboring sphere on the conduction heat transfer from a sphere

temperature gradients in the region of the contact point must be small, contribute little to the overall heat transfer, and produce a relatively small temperature jump.

The temperature distribution in the gas may again be expressed by equation (7). Proceeding as before, we apply the boundary condition at each sphere in turn. Using

$$F(\lambda, \xi) \equiv c_1(\lambda) \cos h \lambda \xi + c_2(\lambda) \sinh \lambda \xi \quad (24)$$

and equation (8), we obtain

$$\int_0^\infty [F(\lambda, \xi) - \exp(-\lambda |\xi|)] J_0(\lambda \eta) d\lambda = \mp C_t l \int_0^\infty [\xi F(\lambda, \xi) + (\xi^2 + \eta^2) \frac{\partial}{\partial \xi} F(\lambda, \xi)] \cdot J_0(\lambda \eta) d\lambda \quad (25)$$

at  $\xi$  equal to  $\xi_I$  and  $-\xi_{II}$ , respectively.

Because of the presence, on the right-hand side of (25), of the integral

$$I = \int_0^\infty \frac{\partial}{\partial \xi} F(\lambda, \xi) \eta^2 J_0(\lambda \eta) d\eta \quad (26)$$

further rearrangement must precede the extraction of a differential equation governing the coefficients in  $F(\lambda, \xi)$ . Since  $J_0(\lambda \eta)$  satisfies Bessel's equation

$$\lambda \frac{\partial}{\partial \lambda} \left[ \lambda \frac{\partial}{\partial \lambda} J_0(\lambda \eta) \right] + \eta^2 \lambda^2 J_0(\lambda \eta) = 0 \quad (27)$$

we may write the integral as

$$I = - \int_0^\infty \frac{\partial}{\partial \xi} F(\lambda, \xi) \frac{1}{\lambda} \frac{\partial}{\partial \lambda} \left[ \lambda \frac{\partial}{\partial \lambda} J_0(\lambda \eta) \right] d\lambda \quad (28)$$

Now, integrating by parts repeatedly and using the definition (24) of  $F(\lambda, \xi)$ , there results

$$I = - \int_0^\infty \frac{\partial}{\partial \lambda} \left\{ \lambda \frac{\partial}{\partial \lambda} \left[ \frac{1}{\lambda} \frac{\partial}{\partial \xi} F(\lambda, \xi) \right] \right\} J_0(\lambda \eta) d\lambda \quad (29)$$

Substituting into (25), the boundary condition becomes

$$F(\lambda, \xi) \pm C_t l \xi (F(\lambda, \xi) + \xi \frac{\partial}{\partial \xi} F(\lambda, \xi) - \frac{1}{\xi} \frac{\partial}{\partial \lambda} \left[ \lambda \frac{\partial}{\partial \lambda} \left[ \frac{1}{\lambda} \frac{\partial}{\partial \xi} F(\lambda, \xi) \right] \right]) = \exp(-\lambda |\xi|) \quad (30)$$

at each surface. Accordingly, in place of equations (9) and (10), we have

$$c_1 \cosh \lambda \xi_I + c_2 \sinh \lambda \xi_I - C_t l \left[ \frac{dc_1}{d\lambda} (\sinh \lambda \xi_I + 2\lambda \xi_I \cosh \lambda \xi_I) + \lambda \frac{d^2 c_1}{d\lambda^2} \sinh \lambda \xi_I + \frac{dc_2}{d\lambda} (\cosh \lambda \xi_I + 2\lambda \xi_I \sinh \lambda \xi_I) + \lambda \frac{d^2 c_2}{d\lambda^2} \cosh \lambda \xi_I \right] = \exp(-\lambda \xi_I) \quad (31)$$

and

$$c_1 \cosh \lambda \xi_{II} - c_2 \sinh \lambda \xi_{II} - C_t l \left[ \frac{dc_1}{d\lambda} (\sinh \lambda \xi_{II} + 2\lambda \xi_{II} \cosh \lambda \xi_{II}) + \lambda \frac{d^2 c_1}{d\lambda^2} \sinh \lambda \xi_{II} - \frac{dc_2}{d\lambda} (\cosh \lambda \xi_{II} + 2\lambda \xi_{II} \sinh \lambda \xi_{II}) - \lambda \frac{d^2 c_2}{d\lambda^2} \cosh \lambda \xi_{II} \right] = \exp(-\lambda \xi_{II}) \quad (32)$$

Fortunately, there is no need to seek an exact solution of these equations to yield  $c_1$  and  $c_2$  as functions of  $\lambda$ . The boundary condition, equation (23), is valid only to first order in the Knudsen number. Consequently, there is no reason to seek a solution to equations (31) and (32) that is valid to any higher order. Accord-

ingly, we express the coefficients in terms of an expansion in powers of  $C_t l / a_I$  or equivalently,  $2C_t l \xi_I$ .

$$c_1 = c_{1,0} + 2C_t l \xi_I c_{1,1} + \dots \quad (33)$$

$$c_2 = c_{2,0} + 2C_t l \xi_I c_{2,1} + \dots \quad (34)$$

The zeroth order coefficients,  $c_{1,0}$  and  $c_{2,0}$ , are given by equations (11) and (12). The first order corrections,  $c_{1,1}$  and  $c_{2,1}$ , are then found by substituting into equations (31) and (32), gathering terms of first power in  $2C_t l \xi_I$  and then solving the resultant set of linear algebraic equations. Finally, substitution into equation (19), followed by appropriate integration, yields the Nusselt number of sphere I. We present detailed results only for the case of equal sized spheres.

For equal sized spheres,

$$\xi_I = \xi_{II} \equiv \xi_0 \quad (35)$$

so that

$$c_2 = 0 \quad (36)$$

and the zeroth order coefficient,  $c_{1,0}$ , reduces to

$$c_{1,0} = \frac{2}{1 + \exp(2\lambda \xi_0)} \quad (37)$$

Substituting equations (33) and (35)–(37) into either equation (31) or (32), we find the first order correction

$$c_{1,1} = \frac{2 \exp(2\lambda \xi_0) [1 - 8\lambda \xi_0 \exp(2\lambda \xi_0) - \exp(4\lambda \xi_0)]}{[1 + \exp(2\lambda \xi_0)]^4} \quad (38)$$

With these terms, equations (33) and (36) are substituted into equation (19), the expression for the Nusselt number. The result reduces to

$$\text{Nu} = 2 \ln 2 - C_t \frac{l}{a} \left( \frac{1}{2} + 8 \int_0^\infty \frac{x \exp(2x)}{[1 + \exp(x)]^4} dx \right)$$

The final integral is evaluated numerically using Gaussian quadrature. The Nusselt number for a sphere with an identical neighbor is

$$\text{Nu} = 2 \ln 2 - 1.091 \cdot C_t \frac{l}{a}$$

## Conclusions

Conduction heat transfer from an aggregate of two touching spheres at small Knudsen number has been analyzed. The effects of the neighboring sphere and of temperature jump are to reduce the Nusselt number of either sphere. For a pair of equal sized spheres, a numerical result was obtained. For small particles as are treated here, convection effects are negligible.

## References

- 1 Chapman, S., and Cowling, T. G., *The Mathematical Theory of Non-Uniform Gases*, Cambridge University Press, Cambridge, 1952.
- 2 Eckert, E. R. G., and Drake, R. M., Jr., *Analysis of Heat and Mass Transfer*, McGraw-Hill, New York, 1972.
- 3 Loyalka, S. K., "Momentum and Temperature-Slip Coefficients With Arbitrary Accommodation at the Surface," *Journal Chem. Physics*, Vol. 48, 1968, pp. 5432–5436.
- 4 Loyalka, S. K., "Approximate Method in the Kinetic Theory," *Physics of Fluids*, Vol. 14, 1971, pp. 2291–2294.
- 5 Acrivos, A., and Taylor, T. D., "Heat and Mass Transfer From Single Spheres in Stokes Flow," *Physics of Fluids*, Vol. 5, 1962, pp. 387–394.
- 6 Rimmer, R. L., "Heat Transfer From a Sphere in a Stream of Small Reynolds Number," *Journal Fluid Mechanics*, Vol. 32, 1968, pp. 1–7; "Corrigenda," Vol. 35, 1969, pp. 827–829.
- 7 Proudman, I., and Pearson, J. R. A., "Expansions at Small Reynolds Numbers for the Flow Past a Sphere and a Circular Cylinder," *Journal Fluid Mechanics*, Vol. 2, 1957, pp. 237–262.



- 8 Taylor, T. D., "Heat Transfer From Single Spheres in a Low Reynolds Number Slip Flow," *Physics of Fluids*, Vol. 6, 1963, pp. 987-992.
- 9 Kavanau, L. L., "Heat Transfer From Spheres to a Rarified Gas in Subsonic Flow," *TRANS. ASME*, Vol. 77, 1955, pp. 617-623.
- 10 Russell, A., "The Coefficients of Capacity and the Mutual Attractions or Repulsions of Two Electrified Spherical Conductors When Close Together," *Proceedings of the Royal Society*, Vol. A32, 1909, pp. 524-531.
- 11 Cornish, A. R. H., "Note on Minimum Possible Rate of Heat Transfer From a Sphere When Other Spheres are Adjacent to It," *Trans. Instn. Chem. Engrs.*, Vol. 43, 1965, pp. 332-333.
- 12 Moon, P., and Spencer, D. E., *Field Theory Handbook*, Springer-Verlag, Berlin, 1961.
- 13 Abramowitz, M., and Stegun, I. A., eds., *Handbook of Mathematical Functions*, U.S. Government Printing Office, Washington, D.C., 1964.

M. F. Modest<sup>1</sup>  
National Aeronautics and  
Space Administration,  
Lyndon B. Johnson Space Center,  
Houston, Texas

# Two-Dimensional Radiative Equilibrium of a Gray Medium in a Plane Layer Bounded by Gray Nonisothermal Walls

*Radiative equilibrium temperature and surface heat flux distributions are calculated for an absorbing-emitting gray medium in an infinite plane layer bounded by gray diffuse walls with arbitrary temperature distributions. Superposition is used to obtain the solution for the differential approximation, which yields good accuracy for the optically thick medium. To also obtain accurate results for optically thin and intermediate regimes, the differential approximation is subsequently improved by a number of geometrical parameters, which are derived from the exact expression for the intensity. As an example, the case of constant temperature at the upper wall and a temperature step at the lower wall without heat generation in the medium is presented. Comparison with other available results shows excellent agreement.*

## Introduction

Due to its mathematical complexity only very few studies of radiative transfer in absorbing-emitting media have been concerned with two and three-dimensional problems. Some numerical calculations have been performed by use of the Monte-Carlo method [1, 2]<sup>2</sup> and Hottel's zonal method [3, 4]. Recently Breig and Crosbie presented some two-dimensional numerical solutions for a semi-infinite medium [5, 6] and for a plane layer [7]. However, numerical computations generally require a large amount of computer time and are not necessarily very accurate.

The first approximate analysis was introduced by Taitel [8] for the case of an infinite plane layer bounded by walls with a single step in surface temperature. An iterative integral method was used which yields accurate results for relatively small optical thickness. Olfe [9] discussed several approximate methods of solution for radiative equilibrium in a semi-infinite medium with sinusoidal wall temperature. Recently Glatt and Olfe [10] presented temperature calculations for a rectangular enclosure based on a simplified version of the modified differential approximation developed by Olfe [11].

The present study is concerned with the infinite plane layer

bounded by gray diffuse walls with arbitrary temperature distribution. The solution for the differential approximation is found by use of superposition (Duhamel's integral), which yields good accuracy for optically thick situations. To obtain accurate results for all optical thicknesses, the emission term in the exact expression for the intensity is expanded into a truncated Taylor series. This results in a number of geometrical parameters, which are used to improve the results of the differential approximation.

To demonstrate the simplicity and accuracy of the present model, the case of constant temperature at the upper wall and a single step in temperature at the lower wall is treated in detail. Comparison with other available results [1, 8] shows excellent agreement.

## Solution for the Differential Approximation

The ordinary differential approximation (Eddington approximation) assumes an isotropic intensity distribution in the absorbing-emitting medium. It, therefore, describes accurately the radiative heat transfer in optically sufficiently thick situations. For a gray gas at radiative equilibrium, the heat flux  $\bar{q}^*$  and integrated intensity  $I_0^*$  satisfy the following equations:

$$\nabla \cdot \bar{q}^* = -\alpha(u_0^* - 4\pi B^*) = S \quad (1)$$

$$\nabla I_0^* = -3\alpha \bar{q}^* \quad (2)$$

where the asterisk denotes values obtained from the differential approximation,  $B = \sigma T^4/\pi$  is the Planck function,  $\alpha$  is the constant absorption coefficient and  $S$  is heat generation per unit volume if present. The appropriate boundary conditions are at any wall:

<sup>1</sup>Postgraduate Research Associate of the National Research Council, currently at the Division of Engineering, San Francisco, State University, San Francisco, Calif.

<sup>2</sup>Numbers in brackets designate References at end of paper.

Contributed by the Heat Transfer Division for publication in the JOURNAL OF HEAT TRANSFER. Manuscript received by the Heat Transfer Division, January 21, 1974. Paper No. 75-HT-G.

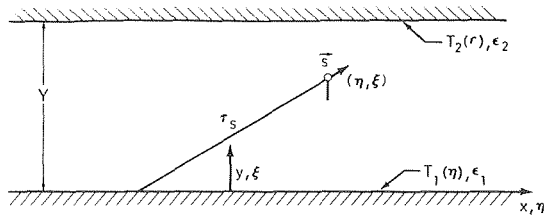


Fig. 1 Geometry and notation

$$2\vec{q}^* \cdot \vec{n} = \frac{\epsilon}{2 - \epsilon} (4\sigma T_w^4 - I_0^*) \quad (3)$$

where  $\vec{n}$  is the outward surface normal and  $\epsilon$  is the surface emissivity.

The heat flux can be eliminated from equations (1) and (2) so that for two dimensions in cartesian coordinates:

$$Y^2 \nabla^2 I_0^* = \frac{\partial^2 I_0^*}{\partial \eta^2} + \frac{\partial^2 I_0^*}{\partial \xi^2} = -3 \frac{S\tau_0^2}{\alpha} \quad (4)$$

where  $\eta = x/Y$ ,  $\xi = y/Y$ , and  $\tau_0 = \alpha Y$  is the optical distance between the parallel plates (Fig. 1). The boundary conditions for equation (4) become:

$$\text{Lower wall } \xi = 0: \quad \frac{\partial I_0^*}{\partial \xi} = -\frac{3}{2} \tau_0 \frac{\epsilon_1}{2 - \epsilon_1} (4\sigma T_1^4 - I_0^*) \quad (5)$$

$$\text{Upper wall } \xi = 1: \quad \frac{\partial I_0^*}{\partial \xi} = \frac{3}{2} \tau_0 \frac{\epsilon_2}{2 - \epsilon_2} (4\sigma T_2^4 - I_0^*) \quad (6)$$

$$\text{and} \quad \eta \rightarrow \pm \infty: \quad \frac{\partial I_0^*}{\partial \eta} = 0 \quad (7)$$

where the wall temperatures  $T_1$  and  $T_2$  may be arbitrary functions in  $\eta$ . It will be assumed here that the emissivities  $\epsilon$  are constant along each surface.

Equation (4) together with its boundary conditions (5) to (7) is the two-dimensional nonhomogeneous Laplace equation with boundary conditions of the third kind. As equation (4) is linear in  $I_0^*$  superposition can be applied. The solution will be of the following form (Duhamel's theorem) [12]:

$$I_0^*(\eta, \xi) = I_{0,s}^*(\xi) + \int_{-\infty}^{\infty} 4\sigma T_1^4(\lambda) \frac{dw}{d\lambda}(\eta - \lambda, \xi, \epsilon_1, \epsilon_2) d\lambda + \int_{-\infty}^{\infty} 4\sigma T_2^4(\lambda) \frac{dw}{d\lambda}(\eta - \lambda, 1 - \xi, \epsilon_2, \epsilon_1) d\lambda \quad (8)$$

where  $I_{0,s}^*(\xi)$  is the contribution of the source term and  $dw(\eta - \lambda, \xi, \epsilon_1, \epsilon_2)$  is the contribution of the walls if only the lower wall is heated to unity temperature between  $\lambda \leq \eta \leq \lambda + d\lambda$ . Duhamel's theory was preferred here to the often used Fourier-integral approach as it results in closed-form solutions for a large number of wall temperatures (cf. equation (10)). The inversion of the Fourier

transform, on the other hand, generally results in complicated integrals, which must be solved numerically.

The source contribution  $I_{0,s}^*(\xi)$  is readily found to be

$$I_{0,s}^*(\xi) = \frac{3}{2} \frac{S\tau_0^2}{\alpha} \times \left\{ \frac{[2(1/\epsilon_2 - 1/2) + 3\tau_0/4][\xi + (1/\epsilon_1 - 1/2)4/3\tau_0]}{1/\epsilon_1 + 1/\epsilon_2 - 1 + 3\tau_0/4} - \xi^2 \right\} \quad (9)$$

where, for clarity, it was assumed that  $S = \text{const}$ .

The function  $dw(\eta - \lambda, \xi, \epsilon_1, \epsilon_2)$  can be determined by the method of separation of variables. After some algebraic manipulation, the Planck function for the differential approximation can be obtained as:

$$4\pi B^*(\eta, \xi) = \frac{S}{\alpha} + I_{0,s}^*(\xi) + \sum_{n=1}^{\infty} C_n(h_1, h_2) \{ \beta_n \cos \beta_n \xi + h_1 \sin \beta_n \xi \} \int_{-\infty}^{\infty} 4\sigma T_1^4(\lambda) e^{-\beta_n |\eta - \lambda|} d\lambda + \sum_{n=1}^{\infty} C_n(h_2, h_1) \{ \beta_n \cos \beta_n (1 - \xi) + h_2 \sin \beta_n (1 - \xi) \} \int_{-\infty}^{\infty} 4\sigma T_2^4(\lambda) e^{-\beta_n |\eta - \lambda|} d\lambda \quad (10)$$

where

$$h_k = \frac{3\tau_0}{4} / \left( \frac{1}{\epsilon_k} - \frac{1}{2} \right); \quad k = 1, 2, \quad (11)$$

$$C_n(h_1, h_2) = \frac{h_1}{\beta_n^2 + h_1^2} / \left( 1 + \frac{h_1}{\beta_n^2 + h_1^2} + \frac{h_2}{\beta_n^2 + h_2^2} \right) \quad (12)$$

The eigenvalues  $\beta_n$  are the roots of the equation

$$\tan \beta_n = (h_1 + h_2)\beta_n / (\beta_n^2 - h_1 h_2) \quad (13)$$

The heat flux in the direction perpendicular to the walls follows immediately from equation (2) as:

$$q_{\xi}^*(\eta, \xi) = -\frac{1}{3\tau_0} \frac{\partial I_0^*}{\partial \xi} \quad (14)$$

### Improvement of the Differential Approximation

For the differential approximation it has been assumed that the distribution of intensity is more or less isotropic. In optically thin situations, however, radiation from the surfaces comprises the largest part of the intensity and its distribution may, in general, become strongly anisotropic. For these cases results from the differential approximation cannot be expected to be accurate and must be improved. Consider the exact formulation for the intensity in the medium:

### Nomenclature

$B$ = Planck function, $\sigma T^4/\pi$	$\vec{n}$ = outward surface normal	$\beta_n$ = eigenvalues for generalized Fourier series
$C_n$ = coefficients for generalized Fourier series	$\vec{q}$ = heat flux	$\gamma^i$ = wall contribution factor for unit step function
$E_n(x)$ = exponential integral, $\int_0^1 e^{-x/\mu} \mu^{n-2} d\mu$	$\vec{s}$ = unit direction vector	$\Gamma_k^i$ = wall contribution factor
$G_k^i$ = correction factor for nonblack surfaces, equation (38)	$S$ = heat generation (per unit volume)	$\delta_i$ = parameter for $I^i$
$h_k$ = coefficient for boundary conditions, equation (11)	$T$ = temperature	$\epsilon$ = wall emissivity
$I$ = intensity	$x$ = horizontal distance parallel to plates	$\eta$ = nondimensional horizontal distance
$I^i$ = integral defined by equation (26)	$y$ = vertical distance normal to plates	$\xi$ = nondimensional vertical distance
$I_0$ = integrated intensity	$Y$ = distance between plates	$\tau_0$ = optical distance between plates
	$\alpha$ = absorption coefficient	$\tau_s$ = optical distance to wall in direction $s$

$$I(\vec{s}) = B_w e^{-\tau_s} + \int_0^{\tau_s} B e^{-s} ds \quad (15)$$

where  $\pi B_w$  is the surface radiosity and  $\tau_s$  is the optical distance between the point under consideration and the wall in the direction of  $\vec{s}$  (Fig. 1). The first term is the intensity originating from the surface attenuated by absorption. The integral term describes emission in the gas along  $\tau_s$ .

One common method for the solution of integral equations is through successive approximation, starting with some approximate solution. In the case of equation (15) the first iteration already can prove to be very tedious as the emission term must also be integrated over all solid angles resulting in a complicated triple integral. On the other hand, equation (15) can be used to improve the differential approximation in a relatively simple manner. This is accomplished by approximating the emission integral by an algebraic expression which combines the optically thick solution with a number of geometrical parameters, which become important in optically thin situations. Thus:

$$\int_0^{\tau_s} B e^{-s} ds \cong B^*(1 - e^{-\tau_s}) + \frac{1}{4\pi} (3\bar{q}^* - \nabla \frac{S}{\alpha^2}) \cdot \vec{s} [1 - (1 + \tau_s) e^{-\tau_s}] \quad (16)$$

where the Planck function has been replaced by values obtained from the differential approximation and was then expanded into a Taylor series around  $s = 0$  and truncated after two terms. This approximation reduces to the correct optically thin and thick limits and, if  $B^*$  is a linear function in  $s$ , results in the exact value for the integral with  $B$  replaced by  $B^*$  ("first iteration").

Using this approximation improved values for the Planck function and radiative heat flux can be calculated from

$$4\pi B(\eta, \xi) = \frac{S}{\alpha} + \sum_k \Gamma_k^0(\eta, \xi) + 4\pi B^*(1 - \psi^{00})(\eta, \xi) - (3\bar{q}^* - \nabla \frac{S}{\alpha^2}) \cdot (\bar{\psi}^{10} + \bar{\psi}^{11})(\eta, \xi) + R_B \quad (17)$$

$$\bar{q}(\eta, \xi) = \sum_k \bar{\Gamma}_k^1(\eta, \xi) - 4\pi B^* \bar{\psi}^{10}(\eta, \xi) + (\bar{q}^* - \frac{1}{3} \nabla \frac{S}{\alpha^2})(\eta, \xi) - (3\bar{q}^* - \nabla \frac{S}{\alpha^2}) \cdot (\bar{\psi}^{20} + \bar{\psi}^{21})(\eta, \xi) + \bar{R}_q \quad (18)$$

where

$$\psi^{ij}(\eta, \xi) \equiv \frac{1}{4\pi} \int_{\Omega_k} \tau_s^j(\vec{s})^{(i)} e^{-\tau_s} d\omega; \quad i = 0, 1, 2; \quad j = 0, 1, \quad (19)$$

$$\Gamma_k^i(\eta, \xi) \equiv \int_{\Omega_k} B_k(\vec{s})^{(i)} e^{-\tau_s} d\omega; \quad i = 0, 1, \quad (20)$$

and  $(s)^{(i)}$  is an  $i$ th rank tensor, e.g.,  $(\vec{s})^{(2)} = \vec{s}\vec{s}$ . The integration in equation (20) is over the solid angle of  $\Omega_k$  subtended by the  $k$ th subsurface when viewed from the point under consideration.

Equations (17) and (18) are subject to two types of errors. One arises from the fact that the Planck function in equation (15) has been replaced by the value found from the differential approximation,  $B^*$ :

$$\left\{ \frac{R_B^*}{R_q^*} \right\} = 4\pi(B - B^*) \left\{ \frac{(1 - \psi^{00})}{-\bar{\psi}^{10}} \right\} + 4\pi \frac{1}{\alpha} \nabla(B - B^*) \cdot \left\{ \frac{-(\bar{\psi}^{10} + \bar{\psi}^{11})}{\bar{\delta}/3 - \bar{\psi}^{20} - \bar{\psi}^{21}} \right\} \quad (21)$$

where  $\bar{\delta}$  is the unit tensor. The magnitude of this error is difficult to estimate. However, it is readily seen from equation (19) that for optically thin situations the bracketed terms on the right-hand side of equation (21) vanish, while in optically thick situations  $(B - B^*) \rightarrow 0$ .

Furthermore, if  $R_B^*$  and  $\bar{R}_q^*$  are the only error terms present, equations (17) and (18) are identical to the first iteration of successive approximations and  $B$  and  $\bar{q}$  must fall in between the exact values and results obtained from the differential approxi-

**Table 1 Comparison of Nondimensional Heat Fluxes  $q/\sigma(T_1^4 - T_2^4)$  For The Planar Case**

(ODA = ordinary diff. appr.; IDA = improved diff. appr.; MDA = modified diff. appr., MDE = MDA with exponential appr.)

$\tau_0$	ODA, MDE	IDA, MDA	Exact
0	1	1	1
.1	.9302	.9160	.9157
.2	.8696	.8502	.8491
.5	.7272	.7082	.7040
1.0	.5714	.5603	.5532
2.0	.4000	.3970	.3900

mation. Lee and Olfe [13] employed the method of successive approximations to the case of one-dimensional concentric spheres. Their results demonstrate the excellent accuracy of the complete first iteration.

A second error arises from the fact that only the first two terms of the Taylor series in equation (16) were retained. This results in a truncation error of

$$\left\{ \frac{R_B^T}{R_q^T} \right\} = 4\pi \frac{1}{\alpha^2} \left( \frac{d^2 B}{dr^2} \right) \left\{ \frac{1 - \psi^{00} - \psi^{01} - \psi^{02}}{-(\bar{\psi}^{10} + \bar{\psi}^{11} + \bar{\psi}^{12})} \right\} \quad (22)$$

where  $(d^2 B/dr^2)$  is the curvature of the Planck function at some point and direction inside the medium. Again, in optically thin situations, the optical parameters vanish so that  $R_B^T, \bar{R}_q^T \rightarrow 0$ . In optically thick media the optical parameters for  $\bar{R}_q^T$  also vanish while for  $R_B^T$  they do not. However, in most engineering applications the curvature of the Planck function,  $(d^2 B/dr^2)/\alpha^2$ , approaches zero in this case. In the rare situation of an optically thick situation with rapidly oscillating Planck function ( $\alpha\lambda$  small, where  $\lambda$  is the wavelength of oscillation) it is then advantageous to drop the  $\bar{q}^*$  term in equation (17).

To give some indication of the accuracy of the present improved differential approximation (IDA) wall fluxes have been computed for the one-dimensional planar case. In Table 1 the results are compared for various optical thicknesses with values obtained from the ordinary differential approximation (ODA), Olfe's modified differential approximation [11] (MDA) and the exact solution. It is seen that the present model offers substantial improvement over the differential approximation and—for the one-dimensional planar case—coincides with the modified differential approximation. However, to obtain a solution for the MDA in multidimensional systems it is usually necessary to introduce an exponential approximation as a further simplification (MDE), which—in the planar case—reduces its accuracy to that of the ordinary differential approximation.

For the plane layer the  $\psi^{(ij)}$  is readily calculated and

$$4\pi B(\eta, \xi) = \frac{S}{\alpha} + \sum_{k=1}^2 \Gamma_k^0(\eta, \xi) + 2\pi B^*(\eta, \xi) \{ 2 - E_2(\tau_0 \xi) - E_2(\tau_0(1 - \xi)) \} - \frac{1}{2} (3\bar{q}_\xi^* - \frac{1}{\tau_0} \frac{\partial}{\partial \xi} \frac{S}{\alpha})(\eta, \xi) \{ E_3(\tau_0 \xi) + \tau_0 \xi E_2(\tau_0 \xi) - E_3(\tau_0(1 - \xi)) - \tau_0(1 - \xi) E_2(\tau_0(1 - \xi)) \} \quad (23)$$

$$\bar{q}_\xi(\eta, \xi) = \sum_{k=1}^2 \bar{\Gamma}_k^1(\eta, \xi) - 2\pi B^*(\eta, \xi) \{ E_3(\tau_0 \xi) - E_3(\tau_0(1 - \xi)) \} + \frac{1}{2} (3\bar{q}_\xi^* - \frac{1}{\tau_0} \frac{\partial}{\partial \xi} \frac{S}{\alpha})(\eta, \xi) \left\{ \frac{2}{3} - E_4(\tau_0 \xi) - \tau_0 \xi E_3(\tau_0 \xi) - E_4(\tau_0(1 - \xi)) - \tau_0(1 - \xi) E_3(\tau_0(1 - \xi)) \right\} \quad (24)$$

where  $E_n$  is the exponential integral.

To calculate the  $\Gamma_1^1(\eta, \xi)$  (lower surface) consider first the case

of a step function in wall radiosity at the lower surface, i.e.,  $4\pi B_1 = H(\eta)$ , where  $H(\eta)$  is Heaviside's unit function, i.e.,  $H(\eta) = 1$  for  $\eta < 0$  and  $H(\eta) = 0$  for  $\eta > 0$ . Denoting the solution to equation (20) for this particular case by  $\gamma^i(\eta, \xi)$  it follows that

$$\gamma^i(\eta, \xi) = \frac{1}{4} E_{2+i}(\tau_0 \xi) \left\{ 1 - \text{sgn}(\eta) \left[ 1 - I^i\left(\frac{\eta}{\xi}, \tau_0 \xi\right) / E_{2+i}(\tau_0 \xi) \right] \right\};$$

$$i = 0, 1, \quad (25)$$

where

$$I^i(r, \tau) \equiv \frac{2}{\pi} \int_0^{\pi/2} \int_0^{\cos[\tan^{-1}(|r|/\cos\phi)]} \mu^i e^{-\tau/\mu} d\mu d\phi. \quad (26)$$

The functions  $I^i(r, \tau)$  have first been introduced by Taitel [8]. An exact calculation of the integrals  $I^i$  is possible in form of slowly converging double series. However, simple and very accurate approximations are easily found to be

$$I^0(r, \tau) \cong \frac{2}{\pi} \tan^{-1} \left| \frac{1}{r} \right| \exp\left(-\frac{2\tau}{1+\tau} |r|\right) E_2(\tau), \quad (27)$$

$$I^1(r, \tau) \cong \left(1 - \frac{|r|}{\sqrt{1+r^2}}\right) \exp\left(-\frac{2\tau}{1+\tau} |r|\right) E_3(\tau). \quad (28)$$

These approximations reduce to the correct limits for  $r = 0$ ,  $r \rightarrow \infty$ ,  $\tau = 0$ ,  $\tau \rightarrow \infty$ , with negligible error in between. The simple solution for a step function is now readily extended to the general case by use of superposition. Thus,

$$\Gamma_1^i(\eta, \xi) = 4\pi \int_{-\infty}^{\infty} B_1(\lambda) \frac{d\gamma^i}{d\lambda}(\eta - \lambda, \xi) d\lambda; \quad i = 0, 1. \quad (29)$$

Finally, the contribution of the upper surface follows immediately from symmetry as

$$\Gamma_2^i(\eta, \xi) = (-1)^i 4\pi \int_{-\infty}^{\infty} B_2(\lambda) \frac{d\gamma^i}{d\lambda}(\eta - \lambda, 1 - \xi) d\lambda; \quad i = 0, 1. \quad (30)$$

In the case of nonblack surfaces, one more difficulty must be overcome: the distribution of the wall radiosity is not readily known because it contains the heat flux at the wall, i.e.,

$$\pi B_k = \sigma T_R^4 - \frac{1 - \epsilon_k}{\epsilon_k} \bar{q}_k \cdot \bar{n}_k. \quad (31)$$

It is felt, however, that the heat flux in equation (31) can be replaced by the value  $\bar{q}^*$  found from the differential approximation. This can be justified by realizing that, if  $\epsilon_k$  is close to unity, the factor  $(1 - \epsilon_k)/\epsilon_k$  renders the second term unimportant. If  $\epsilon_k$  is small, on the other hand, wall effects on the intensity distribution are fairly small so that  $\bar{q}_k^* \cong \bar{q}_k$ .

### Illustrative Example

As an illustrative example the case of constant temperature at the upper wall and constant temperature with a step at  $\eta = 0$  at the lower wall, i.e.,  $T_1^4(\eta) = T_{1R}^4 + (T_{1L}^4 - T_{1R}^4) H(\eta)$ , will be considered. It will be assumed that no heat generation takes place in the medium ( $S \equiv 0$ ).

The solution for the differential approximation follows immediately from equations (10) and (14):

$$4\pi B^*(\eta, \xi) = 4\sigma T_2^4 + \sigma \{ T_{1L}^4 + T_{1R}^4 - 2T_2^4$$

$$+ \text{sgn}(\eta)(T_{1R}^4 - T_{1L}^4) \} \frac{2/\epsilon_2 - 1 + (1 - \xi)3\tau_0/2}{1/\epsilon_1 + 1/\epsilon_2 - 1 + 3\tau_0/4}$$

$$- \text{sgn}(\eta)4\sigma(T_{1R}^4 - T_{1L}^4) \sum_{n=1}^{\infty} \frac{C_n}{\beta_n} (h_1, h_2) e^{-\beta_n |\eta|} \beta_n \cos \beta_n \xi$$

$$+ h_1 \sin \beta_n \xi \} \quad (32)$$

$$q_{\xi}^*(\eta, \xi) = \frac{1}{2} \sigma \{ T_{1L}^4 + T_{1R}^4 - 2T_2^4 + \text{sgn}(\eta)(T_{1R}^4 - T_{1L}^4) \}$$

$$\times \frac{1}{1/\epsilon_1 + 1/\epsilon_2 - 1 + 3\tau_0/4} - \text{sgn}(\eta) \sigma (T_{1R}^4 - T_{1L}^4) \frac{4}{3\tau_0}$$

$$\times \sum_{n=1}^{\infty} C_n (h_1, h_2) e^{-\beta_n |\eta|} \beta_n \sin \beta_n \xi - h_1 \cos \beta_n \xi \} \quad (33)$$

with  $C_n(h_1, h_2)$  given by equation (12) and the eigenvalues  $\beta_n$  are the roots of equation (13).

Equations (32) and (33) are then employed to improve values for the Planck function  $B(\eta, \xi)$  and vertical heat flux  $q_{\xi}(\eta, \xi)$  (equations (23) and (24)). The  $\Gamma_k^i(\eta, \xi)$  are readily calculated from equations (29) and (30) so that

$$\Gamma_1^0(\eta, \xi) = \{ \sigma(T_{1L}^4 + T_{1R}^4) - \text{sgn}(\eta)\sigma(T_{1L}^4 - T_{1R}^4) \}$$

$$\times \left( 1 - \frac{2}{\pi} \tan^{-1} \left| \frac{\xi}{\eta} \right| e^{-\frac{2\tau_0 \eta}{1+\tau_0 \xi}} \right) + G_1^0(\eta, \xi) E_2(\tau_0 \xi) \quad (34)$$

$$\Gamma_2^0(\eta, \xi) = \{ 2\sigma T_2^4 + G_2^0(\eta, 1 - \xi) \} E_2(\tau_0(1 - \xi)) \quad (35)$$

$$\Gamma_1^1(\eta, \xi) = \{ \sigma(T_{1L}^4 + T_{1R}^4) - \text{sgn}(\eta)\sigma(T_{1L}^4 - T_{1R}^4) \}$$

$$\times \left[ 1 - \left( 1 - \frac{|\eta|}{\sqrt{\eta^2 + \xi^2}} \right) e^{-\frac{2\tau_0 |\eta|}{1+\tau_0 \xi}} \right] + G_1^1(\eta, \xi) E_3(\tau_0 \xi) \quad (36)$$

$$\Gamma_2^1(\eta, \xi) = -\{ 2\sigma T_2^4 + G_2^1(\eta, 1 - \xi) \} E_3(\tau_0(1 - \xi)) \quad (37)$$

where the  $G_k^i(\eta, \xi)$  are correction factors for nonblack surfaces:

$$G_k^i(\eta, \xi) = (-1)^k \sigma \{ T_{1L}^4 + T_{1R}^4 - 2T_2^4$$

$$+ \text{sgn}(\eta)(T_{1R}^4 - T_{1L}^4) \} \frac{1/\epsilon_k - 1}{1/\epsilon_1 + 1/\epsilon_2 - 1 + 3\tau_0/4}$$

$$+ (1/\epsilon_k - 1) \text{sgn}(\eta) \sigma (T_{1L}^4 - T_{1R}^4) \frac{4}{3\tau_0} \{ (k - 2)$$

$$\times \left[ \left( \frac{3\tau_0/4}{1/\epsilon_1 + 1/\epsilon_2 - 1 + 3\tau_0/4} + 2h_1 \sum_{n=1}^{\infty} C_n(h_1, h_2) \right) \frac{I^i(\eta/\xi, \tau_0 \xi)}{E_{2+i}(\tau_0 \xi)} \right.$$

$$\left. + \sum_{n=1}^{\infty} 2h_k [(-1)^n]^{k-1} C_n(h_1, h_2) \left( \frac{\beta_n^2 + h_1^2}{\beta_n^2 + h_2^2} \right)^{\frac{k-1}{2}} \right.$$

$$\left. \times \frac{\beta_n^2 e^{-\delta_i |\eta|} - \delta_i^2 e^{-\beta_n |\eta|}}{\beta_n^2 - \delta_i^2} \right\}; \quad k = 1, 2; \quad i = 0, 1 \quad (38)$$

with

$$\delta_i(\xi) = \left[ \left( \frac{2}{\pi} \right)^{1-i} + \frac{2\tau_0 \xi}{1 + \tau_0 \xi} \right] \frac{1}{\xi}; \quad i = 0, 1. \quad (39)$$

To make a straight forward integration in equations (29) and (30) possible, a somewhat cruder approximation of

$$I^i\left(\frac{\eta}{\xi}, \tau_0 \xi\right) \cong e^{-\delta_i |\eta|} E_{2+i}(\tau_0 \xi) \quad (40)$$

was used in the evaluation of the  $G_k^i(\eta, \xi)$ .

Some results for the dimensionless temperature distribution and for the wall fluxes are shown in Figs. 2 to 7. Fig. 2 depicts the temperature distribution for an optically thin, black enclosure calculated by the present method. As expected, these temperature profiles virtually coincide with those of Taitel [8] as both methods are exact in the optically thin limit. (Taitel's results have not been included in the figures to avoid crowding of the graphs.) It should be noted here that the temperature distribu-

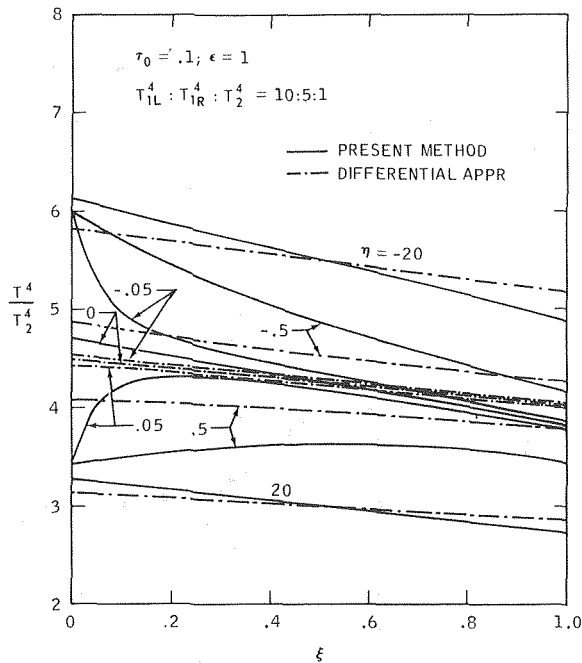


Fig. 2 Nondimensional temperature profiles for  $\tau_0 = 0.1$ ,  $\epsilon = 1$

tion for small positive  $\eta$  displays a maximum close to the lower wall. This is due to the influence of the walls, demonstrating clearly the action-at-a-distance character of radiative transfer in optically thin media. At  $\eta > 0$  the gas "sees" more of the hot surface for larger  $\xi$ . If the optical thickness is small so that the surface radiation is not significantly attenuated by absorption, a maximum in temperature occurs. This characteristic cannot be obtained with the differential approximation, which is included in Fig. 2 for comparison. The temperature profiles of the differential approximation show little curvature and change far too slowly for increasing  $\eta$ . In fact, for the optically thin limit,  $\tau_0 \rightarrow 0$ , the differential approximation predicts a constant temperature throughout the entire medium. Fig. 3 shows another comparison between the present method and the differential approximation,

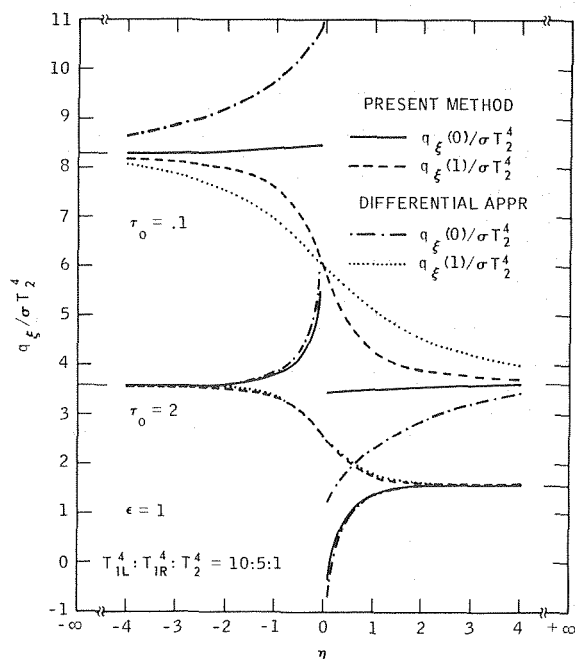


Fig. 3 Nondimensional surface heat flux for black walls

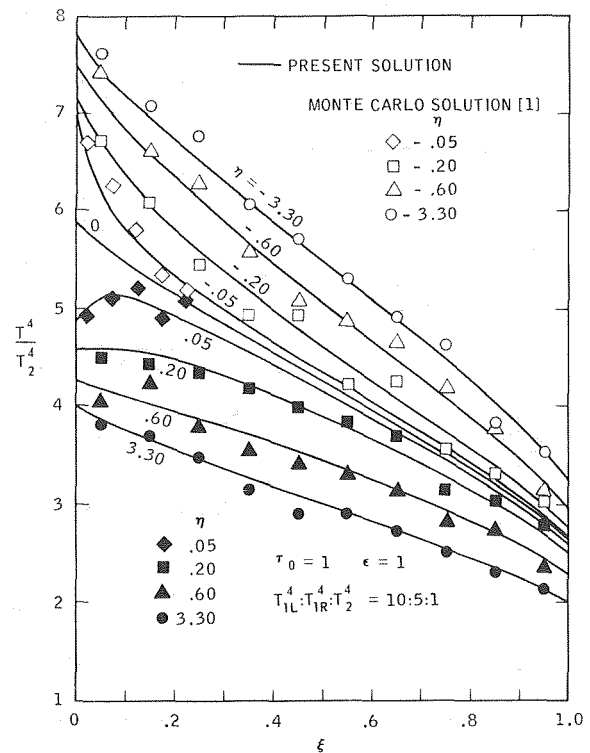


Fig. 4 Nondimensional temperature profiles for  $\tau_0 = 1$ ,  $\epsilon = 1$

depicting heat fluxes at the upper and lower surfaces in a black enclosure as functions of horizontal distance  $\eta$ . It is seen that for an optical thickness of  $\tau_0 \geq 2$  the differential approximation predicts surface heat fluxes very accurately. (This is, however, not true for temperature distributions as it cannot predict the curvature of temperature profiles close to  $\eta = 0$ .) At  $\tau_0 = 2$  the general level of the differential-approximation profiles is high by 2.5 percent corresponding to the error of this method for the one-dimensional planar case. At optical thicknesses below  $\tau_0 = 2$  the differential approximation displays large errors close to the wall-temperature jump until, in the optically transparent case, it is not able any more to even reach the one-dimensional limit for  $\eta \rightarrow \pm \infty$ .

Fig. 4 compares the present method with numerical results obtained by Murakami [1] using the Monte Carlo method. The agreement is excellent and, due to the spread of the Monte Carlo data, the accuracy of the present approximation is obviously comparable to this numerical solution. (Taitel's solution does not fit the data points quite as well because its accuracy diminishes with growing optical thickness.)

Fig. 5 depicts the surface heat fluxes for various optical thicknesses  $\tau_0$  in comparison with the Monte Carlo technique. Again, the agreement is excellent for all optical thicknesses. (Taitel's solution approaches the numerical data for  $\tau_0 = 0.1$  while, as expected, it cannot approximate accurately the steep gradients close to  $\eta = 0$  for larger optical thicknesses.)

Figs. 6 and 7 show results for diffuse gray walls with emissivities  $\epsilon_1 = \epsilon_2 = 0.5$ . Also in this case the agreement with the Monte Carlo data is very good for temperature distributions as well as for wall fluxes. Thus, the assumption that  $q$  can be replaced by  $\bar{q}^*$  (differential approximation) in equation (31) has been justified. Obviously, good results will be obtained at least for surface emissivities of  $\epsilon \geq 0.5$ .

### Summary and Conclusions

An effort has been made to predict temperature and heat flux distributions in an infinite two-dimensional plane layer of a gray

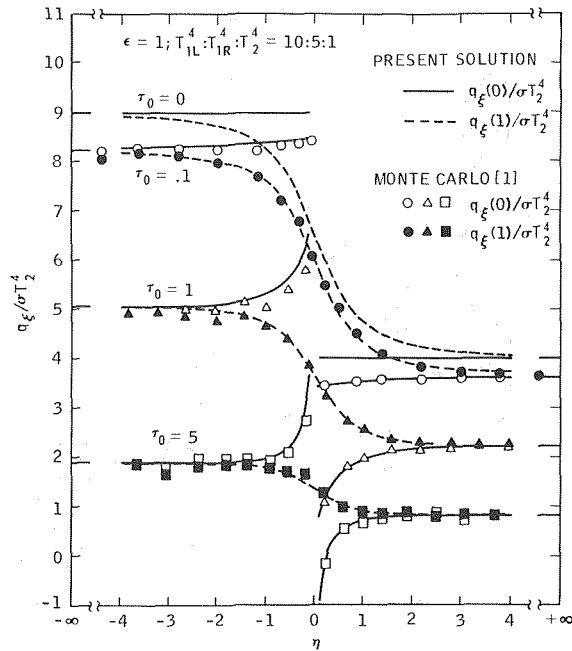


Fig. 5 Nondimensional surface heat flux for black walls

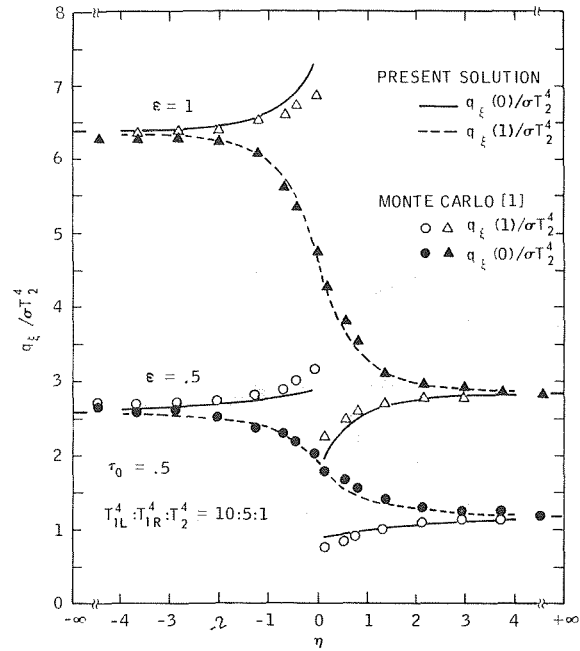


Fig. 7 Nondimensional surface heat flux for gray walls

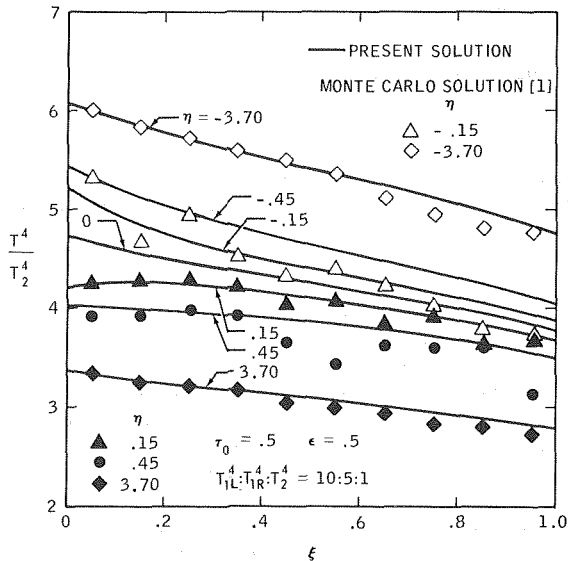


Fig. 6 Nondimensional temperature profiles for gray walls

medium at radiative equilibrium. The present approach was chosen over other available methods for its relative simplicity and generality: Taitel's approximation [8] requires the numerical solution of an integral equation and can only be considered accurate for an optically thin medium. The modified differential approximation by Olfe [11], although accurate for all optical regimes, requires the numerical solution of the nonhomogeneous Laplace equation. Both methods cannot be used if internal heat generation is present. If the bounding walls are nonblack, Taitel's method is not applicable while the modified differential approximation results in an integral equation, thus defeating the original purpose of introducing an approximate method of solution. The present approach resulted in a relatively simple closed-form solution for the distributions of gas temperature and heat flux for the general case.

Comparison with known numerical results demonstrated the

excellent accuracy of the method presented here. The solution to the differential approximation can be found for many two- and three-dimensional cases while the geometrical parameters for its improvement can conveniently be approximated or integrated numerically. It is felt that a substantial number of other multidimensional problems can be solved in a relatively simple manner by the method presented in this article.

## References

- 1 Murakami, M., "Direct Monte Carlo Simulation of Two-Dimensional Radiative Heat Transfer in Absorbing-Emitting Medium Bounded by the Non-Isothermal Gray Walls," 9th Int. Symposium on Space Technology and Science, Proceedings, Agne Publ. Inc., 1971, pp. 407-416.
- 2 Taniguchi, H., "Radiative Heat Transfer of Gas in a Three-Dimensional System Calculated by Monte Carlo Method," *Bull. Japan. Soc. Mech. Engrs.*, Vol. 12, No. 49, 1969, pp. 67-78.
- 3 Hottel, H. C., and Cohen, E. S., "Radiant Heat Exchange in a Gas-Filled Enclosure: Allowance for Non-Uniformity of Gas Temperature," *AIChE Journal*, Vol. 4, No. 1, 1958, pp. 3-14.
- 4 Hottel, H. C., and Sarofim, A. F., *Radiative Transfer*, McGraw-Hill, New York, Chapter 11, 1967.
- 5 Breig, W. F., and Crosbie, A. L., "Two-Dimensional Radiative Equilibrium: A Semi-Infinite Medium Subjected to Cosine Varying Radiation," *J. Quant. Spectrosc. Radiat. Transfer*, Vol. 13, 1973, p. 1395.
- 6 Breig, W. F., and Crosbie, A. L., "Two-Dimensional Radiative Equilibrium: A Semi-Infinite Medium Subjected to a Finite Strip of Radiation," *J. Quant. Spectrosc. Radiat. Transfer*, Vol. 14, 1974, p. 189.
- 7 Breig, W. F., and Crosbie, A. L., "Two-Dimensional Radiative Equilibrium," *J. Math. Anal. Applic.*, Vol. 46, 1974, p. 104.
- 8 Taitel, Y., "Formulation of Two-Dimensional Radiant Heat Flux for Absorbing-Emitting Plane Layer With Nonisothermal Bounding Walls," *AIChE Journal*, Vol. 7, No. 10, 1969, pp. 1832-1837.
- 9 Olfe, D. B., "Radiative Equilibrium of a Gray Medium Bounded by Nonisothermal Walls," *Progress in Astronautics and Aeronautics*, Vol. 23, 1970, pp. 295-317.
- 10 Glatt, L., and Olfe, D. B., "Radiative Equilibrium of a Gray Medium in a Rectangular Enclosure," *J. Quant. Spectrosc. Radiat. Transfer*, Vol. 13, 1973, pp. 881-895.
- 11 Olfe, D. B., "Application of a Modified Differential Approximation to Radiative Transfer in a Gray Medium Between Concentric Spheres and Cylinders," *J. Quant. Spectrosc. Radiat. Transfer*, Vol. 8, 1968, pp. 899-907.
- 12 Carslaw, H. S., and Jaeger, J. C., *Conduction of Heat in Solids*, Oxford University Press, 1959.
- 13 Lee, R. L., and Olfe, D. B., "An Iterative Method for Non-Planar Radiative Transfer Problems," *J. Quant. Spectrosc. Radiat. Transfer*, Vol. 9, 1969, pp. 297-308.

C. A. Deavours  
 Assoc. Professor,  
 Mathematics Department,  
 Kean College of New Jersey,  
 Union, N. J.

# An Exact Solution for the Temperature Distribution in Parallel Plate Poiseuille Flow

*This paper finds by an exact method the temperature distribution in a viscous fluid undergoing Poiseuille flow between two infinite parallel plates. The upstream portion of the plates is assumed to be at temperature  $T = T^-$  and downstream portion of the plates to be at temperature  $T = T^+$ . Results are obtained numerically for the "entrance region" temperature profiles. These tend rapidly to zero away from the point where the wall temperature changes abruptly. Using asymptotic expansions for the functions involved estimates are made for the number of terms required to achieve a given level of accuracy for a given Peclet number (Pe). Typical results for  $Pe = 1$  and  $10$  are shown graphically.*

## 1 Introduction

This paper finds by an exact method the temperature distribution for fluid flow between parallel plates occupying the region  $y = \pm L$ ,  $-\infty < X < +\infty$  with the right half of the walls,  $X > 0$ , maintained at a constant temperature  $T = T^+$  and the left half of the walls,  $X < 0$ , maintained at a constant temperature  $T = T^-$ . The formula obtained for the temperature distribution can be found for any given fluid velocity profile, and holds for any range of Peclet numbers. The result is demonstrated numerically for Poiseuille flow and a range of Peclet numbers.

Problems of this sort have been treated previously [1-4],<sup>1</sup> under various simplifying assumptions. The usual method of utilizing infinite systems of linear equations which are then solved approximately by truncation is avoided here as it is possible to find an exact formula for the answer. The form of the answer allows easy estimation of the part played by entrance region effects in the relevant physical process.

## 2 Problem Formulation

For parallel plate fluid flow with velocity  $v(y)$  the steady-state Fourier-Kirchhoff-Neumann energy equation becomes

$$\frac{\partial^2 T}{\partial x^2} + \frac{\partial^2 T}{\partial y^2} = \frac{\rho c v}{k} \frac{\partial T}{\partial x} - \frac{\mu (\partial v)^2}{k \partial y^2} \quad (1)$$

with boundary condition

$$T(x, \pm L) = T^+, \quad x > 0 \quad (2)$$

$$T(x, \pm L) = T^-, \quad x < 0 \quad (3)$$

plus some boundary conditions as  $X \rightarrow \pm\infty$  which arise later in a natural manner.

Equation (1) may be nondimensionalized by introduction of the variables

$$\Phi = \frac{T - T^-}{[T]} \quad (4)$$

$$p = v/\bar{v} \quad (5)$$

$$Pe = 2\bar{v}L\rho c/k \quad (6)$$

$$\xi = kx/\rho c \bar{v} L^2 = 2x/LPe \quad (7)$$

$$\eta = y/L \quad (8)$$

where  $[T] = T^+ - T^-$  and  $\bar{v}$  is the mean fluid velocity in the channel. Equation (1) now becomes

$$(2/Pe)^2 \frac{\partial^2 \Phi}{\partial \xi^2} + \frac{\partial^2 \Phi}{\partial \eta^2} = p(\eta) \frac{\partial \Phi}{\partial \xi} + f(\eta) \quad (9)$$

where

$$f(\eta) = -(\mu \bar{v}^2/k[T]) \left(\frac{\partial p}{\partial \eta}\right)^2 \quad (10)$$

The boundary conditions (2) and (3) now become

$$\Phi(\xi, \pm 1) = 1, \quad \xi > 0 \quad (11)$$

$$\Phi(\xi, \pm 1) = 0, \quad \xi < 0. \quad (12)$$

Let  $\Phi_1$  denote the solution for  $\xi < 0$  and  $\Phi_2$  be the solution for  $\xi > 0$ . We shall find separate expressions for these solutions and then match them at  $\xi = 0$  by requiring that the solution and its normal derivative (and hence and higher order derivatives) be continuous at  $\xi = 0$ , i.e.,

<sup>1</sup> Numbers in brackets designate References at end of paper.

Contributed by the Heat Transfer Division for publication in the JOURNAL OF HEAT TRANSFER. Manuscript received by the Heat Transfer Division August 28, 1973. Paper No. 75-HT-F.



$$\Phi_1(0, \eta) = \Phi_2(0, \eta), \quad -1 < \eta < +1 \quad (13)$$

$$\frac{\partial \Phi_1}{\partial \xi}(0, \eta) = \frac{\partial \Phi_2}{\partial \xi}(0, \eta), \quad -1 < \eta < +1. \quad (14)$$

Since the boundary conditions are themselves discontinuous at  $\eta = \pm 1$  so will be the solution. Thus the matching conditions (13) and (14) are not valid for these two points.

### 3 Solution

Consider first the solution for  $\xi > 0$ . Assuming that  $\Phi$  tends uniformly to some function independent of  $\xi$  as  $\xi \rightarrow \infty$  then, in the limit (9) becomes

$$\frac{d^2 \Phi_\infty}{d\eta^2} = f(\eta) \quad (15)$$

whose general solution is readily found to be

$$\Phi_\infty = a + b\eta + \int_0^\eta (\eta - s)f(s)ds \quad (16)$$

in view of (11) we need

$$a = 1 - \int_0^1 (1 - s)f(s)ds \quad (17)$$

$$b = 0. \quad (18)$$

We have assumed  $p(\eta) = p(-\eta)$  for algebraic convenience. This also implies that  $f(\eta) = f(-\eta)$ .

As  $\xi \rightarrow \infty$  we obtain for (9)

$$\frac{d^2 \Phi_{-\infty}}{d\eta^2} = f(\eta) \quad (19)$$

whose general solution is

$$\Phi_{-\infty} = c + d\eta + \int_0^\eta (\eta - s)f(s)ds \quad (20)$$

so that, using (12), we have

$$c = - \int_0^1 (1 - s)f(s)ds \quad (21)$$

$$d = 0. \quad (22)$$

Luckily the solutions  $\Phi_{\pm\infty}$  are also particular solutions of (9) for  $\xi < 0$  and  $\xi > 0$ , respectively. Let

$$\Phi_1 = \Phi_{-\infty} + \phi_1 \quad (23)$$

$$\Phi_2 = \Phi_{+\infty} + \phi_2 \quad (24)$$

then  $\phi_1$  must satisfy the equation

$$\left(\frac{2}{Pe}\right)^2 \frac{\partial^2 \phi_1}{\partial \xi^2} + \frac{\partial^2 \phi_1}{\partial \eta^2} = p \frac{\partial \phi_1}{\partial \xi} \quad (25)$$

$$\phi_1(\xi, \pm 1) = 0. \quad (26)$$

The function  $\phi_2$  satisfies the same equation and boundary condition as  $\phi_1$  but for  $\xi > 0$ .

We seek separated solutions of (25) in the form

$$\phi_{\text{sep}} = \psi(\eta)e^{-\lambda\xi}. \quad (27)$$

Substitution into (25) yields the equation for  $\psi$  which is

$$\psi'' + \left(\frac{2}{Pe}\right)^2 \lambda^2 + \lambda p \psi = 0 \quad (28)$$

along with boundary conditions  $\psi(\pm 1) = 0$  to satisfy (26). Equation (28) and its associated boundary conditions constitute an eigenvalue problem though not of the classical Sturm-Liouville variety since the eigenvalues occur nonlinearly in (28). Equation (28) has two sets of complete eigenfunctions, [5], one set corresponding to the denumerable positive eigenvalues,  $\lambda_n$ , and one set corresponding to the negative eigenvalues. An arbitrary function on the interval  $[-1, +1]$  may be expanded in terms of either set of eigenfunctions, but since they are not orthogonal, the coefficients in the expansion are not calculable exactly.

Thus, the most general separated solution of (25) which is bounded as  $\xi \rightarrow -\infty$  is seen to be

$$\phi_1(\xi, \eta) = \sum_{\lambda_n < 0} c_n \psi_n(\eta) e^{-\lambda_n \xi} \quad (29)$$

where  $\psi_n$  is the eigenfunction corresponding to the eigenvalue  $\lambda_n$ , the  $C_n$  are constants, and the summation extends only over the negative eigenvalues.

Similarly,

$$\phi_2(\xi, \eta) = - \sum_{\lambda_n > 0} c_n \psi_n(\eta) e^{-\lambda_n \xi} \quad (30)$$

where the minus sign is introduced for convenience.

The matching conditions, (13) and (14), now require

$$\phi_1(0, \eta) + \Phi_{-\infty}(\eta) = \phi_2(0, \eta) + \Phi_{+\infty}(\eta) \quad (31)$$

$$\frac{\partial \phi_1}{\partial \xi}(0, \eta) = \frac{\partial \phi_2}{\partial \xi}(0, \eta) \quad (32)$$

or,

$$\sum_{\lambda_n < 0} c_n \psi_n(\eta) + \sum_{\lambda_n > 0} c_n \psi_n(\eta) = \Phi_{+\infty} - \Phi_{-\infty} \quad (33)$$

$$\sum_{\lambda_n < 0} \lambda_n c_n \psi_n(\eta) + \sum_{\lambda_n > 0} \lambda_n c_n \psi_n(\eta) = 0 \quad (34)$$

### Nomenclature

$A$  = matrix defined in (42)  
 $a_n$  = coefficient defined in (51)  
 $b_n = \lambda_n C_n$   
 $C = \begin{pmatrix} 0 & 1 \\ 1 & 0 \end{pmatrix}$   
 $c_n$  = expansion coefficients of  $\phi_1, \phi_2$   
 $f$  = defined in (10)  
 $f_1, f_2$  = components of vector  $f$   
 $k$  = thermometric conductivity  
 $L$  = distance between plates  
 $N_n$  = normalization constants for  $Z_n$   
 $p$  = nondimensional velocity =  $\frac{v}{V}$

$Pe$  = Peclet number  
 $T$  = temperature in fluid  
 $T^\pm$  = temperature of left and right half plates  
 $[T] = T^+ - T^-$   
 $v$  = fluid velocity  
 $\bar{v}$  = average fluid velocity  
 $x$  = horizontal coordinate along center of channel  
 $y$  = vertical coordinate measured from center of channel  
 $Z_n$  = solutions of equation (41)

$\delta$  = Dirac delta function  
 $\eta = y/L$   
 $\lambda_n$  = eigenvalue of (12)  
 $\mu$  = fluid viscosity  
 $\xi = 2x/(LPe)$   
 $\rho$  = fluid density  
 $\Phi = (T - T^-)/[T]$   
 $\Phi_{\pm\infty}$  = particular solutions of (9)  
 $\phi_1$  = entrance region temperature for  $\xi < 0$   
 $\phi_2$  = entrance region temperature for  $\xi > 0$   
 $\psi_n$  = defined in (28)

Since  $\Delta\Phi \equiv \Phi_{+\infty} - \Phi_{-\infty}$  satisfies  $d^2/d\eta^2(\Delta\Phi) = 0$  with  $\Delta\Phi(\pm 1) = 1$ , then  $\Delta\Phi(\eta) = 1$  as may be verified from previous expressions for  $\Phi_{+\infty}$  and  $\Phi_{-\infty}$ .

Thus (33) and (34) become

$$\sum_{\lambda_n} c_n \psi_n(\eta) = \Delta\Phi = 1 \quad (35)$$

$$\sum_{\lambda_n} \lambda_n c_n \psi_n(\eta) = 0 \quad (36)$$

where the series are required to converge for  $-1 < \eta < +1$  in the manner of a trigonometric Fourier series expansion.

The series of (35) will be required only to possess the property that its value approach 1 as  $\eta \rightarrow \pm 1$  since  $\psi_n(\pm 1) = 0$ .

Because the  $\psi_n$  are not orthogonal, approximate methods would seem appropriate at this point. Instead, we shall convert equations (35) and (36) to an equivalent vector system of differential equations in which orthogonality is restored. Let

$$Z_{1n} = \psi_n \quad (37)$$

$$Z_{2n} = \psi_n' / \lambda_n \quad (38)$$

then

$$Z_{1n}' = \lambda_n Z_{2n} \quad (39)$$

$$Z_{2n}' = -\left(\left(\frac{2}{Pe}\right)^2 \lambda_n + p\right) Z_{1n} \quad (40)$$

where prime ' denotes differentiation with respect to  $\eta$ . These two equations may be combined into the single vector equation

$$\mathbf{Z}_n' = \lambda_n \mathbf{A} \mathbf{Z}_n + \mathbf{B} \mathbf{Z}_n \quad (41)$$

with  $Z_{1n}(\pm 1) = 0$ . In the foregoing,

$$\mathbf{A} = \begin{pmatrix} 0 & 1 & 0 & 0 \\ -\left(\frac{2}{Pe}\right)^2 & 0 & -p & 0 \end{pmatrix}, \quad \mathbf{B} = \begin{pmatrix} 0 & 0 \\ 0 & 0 \end{pmatrix} \quad (42)$$

$$\mathbf{Z}_n = (Z_{1n}, Z_{2n}) \quad (43)$$

Equations of type (41) have been extensively studied [6]. The orthogonality property is easily proved as is shown. Suppose  $\mathbf{Z}_m$  is the eigenvector corresponding to an eigenvalue  $\lambda_m$ . Then

$$\mathbf{Z}_m' = \lambda_m \mathbf{A} \mathbf{Z}_m + \mathbf{B} \mathbf{Z}_m \quad (44)$$

with  $Z_{1m}(\pm 1) = 0$ . Multiplying (41) on the left by the matrix,

$$\mathbf{C} = \begin{pmatrix} 0 & 1 \\ -1 & 0 \end{pmatrix} \quad (45)$$

and taking the dot product of both sides of the resulting equation with  $\mathbf{Z}_m$  yields

$$(\mathbf{Z}_m \cdot \mathbf{C} \mathbf{Z}_n)' = \lambda_n \mathbf{Z}_m \cdot \mathbf{C} \mathbf{A} \mathbf{Z}_n + \mathbf{Z}_m \cdot \mathbf{C} \mathbf{B} \mathbf{Z}_n \quad (46)$$

Interchanging  $m$  and  $n$  in (46) and subtracting the resulting equation from (46) yields, after some algebra,

$$(\mathbf{Z}_m \cdot \mathbf{C} \mathbf{Z}_n)' = (\lambda_n - \lambda_m) \mathbf{Z}_m \cdot \mathbf{C} \mathbf{A} \mathbf{Z}_n \quad (47)$$

whence we find

$$(\lambda_n - \lambda_m) \int_{-1}^{+1} \mathbf{Z}_m \cdot \mathbf{C} \mathbf{A} \mathbf{Z}_n d\eta = \mathbf{Z}_m \cdot \mathbf{C} \mathbf{Z}_n \Big|_{-1}^{+1} = 0 \quad (48)$$

Thus

$$\int_{-1}^{+1} \mathbf{Z}_m \cdot \mathbf{C} \mathbf{A} \mathbf{Z}_n d\eta = 0 \quad (49)$$

for  $\lambda_n \neq \lambda_m$  and the eigenvectors are orthogonal on the interval  $(-1, +1)$  with respect to the matrix

$$\mathbf{C} \mathbf{A} = \begin{pmatrix} -\left(\frac{2}{Pe}\right)^2 & 0 \\ 0 & -1 \end{pmatrix} \quad (50)$$

An arbitrary vector  $(f_1, f_2)$  is expandable in terms of the eigenvectors  $\mathbf{Z}_m$  as a series of the form

$$\mathbf{F} = \begin{pmatrix} f_1 \\ f_2 \end{pmatrix} = \sum_{\lambda} a_n \mathbf{Z}_n \quad (51)$$

where

$$a_n = \frac{1}{N_n} \int_{-1}^{+1} \mathbf{F} \cdot \mathbf{C} \mathbf{A} \mathbf{Z}_n d\eta \quad (52)$$

with

$$N_n = \int_{-1}^{+1} \mathbf{Z}_n \cdot \mathbf{C} \mathbf{A} \mathbf{Z}_n d\eta \quad (53)$$

The convergence, termwise differentiation, and integration properties of these types of eigenvector expansions are similar to those of ordinary Fourier expansions. The reader is referred to [6] for details.

Equations (35) and (36) can be written as

$$\sum_{\lambda_n} b_n Z_{2n} = (\Delta\Phi)' \quad (54)$$

$$\sum_{\lambda_n} b_n Z_{1n} = 0 \quad (55)$$

where

$$b_n = \lambda_n c_n.$$

Equation (54) requires further discussion. It was obtained from termwise differentiation of (35). Even though  $\Delta\Phi \equiv 1$  for  $-1 \leq \eta \leq +1$  (35) cannot converge to 1 at  $\eta = \pm 1$  since all of the  $\psi_n$ 's vanish at these points. Therefore, the series in (35) converges to the value 1 for  $-1 < \eta < +1$  and to 0 for  $\eta = \pm 1$ . The convergent series has unit jumps at  $\eta = \pm 1$  and is constant otherwise. When (35) is differentiated,  $\Delta\Phi = 0$  for  $-1 \leq \eta \leq +1$  but the series has a zero derivative everywhere *inside* the interval and the endpoint jumps result in the terms  $\delta(\eta + 1)$  and  $-\delta(\eta - 1)$  at the left and right endpoints, respectively, where  $\delta$  is the usual Dirac delta function. See [7] for examples of this type of generalized differentiation. This type of phenomenon is familiar from ordinary Fourier series expansions. For instance

$$1 = \sum_{n=0}^{\infty} \left( (-1)^n / \left(n + \frac{1}{2}\right) \pi \right) \cos\left(n + \frac{1}{2}\right) \pi x \quad (56)$$

for  $-1 < x < +1$  however, the termwise derivative of the series in (56) is the well known delta function series

$$\begin{aligned} -\sum_{n=0}^{\infty} (-1)^n \sin\left(n + \frac{1}{2}\right) \pi x \\ = \delta(x + 1) - \delta(x - 1), \quad -1 \leq x \leq +1. \end{aligned}$$

Since these jumps lie at the endpoints of the interval,  $\delta$  could also be replaced by  $\delta/2$  or any other consistently followed notation [7].

In reality then, (54) and (55) become

$$\sum_{\lambda_n} b_n Z_{2n} = \delta(\eta + 1) - \delta(\eta - 1) \quad (57)$$

$$\sum_{\lambda_n} b_n Z_{1n} = 0 \quad (58)$$

which can be written in vector form

$$\sum_{\lambda_n} b_n \mathbf{Z}_n = \begin{pmatrix} 0 \\ \delta(\eta + 1) - \delta(\eta - 1) \end{pmatrix} \quad (59)$$

It now follows from (52) that the coefficients  $b_n$  are given by the formula

$$\begin{aligned} b_n &= \frac{-1}{N_n} \int_{-1}^{+1} (\delta(\eta + 1) - \delta(\eta - 1)) \begin{pmatrix} 0 \\ (\frac{2}{Pe})^2 & 0 \\ 0 & 1 \end{pmatrix} \begin{pmatrix} Z_{1n} \\ Z_{2n} \end{pmatrix} d\eta \\ &= \frac{-1}{N_n} \int_{-1}^{+1} (\delta(\eta + 1) - \delta(\eta - 1)) Z_{2n} d\eta \\ &= \frac{-1}{\lambda_n N_n} \int_{-1}^{+1} (\delta(\eta + 1) - \delta(\eta - 1)) \psi_n' d\eta \\ &= \frac{-1}{\lambda_n N_n} (\psi_n(-1) - \psi_n(+1)). \end{aligned} \quad (60)$$

It can be shown that all of the eigenfunctions  $\psi_n$  are either odd or even functions of  $\eta$ ; if  $\psi_n$  is odd then  $\psi_n'$  is even, and conversely. Thus the last term reduces to

$$b_n = \begin{cases} 0 & \psi_n \text{ odd} \\ \frac{1}{2} \psi_n(-1)/\lambda_n N_n & \psi_n \text{ even} \end{cases} \quad (61)$$

The complete solution of the problem is now given as

$$\Phi_1(\xi, \eta) = \Phi_{-\infty}(\eta) + \sum_{\lambda_n < 0} c_n \psi_n(\eta) e^{-\lambda_n \xi} \quad (62)$$

$$\Phi_2(\xi, \eta) = \Phi_{\infty}(\eta) - \sum_{\lambda_n > 0} c_n \psi_n(\eta) e^{-\lambda_n \xi} \quad (63)$$

with

$$c_n = b_n/\lambda_n.$$

For purposes of numerical calculation we will now derive a formula for the  $N_n$ , the normalization constants in the vector expansion.

Let  $\mathbf{Z}(\eta, \lambda) = (Z_1(\eta, \lambda), Z_2(\eta, \lambda))$  be a solution of

$$\mathbf{Z}' = \lambda \mathbf{A} \mathbf{Z} + \mathbf{B} \mathbf{Z} \quad (64)$$

satisfying the initial condition

$$\mathbf{Z}(-1, \lambda) = \mathbf{Z}_n(-1). \quad (65)$$

Then

$$\lim_{\lambda \rightarrow \lambda_n} \mathbf{Z}(\eta, \lambda) = \mathbf{Z}_n(\eta) \quad (66)$$

Following the usual cross-multiplication process used before, we find that

$$(\mathbf{Z} \cdot \mathbf{C} \mathbf{Z}_n)' = (\lambda_n - \lambda) \mathbf{Z} \cdot \mathbf{C} \mathbf{A} \mathbf{Z}_n \quad (67)$$

or

$$\begin{aligned} \int_{-1}^{+1} \mathbf{Z} \cdot \mathbf{C} \mathbf{A} \mathbf{Z}_n d\eta &= \mathbf{Z} \cdot \mathbf{C} \mathbf{Z}_n / (\lambda_n - \lambda) \Big|_{-1}^{+1} \\ &= \mathbf{Z}(1, \lambda) \cdot \mathbf{C} \mathbf{Z}_n(1, \lambda) / (\lambda_n - \lambda) \end{aligned} \quad (68)$$

since the lower limit vanishes because of the initial conditions.

Letting  $\lambda \rightarrow \lambda_n$  on both sides of this last equation yields

$$\begin{aligned} N_n &= \lim_{\lambda \rightarrow \lambda_n} \int_{-1}^{+1} \mathbf{Z} \cdot \mathbf{C} \mathbf{A} \mathbf{Z}_n d\eta = \lim_{\lambda \rightarrow \lambda_n} \mathbf{Z} \cdot \mathbf{C} \mathbf{Z}_n / (\lambda_n - \lambda) \Big|_{-1}^{+1} \\ &= \lim_{\lambda \rightarrow \lambda_n} \mathbf{Z}(1, \lambda) \cdot \mathbf{C} \mathbf{Z}_n(1, \lambda) / (\lambda_n - \lambda) \\ &= \lim_{\lambda \rightarrow \lambda_n} Z_{1n}(1, \lambda) Z_{2n}(1) / (\lambda_n - \lambda) \end{aligned} \quad (69)$$

Both  $Z_{1n}(1, \lambda)$  and  $\lambda_n - \lambda$  approach 0 as  $\lambda \rightarrow \lambda_n$ , and hence this last quantity is indeterminate. Using L'Hôpital's rule

$$\begin{aligned} \lim_{\lambda \rightarrow \lambda_n} Z_{1n}(1, \lambda) Z_{2n}(1) / (\lambda_n - \lambda) &= \frac{d}{d\lambda} Z_{1n}(1, \lambda) Z_{2n}(1) \\ &= \frac{d\psi_n}{d\lambda}(1, \lambda_n) \psi_n'(1) / \lambda_n. \end{aligned} \quad (70)$$

Thus the coefficients  $c_n$  in our solution are zero for odd  $\psi_n$  and are

$$c_n = b_n/\lambda_n = -2\psi_n'(-1)/\lambda_n N_n = -2/d\psi/d\lambda(1, \lambda_n) \quad (71)$$

for  $\psi_n$  even.

#### 4 Numerical Results

The solution consists of particular solutions  $\Phi_{-\infty}$ ,  $\Phi_{+\infty}$  and entrance region solutions  $\phi_1$ ,  $\phi_2$ .

For Poiseuille flow,  $p(\eta) = (3/2)(1 - \eta^2)$ . Thus our previous formulas yield for the particular solutions

$$\Phi_{+\infty} = 1 + \frac{3}{4} h(1 - \eta^4) \quad (72)$$

$$\Phi_{-\infty} = \Phi_{+\infty} - 1 \quad (73)$$

where  $h = \mu \bar{v}^2 / [TK]$ . The coefficients  $c_n$  in the series expressions for  $\phi_1$  and  $\phi_2$  may be calculated by utilizing the formula (71) with enough terms in the series retained to arrive at any desired accuracy. The first twelve positive eigenvalues corresponding to even eigenfunctions for (28) may be found from those previously calculated by Tan and Hsu [8] correct to six places for Peclet numbers of 1, 5, 10, 100 if one notes the relation  $\lambda_n = \frac{2}{3} \epsilon_n^2$  where the  $\epsilon_n$  are their set of eigenvalues.

Calculations for several selected Peclet numbers were carried out using a Hewlett-Packard 9820A programmable calculator and, to a lesser extent, an IBM 1130 computer. The derivatives of  $\psi$  with respect to the eigenvalue parameter lambda were approximated correct to three decimal places using the well known relation

$$\begin{aligned} d\psi/d\lambda(1, \lambda_n) &= (\psi(1, \lambda_n + \Delta\lambda) - \psi(1, \lambda_n - \Delta\lambda)) / 2\Delta\lambda + O(\frac{1}{|\lambda|^2}) \end{aligned} \quad (74)$$

The equation for  $\psi$ , (28), was integrated numerically using the standard fourth order Runge-Kutta scheme, and negative eigenvalues were found by a "shooting method" on the Hewlett-Packard calculator.

Table 1 shows sample results obtained for the lambda derivatives with  $Pe = 1$ . Six terms in the series solution were retained in all subsequent calculations of the entrance region temperature profiles.

Fig. 1 shows typical entrance region temperature profiles for  $Pe = 1$  at various stations along the positive half of the walls. The curve for  $\xi = 0.3$  is shown by a dotted line since, at this point, not enough terms had been retained in the series solution to fix the solution to better than  $\pm 0.01$ ; the curve shown is a mean curve drawn through the resulting scattered points. Figs. 2 and 3 show similar results for  $Pe = 1$  in the negative portion of the walls and for  $Pe = 10$  in the positive portion, respectively.

Near the outer walls the temperature is seen to be monotonically decreasing as  $\xi \rightarrow \infty$ , whereas near the center of the channel

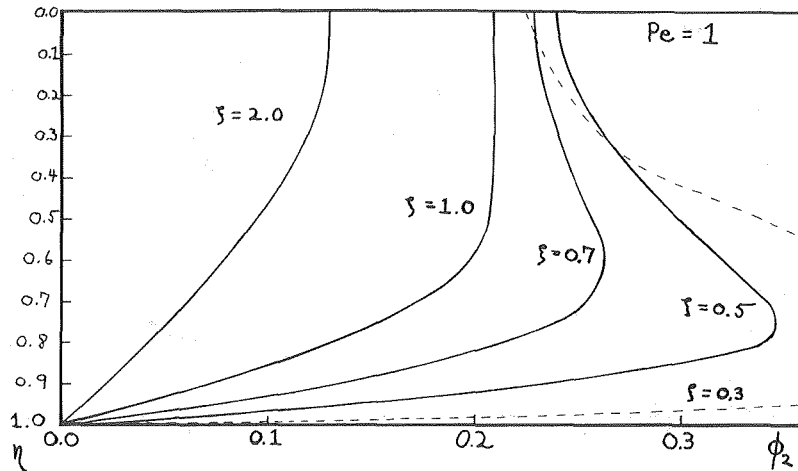


Fig. 1 Axial temperature profiles for  $Pe = 1$  downstream of the point where temperature changes abruptly

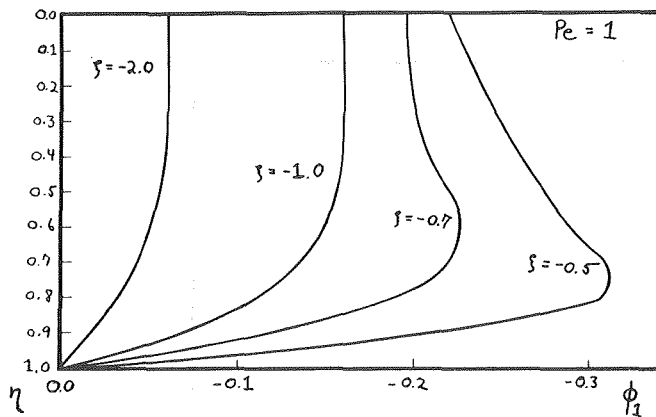


Fig. 2 Axial temperature profiles for  $Pe = 1$  upstream of the point where temperature changes abruptly

close to the entrance,  $\xi = 0$ , the crossing of temperature plots shows the existence of a "hot spot" just removed from the entrance. This phenomenon may be seen more clearly in Fig. 4 where the temperature profiles along the center of the channel ( $\eta = 0$ ) for  $\xi > 0$  are shown for  $Pe = 1, 5, 10$ . The temperature rises just inside the entrance,  $\xi = 0$ , over a distance which decreases with increasing Peclet number and thereafter decreases steadily for  $\xi \rightarrow \infty$ . This effect is more pronounced with increasing Peclet number.

### 5 Asymptotic Results

Asymptotic expressions for the eigenvalues and eigenfunctions of (28) are obtainable through standard procedures [9]. We find that the eigenvalues of (28) are

$$\lambda_n = \left(\frac{n\pi}{4} - \frac{Pe}{8}\right)Pe + O\left(\frac{1}{n}\right) \quad (75)$$

The corresponding eigenfunctions of (28) are given by

$$\psi_n = \frac{Pe}{2\lambda_n} \sin Q(\eta, \lambda_n) + O(1/n) \quad (76)$$

where

$$Q(\eta, \lambda_n) = \frac{2\lambda_n}{Pe}(\eta + 1) + \frac{Pe}{4} \int_{-1}^{\eta} p(s) ds.$$

Table 1 First six positive and negative eigenvalues with corresponding  $\psi$  derivatives for  $Pe = 1$

Downstream Solution		Upstream Solution	
$\lambda_n$	$\frac{d\psi}{d\lambda}(1, \lambda_n)$	$\lambda_n$	$\frac{d\psi}{d\lambda}(1, \lambda_n)$
0.638970	- 2.737	- 0.964735	2.409
2.230631	- 0.892	- 2.48918	0.808
3.802770	- 0.526	- 4.05585	0.494
5.373682	- 0.372	- 5.62527	0.356
6.944420	- 0.288	- 7.19540	0.278
8.515141	- 0.235	- 8.76585	0.228

The expression (75) agrees to two decimal places with the exact value of  $\lambda_n$  for  $|\lambda_n| > 2$  and to three places for  $|\lambda_n| > 8$  if  $Pe = 1$ . As  $Pe$  increases, the accuracy of the asymptotic results improves considerably. Comparable accuracy occurs for the asymptotic eigenfunction expansions (76).

Using (75) and (76), asymptotic expressions for the normalization constants,  $N_n$  are found to be

$$N_n = -\frac{2}{\lambda_n^2} + \frac{1}{\lambda_n^3} \frac{Pe}{4} \sin\left(\frac{8\lambda_n}{Pe} + \frac{Pe^2}{2}\right) + O\left(\frac{1}{n^4}\right) \quad (77)$$

From the foregoing results, useful formulas for predicting the average number of terms needed in the series expansion of the entrance region temperatures  $\phi_1$  and  $\phi_2$  can be obtained. For example, since

$$\phi_2(\eta, \xi) = 2 \sum_{\substack{n=1 \\ n \text{ odd}}}^{\infty} \frac{\psi_n'(1)}{\lambda_n N_n} \psi_n(\eta) e^{-\lambda_n \xi} \quad (78)$$

the error made in approximating  $\phi_2$  by a truncated series containing terms up to and including  $n = N$  is

$$R_N = 2 \sum_{\substack{n=2N+2 \\ n \text{ odd}}}^{\infty} \frac{\psi_n'(1)}{\lambda_n N_n} \psi_n(\eta) e^{-\lambda_n \xi} \quad (79)$$

This error term series,  $R_N$ , can be summed approximately by utilizing asymptotic expansions (75), (76), (77) in the series for  $R_N$ .

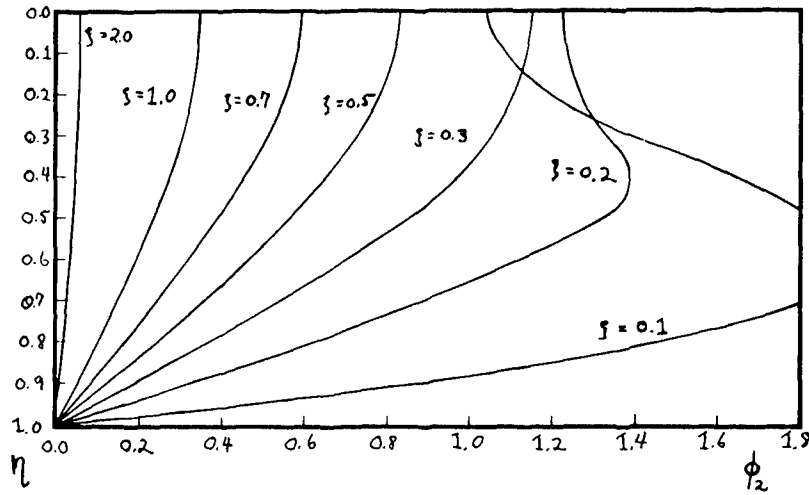


Fig. 3 Axial temperature profiles for  $Pe = 10$  downstream of the point where temperature changes abruptly

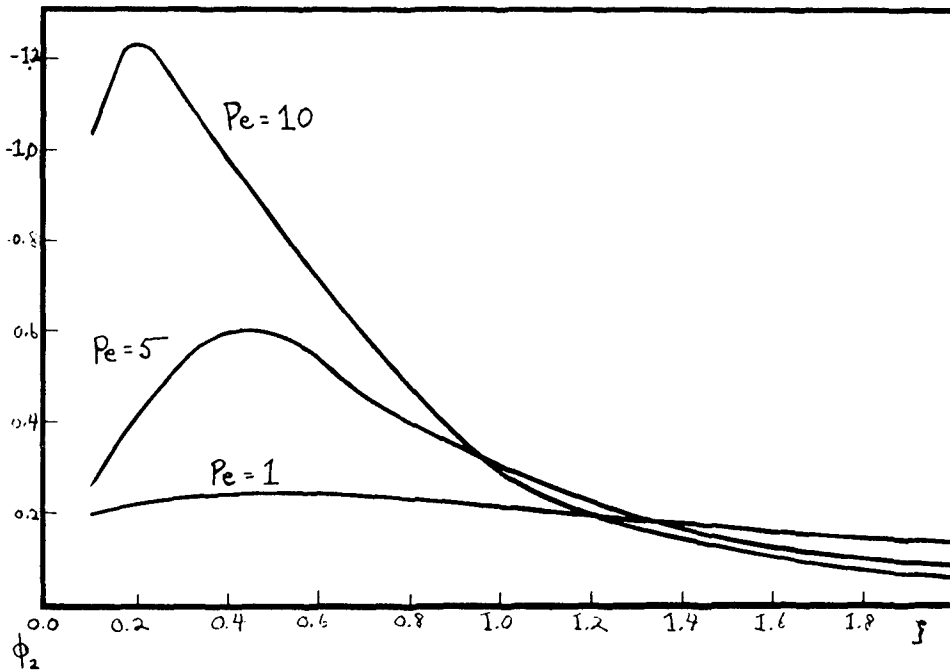


Fig. 4 Typical center-line temperature distributions for the Right-Half Channel

Table 2 Number of series terms needed to obtain error of less than 0.01 at various downstream axial locations for typical Peclet numbers

$\xi$	0.1	0.2	0.3	0.4	0.5	0.6	0.7	0.8	0.9	1.0
$Pe = 10$	3	1	1	1	1	1	1	1	1	1
$Pe = 5$	5	3	2	1	1	1	1	1	1	1
$Pe = 1$	15	8	6	5	4	4	3	3	2	2
$Pe = 0.5$	21	11	7	5	5	5	4	4	4	4
$Pe = 0.1$	23	13	11	8	5	5	4	3	3	3

Table 3 Number of series terms needed to obtain error of less than 0.001 at various downstream axial locations for typical Peclet numbers

$\xi$	0.1	0.2	0.3	0.4	0.5	0.6	0.7	0.8	0.9	1.0
$Pe = 10$	4	2	1	1	1	1	1	1	1	1
$Pe = 5$	9	4	3	2	2	1	1	1	1	1
$Pe = 1$	30	15	12	8	7	5	5	4	4	4
$Pe = 0.5$	30	24	17	13	11	9	8	7	7	6
$Pe = 0.1$	120	65	46	37	28	22	18	17	17	16

The result is an algebraically messy series which can be summed exactly using the formulas involved. By selecting a given accuracy level e.g.,  $|R_N| < 0.01$  one can then estimate the average number of terms required to obtain this desired accuracy for a given  $Pe$  and  $\xi$  values. Results obtained are shown in Tables 2 and 3 and were found to be in excellent agreement with previous numerical calculations over all calculated ranges of values.

It is apparent from these results the disproportionate difficulty in obtaining accurate results for small values of  $\xi$  near the entrance. In such cases, mean curves constructed through the resulting scattered collection of points often yield fairly accurate results.

## References

- 1 Agrawal, H. C., "Heat Transfer in Laminar Flow Between Parallel Plates at Small Péclet Numbers, *Applied Scientific Research*, Sect. A, Vol. 9, 1959-1960, pp. 177-189.
- 2 Van Der Does De Bye, J. A. W., and Schenk, J., "Heat Transfer in Laminar Flow Between Parallel Plates" *Applied Scientific Research*, Sect. A, Vol. 3, 1951, pp. 308-316.
- 3 Schenk, J., "A Problem of Heat Transfer in Laminar Flow Between Parallel Plates," *Applied Scientific Research*, Sect. A, Vol. 4, 1954, pp. 241-244.
- 4 Davies, J. E., *Canadian J. Chem. Engin.*, Vol. 51, 1973, pp. 562-572.
- 5 Deavours, C., Sc.D. thesis, University of Virginia, 1969.
- 6 Langer, R. E., "The Expansion Problem in the Theory of Ordinary Linear Differential Systems of the Second Order," *Transactions of the American Math. Society*, Oct. 1929, pp. 868-906.
- 7 Friedman, B., *Principles and Techniques of Applied Mathematics*, Wiley, New York, 1956, p. 154.
- 8 Tan, C. W., and Hsu, C. J., "Mass Transfer of Aerosols With Axial Diffusion in Narrow Rectangular Channels," *Applied Scientific Research*, Sect. A, Vol. 25, 1972, pp. 295-312.
- 9 Erdelyi, A., *Asymptotic Expansions*. Dover Publications, Chapter IV, 1956.

M. Cumo  
G. E. Farello  
G. Ferrari  
G. Palazzi

Laboratorio Tecnologie Reattori,  
Centro di Studi Nucleari della Casaccia,  
Comitato Nazionale per l'Energia Nucleare,  
Rome, Italy

## On Two-Phase Highly Dispersed Flows

*Experimental research on highly dispersed, two-phase, turbulent flows was performed employing Freon 12 at different pressures up to the critical value. By means of visualization techniques it was possible to study the droplet size distribution, their spatial concentration, and the relationships among the deduced law of distribution and the main thermo-hydraulic parameters for different thermo-hydraulic conditions (pressure, mass velocity, and quality). Simple relations were developed which make it possible to determine, at least for some reference thermo-hydraulic situations, all of the characteristics of the liquid dispersed phase.*

### Considerations on the Constitution of Two-Phase, Liquid-Vapor Mixtures at High Qualities

The present study extends a previous one [1]<sup>1</sup> which analyzed the influence of vapor quality on the constitution of two-phase mixtures, mainly evaluating the degree of thermodynamic nonequilibrium obtained in such mixtures. The fluid employed is Freon 12 which has advantages for experimental use (low vapor tension, low latent heat) and models the thermodynamic conditions of the most commonly employed fluid, water [2, 3].

This research is concerned with the influence of pressure on the constitution of a two-phase mixture at high vapor quality. Such mixtures are characteristic of the flow region in heated channels called "post burnout" or "post dryout" which is between the dryout point and the point at which the last droplets disappear via evaporation.

This two-phase flow is characterized by some specific parameters. For a vertical upward flow in a tubular uniformly heated channel with given fluid and geometry these parameters are: the pressure  $p$  (or the reduced pressure  $\pi = p/p_{cr}$ ), the mass velocity  $G$ , the quality  $X$ , and the heat flux  $\phi$ .

As shown in the previous study, the heat flux may affect the mixture constitution, because depending on the value of  $\phi$  it is possible to have different degrees of thermodynamic nonequilibrium (superheating of the steam in presence of the liquid phase, with consequent differences between the equilibrium and actual qualities). The quality  $X$  used here refers exclusively to the calculated equilibrium quality obtained by an enthalpy balance.

### Experimental Apparatus

The experimental facility consists of a stainless steel loop sketched in Fig. 1. The vertical test section is electrically heated. A detailed description of the plant may be found in [4]. The

working fluid is Freon 12, which has been already successfully employed to simulate water in burnout power measurements [3].

In this loop a visual test section having the same cross-sectional area as the tubular duct was installed (Fig. 2). The visual test section was constructed so as to have an adiabatic flow which maintained the constitutive characteristics of the highly dispersed mixture which was generated in the heated section. There is no influence of the flow passage width on droplet size and distribution, since the droplet diameters are much smaller than the tube diameter ( $\sim 100 \mu$  versus  $5000 \mu$ ). In addition, no interaction has been noted between droplets and sight glass. The whole depth of the flow passage has been focused in the optical system. The optical resolution, with  $20\times$  magnification, is  $0.1 \text{ mm}$ ; this  $0.1 \text{ mm}/20 = 5$  is the obtainable resolution.

The optical system includes a light source, able to give  $1\text{-}\mu$  light pulses, and a camera installed on an optical bench [1]. This system provides photographs of the flow which, in turn, enable determination of the droplets' spatial distribution and their characteristic dimensions. The light pulses have a continuous spectrum.

The experimental research was performed with particular reference to the influence of pressure on the two-phase flow; hence, the pressure value was systematically varied up to the critical point. The other two main parameters, namely the mass velocity and quality, were kept constant. In all the tests, dispersed flow existed over the entire visual test section.

### Constitution of the Two-Phase Mixture

Some examples of the photographs obtained are given in Figs. 3, 4, and 5. In these photographs the droplets and their spatial distribution are clearly visible. The influence of the pressure parameter is clear: at increasing pressures, the droplet volume decreases, until it disappears when the critical pressure is reached. From these photographs and from many similar ones, some quantitative characteristics of the two-phase mixture have been deduced. The droplet size distribution curves were directly measured using the same photographs after suitable enlargement. Figs. 6 and 7 collect a series of 14 thermo-hydraulic situations, chosen so as to show the effect of the pressure parameter at essentially constant values of mass velocity and quality. Qualita-

<sup>1</sup> Numbers in brackets designate References at end of paper.

Contributed by the Heat Transfer Division of THE AMERICAN SOCIETY OF MECHANICAL ENGINEERS and presented at the ASME-ATChE Heat Transfer Conference, Atlanta, Ga., August 5-8, 1973. Journal manuscript received by the Heat Transfer Division September 24, 1973. Paper No. 73-HT-18.

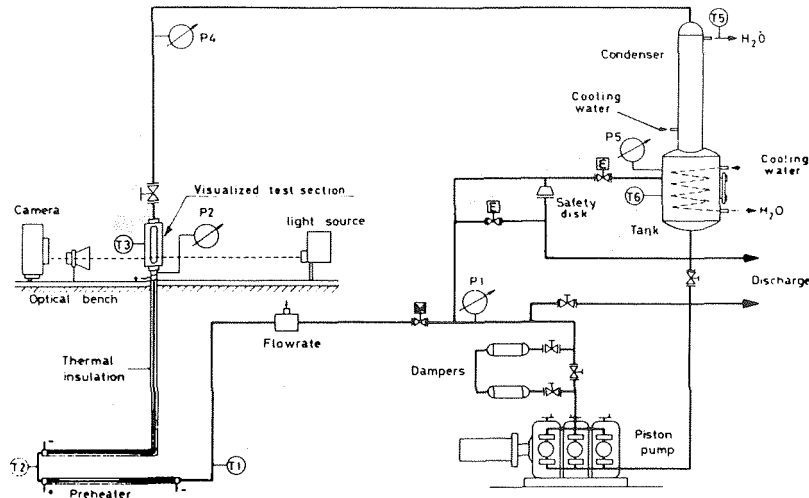


Fig. 1 Sketch of the experimental loop with indication of the main components

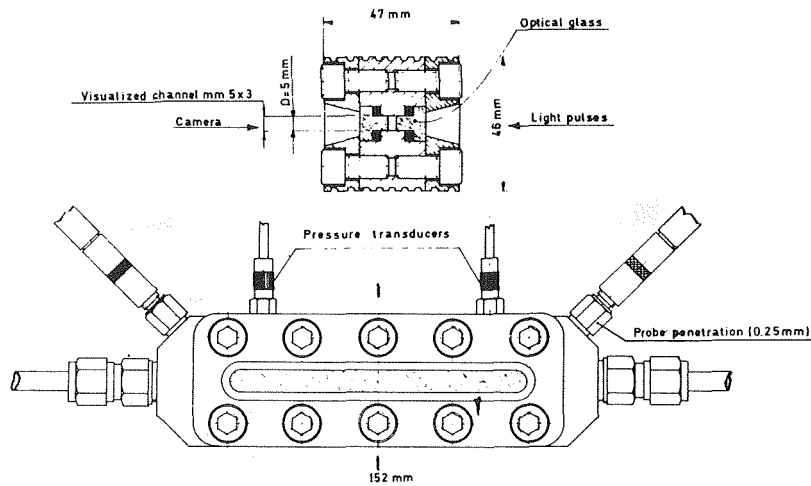


Fig. 2 Sketch of the visual test section

tively, the distribution curves suitably normalized, are such that with increasing  $\pi$  their maximum moves toward minor diameters and at the same time the whole curve tightens to denote a minor size scattering of the droplets. The distribution curves have roughly a Maxwellian shape. A characteristic parameter of the mixtures relative to the different thermo-hydraulic situation is the droplet mean diameter,  $\bar{d}$ , defined by the relationship:

$$\bar{d} = \frac{\int_0^{\infty} n(d) \cdot d \cdot \delta d}{\int_0^{\infty} n(d) \cdot \delta d} \quad (1)$$

It is interesting to see how this mean diameter depends on the

### Nomenclature

$C$  = spatial concentration of the droplets  
 $d$  = droplet diameter  
 $\bar{d}$  = mean droplet diameter  
 $d_*$  = most probable droplet diameter  
 $d_{\max}$  = maximum droplet diameter  
 $D$  = main side of cross section of the visual channel  
 $G$  = specific mass flowrate  
 $H$  = enthalpy

$m(d)$  = mass percentage of droplets having diameter  $< d$   
 $M$  = total mass relative to the examined droplets  
 $n(d)$  = droplet size distribution  
 $N$  = total number of droplets  
 $p$  = system pressure  
 $X$  = vapor quality,  $(H_b - H_{\text{sat}})/\lambda$   
 $y$  = distance from the wall

$\lambda$  = enthalpy of vaporization  
 $\mu$  = dynamic viscosity  
 $\pi$  = reduced pressure  
 $\rho$  = density  
 $\varphi$  = heat flux

### Subscripts

$b$  = bulk  
 $l$  = liquid



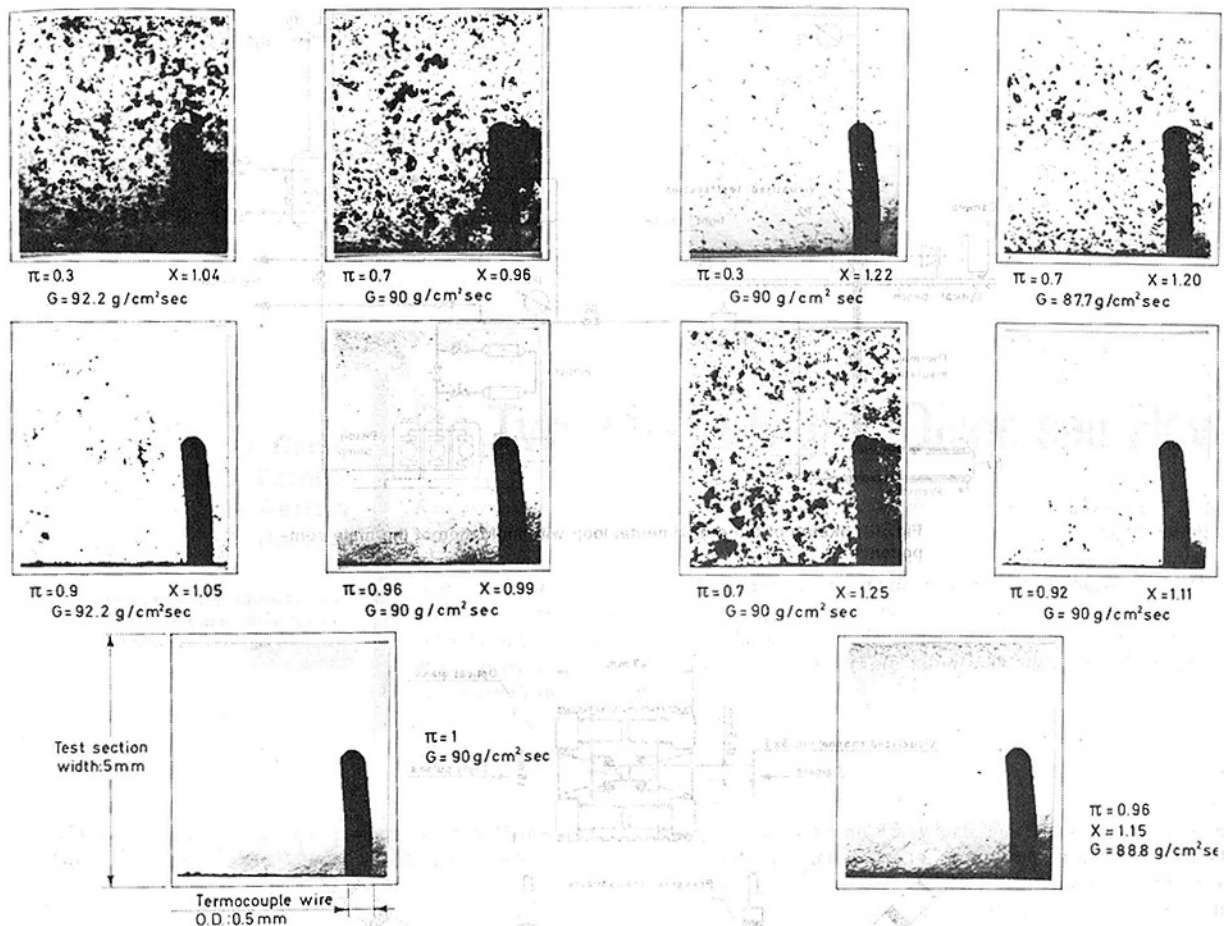


Fig. 3 Pictures showing the influence of pressure on droplet size

Fig. 4 Pictures showing the influence of pressure on droplet size

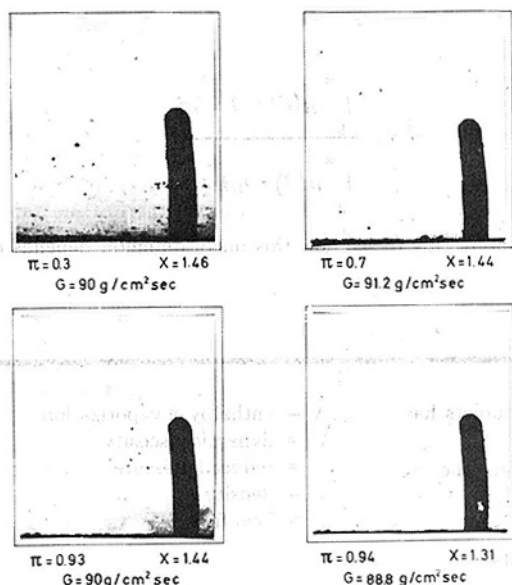


Fig. 5 Pictures showing the influence of pressure on droplet size

experimental situations. Fig. 8 shows, for three qualities ( $X \approx 1$ ,  $X \approx 1.20$  and  $X \approx 1.40$ ), the trend of  $\bar{d}$  versus  $\pi$ . This trend systematically indicates a decrease of  $\bar{d}$  which becomes more pronounced when  $\pi$  approaches unity. There is a strong variation within  $\pi = 0.7$  and  $\pi = 1$ , while in the range  $\pi = 0.3-0.7$ ,  $\bar{d}$  appears substantially constant. It should be noted that the reference qualities for the single experimental points, although grouped close to the three values indicated, are not exactly equal for each situation.

If there were a strong influence of the quality on the dimensions of the droplets, this influence might mask the same influence of the pressure. This is not the real situation as indicated in Fig. 9; for small variations of  $X$ ,  $\bar{d}$  is almost constant.

Let us now consider the droplet size distribution curves for the various thermo-hydraulic situations, partially represented in the diagrams of Figs. 6 and 7. A study of the structure of the  $n(d)$  curves has indicated the following analytic expression:

$$n(d) = \frac{d}{d_*^2} e^{-d/d_*} \quad (2)$$

where  $d_*$  is the diameter corresponding to the maximum of  $n(d)$ , i.e., the most probable diameter.

This expression is very simple and Figs. 6 and 7 show a set of experimental data which gives a particularly good fit to equation (2).

The value of the droplet mean diameter may be calculated from equation (2) and the general expression for mean diameter for this distribution is  $\bar{d} = 2 d_*$ . This relationship shows the connection between the mean diameter and the most probable diameter.

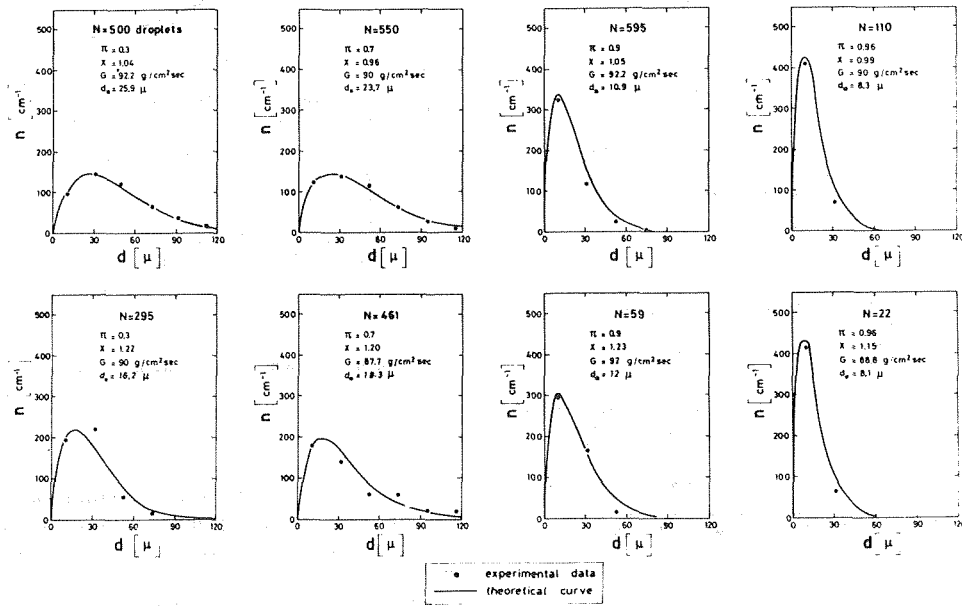


Fig. 6 Size distributions of droplets for different thermo-hydraulic conditions

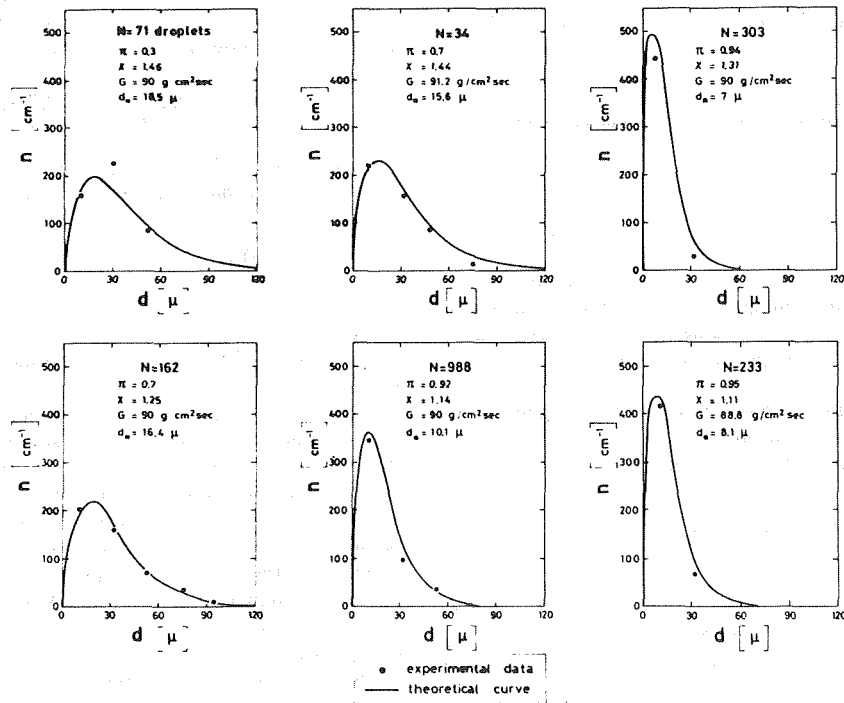


Fig. 7 Size distributions of droplets for different thermo-hydraulic conditions

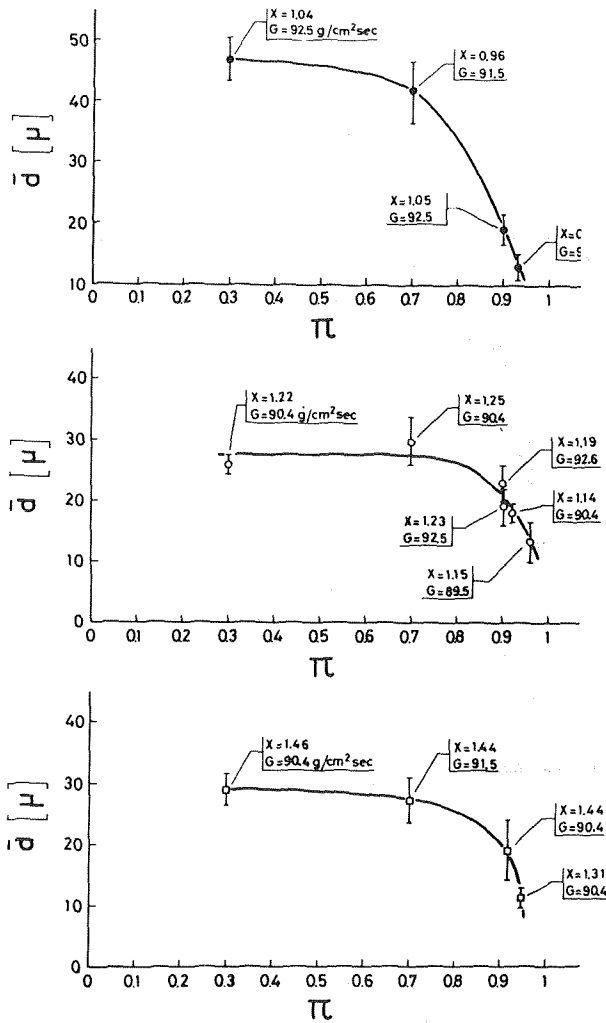


Fig. 8 Mean diameter of droplets versus reduced pressure

Two interesting parameters of two-phase mixture and droplet size distribution are the percentage of the mass of droplets having diameter less than a determined value  $d$ , that is "cumulative mass," and the mass percentage distribution as a function of droplet diameter.

The analytical expression for both these parameters may be calculated from the distribution law, equation (2).

The equation for the cumulative mass becomes

$$m(d) = \frac{100}{M} \frac{\pi}{6} \rho_l \int_0^d d_*^3 \cdot n(d) \cdot \delta d$$

$$= \frac{400}{M} \pi \cdot \rho_l \cdot d_*^3 \cdot \left[ 1 - e^{-d/d_*} \sum_{i=0}^4 \frac{(d/d_*)^i}{i!} \right] \quad (3)$$

where  $M$  is the total mass of measured droplets. Some experimental points, calculated from the histograms of Fig. 6, are compared with equation (3) and the results are shown in Fig. 10.

If we differentiate the expression (3), we get the mass percentage distribution of liquid phase as a function of droplet diameter

$$\frac{\partial m}{\partial d} = \frac{\pi}{6} \cdot \frac{\rho_l}{M} \cdot \frac{d^4}{d_*^2} e^{-d/d_*} \quad (4)$$

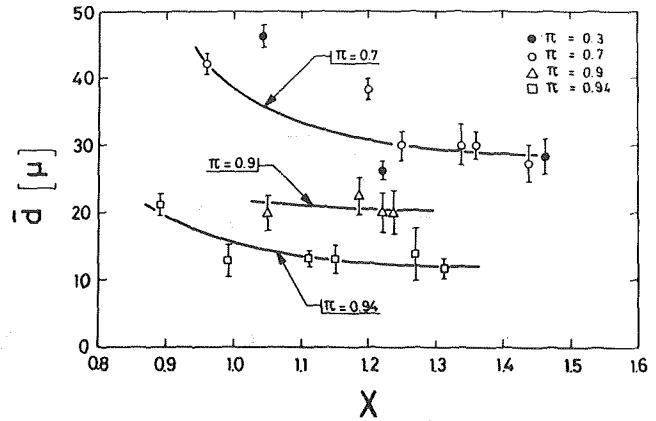


Fig. 9 Mean diameter of droplets versus equilibrium quality

The comparison with some experimental results is shown in Fig. 10 where the corresponding values of  $d_*/d_{max}$  are also given;  $d_{max}$  is the maximum measured droplet diameter for each photograph.

The maximum droplet diameter is a particular parameter because it shows clearly the maximum dimension that a droplet can have in the particular conditions of turbulent flow and it constitutes in a certain sense a measure of the external forces which act on the droplets and which oppose surface-tension forces. The droplet size distribution law is characterized, of course, by the most probable droplet diameter  $d_*$ . It is dependent on the main thermo-hydraulic parameters characterizing the situation of two-phase, highly dispersed flows. Therefore, if we group the main quantities as a nondimensional number, that is mean flowrate, quality, viscosity, and the most probable droplet diameter, we obtain a kind of a Reynolds number referring to  $d$ .

$$Re_* = \frac{(GX)d_*}{\mu_l}$$

We are interested in finding the ratio between  $Re_*$  and the parameter studied, that is the reduced pressure  $\pi$ :  $Re_* = j(\pi)$ . In our case:

$$\frac{(GX)d_*}{\mu_l} = 123.1(1 - \pi)^{0.31} \quad (5)^2$$

has been found.

Fig. 11 shows the experimental results compared with the theoretical curve.

To sum up, with reference to the geometry and fluid used in our experiment, it is possible to characterize, with equations (5), (2), (3), and (4), the configuration of two-phase, highly dispersed flows in a satisfactory and complete way.

We consider now another physical quantity which is important for the understanding of a possible wall effect: the spatial concentration  $C$  of the droplets throughout the flow region, that is the number of droplets (of any size) per unit volume at various distances,  $y$ , from the solid wall, across the visual test section (side of length  $D$ ).

Therefore the pictures obtained, suitably enlarged, have been subdivided crosswise to the flow in several zones to measure the relative droplet density  $C$  for each zone. Because of the symmetry of the test section and the flow, the observation could be limited

<sup>2</sup>Relation (5), obviously, applies only to Freon 12, being empirical in nature. Generally speaking, in the Reynolds number, the use of vapor viscosity, not liquid, referring to the continuous phase, would be more appropriate.

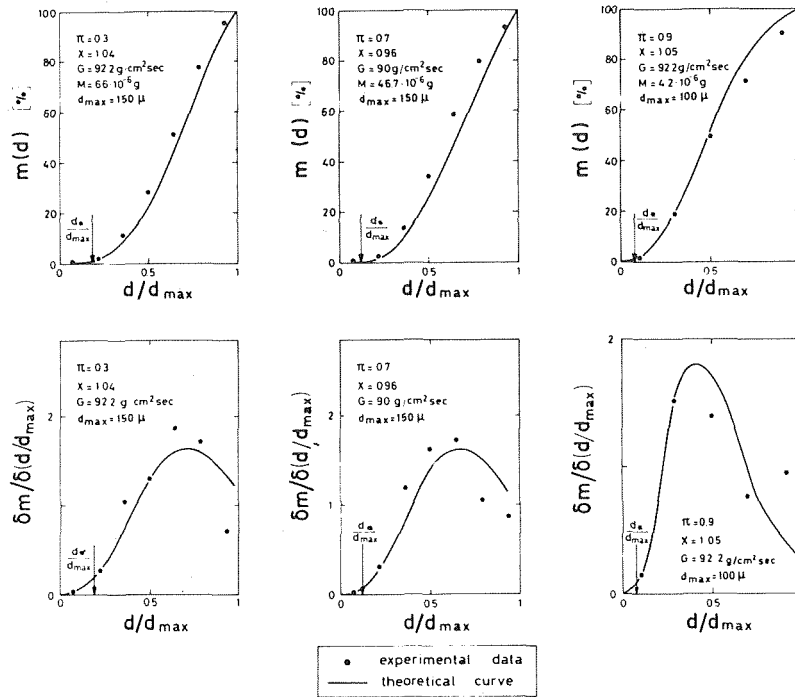


Fig. 10 Mass percentage of liquid phase of all droplets having diameter less than or equal to  $d$  and percentage distribution of the liquid phase versus droplet diameter

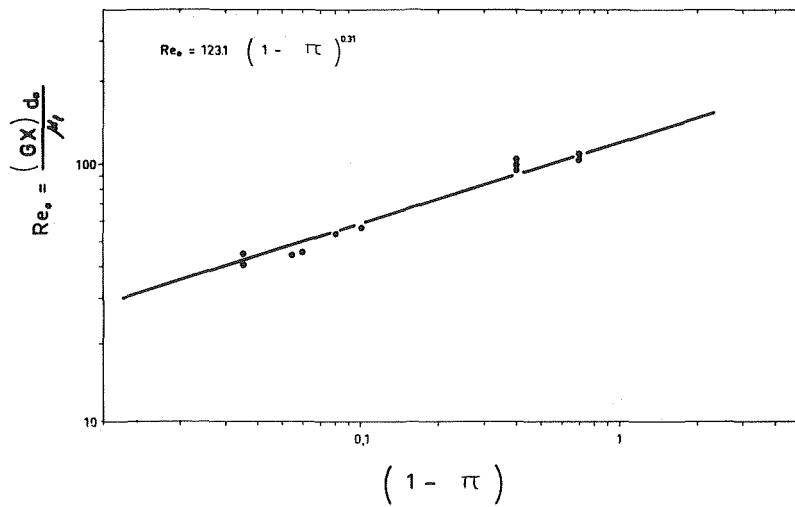


Fig. 11 Comparison of relationship (5) with experimental values

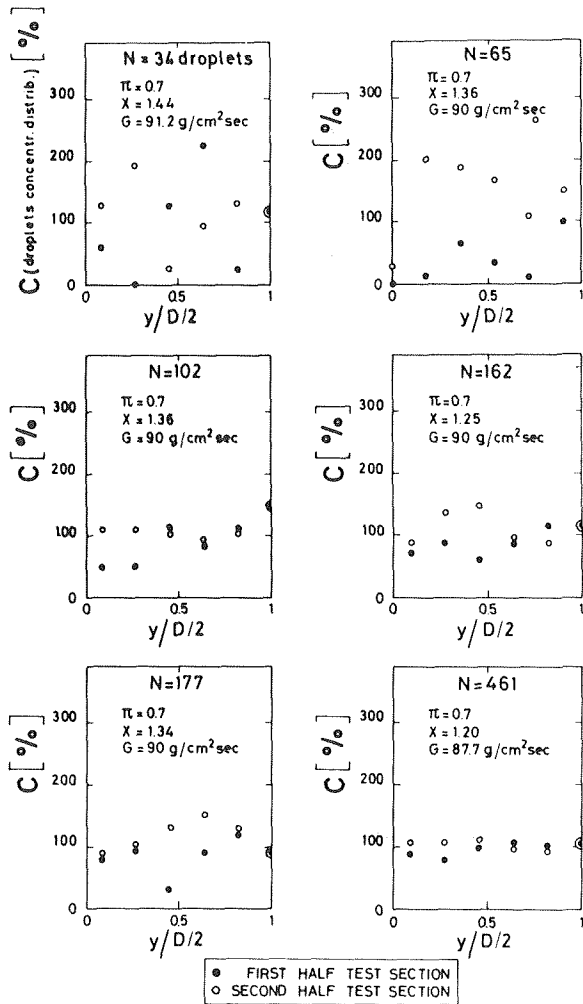


Fig. 12 Concentration of droplets versus the distance from the wall (two different symbols (● ○) refer to measurements obtained in two symmetrical parts into which the visual test section has been divided along the direction of the flow)

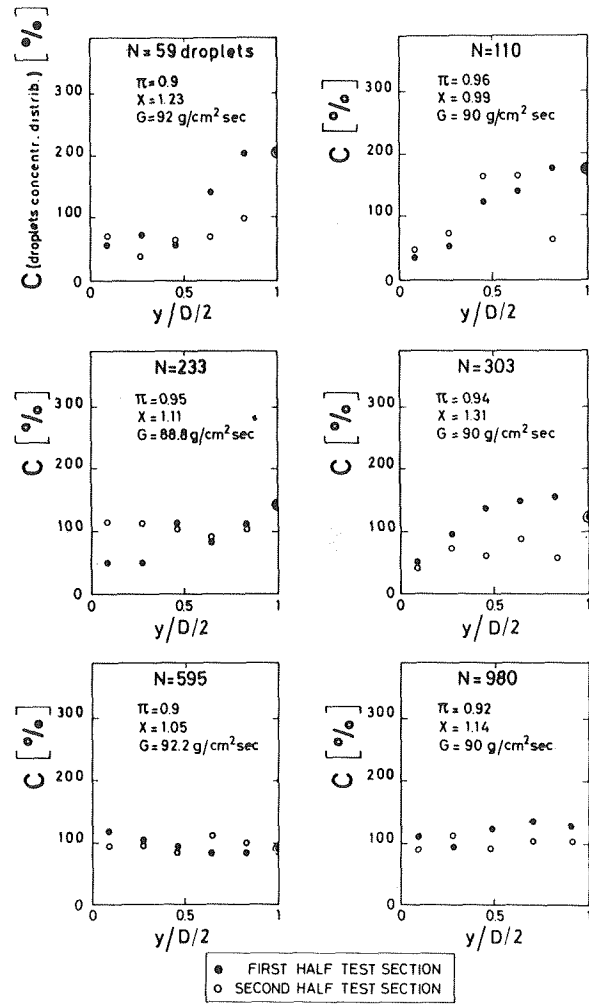


Fig. 13 Concentration of droplets versus the distance from the wall (two different symbols (● ○) refer to measurements obtained in two symmetrical parts into which the visual test section has been divided along the direction of the flow)

to half of the test section, but considering the statistical constitution of the flow, measurements of the two halves of the test section were taken, to make evident, at the same time, the statistical fluctuations, as well as for precision of results.

Figs. 12 and 13 collect some of these results. From them, and from other similar results, there appears to be no effect of the pressure, nor of the quality upon the spatial concentration of the droplets, whose distribution appears to be statistical. This confirms some preliminary conclusions reached in [1].

When the droplets number  $N$  increases, the spatial distribution becomes more and more uniform and the  $C$  profile flattens out.

This result is very useful when formulating two-phase flow models, because the problem is obviously simplified with the hypothesis of a uniform distribution of discontinuous phase in the continuous one.

From the study of the pictures obtained it has been possible to answer another important problem: Does the numerical droplet concentration in the flow region depend on the droplet size? For example, if the larger droplets crowd together close to the solid walls, the smaller droplets could be expected to be entrained more easily by the vapor flow.

To explore this, a mean size,  $d = 50 \mu$ , was selected to divide the "large" from the "small" droplets and, with these values, the measurements of the spatial distribution across the test section were repeated.

Fig. 14 collects some examples. It appears obvious that as regards droplet sizes, too, there is no preferential dependence on concentration, and the droplet distribution appears to be quite uniform across the flow region, especially as the number of observed values is increased.

This last fact also, that is large and small droplets, uniformly mixed without any separation along the flow for different velocities of the entraining vapor phase, simplifies greatly any mathematical formulation of a two-phase flow model.

## Conclusions

The research carried out may be summarized in the following conclusions:

1 Two-phase, highly dispersed, turbulent flows are characterized by a uniform (statistically) spatial distribution of the droplets entrained within the duct flow.

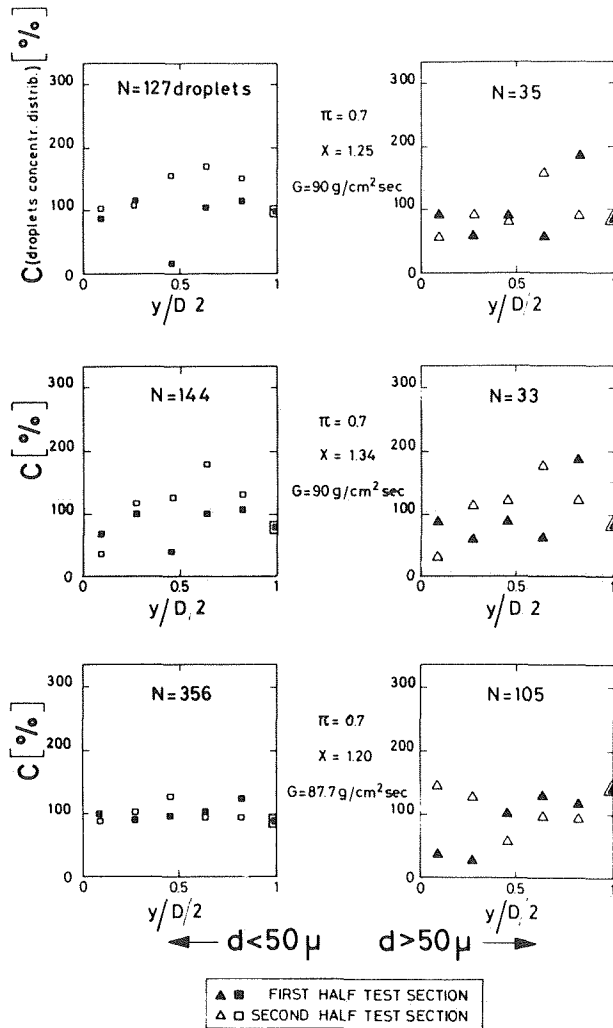


Fig. 14 Concentration of droplets depending on their sizes with the distinction of droplet diameter greater or less than  $50 \mu$

2 The droplets are uniformly (statistically) mixed independently of their dimensions; "big" droplets and "small" droplets are spaced in the cross section of the duct flow independently of the local vapor velocity, and there is no separation independent of vapor velocity or velocity gradient.

3 The droplets dimensional distribution is characterized by a most probable value of droplet diameter,  $d^*$ , which for the present Freon 12 experiments is given by equation (5).

4 The law of the droplets' size distribution (normalized) is expressed by equation (2).

5 The mass percentage of liquid phase relative to droplets with a diameter less than a determined value  $d$  is given, consequently, by equation (3).

6 The mass percentage distribution of liquid phase as a function of droplet diameter is then expressed by equation (4).

The relationships developed in this study are sufficient to characterize the constitution of a highly dispersed two-phase mixture, at least for the present experimental situation.

#### Acknowledgments

The technicians involved with the experimental program were G. Garofalo and G. Perelli.

#### References

- Cumo, M., Farello, G. E., and Ferrari, G., "A Photographic Study of Two-Phase, Highly Dispersed Flows," XXV Congresso Nazionale ATI, Trieste, Oct. 1970.
- Eastwood, W. S., "The Scaling of Two-Phase Flow Using Freon," II European Meeting on Two-Phase Flow, Ispra, June 1966.
- Barnett, P. G., "The Prediction of Burn-Out in Non-Uniformly Heated Rod Clusters From Burn-Out Data for Uniformly Heated Round Tubes," Report AEEW R362, Winfrith, Dorchester, 1964.
- Farello, G. E., "Rapporto di sicurezza: circuito CF-1," C.N.E.N. RT/TR (68) STAV 11, 1968.
- Mugele, R. A., and Evans H. D., "Droplet Size Distribution in Sprays," *Industrial and Engineering Chemistry*, Vol. 43, No. 6, June 1951, pp. 1317-1324.
- Dr. Gardner, Personal Communication, Central Electricity Generating Board, C.E.R.L., Leatherhead, Surrey.
- Silvestri, M., *Advances in Heat Transfer*, Academic Press, New York, London, 1964.
- Abramovich, G. N., "Effect of Solid-Particle or Droplet Admixture on the Structure of a Turbulent Gas Jet," *International Journal of Heat and Mass Transfer*, Vol. 14, 1971, pp. 1039-1045.
- Rohsenow, W. M., and Fedorovich, E., "Post Burn-Out Heat Transfer to Mist Flow," *Heat and Mass Transfer*, Vol. 2, Beograd, 1970, pp. 683-699.

F. W. Paul  
Mechanical Engineering Department,  
Carnegie-Mellon University,  
Pittsburgh, Pa.

K. J., Riedle  
Siemens  
Forschung Szentrum, RT 51,  
852 Erlangen,  
West Germany

# Experimental Frequency Response Characteristics for Diabatic Two-Phase Flow in a Vertical Monotube Vapor Generator

*This paper presents experimental data on the dynamic behavior of diabatic two-phase flow in a vertical tube with Refrigerant-11 as the working fluid. A detailed description is included of the experimental test facility as well as the instrumentation used for monitoring the variables of pressure, flow, heat flux, and void fraction.*

*Experimental data are presented in frequency response form for inlet impedance ( $\Delta P_1/\Delta W_1$ ) and exit void fraction ( $\Delta \alpha_3/\Delta W_1$ ) at constant heat flux over a frequency range of 0.01 to 10.0 Hz. The data cover inlet subcooling conditions of 14°F and 79°F and two heat flux levels.*

*The experimental results show that the inlet impedance characteristics have fluctuations in amplitude and phase lag with frequency which lead to resonant peaks in the overall frequency response behavior. Exit void fraction characteristics show similar resonant behavior with large phase lag at frequencies above 1 Hz.*

## Introduction

The knowledge of the dynamic behavior of thermal systems which operate in forced convection flow-boiling is important for the prediction and understanding of their local and global stability. The control and overall stability of specific thermodynamic systems requires an understanding and knowledge of the dynamic behavior of the vapor generating component (boiler) and how this device interacts with other system components. Numerous thermal-hydraulic systems, such as nuclear reactors, tubular chemical reactors, distillation plants, refrigeration systems, and rankine cycle engines, utilize this type of component with the attendant need for basic understanding of the boiler dynamics if safe, reliable, and controllable designs are to be realized.

The purpose of this paper is to present experimental data for the inlet impedance and exit void fraction frequency response characteristics for forced inlet diabatic two-phase flow in a vertical monotube vapor generator. Data is presented for inlet subcoolings of 14°F and 79°F, two magnitudes of uniform heat flux, and a constant mass flux. Detailed discussion of the results is included to elucidate the dynamic behavior of the vapor generator.

## Previous Work

A limited amount of experimental data exists which presents the dynamic behavior of a diabatic monotube boiler over a broad

frequency spectrum. Such experimental data can be characterized in the frequency domain by numerous different magnitude-phase ratios as listed in the following indicated functionally in Figure 1.

- 1  $\Delta P_1/\Delta W_1(j\Omega)$  for  $\Delta q'' = 0$
- 2  $\Delta P_3/\Delta W_1(j\Omega)$  for  $\Delta q'' = 0$
- 3  $\Delta \alpha_3/\Delta W_1(j\Omega)$  for  $\Delta q'' = 0$
- 4  $\Delta P_1/\Delta q''(j\Omega)$  for  $\Delta W_1 = 0$
- 5  $\Delta P_3/\Delta q''(j\Omega)$  for  $\Delta W_1 = 0$
- 6  $\Delta \alpha_3/\Delta q''(j\Omega)$  for  $\Delta W_1 = 0$

Experimental frequency response results have been presented for ( $\Delta \alpha_3/\Delta q''$ ) by St. Pierre [1]<sup>1</sup> using water, for ( $\Delta \alpha_3/\Delta W_1$ ) and ( $\Delta \alpha_3/\Delta q''$ ) by Staub, Zuber, and Bijwaard [2] and Staub and Zuber [3] using Refrigerant-22, and for ( $\Delta \alpha_3/\Delta q''$ ) and ( $\Delta P_1/\Delta q''$ ) by Dijkman [4] using water. Neal Zivi, and Wright [5] also show experimental frequency response data for ( $\Delta \alpha_3/\Delta W_1$ ) magnitude only using water as the working fluid.

Recently Dorsch [6], Krejsa, Goodykoontz, and Stevens [7, 8, 9, 10], and Krejsa [11] have presented experimental frequency response data for inlet impedance characteristics ( $\Delta P_1/\Delta W_1$ ) using Refrigerant-113. These results appear to present the only experimental data for hydrodynamic inlet impedance characteristics in two-phase flow.

Contributed by the Heat Transfer Division for publication in the JOURNAL OF HEAT TRANSFER. Journal manuscript received by the Heat Transfer Division, June 12, 1974.

<sup>1</sup> Numbers in brackets designate References at end of paper.

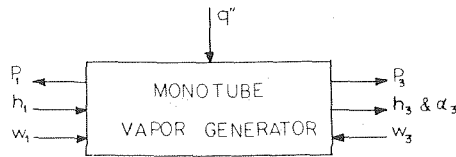


Fig. 1 Functional representation

### Experimental Test Facility

This experimental investigation was carried out on an experimental test apparatus which utilized Refrigerant-11 as the working fluid. The use of this fluid permitted the tests to be conducted at a reduced pressure  $P'$  of approximately 0.3, reducing the costs of operating the test facility.

Fig. 2 shows a schematic of the experimental test facility. Pressure and flow are supplied by a 40 HP d-c motor-centrifugal pump combination, while a positive displacement make-up pump maintains the system pressure level. The main centrifugal pump capacity is approximately 100 gpm with a pressure rise of 80 psi, and a maximum system pressure level of 600 psia.

The capability of the loop centrifugal pump is such that substantial throttling is possible prior to the test section to provide a stiff system and decouple the pump, condenser, and fluid supply system from the test section. No accumulators or fluid surge chambers are included in the loop to minimize the possibility of flow oscillations due to system component interactions. Such component interactions can lead to misleading experimental dynamic measurements which reflect the behavior of the loop rather than those of the vapor generator.

The centrifugal pump supplies flow to the loop preheater which permits the automatic regulation of the test section inlet temperature and subcooling. Approximately 10 percent of the total pump flow goes to the experimental test section with the remaining 90 percent bypassed to the condenser through a throttling valve. This permits the test section to operate at approximately constant pressure drop during transient testing and in addition decouples the test section from the experimental loop.

Refrigerant-11 flows in an upward vertical direction in a 304 stainless steel tube. This tube had a mean outside diameter of 0.999 in. with a wall thickness of 0.066 in. The test section was made of two joined 96 in. long tubes, giving a total heated length of 192 in. During the experimental testing program, the tube was enclosed with asbestos and fiberglass insulation to minimize heat transfer to the surrounding environment.

Heat is supplied directly to the resistance test section for forced flow boiling conditions using a d-c power supply with a capability of 400 KW of regulated power. The heated Refrigerant-11 exits from the test section to a plenum where it mixes with the bypass flow and then flows into the downstream condenser. The loop condenser capacity is greatly in excess of that required to decouple the fluid flow downstream of the test section from the remainder of the loop.

Fig. 3 shows the location of the inlet throttling valve, flow modulating valve, turbine flowmeter, and test section. The hydraulic servo-controlled flow modulating valve was used to sinusoidally

generate flow oscillations at the experimental test section inlet. A downstream turbine flow meter was used to measure and control the inlet flow perturbations and close the servo-controlled flow loop. Due to physical limitations the flow modulating valve and flowmeter could not be located directly before the test section inlet. Calculations showed that the delay time and attenuation inherent in the flow signal from the flow transducer to the test section inlet is insignificant at frequencies less than 10 Hz.

### Instrumentation

Test section instrumentation was provided to measure steady-state values of absolute and differential pressure, inlet flow, external tube wall temperature, flowing bulk fluid temperature, exit void fraction, and power input to the test section. Transient instrumentation was included to measure inlet pressure, inlet flow, and exit void fraction. The confidence limits of the various measurements were estimated to be as follows:

Power input:	$\pm 2$ percent unaccounted for losses to the environment
Flow rate:	$\pm 2$ percent
Absolute pressure:	$\pm \frac{1}{2}$ psi
Differential pressure:	$\pm 0.1$ in. Hg
Temperature:	$\pm 0.5^\circ\text{F}$
Void fraction:	less than 20 percent absolute value; less than 5 percent transient change.

The bandwidth capability of all the dynamic instrumentation was in excess of 20 Hz. The transient flow was measured with a turbine-type meter which was statically calibrated against a  $\frac{1}{2}$  in. standard orifice flow meter and a digital counter. This transducer was used in conjunction with a closed-loop servo system for inlet flow excitation having a bandwidth in excess of 15 Hz.

The transient inlet pressure was measured as a differential value between the inlet to the test section and the exit plenum reference pressure with a 50 psia differential pressure transducer having a bandwidth of 50 Hz. The steady-state pressure differential was measured using a high pressure u-tube mercury manometer. In addition, the steady-state exit plenum pressure was monitored using a 600 psia absolute pressure gauge readable to  $\frac{1}{2}$  psi.

External tube wall temperatures were monitored with iron-constantan thermocouples secured to the wall using electrical insulating and heat conducting tape. In addition, the bulk fluid temperatures were measured at the inlet, midpoint, and exit of the test section with immersed thermocouples located at test section half depth. These steady-state temperatures were monitored on a commercially available temperature recorder.

The electrical d-c power applied to the resistance test section was calculated from measurements of test section voltage drop and current flow. The voltage was measured directly across the test section while the current was monitored across a 300 amp/mV series shunt. Power losses were measured to be less than 7 percent of the supplied test section power.

The average exit test section void fraction was monitored with a commercially manufactured capacitance void measurement system. This instrument had the disadvantage of not being movable along the test section length for ascertaining the axial void distri-

### Nomenclature

$G$ = mass flux [lb <sub>m</sub> /hr-ft <sup>2</sup> ]	$T_1, T_2, T_3$ = inlet, midpoint, exit bulk centerline fluid temperature, respectively, [°F]	$(\alpha_A), (\alpha_M)$ = actual and sensor measured average void fraction [percent]
$h$ = enthalpy [Btu/lb <sub>m</sub> ]	$T_f$ = fluid temperature [°F]	$\rho_1$ = inlet fluid density [lb <sub>m</sub> /ft <sup>3</sup> ]
$P' \equiv P_R/P_C$ = ratio of exit plenum reference pressure to fluid critical pressure	$W_1$ = volume flow [gal/min] note that mass flow $W_1'$ is given by $W_1' = \rho_1 W_1 / 7.4806$	$\Omega$ = frequency [Hertz = 1 cycle/s]
$P_1, P_2, P_3$ = inlet, midpoint, exit pressure, respectively, [psi]	$(\alpha_3)$ = average exit void fraction [percent]	$\Delta$ = indicates small perturbation change from steady-state for frequency response
$P_R$ = exit plenum reference pressure [psia]		
$q''$ = heat flux [Btu/hr-ft <sup>2</sup> ]		



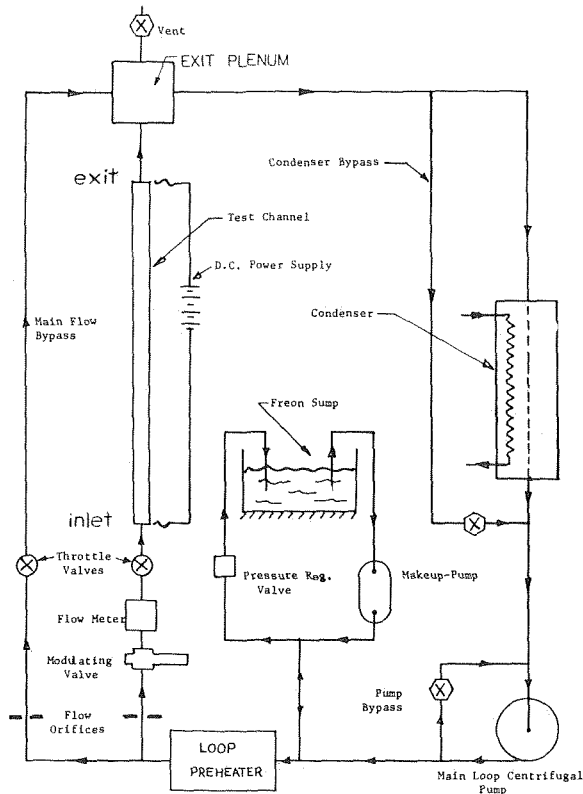


Fig. 2 Experimental loop schematic

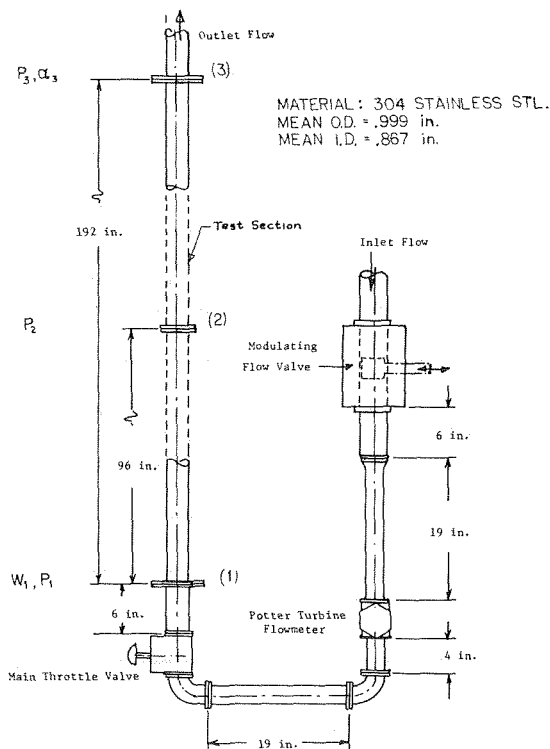


Fig. 3 Experimental flow channel

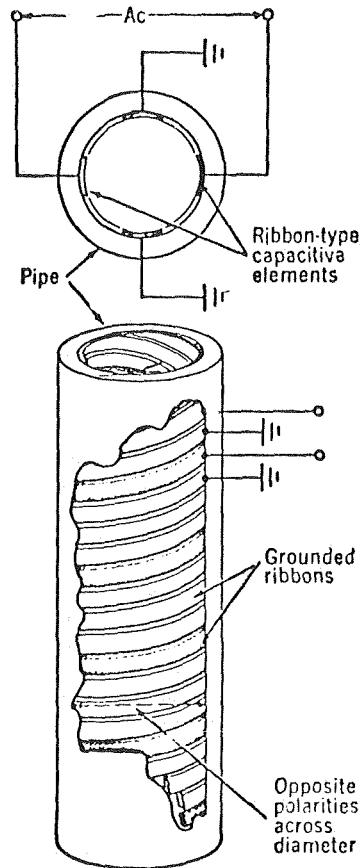
bution, but was used because of its operating simplicity and ease of installation. Further discussion is presented in the next section on the void measuring system performance.

### Void Measurement

For any two-phase single component flow channel in forced convection, a spatial and temporal knowledge of the void fraction

permits an improved understanding of:

- (a) The density changes in the two-phase mixture which affect the gravity pressure drop in non-horizontal channels.
  - (b) Pressure drop changes due to momentum changes and acceleration of the flowing fluid phases.
  - (c) The flow pattern distribution within the flowing channel.
- This paper presents experimental data for the exit test section void fraction and its temporal behavior at this axial location.



Bulk dielectric constant of flowing fluid is sensed across a series of diameters because of spiral design.

Fig. 4 Sensor design

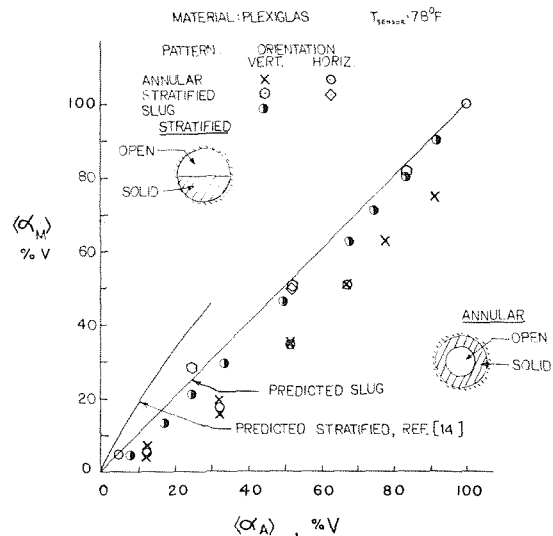


Fig. 5 Sensor flow pattern bench test-I

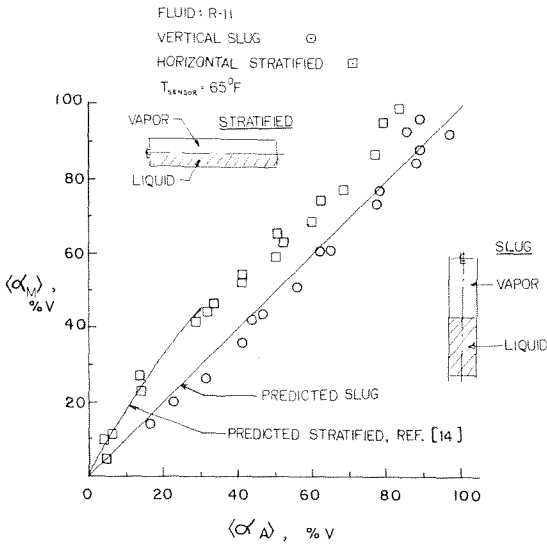


Fig. 6 Sensor flow pattern bench test-II

Gouse [12] presents a comprehensive review on void fraction measurement up to 1964. This study reviews direct and indirect measurement techniques, presenting a synopsis of the difficulties encountered when experimental determination of this variable is desired. Cimorelli and Evangelisti [13] present results of work with a capacitive type measurement system for adiabatic flow boiling. Their capacitive device consisted of two concentric cylin-

drical tubes as integral parts of the experimental test section. Discussed is the strong influence of the hydrodynamic flow pattern on the measured void fraction.

Recently, Murphy and Bergles [14] presented data utilizing a commercially available void measuring system like that utilized for the research work presented in this paper. Their results showed that this device was sensitive to temperature and flow pattern using simple analytic models and experimental measurements.

### Void Measurement Instrumentation

The averaging capacitive void sensor used for experimental measurements operated on the measurement of the apparent bulk dielectric constant  $\epsilon_{TP}$  which existed within the finite length tubular sensor. Fig. 4 shows a sketch of the sensor element and a schematic of the electrical capacitive elements. The primary capacitive path is diametrical, with spacer grounded ribbon elements used to minimize coupling effects. The sensor for this work had an active length of  $6\frac{1}{4}$  in. over which the void fraction measurement was averaged.

To establish confidence in the values of void fraction determined from bulk dielectric constant measurements, experimental evaluations were conducted to establish the temperature and flow pattern sensitivity. The sensor was calibrated at  $70^\circ\text{F}$  ( $\pm 2^\circ\text{F}$ ) for liquid and vapor dielectric constants and then evaluated for static temperature sensitivity. This static temperature correction was incorporated into the steady-state experimental measurements of void fraction.

The variation of void fraction with two-phase flow pattern required a direct visual or quantitative measurement method. A room temperature bench test approach was selected using Refrig-

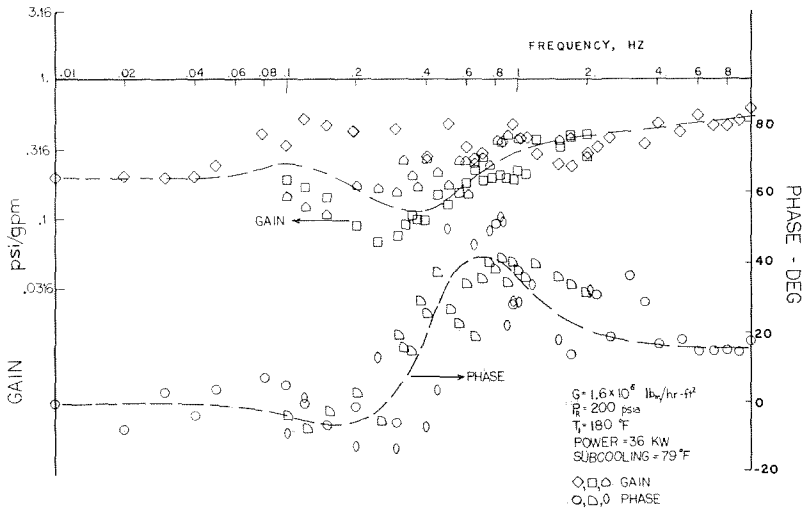


Fig. 7(a) Frequency response— $\Delta P_1 / \Delta W_1(j\omega)$

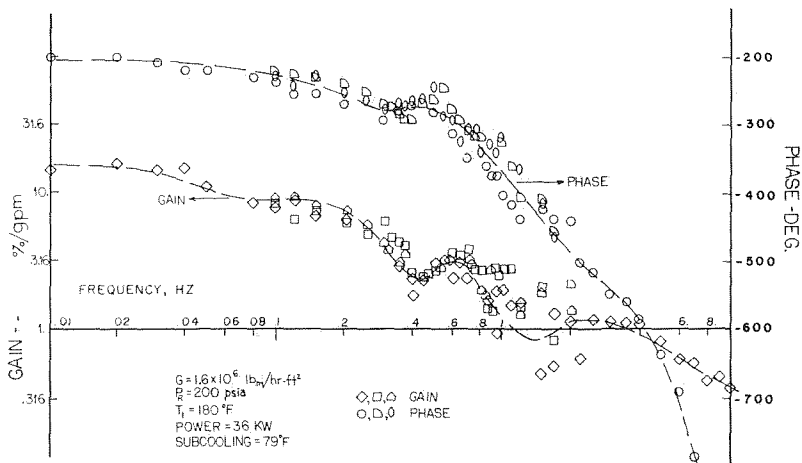


Fig. 7(b) Frequency response— $\Delta \alpha_3 / \Delta W_1(j\omega)$

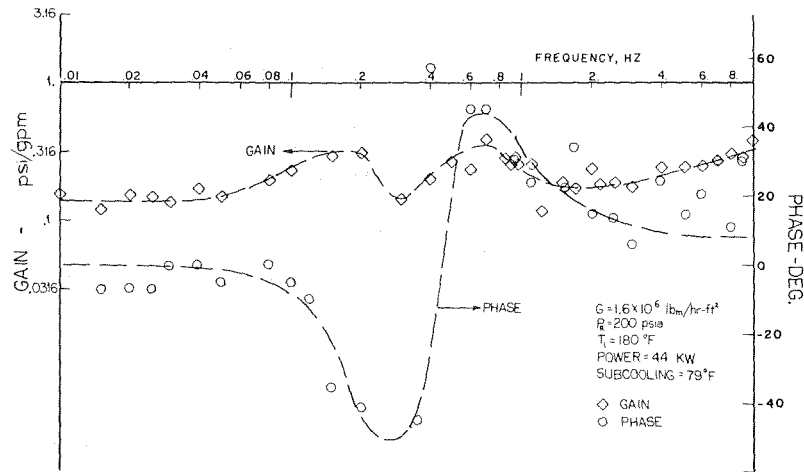


Fig. 8(a) Frequency response— $\Delta P_1/\Delta W_1(j\omega)$

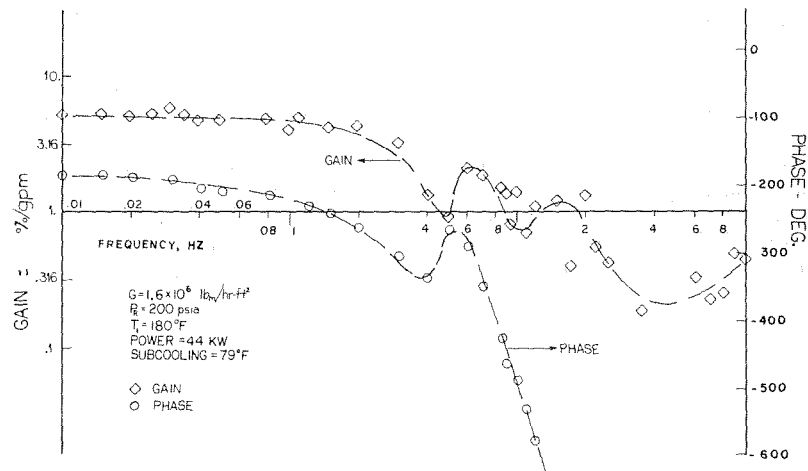


Fig. 8(b) Frequency response— $\Delta \alpha_3/\Delta W_1(j\omega)$

erant-11 and specially manufactured plexiglass sections to represent void distributions. Three flow patterns easy to identify and use for these equilibrium tests were vertical slug (plug), horizontal, stratified, and annular.

Figs. 5 and 6 show the results of bench test measurements using the plexiglass sections and Refrigerant-11, respectively. A comparison of these data for the slug pattern orientation shows good agreement, while dissimilar results are obtained for the stratified flow pattern. The stratified pattern bench tests indicate a shift in slope of the characteristic with the same data trend. Repeated experimental tests did not resolve this difference. Fig. 5 also shows the results of an annular flow condition using the plexiglass sections. No data using Refrigerant-11 was obtained for this case.

Caution must be exercised in the direct interpretation of this equilibrium bench test void fraction data to steady-state non-equilibrium flow boiling patterns. These results indicate that an absolute void measurement using this capacitive type instrument is sensitive to steady-state flow pattern, but also that the slope of the  $\langle \alpha_M \rangle$  vs.  $\langle \alpha_A \rangle$  in the void range of 20 to 90 percent is relatively constant. This suggests that absolute void fraction measurements which are corrected for known fluid temperature conditions but not for unknown flow pattern sensitivity may be in error by twenty percent. Measurements of small transient changes (perturbations) in void fraction, as is done in frequency response testing, should produce magnitude errors of less than five percent in the transient data due to the relative constancy of the slope of the  $\langle \alpha_M \rangle$  versus  $\langle \alpha_A \rangle$  curve for approximately constant temperature conditions.

### Experimental Test Procedure

Experimental test operations were begun by initially pressurizing the test facility, raising the temperature of the operating fluid, and then bleeding off trapped and dissolved gases in the test loop and instrumentation. Next a series of steady-state tests were conducted to provide experimental data on test section pressure drop, exit void fraction, and wall and bulk fluid temperatures. For these tests a constant heat flux is set for the test channel and the mass flux was varied between  $0.9 \times 10^6$  and  $2.5 \times 10^6$  ( $\text{lb}_m/\text{hr-ft}^2$ ), while the inlet fluid temperature was maintained constant.

Frequency response tests were initiated by establishing a nominal operating condition in heat flux, inlet subcooling, mass flux, and system reference pressure. Sinusoidal variations in mass flux were then introduced into the system. The flow amplitude variations were adjusted to be less than or equal to plus and minus ten percent of the nominal flow rate to minimize nonlinear system behavior. Data was obtained using a commercial frequency response analyzer.

### Experimental Results—Frequency Response Characteristics

Experimental data were obtained for uniform heat flux input to the test section, approximately constant mass flux, and both high and low inlet subcoolings. Fig. 7 through 10 present experimental frequency response data for inlet impedance and exit void fraction for disturbances in inlet flow at constant heat flux. The input frequencies ranged between 0.01 and 10.0 Hz. Two inlet

subcoolings of 79°F and 14°F were studied at a nominal volume flow rate of 10 gpm, with flow perturbations of  $\pm 10$  percent of steady-state. Additionally at each inlet subcooling two magnitudes of heat flux were considered. Figs. 10(a),(b) and 13(a),(b) show the repeatability of the test data, with each run denoted by a separate symbol. The largest variation in data occurred for the inlet impedance ( $\Delta P_1/\Delta W_1$ ) characteristic at the 79°F inlet subcooling condition.

A comparison of the inlet impedance characteristics for 79°F and 14°F (Figs. 7(a), 8(a), 9(a), and 10(a)) shows that at low frequency the gain of the flow to inlet pressure curve is larger for the 14°F subcooling. This result is consistent since a larger portion of the boiler tube is in two-phase flow regimes, resulting in a larger slope on the static pressure drop versus flow characteristic.

A decrease in the inlet subcooling to the diabatic flow channel results in a "softer" behaving system with a subsequent increase in the resonant peak amplitudes and phase angles. Close observation of the curves indicates that as a larger portion of the tube becomes vapor, the number of resonant peaks occurring at frequencies less than 10 Hz increases. This dynamic characteristic when coupled with other power system components such as pumps, condensers, and piping can result in slower responding and less stable systems behavior, although the vapor generator itself has improved stability, i.e., an elimination of the density-wave oscillation instability.

The exit void fraction frequency response characteristics are shown in Figs. 7(b), 8(b), 9(b), and 10(b). Decreasing the inlet

subcooling reduced the inlet flow to exit void fraction low frequency gain characteristic. The exit void fraction must also have a zero frequency phase shift of minus 180 deg for changes in inlet flow, since an increase of the flow leads directly to a decrease in exit void fraction. The phase lag in exit void increases at an increased rate above 0.1 Hz. This is expected because of the transport delay between inlet flow and exit void fraction. Any distributed or lumped mathematical model developed for analytic purposes should account for this effect.

The effect of changing the uniform constant heat flux supplied to the flow channel can be observed by comparing Figs. 7 and 8 for 70°F subcooling and Figs. 9 and 10 for 14°F subcooling. Increased heat flux reduces the amount of liquid phase in the channel resulting in a softer system with larger resonant peaks and phase shifts.

### Conclusions

This paper has presented experimental frequency response data for inlet pressure and exit void fraction for perturbations in inlet flow at constant uniform heat flux. In support of the data, a detailed description of the experimental test facilities and instrumentation used for this work was presented. A specific evaluation conducted to show the performance of the averaging capacitive void measuring system was included.

The experimental measurements indicated that:

1 A decrease in the inlet subcooling for constant heat flux gives rise to a softer or "more spongy" vapor generator with in-

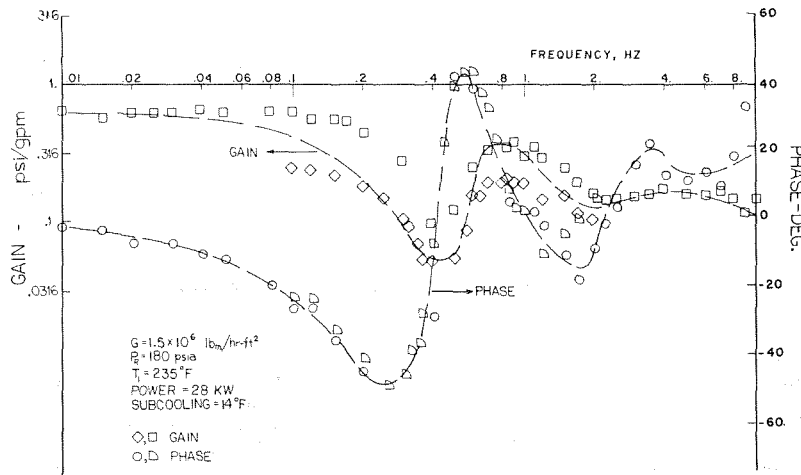


Fig. 9(a) Frequency response— $\Delta P_1/\Delta W_1(j\omega)$

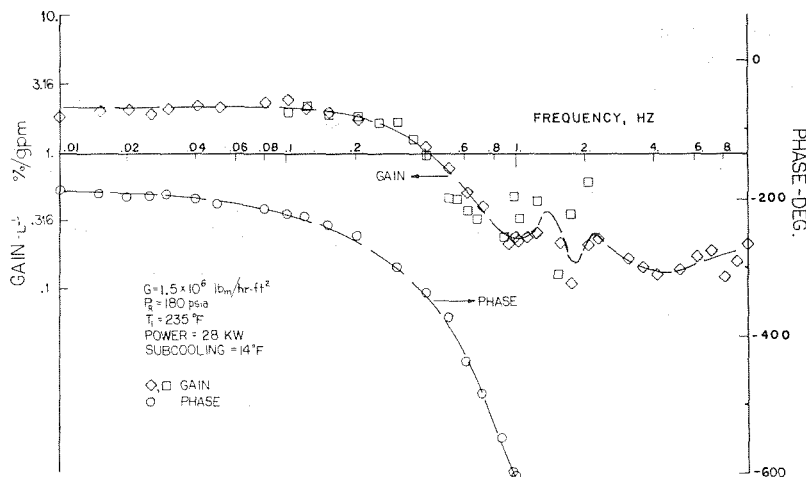


Fig. 9(b) Frequency response— $\Delta \alpha_3/\Delta W_1(j\omega)$

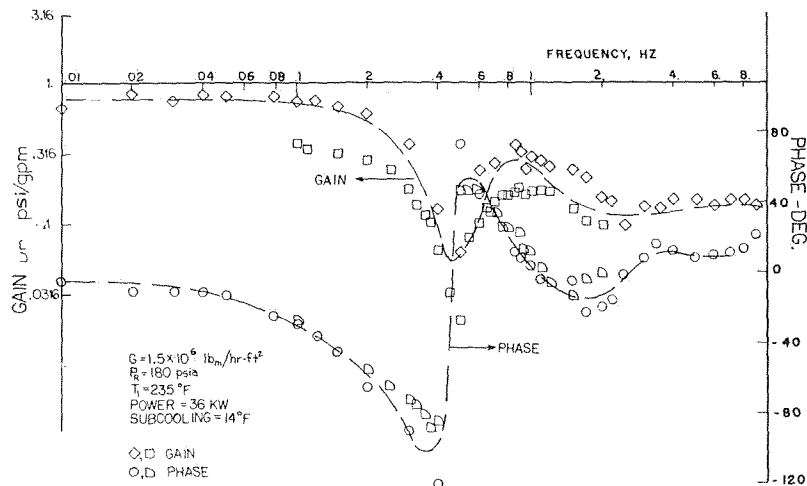


Fig. 10(a) Frequency response— $\Delta P_1/\Delta W_1(j\omega)$

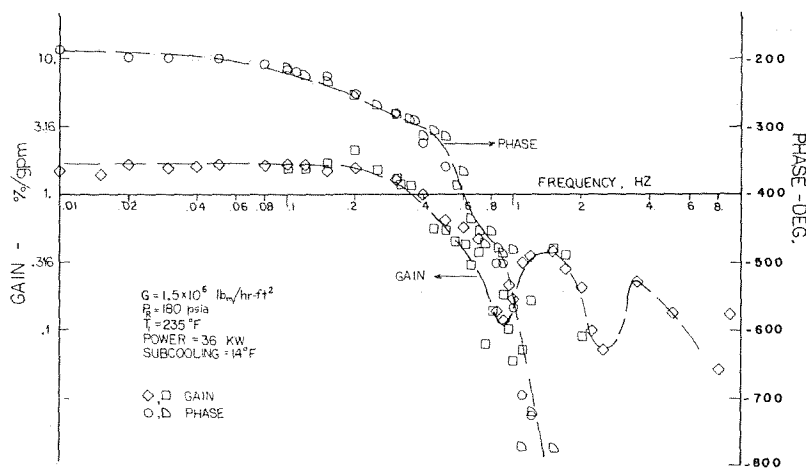


Fig. 10(b) Frequency response— $\Delta \alpha_3/\Delta W_1(j\omega)$

creased amplitudes and lower resonant frequencies;

2 An increase in heat flux at constant inlet subcooling also gives a softer dynamic system;

3 Large phase shifts occur in exit void fraction for frequencies above 1 Hz indicative of the transport delay line behavior of monotube boilers.

#### Acknowledgment

This work was supported by the Office of Naval Research, Power Office, Code 473, Arlington, Virginia, under Contract No. N00014-67-A-0314-003 and was carried out in the Department of Mechanical Engineering, Carnegie-Mellon University.

#### References

- 1 St. Pierre, C. C., "Frequency-Response Analysis of Steam Voids to Sinusoidal Power Modulation in a Thin-Walled Boiling Water Coolant-Channel," ANL-7041, May 1965.
- 2 Staub, F. W., Zuber, N. and Bijwaard, G., "Experimental Investigation of the Transient Response of the Volumetric Concentration in a Boiling Forced-Flow System," *Nuc. Sci. and Engr.*, Vol. 30, 1967, pp. 279-295.
- 3 Staub, F. W., and Zuber, N., "Void Response to Flow and Power Oscillations in a Forced-Convection Boiling System with Axially Nonuniform Power Input," *Nuc. Sci. and Engr.*, Vol. 30, 1967, pp. 296-303.
- 4 Dijkman, F. J. M., "Some Hydrodynamic Aspects of a Boiling Water Channel," PhD thesis, Eindhoven University of Technology, The Netherlands, 1969.

lands, 1969.

5 Neal, L. G., Zivi, S. M., and Wright, R. W., "The Mechanisms of Hydrodynamic Instabilities in Boiling Systems," Paper 8.1, Symposium on Two-Phase Flow Dynamics, Eindhoven, 1967.

6 Dorsch, R. G., "Frequency Response of a Forced-Flow Single-Tube Boiler," Paper 2.1, Symposium on Two-Phase Flow Dynamics, Eindhoven, 1967; see also NASA TM X-52306.

7 Krejsa, E. A., Goodykoontz, J. H., and Stevens, G. H., "Frequency Response of Forced-Flow Single-Tube Boiler," NASA TN D-4039, June 1967.

8 Goodykoontz, J. H., Stevens, G. H., and Krejsa, E. A., "Frequency Response of Forced-Flow Single-Tube Boiler with Inserts," NASA TN D-4189, Oct. 1967.

9 Stevens, G. H., Krejsa, E. A., and Goodykoontz, J. H., "Frequency Response of a Forced-Flow Single-Tube Boiler with Inserts and Exit Restriction," NASA TN D-5023, Feb. 1969.

10 Stevens, G. H., Goodykoontz, J. H., and Krejsa, E. A., "Experimental Evaluation of Four Transfer Functions for a Single Tube Boiler Which are Dynamically Independent of Exit Restrictions," NASA TM X-2247, Mar. 1971.

11 Krejsa, E. A., "Model for Frequency Response of a Forced Flow, Hollow, Single Tube Boiler," NASA RM X-1528, Mar. 1968.

12 Gouse, S. W., Jr., "Void Fraction Measurement," Report No. DSR 8734-2, Dept. of M.E., EPL, MIT, 1964.

13 Cimorelli, L., and Evangelisti, R., "The Application of the Capacitance Method for Void Fraction Measurement in Bulk Boiling Conditions," *International Journal of Heat and Mass Transfer*, Vol. 10, 1967, pp. 277-288.

14 Murphy, R. E., and Bergles, A. E., "Subcooled Flow Boiling of Fluorocarbons," Report No. DSR 71903-72, Dept. of M.E., EPL, MIT, 1971.

P. G. LaHaye

President,  
Hague International Corp.,  
South Portland, Me.

F. J. Neugebauer

Technical Consultant,  
Green Valley, Ariz.

R. K. Sakhuja

Senior Development Engineer,  
Thermo Electron Corp.,  
Waltham, Mass. Assoc. Mem. ASME

# A Generalized Prediction of Heat Transfer Surfaces

*A new way of presenting the heat transfer data is shown. This leads to a dimensionless performance plot between a "heat transfer performance factor" and a "pumping power factor" with a nondimensional "flow length between major boundary layer disturbances" as a varying parameter. This approach leads to the possibility of approximately presenting all surface geometries on a single "idealized" performance plot, the nondimensional "flow length" being a geometrical characteristic of each surface. The method can be used to predict approximately the heat transfer performance characteristics of a new, untested surface. The plot permits the rapid assessment and comparison of various heat transfer geometries for a given application. The performance plot is valid only in the turbulent flow regime. The method will prove invaluable in optimizing a design accounting for space limitations, economic restraints, and system considerations such as pumping power and effectiveness tradeoffs.*

## Introduction

The performance data of a heat transfer surface geometry are customarily presented as the heat transfer factor " $j$ " and the pressure-drop factor " $f$ " as functions of Reynolds number. The curves for  $j$  and  $f$  vary over a wide range, in magnitude as well as in slope. Except for very simple geometries, it was not possible in the past to predict them even approximately. Experiment has been the only way to know the performance of a new surface.

It has long been recognized that the flow length between boundary layer disturbances has some bearing on the performance of a heat transfer surface [1, 2].<sup>1</sup> The importance of this fact can be realized from the following quotation from reference [1]: "One of the most widely used ways of increasing conductance is to interrupt the wall surfaces so that the boundary layers can never become thick." Hence, plotting the factors  $j$  and  $f$  and their slope exponents versus the ratio of flow length between major boundary layer disturbances to the equivalent diameter, " $l/D_{eq}$ ," suggests itself automatically. This is done for a large number of surface geometries listed in reference [1]. Figs. 1 and 2 show the disappointing results. While the trend is visible, the scattering of the test data is so large that the ratio  $l/D_{eq}$  does not appear to be a single useful criterion. The tested pressure-drop factors and their slope exponents spread over a wide area (Fig. 2); the plotting of the slope exponents of the pressure-drop factor does not even show a trend.

The seemingly hopeless situation suddenly changes when the

factors  $j$  and  $f$  are replaced by two new dimensionless groupings, as shown in the next section.

In order to present the principles involved in a clear and concise form, the paper is confined to gas-to-gas heat exchangers, in the turbulent range, with specified total pumping power. Other applications are possible, and the method can be adapted to other problems.

## The Dimensionless Performance Plot

### Definitions.

**Surface Geometry.** The geometric proportions of a surface. Note that the dimensions of a surface can be scaled up or down in geometric similarity without changing the surface geometry.

**Surface Configuration.** A surface of fixed geometry and dimensions. Surfaces of the same surface geometry can be executed in different surface configurations, i.e., in different dimensions.

**Standard Performance Plot.** A graph in which the heat transfer performance per unit volume is plotted versus the pumping power per unit volume based on arbitrarily assumed "standard" fluid properties and a surface effectiveness of  $\eta_s = 1.0$  [3, p. 289].

**Dimensionless Performance Plot.** Plotting of the dimensionless values  $J$  and  $F$  (Figs. 4, 5, and 13). The Standard performance plot compares "Surface Configurations." It all started with the plot shown in Fig. 3 (Figs. 11-16 from reference [3]). This plot shows the heat transfer performance per unit core volume at a surface effectiveness of  $\eta_s = 1.0$  versus the pumping power applied per unit core volume. The "dimensionless pumping power factor" is defined as

$$F = \frac{P}{V} \frac{2g_c \rho^2 D_{eq}^3}{\beta \mu^3} = f N_{Re}^3$$

In the same way, we define the "dimensionless transfer performance factor"

<sup>1</sup> Numbers in brackets designate References at end of paper.

Contributed by the Heat Transfer Division and presented at the Winter Annual Meeting New York, N. Y., November 26-30, 1972, of THE AMERICAN SOCIETY OF MECHANICAL ENGINEERS. Journal manuscript received by the Heat Transfer Division, March 11, 1974. Paper No. 72-WA/HT-55.

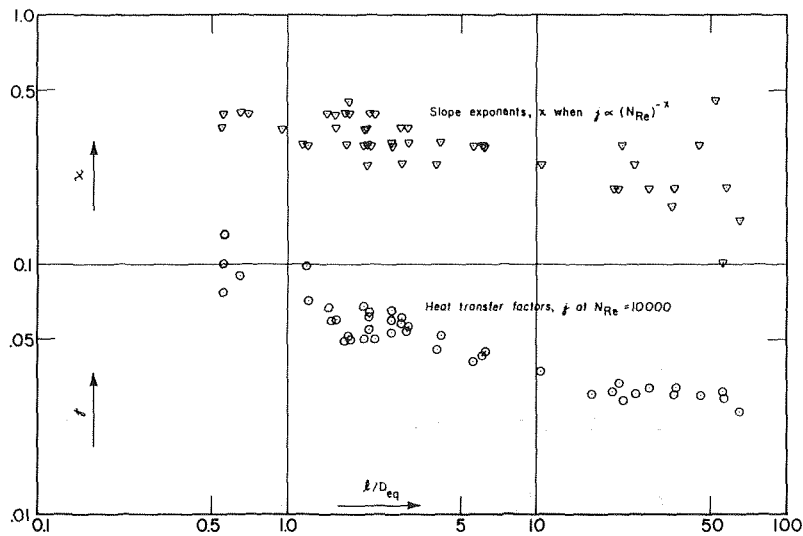


Fig. 1 Heat-transfer factors and their slopes versus specific flow length between major boundary layer disturbances

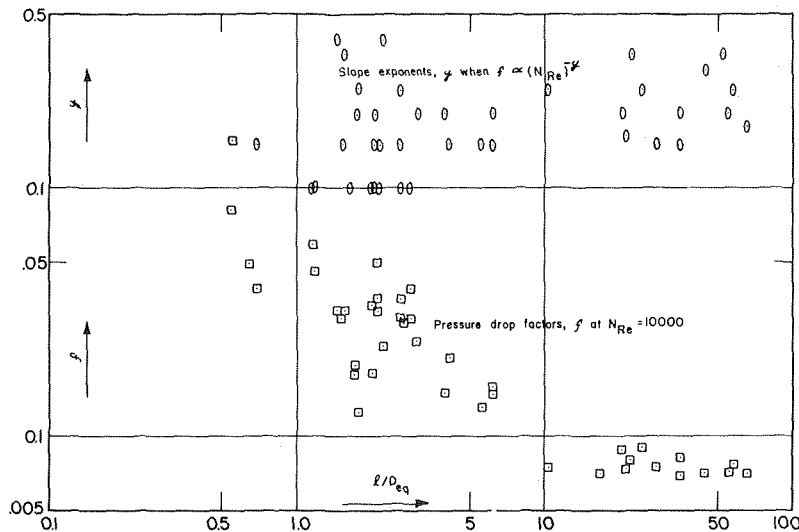


Fig. 2 Pressure drop factors and their slopes versus specific flow length between major boundary layer disturbances

$$J = (\beta h) \frac{N_{Pr}^{2/3} D_{eq}}{\beta c_p \mu} = j N_{Re}$$

Plotting the transfer performance factor versus the pumping power factor delivers the "dimensionless performance plot;" an example is shown in Fig. 4. The points are directly obtained from a customary  $j$  and  $f$  graph by plotting  $j N_{Re}$  versus  $f N_{Re}^3$ . From

here on, we will use the  $J$  factor at  $F = 10^9$ ,  $J_{10^9}$ , and the slope exponent "n" of the performance line to characterize the straight portion of this line.

It will prove helpful in the pursuit of our goal to have the Reynolds number plotted on top of the performance line.

For reasons to be discussed in the following, Fig. 4 is regarded to be a more useful presentation of the performance of a surface

### Nomenclature

$A$  = total heat transfer area  
 $A_c$  = minimum free flow area  
 $c_p$  = specific heat  
 $D_{eq}$  = equivalent diameter ( $D_{eq} = 4AcL/A$ )  
 $F$  = pumping-power factor ( $F = f N_{Re}^3$ )  
 $f$  = pressure-drop factor  
 $g_c$  = proportionally constant in Newton's second law  
 $h$  = surface heat transfer coefficient

$J$  = transfer performance factor, ( $J = j N_{Re}$ )  
 $j$  = heat transfer factor  
 $L$  = total flow length  
 $l$  = flow length between major boundary layer disturbances, Fig. 6  
 $n$  = slope exponent in the dimensionless performance ( $J$  versus  $F$ ) plot  
 $N_{Re}$  = Reynolds number

$N_{Pr}$  = Prandtl number  
 $P$  = pumping power  
 $V$  = core volume between plates  
 $\beta$  = ratio of total transfer area on one side of a plate-fin heat exchanger to the volume between the plates on this side,  $A/V$   
 $\eta_s$  = surface effectiveness  
 $\mu$  = viscosity  
 $\rho$  = density

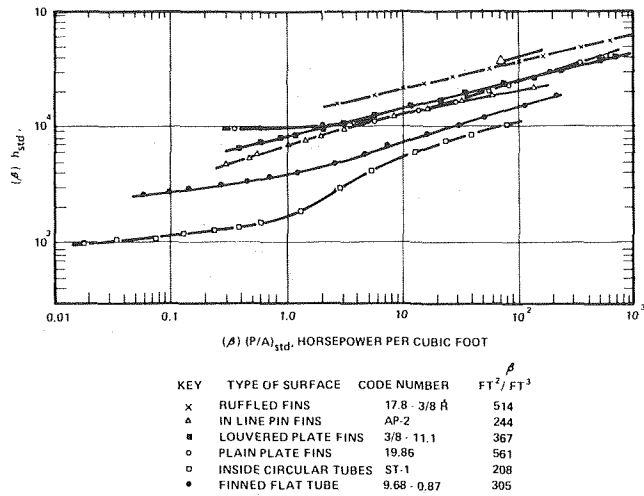


Fig. 3 Standard performance plot (this figure is reproduced from [3, p. 289])

geometry than the  $j$  and  $f$  plot previously used. Note that the plot, since dimensionless, compares "geometries" and not merely "configurations."

**Evaluation of Numerous Tested Surfaces.** Fig. 5 shows dimensionless performance lines for four typical surface geometries of greatly different  $l/D_{eq}$  ratios. The trend toward higher performance at smaller  $l/D_{eq}$  ratios is already clearly visible.

Eight-three surface geometries listed in reference [1] were eval-

uated in this way. They include banks of bare tubes, banks of circularly finned tubes, continuous fins on flat tubes, plain continuous fins, louvered fins, strip-fins, and pin-fins. Only the parts of the  $j$  and  $f$  curves which show a strong influence of turbulence are included. The  $f$  and  $j$  characteristics illustrated in reference [1] clearly show a distinct variation in slope from low to high Reynolds numbers. The behavior exhibited in the turbulent range (high Reynolds number) is much more orderly (constant slope) and therefore the presentation here is only made for turbulent range for purposes of simplification. It is believed that a similar approach can also be used for laminar flow regime.

The characteristic values " $J_{10^9}$ " and  $n$  of the scrutinized surfaces are listed in Table 1. The last column of the table was reserved for the ratio  $l/D_{eq}$ . Examples for measuring the flow length between major boundary layer disturbances are presented in Fig. 6. It is noteworthy that " $l$ " is selected between the points at which the same flow pattern or its mirror image recurs.

**The Predominant Influence of the " $l/D_{eq}$ " Ratio.** The big surprise comes when the characteristic values  $J_{10^9}$  and  $n$  are plotted versus the specific length between major boundary layer disturbances, i.e.,  $l/D_{eq}$  (Fig. 7). The figure shows clear trends. The scattering of the points is regarded to be small, especially if it is kept in mind that the uncertainty of measuring the factor  $j$  is only  $\pm 5$  percent, and of  $f$  is  $\pm 5$  percent [1, p. 135]. The number of "runaway points" is also small. (For some tube banks and finned tube surfaces, the uncertainty is higher [8]).

Figs. 8 through 12 show the scatter of data for various surface geometries on the dimensionless performance plot. Some surfaces (e.g., Plain Plate fins, Louvered Plate fins, Strip fins, Wavy fins, etc.) showed less scatter than others. Generally the scatter of the points is regarded to be small and considered reasonable in com-

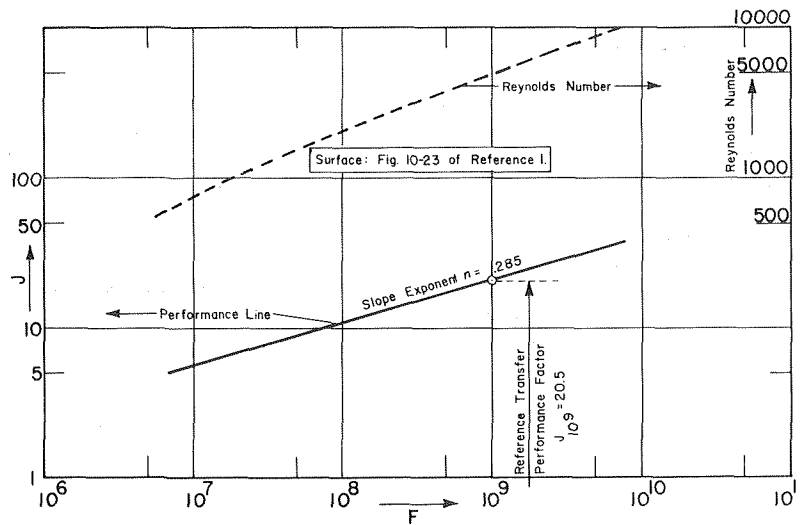


Fig. 4 Example of a dimensionless performance plot

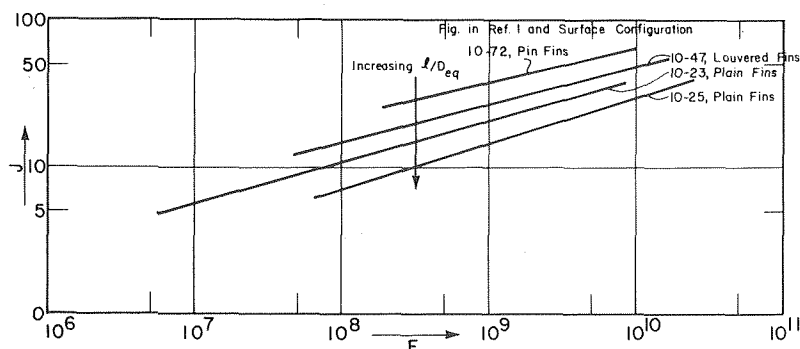


Fig. 5 Typical dimensionless performance plots for four different surface configurations



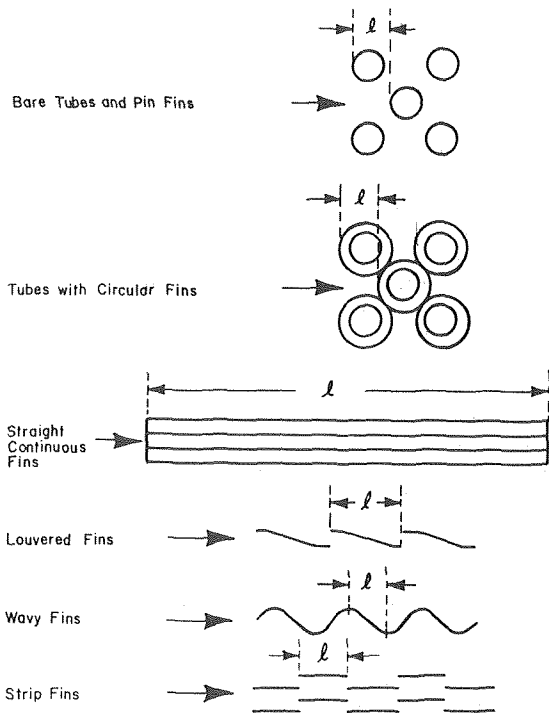


Fig. 6 Examples of measuring the flow length between major boundary layer disturbances

mon heat transfer correlations, especially, keeping in mind that this is an approximate presentation which guides the designer in the vicinity of optimum solutions.

What is the reason for the striking difference between the plots of Fig. 2 and Fig. 7? The casual relationship between  $f$  and  $j$  provides the answer. As a rule, a geometry of greater flow resistance also yields higher heat transfer so that, while  $j$  and  $f$  may vary greatly, the functional relationship between pumping power and heat transfer performance remains more or less intact.

Curves for  $J_{10^9}$  and  $n$  are drawn in Fig. 7, with the consideration that they have to level out at infinitely large  $l/D_{eq}$ . These two curves now allow the design of the "idealized dimensionless performance plot," Fig. 13. In Fig. 5, surface types were used as a parameter; they have disappeared in Fig. 13 and are replaced by the characteristic dimensionless numerical value  $l/D_{eq}$ . In this

way, Fig. 13 is a general performance plot for practically all geometries in the turbulent region.

The lines of constant Reynolds numbers in Fig. 13 are taken from Fig. 14, in which all the evaluated Reynolds numbers are plotted.

#### The Significance of the Idealized Dimensionless Performance Plot.

1 The idealized plot, Fig. 13, provides a convenient comparison of the effect of  $l$  on heat transfer surface performance at the same " $D_{eq}$ " and " $\beta$ ," since for the same  $D_{eq}$  and  $\beta$ , " $F$ " is proportional to " $P/V$ " (pumping power per unit volume) and " $J$ " is proportional to " $\beta_h$ " (heat transfer per unit volume). With these restrictions, Fig. 13 shows that surface designed to operate at the same  $P/V$  would result in an increase in  $\beta_h$  between 80 and 250 per cent by decreasing boundary layer interruption length  $l/D_{eq}$  from 200 to 0.5.

2 The numerical effect of surface modifications can be estimated from Fig. 13. Assume, for example, a continuous-fin surface with an  $l/D_{eq}$  ratio of 50. If boundary layer interrupting slots are cut into this surface in such distances that  $l/D_{eq}$  becomes equal to 2, then it can be read from Fig. 8 that the transfer performance factor  $J_{10^9}$  will rise from 15 to 26, i.e., approximately 70 per cent, and that the slope exponent  $n$  will change from 0.3 to 0.24.

3 The prospective performance of newly designed, but not yet tested, surface geometries can be fairly well predicted if a value for the ratio  $l/D_{eq}$  can be established. Performance plots based on experimental evidence should, however, always be used for the final design.

#### Discussion

The basis of this work, namely that more frequent boundary layer interruptions lead to higher heat transfer coefficients for a given power, has been established for a long time. A number of dimensionless groupings like  $j$ ,  $f$ ,  $j/f$ ,  $(j^3/f)$ , etc., have been considered for presenting the heat transfer data by various authors [4, 5, 6], but none has resulted in a presentation so simple and universal with the potential of describing all the surfaces on one plot, as presented in this work. It is well known that higher resistance to the flow path leads to higher heat transfer. While  $j$  and  $f$  may vary greatly, the functional relationship between pumping power and heat transfer performance remains more or less intact. The presentation in terms of  $F$  and  $J$  factors was primarily selected because it synoptically correlates heat transfer and pumping power better than any other parameters.

A more precise definition of  $l/D_{eq}$  is certainly desirable from a

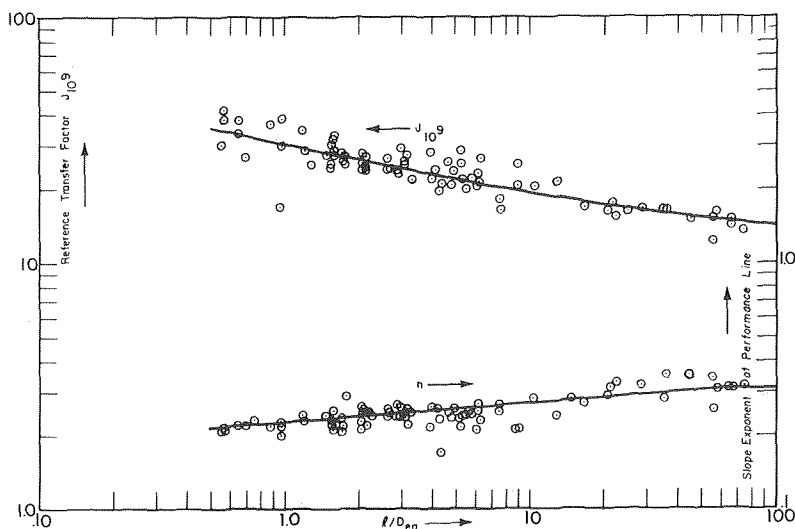


Fig. 7 Characteristics of the dimensionless performance plot versus specific flow length between major boundary layer disturbances

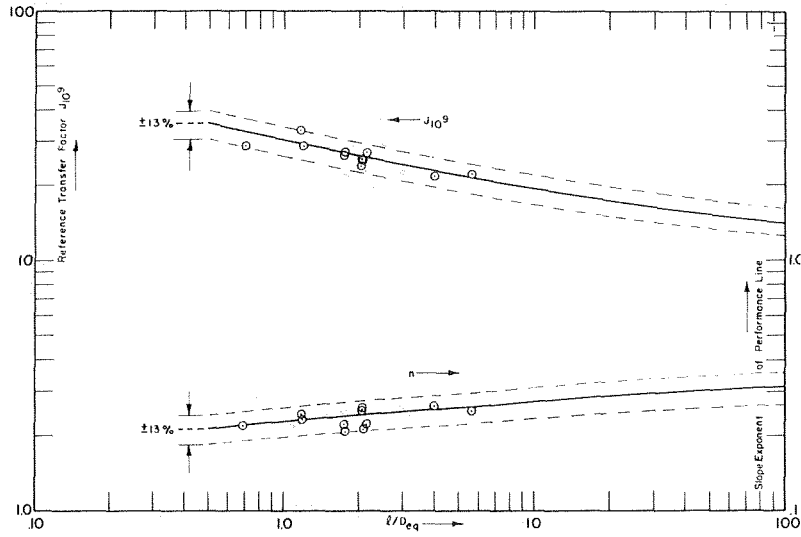


Fig. 8 Characteristics of the dimensionless plot for 13-strip fin configuration

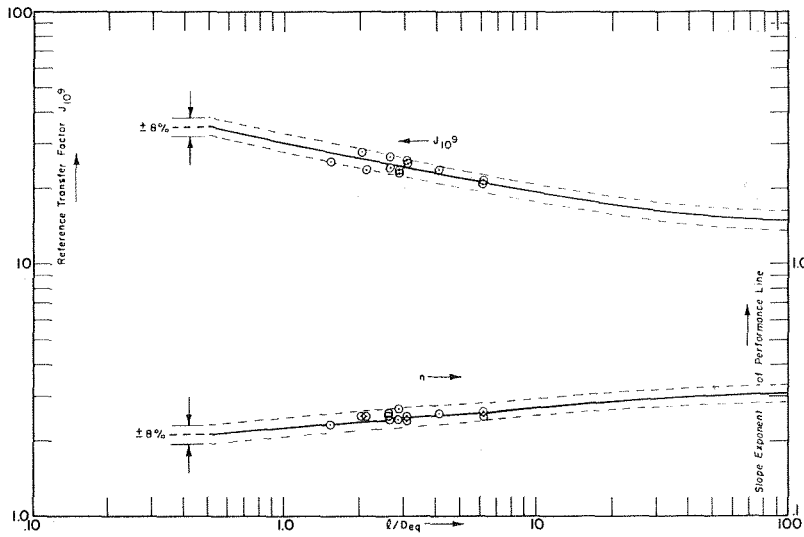


Fig. 9 Characteristics of the dimensionless performance plot for 14 lowered plate fin configurations

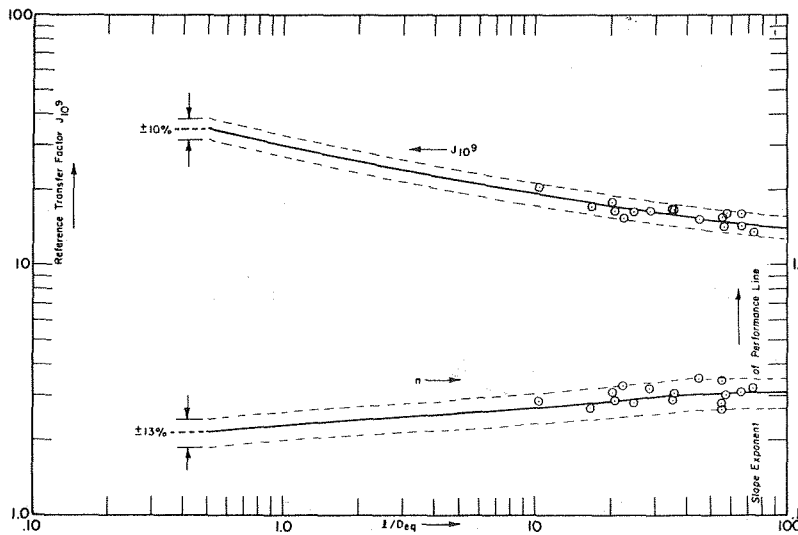


Fig. 10 Characteristics of the dimensionless performance plot for 16 plate fin configurations

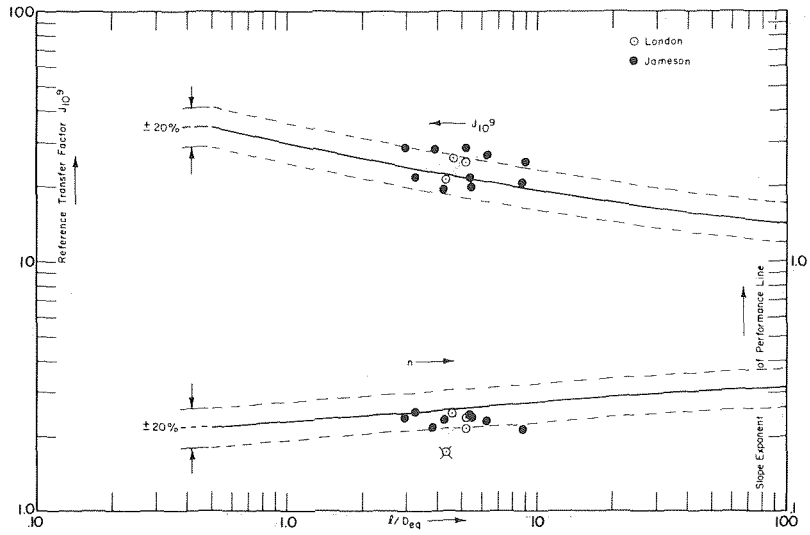


Fig. 11 Characteristics of the dimensionless performance plot for 13 circular finned tube configurations

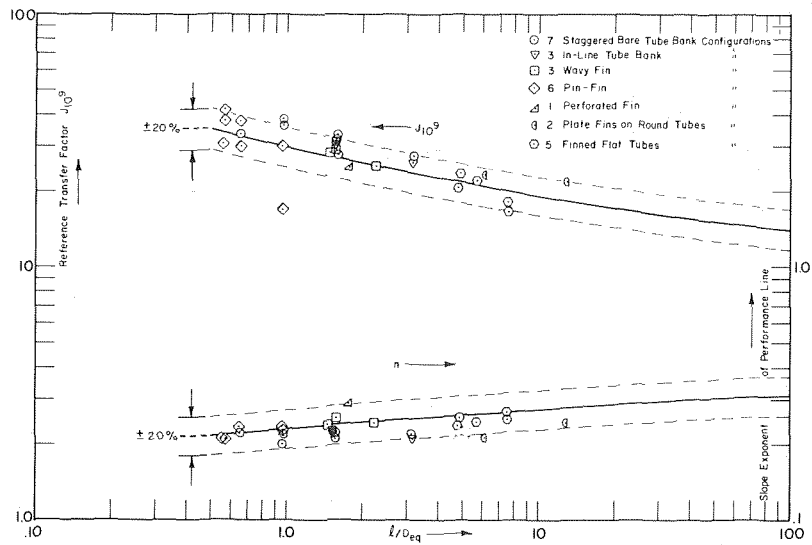


Fig. 12 Characteristics of the dimensionless performance plot for 27 miscellaneous configurations

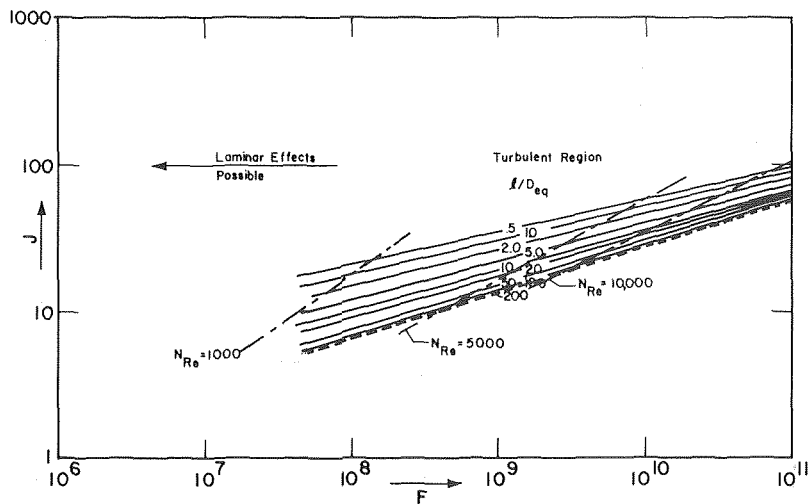


Fig. 13 Idealized dimensionless performance plot

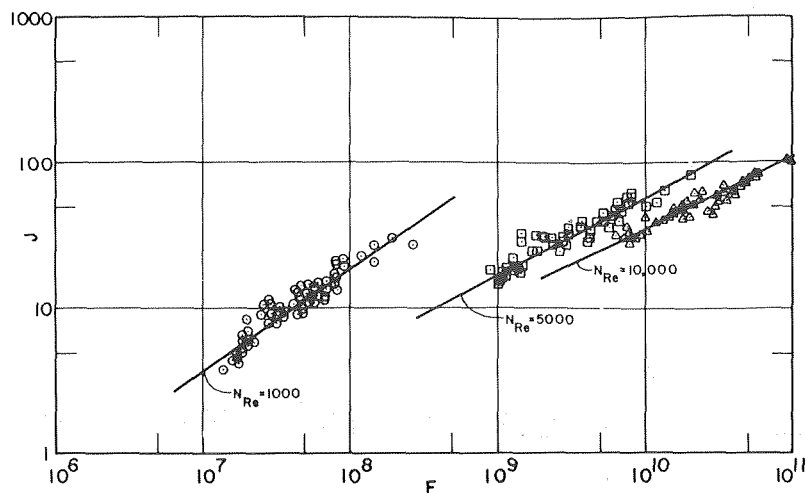


Fig. 14 Plotting points of constant Reynolds number in the dimensionless performance plot

Table 1

Fig. in Ref. 1	n	$J_{10^9}$	$l/D_{eq}$	Fig. in Ref. 1	n	$J_{10^9}$	$l/D_{eq}$
10-4	.21	32	1.565	10-21	.352	16.5	35.5
10-5	.22	33	1.575	10-23	.285	20.5	10.3
10-6	.22	27.2	3.12	10-24	.342	15.2	55
10-7	.22	27.4	1.59	10-25	.31	14.2	65
10-8	.22	33.3	.645	10-26	.29	16.1	20.6
10-9	.20	38.5	.96	10-27	.30	16	57.8
10-10	.22	36.8	.869	10-28	.28	16.2	24.7
10-12	.225	30.2	1.565	10-29	.31	16	65
10-13	.215	31.2	1.575	10-30	.285	16.5	35
10-14	.21	25.5	3.16	10-31	.27	17	16.6
10-19	.31	17.7	21.1	10-32	.35	15.1	44.4
10-20	.32	16.3	28.2	10-33	.33	15.2	22.1
10-34	.32	13.4	73.8	10-63	.235	28	1.7
10-35	.265	14.1	55.3	10-64	.26	24.5	2.025
10-38	.25	23.1	2.14	10-65	.24	27.5	1.475
10-39	.25	24	2.14	10-66	.252	28.5	1.575
10-40	.265	23	2.85	10-67	.24	25	2.24
10-41	.24	23.5	2.85	10-68	.21	33	.658
10-42	.24	24	2.605	10-69	.23	30	.682
10-43	.255	24	2.605	10-70	.225	17	.96
10-44	.23	25.3	1.54	10-71	.21	42	.56
10-45	.25	26.2	2.6	10-72	.215	38	.56
10-46	.25	27.5	2.06	10-73	.23	38	.644
10-47	.25	25	3.08	10-74	.29	25	1.79
10-48	.24	25.8	3.08	10-75	.17	21	4.32
10-49	.255	23.8	4.12	10-76	.215	25	5.2
10-50	.25	21.1	6.16	10-77	.245	25.2	4.6
10-51	.26	21	6.16	10-79	.235	28.5	5.12
10-52	.25	23.8	2.06	10-80 A	.23	26.5	6.26
10-53	.22	28.5	.696	10-80 B	.235	29	2.94
10-54	.23	28.7	1.2	10-81 A	.21	20.2	8.67
10-55	.242	34.8	1.188	10-81 B	.24	21.2	5.29
10-56	.25	22	5.6	10-81 C	.25	21.8	3.28
10-57	.26	21.3	3.96	10-81 D	.23	19.5	4.21
10-58	.22	26	1.715	10-81 E	.24	19.9	5.45
10-59	.205	27	1.76	10-82 A	.21	25	8.95
10-60	.22	27	2.13	10-82 B	.215	28	3.88
10-61	.21	25	2.07	10-83	.21	23	6.05
10-62	.255	25.2	2.05	10-84	.24	21.3	12.8
				10-85	.265	16.4	7.5
				10-86	.235	20.3	4.79
				10-87	.25	18	7.5
				10-88	.255	23.2	4.86
				10-89	.245	22	5.7

scientific point of view. The effects of parameters like fin thickness (which may be important for relatively thick fins) gaps between successive elements in a row, etc., have not been included and could be considered in refining the definition of  $l/D_{eq}$ . The practical achievement which could be obtained, however, will probably be disappointingly small as compared to the effort spent. Test data of surfaces considered in this paper have ap-

proximately the same error band as the spread shown in Fig. 7. Hence, this error band may overshadow the accuracy of the definition of  $l/D_{eq}$ .

Smith [7] also considered an alternative approach to the conventional approach of  $j$  and  $f$  factors. In his paper, he does mention the dimensionless groupings  $J$  and  $F$ , but he does not recognize the universal dependence of the "reference transfer performance factor" on the dimensionless flow length, which is the basis of this paper.

### Conclusions

1 The flow length between major boundary layer disturbances is predominantly and within rather narrow limits responsible for the numerical merits of a surface geometry.

2 It is possible to present all surface geometries approximately in one single idealized performance plot. The surface effectiveness can also be incorporated.

3 It is possible to predict the approximate performance of untested geometries and surface modification when the appropriate  $l$  is established.

### Acknowledgment

The authors are grateful to Prof. W. M. Rohsenow, of the Massachusetts Institute of Technology, Cambridge, Massachusetts, for his valuable suggestions.

### References

- 1 Kays, W., and London, A. L., *Compact Heat Exchangers*, McGraw-Hill, New York, 1964.
- 2 Norris, R. H., and Spofford, W. A., "High Performance Fins for Heat Transfer," TRANS. ASME, Vol. 64, July 1942, pp. 489-496.
- 3 McAdams, W. H., *Heat Transmission*, Third ed., 1954.
- 4 Neugebauer, F. J., "Sizing Heat Exchangers," *Product Engineering*, Sept. 14, 1964.
- 5 Bergwerk, W., "The Utilization of Research Data in Heat Exchanger Design," Institute of Mechanical Engineers, Paper No. 6, Apr. 1964.
- 6 Norris, R. H., "Concepts of Efficiency of Heat Transfer and Pressure Drop Relations in Heat Exchangers," *Proceedings of the Fifth International Congress for Applied Mechanics*, 1939, p. 585.
- 7 Smith, J. L., Jr., "The Presentation of Heat Transfer and Friction Factor Data for Heat Exchanger Design," ASME Paper No. 66-WA/HT-59.
- 8 Jameson, S. L., "Tube Spacing in Finned-Tube Banks," TRANS. ASME, Vol. 67, 1945.

M. R. Berry, Jr.  
Assoc. Mem. ASME

R. W. Parker

R. W. Dickerson, Jr.  
Mem. ASME

Food Engineering Branch,  
Bureau of Foods,  
Food and Drug Administration,  
Department of Health, Education, and Welfare,  
Cincinnati, Ohio

# A Dry Materials Heat Exchanger With Regeneration

*The concept of regeneration is successfully demonstrated for the heat processing of sorptive materials in a continuous-flow heat exchanger. Data are presented for oats, cracked corn, and black peppercorns. Regeneration efficiency depends on the relative flow rates of the air and the product. Maximum efficiency was attained with the ratio of the air-to-product heat capacity fluxes near unity. Regeneration efficiency is also dependent on the moisture content of the product entering the heat exchanger. A maximum efficiency of 57 percent was obtained for black peppercorns that entered the heat exchanger with moisture contents of 5 to 8 percent (dry basis) and were processed to a holding temperature of 175° F (79.5° C).*

*Significant drying of the product was realized in the heat exchanger/regenerator. For oats, processed at 200° F, approximately half the moisture was removed in a single pass when the inlet moisture content was 13.7 percent. The amount of drying decreased as the moisture content of the product entering the heat exchanger was lowered. Drying also decreased when the processing temperature was lowered. Considerable energy is consumed by drying, and thus the regeneration effect for high moisture products is not as apparent.*

## Introduction

Because of the very wet harvest season of 1972 and the nationwide energy shortage, many farm crops were in danger of being lost since fuel was not immediately available to dry them sufficiently for marketing or storage. Crop drying is normally a bulk process whereby heated air is passed over or through thin layers of the product; often it requires several hours [1].<sup>1</sup> Much of the energy that is lost to the environment could be used for additional drying. A technique for retrieving some of this energy would not only reduce drying costs, but would also help to alleviate the energy shortage.

Another area that would benefit greatly from energy conservation techniques is that of pasteurizing foods, animal feeds, and feed ingredients to rid them of potentially harmful microorganisms. It is known that spices, for example, are often contaminated with bacteria, yeasts, and molds that cause spoilage of foods [2, 3]. Recently it was recommended that all animal feeds and cereal grains be pasteurized [4], and, in fact, salmonella has been found in approximately 17 percent of the ingredients used to manufacture animal feeds [5]. Pasteurization would eliminate this pathogen and greatly reduce its chances of ever reaching the retail food level, but pasteurization by present methods is economically prohibitive because of the relatively low dollar value of

the product and the high cost of the energy required to heat it. The heating of dry products is currently performed in bulk processes or in continuous-flow heat exchangers. These heat exchangers are normally fluidized beds or indirect heat exchangers where the heating medium (normally steam) passes through the inside of a screw conveyor. Once the dry product has been heated to the prescribed processing temperature, however, much of its energy could be recovered. Such a step would serve a dual purpose: the product would be returned to its initial temperature and the recovered energy could be used to heat the incoming product to pasteurization temperature, thereby significantly reducing the total energy requirements for pasteurization.

To make the drying and/or pasteurization process for granular dry materials more feasible economically, the concept of regeneration was incorporated in a dry materials heat exchanger, and its performance as a pasteurizer and a dryer was evaluated.

## Experimental

A schematic of the heat exchanger with regeneration developed for this experimental investigation is shown in Fig. 1. Air is the heat exchange medium that passes in counterflow through the dry product. The product flows vertically downward because of gravity. The device consists of four main sections: (1) a heat exchanger where the temperature of the dry product is raised to the processing temperature by heated air, (2) a holding tube where the product is held at processing temperature, (3) a regenerator where the product is cooled and the air is preheated, and (4) a metering tube that controls the flow rate of the product. The flow of air which bypasses the holding tube is heated in the heater to the temperature necessary for the process.

**Apparatus.** A bench model of the dry materials heat exchang-

<sup>1</sup> Numbers in brackets designate References at end of paper.

Contributed by the Heat Transfer Division and presented at the Winter Annual Meeting, Detroit, Mich., November 11-15, 1973 of THE AMERICAN SOCIETY OF MECHANICAL ENGINEERS. Journal manuscript received by the Heat Transfer Division February 5, 1974. Paper No. 73-WA-HT-14.

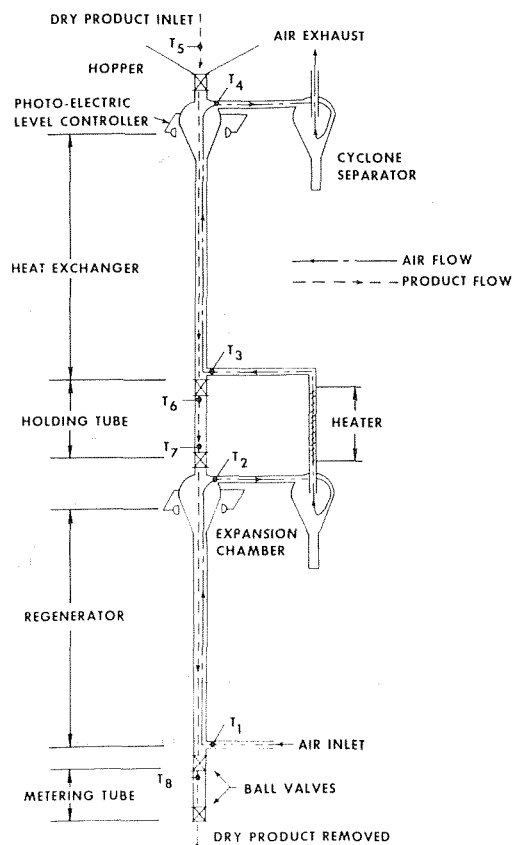


Fig. 1 Schematic of dry materials heat exchanger with regeneration

er with regeneration was fabricated using 1½-in. (38.1-mm) ID Pyrex glass tubing. The heat exchanger and regenerator sections each had an effective length of 42 in. (1.07 m). This included an expansion chamber at the top of the respective sections. The purpose of the expansion chamber was to reduce the air velocity thereby allowing airborne particles of product to fall out before leaving the section. Any fine particles that are exhausted from either the heat exchanger or the regenerator are removed by means of Pyrex glass cyclone separators. Both the expansion chambers and the cyclone separators were custom fabricated from 2000-ml Erlenmeyer flasks. The length of the holding tube could be varied to allow for a wide range of holding times. If this apparatus were being used to pasteurize animal feeds, the holding time required at pasteurization temperature to facilitate a sufficient kill of salmonella would vary with the pasteurization temperature and moisture content of the feed [6, 7, 8]. A holding tube length of 18 in. (0.46 m) was used throughout this investigation. The preheated air that bypasses the holding tube was further heated by spiral-finned electric heaters. A temperature controller monitoring the air temperature at the inlet to the heat exchanger controlled the heaters.

## Nomenclature

$c$  = constant pressure specific heat, Btu/lb°F  
 $d.b.$  = dry basis, weight of water per weight of dry material  
 $m$  = mass flow, lb/hr  
 $mc$  = heat capacity flux, Btu/hr°F  
 $M$  = percent moisture content of the product, dry basis ( $d.b.$ )

$q$  = heat flow, Btu/hr  
 $T$  = temperature, °F  
 $w.b.$  = wet basis, weight of water per weight of dry material and water  
 $W$  = moisture content of the product, wet basis ( $w.b.$ )  
 $\beta$  = thermal effectiveness

$\eta$  = regeneration efficiency

## Subscripts

$a$  = air  
 $h$  = heater  
 $p$  = dry product  
 $r$  = regenerator  
 1-8 = thermocouple locations (see Fig. 1)

Product flow was controlled automatically by electric timers cycling the five pneumatically actuated 1½-in. (38.1 mm) ID ball valves shown in Fig. 1. A cycle consisted of three operations: the fill, the pulse, and the dwell. The first operation, the fill, has 5 s in which to fill the regenerator with product held in the holding tube and empty the metering tube. When the regenerator fills to the proper level, the filling is interrupted by a photo-electric level controller located in the expansion chamber of the regenerator; thus a constant level of product is maintained in the regenerator. During the pulse, which is 10 s long, the holding tube and the metering tube are simultaneously filled. The remainder and the majority of the cycle, the dwell, is limited to 5 min. During the first few seconds of the dwell, the heat exchanger is filled from the hopper. The amount of product entering the heat exchanger is also controlled by a photo-electric level controller located in the expansion chamber. Product flow is halted until the end of the dwell and the beginning of a new cycle. The duration of the dwell controls the rate of flow of the dry product. The metering tube, which holds 20 cu in. (328 ml), is emptied once per cycle, giving a continuous, slug-type flow of dry product at the rate of 2.1 cu ft (59 l) per hr for a 3-min cycle time.

**Maintaining Continuous Flow.** A continuous flow of air opposing the flow of the product tended to plug or mass the dry material in both the heat exchanger and the regenerator. Once a plug formed, the flow of the product ceased. Several techniques were employed to eliminate plugging. Vibrators installed on the walls of the heat exchanger and regenerator were of some help but did not reliably eliminate the phenomenon. In a scale-up of the heat exchanger/regenerator, plugging is not expected to be as much of a problem since a product with a given particle size should flow more freely in a larger flow channel. For the bench model, however, the inclusion of a turbulence promoter and a pulsating air supply was necessary to attain a continuous flow of the dry product. The turbulence promoter was a 7/8-in. (22.2-mm) OD spiral, wound with a 1½-in. (38.1-mm) throw from 1/8-in. (3.18-mm) OD, thin-wall, stainless steel tubing. A spiral was suspended in the center of both the heat exchanger and the regenerator sections and extended into the expansion chambers. The air entering at both the heat exchanger and the regenerator was pulsed by solenoid valves. Pulses of ¼ s with a frequency of two per second proved most effective. The combined effect of the turbulence promoter and the pulsed air supply was to vigorously agitate the dry product, thereby forming a fluidlike suspension that would flow without plugging. This procedure also induces intimate contact between the dry product and the air, a necessary characteristic for effective heat and moisture transfer.

**Insulation.** The low flow rate and associated energy of the product compared with the large surface area for heat loss to the surroundings made thorough insulation of the column mandatory. The heat exchanger and regenerator tubes were fitted with 2-in. (50.8-mm) thick, canvas-covered, fiberglass insulation. Irregular portions of the column such as the expansion chambers and ball valves were covered with 3½-in. (88.9-mm) fiberglass home insulation. The holding tube was wrapped with flexible electric heating tape. Voltage to the tape was regulated so that the product temperature at the holding tube outlet equaled that at the inlet. This step guarded the holding tube from heat losses to the surroundings.

**Dry Products.** Three dry products were selected for this investigation: coarse cracked corn, since it is one of the primary ingredients of all poultry feeds; oats, since it is a representative feed; and black peppercorns, since it requires drying and is one of the more heavily contaminated spices [2, 3]. All three products were heated to a processing temperature of 175° F (79.5° C). In addition, a series of runs were made with oats at 200° F (93.3° C). Each series of runs consisted of varying air and product flow rates to obtain air-to-product heat capacity flux ratios ( $m_a c_a / m_p c_p$ ) between 0.6 and 3.6. This was accomplished with air flows between 8 and 28 lb/hr (3.6 to 12.7 kg/hr) with cycle times of 45 s to 5 min. For each series, from 10 to 25 runs were conducted with the moisture content of the dry product entering the column equilibrated to between 5 and 8 percent moisture content, dry basis (*d.b.*). In addition, approximately 5 runs were made for each product with moisture contents above 8 percent and below 5 percent.

**Procedure.** The dry product, preconditioned to a prescribed temperature and moisture content, was supplied to the column by way of a 1½-cu-ft (42.5-l), cone-shaped hopper. Once steady-state conditions were attained, temperatures were recorded by a multipoint, strip-chart recorder. Air and product temperatures were taken at the inlet and outlet of both the heat exchanger and regenerator. Thermocouples (copper-constantan) were located as shown in Fig. 1. The thermocouples were fabricated from 24-ga nylon wire and inserted through the gaskets connecting the glass sections so as to be free-standing at the midpoint of the column. Pressure drops across the heat exchanger and regenerator were also recorded. The air flow rate was measured with a rotometer and the dry product flow rate was determined by weighing the product leaving the column. Samples of the dry product before and after processing were taken so that the amount of drying could be determined. Moisture content was determined by oven-drying [9].

## Results and Discussion

The performance of the heat exchanger and regenerator is best characterized by defining a regeneration efficiency, which is defined as the ratio of the regenerated energy to the total energy required for the process. In terms of the energy associated with the air flow, the regeneration efficiency is defined as

$$\eta = \frac{q_r}{q_r + q_h} \quad (1)$$

Or, since the air behaves as an ideal gas

$$\eta = \frac{m_a c_a (T_2 - T_1)}{m_a c_a (T_2 - T_1) + m_a c_a (T_3 - T_2)} \quad (2)$$

or

$$\eta = \frac{T_2 - T_1}{T_3 - T_1} \quad (3)$$

The regeneration efficiency is then the ratio of the temperature rise of the air through the regenerator to the total rise in air temperature through both the regenerator and the heater sections. The regeneration efficiency will vary with the air and product flow rates. This effect is shown in Fig. 2 by way of temperature distributions typical of counterflow heat exchangers. Constant product flow rate and a constant holding temperature are assumed. Insufficient air flow gives rise to excessively high air temperatures entering the heat exchanger and incomplete cooling of the dry product in the regenerator. With excess air, regeneration efficiencies are lowered because of both low regeneration temperatures and hot air being exhausted from the heat exchanger. Also, with excess air, velocities are such that large amounts of product are lost by way of the cyclone separators. For the proper ratio of air-to-product flow rates, temperature differences between the air and the product are minimized, thus giving maximum regeneration temperatures and requiring a minimum of energy from the

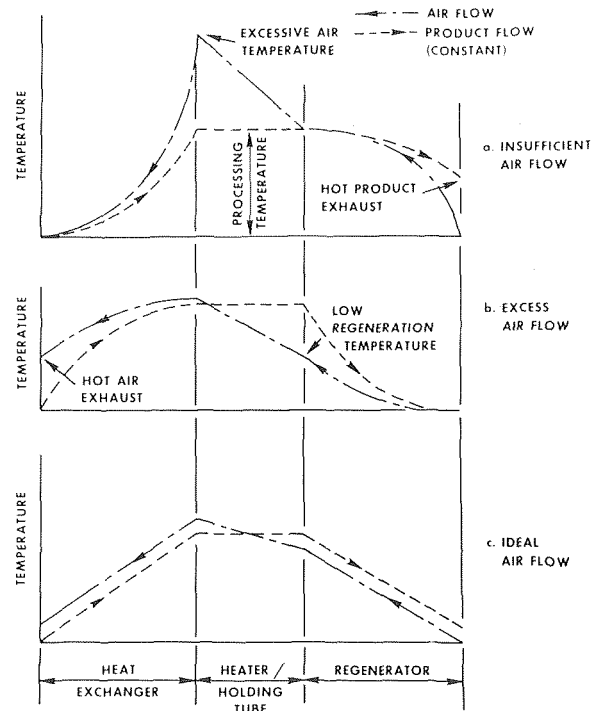


Fig. 2 Effect of air flow on regeneration efficiency

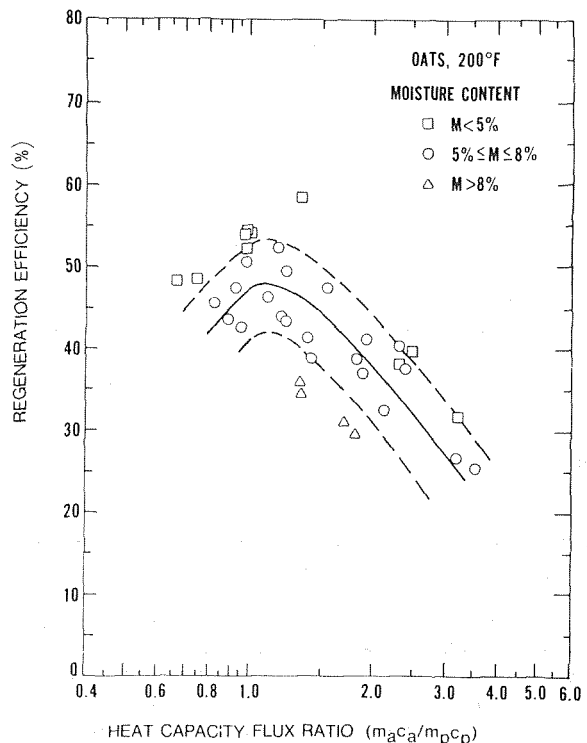


Fig. 3 Regeneration efficiencies for oats at 200° F, various moisture contents

heater. The effect of drying on the regeneration efficiency is about the same as insufficient air flow (Fig. 2). The energy required to vaporize the moisture and remove it from the product must be supplied by the air. Therefore, when drying is accomplished, regeneration efficiencies will be lower and a strong function of the amount of drying that takes place.

**Regeneration Performance.** The regeneration efficiency as a function of heat capacity flux ratio is shown in Fig. 3 for oats with

a processing temperature of 200° F. The upper and lower dashed lines indicate the bounds of the experimental data for an entering product moisture content of less than 5 percent and greater than 8 percent, respectively. In other words, all the experimental data for moisture content from 5 to 8 percent lie between the dashed curves. The solid curve represents the average of this data. Fig. 3 is typical of all products. The regeneration efficiency is seen to be not only a strong function of moisture content, but also highly dependent on the ratio of air-to-product heat capacity fluxes. Curves for the average regeneration efficiencies of the various products tested with moisture contents between 5 and 8 percent (*d.b.*) are shown in Fig. 4. For all products, the maximum regeneration efficiency occurred at a ratio of heat capacity fluxes equal to or slightly higher than unity. Comparison of the two curves for oats at 175 and 200° F indicate that higher efficiencies can be obtained by lowering the processing temperature. This effect should not be interpreted as due to the heat transfer characteristics alone. The energies associated with the mass transfer are also altered when the temperature is lowered. This effect is discussed in the next section.

The influence of column diameter or column length on regeneration efficiency was not determined.

**Thermal Properties.** The specific heats of the dry products used in this investigation are dependent on moisture content. The specific heat of oats at 59° F (15° C) is given by Haswell [10] as a function of moisture content on a wet basis as

$$c = 0.305 + 0.0078W \quad (4)$$

For yellow dent corn at an average temperature of 69° F (20.6° C), Kazarian and Hall [11] report

$$c = 0.350 + 0.0085W \quad (5)$$

Both investigators used calorimeters to measure the specific heats directly.

The specific heat of black peppercorns was not found in the lit-

erature. The thermal diffusivity and the thermal conductivity of the pepper were measured by techniques described by Dickerson [12]. The specific heat was calculated from the definition of thermal diffusivity, and at an average temperature of 100° F (37.8° C), it is given by

$$c = 0.24 + 0.016W \quad (6)$$

This is an apparent specific heat that was indirectly obtained by measuring other thermal properties in a closed container. There was a significant air space within the product. Similar tests for oats and corn gave apparent specific heats approximately 17 percent lower than the specific heats from equations (4) and (5) at the same temperature.

The specific heats used in the data reduction were calculated from equations (4), (5), and (6) using the average of the inlet and outlet moisture contents converted to a wet basis.

**Effect of Moisture.** All data collected for this investigation were obtained using sorptive materials. Because of the extremely low relative humidity of the heated air entering the heat exchanger, some drying of the product was realized. Despite the drying effect, the data (Fig. 3) show that optimum performance was accomplished at a heat capacity flux ratio of approximately unity. Consequently, the amount of drying does not affect the optimum operating point for a given inlet moisture content. The amount of drying does, however, affect the temperature of the air entering the heat exchanger and therefore the regeneration efficiency. Regeneration efficiency was a function of the moisture content of the oats entering the column and increased as moisture content decreased (Fig. 5). If this curve were extrapolated to zero moisture content, it appears that in the absence of drying, efficiencies as high as 90 percent could be realized. Conversely, for very high moisture contents, the regeneration effect is overshadowed by the very high energy requirements of the drying process. But even a regeneration efficiency of only 30 percent indicates a 30 percent reduction in the energy cost of processing.

**Drying Performance.** The removal of moisture from grains

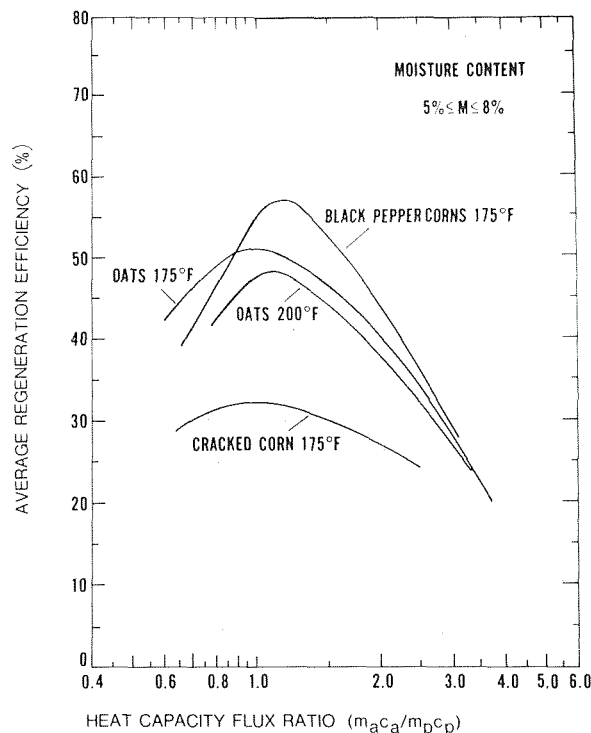


Fig. 4 Regeneration efficiencies for various products, 5 percent to 8 percent moisture content (dry basis)

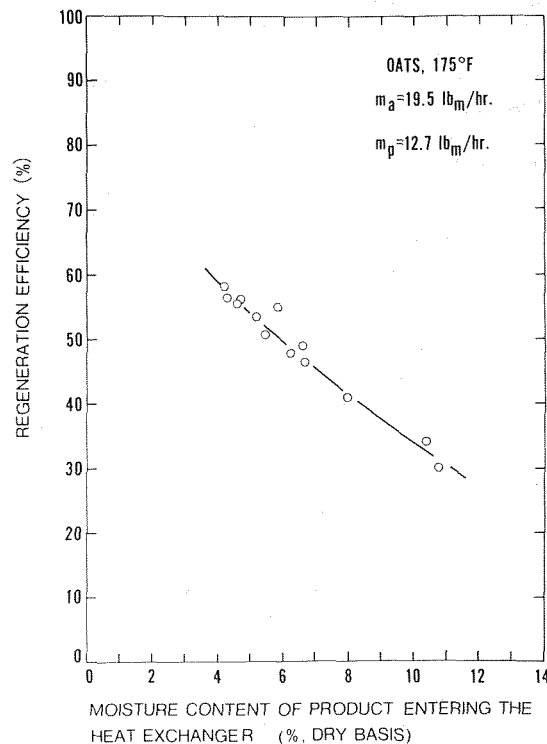


Fig. 5 Effect of moisture content on the regeneration efficiency of oats at 175° F



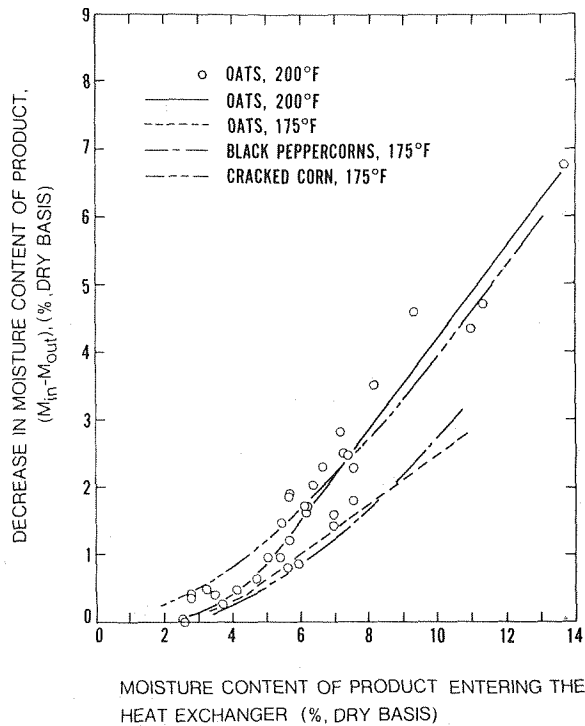


Fig. 6 Drying curves for various products

and feeds is usually performed at relatively low air temperatures and requires extended drying times of several hours [1]. Yet as product temperature is increased at constant moisture content, its equilibrium relative humidity is increased significantly; and if product temperature is raised high enough, some of the previously adsorbed moisture is converted to free moisture within the product [9]. Raising the temperature of oats to 200° F should result in significantly increased drying rates. The amount of drying accomplished in the heat exchanger/regenerator is shown in Fig. 6. The change in moisture content is a function of the moisture content of the product entering the heat exchanger. Only one set of data points is shown, those for oats at a processing temperature of 200° F. The curve shown for oats at 200° F represents the average of these data. The remaining curves of Fig. 6 were obtained in a similar manner. A comparison of the curves for oats at 175 and 200° F indicates that drying is dependent on holding temperature.

The amount of drying for the cracked corn was higher than that for the other products at the same temperature. This fact, together with a high heat of desorption for corn [9], accounts for the low regeneration efficiencies obtained with the corn (see Fig. 4).

The rate of drying decreases as the moisture content of the product entering the heat exchanger decreases. For moisture contents below about 12 percent (*d.b.*), the water in sorptive material such as those used in this study is no longer free or surface water. Increased amounts of energy are thus required to remove it since it is tightly bound by the material. As much as 50 percent additional energy is required to remove moisture from feeds and feed ingredients at low moisture contents [9].

For product inlet moisture contents above 8 percent (*d.b.*), the apparatus is an effective dryer; for oats processed at 200° F, approximately half of the moisture was removed when the product inlet moisture content was 13.7 percent (Fig. 6). This was accomplished in an average process time of approximately 30 min, depending on cycle time.

Fig. 6 shows the amount of moisture removed from the product but does not indicate where in the apparatus it was removed. Since no air moves through the holding tube, it is unlikely that substantial moisture was removed in this section. By identifying

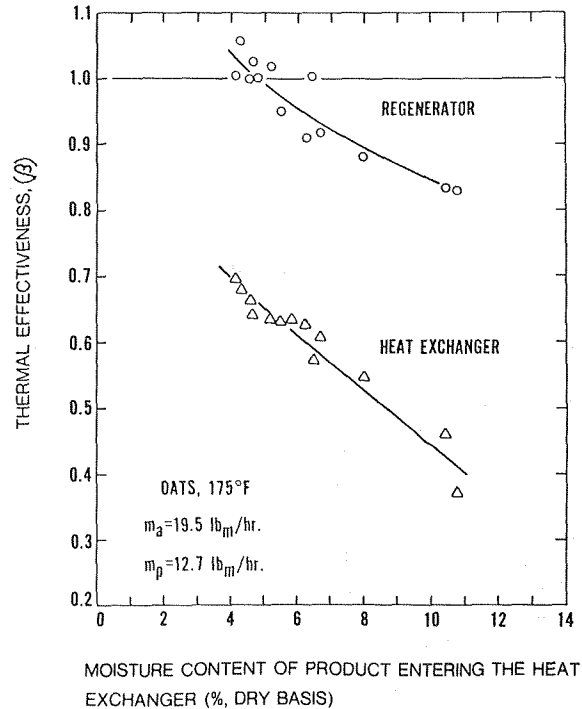


Fig. 7 Thermal effectiveness of the heat exchanger and the regenerator

the term "thermal effectiveness," it is possible to obtain estimates of the degree of vaporization and condensation. For the regenerator, thermal effectiveness is the ratio of the sensible portion of the energy added to the air to the sensible energy removed from the product.

$$\beta_r = \frac{m_a c_a (T_1 - T_2)}{m_p c_p (T_7 - T_8)} \quad (7)$$

Assuming negligible heat losses to the surroundings, this quantity could be greater than unity only if moisture were added to the product. Similarly, for the heat exchanger, the quantity of sensible energy added to the product divided by the sensible energy removed from the air is

$$\beta_e = \frac{m_p c_p (T_6 - T_5)}{m_a c_a (T_3 - T_4)} \quad (8)$$

These thermal effectiveness values are shown in Fig. 7 for constant flow rates of air and oats, with the oats entering at various moisture contents. The thermal effectiveness of both the heat exchanger and the regenerator decrease with increased inlet moisture content, indicating increased drying activity. For product inlet moisture contents of less than 5 percent (*d.b.*), the regenerator thermal effectiveness is greater than unity, indicating some adsorption of moisture by the product. This effect was caused, however, by inlet air conditions. The relative humidity of the air entering the regenerator was consistently between 15 and 20 percent for all tests. This would correspond to a moisture content in the oats of 4 to 5 percent (*d.b.*) if the feeds were allowed to come into equilibrium with the air [9]. Furthermore, when a product entered the regenerator with a moisture content higher than 5 percent (*d.b.*), the regenerator further decreased the moisture content. For the entire range of product inlet moisture contents, thermal effectiveness in the regenerator varied from only 0.85 to 1.05, indicating no appreciable drying of the product.

In the heat exchanger, thermal effectiveness ranged between 0.4 and 0.7, demonstrating considerable drying. With the product inlet moisture content at 10.5 percent (*d.b.*), more than half the

energy supplied by the air was used to vaporize and remove moisture (Fig. 7).

**Effect of Heat Transfer on Drying.** Sorptive materials respond much more slowly to moisture changes than to temperature changes [13, 14]. To increase the temperature of a dry material, it is necessary only to supply the sensible heat requirement of the dry material and adsorbed moisture. When removing moisture, however, the energies of vaporization and desorption must also pass through the heat transfer barrier at the surface of the particle. Consequently, drying rates are influenced by the surface heat transfer coefficient of the solid material.

When drying small samples in an oven, surface heat transfer coefficients are quite low, and approximately 100 hr of drying time is required to reach moisture equilibrium [1]. With forced air convection, equilibrium times can be reduced to about 50 hr [9]. In this apparatus, the air is blown directly through the product, causing vigorous, localized agitation of the product. The high heat transfer coefficient at the surface of the product particle is responsible for the extremely short drying times achieved.

High heat transfer coefficients do not represent the total effect, however. Raising the temperature of the product markedly increases drying rates [1]. The processing temperature of 200° F used on the oats yielded a marked improvement in drying rates over a processing temperature of 175° F (Fig. 6).

No measurement was made of how product quality is affected by processing oats at 200° F, a temperature that is beyond the normal range for product processing. The time of exposure, however, was quite brief. Depending on cycle time, the product was heated from room temperature to 200° F in less than 15 min, held for about 8 min, and cooled to room temperature in less than 15 min. Research on product quality will be required to assess the effect of the short term, high temperature exposure.

## Conclusions

A bench model of a continuous-flow, dry materials heat exchanger with regeneration was fabricated. Based on data obtained from the series of runs made with oats, cracked corn, and black peppercorns, the following points are summarized:

- 1 The concept of a regenerative heat exchanger has been successfully demonstrated for granular dry materials.
- 2 Regeneration efficiency is a function of the relative flow rates of the air and the product. Highest efficiencies are attained at a ratio of air-to-product heat capacity fluxes equal to or slightly higher than unity.
- 3 Higher regeneration efficiencies can be obtained by lowering the processing temperature.
- 4 Regeneration efficiencies increase as the moisture contents of the dry products decrease.
- 5 The apparatus effectively dries sorptive materials. The regenerator section provides additional drying for all products with

moisture contents above about 5 percent (*d.b.*) before processing.

6 The amount of drying depends on the moisture level of the product entering the heat exchanger. The amount of moisture removed decreases with decreasing moisture content of the product.

7 Additional drying can be obtained by raising the processing temperature.

In conclusion, a dry products heat exchanger with regeneration of a specific geometry has been evaluated as both a heat exchanger and a dryer. For sorptive materials, such as those tested in this investigation, the two functions cannot be separated. The final design for any application must therefore be a trade-off between high regeneration efficiency and effective drying.

## Acknowledgment

The authors wish to acknowledge L. F. Tekulve for his contributions during certain phases of this investigation.

## References

- 1 Hall, C. W., *Drying Farm Crops*, AVI Publishing Co., Westport, Conn., 1957, pp. 76, 186, 258.
- 2 Christensen, C. M., "Pure Spices-How Pure?," *Amer. Soc. Microbio. News*, Vol. 38, No. 4, Apr. 1972, p. 165.
- 3 Krishnaswamy, M. A., Patel, J. D., and Parthasarathy, N., "Enumeration of Micro-organisms in Spices and Spice Mixtures," *J. Food Sci. Technol.*, Vol. 8, No. 4, Dec. 1971, p. 191.
- 4 Weckel, K. G., et al., "Prevention of Contamination of Raw Agricultural and Marine Products," *Proceedings of the 1971 National Conference on Food Protection*, U. S. Department of Health, Education, and Welfare, Food and Drug Administration Publication (FDA) 72-2015, U. S. Government Printing Office, Washington, D. C., 1972, p. 47.
- 5 Pomeroy, B. S., and Grady, M. K., "Salmonella Organisms From Feed Ingredients," *Proceedings, U. S. Livestock Sanitary Association*, 65th Annual Meeting, Nov. 1961, p. 449.
- 6 Liu, T. S., Snoeyenbos, G. H., and Carlson, V. L., "Thermal Resistance of Salmonella Senftenberg 775W in Dry Animal Feeds," *Avian Diseases*, Vol. 8, No. 3, Aug. 1969, p. 611.
- 7 Rasmussen, O. G., Hansen, R., Jacobs, N. J., and Wilder, O. H. M., "Dry Heat Resistance of Salmonella in Rendered Animal By-Products," *Poultry Sci.*, Vol. 43, 1964, p. 1151.
- 8 Riemann, H., "Effect of Water Activity on the Heat Resistance of Salmonella in 'Dry' Materials," *Appl. Microbio.*, Vol. 16, No. 10, Oct. 1968, p. 1621.
- 9 Berry, M. R., and Dickerson, R. W., "Moisture Adsorption Isotherms for Selected Feeds and Ingredients," *Trans. Amer. Soc. Agr. Eng.*, Vol. 16, No. 1, Jan. 1973, p. 137.
- 10 Haswell, G. A., "A Note on the Specific Heat of Rice, Oats, and Their Products," *Cereal Chem.*, Vol. 31, No. 4, 1954, p. 341.
- 11 Kazarian, E. A., and Hall, C. W., "Thermal Properties of Grain," *Trans. Amer. Soc. Agr. Eng.*, Vol. 8, No. 1, Jan. 1965, p. 33.
- 12 Dickerson, R. W., and Read, R. B., "Calculation and Measurement of Heat Transfer in Foods," *Food Technol.*, Vol. 22, No. 12, Dec. 1968, p. 1533.
- 13 Sutherland, J. W., Banks, P. J., and Griffiths, H. J., "Equilibrium Heat and Moisture Transfer in Air Flow through Grain," *J. Agr. Eng. Res.*, Vol. 16, No. 4, Dec. 1971, p. 368.
- 14 Myklestad, O., "An Analysis of Transient Flow of Heat and Moisture During Drying of Granular Beds," *Int. J. Heat Mass Transfer*, Vol. 11, No. 4, Apr. 1968, p. 675.

M. F. Blair

Research Engineer,  
United Aircraft Research Laboratories,  
East Hartford, Conn.  
Mem. ASME

# An Experimental Study of Heat Transfer and Film Cooling on Large-Scale Turbine Endwalls

*Experiments were conducted to determine the film cooling effectiveness and convective heat transfer coefficient distributions on the endwall of a large-scale turbine vane passage. The vane test models employed simulated the passage geometry and upstream cooling slot geometry of a typical first stage turbine. The test models were constructed of low thermal conductivity foam and foil heaters. The tests were conducted at a typical engine Reynolds number but at lower than typical Mach numbers. The film cooling effectiveness distribution for the entire endwall and the heat transfer distribution for the downstream one-half of the endwall were characterized by large gapwise variations which were attributed to a secondary flow vortex.*

## Introduction

In future gas turbine engines, which will employ maximum turbine inlet temperatures to achieve high cycle efficiencies and power, the components subjected to these high temperatures must be cooled. Since the total amount of cooling air required must be minimized to achieve the maximum cycle and turbine efficiency benefits of the high turbine inlet temperature, the heat transfer systems for these components must be highly sophisticated. Development of the required heat transfer design systems requires knowledge of the mechanisms influencing the heat transfer.

Previous aerodynamic studies have shown that large secondary flows occur within turbine blade (or vane) passages. These secondary flows take the form of streamwise vortices of differing kinds, which alter the primary flow through the blade passages. The amount of heat transferred to the endwall of a turbine is expected to depend strongly on the various secondary flows which occur in the blade (or vane) passages. At least three mechanisms exist for producing these secondary flows. The turning of the mainstream flow as it passes through the blade (or vane) passage produces cross-channel flow near the endwall from the pressure surface of one blade to the suction surface of an adjacent blade. This flow is turned away from the endwall at the suction surface and rolls up to form a passage vortex in the corner formed by the endwall and suction surface. A second source of secondary flow occurs when there is clearance between the blade (or vane) tip and endwall. This clearance causes tip leakage flow, which tends to form a vortex in

the same location as the passage vortex, but with swirl in the opposite direction. A third source of secondary flow is the relative motion between a blade tip and endwall. For a turbine the endwall moves toward the suction surface of the blades and, at sufficiently high rotation speeds, a scraping vortex is formed along the suction surface with swirl in the same direction as the passage vortex. All of these secondary flows have been observed in flow visualization studies by Allen and Kofskey [1]<sup>1</sup> and Herzig, et al. [2]. The relative strengths of the secondary flows depend on turbine design and operating conditions.

The present study was restricted to investigating phenomena associated with the first source, that is, the cross-channel flow and the resulting corner vortex. This experimental investigation was directed toward obtaining a greater understanding of the mechanisms governing the film cooling of and the heat transfer to the endwall of turbines by obtaining local film effectiveness and heat transfer coefficients on a large-scale model of a typical turbine vane passage. Although the results obtained from the present investigation are strictly applicable only to the endwall region between vanes, the same basic heat transfer mechanisms are expected to be involved in the rotor case.

## Description of Test Equipment

Two vane passage test sections were employed in the present investigation: one with rounded leading edges and the other with sharp leading edges. A scale drawing of the vane passage test sections is presented in Fig. 1. The rounded leading edge passage was constructed to simulate a typical first stage turbine vane. Suction and pressure surface static pressure distributions, which simulate

Contributed by the Heat Transfer Division for publication in the JOURNAL OF HEAT TRANSFER. Manuscript received by the Heat Transfer Division June 11, 1974. Paper No. 74-GT-33.

<sup>1</sup> Numbers in brackets designate References at end of paper.

typical vane flow conditions, are obtained by adjusting both the exit tailboards (which set the mean exit angle of the flow and the passage back pressure) and the leading edge flow adjustment slots. To simulate endwall film cooling, coolant air was injected through a slot located in the vertical wall immediately upstream of the leading edge plane. Bleed slots, located on the upper and lower horizontal surfaces of the upstream duct and on the vertical wall immediately upstream of the coolant injection slot, were used for removing boundary layer flow from these surfaces. The sharp leading edge vane passage was designed to eliminate the secondary flows generated in the immediate region of the leading edge and differs from the rounded leading edge passage only in the immediate region of the leading edge. Results from tests with this configuration provide information regarding the influence of these leading edge generated secondary flows on the endwall heat transfer and data for evaluating analytical procedures being developed at UARI, for predicting the endwall heat transfer in turbine vane passages.

All tests were conducted in the vane passage wind tunnel, shown schematically in Fig. 2. This tunnel is a large-scale, low-speed, continuous flow wind tunnel designed to permit detailed study of the flow in simulated turbine vane passages. Immediately downstream of the blower the air flows through a honeycomb section and three screens in order to reduce turbulence and to obtain a uniform velocity distribution. The widths of the test section and the upstream duct are 20 in.; the height of the upstream duct is 8.25 in.

The adiabatic endwall assembly, which was used in the film cooling effectiveness tests, was fabricated by casting a 1-in.-thick rigid urethane foam layer on a Micarta backing plate. By using a material with such a low thermal conductivity ( $k = 0.02 \text{ Btu/hr } ^\circ\text{F ft}$ ), local surface temperatures very close to the true local adiabatic wall recovery values were achieved. The test surface extended from an upstream injection slot to the vane trailing-edge line across the entire vane gap. A coolant plenum provided uniform flow along the entire injection slot. The endwall test region was instrumented with 96 chromel-alumel thermocouples, 60 of which were located in the upstream 1/3 of the test surface, where the largest local temperature gradients were anticipated.

Local convective heat transfer rates on the endwall of the vane passages were determined by measuring the power required to maintain thermally isolated segments of a plate assembly at an isothermal level in excess of the mainstream temperature. A cross-sectional sketch of the endwall showing the details of the endwall construction and the heater installation is presented in Fig. 3. The basic structure of the endwall consists of rigid urethane foam backed by a printed circuit board. Heater elements, consisting of a thin etched foil with Kapton substrate (0.008-in. thick), were attached to the foam. Copper segments (0.032-in. thick), attached to the heater elements, promote an even distribution of surface temperature and form the surface in direct contact with the airstream. The small gaps (0.020 in.) between the copper segments were filled with a low thermal conductivity foam adhesive ( $k = 0.1 \text{ Btu/hr } ^\circ\text{F ft}$ ). The endwall was painted with carbon black paint to obtain a surface with an emissivity approximately equal to one. Power was

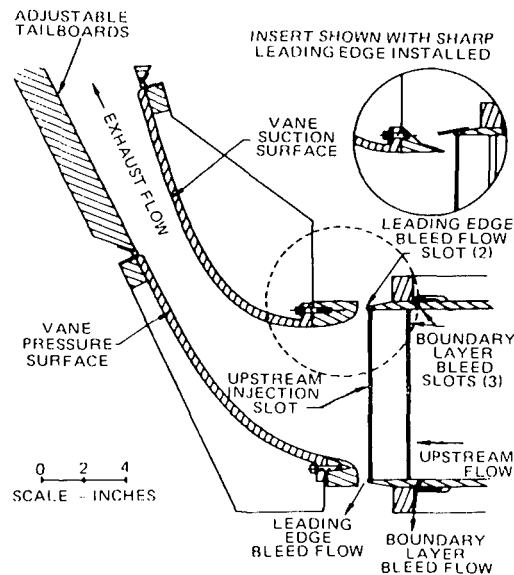


Fig. 1 Vane passage test section with rounded and sharp leading edges

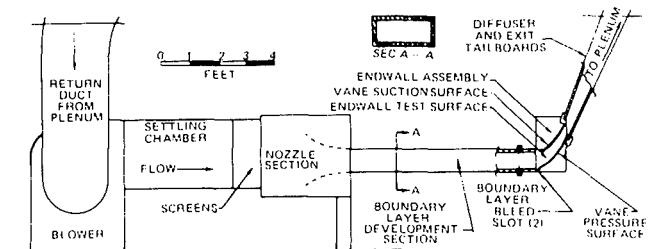


Fig. 2 Vane passage wind tunnel

supplied to the individual foil heaters through copper coated steel rods, which were welded to the power tabs of the heaters and soldered to their respective tracks on the printed circuit board. These tracks led to connectors that were wired to a bank of individual constant voltage power supplies. Chromel-alumel thermocouples, mounted in each copper surface block, were used to monitor the plate surface temperature distribution. For all heat transfer tests described herein, each heater was adjusted until all were at a uniform temperature level. When the adjustments for individual heater power were completed, the power dissipated in each heater was measured. Because of the thermal isolation of the heater segments, the heater power was essentially a direct measure of the local convective and radiative heat transfer rate. The radiative heat flux from the test surface was calculated for a surface emissivity assumed equal to one and was subtracted from the total power to determine the convective heat transfer rate. The endwall test surface was divided into a mosaic pattern (Fig. 4) for which foil heaters were designed and fabricated. The density of the elements was

## Nomenclature

$C_p$  = pressure coefficient,  $(P - P_e)/q_e$ , dimensionless  
 $h$  = convective heat transfer coefficient,  $\text{Btu/s sq ft } ^\circ\text{F}$   
 $M$  = blowing parameter,  $\rho_c U_c / \rho_e U_e$ , dimensionless  
 $P$  = static pressure,  $\text{lb}_f/\text{sq ft}$   
 $q$  = dynamic pressure,  $\rho_e U_e^2 / 2g$ ,  $\text{lb}_f/\text{sq ft}$   
 $Re$  = axial chord Reynolds number,  $U_e C_x / \nu_e$

$Re_x$  = Reynolds number based on distance from boundary layer origin,  $U_e x / \nu_e$ , dimensionless  
 $S$  = slot characteristic dimension, ft  
 $S_t$  = Stanton number,  $h / (\rho_e U_e C_p)$ , dimensionless  
 $T$  = temperature,  $^\circ\text{R}$   
 $U$  = velocity,  $\text{ft/s}$   
 $U_x$  = local velocity at location  $x'$ ,  $\text{ft/s}$   
 $x'$  = distance along curved locus (Figs.

6, 7), ft  
 $\eta$  = effectiveness parameter,  $(T_e - T_{aw}) / (T_e - T_c)$ , dimensionless

## Subscripts

$aw$  = adiabatic wall  
 $c$  = coolant  
 $e$  = free-stream value upstream of the leading edge  
 $w$  = nonadiabatic wall

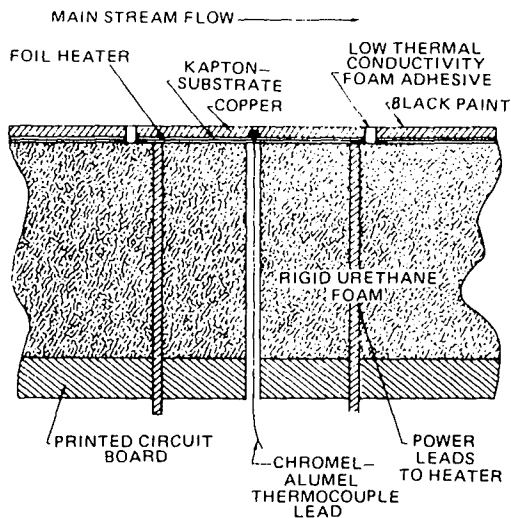


Fig. 3 Typical cross section of heated plate

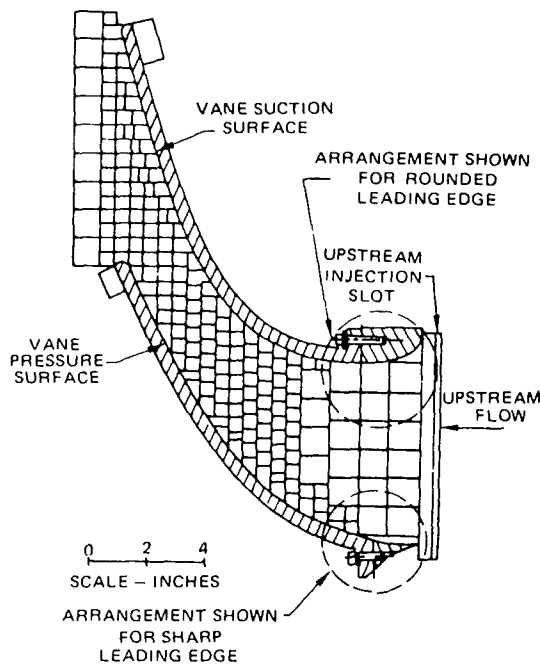


Fig. 4 Heater arrangement for vane passage endwall

maximized in regions of the endwall where the greatest spatial variations of heat transfer were anticipated. These include the regions near both the suction and pressure surfaces and the mid-chord region across the entire gap. Guard heaters fit against the ends of the vane suction and pressure surfaces and prevented heat loss by conduction from the rows of heaters in the suction and pressure corners.

### Discussion of Tests and Results

Endwall film cooling effectiveness and heat transfer distributions were obtained for several coolant flow conditions and for the two leading edge geometries, i.e., (a) film cooling effectiveness distributions were determined for the rounded-leading-edge configuration with three coolant injection rates, (b) heat transfer distributions were measured for the rounded-leading-edge configuration with both natural and forced endwall boundary layer transition and with upstream coolant injection, and (c) the heat transfer distribution was measured for the sharp-leading-edge configuration with forced endwall boundary layer transition.

The static pressure distributions measured on the vane surfaces for these tests are presented in Fig. 5. In addition, the presence of endwall cross-channel secondary flow, such as described in the introduction, was confirmed through the use of ink-streak flow visualization.

Endwall adiabatic film cooling effectiveness distributions associated with upstream coolant injection were determined for a range of coolant flows using the adiabatic endwall assembly described previously. Wall temperature distributions were measured for the rounded-leading-edge configuration at three coolant flow rates ( $M = \rho_c U_c / \rho_c U_c = 0.5, 0.75, \text{ and } 1.0$ ). The results for  $M = 0.75$  are presented in Fig. 6 in terms of the standard film cooling effectiveness parameter,  $\eta = (T_c - T_{aw}) / (T_c - T_e)$ . Included in Fig. 6 is a diagram of the upstream injection slot. Iso-effectiveness contours were constructed from the data by linear interpolation between the endwall thermocouple locations. For all cases, the upstream velocity was 94 fps and the free-stream temperature was 98 °F. These conditions resulted in an axial chord Reynolds number,  $Re_{axial\ chord} = 4.6 \times 10^5$ , which is typical of current gas turbine engines. The coolant injection temperature for all cases was 70 °F. For  $M = 0.75$  the Reynolds number based on slot height was 2250 and the slot flow was probably transitional. The principal characteristic of the film cooling distributions was that the effectiveness showed extreme variations across the vane gap. Secondary flow on the endwall moving from the pressure-surface corner toward the suction surface evidently sweeps the slot coolant across the channel, resulting in greatly extended cooling near the suction corner and reduced cooling near the pressure corner. The extent of endwall cooling increases somewhat with increasing coolant mass flow.

Film cooling effectiveness values for all three injection rates are compared with the results of a previous accelerated flow film cool-

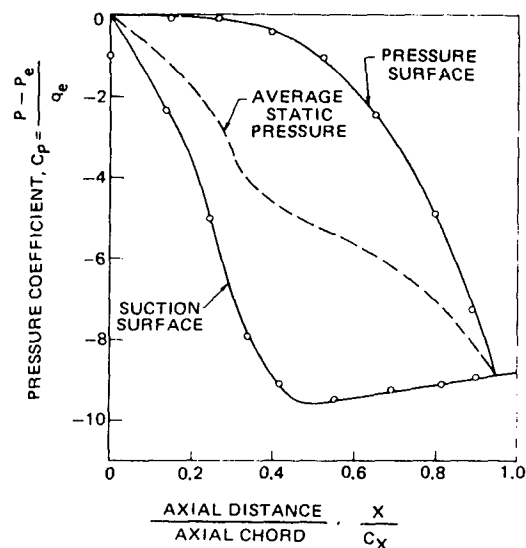
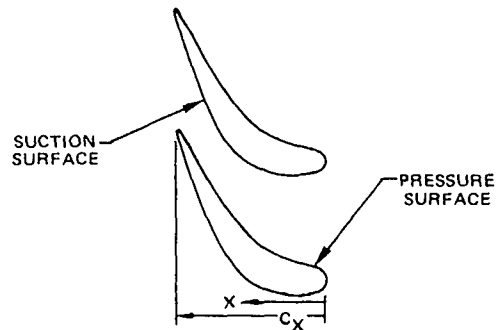


Fig. 5 Measured vane surface static pressure distribution

ing study by Hartnett, Birkebak, and Eckert [3] in Fig. 7. Hartnett, et al., employed a similar coolant slot and a flat plate along which various flow accelerations were imposed by means of wall contours. For the present study, the distance from the slot ( $x'$ ) was determined along the curved channel loci labeled in Fig. 6. An approximate value of the local velocity ( $U_{x'}$ ) along the near suction, near pressure, and midchannel loci was determined from the local static pressure measured on the vane suction and pressure surfaces and from an average of the two local pressures, respectively. This method for determining the approximate local velocity ( $U_{x'}$ ) is believed to be sufficiently accurate for the present comparison because the acceleration correction of Hartnett, et al., is relatively small and because the majority of the data are located near the leading edge, where little flow acceleration has occurred. The effectiveness values recorded midway between the suction and pressure surface of all three injection rates agree within  $\pm 20$  percent of the correlation of Hartnett, et al., from the coolant slot location to a value of  $x'/MS = 150$ . Data recorded along a locus near the pressure surface show a more rapid decrease in the film effectiveness with increasing value of  $x'/MS$  than occurred at midgap. The effectiveness results recorded near the suction surface are as much as 50 percent greater than the correlation of Hartnett, et al., at  $x'/MS = 130$ . One explanation of the higher film cooling effectiveness near the suction corner is that a concentration of coolant resulted at this location from the endwall secondary flow. It is less likely that curved wall boundary layer effects, such as might be expected on the pressure and suction surfaces, produced the endwall effectiveness variations, because the coolant film was on the surface perpendicular to the curved walls. The results of this comparison demonstrate the failure of presently available correlations of film cooling effectiveness to predict adequately the extreme gapwise effectiveness variations that occur on turbine endwalls.

Endwall heat transfer distributions were measured with the heated, segmented endwall assembly described previously. For all

tests the upstream velocity was 94 fps and the free-stream temperature was 92°F. The heated, segmented flat plate was adjusted to an operating temperature of 126°F. Results for the endwall heat transfer tests are presented in the form of the dimensionless Stanton number,  $St = h/\rho_e U_e c_p$ . Contours of constant Stanton number were constructed by drawing dividing boundaries between regions of elemental heaters that measured heat transfer larger and smaller than the contour in question. The endwall heat transfer distribution measured for the rounded-leading-edge configuration with a smooth endwall surface and no coolant injection is presented in Fig. 8. The distribution shows a rapid decrease in Stanton number immediately downstream of the coolant injection slot in the midgap region. In this region the heat transfer coefficients measured along the midgap locus agree with a correlation for zero pressure gradient laminar flow. Comparison of the results of the present study to zero pressure gradient data in the midgap leading-edge region is considered valid because little flow acceleration occurred from the leading edge to this chordwise location. From this comparison it was concluded that the endwall boundary layer remained laminar for at least 2 in. downstream of the injection slot for the case of no coolant injection. An additional result (Fig. 8) is that, in the leading-edge region of this configuration, the heat transfer is greater near the leading edges of both the suction and pressure surfaces than in the midgap region. This increase in heat transfer probably results from the leading edge vortex that is formed at the intersection of the blade leading edge and the endwall and distorts the local endwall boundary layer. The rapid increase to much higher measured heat transfer coefficients following the upstream third of the test section indicates that the endwall boundary layer underwent transition to turbulent flow within this region. For intermediate axial chord stations, the lines of constant endwall transfer are approximately straight and perpendicular to the vane surfaces, indicating that the passage secondary flows are not strongly influencing the endwall heat transfer in this region. The heat transfer distribution for the downstream 1/3 of the test surface is marked by extreme gapwise variations and a region of maximum heat transfer; Stanton numbers in this region are 33 percent greater than those measured at the leading edge of the endwall test surface. The region of maximum heat transfer extended downstream from about the 2/3 chordal point on the suc-

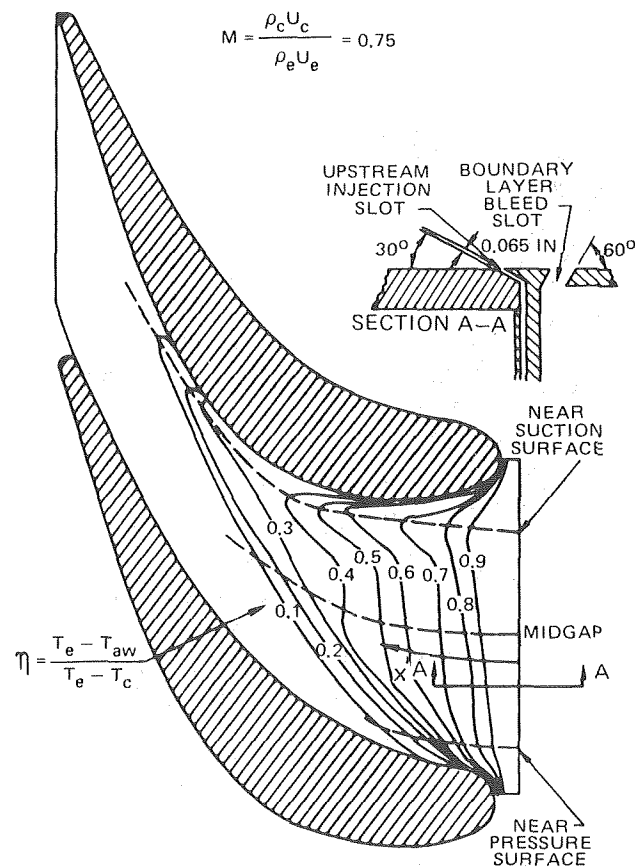


Fig. 6 Effectiveness distribution for rounded-leading-edge configuration

GAPWISE LOCATION (SEE FIG. 6)	BLOWING PARAMETER, M		
	0.5	0.75	1.0
MIDGAP	○	△	□
NEAR SUCTION SURFACE	●	▲	■
NEAR PRESSURE SURFACE	◐	◑	◒

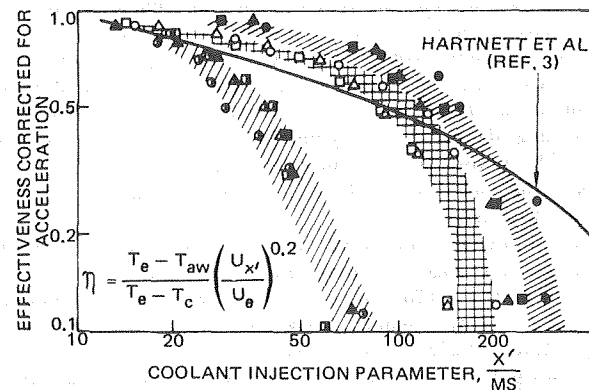


Fig. 7 Comparison of effectiveness results for three blowing rates with previous flat plate studies

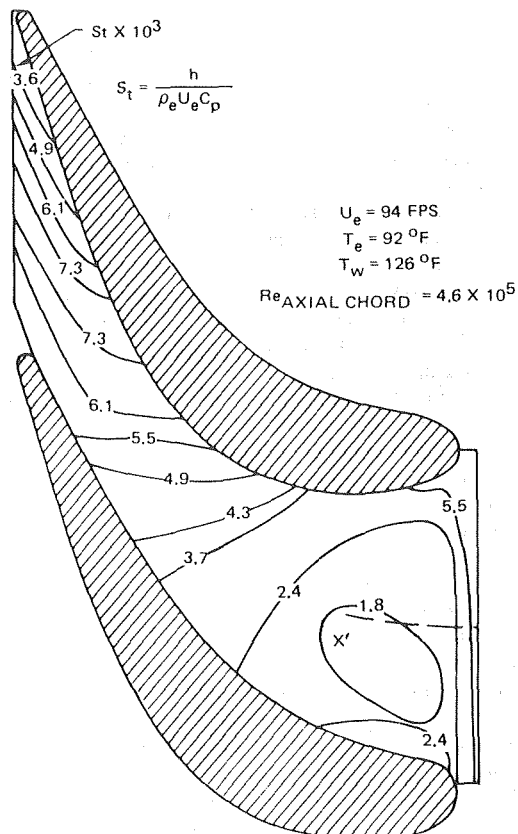


Fig. 8 Heat transfer distribution for rounded-leading-edge configuration with no coolant injection and natural transition

tion surface to approximately midgap at the vane trailing-edge line. This region of maximum heat transfer is believed to correspond approximately to the location of the periphery of the corner vortex, the increased heat transfer probably resulting from the transport of free-stream fluid toward the endwall by the vortex.

The endwall heat transfer distribution was also determined for the rounded-leading-edge configuration with no coolant injection and a 0.035-in.-dia trip wire located on the endwall surface along the leading-edge line. The objective of this test was to alter the location of endwall boundary layer transition from the smooth endwall case and determine the resulting effects on the heat transfer distribution. The decrease in heat transfer immediately downstream of the injection slot was less rapid for this case than for the smooth endwall configuration, and the coefficients measured along a midgap locus agree reasonably well with a zero pressure gradient correlation for fully turbulent flow. The differences between the heat transfer for the smooth endwall and for the endwall with the trip wire installed indicate that the endwall boundary layer was successfully forced to transit at the wire. As with the smooth endwall rounded leading edge case, there is a local region of increased heat transfer near the suction leading edge. No corresponding region of increased heat transfer was observed near the pressure surface leading edge for this configuration. The heat transfer distribution for the downstream two thirds of the test surface was identical for both the smooth endwall configuration and the configuration with trip wire installed.

The endwall heat transfer distribution was also measured for the rounded-leading-edge configuration with a coolant injection rate of  $M = \rho_c U_c / \rho_e U_e = 0.75$ . For this case the trip wire was removed. The coolant injection temperature was set equal to the free-stream temperature of 92°F to isolate the effect of local wall recovery temperature distribution from the effect of the endwall boundary layer on the heat transfer. The coefficients determined in the leading-edge region for the coolant injection case were slightly less

than those for the forced transition case except in the region immediately downstream of the injection slot where the heat transfer for the injection case was larger. The similarity between the heat transfer distributions measured for the forced transition case and for the injected coolant case indicates that both were turbulent and that the coolant must have acted to promote transition in the endwall boundary layer. The somewhat reduced heat transfer coefficients for the coolant injection case probably resulted from the injected coolant increasing the thickness of the endwall boundary layer to a value greater than that for the uncooled forced transition case. The higher heat transfer measured immediately downstream of the slot with coolant injection is believed to be a local effect noted in previous film cooling investigations (e.g., [3]). No region of increased heat transfer was observed near the leading edge of either suction or pressure surfaces for this configuration. The heat transfer distribution for the middle 1/3 of the test surface was essentially unchanged from the previous two rounded-leading-edge cases. The coefficients measured in the region of maximum heat transfer near the trailing edge were approximately 10 percent less than those recorded for the two uncooled rounded-leading-edge cases. However, the location of the region of maximum heat transfer appeared to be essentially unchanged. These results suggest that the character of the corner vortex was not affected significantly by the coolant film.

The endwall heat transfer distribution determined for the sharp-leading-edge configuration is presented in Fig. 9. For this case, a 0.035-in.-dia trip wire was located on the endwall at the leading-edge line. The heat transfer distribution for this case was very similar to that measured for the rounded-leading-edge configuration with forced transition with the exception of the leading-edge region. For the sharp-leading-edge case, no increase in heat transfer near the suction and pressure surface leading edges, which could be attributed to leading-edge vortices, was present. The results for all the flow conditions investigated may be obtained from reference [4].

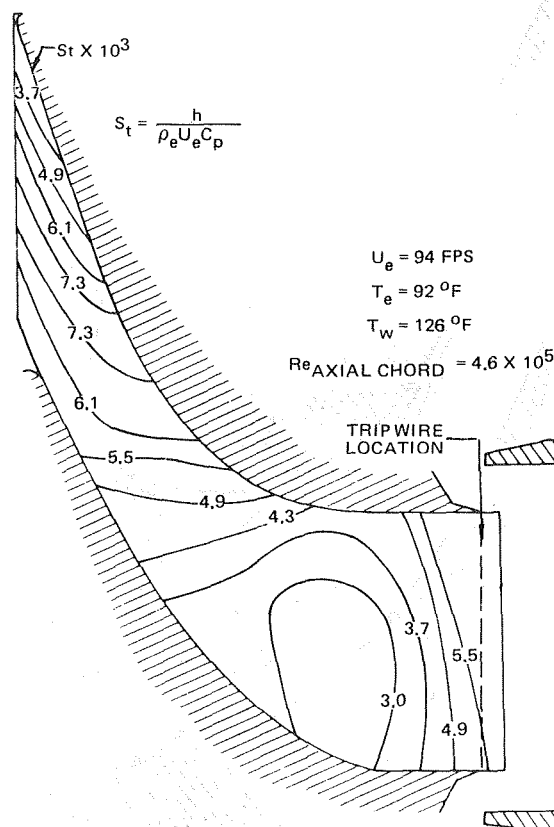


Fig. 9 Heat transfer distribution for sharp-leading edge configuration with no coolant injection and forced transition

### Comparison of Measured Heat Transfer With Predictions.

The endwall heat transfer distribution measured for the rounded-leading-edge configuration with no coolant injection and forced transition at the leading edge was compared to the heat flux predicted by the two-dimensional boundary layer calculation procedure of reference [5]. Heat transfer predictions were calculated for the following three pressure distributions external to a two-dimensional boundary layer: (1) the measured vane suction surface static pressure distribution, (2) the measured vane pressure surface static pressure distribution, and (3) a static pressure distribution obtained by gapwise averaging of the measured pressure and suction surface pressure distributions. These pressure distributions are presented in Fig. 5 and the resulting heat transfer predictions in Fig. 10. For these calculations the boundary layer transition occurred at the streamwise location of the endwall trip wire. The heat transfer distributions predicted by the two-dimensional boundary layer procedure for both the suction surface and gapwise averaged static pressure distributions are as much as 50 and 100 percent higher than the measured gapwise averaged values. Although the gapwise averaged measured heat transfer coefficients agree along the entire chord within  $\pm 17$  percent of the values calculated by the procedure for the pressure surface static pressure distribution, this agreement should be viewed with caution until more extensive comparisons can be conducted. The inability of the two-dimensional procedure to predict the extreme gapwise variations present along the chord (e.g., at the trailing edge  $h_{max}/h_{min} \approx 2$ ) is, of course, evident.

### Conclusion

The conclusion from the foregoing results was that the vane passage endwall heat transfer is strongly influenced by the existence of the large vortex located in the corner between the endwall and the suction surfaces which produces large variations of heat transfer across the vane gap in the trailing edge region. The limited results of this study also show that the influence of this corner vortex is relatively unaffected by the location of endwall boundary layer transition or the existence of a coolant film injected upstream of the vane leading-edge line.

### Acknowledgment

This study was supported by the Naval Air Systems Command under Contract N00019-72-C-0365 with Dr. H. J. Mueller as the Project Officer.

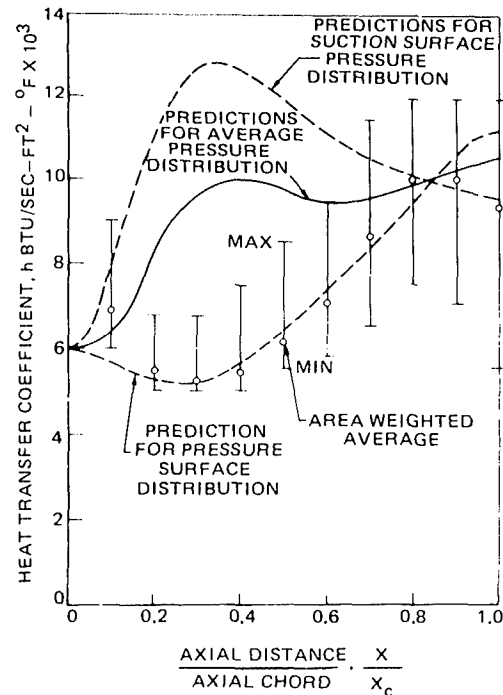


Fig. 10 Comparison between measured heat transfer distribution for the rounded-leading-edge configuration and predictions of the two-dimensional boundary layer deck procedure of reference [5]

### References

- 1 Allen, H. W., and Kofskey, M. G., "Visualization Study of Secondary Flows in Turbine Rotor Tip Regions," NACA TN 3519, 1955.
- 2 Herzig, H. Z., Hansen, A. G., and Costello, G. R., "A Visualization Study of Secondary Flows in Cascades," NACA Report 1163, 1954.
- 3 Hartnett, J. P., Birkebak, R. C., and Eckert, E. R. G., "Velocity Distributions, Temperature Distributions, Effectiveness, and Heat Transfer in Film Cooling of a Surface With a Pressure Gradient," University of Minnesota Heat Transfer Laboratory Technical Report No. 34, 1961.
- 4 Blair, M. F., "Investigation of Factors Affecting Heat Transfer to Turbine Endwalls," UARL Report L911324-3, Dec. 1972.
- 5 McDonald, H., and Fish, R. W., "Practical Calculations of Transitional Boundary Layers," *International Journal of Heat and Mass Transfer*, Vol. 16, No. 9, 1973, pp. 1729-1744.



G. I. Sivashinsky  
Faculty of Mechanical Engineering,  
Technion—Israel Institute of Technology,  
Haifa, Israel

# The Diffusion Stratification Effect in Bunsen Flames

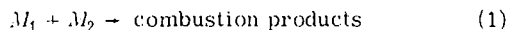
*The thermal diffusion flame model for a bimolecular reaction under stoichiometry conditions of the fresh mixture was examined. The structure of the flame tip of the Bunsen cone was studied. A local breakdown in the stoichiometry in the vicinity of the reaction zone was found such that the light component is always insufficient. For Lewis numbers greater than unity, the flame front is continuous. The temperature at the exit from the reaction zone exceeds the adiabatic temperature of the combustion products. For a Lewis number of the light component less than unity, either a flame with a continuous front, the temperature of which is less than the adiabatic temperature, or a flame with an exposed tip is possible. The problem is solved on the assumption of a strong temperature dependence of the reaction rate.*

## 1 Introduction

A Bunsen burner, in general, is a tube into which an explosive mixture of gases is introduced. This mixture is ignited at the open end of the tube and the flame obtained takes on a form similar to a conic surface.

In the flame, it is generally possible to distinguish two zones—the internal cone and an external mantle, the so-called external cone. In the internal cone the combustion of the original mixture takes place. If the mixture contains a surplus of the combustible, the burning in the internal cone does not bring about a complete combustion, and the unburnt part is oxidized by atmospheric oxygen in the external cone which represents a diffusion flame. This secondary process of combustion in the external cone will not be discussed here. The existence of such an external cone in the Bunsen burner is not necessary. If the combustion mixture is placed in a pipe with no admission of air the unburnt gas of the internal cone has nothing to burn in, the external cone disappears, and we observe only a stable and very luminous internal cone. A sole internal cone is also observed if a mixture with a surplus of oxygen is blown into the burner [1].<sup>1</sup> We shall examine the flame front at distances close to the tip of this cone.

In the present work we examine a flame of a very simple chemical reaction of the type



We shall assume that the concentrations of both components in the oncoming flow of the fresh mixture are equal, that is, according to (1), the condition of a stoichiometric mixture is fulfilled. Hence, in the case of flat steady-state (normal) flame propagation, the reaction is limited by both mixture components. In

curved flames which we obtain in a Bunsen burner, the condition of stoichiometry in the oncoming flow is not yet sufficient for stoichiometry of the mixture in the vicinity of the reaction zone. Various diffusion properties of the reacting components may lead to a breakdown in the stoichiometry on approaching the reaction zone.

The first indication of such type of effect appeared in 1914 in the experiments of Bubnoff [2] in which the combustion products collected at the top of the flame of a previously mixed mixture of benzene and ether with air correspond to richer composition than the products taken from the side of the flame. Haber [2] further established that for hydrogen-air mixtures, samples taken at flame tips correspond to leaner mixtures than for samples taken from the sides. On the basis of these results, Haber concluded that the heavier component of the mixture always tends towards the tip of the flame, that is, the component having the greater diffusion coefficient (either the fuel or the oxidant) is always insufficient.

As is known, a flame is a reaction wave propagating relative to the gas with some velocity. In this wave, diffusion and heat transfer processes occur accompanied by the evolution of chemical energy in the form of heat as well as by thermal expansion of the gas.

For flat, steady-state (normal) flame propagation, combustion at the flame front is characterized by the adiabatic temperature of the combustion products  $T_b$ . Here the only characteristic dimension outside the reaction zone is the width of the preheating zone  $l_T$ . The propagation of a curved flame, generally speaking, is accompanied by change in the temperature along the flame front and, consequently, by sharp change in the chemical reaction rate due to a large value for  $E/R^0T_b$ .

As shown in the following, the characteristic distance from the symmetry axis at which the front curvature begins to have a significant effect on the change in the velocity of flame propagation is  $(E/R^0T_b)l_T$ , which substantially exceeds the thermal structure of the flame.

In order to simplify the problem and clarify the role of diffusion

<sup>1</sup> Numbers in brackets designate References at end of paper.  
Contributed by the Heat Transfer Division for publication in the JOURNAL OF HEAT TRANSFER. Manuscript received by the Heat Transfer Division, February 11, 1974. Paper No. 75-HT-A.

and thermal conductivity,<sup>2</sup> we proceed from a flame model not taking into consideration thermal expansion of the gas, that is, we shall consider the density everywhere to be constant. Then, change in temperature will not affect the gas stream which will be considered a flow of constant velocity. Thus, the proposed purely thermal diffusion model does not describe the refraction of the streamlines at the flame front and related effects. A general view of the Bunsen cone flame with a continuous front is depicted in Fig. 1.

On the basis of the simplification made, the flame will be described fully by a system of diffusion equations for each reaction component of the gas and thermal conductivity equation.

For the case of cylindrical symmetry, this system of equations for the appropriate selection of dimensionless variables takes the form:

Equation for the diffusion of component  $M_i$  ( $i = 1, 2$ ):

$$\frac{1}{\sin \alpha} \frac{\partial C_i}{\partial z} = \frac{1}{L_i} \frac{1}{r} \frac{\partial}{\partial r} (r\kappa \frac{\partial C_i}{\partial r}) + \frac{1}{L_i} \frac{\partial}{\partial z} \kappa \frac{\partial C_i}{\partial z} - W \quad (2)$$

Thermal conductivity equation:

$$\frac{1}{\sin \alpha} \frac{\partial T}{\partial z} = \frac{1}{r} \frac{\partial}{\partial r} (r\kappa \frac{\partial T}{\partial r}) + \frac{\partial}{\partial z} (\kappa \frac{\partial T}{\partial z}) + (1 - \epsilon)W \quad (3)$$

Here,  $1/\sin \alpha$  is the ratio of the velocity of the oncoming flow (from  $z = -\infty$ ) to the normal flame velocity  $U$ ,  $\alpha$  is the angle of inclination of the flame front surface to the symmetry axis as  $z \rightarrow -\infty$ , and  $\epsilon$  is the ratio of the temperature of the fresh mixture  $T_0$  to the adiabatic temperature of the combustion products  $T_b$ . The velocity of the chemical reaction  $W$  is given by the Arrhenius equation

$$W = AZ(T)N^3 C_1 C_2 \exp N(1 - \frac{1}{T}) \quad (4)$$

Here,  $A$  is a dimensionless constant defined by the parameters for normal (flat, steady-state) flame propagation

$$A = 2Z_b C_0 \rho^{-1} \kappa_b c_p^{-1} U^{-2} N^{-3} \exp(-N) \quad (5)$$

<sup>2</sup>The following is a description of the flame using the Shvab-Zeldovich approach which excludes the effects of thermo-diffusion, diffusion thermal conductivity and barodiffusion [3]. This approach is justified if, for example, it is supposed that the reacting components  $M_i$  are only small additions to some "inert" gas  $M_0$ . In this case the mutual diffusion of the reacting components may also be neglected. The diffusion coefficient will be determined only by the binary diffusion of the components  $M_i$  and  $M_0$ . The lighter of the reacting components will have a higher diffusion coefficient (greater mobility) and therefore a smaller Lewis number.

## Nomenclature

$A$  = defined in (5)  
 $C_i$  = dimensionless concentration of  $M_i$ , referred to  $C_0$   
 $C_0$  = concentration reactants in the fresh mixture  
 $c_p$  = specific heat at constant pressure  
 $E$  = activation energy  
 $G$  = defined in (12)  
 $I$  = defined in (27)  
 $L_i$  = Lewis number of component  $M_i$  ( $= \kappa_b / \rho_b D_{bi} c_p$ )  
 $l_T$  = preheating zone width ( $= \kappa_b / \rho_b U_b c_p$ )  
 $M_i$  = chemical symbol  
 $N$  = dimensionless activation energy ( $= E/R^0 T_b$ )  
 $Q$  = intensity of the concentrated source  
 $R^0$  = universal gas constant

$R$  = defined in (11)  
 $r$  = dimensionless radial coordinate, referred to  $l_T$   
 $S_i$  = defined in (46)  
 $T$  = dimensionless temperature, referred to  $T_b$   
 $T_b$  = adiabatic temperature of the combustion products  
 $T_0$  = temperature of the fresh mixture  
 $U$  = normal flame velocity relative to the burned gas  
 $W$  = defined in (14)  
 $Y$  = defined in (45)  
 $Z$  = dimensionless frequency factor, referred to  $Z_b$   
 $Z_b$  = frequency factor at temperature  $T_b$   
 $z$  = dimensionless vertical coordinate, referred to  $l_T$

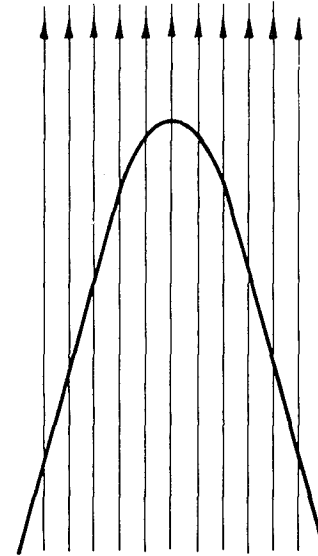


Fig. 1 Continuous flame front (the arrows indicate the direction of gas flow)

$Z_b$  is the frequency factor at temperature  $T_b$ ,  $C_0$  is the concentration of component  $M_i$  in the fresh mixture, and  $N$  is the dimensionless activation energy defined as  $E/R^0 T_b$ .

In the theory for thermal flame propagation, it is always taken for granted that  $N \gg 1$ , that is, that there is a strong temperature dependence of the reaction rate. Then, as will be shown in Section 4, constant  $A$  is on the order of unity relative to  $1/N$  while reaction zone width is on the order of  $1/N$  relative to  $l_T$ . Thus, velocity  $U$  is on the order of  $N^{-3/2} \exp -\frac{1}{2}N$  relative to velocity for zero activation energy.<sup>3</sup>

In the oncoming flow, the temperature  $T_0$  is so low that there is practically no reaction, the reactant concentration do not change and remain equal to  $C_0$ .

As already noted, in a curved flame the condition of the limitation of the reaction by two components may turn out to be too strong. Therefore, we shall assume that the reaction is limited by the component  $M_1$  the concentration of which  $C_1$  becomes zero at the exit from the reaction zone. The concentration  $C_2$  of component  $M_2$  generally speaking, does not become zero at the exit

<sup>3</sup>On the application of asymptotic methods to the theory of flames with high activation energies, see also [4-6].

from the reaction zone and the temperature is not equal to the adiabatic temperature of the combustion products  $T_b$ . However, in the combustion product regions sufficiently far away from the front tip, these temperature and concentration perturbations arising from curvature of the front should dissipate inevitably. Thus, as  $z \rightarrow +\infty$  concentration  $C_2$ , the unreacted portion of component  $M_2$  also becomes zero and the temperature of the reaction products assumes the value  $T_b$ .

In dimensionless variables, the conditions presented have the following form:

$$\left. \begin{aligned} T(-\infty, r) &= \epsilon; & C_i(-\infty, r) &= 1 \\ T(+\infty, r) &= 1; & C_i(+\infty, r) &= 0 \end{aligned} \right\} \quad (6)$$

## 2 Derivation of the Equation for the Flame Front Surface

The major release of heat resulting from the chemical reaction is concentrated in the vicinity of a certain surface known as the flame front.

As the reaction zone width is of the order  $1/N$  relative to the width of the preheating zone, the reaction zone should be considered a concentrated source, at distances from the front of many large  $1/N$ . Thus, in equations (2) and (3), the reaction rate  $W$  may be substituted by the corresponding surface  $\delta$ -function of some intensity  $Q$ .

$$W \rightarrow Q\sqrt{1 + (d\phi/dr)^2} \cdot \delta(z - \phi(r)) \quad (7)$$

where  $z = \phi(r)$  is the equation for the flame front surface.

Condition (7) is equivalent to the following conditions for a jump of the heat and material fluxes at  $z = \phi(r)$

$$[\kappa dT/dn] = -(1 - \epsilon)Q; \quad \frac{1}{L_i} [\kappa \frac{dC_i}{dn}] = Q \quad (8)$$

( $d/dn$  indicates the derivative with respect to the normal to the front surface  $z = \phi(r)$ ).

As will be shown, as the result of an examination of the structure of the reaction zone (Section 4), in the zero-order approximation in  $1/N$  for the intensity  $Q$ , the following representation holds

$$\left. \begin{aligned} Q &\approx \sqrt{1 + \frac{1}{2}N \frac{1-\epsilon}{L_2} C_2} \exp \frac{1}{2}N(T-1) \\ \text{where } T-1 &\sim C_2 \sim 1/N \\ z &= \phi(r) \end{aligned} \right\} \quad (9)$$

In our subsequent examination, it is convenient to study the problem in the  $(r, \eta)$  coordinate system related to the flame front surface

$$\eta = z - \phi(r) \quad (10)$$

As we expect that the characteristic distance from the symmetry axis at which the curvature of the flame front begins to have a substantial effect on the processes in the combustion zone is on the order of  $Nl_T$ , then it will be convenient to introduce the following transformation

$$r = NR; \quad \phi(r) = N\Phi(R) \quad (11)$$

The correctness of the scales of stretching selected will be verified *a posteriori* through the requirements of asymptotic matching principle.

In conjunction with (7) to (11), the set (2) and (3) becomes

$$\begin{aligned} \frac{1}{NR} \frac{\partial}{\partial R} (R\kappa \frac{\partial T}{\partial \eta} - \frac{1}{N} R\kappa \frac{\partial T}{\partial R}) + \frac{\partial}{\partial \eta} (\frac{1}{N} \kappa G \frac{\partial T}{\partial R} - \kappa(1 + G^2) \frac{\partial T}{\partial \eta}) \\ + \frac{1}{\sin \alpha} T = (1 - \epsilon)\sqrt{1 + G^2} Q\delta(\eta) \end{aligned} \quad (12)$$

where  $G = d\Phi/dR$

$$\begin{aligned} \frac{1}{NR} \frac{\partial}{\partial R} (\frac{1}{L_i} R\kappa \frac{\partial C_i}{\partial \eta} - \frac{1}{NL_i} R\kappa \frac{\partial C_i}{\partial R}) + \frac{\partial}{\partial \eta} (\frac{1}{NL_i} \kappa G \frac{\partial C_i}{\partial R} - \frac{\kappa}{L_i} (1 \\ + G^2) \frac{\partial C_i}{\partial \eta} + \frac{1}{\sin \alpha} C_i) = -\sqrt{1 + G^2} Q\delta(\eta) \end{aligned} \quad (13)$$

We shall seek the values for  $C_i$ ,  $T$ ,  $Q$ , and  $G$  in the form of the following asymptotic expansions in  $1/N$

$$\left. \begin{aligned} C_i &= C_i^0 + \frac{1}{N} C_i^1 + \dots; & T &= T^0 + \frac{1}{N} T^1 + \dots \\ G &= G_0 + \frac{1}{N} G_1 + \dots; & Q &= Q_0 + \frac{1}{N} Q_1 + \dots \end{aligned} \right\} \quad (14)$$

Furthermore, we assume that for  $\eta > 0$

$$T^0 = 1; \quad C_i^0 = C_2^0 = 0 \quad (15)$$

In the zero-order approximation in  $1/N$ , the system of equations (12) and (13) reduces to a system of equations for quasi-one-dimensional flame propagation. The solutions of the latter taking into account conditions (14) and (15) may be represented in the form

$$\left. \begin{aligned} \frac{1}{\sin \alpha} (T^0 - \epsilon) &= (1 + G_0^2) \kappa^0 \frac{\partial T_0}{\partial \eta} & \text{for } \eta < 0 \\ T^0 &= 1 & \text{for } \eta > 0 \end{aligned} \right\} \quad (16)$$

Here,  $\kappa^0 = \kappa(T^0)$

$$C_i^0 = 1 - (\frac{T^0 - \epsilon}{1 - \epsilon})^{L_i} \quad (17)$$

Subsequently, integrating equation (12) in the vicinity of the point  $\eta = 0$ , and taking into account the solution (16), in the zero-order approximation in  $1/N$ , we have

$$\frac{1}{\sin^2 \alpha (1 + G_0^2)} = Q_0^2; \quad \eta = 0 \quad (18)$$

in which, according to (9)

$$Q_0^2 = [1 + \frac{1}{2L_2} (1 - \epsilon) C_2^1] \exp T^1; \quad \eta = 0 \quad (19)$$

In order to obtain another two equations relating to  $C_2^1(0, R)$  and  $T^1(0, R)$  with  $G_0(R)$ , we must go to the next approximation in  $1/N$ .

For  $\eta > 0$  in the first approximation in  $1/N$ , it follows from equation (12) that

$$\frac{1}{\sin \alpha (1 + G_0^2)} \frac{\partial T^1}{\partial \eta} = \frac{\partial^2 T^1}{\partial \eta^2} \quad (20)$$

The only solution of equation (20) which matches with the solution of the corresponding outer problem<sup>4</sup> as  $\eta \rightarrow \infty$  has the form

$$T^1(\eta, R) = T^1(0, R) \quad (21)$$

$$C_2^1(\eta, R) = C_2^1(0, R) \quad (22)$$

Henceforward, we shall proceed from a linear combination of equations (12) and (13) constructed according to the following scheme, (12) + (1 -  $\epsilon$ ) (13):

$$\begin{aligned} \frac{1}{NR} \frac{\partial}{\partial R} R[\kappa G \frac{\partial}{\partial \eta} (T + \frac{1-\epsilon}{L_i} C_i) - \frac{\kappa}{N} \frac{\partial}{\partial R} (T + \frac{1-\epsilon}{L_i} C_i)] \\ = \frac{\partial}{\partial \eta} [-\frac{1}{\sin \alpha} (T - 1 + (1 - \epsilon) C_i) + (1 + G^2) \kappa \frac{\partial}{\partial \eta} T] \end{aligned}$$

<sup>4</sup>This outer solution, the characteristic variable of which is  $N^2\eta$ , provides for dissipation of temperature and concentration perturbations and, thus, satisfaction of the boundary condition (6) as  $z \rightarrow \infty$ .

$$+ \frac{1-\epsilon}{L_i} C_i - \frac{\kappa}{N} G \frac{\partial}{\partial \eta} (T + \frac{1-\epsilon}{L_i} C_i) \quad (23)$$

We integrate (23) with respect to  $\eta$  from  $-\infty$  to 0

$$\begin{aligned} \frac{1}{NR} \frac{\partial}{\partial R} R \int_{-\infty}^0 [\kappa G \frac{\partial}{\partial \eta} (T + \frac{1-\epsilon}{L_i} C_i) - \frac{\kappa}{N} \frac{\partial}{\partial R} (T \\ + \frac{1-\epsilon}{L_i} C_i)] d\eta = - \frac{T(0, R) - 1 + (1-\epsilon) C_i(0, R)}{\sin \alpha} \\ - \frac{1}{N} \kappa (T(0, R)) G \frac{\partial}{\partial R} [T(0, R) + \frac{1-\epsilon}{L_i} C_i(0, R)] + (1 \\ + G^2) \kappa (T(0, R)) \frac{\partial T(+0, R)}{\partial \eta} + \frac{1-\epsilon}{L_i} \kappa (T(0, R)) \frac{\partial C_i(+0, R)}{\partial \eta} \quad (24) \end{aligned}$$

Hence, in the first approximation in  $1/N$  we have

$$\begin{aligned} \frac{1}{R} \frac{\partial}{\partial R} R \int_{-\infty}^0 [\kappa^0 G_0 \frac{\partial}{\partial \eta} (T^0 + \frac{1-\epsilon}{L_i} C^0)] d\eta \\ = - \frac{1}{\sin \alpha} [(1-\epsilon) C_i^1(0, R) + T^1(0, R)] \quad (25) \end{aligned}$$

Thus,  $T^1(0, R)$  and  $C_i^1(0, R)$  may be found from the zero-order approximation of the problem.

Employing (17) we proceed from integration with respect to variable  $\eta$  to integration with respect to  $T^0$ .

Relationship (25) transforms to

$$- \sin \alpha I(L_i) \frac{1}{R} \frac{d}{dR} R G_0 = (1-\epsilon) C_i^1(0, R) + T^1(0, R) \quad (26)$$

where

$$I(L_i) = \int_{\epsilon}^1 \kappa(T) [1 - (\frac{T-\epsilon}{1-\epsilon})^{L_i-1}] dT \quad (27)$$

As  $C_1^1(0, R) = 0$ , then relationships (18) and form a system of three equations for the determination of  $C_2^1(0, R)$ ,  $T^1(0, R)$ , and  $G_0(R)$ .

$$(1-\epsilon) C_2^1(0, R) = T^1(0, R) \frac{I(L_2) - I(L_1)}{I(L_1)} \quad (28)$$

$$\sin \alpha I(L_1) \frac{1}{R} \frac{d}{dR} R G_0 = -T^1(0, R) \quad (29)$$

$$\frac{1}{\sin^2 \alpha (1 + G_0^2)} = [1 + \frac{I(L_2) - I(L_1)}{2L_2 I(L_1)} T^1(0, R)] \exp T^1(0, R) \quad (30)$$

We introduce new terms

$$R = \xi \sin \alpha I(L_1) \quad (31)$$

$$\frac{I(L_2) - I(L_1)}{2L_2 I(L_1)} = \lambda \quad (32)$$

Then, from (29) to (32) we easily obtain one differential nonlinear equation for  $G_0$

$$\sin^{-2} \alpha (1 + G_0^2)^{-1} = (1 - \lambda \frac{1}{\xi} \frac{d}{d\xi} \xi G_0) \exp (-\frac{1}{\xi} \frac{d}{d\xi} \xi G_0) \quad (33)$$

As concentration may not take negative values, then from (26)

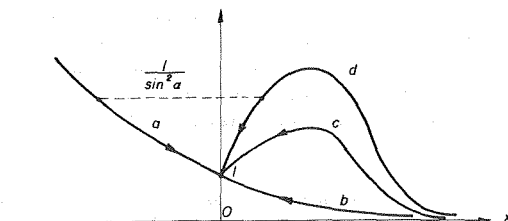


Fig. 2 Trajectory of the solutions of equation (33) in the  $(x, y)$  plane (the arrows indicate the direction from the flame tip)

we have an additional condition: for equation (33)

$$\lambda \frac{1}{\xi} \frac{d}{d\xi} \xi G_0 < 0 \quad (34)$$

It is apparent from (31) that  $\xi > 0$  corresponds to the problem in which  $L_1 > 1$  while  $\xi > 0$  corresponds to the problem for  $L_1 < 1$ . The case in which  $L_1 = 1$  corresponds to constant temperature at the front when the asymptotic treatment presented is unsuitable. As  $R \rightarrow \infty$  ( $\xi \rightarrow \pm \infty$ ), the flame front surface should go over to an ideal geometric cone.

Hence,

$$G_0(R = \infty) = -1/\tan \alpha \quad (35)$$

Condition (35) serves as a boundary condition for equation (33).

### 3 Solutions of Equation (33) and Their Physical Significance

From boundary condition (35) it follows directly that as  $R \rightarrow \infty$

$$-\lambda \frac{1}{\xi} \frac{d}{d\xi} \xi G_0 \approx \frac{I(L_2) - I(L_1)}{2L_2 R} \cos \alpha \quad (36)$$

Then, on the basis of condition (34), we have that

$$L_2 > L_1 \quad (37)$$

Thus, the known experimental fact that in a Bunsen flame the lighter component is always insufficient<sup>5</sup> is correlated.

On the basis of (37) it now follows from (28) that

$$T^1(0, R) > 0 \quad \text{for } L_1 > 1 \quad (38)$$

that is, the temperature at the flame front is higher than the adiabatic one

$$T^1(0, R) < 0 \quad \text{for } L_1 < 1 \quad (39)$$

that is, the temperature is lower than the adiabatic one. It will be convenient to conduct the subsequent examination in the  $(x, y)$  plane where

$$x = \frac{1}{\xi} \frac{d}{d\xi} \xi G_0; \quad y = \sin^{-2} \alpha (1 + G_0^2)^{-1} \quad (40)$$

The solution of equation (33) upon change in  $\xi$  will pass through points on the curve on the  $(x, y)$  plane.

Four cases corresponding to qualitatively different effects are possible:

$$(a) \lambda > 0, \quad x < 0$$

$$(b) -1 < \lambda < 0, \quad x > 0$$

$$(c) -\infty < \lambda < -1, \quad -\lambda \exp(-\frac{1+\lambda}{\lambda}) < \sin^{-2} \alpha, \quad x > 0$$

$$(d) -\infty < \lambda < -1, \quad -\lambda \exp(-\frac{1+\lambda}{\lambda}) > \sin^{-2} \alpha, \quad x > 0$$

Each of these cases corresponds to one of the curves of equation (41) on the  $(x, y)$  plane (see Fig. 2) and a region on the  $(L_1, L_2)$  plane (see Fig. 3).

Point (0,1) in the  $(x, y)$  plane corresponds to the flame front surface infinitely far from the flame tip. Here, the front takes the form of an ideal cone. The flame goes over to the solution for normal propagation relative to the gas. Combustion takes place at the front at the adiabatic temperature. Component  $M_2$  is depleted completely in the reaction zone.

In case (a), on approaching the flame tip, the temperature in the reaction increases monotonically along with the concentration of the unreacted portion of component  $M_2$ . The reaction rate in-

<sup>5</sup>This property of diffusion stratification is not general. For example, in the flame of an inverted Bunsen cone when  $G_0(\infty) = 1/\tan \alpha$ , the heavier component will be insufficient.

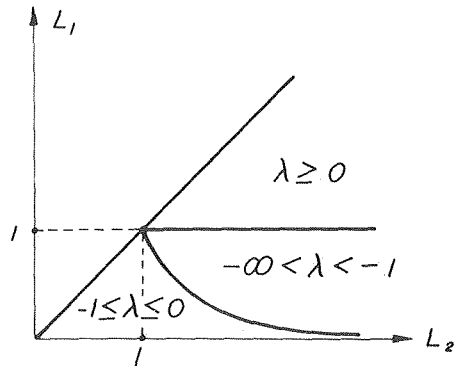


Fig. 3 Region of change of Lewis numbers corresponding to cases (a)-(d)

increases along with the rate of flame propagation relative to the gas. The general view of the flame front surface is presented in Fig. 1.

In case (b), on approaching the flame tip, the temperature in the reaction zone constantly decreases from the adiabatic temperature down to  $-\infty$ . The concentration of the unreacted portion of component  $M_2$  increases from zero to  $+\infty$ . The flame front is bent such that flame velocity relative to the gas on approaching the tip falls to zero (see Fig. 4(b)). These properties of the flame which formally follow from equation (33) indicate the applicability of the asymptotic constructed only at a sufficient distance from the flame tip. Actually, in order for a flame to exist, the temperature reduction in the reaction zone may not exceed a certain value  $\sim T_b^2 R^0/E$  or the flame will be extinguished [7].

In case (c), as in case (b), on approaching the tip, the temperature in the reaction zone drops monotonically. However, the flame bends at a distant sufficiently far from the tip such that the flame propagation temperature relative to the gas becomes more than normal.

This effect is related to the onset of diffusion stratification which, despite the drop in temperature at the front, increases the reaction rate on account of an excess of the heavy component.

Nevertheless, close to the tip, the temperature drop effect becomes stronger. The flame velocity relative to the gas begins to decrease. At some place, the continuation of combustion becomes impossible and the flame disappears. This change in the combustion mode along the front is indicated by an inflection point on the front surface (Fig. 4(c)).

In case (d), the diffusion stratification effect is so strong, that despite the drop in temperature at the front, the reaction rate nevertheless increases on approaching the tip. Hence, the front velocity relative to the gas also increases continuously.

The front takes the form of a smooth continuous surface (Fig. 4(d)) similar to the surface obtained in case (a).

We note that for  $-\infty < \lambda < -1$  we are able to go from a front with an exposed tip at high velocities to a continuous front at relatively low velocities only due to a change in the oncoming flow (i.e., angle  $\alpha$ ).

It is interesting to note that conic flames with exposed tips are observed, for example, for hydrogen-air mixtures [8]. The disappearance of the flame at the tip occurs when the reaction is clearly limited by hydrogen, that is, the light component for which  $L_1 < 1$ .

Thus, under the conditions of stoichiometry of the fresh mixture and at high activation energy, the reaction rate is as sensitive to change in the composition of the mixture in the reaction zone, as to change in the temperature. The diffusion stratification effect always acts to increase the reaction rate and under some conditions, may repress the tendency to a reduction in the rate upon a drop in the temperature. The diffusion stratification effect appears only on components which limit the reaction under normal flame propagation. If the condition of stoichiometry is not maintained in the oncoming flow of the fresh mixture, then a

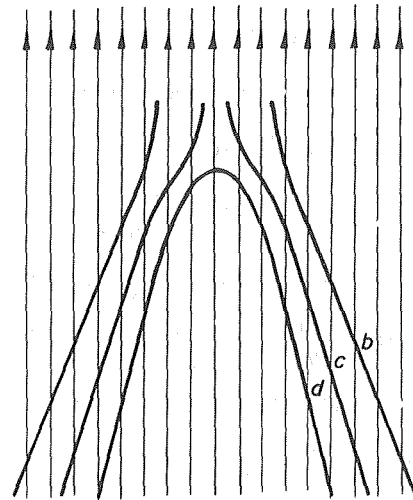


Fig. 4 Types of flame front surfaces for  $L_1 < 1$  (the arrows indicate the direction of gas flow)

change in the composition may also occur in the vicinity of the reaction zone in a curved flame. However, in this case, diffusion stratification cannot significantly affect the reaction rate.<sup>6</sup> Change in the flame velocity in this case will be determined only by the diffusion of the limiting component and the temperature. In the problem examined, this situation corresponds to the case in which  $L_1 = L_2$  ( $\lambda = 0$ ) when the bimolecular reaction becomes formally indistinguishable from a second order monomolecular reaction.

This case of limiting the reaction by one of the components independently of selective diffusion is of intrinsic importance. By computing the results for such a case it can be shown that if the Lewis number ( $L$ ) of the limiting component is greater than 1 the flame front is not broken, whereas for  $L < 1$  around the summit of the cone the flame is extinguished.

#### 4 Justification of the Asymptotic Formula (9)

In order to conjugate the heat and material fluxes on both sides of the reaction zone, we employ the relationships

$$\sqrt{1 + G_0^2} \frac{\partial T^0(-0, R)}{\partial \eta} = (1 - \epsilon) \sqrt{1 + \frac{1}{2L_2}(1 - \epsilon)C_2^1(0, R)} \exp \frac{1}{2} T^1(0, R) \quad (42)$$

$$\frac{1}{L_i} \sqrt{1 + G_0^2} \frac{\partial C_i^0(-0, R)}{\partial \eta} = -\sqrt{1 + \frac{1}{2L_2}(1 - \epsilon)C_2^1(0, R)} \exp \frac{1}{2} T^1(0, R) \quad (43)$$

which are a consequence of conditions (6) and the proposed asymptotic (9).

We shall show that (42) to (43) are rigorous consequences of the conditions for the matching of the asymptotic solutions corresponding to the structure of the reaction zone and with the asymptotic solutions outside of this zone. Thus, the correctness of (9) will be proven in the zero-order approximation in  $1/N$ .

We shall proceed from a system of equations for diffusion and thermal conductivity with disperse heat and material sources. To this end, the concentrated source in equations (12) to (13) must again be replaced by the corresponding chemical reaction rate  $W$

<sup>6</sup>These propositions conform with the paper [9] which shows that the stability of the flame front in a multi-component mixture is fully determined by the limiting component. But the case of a limiting reaction with two components is not discussed in [9] and, therefore, the question of the effect of selective diffusion on the stability of the flame remains open.

$$\sqrt{1 + G_0^2} Q\delta(\eta) = W(C_1, C_2, T) \quad (44)$$

As we presume that the reaction zone width is of the order of  $1/N$  relative to the preheating zone width, then we take as the characteristic variable for the region of the reaction zone

$$Y = yN \quad (45)$$

In this region, the asymptotic expansions for temperature, concentration, and the constant  $A$  are sought in the form

$$\left. \begin{aligned} T &= 1 + \frac{1}{N}\theta(Y, R) + \dots \\ C_i &= \frac{1}{N}S_i(Y, R) + \dots \\ A &= A_0 + \dots \end{aligned} \right\} \quad (46)$$

Then, from system (12) to (13) taking into account (44) to (46) for the zero'th approximation in  $1/N$  in the reaction zone region, we have

$$(1 + G_0^2) \frac{\partial^2 \theta}{\partial Y^2} + (1 - \epsilon)A_0 S_1 S_2 \exp \theta = 0 \quad (47)$$

$$\frac{1}{L_1}(1 + G_0^2) \frac{\partial^2 S_1}{\partial Y^2} - A_0 S_1 S_2 \exp \theta = 0 \quad (48)$$

$$\frac{1}{L_2}(1 + G_0^2) \frac{\partial^2 S_2}{\partial Y^2} - A_0 S_1 S_2 \exp \theta = 0 \quad (49)$$

As for  $\eta > 0$ ,  $T^0(\eta, R) = 1$ ,  $C_1(\eta, R) = 0$ ,  $C_2^1(\eta, R) = C_2^1(0, R)$ , then the condition for matching the solutions of system (47) to (49) with the solutions of the outer problem have the form

$$\theta(+\infty, R) = T^1(0, R) \quad (50)$$

$$\frac{\partial \theta(-\infty, R)}{\partial Y} = \frac{\partial T^0(-0, R)}{\partial \eta} \quad (51)$$

$$S_1(+\infty, R) = 0 \quad (52)$$

$$\frac{\partial S_1(-\infty, R)}{\partial Y} = \frac{\partial C_1^0(-0, R)}{\partial \eta} \quad (53)$$

$$S_2(+\infty, R) = C_2^1(0, R) \quad (54)$$

$$\frac{\partial S_2(-\infty, R)}{\partial Y} = \frac{\partial C_2^0(-0, R)}{\partial \eta} \quad (55)$$

From (47) to (49) taking into account (50), (52), and (54), we have

$$\theta + \frac{1 - \epsilon}{L_1} S_1 = T^1(0, R) \quad (56)$$

$$\theta + \frac{1 - \epsilon}{L_2} S_2 = T^1(0, R) + \frac{1 - \epsilon}{L_2} C_2^1(0, R) \quad (57)$$

System (47) to (49) may now be reduced to one equation for

$$(1 + G_0^2) \frac{\partial^2 \theta}{\partial Y^2} + \frac{A^0 L_1 L_2}{(1 - \epsilon)} (T^1 - \theta) \left( T^1 + \frac{1 - \epsilon}{L_2} C_2^1 - \theta \right) \exp \theta \quad (58)$$

Hence, on the basis of (50)

$$(1 + G_0^2) \left( \frac{\partial \theta}{\partial Y} \right)^2 = - \frac{2A^0 L_1 L_2}{(1 - \epsilon)} \int_{T^1}^{\theta} (T^1 - \theta) \left( T^1 + \frac{1 - \epsilon}{L_2} C_2^1 - \theta \right) \exp \theta d\theta \quad (59)$$

Thus,

$$(1 + G_0^2) \left( \frac{\partial \theta(-\infty, R)}{\partial Y} \right)^2 = \frac{2A^0 L_1 L_2 \exp T^1}{(1 - \epsilon)} \int_{-\infty}^0 (-z) \left( \frac{1 - \epsilon}{L_2} C_2^1 - z \right) \exp z dz = \frac{2A^0 L_1 L_2}{1 - \epsilon} \exp T^1 \left( 2 + \frac{1 - \epsilon}{L_2} C_2^1 \right) \quad (60)$$

For normal flame propagation,

$$G_0 = 0, \quad \frac{\partial T^0(-0, R)}{\partial Y} = 1 - \epsilon, \quad T^1(0, R) = C_2^1(0, R) = 0 \quad (61)$$

Then, from (51) and (60) to (61), it follows that

$$A^0 = \frac{(1 - \epsilon)^3}{4L_1 L_2} \quad (62)$$

$A^0$  determines the major term for the asymptotic of normal flame propagation  $U$ , (9).

Then, from (61) and (59), we have

$$\sqrt{1 + G_0^2} \frac{\partial \theta(-\infty, R)}{\partial Y} = (1 - \epsilon) \sqrt{1 + \frac{1 - \epsilon}{2L_2} C_2^1} \exp \frac{1}{2} T^1 \quad (63)$$

which according to (51), is equivalent to relationship (42) sought. Relationship (43) is a simple consequence of (56) to (57), and (62).

## References

- 1 Zel'dovich, Ya. B., and Voevodsky, V. V., *Teplovai Vzriv i rasprostranenie plameni v gazah, (Thermal Explosion and Flame Propagation in Gases)* Moscow, Publ. Moscow Mech. Inst., 1947, pp. 182-183.
- 2 *Nonsteady Flame Propagation*, G. I. Markstein, ed., Pergamon Press, 1964, pp. 9-12.
- 3 Williams, F. A., *Combustion Theory*, Addison-Wesley, Reading, Mass., Palo Alto, London, 1964, pp. 9-13.
- 4 Bush, W. B., and Fendell, F. E., "Asymptotic Analysis of Laminar Flame Propagation for General Lewis Numbers," *Combustion Science and Technology*, Vol. 1, 1970, pp. 421-428.
- 5 Fendell, F. E., "Asymptotic Analysis of Premixed Burning With Large Activation Energy," *Journal of Fluid Mechanics* Vol. 56, Part 1, 1972, pp. 81-95.
- 6 Sivashinsky, G. I., "On a Steady Corrugated Flame Front," *Astronautica Acta.*, Vol. 18, 1973, pp. 253-260.
- 7 Frank-Kamenetskii, D. A., *Diffusion and Heat Transfer in Chemical Kinetics*, Plenum, New York, Second and revised ed., 1969, pp. 365-369.
- 8 Lewis, B., and Von Elbe, G., *Combustion, Flames and Explosions of Gases*, Academic Press, New York, London, 1951, pp. 178-279.
- 9 Parlange, J.-Y., "Influence of Preferential Diffusion on the Stability of a Laminar Flame," *The Journal of Chemical Physics*, Vol. 48, No. 4, 1968, pp. 1843-1849.

P. M. Wathen<sup>1</sup>  
Research Assistant.

J. W. Mitchell  
Professor.

W. P. Porter  
Associate Professor.

The University of Wisconsin,  
Madison, Wisc.

# Heat Transfer From Animal Appendage Shapes—Cylinders, Arcs, and Cones

The heat transfer relationships for shapes that approximate animal appendages have been experimentally determined. Finite length hollow cylinders, arcs, and cones with different amounts of closure were tested over a wide range of pitch and yaw angles at different wind speeds. The data for all of these shapes are within  $\pm 70$  percent of the standard correlation for circular cylinders. Pitch and yaw variations have little effect on the heat transfer coefficient. Shorter length geometries and those with less enclosure have higher heat transfer than the longer and more enclosed geometries. The application of these results to modeling the heat transfer from animal appendages is illustrated.

## Introduction

The appendages of an animal may have an important role in the overall temperature regulation of that animal. Rabbit ears, fox ears, and deer antlers are some of the many examples of appendages which transfer some portion of the metabolic heat to the surroundings. Thermal energy is carried from the central core of the animal to the appendage by blood flow, with the flow rate regulated by temperature of the animals. Heat is then transferred to the surroundings by convection and radiation. In the natural outdoor environments, convective heat transfer to the air is the predominate mode of heat transfer from the appendage. Thus, the role of the appendage in transferring a significant proportion of the metabolic heat is governed by the convective properties of the appendage.

Model studies of the thermal energy flows between an animal and its environment have aided in determining the influence of the thermal environment on animal behavior [1-4].<sup>2</sup> In such studies, the convective heat-transfer coefficient for the appendage has usually been taken to be that for an equivalent circular cylinder normal to an air stream. There are virtually no heat-transfer data available in either the engineering or biological literature for shapes that more closely approximate appendage shapes and orientations. Some data exist on noncircular cylinders [5] and plates at various orientations [6, 7], but the Reynolds number range for the data is much higher than that experienced by an animal in

the outdoor environment.

In this paper, experimental heat-transfer relations for shapes that approximate animal appendages are presented. While these shapes have been chosen to model animal appendages, the results and conclusions are also applicable to more conventional heat-transfer situations. The geometries tested are described in Fig. 1 and Table 1, and consist of:

- 1 Circular cylindrical sections of two finite lengths and four amounts of closure
- 2 Circular arcs of three lengths
- 3 Conical sections of two heights and four amounts of closure.

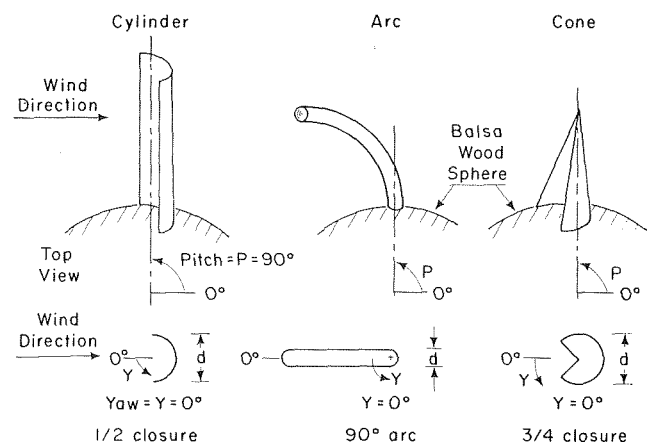


Fig. 1 Schematic representation of appendage models showing model geometry and orientation

<sup>1</sup> Current address: Peace Corps, Zaire, Africa.

<sup>2</sup> Numbers in brackets designate References at end of paper.

Contributed by the Bioengineering Division of THE AMERICAN SOCIETY OF MECHANICAL ENGINEERS and presented at the Winter Annual Meeting, Detroit, Michigan, November 11-15, 1973. Journal manuscript received at ASME Headquarters December 20, 1973. Paper No. 73-WA/Bio-10.

**Table 1 Model geometries**

Model	Tall			Short		
	dia (in)	height (in)	height/dia	dia (in)	height (in)	height/dia
<b>Cylinders</b>						
whole, $\frac{3}{4}, \frac{1}{2}$	1.1	6.8	6.2	2.1	2.1	1.0
$\frac{1}{4}$ closure	1.1	6.8	6.2	1.5	2.1	1.4
<b>Cones</b>						
whole, $\frac{3}{4}, \frac{1}{2}, \frac{1}{4}$	1.1	3.0	3.1	1.1	1.1	1.0
<b>Arc</b>						
	dia (in)	length (in)	length/dia			
90° arc	.63	5.1	8.1			
180° arc	.63	9.8	15.6			
270° arc	.63	13.8	27.0			

**Test Procedure**

The test specimens were made from copper tubing or copper sheet material with thickness of 0.030 to 0.085 in. The dimensions of the various models are given in Table 1. For the cylinders and cones, the amount of closure is the circumference fraction of a complete cylinder or cone. The specimens were gold plated after fabrication to minimize thermal radiation, and cooper-constantan thermocouples were soldered to the base for temperature determinations. In order to provide a support for the specimens and to model the influence of the head of the animal on the airflow, most of the specimens were mounted on a 3-in. balsa wood sphere. The short cylinders were mounted on a 5-in. sphere of styrofoam. The influence of this sphere on the convective and conductive heat transfer from the model will be discussed later.

The sphere with the appendage model attached was placed in the center of the 28- x 28-in. test section of a low-speed wind tunnel. The air velocity was varied over the range of 1.4 to 10 fps (1 to 7 mph). Air velocity was measured with a Hastings hot wire anemometer (estimated accuracy of ±5 percent).

Heat-transfer coefficients were obtained using a transient technique [8]. The copper specimen was heated with a hot air gun to a temperature about 30 F higher than the temperature of the air stream and allowed to cool. The temperature difference between the model and the air stream was recorded as a function of time. In determining the heat-transfer coefficient by this technique, all of the thermal resistance is assumed to be in the boundary layer, with the copper specimen the only thermal capacitance. The mean heat-transfer coefficient is calculated from

$$h = [mc/A(\tau - \tau_i) \cdot \ln[(t_i - t_{air})/(t - t_{air})]] \quad (1)$$

**Nomenclature**

<p><math>A</math> = heat-transfer area, sq ft</p> <p><math>c</math> = specific heat of model specimens, Btu/lb<sub>m</sub>-F</p> <p><math>d</math> = diameter, ft</p> <p><math>g</math> = acceleration due to gravity, ft/s<sup>2</sup></p> <p><math>Gr = g\beta(t - t_{air})l^3/\nu^2</math>, Grashof number, dimensionless</p> <p><math>h</math> = average heat-transfer coefficient, Btu/hr-sq ft-F</p>	<p><math>k</math> = air thermal conductivity, Btu/hr-ft-F</p> <p><math>l</math> = characteristic length for free convection, ft</p> <p><math>m</math> = mass of model specimen, lb<sub>m</sub></p> <p><math>Nu = hd/k</math>, Nusselt number, dimensionless</p> <p><math>P</math> = pitch angle, deg</p> <p><math>Re = ud/\nu</math>, Reynolds number, dimensionless</p>	<p><math>t</math> = model temperature, F</p> <p><math>t_i</math> = initial model temperature, F</p> <p><math>t_{air}</math> = air temperature, F</p> <p><math>u</math> = air velocity, fps</p> <p><math>Y</math> = yaw angle, deg</p> <p><math>\beta</math> = air coefficient of thermal expansion, 1/F</p> <p><math>\nu</math> = air kinematic viscosity, sq ft/s</p> <p><math>\tau</math> = time measured from start of test, hr</p> <p><math>\tau_i</math> = starting time, hr</p>
--	--	---

The heat-transfer coefficient calculated from equation (1) is thus an average coefficient over both time and position along the model. A least-mean-squares fit of equation (1) using temperatures at several times was employed to compute the best value of the heat-transfer coefficient.

The internal, conductive resistance for the copper specimens, both across the specimen thickness and around the circumference, was an order of magnitude less than the external, convective thermal resistance. Thus, temperature differences inside the model may be neglected, and the transient techniques is valid. Radiation was estimated to be less than 1 percent of the total heat transfer at the lowest speeds and was neglected. Conduction into the balsa wood sphere was estimated to be ±2 percent of the total heat flow at most, and was neglected.

A measure of the effect of free convection on the heat-transfer coefficient is the ratio,  $Gr/Re^2$ . During the experimental determination of the heat-transfer coefficient, the temperature difference varied from about 20 F at the start of the test to 5 F at the end of the test. Based on the average value of Grashof number during a test, the ratio,  $Gr/Re^2$ , was less than 0.6 at the lowest velocities and decreased as velocity increased for all but the tall cylinder tests. For the tall cylinder tests, the ratio,  $Gr/Re^2$ , varies from about 20 at low velocities to 0.2 at high velocities. This implies that the low velocity results, especially for the tall cylinders, may be significantly affected by free convection. However, the data obtained for all models show a consistent forced convection-type correlation for all velocities, and thus the free convection effect apparently does not significantly alter the forced convection flow.

**Results**

**Cylinders.** The eight cylinder models were tested at pitch angles of 45 and 90 deg, and at yaw angles of 0, 90, and 180 deg. Heat-transfer results for the tall cylinder with  $\frac{1}{4}$  closure are shown in Fig. 2(a). These results are typical of the eight cylinders tested.

For all cylinders, it was found that a better correlation of the data was obtained using the diameter of the cylindrical section in the calculation of Reynolds and Nusselt number than using other characteristic dimensions. For attached flow on the front of the model, it is expected that the flow length is the characteristic dimension. Experiments on two-dimensional bluff bodies [7, 9, 10] indicate that the smaller dimension perpendicular to the air stream is the characteristic dimension for heat transfer in the separated region, but that the shape of the body prior to the point of separation is also important. For any one model tested, using, as the characteristic dimension, the dimension perpendicular to the air stream produced a 3 to 1 spread in Nusselt number at any Reynolds number, while the use of the diameter,  $d$ , produces a spread of about 1.4 to 1.

For any one geometry, there is no consistent effect of pitch or yaw angles on the heat-transfer. The spread of Nusselt number at any Reynolds number is about 1.4 to 1 for all of cylindrical mod-

The short cylinders have about 1.3 times higher heat-transfer coefficients than the corresponding tall cylinders. The heat transfer also decreases as the amount of closure increases. Nusselt



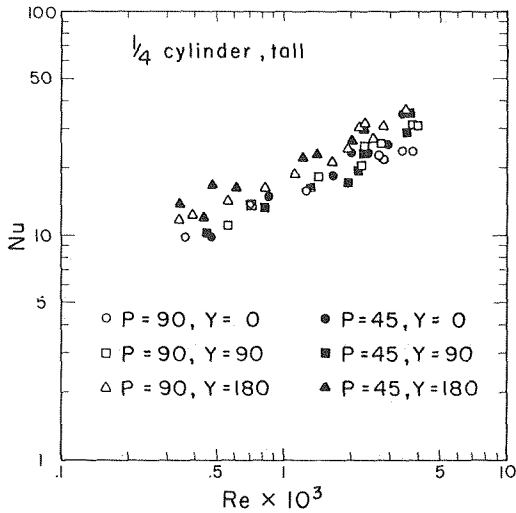


Fig. 2(a) Nusselt number as a function of Reynolds number for the  $\frac{1}{4}$  closure tall cylinder

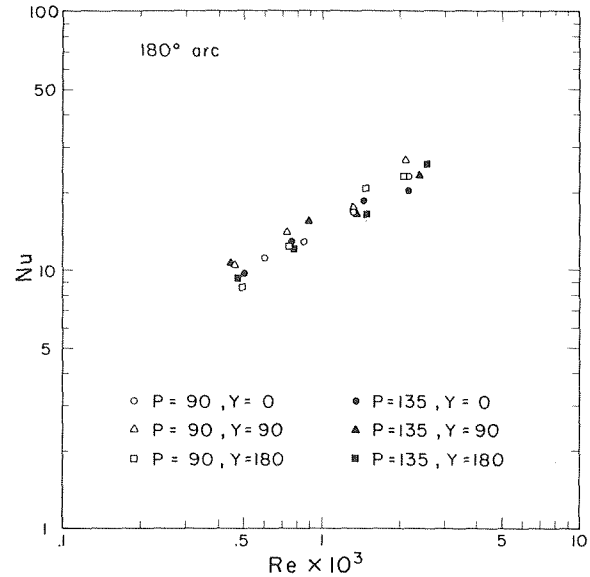


Fig. 3(a) Nusselt number as a function of Reynolds number for the 180 deg arc model

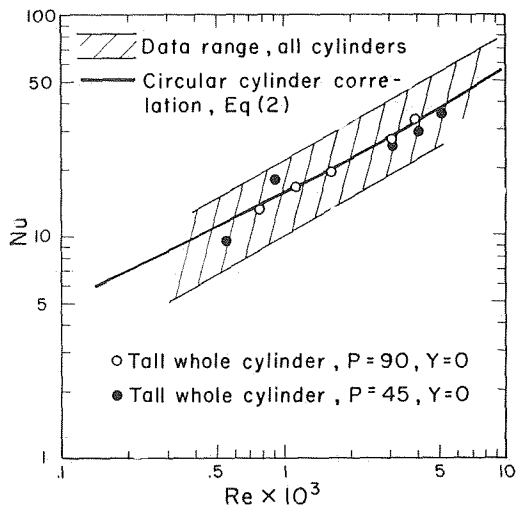


Fig. 2(b) Summary plot of Nusselt number as a function of Reynolds number for all cylindrical sections

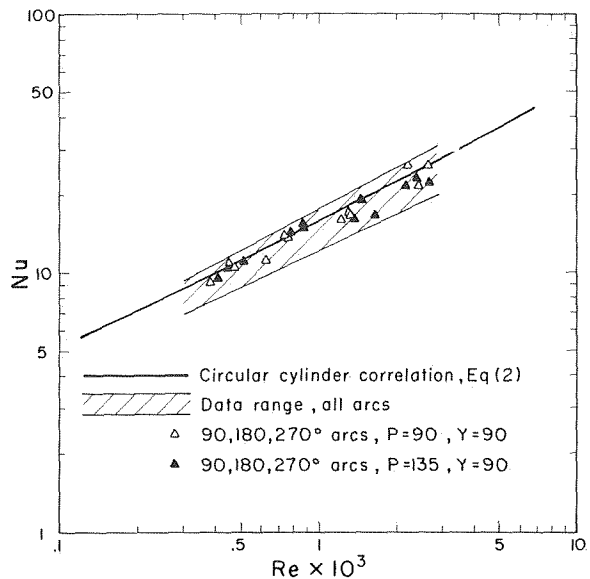


Fig. 3(b) Summary plot of Nusselt number as a function of Reynolds number for all arc models

number drops by about 15 percent as the closure increases from  $\frac{1}{4}$  to  $\frac{3}{4}$ . The value for a whole cylinder is 10 percent greater than that for the  $\frac{1}{4}$  closure cylinder. These effects are consistent with the observations that heat transfer in the separated region is quite high and that the magnitude of the heat-transfer coefficient is proportional to the extent of the wake [7, 10, 11].

A summary of all of the cylinder data is presented in Fig. 2(b). The data range is shown in comparison with the standard cylinder correlation [12], which over the Reynolds number range of the data is given by

$$Nu = 0.615 Re^{0.466} \quad (2)$$

The data spreads about  $\pm 50$  percent about the standard correlation.

Also shown in Fig. 2(b) are the data for the whole tall cylinder at pitches of 90 and 45 deg. The data for these cylinders agree with the correlation for infinite length cylinders, which establishes confidence in the experimental procedure. This agreement also demonstrates that the influence of the sphere on which the models are mounted does not have a significant effect on the heat transfer. The short cylinder data show greater disagreement due, in part, to the proportionately greater surface area of the cylindrical

cap on the top of the cylinder. In the tall cylinder, this area is 4 percent of the total area, while in the short cylinder, it is 20 percent.

**Arcs.** The 90-, 180-, and 270-deg arcs were tested at pitch angles of 90 and 135 deg and yaw angles of 0, 90, and 180 deg. Results for the 180-deg arc, which are representative of the other two arcs, are presented in Fig. 3(a). There are no consistent effects on heat transfer of either pitch or yaw angle for any one geometry.

A summary of all of the data for arcs is presented in Fig. 3(b) in comparison with the circular cylinder correlation. The data scatter very tightly around the correlation as might be expected. The spread of the data is about  $\pm 20$  percent.

In Fig. 3(b) are also shown the results for arcs at yaw angles of 90 deg. These orientations correspond closely to the cylindrical geometry on which the correlation is based, and the agreement between data and correlation is quite good.

**Cones.** The eight cone specimens were tested at pitch angles of 45, 90, 135, and 180 deg and at yaw angles of 0, 90, and 180 deg.

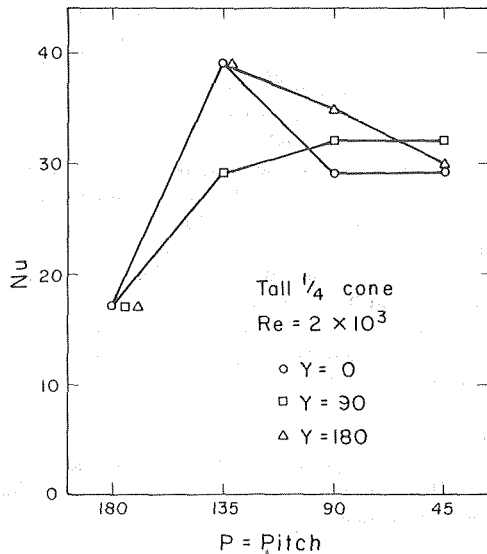


Fig. 4 Nusselt number at a Reynolds number of  $2 \times 10^3$  as a function of pitch angle for the  $1/4$  closure tall cone

Both pitch angle and amount of closure significantly affect the heat transfer.

In Fig. 4, the Nusselt number at a Reynolds number of  $2 \times 10^3$  is plotted as a function of pitch angle for the tall  $1/4$  cone. These results are representative of the other cones. The Nusselt number at a pitch of 180 deg (cone pointed into the air stream) for all cones is always 50 to 65 percent of that for pitch angles of 135, 90, and 45 deg. The use of the slant height instead of the base diameter in the definition of Nusselt and Reynolds number for the pitch = 180-deg tests would make the Nusselt numbers essentially the same at all pitch angles. There is no consistent effect of other pitch angles or yaw angle on the heat transfer.

Increased closure on cones reduces the heat transfer. The drop is approximately 25 percent in Nusselt number for the  $3/4$  cone compared to the tall whole cone. The short cones have approximately 30 percent higher heat transfer than the tall cones. These effects of closure and height, which are similar to the effects ob-

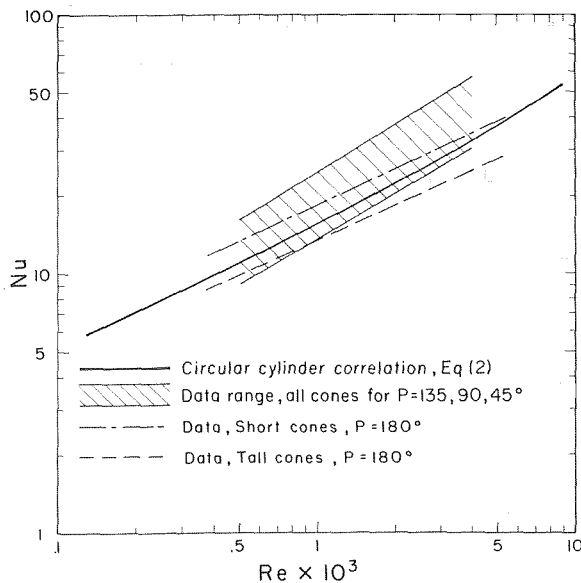


Fig. 5 Summary plot of Nusselt number as a function of Reynolds number for all conical section models

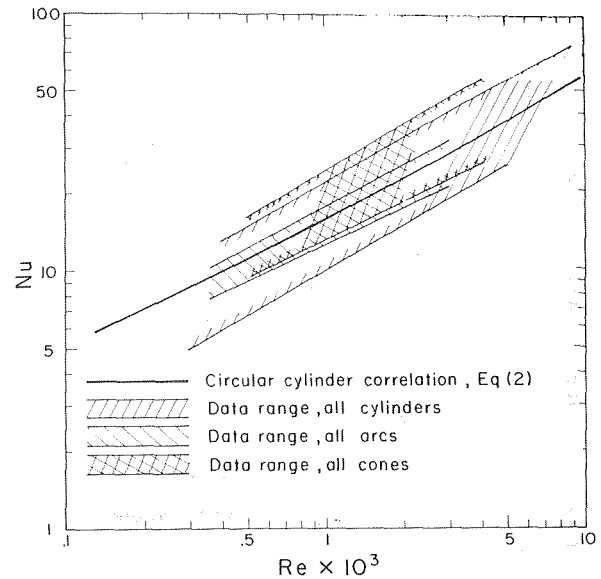


Fig. 6 Summary plot of Nusselt number as a function of Reynolds number for all appendage models

served with cylinders, are probably due to the very active wakes in the shorter, more open models.

The data are summarized in Fig. 5, with the data for cones with a pitch angle of 180 deg separated from the remainder of the data. Also shown is the circular cylinder correlation, equation (2). The data for a pitch angle of 180 deg are within about 20 percent of the cylinder correlation. For other pitch angles, the data are higher than the correlation by an average of about 20 percent, with a data spread of approximately 2 to 1.

### Summary and Conclusion

Heat-transfer data have been obtained from cylindrical sections, arcs, and conical sections in orientations that simulate animal appendages. The heat-transfer results from all of these models are summarized in Fig. 6. The data spread around the established correlation for circular cylinders, equation (2), within about  $\pm 70$  percent.

In general, orientation (pitch and yaw) with respect to the air stream had little effect on the heat-transfer coefficient. Shorter cylinders and cones had higher coefficients than larger cylinders and cones by approximately 30 percent. Models with more encl-

Table 2 Average ratio of Nusselt number to that for an infinitely long cylinder

Geometry	Cylinders* Nu/Nu <sub>cyl</sub>	Cones† Nu/Nu <sub>cyl</sub>
Short	1/4	1.13
	1/2	1.27
	3/4	1.04
	whole	1.50
Long	1/4	1.00
	1/2	0.97
	3/4	0.80
	whole	1.00

\*For all pitch and yaw angles

†For all yaw angles and all pitch angles except 180 degrees.

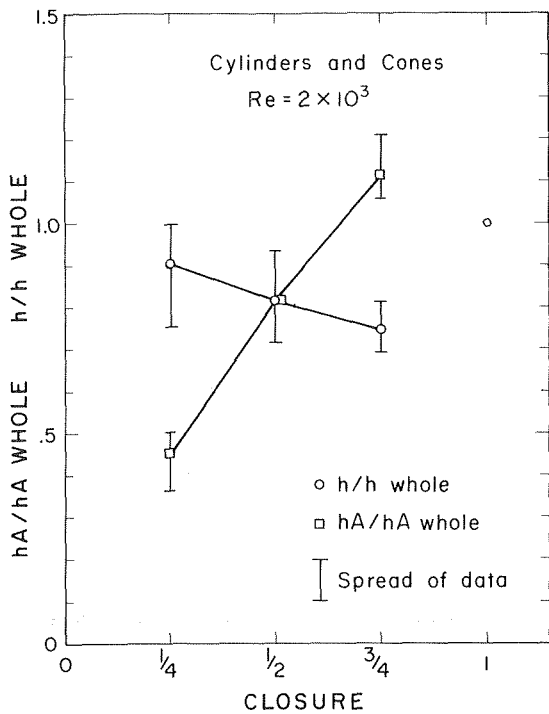


Fig. 7 Normalized heat transfer coefficient and  $hA$  product as a function of closure for cylinders and cones— $Re = 2 \times 10^3$

sure of the region exposed to separated flow than others had lower heat-transfer coefficients. For bluff bodies such as these, the heat transfer in the separated region is of equal importance to that in the attached regions. Thus, geometries that restrict the size of the wake and the circulation in the separated region have lower overall heat transfer.

For heat transfer from an appendage, the product of the heat-transfer coefficient and surface area ( $hA$ ) is more important than the value of the heat-transfer coefficient ( $h$ ) itself. The models with small closure have higher coefficients but less surface area than those with more closure. The values of  $h$  and  $hA$  for cylinders and cones with different amounts of closure, normalized with respect to the values for the whole cylinder, are presented in Fig. 7. It is seen that even though increased closure reduces the heat-transfer coefficient, the increased area produces an increase in the

overall heat transfer. The whole geometries have only area on the outside of the surface and on the cap, while the other models have area on both inside and outside. Thus, there is not a continuous variation with closure to the whole cylinder.

The following procedure is suggested for modeling a shape approximated by one of the models tested here. The cylinder relation, equation (2), is used as the basic relation for the heat-transfer coefficient as a function of velocity, specimen diameter, and air properties. The multiplicative coefficient, 0.615, is altered by the length and closure as discussed in the text and given by Fig. 7. For example for a  $1/4$  cone at pitch angles other than  $180$  deg, the coefficient would be  $0.9 \times 0.615 = 0.554$ . The effects of pitch and yaw on the heat transfer coefficient may be neglected. The resulting relation should be adequate for modeling animal appendages under field conditions.

#### Acknowledgments

This study was supported by National Science Foundation Grant No. GB-15499. Trina Schulte and Jim Vignale aided testing of some of the models.

#### References

- Barlett, P. N., and Gates, D. M., "The Energy Budget of a Lizard on a Tree Trunk," *Ecology*, Vol. 48, 1967, pp. 315-322.
- Porter, W. P., and Gates, D. M., "Thermodynamic Equilibria of Animals With Environment," *Ecological Monograph*, Vol. 39, 1960, pp. 245-270.
- Wathen, P., Mitchell, J. W., and Porter, W. P., "Theoretical and Experimental Studies of Energy Exchange From Jack Rabbit Ears and Cylindrically Shaped Appendages," *Biophysical Journal*, Vol. 11, 1971, pp. 1030-1047.
- Beckman, W. A., Mitchell, J. W., and Porter, W. P., "Thermal Model for Prediction of a Desert Iguana's Daily and Seasonal Behavior," *JOURNAL OF HEAT TRANSFER, TRANS. ASME* (to be published).
- Jakob, M., *Heat Transfer*, Wiley, New York, Vol. 1, 1949.
- Sogin, H. H., Burkhard, K., and Richardson, P. D., "Heat Transfer in Separated Flows," Report ARL-4, Brown University, Jan. 1961.
- Sogin, H. H., "A Summary of Experiments on Local Transfer From the Rear of Bluff Obstacles to a Low Speed Airstream," *JOURNAL OF HEAT TRANSFER, TRANS. ASME, Series C*, Vol. 86, 1964, pp. 200-202.
- London, A. L., Nottage, H. B., and Boelter, L. M. K., "Determination of Unit Conductances in Heat and Mass Transfer by the Transient Method," *Ind. & Engr. Chem.*, Vol. 33, 1941, p. 467.
- Roshko, A., "On the Drag and Shedding Frequency of Two-Dimensional Bluff Bodies," NACA TN3169, July 1954.
- Mitchell, J. W., "Base Heat Transfer in Two-Dimensional Subsonic, Fully Separated Flows," *JOURNAL OF HEAT TRANSFER, TRANS. ASME, Series C*, Vol. 93, 1971, pp. 342-348.
- Geidt, W. H., "Investigation of Variation of Point Unit Heat Transfer Coefficient Around a Cylinder Normal to an Air Stream," *TRANS. ASME*, Vol. 71, 1949, p. 375.
- McAdams, W. H., *Heat Transmission*, McGraw Hill, Third ed. New York, 1954, p. 259.

This section consists of contributions of 1500 words or less (about 5 double-spaced typewritten pages, including figures). Technical briefs will be reviewed and approved by the specific division's reviewing committee prior to publication. After approval such contributions will be published as soon as possible, normally in the next issue of the journal.

## Storage of Thermal Energy by Solid-Liquid Phase Change—Temperature Drop and Heat Flux

N. Shamsundar<sup>1</sup> and E. M. Sparrow<sup>1</sup>

### Introduction

Present day studies of alternative energy sources such as the sun and the winds have underscored the need for energy storage techniques. One of the techniques being examined for the storage of thermal energy is solid-liquid phase change. Although the heat conduction aspects of such phase change processes were studied extensively in the past, the results were aimed at applications other than energy storage. Consequently, even though surface heat flux rates and solid phase temperature differences are of prime importance in thermal storage applications, such results are rarely presented in the published literature.

In the present paper, a related pair of phase-change heat conduction problems is solved, and results relevant to energy storage are presented and discussed. The physical situation selected for analysis is a circular tube filled with a phase change material (pcm) which may, for example, be a salt or a metal. The tube is situated in a fluid environment and may be one of several in a bundle. During periods of time when energy is being stored, heat flows from the fluid environment into the pcm, thereby causing the pcm to melt. On the other hand, during the heat extraction period, heat flows from the pcm to the fluid environment, as the pcm solidifies.

The extraction period is especially critical inasmuch as the solidifying pcm takes on the role of the heat source for the power producing system. If there is a substantial temperature drop across the solidified layer of pcm, there is a corresponding decrease in the temperature at which the energy is available and a consequent reduction of the efficiency.<sup>2</sup> Another relevant consid-

eration to the functioning of the power-producing device is the time dependence of the heat release by the pcm.

To illustrate the type of results that are relevant to thermal storage systems, consideration is given here to the two limiting cases described in the following, both of which pertain to the period of energy extraction. In both cases, the pcm is in the liquid phase and at its saturation temperature when the extraction period begins.

The first of the aforementioned cases appears not to have been analyzed in the published literature. The second case has been analyzed by a number of solution methods, but no results of the type that are relevant to thermal storage systems have been presented.

### Analysis and Solutions

A schematic diagram of the physical problem is given in the inset of Fig. 1. A circular tube of radius  $R$  contains a pcm which, at any time  $t > 0$ , has both liquid ( $L$ ) and solid ( $S$ ) phases as in-

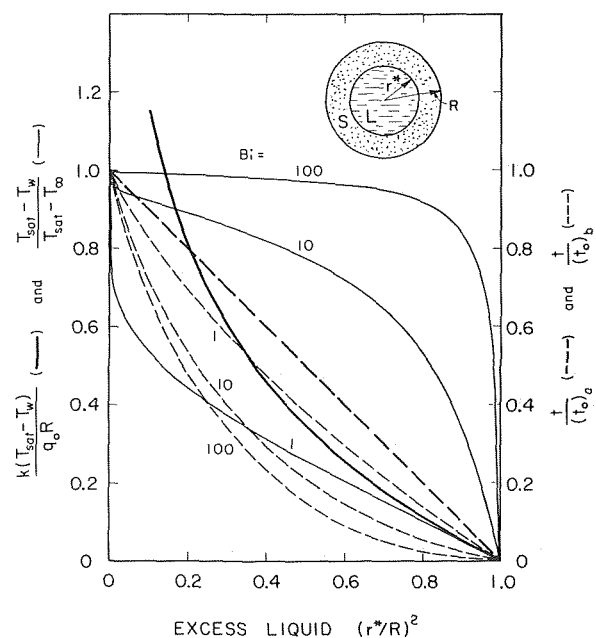


Fig. 1 Results for temperature drop and time history of freezing front

<sup>1</sup> Department of Mechanical Engineering, University of Minnesota, Minneapolis, Minn.

<sup>2</sup> During the period when energy is being stored in the pcm, the temperature of the fluid is higher than that of the pcm. Thus, the temperature of the pcm does not affect the thermodynamic efficiency.

Contributed by the Heat Transfer Division of THE AMERICAN SOCIETY OF MECHANICAL ENGINEERS. Manuscript received by the Heat Transfer Division, November 16, 1973.

indicated in the figure. The phase boundary is assumed to be axisymmetric with radius  $r = r^*$  and the density difference associated with the change of phase is neglected. At time  $t = 0$ , the contents of the tube is pure liquid at its saturation temperature  $T_{\text{sat}}$ .

$$\dot{\eta}^* = \frac{-2 \text{Ste}_a}{\eta^*(1 + \sqrt{1 - 4 \text{Ste}_a \ln \eta^*})} \quad (9)$$

$$\dot{\eta}^* = \frac{-2 \text{Ste}_b \text{Bi}}{\eta^* \{ \sqrt{1 - \text{Bi} \ln \eta^*} - 2 \text{Ste}_b \text{Bi} \ln \eta^* (2 - \text{Bi} \ln \eta^*) + (1 - \text{Bi} \ln \eta^*) \}} \quad (10)$$

The phase boundary moves inward toward smaller radii as heat is extracted from the surface of the tube. The heat extraction is either as a uniform heat flux  $q_0$  (case *a*) or via a constant convective heat transfer coefficient  $h$  to a fluid environment with constant temperature  $T_{\infty}$  (case *b*).

Within the solidified layer, the heat conduction process is governed by

$$\partial T / \partial t = (\alpha / r) \partial / \partial r (r \partial T / \partial r), \quad r^* \leq r \leq R \quad (1)$$

where the thermophysical properties appearing in equation (1) and in subsequent equations are those of the solid. At the phase boundary, continuity of temperature and heat flux are expressed as

$$T = T_{\text{sat}}, \quad k(\partial T / \partial r) = \rho \lambda (dr^* / dt), \quad r = r^* \quad (2)$$

in which  $\lambda$  is the latent heat of fusion. At the surface of the tube, the respective boundary conditions for problems (*a*) and (*b*) are

$$(a) -k(\partial T / \partial r) = q_0, \quad (b) -k(\partial T / \partial r) = h(T - T_{\infty}), \quad r = R \quad (3)$$

To initiate the solutions, it is appropriate to introduce the following dimensionless variables

$$\theta_a = k(T_{\text{sat}} - T) / q_0 R, \quad \theta_b = (T_{\text{sat}} - T) / (T_{\text{sat}} - T_{\infty}) \quad (4a)$$

$$\eta = r / R, \quad \eta^* = r^* / R, \quad Fo = \alpha t / R^2 \quad (4b)$$

along with the dimensionless parameters

$$\text{Ste}_a = \frac{c(q_0 R / k)}{\lambda}, \quad \text{Ste}_b = \frac{c(T_{\text{sat}} - T_{\infty})}{\lambda}, \quad \text{Bi} = \frac{hR}{k} \quad (5)$$

The magnitude of the Stefan number  $\text{Ste}$  is a measure of the importance of heat capacity relative to the latent heat.

The solutions themselves are found by applying a method due to Megerlin [1]<sup>3</sup> along with relations derived by him. This method, although approximate, has been demonstrated by comparisons with finite-difference solutions to yield results of high accuracy [2]. The first step in the solution is to expand the dimensionless temperature  $\theta$  in powers of  $\ln(\eta / \eta^*)$ , with coefficients that are independent of  $\eta$  but depend on the Fourier number and the constant parameters of the problem. The coefficients are chosen such that equations (1) and (2) are satisfied exactly at the phase boundary  $\eta = \eta^*$ . These operations give

$$\text{Ste} \theta = -\dot{\eta}^* \eta^* \ln \left( \frac{\eta}{\eta^*} \right) + \frac{1}{2} (\dot{\eta}^* \eta^*)^2 \left[ \ln \left( \frac{\eta}{\eta^*} \right) \right]^2 + \dots \quad (6)$$

where  $\dot{\eta}^* = d\eta^* / dFo$ . This equation applies equally well if subscripts *a* or *b* are appended to  $\text{Ste}$  and  $\theta$ .

The quantity  $\dot{\eta}^*$  is found by applying the boundary conditions (3), so that

$$-\dot{\eta}^* \eta^* + (\dot{\eta}^* \eta^*)^2 \ln(1 / \eta^*) + \dots = \text{Ste}_a \quad (7)$$

$$-\dot{\eta}^* \eta^* + (\dot{\eta}^* \eta^*)^2 \ln(1 / \eta^*) + \dots = \text{Ste}_b \text{Bi} \quad (8)$$

$$-\text{Bi} \left\{ -\dot{\eta}^* \eta^* \ln(1 / \eta^*) + \frac{1}{2} (\dot{\eta}^* \eta^*)^2 \left[ \ln(1 / \eta^*) \right]^2 + \dots \right\}$$

respectively, for cases *a* and *b*. To the order of terms contained in equations (7) and (8), the corresponding solutions for  $\dot{\eta}^*$  are

If equation (9) or equation (10) is substituted in (6), thereby eliminating  $\dot{\eta}^*$ , the resulting equation gives the spatial temperature distribution in the solidified layer, with the freezing front position  $\eta^*$  playing the role of a parameter. Further, by setting  $\eta = 1$ , the temperature drop across the solid is expressed as a function of  $\eta^*$ .

It is now appropriate to consider the physical significance of  $\eta^*$  or, more to the point, of  $(\eta^*)^2$ . Inasmuch as  $(\eta^*)^2 = (r^* / R)^2 = \pi r^{*2} / \pi R^2$ , it follows that  $(\eta^*)^2$  represents the fraction of the original liquid contents of the tube that is still liquid. If the solidification process were to be terminated at a particular value of  $\eta^*$ , then  $(\eta^*)^2$  would correspond to the excess liquid, over and above that which participates in the phase change process. Thus, the equation derived in the preceding paragraph can be employed to compute the temperature drop across the solid as a function of the excess liquid  $(\eta^*)^2$ .

The time required for the freezing front to reach a specified radial position  $\eta^*$  can be evaluated from

$$Fo = - \int_{\eta^*}^1 d\eta^* / \dot{\eta}^* \quad (11)$$

in which  $\dot{\eta}^*$  is expressed by either equation (9) or equation (10). For case *a*, the integration can be carried out in closed form to give

$$2 \text{Ste}_a Fo = \frac{1}{2} (1 - \eta^{*2}) + \frac{1}{2} (1 - \eta^{*2} \sqrt{1 - 4 \text{Ste}_a \ln \eta^*}) + \sqrt{2 \text{Ste}_a} \frac{\sqrt{\pi}}{4} \exp \left( \frac{1}{2 \text{Ste}_a} \right) \left\{ \text{erf} \left( \sqrt{\frac{1}{2 \text{Ste}_a}} - 2 \ln \eta^* \right) - \text{erf} \left( \sqrt{\frac{1}{2 \text{Ste}_a}} \right) \right\} \quad (12)$$

For case *b*, numerical integration is required to evaluate equation (11).

## Results and Discussion

Prior to the evaluation of the results, estimates were made of the values of the Stefan number relevant to the application of [3]. When  $T_{\text{sat}} - T_{\infty}$  was limited to 10 deg C, the computed  $\text{Ste}$  values were on the order of 0.05. Then, when the equations of the foregoing paragraphs were evaluated for  $\text{Ste} = 0.05$ , the results for both cases were found to be hardly distinguishable from those for  $\text{Ste} = 0$  (an extreme of 2–3 percent at  $\eta^{*2} = 0.1$ ), where  $\text{Ste} = 0$  corresponds to the case in which the heat capacity of the solidified layer is neglected altogether. Consequently, in what follows, the results that are presented will correspond to  $\text{Ste} = 0$ .

Fig. 1 portrays, on the left-hand ordinate, dimensionless forms of the temperature drop  $T_{\text{sat}} - T_w$  across the solid for both cases *a* and *b*. The abscissa is the excess liquid  $(r^* / R)^2$ , that is, the fraction of the original liquid contents of the tube which is still liquid at the conclusion of the period of energy extraction. The objective of the figure is to show how  $T_{\text{sat}} - T_w$  responds to the presence of excess liquid for fixed values of the other parameters. It is evident that substantial decreases in the temperature drop can be achieved, but the extent of the gains depends strongly on the thermal boundary conditions at the tube surface and on which quantities are held fixed when comparisons are made. More direct illustrations of the excess liquid effect will be presented shortly for specific pcm's and in terms of dimensional variables.

<sup>3</sup> Numbers in brackets designate References at end of paper.

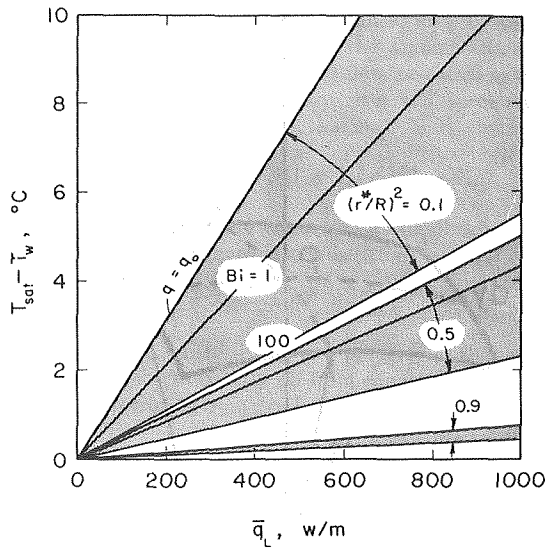


Fig. 2 Temperature drop across solidified layer—lithium fluoride

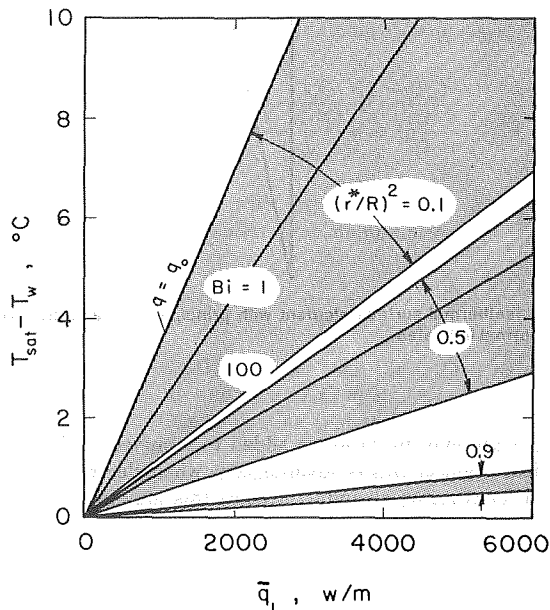


Fig. 3 Temperature drop across solidified layer—tin

On the right-hand ordinate of Fig. 1 is plotted the time that is required for the phase boundary to arrive at  $\eta = \eta^*$ , starting from  $\eta = 1$  when  $t = 0$ . The time scale is made dimensionless by the quantity  $t_0$ , which corresponds to the time required for complete freezing. When the heat capacity of the solid is negligible, it is easily shown that

$$(t_0)_a = \rho\lambda R/2q_0, \quad (t_0)_b = \rho\lambda R^2(1/Bi + 1/2)/2k(T_{sat} - T_\infty) \quad (13)$$

Solid-phase temperature drops for two candidate pcm's—lithium fluoride and tin, one a salt and the other a metal, are shown in Figs. 2 and 3. In each figure,  $T_{sat} - T_w$  is plotted as a function of  $\bar{q}_L$  ( $\approx 2\pi R\bar{q}$ ), where the subscript  $L$  means per unit length of tube. The quantity  $\bar{q}$  is the time-average heat transfer rate corresponding to the period of time during which the phase boundary moves from  $\eta = 1$  to  $\eta = \eta^*$ . The use of  $\bar{q}$  as the abscissa variable places cases  $a$  and  $b$  on an equal footing in that for common values of  $\eta^*$  and  $Fo$ , the value of  $\bar{q}$  for case  $b$  is equal to the value

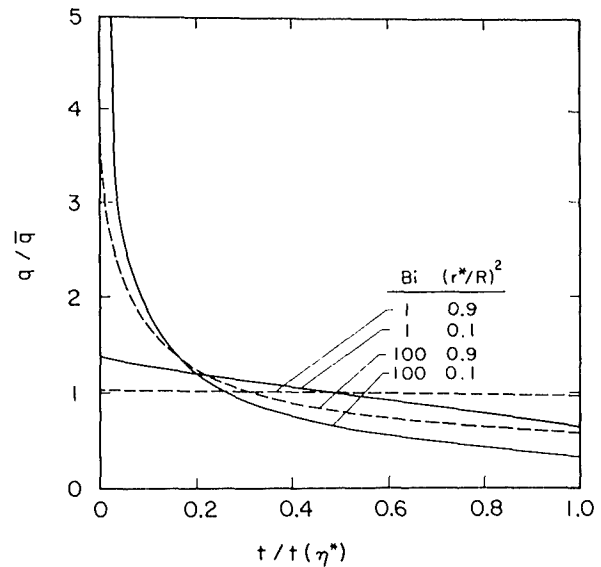


Fig. 4 Variation of surface heat flux with time

of  $q_0$  for case  $a$ , and the total amount of heat transferred is also the same in the two cases. Each figure contains three shaded bands, each of which, respectively, encompasses the results for  $\eta^{*2} = 0.1, 0.5$ , and  $0.9$ . The uppermost line in each band is for case  $a$ , whereas the remainder of the band corresponds to a range of Biot numbers for case  $b$ .

These figures demonstrate the extent to which the presence of excess liquid diminishes the solid phase temperature drop. Furthermore, for any given value of  $\eta^{*2}$ , the temperature drop is highest for case  $a$  and decreases as the Biot number increases for case  $b$ . From this standpoint, it would appear advantageous to design a thermal storage system to have as high a Biot number as possible. However, before accepting this conclusion, it is appropriate to examine the time variations of  $q$  that are encountered in case  $b$ .

Fig. 4 shows curves of  $q/\bar{q}$  as a function of  $t/t(\eta^*)$ , where  $t(\eta^*)$  is the time required for the freezing front to arrive at  $\eta = \eta^*$ . The curves are parameterized by values of  $\eta^{*2}$  and of  $Bi$ . The results indicate that for any fixed  $\eta^*$ , the time variation of  $q$  becomes more marked as  $Bi$  increases. If one of the design objectives is to achieve a relatively constant value of  $q$  during the extraction period, then large values of  $Bi$  are disadvantageous. Indeed, the most uniform time history for  $q$  is achieved at large values of  $\eta^{*2}$  and small values of  $Bi$ .

The foregoing discussion of the role of  $Bi$  reveals one of the trade-offs which will have to be made in the design of a phase-change energy storage system. Of course, when considering the total impact of the temperature drop associated with the storage medium, it is necessary to add the convective drop  $T_w - T_\infty$  to  $T_{sat} - T_w$ . A second trade-off which emerges in connection with the solid-phase temperature drop is a balancing out of the amount of excess liquid against the radius of the storage tube. Lower temperature drops can be achieved by using either additional excess liquid or tubes of smaller radius. Economic considerations will, in all likelihood, be decisive in resolving these questions.

## References

- 1 Megerlin, F., "Geometrisch eindimensionale Wärmeleitung beim Schmelzen und Erstarren," *Forsch. Ing.-Wes.*, Vol. 34, 1968, p. 40.
- 2 Stephan, K., "Schmelzen und Erstarren Geometrisch einfacher Körper," *Kältetechnik-Klimatisierung*, Vol. 23, 1971, p. 42.
- 3 "Research Applied to Solar-Thermal Power Systems," Appendix 13, Progress Reprint No. 1, University of Minnesota and Honeywell, Inc., Minneapolis, Minn., Jan., 1973.

## Acknowledgment

this paper was prepared under Grant No. GI-34871 from the National Science Foundation, Advanced Technology Application Division of RANN.

# The Critical Curvature for Maximum Heat Flow From a Surface

Niels Madsen<sup>1</sup>

## Nomenclature

- $A$  = heat-transfer area on isothermal surface, m<sup>2</sup>  
 $h$  = unit total conductance, W/m<sup>2</sup>K  
 $k$  = thermal conductivity, W/mK  
 $K_{\text{crit}}$  = critical mean curvature of surface, 1/m  
 $L$  = thickness of insulation, m  
 $L_{\text{cr}}$  = critical thickness of insulation, m  
 $n$  = distance from isothermal surface, m  
 $P$  = point on isothermal surface  
 $q$  = rate of heat flow, W  
 $r_1, r_2$  = principal radii of curvature of isothermal surface, m  
 $R_1, R_2$  = principal radii of curvature of body surface, m  
 $S$  = heat-transfer area of body surface, m<sup>2</sup>  
 $T$  = temperature of isothermal surface, K or °C  
 $T_s$  = temperature of body surface, K or °C  
 $T_\infty$  = temperature of ambient fluid, K or °C  
 $x$  = distance along surface in first principal direction, m  
 $y$  = distance along surface in second principal direction, m

## Introduction

The purpose of this communication is to derive a general expression for the critical mean curvature of a surface in terms of the local, unit total conductance of the surface and the thermal conductivity of the body; then the critical radius of the sphere, and of the right circular cylinder become special cases of this general expression. It is well-known that the rate of heat transfer between an ambient fluid and the two simple one-dimensional bodies, the sphere, and the long, right, circular cylinder at first increases, passes through a maximum, and then decreases asymptotically to zero as their respective radii are made greater and greater. This was predicted, and a solution was proposed, for the sphere by Lord Kelvin then known as W. Thomson [1]<sup>2</sup> in 1886. The critical radius (the radius at which the heat flow is a maximum) was evaluated analytically for the circular cylinder and the result confirmed through extensive experimental data by A. W. Porter and T. R. Martin [2] in 1910, and subsequently by V. S. Day [3] in 1920.

## Applications

The original note by Lord Kelvin was concerned with the efficiency of clothing, whereas the two later publications discussed the engineering importance of the fact that heat flow may in-

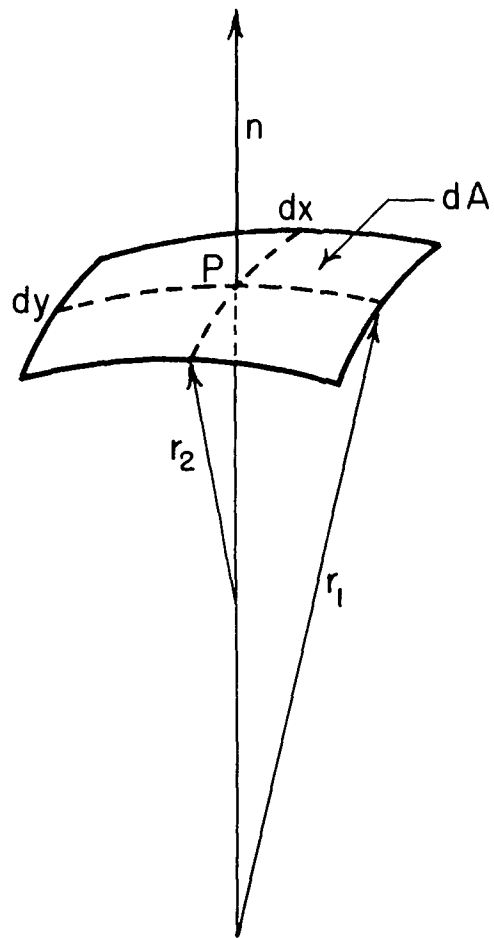


Fig. 1 Isothermal surface element with principal radii and the direction of the normal indicated

crease if thermal insulation is added to a curved surface. To the electrical engineer this is advantageous when electrical insulation is used for covering a conductor since this may improve the rate of cooling; but it is a disadvantage in thermal engineering particularly in the design of refrigeration equipment where small-diameter pipes are employed, lagging of their surfaces may increase the heat flow rather than decrease it. Theoretical biologists are also interested in the critical radius effect. T. H. Strunk [4].

## Analysis

Over a small region  $dA$  a curved surface can always be described in terms of two radii of curvature in mutually orthogonal planes. These are known as the principal radii of curvature  $r_1$  and  $r_2$ , Fig. 1. Assume that  $dA$  is maintained at a constant temperature  $T$  by a heat source below it. Now let a thickness,  $L$ , of insulation be applied to the surface; the area available for heat flow through it will depend on the distance,  $n$  from the isothermal surface as measured along the normal to this surface. This area will be related to the area on the isothermal surface by the equation

$$dS = \left(\frac{r_1 + n}{r_1}\right) \left(\frac{r_2 + n}{r_2}\right) dx dy = (1 + n/r_1)(1 + n/r_2)dA \quad (1)$$

where  $dA = dx dy$ , and  $r_1$  and  $r_2$  are the principal radii of curvature of the isothermal surface at  $P$ . The local unit rate of heat flow through the body surface,  $dq/dS$  may be expressed by the Newton rate equation

$$dq/dS = h(T_s - T_\infty) \quad (2)$$

<sup>1</sup>Department of Chemical Engineering, University of Rhode Island, Kingston, R. I.

<sup>2</sup>Numbers in brackets designate References at end of technical brief.

Contributed by the Heat Transfer Division of THE AMERICAN SOCIETY OF MECHANICAL ENGINEERS. Manuscript received by the Heat Transfer Division, April 9, 1974.

## Acknowledgment

this paper was prepared under Grant No. GI-34871 from the National Science Foundation, Advanced Technology Application Division of RANN.

# The Critical Curvature for Maximum Heat Flow From a Surface

Niels Madsen<sup>1</sup>

## Nomenclature

- $A$  = heat-transfer area on isothermal surface, m<sup>2</sup>  
 $h$  = unit total conductance, W/m<sup>2</sup>K  
 $k$  = thermal conductivity, W/mK  
 $K_{\text{crit}}$  = critical mean curvature of surface, 1/m  
 $L$  = thickness of insulation, m  
 $L_{\text{cr}}$  = critical thickness of insulation, m  
 $n$  = distance from isothermal surface, m  
 $P$  = point on isothermal surface  
 $q$  = rate of heat flow, W  
 $r_1, r_2$  = principal radii of curvature of isothermal surface, m  
 $R_1, R_2$  = principal radii of curvature of body surface, m  
 $S$  = heat-transfer area of body surface, m<sup>2</sup>  
 $T$  = temperature of isothermal surface, K or °C  
 $T_s$  = temperature of body surface, K or °C  
 $T_\infty$  = temperature of ambient fluid, K or °C  
 $x$  = distance along surface in first principal direction, m  
 $y$  = distance along surface in second principal direction, m

## Introduction

The purpose of this communication is to derive a general expression for the critical mean curvature of a surface in terms of the local, unit total conductance of the surface and the thermal conductivity of the body; then the critical radius of the sphere, and of the right circular cylinder become special cases of this general expression. It is well-known that the rate of heat transfer between an ambient fluid and the two simple one-dimensional bodies, the sphere, and the long, right, circular cylinder at first increases, passes through a maximum, and then decreases asymptotically to zero as their respective radii are made greater and greater. This was predicted, and a solution was proposed, for the sphere by Lord Kelvin then known as W. Thomson [1]<sup>2</sup> in 1886. The critical radius (the radius at which the heat flow is a maximum) was evaluated analytically for the circular cylinder and the result confirmed through extensive experimental data by A. W. Porter and T. R. Martin [2] in 1910, and subsequently by V. S. Day [3] in 1920.

## Applications

The original note by Lord Kelvin was concerned with the efficiency of clothing, whereas the two later publications discussed the engineering importance of the fact that heat flow may in-

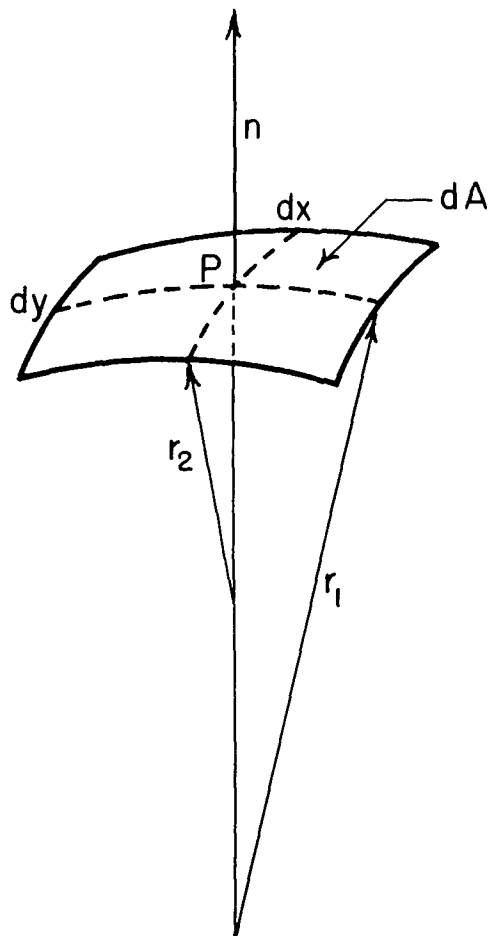


Fig. 1 Isothermal surface element with principal radii and the direction of the normal indicated

crease if thermal insulation is added to a curved surface. To the electrical engineer this is advantageous when electrical insulation is used for covering a conductor since this may improve the rate of cooling; but it is a disadvantage in thermal engineering particularly in the design of refrigeration equipment where small-diameter pipes are employed, lagging of their surfaces may increase the heat flow rather than decrease it. Theoretical biologists are also interested in the critical radius effect. T. H. Strunk [4].

## Analysis

Over a small region  $dA$  a curved surface can always be described in terms of two radii of curvature in mutually orthogonal planes. These are known as the principal radii of curvature  $r_1$  and  $r_2$ , Fig. 1. Assume that  $dA$  is maintained at a constant temperature  $T$  by a heat source below it. Now let a thickness,  $L$ , of insulation be applied to the surface; the area available for heat flow through it will depend on the distance,  $n$  from the isothermal surface as measured along the normal to this surface. This area will be related to the area on the isothermal surface by the equation

$$dS = \left(\frac{r_1 + n}{r_1}\right) \left(\frac{r_2 + n}{r_2}\right) dx dy = (1 + n/r_1)(1 + n/r_2) dA \quad (1)$$

where  $dA = dx dy$ , and  $r_1$  and  $r_2$  are the principal radii of curvature of the isothermal surface at  $P$ . The local unit rate of heat flow through the body surface,  $dq/dS$  may be expressed by the Newton rate equation

$$dq/dS = h(T_s - T_\infty) \quad (2)$$

<sup>1</sup>Department of Chemical Engineering, University of Rhode Island, Kingston, R. I.

<sup>2</sup>Numbers in brackets designate References at end of technical brief.

Contributed by the Heat Transfer Division of THE AMERICAN SOCIETY OF MECHANICAL ENGINEERS. Manuscript received by the Heat Transfer Division, April 9, 1974.



where  $h$  is the local unit total conductance, and  $T_s$  and  $T$  the temperature of the body surface and the ambient fluid. For a thickness of insulation,  $L$  the unit heat flow measured as it passes through  $A$  may be found by substituting  $n = L$  in equation (1) and this value for  $dS$  in equation (2), that is

$$dq/dA = h(1 + L/r_1)(1 + L/r_2)(T - T_\infty) \quad (3)$$

The elementary Fourier rate equation for one-dimensional conduction in the steady state must also be satisfied

$$dq/dS = -k dT/dn|_{at S}$$

where the thermal conductivity,  $k$  is a property of the insulation material added. Substituting for  $dS$  from equation (1), separating variables, and integrating from 0 to  $L$  and from  $T$  to  $T_s$

$$dq/dA \int_0^L \frac{dn}{(1 + n/r_1)(1 + n/r_2)} = -k \int_T^{T_s} dT \quad (5)$$

or after integration and the substitution of the limits

$$\frac{dq/dA}{1/r_2 - 1/r_1} \ln \frac{1 + L/r_2}{1 + L/r_1} = k(T - T_s) \quad (6)$$

Solving equations (3) and (6) for their respective temperature drops, adding the two equations to eliminate  $T_s$ , and rearranging

$$dq/dA = \frac{k(1/r_2 - 1/r_1)(T - T_\infty)}{\frac{(k/h)(1/r_2 - 1/r_1)}{(1 + L/r_1)(1 + L/r_2)} + \ln \frac{1 + L/r_2}{1 + L/r_1}} \quad (7)$$

differentiating equation (7) with respect to  $L$  and setting  $d(dq/dA)/dL$  equal to zero, yields after some manipulation

$$\frac{d}{dL} \left( \frac{dq}{dA} \right) = \frac{1}{L_{cr} + r_1} + \frac{1}{L_{cr} + r_2} - \frac{h}{k} = 0 \quad (8)$$

as  $L_{cr}$  changes from a value smaller than the critical to a value larger than the critical, the sign of  $d(dq/dA)/dL$  changes from positive to negative, thus indicating that the extremum given by equation (8) is a maximum. Since  $L_{cr} + r_1$  and  $L_{cr} + r_2$  are the principal radii of the critically insulated surface  $R_1$  and  $R_2$ , we can rewrite the equation

$$\frac{h}{k} = \frac{1}{R_1} + \frac{1}{R_2} = K_{m_{cr}} \quad (9)$$

where  $K_{m_{(cr)}}$  is the critical mean curvature of the fluid-solid interface. Equation (8) may be solved for the critical insulation thickness

$$\frac{hL_{cr}}{k} = 1 - \frac{h(r_1 + r_2)}{2k} \pm \left[ 1 + \left[ \frac{h(r_1 - r_2)}{2k} \right]^2 \right]^{1/2} \quad (10)$$

but when  $r_1$  or  $r_2 \rightarrow \infty$  the solution becomes difficult to evaluate.

## Discussion

For the sphere where  $R_1 = R_2 = R$  equation (9) yields  $h/k = 2/R_{cr}$ , and for the long, right circular cylinder where one principal radius approaches infinity  $h/k = 1/R_{cr}$ , thus equation (9) is in agreement with the two solutions for one-dimensional heat flow as given by Schneider [5]. It follows as a consequence of equation (9) that when  $h$  is known as a function of the location on a surface, a surface may be described that will be the boundary of a volume of maximum heat transfer. The special case of a right cylinder with variable unit conductance has been considered by E. M. Sparrow [6]. The assumption, made in the derivation of equation (9), that the heat flow is normal to the surface, may be invalid if the thermal resistance normal to the surface is large compared to the resistance parallel to the surface.

## References

- 1 Thomson, W., *Nature*, Vol. XXIX, 1884, p. 567.
- 2 Porter, A. W., and Martin, T. R., *Phil. Mag.*, Vol. 20, 1910, pp. 511-522.
- 3 Day, V. S., *Univ. Ill. Eng. Expt. Sta. Bull.*, 117, 1920.
- 4 Strunk, T. H., *Theoret. Biol.*, Vol. 33, 1971, pp. 35-61.
- 5 Schneider, J. P., *Conduction Heat Transfer*. Addison Wesley, Cambridge, Ma., 1955.
- 6 Sparrow, E. M. *A.I.Ch.E. J.*, Vol. 16, 1970, p. 149.

## Optimization of Inclined Convective Fins

David Pnueli<sup>1</sup>

A new type of fins has been recently used in the electronics industry in cases where large quantities of heat must be removed from small spaces. These fins are rather short and thick. They come out of a heavy backplate and have the properties that: (a) temperature variations between the fin's root and fin's tip are negligible, i.e., the fin is isothermal in the direction perpendicular to its backplate, and (b) convection coefficients vary in the streamwise direction. The need for such designs has led to the analytical and experimental investigations in references [1-3].<sup>2</sup>

The over-all size of the finned walls ( $B$ ,  $H$ , Fig. 1) are usually determined by the size of the electronic equipment. The thickness, the number and length ( $d$ ,  $b$ ,  $L$ , Fig. 1) of the fins are determined by heat transfer considerations (references [1], [3]), by manufacturing considerations, by structural requirements and by the tendency to use standard elements whenever possible.

The heat dissipated from such vertical fins can be increased by inclining them to some angle to the direction of the gravity force. This note demonstrates this possibility.

The local convection coefficient for closely spaced vertical fins decreases with increasing fin length, because the air flowing along the fins is already heated by their lower sections. Inclining the fins has two opposite physical effects. It can cause their length to decrease (Fig. 2), thus increasing heat transfer coefficients (or to increase, depending on the geometry,  $H$ ,  $B$ ,  $b$ , Figs. 1 and 2, and on the inclination angle). It always, however, weakens the effect of gravity, thus decreasing heat transfer coefficients. The optimal inclination angle is thus obtained when the effect (combined for all fins) of the decrease in the fins' length is just balanced by that of the weakened gravity.

To obtain some general numerical results, the average Nusselt number for heat convection from the fins is now estimated, as being proportional to the Grashof number to the power of  $1/4$ .<sup>3</sup> This estimate is based on results obtained for inclined flat plates (references [4, 5]), for long isothermal fins or large isothermal square fins (reference [1]), for long vertical isothermal conduits (reference [2]), and for parallel plates (references [6, 7]). Thus,

$$Nu \propto Gr^{1/4}$$

<sup>1</sup> Department of Fluid, Thermal and Aerospace Sciences, School of Engineering, Case Western Reserve University, Cleveland, Ohio.

<sup>2</sup> Numbers in brackets designate References at end of technical brief.

<sup>3</sup> This estimate is theoretically justifiable for boundary layer type flows only. For long enough fins the growing boundary layers for each fin of an adjacent pair will eventually merge. However, the same dependence of  $Nu$  on  $Gr$  has been observed for cases with such merged boundary layers, references [1, 2].

Contributed by the Heat Transfer Division of THE AMERICAN SOCIETY OF MECHANICAL ENGINEERS. Manuscript received by the Heat Transfer Division January 17, 1974.

where  $h$  is the local unit total conductance, and  $T_s$  and  $T$  the temperature of the body surface and the ambient fluid. For a thickness of insulation,  $L$  the unit heat flow measured as it passes through  $A$  may be found by substituting  $n = L$  in equation (1) and this value for  $dS$  in equation (2), that is

$$dq/dA = h(1 + L/r_1)(1 + L/r_2)(T - T_\infty) \quad (3)$$

The elementary Fourier rate equation for one-dimensional conduction in the steady state must also be satisfied

$$dq/dS = -k dT/dn|_{at S}$$

where the thermal conductivity,  $k$  is a property of the insulation material added. Substituting for  $dS$  from equation (1), separating variables, and integrating from 0 to  $L$  and from  $T$  to  $T_s$

$$dq/dA \int_0^L \frac{dn}{(1 + n/r_1)(1 + n/r_2)} = -k \int_T^{T_s} dT \quad (5)$$

or after integration and the substitution of the limits

$$\frac{dq/dA}{1/r_2 - 1/r_1} \ln \frac{1 + L/r_2}{1 + L/r_1} = k(T - T_s) \quad (6)$$

Solving equations (3) and (6) for their respective temperature drops, adding the two equations to eliminate  $T_s$ , and rearranging

$$dq/dA = \frac{k(1/r_2 - 1/r_1)(T - T_\infty)}{\frac{(k/h)(1/r_2 - 1/r_1)}{(1 + L/r_1)(1 + L/r_2)} + \ln \frac{1 + L/r_2}{1 + L/r_1}} \quad (7)$$

differentiating equation (7) with respect to  $L$  and setting  $d(dq/dA)/dL$  equal to zero, yields after some manipulation

$$\frac{d}{dL} \left( \frac{dq}{dA} \right) = \frac{1}{L_{cr} + r_1} + \frac{1}{L_{cr} + r_2} - \frac{h}{k} = 0 \quad (8)$$

as  $L_{cr}$  changes from a value smaller than the critical to a value larger than the critical, the sign of  $d(dq/dA)/dL$  changes from positive to negative, thus indicating that the extremum given by equation (8) is a maximum. Since  $L_{cr} + r_1$  and  $L_{cr} + r_2$  are the principal radii of the critically insulated surface  $R_1$  and  $R_2$ , we can rewrite the equation

$$\frac{h}{k} = \frac{1}{R_1} + \frac{1}{R_2} = K_{m_{cr}} \quad (9)$$

where  $K_{m_{(cr)}}$  is the critical mean curvature of the fluid-solid interface. Equation (8) may be solved for the critical insulation thickness

$$\frac{hL_{cr}}{k} = 1 - \frac{h(r_1 + r_2)}{2k} \pm \left\{ 1 + \left[ \frac{h(r_1 - r_2)}{2k} \right]^2 \right\}^{1/2} \quad (10)$$

but when  $r_1$  or  $r_2 \rightarrow \infty$  the solution becomes difficult to evaluate.

## Discussion

For the sphere where  $R_1 = R_2 = R$  equation (9) yields  $h/k = 2/R_{cr}$ , and for the long, right circular cylinder where one principal radius approaches infinity  $h/k = 1/R_{cr}$ , thus equation (9) is in agreement with the two solutions for one-dimensional heat flow as given by Schneider [5]. It follows as a consequence of equation (9) that when  $h$  is known as a function of the location on a surface, a surface may be described that will be the boundary of a volume of maximum heat transfer. The special case of a right cylinder with variable unit conductance has been considered by E. M. Sparrow [6]. The assumption, made in the derivation of equation (9), that the heat flow is normal to the surface, may be invalid if the thermal resistance normal to the surface is large compared to the resistance parallel to the surface.

## References

- 1 Thomson, W., *Nature*, Vol. XXIX, 1884, p. 567.
- 2 Porter, A. W., and Martin, T. R., *Phil. Mag.*, Vol. 20, 1910, pp. 511-522.
- 3 Day, V. S., *Univ. Ill. Eng. Expt. Sta. Bull.*, 117, 1920.
- 4 Strunk, T. H., *Theoret. Biol.*, Vol. 33, 1971, pp. 35-61.
- 5 Schneider, J. P., *Conduction Heat Transfer*. Addison Wesley, Cambridge, Ma., 1955.
- 6 Sparrow, E. M. *A.I.Ch.E. J.*, Vol. 16, 1970, p. 149.

## Optimization of Inclined Convective Fins

David Pnueli<sup>1</sup>

A new type of fins has been recently used in the electronics industry in cases where large quantities of heat must be removed from small spaces. These fins are rather short and thick. They come out of a heavy backplate and have the properties that: (a) temperature variations between the fin's root and fin's tip are negligible, i.e., the fin is isothermal in the direction perpendicular to its backplate, and (b) convection coefficients vary in the streamwise direction. The need for such designs has led to the analytical and experimental investigations in references [1-3].<sup>2</sup>

The over-all size of the finned walls ( $B$ ,  $H$ , Fig. 1) are usually determined by the size of the electronic equipment. The thickness, the number and length ( $d$ ,  $b$ ,  $L$ , Fig. 1) of the fins are determined by heat transfer considerations (references [1], [3]), by manufacturing considerations, by structural requirements and by the tendency to use standard elements whenever possible.

The heat dissipated from such vertical fins can be increased by inclining them to some angle to the direction of the gravity force. This note demonstrates this possibility.

The local convection coefficient for closely spaced vertical fins decreases with increasing fin length, because the air flowing along the fins is already heated by their lower sections. Inclining the fins has two opposite physical effects. It can cause their length to decrease (Fig. 2), thus increasing heat transfer coefficients (or to increase, depending on the geometry,  $H$ ,  $B$ ,  $b$ , Figs. 1 and 2, and on the inclination angle). It always, however, weakens the effect of gravity, thus decreasing heat transfer coefficients. The optimal inclination angle is thus obtained when the effect (combined for all fins) of the decrease in the fins' length is just balanced by that of the weakened gravity.

To obtain some general numerical results, the average Nusselt number for heat convection from the fins is now estimated, as being proportional to the Grashof number to the power of  $1/4$ .<sup>3</sup> This estimate is based on results obtained for inclined flat plates (references [4, 5]), for long isothermal fins or large isothermal square fins (reference [1]), for long vertical isothermal conduits (reference [2]), and for parallel plates (references [6, 7]). Thus,

$$Nu \propto Gr^{1/4}$$

<sup>1</sup> Department of Fluid, Thermal and Aerospace Sciences, School of Engineering, Case Western Reserve University, Cleveland, Ohio.

<sup>2</sup> Numbers in brackets designate References at end of technical brief.

<sup>3</sup> This estimate is theoretically justifiable for boundary layer type flows only. For long enough fins the growing boundary layers for each fin of an adjacent pair will eventually merge. However, the same dependence of  $Nu$  on  $Gr$  has been observed for cases with such merged boundary layers, references [1, 2].

Contributed by the Heat Transfer Division of THE AMERICAN SOCIETY OF MECHANICAL ENGINEERS. Manuscript received by the Heat Transfer Division January 17, 1974.

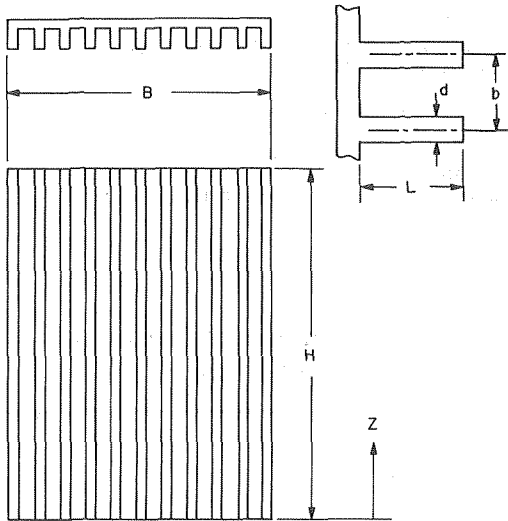


Fig. 1 Geometry of straight fins

The Grashof number depends on the fin's length and on the modified<sup>4</sup> action of gravity:

$$Gr \propto \cos\gamma L^3$$

The total amount of heat transferred from a fin depends of course on the average convection coefficient for that fin and on the fin length:

$$Q \propto h \times L \propto Nu$$

Substitution of the first two equations into the third and summation over all the fins for a given backplate, yield the total heat transferred for that backplate:

$$Q_T = \sum Q \propto \sum (\cos\gamma)^{1/4} \times L_n^{3/4}$$

It is assumed that for a given backplate this quantity must be optimized.

For a particular case several inclination angles can be tried, each individual fin can be considered, and  $Q_T$  can be used for the

<sup>4</sup> For upward-facing inclined surfaces, it has been demonstrated experimentally that a pattern of longitudinal vortices is superposed on the main streamwise natural convection flow. The simple cosine modification of gravity in  $G_R$  is therefore limited to inclination angles which are not too large and to fins which are sufficiently close to each other.

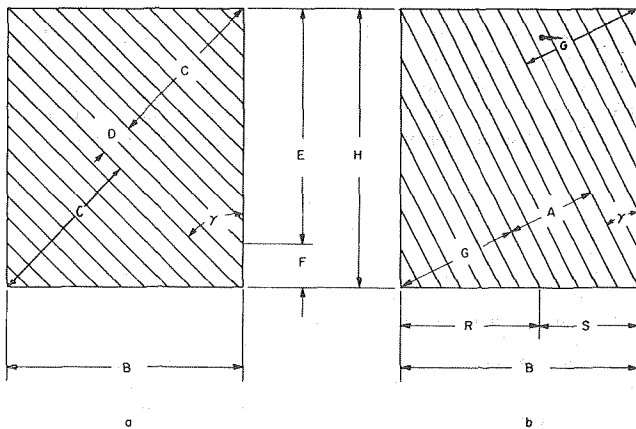


Fig. 2 Tilted fins (note that C and G represent two antisymmetric parts each)

optimization. To obtain some general results it is assumed that the number of the fins is very large, i.e., the gain or loss of a single fin in the summation is not important.

The considered rectangular region, Fig. 2, breaks naturally into two subregions—one in which the length of all the inclined fins is the same ( $D$  in Fig. 2(a),  $A$  in Fig. 2(b)) and one in which they vary ( $C$  in Fig. 2(a),  $G$  in Fig. 2(b)), both consisting of two antisymmetric parts). For very large  $H/B$  values and small tilt angles<sup>5</sup> the  $G$  regions can be neglected with respect to the  $A$  region, while for very small  $H/B$  values the  $C$  regions can be neglected with respect to the  $D$  regions. Since most cases of interest are for moderate  $H/B$  values, all regions must be considered. Because the formulation of the geometry is different for

$$\tan\gamma \geq B/H \quad \text{Case A (Fig. 2(a))}$$

and for

$$\tan\gamma \leq B/H \quad \text{Case B (Fig. 2(b))}$$

it is convenient to consider the two cases separately.

Case A. (Fig. 2(a)),  $\tan\gamma \geq B/H$ .

In the  $D$  Region.

$$D = F \sin\gamma = (H - E) \sin\gamma = H \sin\gamma - B \cos\gamma$$

The number of fins in the  $D$  region is

$$N_D = D/b = (H/b) \sin\gamma - (B/b) \cos\gamma$$

and the length of each fin:

$$L_D = B/\sin\gamma$$

The contribution of all the fins in the  $D$  region to the total heat transfer is

$$Q_D \propto N_D \times L_D \times h = [(H/b) \sin\gamma - (B/b) \cos\gamma] (B/\sin\gamma)^{3/4} (\cos\gamma)^{1/4} \quad (1)$$

In the  $C$  Region.

$$C = B \cos\gamma$$

The number of fins in one of the  $C$  regions is

$$N_C = C/b = (B/b) \cos\gamma$$

The length of these fins vary and they must be counted individually

$$Q_C \propto 2(\cos\gamma)^{1/4} \sum_{n=1}^{N_C} (L_D \times n/N_C)^{3/4} = 2(\cos\gamma)^{1/4} [b/(\sin\gamma \cos\gamma)]^{3/4} \sum_{n=1}^{N_C} N^{3/4} \quad (2)$$

The best tilt angle  $\gamma$  for this case is that which makes the total heat transferred

$$Q_T = Q_D + Q_C \quad (3)$$

a maximum.

Case B. (Fig. 2(b)),  $\tan\gamma \leq B/H$ .

In the  $A$  Region.

$$A = S \cos\gamma = (B - R) \cos\gamma = B \cos\gamma - H \sin\gamma$$

The number of fins in the  $A$  region:

$$N_A = A/b = (B/b) \cos\gamma - (H/b) \sin\gamma$$

and the length of each fin

<sup>5</sup> This will always decrease the heat transferred because the fins become longer.

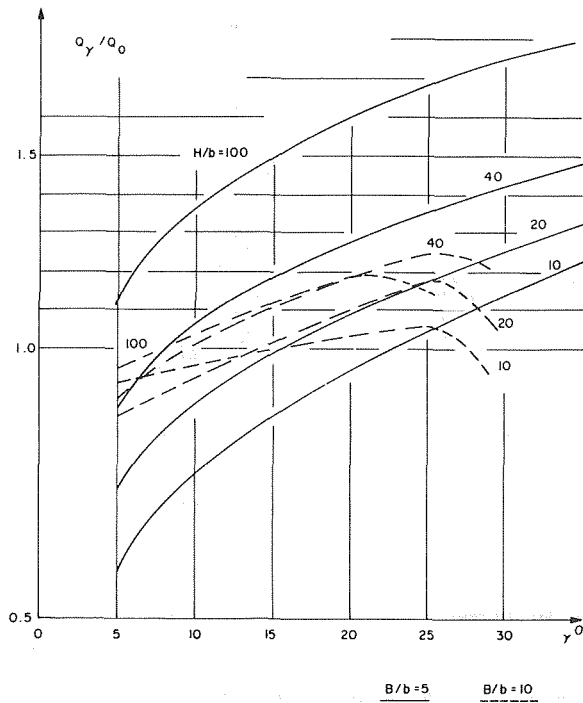


Fig. 3 Ratio of heat transfer improvement at various geometries

$$L_A = H/\cos\gamma$$

In a similar way to Case A, the total heat transfer in the A region:

$$Q_A \propto N_A \times L_A \times h = [(B/b) \cos\gamma - (H/b) \sin\gamma] (H/\cos\gamma)^{3/4} (\cos\gamma)^{1/4} \quad (4)$$

In the G Region.

$$G = H \sin\gamma$$

The number of fins in one of the G regions is

$$N_G = G/b = (H/b) \sin\gamma$$

In a similar way to Case A, the total heat transfer for the two G regions:

$$Q_G \propto 2(\cos\gamma)^{1/4} \sum_{n=1}^{N_G} (L_A \times n/N_G)^{3/4} = 2(\cos\gamma)^{1/4} [b/(\sin\gamma \cos\gamma)]^{3/4} \sum_{n=1}^{N_G} n^{3/4} \quad (5)$$

The best tilt angle  $\gamma$  for this case is that which makes

$$Q_T = Q_A + Q_G \quad (6)$$

a maximum.

The results of the optimizations<sup>6</sup> of equations (3) and (6) must be compared and the larger value is chosen.

Some typical heat transfer modifications are presented in Fig. 3.

For very small  $\gamma$  the region G can be neglected compared to the region A, while all fins in A become longer; thus heat transfer is decreased, i.e.,  $Q_\gamma/Q_0 < 1$ . For very large  $\gamma$ ,  $\cos\gamma$  becomes very

small and again  $Q_\gamma/Q_0 < 1$ . Because for some  $\gamma$ ,  $Q_\gamma/Q_0 > 1$  (as shown by the computed values),  $Q_\gamma/Q_0$  as a function of  $\gamma$  for constant  $H/b$  and  $B/b$  must have a maximum. This maximum is shown for  $B/b = 10$ , while for  $B/b = 5$  it occurs for  $\gamma > 35$  deg, which is approximately the limit to the  $\gamma$  values for which the considerations of this note exactly apply (reference [4]).

While the possibility of increasing total rates of heat transfer by the use of inclined fins has been demonstrated, there is some danger in the direct use of the numerical results, because of the limitations of the assumed Nu-Gr relations. However, the knowledge of these relations for a particular case, will make the computation method directly applicable, and the optimization can be achieved.

## References

- 1 Elenbaas, W., "Heat Dissipation of Parallel Plates by Free Convection," *Physica*, Vol. 9, No. 1, 1942, p. 1.
- 2 Elenbaas, W., "The Dissipation of Heat by Free Convection, The Inner Surface of Vertical Tubes of Different Shapes of Cross-Section," *Physica*, Vol. 9, No. 9, 1942, p. 865.
- 3 Elenbaas, W., "Dissipation of Heat by Free Convection, Part II," *Philips Res. Rep.* Vol. 3, 1948, p. 450.
- 4 Rich, B. R., "An Investigation of Heat Transfer From an Inclined Flat Plate in Free Convection," ASME Paper No. 52-F-20.
- 5 Eckert, E. R. G., and Drake, R. M., *Heat and Mass Transfer*, McGraw-Hill, New York, 1959.
- 6 Ostrach, S., "On Pairs of Solutions of a Class of Internal Viscous Flow Problems With Body Forces," NACA TN 4273, 1958.
- 7 Sparrow, E. M., and Gregg, J. L., "Laminar Free Convection From a Vertical Plate With Uniform Surface Heat Flux," ASME, Paper No. 55-SA-4.

## On Solving the Transient Conducting Slab With Radiating and Convecting Surfaces

J. L. Milton<sup>1</sup>  
W. P. Goss<sup>2</sup>

### Nomenclature

- $\mathcal{F}$  = combined geometry and emissivity factor
- $L$  = characteristic length
- $M$  = maximum number of nodes
- $N$  =  $hL/K$ , Biot number
- $R$  =  $\Delta\tau/(\Delta X)^2$
- $x$  = space coordinate
- $X$  =  $x/L$  dimensionless distance
- $\beta$  = stability parameter
- $\theta_i$  =  $T_i/T_{\text{reference}}$  (cooling- $T_{\text{reference}} = T_0$ ; heating- $T_{\text{reference}} = T_R$ )
- $\tau$  =  $\alpha t/L^2$ , Fourier number
- $\psi$  =  $k/\sigma\mathcal{F}L^3 T_{\text{reference}}^3$  (cooling- $T_{\text{reference}} = T_0$ ; heating- $T_{\text{reference}} = T_R$ ) radiation number

### Superscript

$n, n+1, \dots$  = time sequence

<sup>1</sup> Member of Technical Staff, Bell Telephone Laboratories, Inc., Columbus, Ohio. Assoc. Mem. ASME

<sup>2</sup> Assoc. Professor, Mechanical and Aerospace Engineering, University of Massachusetts, Amherst, Mass. Mem. ASME

Contributed by the Heat Transfer Division of The American Society of Mechanical Engineers. Manuscript received by the Heat Transfer Division April 30, 1974.

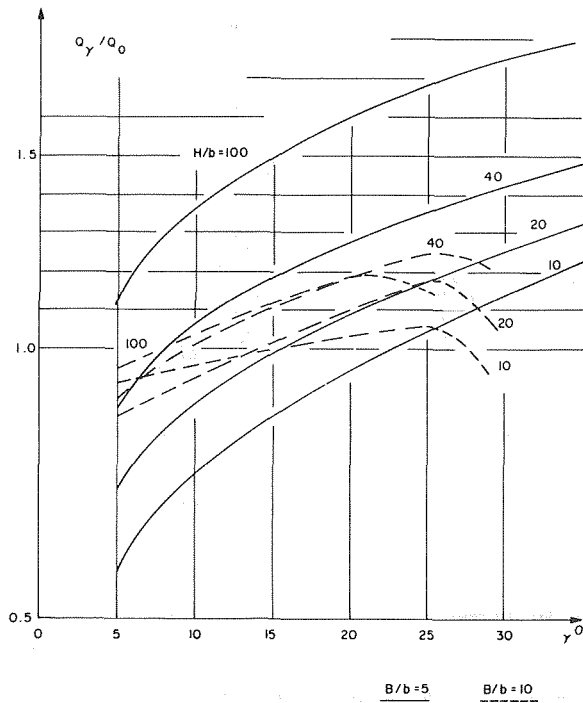


Fig. 3 Ratio of heat transfer improvement at various geometries

$$L_A = H/\cos\gamma$$

In a similar way to Case A, the total heat transfer in the A region:

$$Q_A \propto N_A \times L_A \times h = [(B/b) \cos\gamma - (H/b) \sin\gamma] (H/\cos\gamma)^{3/4} (\cos\gamma)^{1/4} \quad (4)$$

In the G Region.

$$G = H \sin\gamma$$

The number of fins in one of the G regions is

$$N_G = G/b = (H/b) \sin\gamma$$

In a similar way to Case A, the total heat transfer for the two G regions:

$$Q_G \propto 2(\cos\gamma)^{1/4} \sum_{n=1}^{N_G} (L_A \times n/N_G)^{3/4} = 2(\cos\gamma)^{1/4} [b/(\sin\gamma \cos\gamma)]^{3/4} \sum_{n=1}^{N_G} n^{3/4} \quad (5)$$

The best tilt angle  $\gamma$  for this case is that which makes

$$Q_T = Q_A + Q_G \quad (6)$$

a maximum.

The results of the optimizations<sup>6</sup> of equations (3) and (6) must be compared and the larger value is chosen.

Some typical heat transfer modifications are presented in Fig. 3.

For very small  $\gamma$  the region G can be neglected compared to the region A, while all fins in A become longer; thus heat transfer is decreased, i.e.,  $Q_\gamma/Q_0 < 1$ . For very large  $\gamma$ ,  $\cos\gamma$  becomes very

small and again  $Q_\gamma/Q_0 < 1$ . Because for some  $\gamma$ ,  $Q_\gamma/Q_0 > 1$  (as shown by the computed values),  $Q_\gamma/Q_0$  as a function of  $\gamma$  for constant  $H/b$  and  $B/b$  must have a maximum. This maximum is shown for  $B/b = 10$ , while for  $B/b = 5$  it occurs for  $\gamma > 35$  deg, which is approximately the limit to the  $\gamma$  values for which the considerations of this note exactly apply (reference [4]).

While the possibility of increasing total rates of heat transfer by the use of inclined fins has been demonstrated, there is some danger in the direct use of the numerical results, because of the limitations of the assumed Nu-Gr relations. However, the knowledge of these relations for a particular case, will make the computation method directly applicable, and the optimization can be achieved.

## References

- 1 Elenbaas, W., "Heat Dissipation of Parallel Plates by Free Convection," *Physica*, Vol. 9, No. 1, 1942, p. 1.
- 2 Elenbaas, W., "The Dissipation of Heat by Free Convection, The Inner Surface of Vertical Tubes of Different Shapes of Cross-Section," *Physica*, Vol. 9, No. 9, 1942, p. 865.
- 3 Elenbaas, W., "Dissipation of Heat by Free Convection, Part II," *Philips Res. Rep.* Vol. 3, 1948, p. 450.
- 4 Rich, B. R., "An Investigation of Heat Transfer From an Inclined Flat Plate in Free Convection," ASME Paper No. 52-F-20.
- 5 Eckert, E. R. G., and Drake, R. M., *Heat and Mass Transfer*, McGraw-Hill, New York, 1959.
- 6 Ostrach, S., "On Pairs of Solutions of a Class of Internal Viscous Flow Problems With Body Forces," NACA TN 4273, 1958.
- 7 Sparrow, E. M., and Gregg, J. L., "Laminar Free Convection From a Vertical Plate With Uniform Surface Heat Flux," ASME, Paper No. 55-SA-4.

## On Solving the Transient Conducting Slab With Radiating and Convecting Surfaces

J. L. Milton<sup>1</sup>  
W. P. Goss<sup>2</sup>

### Nomenclature

- $\mathcal{F}$  = combined geometry and emissivity factor
- $L$  = characteristic length
- $M$  = maximum number of nodes
- $N$  =  $hL/K$ , Biot number
- $R$  =  $\Delta\tau/(\Delta X)^2$
- $x$  = space coordinate
- $X$  =  $x/L$  dimensionless distance
- $\beta$  = stability parameter
- $\theta_i$  =  $T_i/T_{\text{reference}}$  (cooling- $T_{\text{reference}} = T_0$ ; heating- $T_{\text{reference}} = T_R$ )
- $\tau$  =  $\alpha t/L^2$ , Fourier number
- $\psi$  =  $k/\sigma\mathcal{F}L^3 T_{\text{reference}}^3$  (cooling- $T_{\text{reference}} = T_0$ ; heating- $T_{\text{reference}} = T_R$ ) radiation number

### Superscript

$n, n+1, \dots$  = time sequence

<sup>1</sup> Member of Technical Staff, Bell Telephone Laboratories, Inc., Columbus, Ohio. Assoc. Mem. ASME

<sup>2</sup> Assoc. Professor, Mechanical and Aerospace Engineering, University of Massachusetts, Amherst, Mass. Mem. ASME

Contributed by the Heat Transfer Division of The American Society of Mechanical Engineers. Manuscript received by the Heat Transfer Division April 30, 1974.

## Subscripts

$i$  = spacial nodes  
 $R$  = radiant  
 $\theta$  = initial } temperature  
 $\infty$  = ambient }

## Introduction

Interest in digital and analog computer solutions to transient conducting bodies with radiating surfaces may be seen by the literature in the area; see references [1-3]<sup>3</sup> for a bibliography.

Frequently physical reasoning and engineering judgment may be used to tackle complex physical problems where mathematical theories have not been developed. One particular class of problems where the above procedure has been applied was that of a conducting slab with radiating and convecting surfaces. This slab was characterized by one-dimensional, transient heat transfer. While many approximate solutions have been applied to this problem, little discussion has appeared in the literature on stability criteria for explicit finite-difference solutions to the present problem [4, 5]. This is the scope of the present communication. The difficulty arises from the nonlinear boundary condition due to the  $\theta^4$  term due to thermal radiation.

## Analysis

Such a physical problem is governed by the following dimensionless equation:

$$\partial\theta/\partial\tau = \partial^2\theta/\partial X^2 \quad (1)$$

with initial condition  $\theta(X, 0) = \theta_0$ , symmetry boundary condition

$$\partial\theta(0, \tau)/\partial X = 0, \text{ and}$$

$$-\partial\theta(1, \tau)/\partial X = N[\theta(1, \tau) - \theta_\infty] + \psi^{-1}[(\theta(1, \tau))^4 - \theta_R^4]$$

The second boundary condition above relates the heat transfer governed by the Fourier conduction law to that of the Stefan-Boltzmann radiation law and the Newton "law" of cooling. Further, it may be noted that the standard stability criteria for explicit finite-differences to linear parabolic systems [6, 7] are not applicable.

Equation (1) along with the boundary and initial conditions may be discretized as shown in references [4, 5] and the surface node yields:

$$\Delta\theta_M/\Delta\tau = A - B\theta_M - C\theta_M^4 \quad (2)$$

where

$$\Delta\theta_M = \theta_M^{n+1} - \theta_M^n;$$

$$A = 2[\psi^{-1}\Delta X\theta_R^4 + N\Delta X\theta_\infty + \theta_{M-1}^n]/(\Delta X)^2;$$

$$B = 2[N\Delta X + 1]/(\Delta X)^2, \text{ and } C = 2\psi^{-1}\Delta X/(\Delta X)^2.$$

These results will be used below to develop stability conditions.

## Discussion of Stability Development

Equation (2) is the governing finite-difference relation for the surface node of the slab where  $i = M$ . For a given physical problem, at a given time level,  $\tau^n$ , the quantities  $\psi$ ,  $\Delta X$ ,  $\theta_R$ ,  $\theta_\infty$ , and  $\theta_{M-1}^n$  are all fixed. Then for a slab heating from initial constant temperature,  $\theta_0$ ,  $\Delta\theta_M/\Delta\tau \geq 0$ . Hence equation (2) may be solved for the maximum value of  $\theta_M$  consistent with the physically occurring phenomenon:  $\theta_M^n[\max] \leq A/(B + C(\theta_M^n)^3)$ . Previously it was noted that a nonlinear relation exists for the solution of the surface temperature. From equation (2) with the present restriction of  $\Delta\theta_M/\Delta\tau \geq 0$  it may be noted that the fourth degree polynomial has four roots. Of these four roots two form a complex conjugate pair

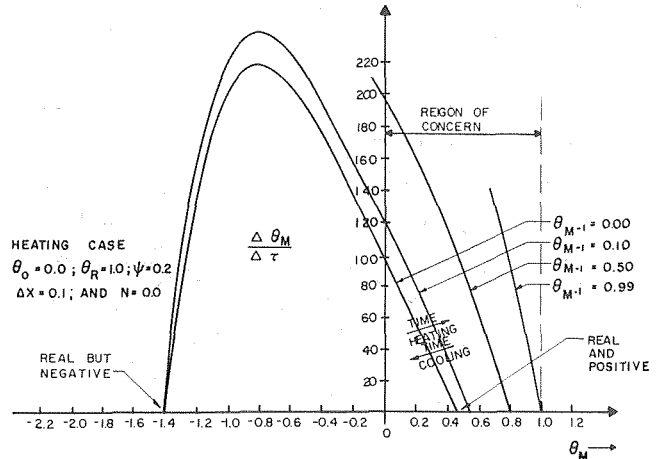


Fig. 1 Plot of  $\Delta\theta_M/\Delta\tau$  versus (real)  $\theta_M$  with  $\theta_{M-1}$  as a parameter

and two are real: 1 positive and 1 negative. Fig. 1 shows a typical plot of the real roots. Since the complex roots and the negative root can be eliminated on physical grounds, the root of interest in the present study is the positive one.

Careful inspection of Fig. 1 reveals that the value of the dimensionless absolute temperature is bounded in the interval  $[0, 1]$ ; this is consistent with physical reality for the range of  $\theta_{M-1}^n$ . The effect of heating versus cooling is also shown on Fig. 1 along with the effect of temperature of the node adjacent to the surface. Space is not available in the present work, but a plot of  $\Delta\theta_M/\Delta\tau$  versus  $\theta_M$  with  $\psi$  as a parameter would reveal that the solution to  $\theta_M^n[\max]$  is very sensitive for small values of  $\psi$ . Thus, physically it may be noted that if the time-step-size is too long, especially with small values of  $\psi$ , thermodynamic principles (the second law) will be violated and temperatures may oscillate violently. This is especially true for cases with high heat fluxes. This physical situation may be seen from the definition of  $\psi$ , i.e., for small values of the thermal conductivity or large values of dimensionless temperature  $\theta_R$ .

It is for the highly nonlinear boundary conditions that the previous stability criteria for linear systems are not adequate. Thus, the instability manifests itself by violent oscillations of calculated values of temperature [5]. But because these oscillating values of temperature violate thermodynamic principles [4, 5], these temperatures are meaningless and must be discarded. However, the derivative method [5] of stability analysis has been found to be stable over the entire range of practical values of parameters. The result of that method is written:  $\partial\theta_M^{n+1}/\partial\theta_M^n \geq 0$  for a heating slab.

Physical reality dictates that for the present heating slab:  $\Delta\theta_M/\Delta\tau \geq 0$ . From equation (2) the solution for the maximum value of  $\theta_M$  consistent with the previously given condition is obtained by iterative numerical computations. This value of  $\theta_M$  is used in the governing equation for node  $M$  to be solved for  $\Delta\tau$  to yield:

$$\Delta\tau \leq (\Delta X)^2 \left\{ \theta_M^n[\max] - \theta_M^n \right\} / 2 \left\{ \theta_{M-1}^n - \theta_M^n \right\} + \psi^{-1} \Delta X \left[ \theta_R^4 - (\theta_M^n)^4 \right] + N \Delta X \left[ \theta_\infty - \theta_M^n \right]$$

This value of  $\Delta\tau$  compares very favorably with the one from the derivative method. Fig. 2 shows the nature of the trend of the value of  $\psi$  on the time-step-size and how  $\Delta\tau$  varies with  $\tau$ . Moreover, the value of  $\Delta\tau$  appears to be bounded above by the constant temperature boundary condition and below by the linearized radiation boundary condition; see Fig. 2.

Here it is noted that the surface node of this slab has the most restrictive stability conditions. For other geometries or boundary conditions, this may not be true [4]. One may prefer to use the "derivative" method to the present "explicit" method because the de-

<sup>3</sup> Numbers in brackets designate References at end of paper.

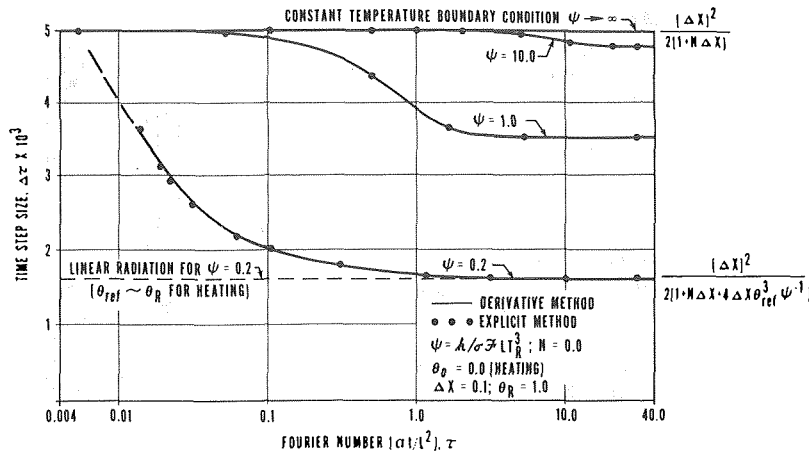


Fig. 2 Comparison of the "explicit method" and the "derivative method" of stability analysis

derivative method can be written in a closed form. The present method requires that the fourth degree polynomial be solved at each time step. And numerical difficulty in predicting  $\Delta\tau$  may be experienced near the steady-state solution. This work should supplement the work presented in [5]. Temperature results from the derivative method [5] were identical to those in the published literature. However, results from stability conditions for linear equations [6, 7] were found to be unstable above critical values of the radiation parameter [5]. And the derivative method yields the method of Dusingherre as a special case. Moreover, heating tended to be more restrictive numerically than did cooling.

While the foregoing discussion centered on the case of a heating slab, a parallel argument holds for the case of a monotonically cooling slab. Note must be given to the difference in definition of  $\psi$  and  $\theta$  for the heating versus the cooling case. Further, for cooling:  $\Delta\theta/\Delta\tau \leq 0$ . With the above limitations, these results, like those of the derivative method, hold equally well for heating and cooling slabs [4], but  $\Delta\tau$  increases with time for the cooling slab.

### Conclusions

The present investigation reports the development of an "explicit" stability criteria consistent with energy conservation principles. Results from the solution of the governing fourth degree polynomial are consistent with those from the "derivative" method. The time-step-size appears to be bounded above by linear heat transfer and below by linearized radiation.

While the present method has been applied to a conducting slab, it appears to be equally applicable to other areas where the parabolic diffusion equation is applicable. Thus, it should prove to be a useful tool for explicit solutions to these problems and aid in understanding stability of a certain class of problems with nonlinearities.

### Acknowledgment

Appreciation is expressed to the University of Massachusetts for providing a University Fellowship to J. L. Milton during the time over which this work was completed.

### References

- Zerkle, R. D., and Sunderland, J. E., "The Transient Temperature Distribution in a Slab Subject to Thermal Radiation," JOURNAL OF HEAT TRANSFER, TRANS. ASME, Series C., Vol. 87, 1965, pp. 117-133.
- Crosbie, A. L., and Viskanta, R., "Transient Heating or Cooling of a Plate by Combined Convection and Radiation," International Journal of Heat and Mass Transfer, Vol. 11, 1968, pp. 305-317.
- Ayers, D. L., "Transient Cooling of a Sphere in Space," JOURNAL OF HEAT TRANSFER, TRANS. ASME, Series C., Vol. 92, 1970, pp. 180-182.
- Milton, J. L., "Stability Criteria for Explicit Finite Difference Solutions of the Parabolic Diffusion Equation With Nonlinear Boundary Condi-

tions," PhD thesis, Mechanical and Aerospace Engineering, University of Massachusetts, 1973.

5 Milton, J. L., and Goss, W. P., "Stability Criteria for Explicit Finite Difference Solutions of the Parabolic Diffusion Equation With Nonlinear Boundary Conditions," Int. J. Num. Meth. Engng. Vol. 7, 1973, pp. 57-67.

6 Dusingherre, G. M., "Numerical Methods for Transient Heat Flow," JOURNAL OF HEAT TRANS., TRANS. ASME, Series C, Vol. 67, 1945, pp. 703-712.

7 Smith, G. D., Numerical Solution of Partial Differential Equations, 1st ed., Oxford University Press, New York, 1965, pp. 60-97.

## The Temperature of Cavity-Type Solar Absorbers With a Circulating Fluid<sup>1</sup>

M. Abrams<sup>2</sup>

### Nomenclature

- $A$  = area  
 $Q$  = radiative flux entering aperture  
 $t$  = dimensionless temperature,  $T/T_{ref}$   
 $u$  = dimensionless overall heat transfer coefficient,  $U/(\sigma T_{ref}^3)$

### Subscripts

- $c$  = cavity  
 $f$  = fluid  
 $i$  = inlet  
 $o$  = outlet  
 $1$  = refers to aperture area  
 $2$  = refers to area of interior surface of cavity

### Superscript

- = refers to average of a quantity

<sup>1</sup> This work was supported by the United States Atomic Energy Commission, Contract Number AT-(29-1)-789.

<sup>2</sup> Aerothermodynamics Division 8111, Sandia Laboratories, Livermore, Calif. Mem. ASME.

Contributed by the Heat Transfer Division of THE AMERICAN SOCIETY OF MECHANICAL ENGINEERS. Manuscript received by the Heat Transfer Division June 20, 1974.

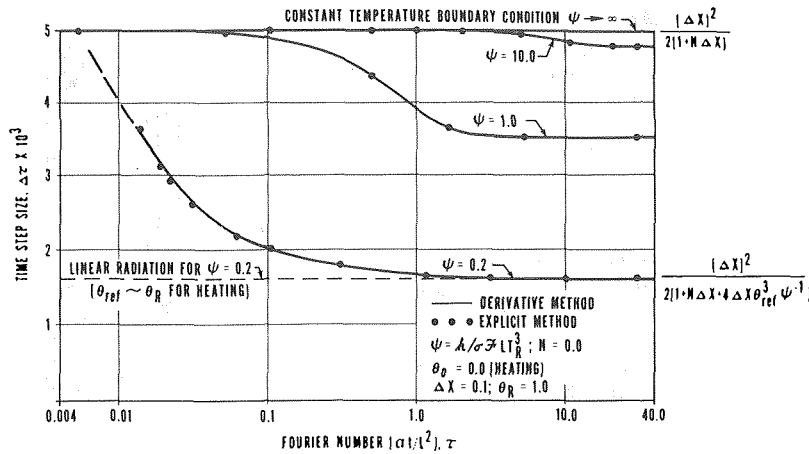


Fig. 2 Comparison of the "explicit method" and the "derivative method" of stability analysis

derivative method can be written in a closed form. The present method requires that the fourth degree polynomial be solved at each time step. And numerical difficulty in predicting  $\Delta\tau$  may be experienced near the steady-state solution. This work should supplement the work presented in [5]. Temperature results from the derivative method [5] were identical to those in the published literature. However, results from stability conditions for linear equations [6, 7] were found to be unstable above critical values of the radiation parameter [5]. And the derivative method yields the method of Dusinger as a special case. Moreover, heating tended to be more restrictive numerically than did cooling.

While the foregoing discussion centered on the case of a heating slab, a parallel argument holds for the case of a monotonically cooling slab. Note must be given to the difference in definition of  $\psi$  and  $\theta$  for the heating versus the cooling case. Further, for cooling:  $\Delta\theta/\Delta\tau \leq 0$ . With the above limitations, these results, like those of the derivative method, hold equally well for heating and cooling slabs [4], but  $\Delta\tau$  increases with time for the cooling slab.

### Conclusions

The present investigation reports the development of an "explicit" stability criteria consistent with energy conservation principles. Results from the solution of the governing fourth degree polynomial are consistent with those from the "derivative" method. The time-step-size appears to be bounded above by linear heat transfer and below by linearized radiation.

While the present method has been applied to a conducting slab, it appears to be equally applicable to other areas where the parabolic diffusion equation is applicable. Thus, it should prove to be a useful tool for explicit solutions to these problems and aid in understanding stability of a certain class of problems with nonlinearities.

### Acknowledgment

Appreciation is expressed to the University of Massachusetts for providing a University Fellowship to J. L. Milton during the time over which this work was completed.

### References

- Zerkle, R. D., and Sunderland, J. E., "The Transient Temperature Distribution in a Slab Subject to Thermal Radiation," *JOURNAL OF HEAT TRANSFER*, TRANS. ASME, Series C., Vol. 87, 1965, pp. 117-133.
- Crosbie, A. L., and Viskanta, R., "Transient Heating or Cooling of a Plate by Combined Convection and Radiation," *International Journal of Heat and Mass Transfer*, Vol. 11, 1968, pp. 305-317.
- Ayers, D. L., "Transient Cooling of a Sphere in Space," *JOURNAL OF HEAT TRANSFER*, TRANS. ASME, Series C., Vol. 92, 1970, pp. 180-182.
- Milton, J. L., "Stability Criteria for Explicit Finite Difference Solutions of the Parabolic Diffusion Equation With Nonlinear Boundary Condi-

tions," PhD thesis, Mechanical and Aerospace Engineering, University of Massachusetts, 1973.

5 Milton, J. L., and Goss, W. P., "Stability Criteria for Explicit Finite Difference Solutions of the Parabolic Diffusion Equation With Nonlinear Boundary Conditions," *Int. J. Num. Meth. Engrg.* Vol. 7, 1973, pp. 57-67.

6 Dusinger, G. M., "Numerical Methods for Transient Heat Flow," *JOURNAL OF HEAT TRANS.*, TRANS. ASME, Series C, Vol. 67, 1945, pp. 703-712.

7 Smith, G. D., *Numerical Solution of Partial Differential Equations*, 1st ed., Oxford University Press, New York, 1965, pp. 60-97.

## The Temperature of Cavity-Type Solar Absorbers With a Circulating Fluid<sup>1</sup>

M. Abrams<sup>2</sup>

### Nomenclature

- $A$  = area  
 $Q$  = radiative flux entering aperture  
 $t$  = dimensionless temperature,  $T/T_{ref}$   
 $u$  = dimensionless overall heat transfer coefficient,  $U/(\sigma T_{ref}^3)$

### Subscripts

- $c$  = cavity  
 $f$  = fluid  
 $i$  = inlet  
 $o$  = outlet  
 1 = refers to aperture area  
 2 = refers to area of interior surface of cavity

### Superscript

- = refers to average of a quantity

<sup>1</sup>This work was supported by the United States Atomic Energy Commission, Contract Number AT-(29-1)-789.

<sup>2</sup>Aerothermodynamics Division 8111, Sandia Laboratories, Livermore, Calif. Mem. ASME.

Contributed by the Heat Transfer Division of THE AMERICAN SOCIETY OF MECHANICAL ENGINEERS. Manuscript received by the Heat Transfer Division June 20, 1974.



## Introduction

The purpose of this brief is to provide a simple analytical expression for the effective temperature of a cavity-type absorber of radiative energy when a heat transfer fluid is circulated through the cavity. By effective temperature, we mean that temperature which characterizes the radiative emission loss from the cavity aperture and which drives the absorbed energy into the heat transfer fluid.

The model of the cavity under consideration is shown in Fig. 1. Fluid flowing at the rate  $\dot{m}$  passes between the walls of the cavity and a perfectly insulated casing, and, by convective heat exchange, experiences the temperature rise  $(T_{f,o} - T_{f,i})$ . Diffuse radiation flux, assumed to be uniformly distributed over the aperture area, enters the cavity, where it is partially absorbed, and this absorbed energy is conducted through the cavity wall into the heat transfer fluid.

In two previous analyses of cavity-type absorbers [1, 2],<sup>3</sup> performance was assessed for an assumed temperature distribution over the interior surface area of the cavity. Actually, however, in many applications the cavity temperature can be strongly influenced by the presence of the heat transfer fluid, and, hence, any *a priori* specification of this temperature can be very uncertain. In general, numerical solutions for the cavity temperature distribution, such as those reported in [3, 4], are required.

The results of this brief are intended for use in estimating the effective cavity temperature (and thereby rank-ordering various cavity design options) and are not intended to supplant any detailed numerical calculations for the temperature distribution.

The principal assumptions made are as follows: All physical properties are independent of temperature and are constants; reflectivity and emissivity are independent of wavelength; the interior surface emits energy in a diffuse manner; and the temperature distribution over this surface is uniform and corresponds to the effective cavity temperature. While a uniform cavity temperature is approached only under certain limiting situations,<sup>4</sup> this assumption is made because it leads to an extremely simple analytical result that accounts for all of the pertinent energy transfer processes: emission and reflection of energy from the cavity, conduction of energy through the cavity walls, and convection of energy by the heat transfer fluid. No restriction is placed upon the shape of the cavity, however, since the effects of cavity shape are incorporated into the apparent emissivity for that shape. (Literature sources for the apparent emissivities of various cavity shapes are cited later.) If the apparent emissivity is unknown for the particular cavity being considered it can be estimated as described herein.

## Theory

An energy balance at the plane of the aperture requires that the difference between the incoming and outgoing radiative energies equals the energy conducted through the cavity wall, i.e.,

$$(Q - R)A_1 = UA_2(T_c - \bar{T}_f) \quad (1)$$

where  $U$  is the effective conductance of the wall plus wall-fluid boundary. The radiative flux leaving the cavity,  $R$ , is simply the sum of the reflected and emitted fluxes and is expressed as

$$R = (1 - \epsilon_a)Q + \epsilon_a \sigma T_c^4 \quad (2)$$

The apparent emissivity,  $\epsilon_a$ , is a function of the actual emissivity of the cavity interior ( $\epsilon$ ) and the cavity geometry. Sparrow and Cess [5] give graphs of  $\epsilon_a$  for cylindrical, conical, and spherical cavities. (Results for the cylindrical and conical cavities are based upon numerical solutions of integral equations, while the results

<sup>3</sup>Numbers in brackets designate References at end of paper.

<sup>4</sup>As examples of such situations, uniform cavity temperature is approached as the magnitude of convective heat losses becomes small compared to radiative heat losses, and also as the transverse conductance of the wall decreases and the longitudinal conductance increases.

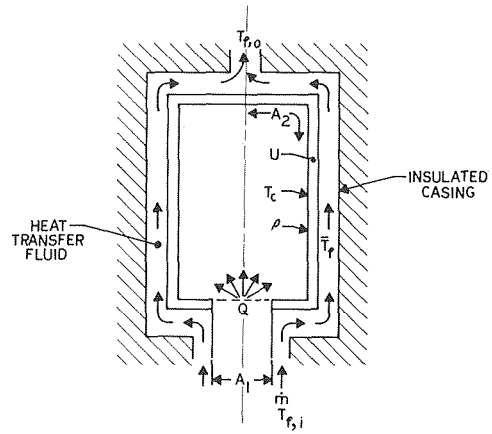


Fig. 1 Radiation-conduction-convection heat transfer model of solar radiation cavity

for the spherical cavity are based upon the analytical solution of reference [6].) A cavity having specularly reflecting surfaces may also be treated by the present formalism if the apparent emissivity of such a cavity is known. When dealing with cavity shapes for which there are not data for  $\epsilon_a$ , it is possible to estimate  $\epsilon_a$  by assuming that the cavity behaves as a two-zone enclosure (the zones being  $A_2$ , the interior surface area, and the fictitious surface formed by  $A_1$ , the area of the aperture; see Fig. 1). For example, it can easily be shown that the apparent emissivity of a cavity having diffusely reflecting walls is given by

$$\epsilon_a = 1/[1 + (A_1/A_2)\rho/\epsilon] \quad (3)$$

Eliminating  $R$  between equations (1) and (2)

$$\sigma T_c^4 + U(T_c - \bar{T}_f)(A_2/A_1)/\epsilon_a - Q = 0 \quad (4)$$

The temperature difference appearing in equation (4) is the so-called log-mean temperature difference (LMTD) that arises in heat exchanger theory. Omitting the details for brevity, it can be shown by an energy balance of the heat transfer fluid [7, p. 301] that,

$$(T_c - \bar{T}_f) = (\dot{m}C_p/UA_2)(T_c - T_{f,i})[1 - \exp(-UA_2/\dot{m}C_p)] \quad (5)$$

Substituting equation (5) into (4), and then normalizing the temperature by  $T_{\text{ref}}$  where

$$T_{\text{ref}} \equiv (Q/\sigma)^{1/4} \quad (6)$$

results in

$$t_c^4 + (t_c - t_{f,i})u(A_2/A_1)(1/\epsilon_a)[1 - \exp(-H)]/H - 1 = 0 \quad (7)$$

Physically,  $T_{\text{ref}}$  is the temperature which would be attained by the cavity in the absence of heat transfer to the fluid;  $T_{\text{ref}}$  is also the effective black-body temperature of the source. The parameter  $H$ , defined as  $UA_2/(\dot{m}C_p)$ , is simply the ratio of heat transfer capacity rate of the wall to heat transfer capacity rate of the fluid. A large value of  $H$  implies that the increase in fluid temperature is large compared with the temperature drop across the wall plus film resistance, and vice versa.

Equation (7) is a quartic equation which, as indicated below, has an exact solution. First, the role of the various terms in this equation is briefly commented upon. The first term represents energy loss from the cavity by emission; the second term is a measure of energy transfer to the fluid and cavity reflection losses; and the constant term  $(-1)$  is the dimensionless radiative flux input to the cavity. When the coefficients of  $(t_c - t_{f,i})$  are small (compared with unity), heat transfer from the cavity by mechanisms other than emission is small, and the cavity temperature approaches its

C. S. Fang<sup>1</sup> and H. W. Prengle, Jr.<sup>2</sup>

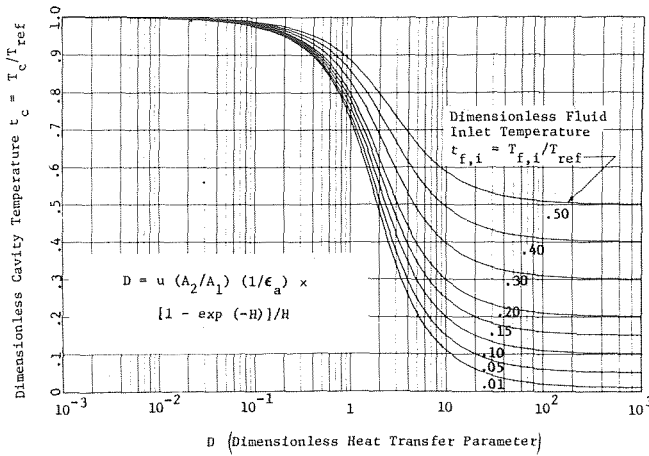


Fig. 2 Dimensionless cavity temperature as a function of the heat loss parameter,  $D$

theoretical maximum value, e.g.,  $t_c = 1$ . On the other hand, when these coefficients become large, the limit  $t_c = t_{f,i}$  is approached.

The solution of equation (7) is obtained following the method outlined in [8]. With the quantities  $D$ ,  $B$ , and  $Y$  respectively defined as

$$D = u(A_2/A_1)(1/\epsilon_a)[1 - \exp(-H)]/H \quad (8)$$

[the coefficient of  $(t_c - t_{f,i})$  in equation (7)]

$$B = \{1 + [(Dt_{f,i} + 1)/3]^3(4/D)^{1/2}\}^{1/2} \quad (9)$$

and

$$Y = (D^2/2)^{1/3}[(B + 1)^{1/3} - (B - 1)^{1/3}] \quad (10)$$

the solution is found to be

$$t_c = (1/2)[(2D/Y^{1/2} - Y)^{1/2} - Y^{1/2}] \quad (11)$$

## Results

The solution of equation (7) is plotted in Fig. 2 as a function of the heat transfer parameter,  $D$ , for several values of the dimensionless fluid inlet temperature,  $t_{f,i}$ . This graph may be employed to obtain the temperature of any cavity shape for which the apparent emissivity is known. If the apparent emissivity for the cavity shape of interest is unknown, it may be estimated from equation (3). Once  $t_c$  has been determined, the dimensionless temperature rise experienced by the heat transfer fluid may be computed from

$$t_{f,0} - t_{f,i} = (t_c - t_{f,i})[1 - \exp(-H)]$$

## References

- Stephans, C. W., and Haire, A. M., "Internal Design Considerations for Cavity-Type Solar Absorbers," *ARS Journal*, July 1961, pp. 896-901.
- Grilikhes, V. A., and Obtemperanskii, F. V., "Analysis of Radiative Heat Exchange Processes in Cylindrical Cavity-Type Collectors of Solar Power Plants," *Appl. Solar Energy*, Vol. 5, No. 1-2, 1969, pp. 59-65.
- Obtemperanskii, F. V., and Grilikhes, V. A., "Approximate Thermal Calculations for Cylindrical Cavity-Type Collectors With Liquid-Metal Heat-Transport Medium," *Appl. Solar Energy*, Vol. 5, No. 3-4, 1969, pp. 61-65.
- Sparrow, E. M., et al., "Radiation From Cavities With Nonisothermal Heat Conducting Walls," *JOURNAL OF HEAT TRANSFER*, TRANS. ASME, Series C, Vol. 96, 1974, pp. 15-20.
- Sparrow, E. M., and Cess, R. D., *Radiation Heat Transfer*, Brooks/Cole Publishing Co., Belmont, Calif. 1967, pp. 163-170.
- Sparrow, E. M., Jonsson, V. K., "Absorption and Emission Characteristics of Diffuse Spherical Enclosures," *JOURNAL OF HEAT TRANSFER*, TRANS. ASME, Series C, Vol. 84, 1962, pp. 188-189.
- Holman, J. P., *Heat Transfer*, 2nd ed., McGraw-Hill, New York, 1968.
- Selby, S. M., Ed., *Standard Mathematical Tables*, 19th Ed., The Chemical Rubber Co., Cleveland, 1967, p. 106.

In recent years there has been considerable interest in the remote sensing of gases using the infrared spectroscopic method. When it is desired to determine the temperature and composition of a remote gas volume, the processing of data involves lengthy computations due to the volumetric integration in the energy transfer equation. As an attempt to solve these problems, this work proposes a simplified equation of radiative energy transfer, using a shape factor to eliminate the volumetric integration. Shape factors for remote gas volumes of various geometries are presented.

The spectral radiant energy flux from an emitting gas volume to the surface of a telescope mirror,  $Q_{\bar{v}}$ , after atmospheric attenuation, is [1]:<sup>3</sup>

$$Q_{\bar{v}} = \int_V \int_{A_m} \frac{K_{\bar{v}} W_{B\bar{v}}(T)}{\pi} \frac{\cos(-\mathbf{b}, \mathbf{n})}{b^2} e^{-K_{\bar{v}} s} e^{-K_{\bar{v}}^{\text{atm}}(b-s)} dA_m dV, \quad (1)$$

where  $V$  and  $A_m$  are, respectively, the volume of gas volume within the field of view and area of the surface of the telescope mirror which receives the radiant energy flux.  $W_{B\bar{v}}$  is the emissive power of the black-body at the gas temperature,  $T$ , and  $s$  is the path-length of the flux beam  $\mathbf{b}$  from  $dV$  to  $dA_m$ .  $K_{\bar{v}}$  and  $K_{\bar{v}}^{\text{atm}}$  are, respectively, the linear absorption coefficients of the gas volume and the atmosphere. The vector  $\mathbf{n}$  is the normal unit vector of  $dA_m$ . Since there are  $n$  components in the gas volume,

$$K_{\bar{v}} = \sum_{i=1}^n K_{\bar{v},i} = \sum_{i=1}^n k_{\bar{v},i} p_i \quad (2)$$

where  $K_{\bar{v},i}$ ,  $k_{\bar{v},i}$ , and  $p_i$  are, respectively, the linear absorption coefficient, absorption coefficient ( $\text{cm}^{-1} \text{atm}^{-1}$ ), and the partial pressure of the  $i$ th component [2, 3].

The temperature of the gas volume is assumed constant; this assumption is acceptable since the field of view usually is small (for example, 1 m in diameter at the distance of 70 m), and it does not cover the entire gas effluent.

The shape of the gas volume depends on the volume itself and the size of the field of view of the telescope. When the field of view is small and completely covered by the gas, the gas volume  $V$  is approximately an inclined-cylindrical volume with one end facing the telescope. When the field of view is larger than the diameter of the gas volume,  $V$  is approximately a vertical-cylindrical volume as shown in Fig. 1. When the diameter of the field of view is equal to the diameter of the gas volume, and  $V$  and  $A_m$  are at the same height from the ground,  $V$  is the volume enclosed by two perpendicular, equal-diameter cylindrical surfaces.

If the gas volume is remote (i.e.,  $Y$  is much larger than the diameter and length of the gas volume, as well as the diameter of  $A_m$ ), equation (1) reduces to:

$$Q_{\bar{v}} = \frac{A_m}{Y^2} \frac{K_{\bar{v}} W_{B\bar{v}}(T)}{\pi} e^{-K_{\bar{v}}^{\text{atm}} Y} \int_V e^{-K_{\bar{v}} s} dV \quad (3)$$

<sup>1</sup> Assist. Professor, Chemical Engineering Department, University of Southwestern Louisiana, Lafayette, La.

<sup>2</sup> Professor, Chemical Engineering Department, University of Houston, Houston, Texas.

<sup>3</sup> Numbers in brackets designate References at end of technical brief.

Contributed by the Heat Transfer Division of THE AMERICAN SOCIETY OF MECHANICAL ENGINEERS. Manuscript received by the Heat Transfer Division January 24, 1974.

C. S. Fang<sup>1</sup> and H. W. Prengle, Jr.<sup>2</sup>

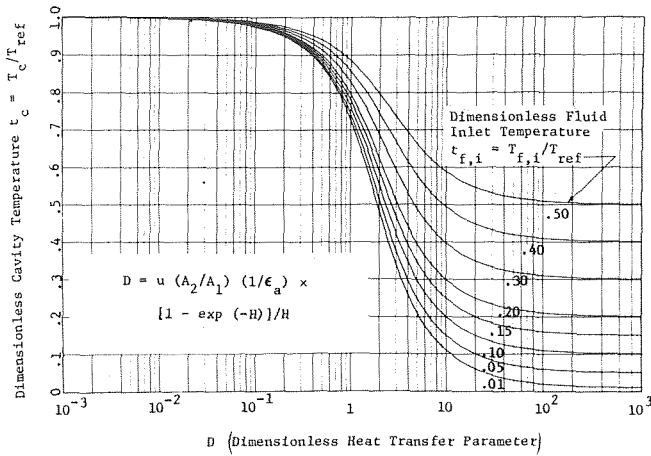


Fig. 2 Dimensionless cavity temperature as a function of the heat loss parameter,  $D$

theoretical maximum value, e.g.,  $t_c = 1$ . On the other hand, when these coefficients become large, the limit  $t_c = t_{f,i}$  is approached.

The solution of equation (7) is obtained following the method outlined in [8]. With the quantities  $D$ ,  $B$ , and  $Y$  respectively defined as

$$D = u(A_2/A_1)(1/\epsilon_a)[1 - \exp(-H)]/H \quad (8)$$

[the coefficient of  $(t_c - t_{f,i})$  in equation (7)]

$$B = \{1 + [(Dt_{f,i} + 1)/3]^3(4/D)^{1/2}\}^{1/2} \quad (9)$$

and

$$Y = (D^2/2)^{1/3}[(B + 1)^{1/3} - (B - 1)^{1/3}] \quad (10)$$

the solution is found to be

$$t_c = (1/2)[(2D/Y^{1/2} - Y)^{1/2} - Y^{1/2}] \quad (11)$$

## Results

The solution of equation (7) is plotted in Fig. 2 as a function of the heat transfer parameter,  $D$ , for several values of the dimensionless fluid inlet temperature,  $t_{f,i}$ . This graph may be employed to obtain the temperature of any cavity shape for which the apparent emissivity is known. If the apparent emissivity for the cavity shape of interest is unknown, it may be estimated from equation (3). Once  $t_c$  has been determined, the dimensionless temperature rise experienced by the heat transfer fluid may be computed from

$$t_{f,0} - t_{f,i} = (t_c - t_{f,i})[1 - \exp(-H)]$$

## References

- Stephans, C. W., and Haire, A. M., "Internal Design Considerations for Cavity-Type Solar Absorbers," *ARS Journal*, July 1961, pp. 896-901.
- Grilikhes, V. A., and Obtemperanskii, F. V., "Analysis of Radiative Heat Exchange Processes in Cylindrical Cavity-Type Collectors of Solar Power Plants," *Appl. Solar Energy*, Vol. 5, No. 1-2, 1969, pp. 59-65.
- Obtemperanskii, F. V., and Grilikhes, V. A., "Approximate Thermal Calculations for Cylindrical Cavity-Type Collectors With Liquid-Metal Heat-Transport Medium," *Appl. Solar Energy*, Vol. 5, No. 3-4, 1969, pp. 61-65.
- Sparrow, E. M., et al., "Radiation From Cavities With Nonisothermal Heat Conducting Walls," *JOURNAL OF HEAT TRANSFER*, TRANS. ASME, Series C, Vol. 96, 1974, pp. 15-20.
- Sparrow, E. M., and Cess, R. D., *Radiation Heat Transfer*, Brooks/Cole Publishing Co., Belmont, Calif. 1967, pp. 163-170.
- Sparrow, E. M., Jonsson, V. K., "Absorption and Emission Characteristics of Diffuse Spherical Enclosures," *JOURNAL OF HEAT TRANSFER*, TRANS. ASME, Series C, Vol. 84, 1962, pp. 188-189.
- Holman, J. P., *Heat Transfer*, 2nd ed., McGraw-Hill, New York, 1968.
- Selby, S. M., Ed., *Standard Mathematical Tables*, 19th Ed., The Chemical Rubber Co., Cleveland, 1967, p. 106.

In recent years there has been considerable interest in the remote sensing of gases using the infrared spectroscopic method. When it is desired to determine the temperature and composition of a remote gas volume, the processing of data involves lengthy computations due to the volumetric integration in the energy transfer equation. As an attempt to solve these problems, this work proposes a simplified equation of radiative energy transfer, using a shape factor to eliminate the volumetric integration. Shape factors for remote gas volumes of various geometries are presented.

The spectral radiant energy flux from an emitting gas volume to the surface of a telescope mirror,  $Q_{\bar{v}}$ , after atmospheric attenuation, is [1]:<sup>3</sup>

$$Q_{\bar{v}} = \int_V \int_{A_m} \frac{K_{\bar{v}} W_{B\bar{v}}(T)}{\pi} \frac{\cos(-\mathbf{b}, \mathbf{n})}{b^2} e^{-K_{\bar{v}} s} e^{-K_{\bar{v}}^{\text{atm}}(b-s)} dA_m dV, \quad (1)$$

where  $V$  and  $A_m$  are, respectively, the volume of gas volume within the field of view and area of the surface of the telescope mirror which receives the radiant energy flux.  $W_{B\bar{v}}$  is the emissive power of the black-body at the gas temperature,  $T$ , and  $s$  is the path-length of the flux beam  $\mathbf{b}$  from  $dV$  to  $dA_m$ .  $K_{\bar{v}}$  and  $K_{\bar{v}}^{\text{atm}}$  are, respectively, the linear absorption coefficients of the gas volume and the atmosphere. The vector  $\mathbf{n}$  is the normal unit vector of  $dA_m$ . Since there are  $n$  components in the gas volume,

$$K_{\bar{v}} = \sum_{i=1}^n K_{\bar{v},i} = \sum_{i=1}^n k_{\bar{v},i} p_i \quad (2)$$

where  $K_{\bar{v},i}$ ,  $k_{\bar{v},i}$ , and  $p_i$  are, respectively, the linear absorption coefficient, absorption coefficient ( $\text{cm}^{-1} \text{atm}^{-1}$ ), and the partial pressure of the  $i$ th component [2, 3].

The temperature of the gas volume is assumed constant; this assumption is acceptable since the field of view usually is small (for example, 1 m in diameter at the distance of 70 m), and it does not cover the entire gas effluent.

The shape of the gas volume depends on the volume itself and the size of the field of view of the telescope. When the field of view is small and completely covered by the gas, the gas volume  $V$  is approximately an inclined-cylindrical volume with one end facing the telescope. When the field of view is larger than the diameter of the gas volume,  $V$  is approximately a vertical-cylindrical volume as shown in Fig. 1. When the diameter of the field of view is equal to the diameter of the gas volume, and  $V$  and  $A_m$  are at the same height from the ground,  $V$  is the volume enclosed by two perpendicular, equal-diameter cylindrical surfaces.

If the gas volume is remote (i.e.,  $Y$  is much larger than the diameter and length of the gas volume, as well as the diameter of  $A_m$ ), equation (1) reduces to:

$$Q_{\bar{v}} = \frac{A_m}{Y^2} \frac{K_{\bar{v}} W_{B\bar{v}}(T)}{\pi} e^{-K_{\bar{v}}^{\text{atm}} Y} \int_V e^{-K_{\bar{v}} s} dV \quad (3)$$

<sup>1</sup> Assist. Professor, Chemical Engineering Department, University of Southwestern Louisiana, Lafayette, La.

<sup>2</sup> Professor, Chemical Engineering Department, University of Houston, Houston, Texas.

<sup>3</sup> Numbers in brackets designate References at end of technical brief.

Contributed by the Heat Transfer Division of THE AMERICAN SOCIETY OF MECHANICAL ENGINEERS. Manuscript received by the Heat Transfer Division January 24, 1974.

where  $Y$  is the distance between the centers of the gas volume and the area  $A_m$ .

As shown in equation (3) the determination of the temperature and concentrations (partial pressures) of the gas volume requires the time-consuming solution of integral equation involving multiple integration for volume  $V$ . To avoid this difficulty the equivalent pathlength,  $L_e$ , is defined so that the radiant energy transfer from  $V$  to  $A_m$  is:

$$Q_{\nu} = (1 - e^{-K_{\nu} L_e}) A_m \frac{A_g}{Y^2} \frac{W_{B\nu}(T)}{\pi} e^{-K_{\nu}^{\text{atm}} Y} \quad (4)$$

where  $A_g$  is the area of the gas volume as observed by the instrument, and can be calculated from a field-of-view equation for the telescope.

In effect, equation (4) implies the conversion of a three-dimensional remote emitting gas volume  $V$  to a measurable two-dimensional surface  $A_g$  with the equivalent pathlength  $L_e$ , while maintaining the concentration-related variable  $K_{\nu}$  in the equation for remote sensing. The equivalent pathlength can be calculated by comparing equations (3) and (4).

The mean beam length reported extensively in the literature is used to calculate the radiant energy from a gas volume to all or part of its bounding surface [1]. The defining equations of the equivalent pathlength and the mean beam length are different due to their different geometries. The most significant difference in the geometry is that the energy receiving surface of the mean beam length is right next to the gas volume, while that of the equivalent pathlength is at some distance away from the gas volume. The definition of  $A_g$  in the equivalent pathlength and the simplifying condition that  $Y$  is much larger than the dimensions of the gas volume are not applicable to the mean beam length. Therefore, it is expected that they have different numerical values, except the spherical gas volume. The equivalent pathlength of a remote spherical gas volume and the mean beam length of a spherical gas volume have the same numerical values at various  $K_{\nu} D$ 's, because of their particular geometry.

For convenience in studying the equivalent pathlength, the shape factor is defined as,

$$\sigma \equiv \frac{L_e}{L_c} \quad (5)$$

where  $L_c$  is a reference length. For the remote inclined-cylindrical gas volume, the reference length is equal to the length of volume, and  $A_g = \pi R^2$ , where  $R$  is the radius of the cylinder. For a remote vertical-cylindrical gas volume,  $L_c = D$  or  $2R$ , and  $A_g = DH = 2RH$ , where  $D$  and  $H$  are, respectively, the diameter and height of the vertical cylinder. For a remote gas volume enclosed by two perpendicular equal-diameter cylindrical surfaces,  $L_c = D$  or  $2R$ , and  $A_g = \pi R^2$ , where  $R$  is the radius of cylinders.

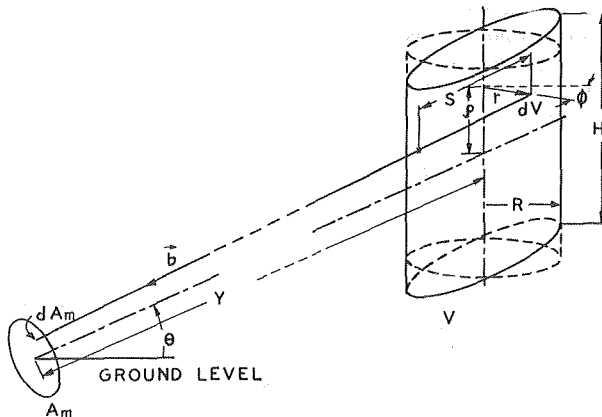


Fig. 1 Remote vertical-cylindrical gas volume

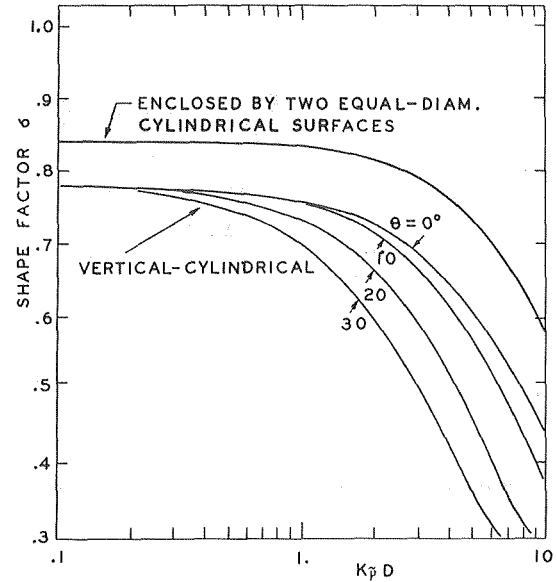


Fig. 2 Shape factors

From equations (3), (4), and (5), the shape factor of the remote inclined-cylindrical gas volume is unity. Similarly, the shape factor of the remote vertical-cylindrical gas volume is given by the following equation,

$$\sigma = \frac{-1}{2K_{\nu} R} \ln \left[ 1 - K_{\nu} R \int_{\rho^*=0}^{0.5} \int_{r^*=0}^1 \int_{\phi=0}^{2\pi} r^* e^{-K_{\nu} R \left( \frac{r^* \cos \phi + \sqrt{1 - (r^* \sin \phi)^2}}{\cos \theta} \right)} d\phi dr^* d\rho^* \right] \quad (6)$$

where  $r^*$  and  $\rho^*$  are, respectively,  $r/R$  (reduced radius vector) and  $\rho/H$  (reduced vertical coordinate), and  $\phi$  is the angular coordinate. The origin of the coordinates is at the center of the volume.  $\theta$  represents the angle between the ground level and the line connecting the centers of  $A_m$  and  $V$ .

The shape factor of a remote gas volume enclosed by two perpendicular equal-diameter cylindrical surfaces is:

$$\sigma = \frac{-1}{2K_{\nu} R} \ln \left[ 1 - \frac{4}{\pi} \int_0^1 \sqrt{1-x^2} (1 - e^{-2K_{\nu} R \sqrt{1-x^2}}) dx \right] \quad (7)$$

where  $x$  is  $r/R$  (reduced radius vector).

Numerical values of shape factors of these two gas volumes at various values of  $K_{\nu} D$  are shown in Fig. 2, and were calculated by equations (6) and (7), using the mechanical cubature method coupled with Weddle's rule [4] in the multiple integrations. For optically thin gases (i.e.,  $K_{\nu} L_e \ll 1$ ), the shape factor is independent of the concentration or  $K_{\nu} L_e$  as shown in the figure.

The spherical gas volume is an interesting case having the smallest shape factor among the various geometries considered. It can be calculated from equations (3) and (4) as others. Its numerical values agree with the results given by Hottel and Sarofim [1].

A real gas volume from an exhaust pipe or stack is approximately a volume enclosed by three or four quadratic surfaces. It appears reasonable to consider the shape of a remote real gas volume to be in between an inclined-cylindrical volume and a vertical-cylindrical volume. Thus, the shape factor of the remote gas volume enclosed by two equal-diameter cylindrical surfaces, given by equation (7), is a reasonable approximation for the shape factor of a remote real gas volume. The interchange factor, similar to the shape factor  $\sigma$ , has been discussed by Edwards and Balakrishnan [5].

In remote sensing  $Q_{\nu}$  is measured at various frequency positions and ranges for determination of the concentrations of the

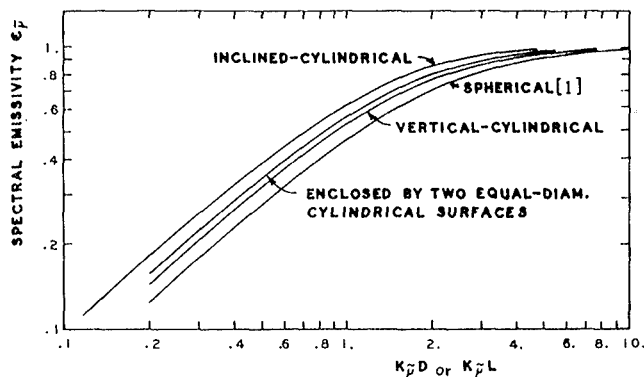


Fig. 3 Spectral emissivities

gases. To determine the temperature of the gas volume,  $Q_{\bar{e}}$  is measured over the total spectral range (e.g., 500–4000  $\text{cm}^{-1}$ ). In either case, equation (4) greatly reduces the time required for the data processing. In refinery or chemical plants, the diameter of the stack or exhaust pipe and its distance  $Y$  are known. Knowing  $Y$ ,  $H$  can be calculated from the field of view equation for the telescope.  $D$  can be estimated from the diameter of the stack and the expansion of the effluent gas [6].

The spectral emissivity of the remote gas volume is  $\epsilon_p$ , and from equation (4) can be calculated by,

$$\epsilon_p = 1 - e^{-K_p \bar{v} L_e} \quad (8)$$

Numerical values for two remote gas volumes were calculated by equation (8) and the results of multiple integrations in equations (6) and (7). A plot of the spectral emissivity versus  $K_p D$  is shown in Fig. 3. The effect of the angle  $\theta$  on the spectral emissivity is negligible. The spectral emissivities of the remote inclined-cylindrical and spherical gas volumes are included for comparison, since they have the largest and smallest shape factors.

Atmospheric attenuation of radiant energy flux exists in the entire spectrum, including the "atmospheric window" region from 8 to 13 microns [7]. It is represented by the last term in equation (4), where  $K_p^{\text{atm}}$  is calculated according to equation (2) for  $\text{CO}_2$  and  $\text{H}_2\text{O}$ -active regions, and the atmospheric window region using Kondratyev's data [7]. The temperature, humidity and  $\text{CO}_2$  partial pressure of the atmosphere are measured at the site of the telescope and assumed constant between the telescope and gas volume.

## References

- 1 Hottel, H. C., and Sarofim, A. F., *Radiative Transfer*, McGraw-Hill, New York, 1967, pp. 276–279.
- 2 Goody, R. M., *Atmospheric Radiation*, Oxford, 1964, p. 123.
- 3 Sparrow, E. M., and Cess, R. D., *Radiation Heat Transfer*, Brooks/Cole Publishing Co., 1966, p. 20.
- 4 Scarborough, J. B., *Numerical Mathematical Analysis*, The Johns Hopkins Press, 1962, p. 170.
- 5 Edwards, D. K., Balakrishnan, A., "Volume Interchange Factors for Nonhomogeneous Gases," *JOURNAL OF HEAT TRANSFER, TRANS. ASME, Series C*, Vol. 94, May 1972, pp. 181–188.
- 6 Perry, R. H., and Chilton, C. H., *Chemical Engineers' Handbook*, 5th ed., McGraw-Hill, New York, 1973, pp. 5–20.
- 7 Kondratyev, K. YA., *Radiation In The Atmosphere*, Academic Press, 1969, pp. 116–117.

## The Initiation of Boiling During Pressure Transients

J. Weisman,<sup>1</sup> G. Bussell,<sup>2</sup> and T. Hsieh<sup>3</sup>

### Nomenclature

- $P_v$  = vapor pressure, dynes/cm<sup>2</sup>  
 $r$  = radius of cavity, cm  
 $P_L$  = system pressure, dynes/cm<sup>2</sup>  
 $\sigma$  = surface tension, dynes/cm

### Introduction

Boiling initiation on metal surfaces during pressure transients has been previously examined using completely degassed water. The previous investigations [1, 2]<sup>4</sup> of boiling during rapid depressurization indicated some bubbles appeared almost immediately. This result is consistent with the pressure-time history model [3, 4] for the conditions examined. In boiling from a reentrant cavity, the incipient superheat is determined from

$$P_v - P_L = \frac{2\sigma}{r} \quad (1)$$

providing noncondensibles are not present. When an overpressure,  $P_L'$ , is applied, the cavity is flooded when

$$P_L' \geq \frac{2\sigma}{r} + P_v \quad (2)$$

If the pressure is reduced, boiling resumes when equation (1) is satisfied with  $r = (P_L' - P_v)/2\sigma$ . High initial superheats are required when  $P_L'$  is appreciable.

Madhavan and Messler [1] applied no overpressure. Surface cavities were unflooded and available for nucleation. Although Kenning and Thirunavukkarasu [2] applied an initial overpressure, the pressure was dropped substantially below saturation very quickly. Within the data accuracy, the pressure reached was low enough to activate unflooded cavities. Bubble growth could thus begin immediately.

When an overpressure is applied with a noncondensable gas present, small bubbles can remain at the cavity base. If pressure is slowly reduced, vapor diffuses into the bubble which then gradually fills the cavity. Boiling can begin at a superheat below that indicated by the maximum radius of the unflooded cavities.

During rapid depressurization, the finite time to fill the cavity may be significant. It is possible that boiling begins at a superheat above that obtained when pressure is slowly reduced but below that computed using the maximum unflooded radius. This research was designed to determine whether such a difference existed.

### Experimental Approach

Bubble growth studies are generally conducted using high speed photography. Since this is cumbersome, an alternative procedure based on a scheme by Ram [5] is used. Ram observed that appearance of bubbles on a surface caused intensity fluctuations in a light beam passing over that surface. In this investigation,

<sup>1</sup>Department of Chemical and Nuclear Engineering, University of Cincinnati, Cincinnati, Ohio.

<sup>2</sup>Department of Chemical and Nuclear Engineering, University of Cincinnati, Cincinnati, Ohio; Presently at Stone and Webster Corp., Boston, Mass.

<sup>3</sup>Department of Chemical and Nuclear Engineering, University of Cincinnati, Cincinnati, Ohio; Presently at University of California at Los Angeles, Los Angeles, Calif.

<sup>4</sup>Numbers in brackets designate References at end of technical brief.

Contributed by the Heat Transfer Division of THE AMERICAN SOCIETY OF MECHANICAL ENGINEERS. Manuscript received by the Heat Transfer Division December 13, 1973.

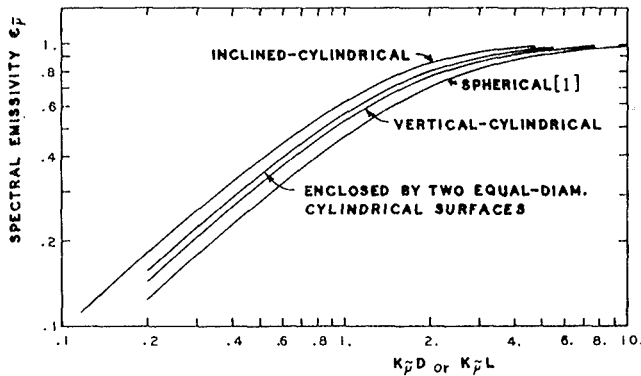


Fig. 3 Spectral emissivities

gases. To determine the temperature of the gas volume,  $Q_{\bar{e}}$  is measured over the total spectral range (e.g., 500–4000  $\text{cm}^{-1}$ ). In either case, equation (4) greatly reduces the time required for the data processing. In refinery or chemical plants, the diameter of the stack or exhaust pipe and its distance  $Y$  are known. Knowing  $Y$ ,  $H$  can be calculated from the field of view equation for the telescope.  $D$  can be estimated from the diameter of the stack and the expansion of the effluent gas [6].

The spectral emissivity of the remote gas volume is  $\epsilon_p$ , and from equation (4) can be calculated by,

$$\epsilon_p = 1 - e^{-K_p \bar{v} L_e} \quad (8)$$

Numerical values for two remote gas volumes were calculated by equation (8) and the results of multiple integrations in equations (6) and (7). A plot of the spectral emissivity versus  $K_p D$  is shown in Fig. 3. The effect of the angle  $\theta$  on the spectral emissivity is negligible. The spectral emissivities of the remote inclined-cylindrical and spherical gas volumes are included for comparison, since they have the largest and smallest shape factors.

Atmospheric attenuation of radiant energy flux exists in the entire spectrum, including the "atmospheric window" region from 8 to 13 microns [7]. It is represented by the last term in equation (4), where  $K_p^{\text{atm}}$  is calculated according to equation (2) for  $\text{CO}_2$  and  $\text{H}_2\text{O}$ -active regions, and the atmospheric window region using Kondratyev's data [7]. The temperature, humidity and  $\text{CO}_2$  partial pressure of the atmosphere are measured at the site of the telescope and assumed constant between the telescope and gas volume.

## References

- 1 Hottel, H. C., and Sarofim, A. F., *Radiative Transfer*, McGraw-Hill, New York, 1967, pp. 276–279.
- 2 Goody, R. M., *Atmospheric Radiation*, Oxford, 1964, p. 123.
- 3 Sparrow, E. M., and Cess, R. D., *Radiation Heat Transfer*, Brooks/Cole Publishing Co., 1966, p. 20.
- 4 Scarborough, J. B., *Numerical Mathematical Analysis*, The Johns Hopkins Press, 1962, p. 170.
- 5 Edwards, D. K., Balakrishnan, A., "Volume Interchange Factors for Nonhomogeneous Gases," *JOURNAL OF HEAT TRANSFER, TRANS. ASME, Series C*, Vol. 94, May 1972, pp. 181–188.
- 6 Perry, R. H., and Chilton, C. H., *Chemical Engineers' Handbook*, 5th ed., McGraw-Hill, New York, 1973, pp. 5–20.
- 7 Kondratyev, K. YA., *Radiation In The Atmosphere*, Academic Press, 1969, pp. 116–117.

## The Initiation of Boiling During Pressure Transients

J. Weisman,<sup>1</sup> G. Bussell,<sup>2</sup> and T. Hsieh<sup>3</sup>

### Nomenclature

- $P_r$  = vapor pressure, dynes/cm<sup>2</sup>  
 $r$  = radius of cavity, cm  
 $P_L$  = system pressure, dynes/cm<sup>2</sup>  
 $\sigma$  = surface tension, dynes/cm

### Introduction

Boiling initiation on metal surfaces during pressure transients has been previously examined using completely degassed water. The previous investigations [1, 2]<sup>4</sup> of boiling during rapid depressurization indicated some bubbles appeared almost immediately. This result is consistent with the pressure-time history model [3, 4] for the conditions examined. In boiling from a reentrant cavity, the incipient superheat is determined from

$$P_v - P_L = \frac{2\sigma}{r} \quad (1)$$

providing noncondensibles are not present. When an overpressure,  $P_L'$ , is applied, the cavity is flooded when

$$P_L' \geq \frac{2\sigma}{r} + P_v \quad (2)$$

If the pressure is reduced, boiling resumes when equation (1) is satisfied with  $r = (P_L' - P_v)/2\sigma$ . High initial superheats are required when  $P_L'$  is appreciable.

Madhavan and Messler [1] applied no overpressure. Surface cavities were unflooded and available for nucleation. Although Kenning and Thirunavukkarasu [2] applied an initial overpressure, the pressure was dropped substantially below saturation very quickly. Within the data accuracy, the pressure reached was low enough to activate unflooded cavities. Bubble growth could thus begin immediately.

When an overpressure is applied with a noncondensable gas present, small bubbles can remain at the cavity base. If pressure is slowly reduced, vapor diffuses into the bubble which then gradually fills the cavity. Boiling can begin at a superheat below that indicated by the maximum radius of the unflooded cavities.

During rapid depressurization, the finite time to fill the cavity may be significant. It is possible that boiling begins at a superheat above that obtained when pressure is slowly reduced but below that computed using the maximum unflooded radius. This research was designed to determine whether such a difference existed.

### Experimental Approach

Bubble growth studies are generally conducted using high speed photography. Since this is cumbersome, an alternative procedure based on a scheme by Ram [5] is used. Ram observed that appearance of bubbles on a surface caused intensity fluctuations in a light beam passing over that surface. In this investigation,

<sup>1</sup>Department of Chemical and Nuclear Engineering, University of Cincinnati, Cincinnati, Ohio.

<sup>2</sup>Department of Chemical and Nuclear Engineering, University of Cincinnati, Cincinnati, Ohio; Presently at Stone and Webster Corp., Boston, Mass.

<sup>3</sup>Department of Chemical and Nuclear Engineering, University of Cincinnati, Cincinnati, Ohio; Presently at University of California at Los Angeles, Los Angeles, Calif.

<sup>4</sup>Numbers in brackets designate References at end of technical brief.

Contributed by THE AMERICAN SOCIETY OF MECHANICAL ENGINEERS. Manuscript received by the Heat Transfer Division December 13, 1973.

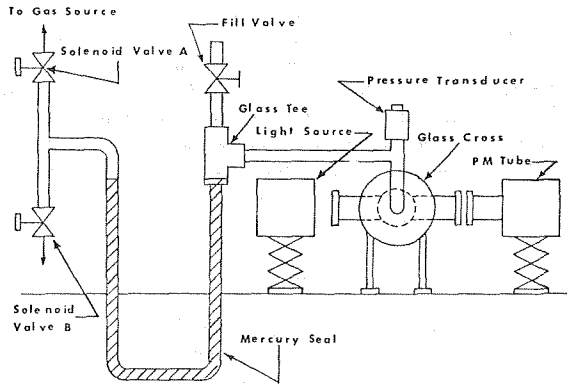


Fig. 1 -Experimental apparatus

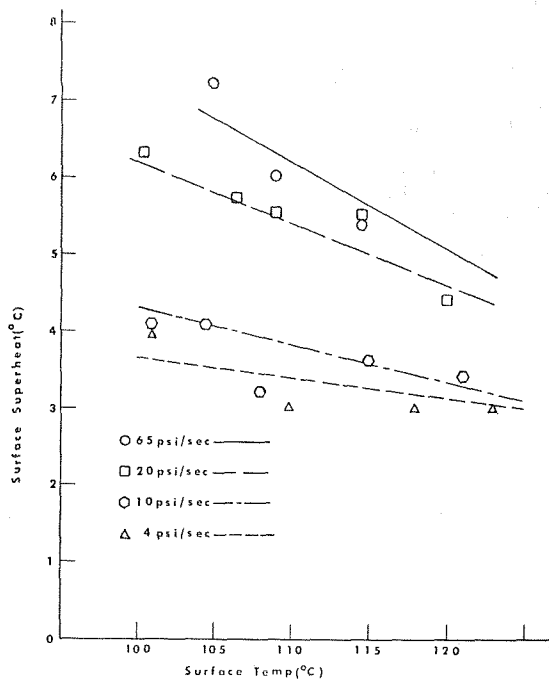


Fig. 2 Wall superheat required to initiate boiling on unheated ribbon

the first appearance of these fluctuations was used to indicate boiling initiation.

The apparatus (Fig. 1) contains the water under study in a  $3 \times 1\frac{1}{2}$  in. glass cross. Glass plates covering the ends of the  $1\frac{1}{2}$  in. arms allow a light beam to traverse the cross. Tubing lines from the flanges affixed to the ends of the 3 in. arms connect the system fluid to a pressure source via a mercury seal. Immersion heaters allow the fluid to be heated as desired.

The boiling surface is a  $\frac{3}{16} \times 10\frac{1}{2}$  in. nichrome ribbon (roughness  $\sim 70 \mu\text{in.}$ ) placed horizontally. The collimated light beam was focused along a 1 inch ribbon section and aligned with the photomultiplier tube. Connection to a battery allowed ribbon heating.

The pressure was measured by a thin film strain gage pressure transducer. The pressure signal and photomultiplier output were fed to a dual beam oscilloscope and data obtained by photographing the oscilloscope traces.

The system was evacuated to 15–20 mm Hg prior to filling and degassed water sucked into the system. It is estimated that this fill procedure left an air partial pressure of about 0.02–0.03 atm.

To conduct a test, the solenoid to the gas source was opened

and high pressure maintained for  $\sim 3$  min. The pressure transient was then produced by simultaneously closing the gas supply solenoid while opening the solenoid to the low pressure chamber. A needle valve in the exhaust line controlled the depressurization rate.

## Experimental Results

The first tests were conducted with the nichrome ribbon unheated. Experiments were initiated at  $\sim 35$  psia and pressure reduced at rates ranging from  $\sim 65$  psi/s to  $\sim 4$  psi/s. These rates are approximate since the fall rate at the beginning of the transient was considerably higher than at the end.

Fig. 2 shows the results expressed in terms of the wall superheat at the onset of boiling. All points shown are the averages of 3 to 5 observations. Since the ribbon was not cooled until boiling began, the wall superheat is the difference between the initial water temperature and the saturation temperature corresponding to the pressure at which boiling began.

Fig. 2 shows the superheat required to initiate boiling increases as the depressurization rate increases. The superheats obtained at the lower depressurization rates approach a single curve. This may be expected since the superheats at the lowest pressure reduction rates can differ only slightly from steady state values. These data are therefore taken as a good approximation of steady state superheats.

The 3–4°C superheats observed at the lowest depressurization rate are significantly below those expected if a noncondensable gas were not present. For example, at 110°C the pressure-time history theory predicts that a 35 psi overpressure requires a superheat  $> 24^\circ\text{C}$ . The low superheats observed can be explained by bubbles being retained at cavity bases during overpressure conditions.

To be certain that the first boiling in the system was on the ribbon, additional tests were run with the ribbon heated at a surface heat flux of  $11 \times 10^3$  Btu/hr ft.<sup>2</sup> Use of this data requires ribbon temperature as a function of heat flux and water temperature. This was obtained by slowly reducing the system pressure until boiling was observed. The inception of boiling was assumed to occur at the steady state superheat previously determined. The ribbon temperature is then the observed saturation temperature plus the steady state superheat.

Superheats in the electrical heating tests were higher than those obtained at comparable pressure reduction rates without heating. A consistent pattern emerges from consideration of the time between the instant the pressure reaches the level at which boiling is expected and the instant at which boiling was observed. The delay time of Fig. 3 is the time interval between the observation of light beam fluctuations and the instant pressure reached the level at which steady state boiling is expected. Delays ranged from 1.6 sec. to 65 ms. Note that the highest and lowest depressurization rates of Fig. 3 used a heated ribbon while the intermediate rate used an unheated ribbon.

As in Fig. 2, the depressurization rates of Fig. 3 have been designated by average values. Fig. 4 shows the actual pressure time histories.

Since observed delay times were longer than expected, the results were verified using high speed photography. The experiment at the 100 psi/s depressurization rate and 126°C ribbon temperature was repeated with photographic observation. The photographs indicated boiling began 0.26 s after transient initiation. This corresponds to a 0.185 s delay time and compares to 0.17 s by the light beam technique.

It may be argued that the calculated delays resulted from temperature or pressure measurement error. Although ribbon temperatures were inferred from steady state conditions, these temperatures were not used to compute delay times. Delays were based on the measurements of the pressure for steady state boiling. Proof that pressure level measurement errors were not responsible is furnished by runs in which essentially all delay time occurred after the pressure reached its lowest value.

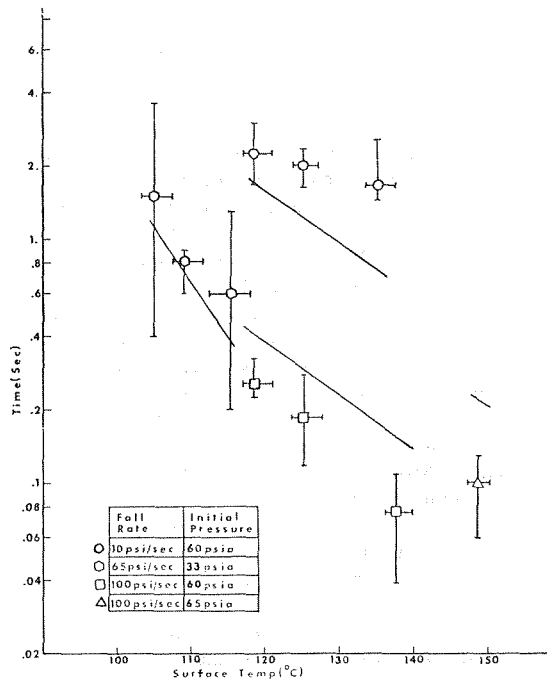


Fig. 3 Boiling delay time

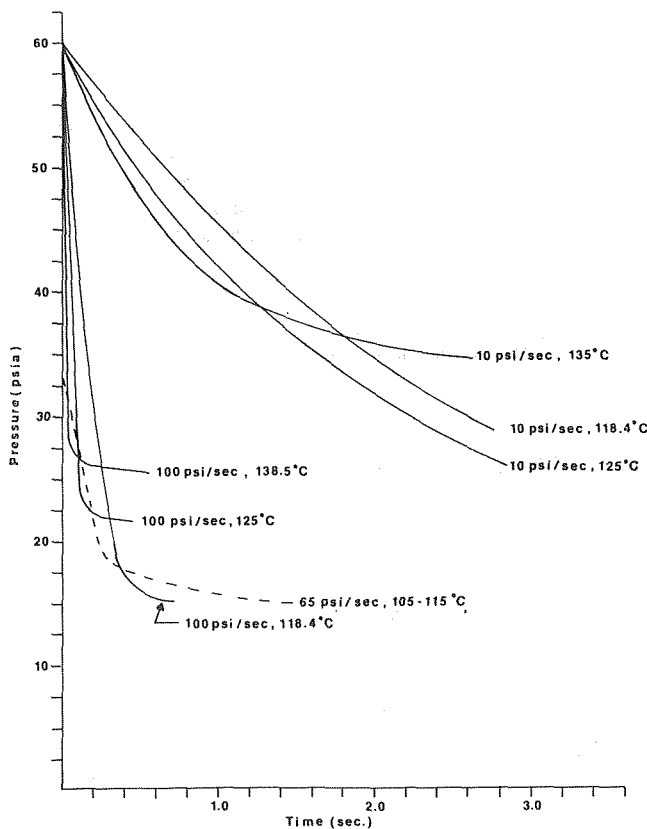


Fig. 4 Pressure-time histories

## Conclusion

Under appropriate conditions, measurable delays in boiling initiation can be encountered. Bussell [6] assumed the delay times represent the time to fill surface cavities. He calculated

delay times taking mass transfer as controlling and  $C$ , the water vaporization coefficient, as having a value of 0.01–0.02 for the temperatures considered [7]. The solid lines of Fig. 3 represent Bussell's calculations. Further verification of this suggestion is required.

## Acknowledgment

The authors wish to acknowledge the financial assistance of the Lewis Research Laboratory of the National Aeronautics and Space Administration under whose sponsorship this research was conducted.

## References

- 1 Madhavan, S., and Mesler, R., "A Study of Bubble Growth on Surfaces," Fourth International Heat Transfer Conference, Vol. V, Paper B 26, 1970.
- 2 Kenning, D. B. R., and Thirunavukkarasu, K., "Bubble Nucleation Following a Sudden Pressure Reduction in Water," Fourth International Heat Transfer Conference, Vol. V., Paper B 2.9, 1970.
- 3 Fabric, S., "Vapor Nucleation on Surfaces Subjected to Transient Heating," Report NE-64-1, Institute of Eng. Research, University of California, Berkeley, 1964.
- 4 Holtz, R. E., "Effect of Pressure-Temperature History Upon Incipient Boiling Superheats," USAEC Report ANL-7184, Argonne National Laboratory 1966.
- 5 Ram, K. S., *Trans. A.N.S.* Vol. 12, No. 1, 1969, p. 301.
- 6 Bussell, G., "Departure From Phase Equilibrium During Boiling Transients," MS thesis, University of Cincinnati, Cincinnati, Ohio, 1973.
- 7 Johnstone, R. K. and Smith, W., "Rate of Condensation on Evaporation During Short Exposures of a Quiescent Liquid," Third International Heat Transfer Conference, *AIChE*, Vol. II, 1966, p. 348.

## Laminar Film Condensation on Submerged Isothermal Bodies

V. K. Dhir<sup>1</sup> and J. H. Lienhard<sup>2</sup>

### Nomenclature

- $A = \mu k \Delta T / (\rho_f - \rho_g) \rho_f h'_{fg}$   
 $c_p$  = specific heat of condensate  
 $g$  = gravitational acceleration  
 $h, \bar{h}$  = heat transfer coefficient; bar denotes average over the body  
 $h_{fg}, h'_{fg}$  = latent heat of vaporization; prime denotes  $h_{fg}$  corrected to include sensible heat of subcooling in the film,  $h'_{fg} = h_{fg} + 0.68 c_p \Delta T$   
 $K$  = configurational constant  
 $k$  = thermal conductivity of condensate  
 $L$  = total length of travel of the condensate  
 $Nu_L$  = Nusselt number,  $\bar{h}L/k$   
 $r$  = characteristic width of the body defined in equation (2)  
 $\alpha$  = angle defined in Table 1  
 $\Delta T$  = difference between saturation temperature and wall temperature  
 $\mu$  = viscosity of condensate  
 $\rho_f, \rho_g$  = densities of liquid and saturated vapor, respectively

<sup>1</sup> Assist. Professor, Energy and Kinetics Department, University of California, Los Angeles, Calif. Assoc. Mem. ASME.

<sup>2</sup> Professor, Mechanical Engineering Department, University of Kentucky, Lexington, Ky. Mem. ASME.

Contributed by the Heat Transfer Division of THE AMERICAN SOCIETY OF MECHANICAL ENGINEERS. Manuscript received by the Heat Transfer Division June 7, 1974.



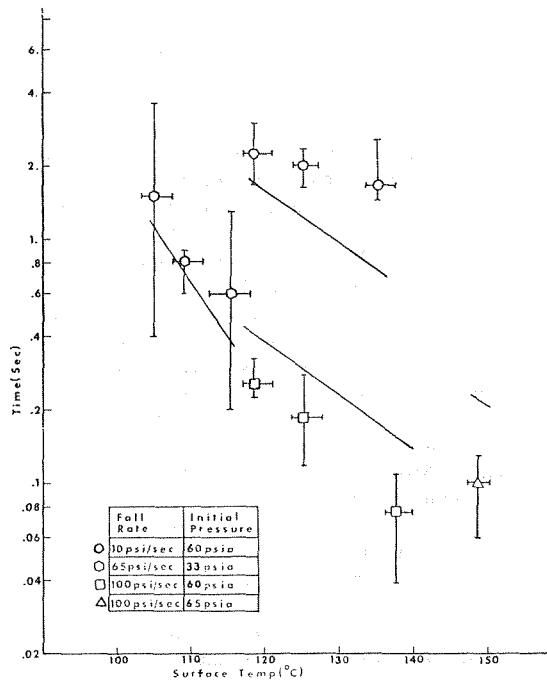


Fig. 3 Boiling delay time

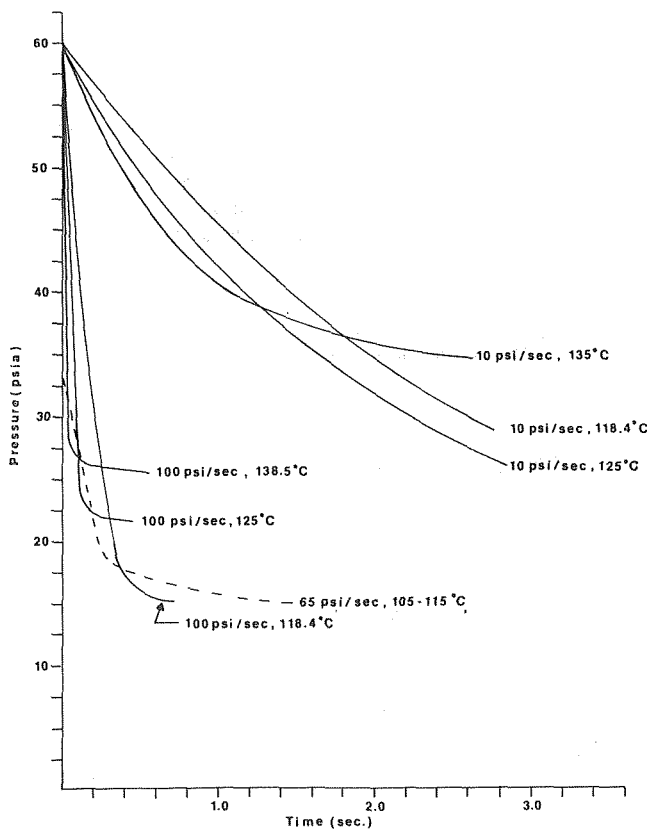


Fig. 4 Pressure-time histories

## Conclusion

Under appropriate conditions, measurable delays in boiling initiation can be encountered. Bussell [6] assumed the delay times represent the time to fill surface cavities. He calculated

delay times taking mass transfer as controlling and  $C$ , the water vaporization coefficient, as having a value of 0.01-0.02 for the temperatures considered [7]. The solid lines of Fig. 3 represent Bussell's calculations. Further verification of this suggestion is required.

## Acknowledgment

The authors wish to acknowledge the financial assistance of the Lewis Research Laboratory of the National Aeronautics and Space Administration under whose sponsorship this research was conducted.

## References

- 1 Madhavan, S., and Mesler, R., "A Study of Bubble Growth on Surfaces," Fourth International Heat Transfer Conference, Vol. V, Paper B 26, 1970.
- 2 Kenning, D. B. R., and Thirunavukkarasu, K., "Bubble Nucleation Following a Sudden Pressure Reduction in Water," Fourth International Heat Transfer Conference, Vol. V., Paper B 2.9, 1970.
- 3 Fabric, S., "Vapor Nucleation on Surfaces Subjected to Transient Heating," Report NE-64-1, Institute of Eng. Research, University of California, Berkeley, 1964.
- 4 Holtz, R. E., "Effect of Pressure-Temperature History Upon Incipient Boiling Superheats," USAEC Report ANL-7184, Argonne National Laboratory 1966.
- 5 Ram, K. S., *Trans. A.N.S.* Vol. 12, No. 1, 1969, p. 301.
- 6 Bussell, G., "Departure From Phase Equilibrium During Boiling Transients," MS thesis, University of Cincinnati, Cincinnati, Ohio, 1973.
- 7 Johnstone, R. K. and Smith, W., "Rate of Condensation on Evaporation During Short Exposures of a Quiescent Liquid," Third International Heat Transfer Conference, *AIChE*, Vol. II, 1966, p. 348.

## Laminar Film Condensation on Submerged Isothermal Bodies

V. K. Dhir<sup>1</sup> and J. H. Lienhard<sup>2</sup>

### Nomenclature

- $A = \mu k \Delta T / (\rho_f - \rho_g) \rho_f h'_{fg}$   
 $c_p$  = specific heat of condensate  
 $g$  = gravitational acceleration  
 $h, \bar{h}$  = heat transfer coefficient; bar denotes average over the body  
 $h_{fg}, h'_{fg}$  = latent heat of vaporization; prime denotes  $h_{fg}$  corrected to include sensible heat of subcooling in the film,  $h'_{fg} = h_{fg} + 0.68 c_p \Delta T$   
 $K$  = configurational constant  
 $k$  = thermal conductivity of condensate  
 $L$  = total length of travel of the condensate  
 $Nu_L$  = Nusselt number,  $\bar{h}L/k$   
 $r$  = characteristic width of the body defined in equation (2)  
 $\alpha$  = angle defined in Table 1  
 $\Delta T$  = difference between saturation temperature and wall temperature  
 $\mu$  = viscosity of condensate  
 $\rho_f, \rho_g$  = densities of liquid and saturated vapor, respectively

<sup>1</sup> Assist. Professor, Energy and Kinetics Department, University of California, Los Angeles, Calif. Assoc. Mem. ASME.

<sup>2</sup> Professor, Mechanical Engineering Department, University of Kentucky, Lexington, Ky. Mem. ASME.

Contributed by the Heat Transfer Division of THE AMERICAN SOCIETY OF MECHANICAL ENGINEERS. Manuscript received by the Heat Transfer Division June 7, 1974.

Since Nusselt's [1]<sup>3</sup> initial analysis, many studies of laminar film condensation heat transfer from submerged isothermal bodies have been made. These studies (e.g., [2, 3]) show that for small film subcooling and for Prandtl number  $\geq 0$  (1), the average Nusselt number for a particular body can be written as:

$$\text{Nu}_L = K[gL^3/A]^{1/4} \quad (1)$$

where  $A \equiv \mu k \Delta T / (\rho_f - \rho_g) \rho_f h'_{fg}$ ,  $L$  is a characteristic length (in this note it will be taken as the total length of travel of the condensate), and  $K$  is a constant which reflects the influence of geometrical configuration of the body and its orientation in relation to the gravitational field.

Nusselt originally showed that  $K = 0.943$  for vertical plates and a number that has subsequently been corrected to 0.815 for horizontal cylinders.<sup>4</sup> We recently [3] showed how to compute  $K$  for a very broad class of problems by replacing  $g$  with an effective gravity that took account of body shape.

Our aim in this note is to show the existence of a commonality in the average laminar condensation heat transfer rates from various bodies. We do this by first showing that the constant,  $K$ , can be approximately correlated with an appropriate configuration parameter for the range of "reasonable" (nonpathological) body shapes. This correlation will make it possible to guess  $K$  for most unknown shapes within a few percent accuracy. The configurational parameter,  $r$ , is defined as:

$$r \equiv \frac{\text{horizontal cross-sectional area of the body}}{\text{run-off area of the condensate}} \quad (2)$$

We neglected the end surface area when evaluating the condensate run-off area of the cylinders as the cylinders are assumed to be infinite.

The constant  $K$  is evaluated numerically using the same method as suggested in [3]. While carrying out the evaluation of the Nusselt number for composite bodies, the condition of continuity of

mass flow rate of condensate had to be imposed at the junction of two bodies. The numerical values of  $K$  for several configurations<sup>5</sup> are listed in Table 1.

We terminated the evaluation of Nusselt number for the bodies of variable shape, as the body becomes increasingly flat. For small angles of inclination the condensate film becomes increasingly thick and is more susceptible to hydrodynamic instability, especially on the underside. The heat transfer is no longer explained by Nusselt's solution. This observation was made earlier by Gerstmann and Griffith [4]. The static head instead of gravity force in the direction of flow takes over as the condensate driving mechanism only for very small angles of inclination. This effect is not appreciable until the surface becomes nearly horizontal. Thus since we suspected strong influences of instability on heat transfer from slightly inclined surfaces, we terminated the calculations arbitrarily. The last entry in Table 1 shows a scale sketch of the body at the point where we have terminated the calculations.

The value of Nusselt number for a diamond cylinder, elliptic cylinder, and abutted cones were first plotted as a function of  $r$  in Fig. 1. The points for a vertical plate, horizontal cylinder, and sphere are also included in the figure. The geometrical configuration of the abutted cones allows the highest heat transfer coefficient whereas the elliptic cylinders have the least. The two extremes remain within  $\pm 10$  percent of the diamond cylinder values.

For any body of hybrid shape we would expect the Nusselt number to lie somewhere between the values for the shapes composing the body. This fact was explicitly brought out when we evaluated the Nusselt number for a circle-diamond cylinder both in the upright and upside-down positions and added these curves to the figure. They both nest nicely between the curves for the diamond and elliptic cylinders as we would expect.

### Conclusion

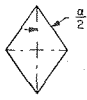
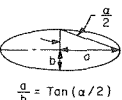
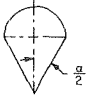
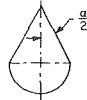
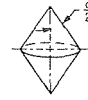



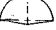


We have evaluated the average Nusselt number for several different bodies most of which have not been treated previously. These evaluations show that an estimate of the average Nusselt number can be made within a few percent of exact value without going through tedious numerical calculations. A similar observa-

<sup>3</sup> Numbers in brackets designate references at end of technical brief.

<sup>4</sup> The constant is 0.729 if  $L$  is defined as the cylinder diameter instead of half the circumference as it is here.

<sup>5</sup> The evaluation of Nusselt number for elliptic cylinder was done by Mr. Amir Karimi. His contribution is gratefully acknowledged.

**Table 1 Numerical evaluation of Nusselt number for various bodies**

$\alpha/2$ (Degrees)										
	$r$	$K$	$r$	$K$	$r$	$K$	$r$	$K$	$r$	$K$
0	0	0.943	0	0.943	0	0.943	0	0.943	0	1.039
5			0.035	0.930						
15			0.113	0.901						
20	0.171	0.928		0.898	0.222	0.895	0.222	0.896	0.171	1.023
30	0.250	0.910			0.280	0.881	0.280	0.880	0.250	1.003
45	0.354	0.864	0.318	0.815						
60	0.433	0.793	0.396	0.742	0.367	0.851	0.367	0.825	0.433	0.874
67			0.430							
80	0.492	0.608			0.387	0.814	0.387	0.749	0.492	
85	0.498				0.388		0.388		0.492	

Last entry is a scale sketch of the body at the point where calculations and the curve are terminated

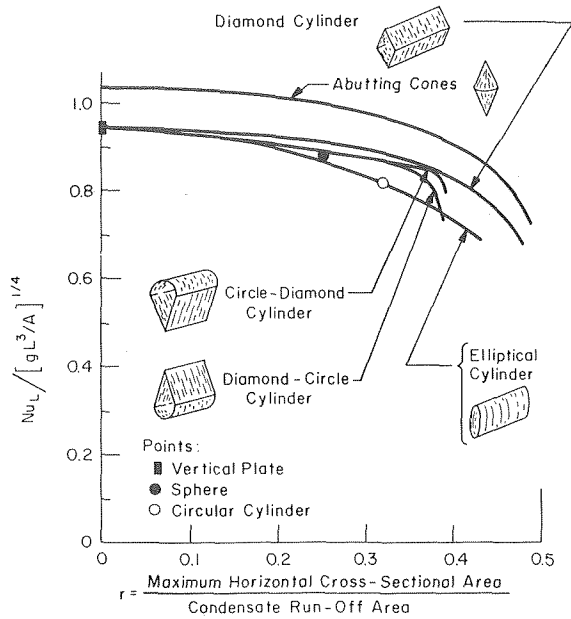


Fig. 1 Average Nusselt number for laminar film condensation on submerged isothermal bodies

tion has been made for natural convection heat transfer from submerged bodies [5].

## References

- 1 Nusselt, W., "Die Oberflächenkondensation des Wasserdampfes," *Z. Ver. Deutsch. Ing.*, Vol. 60, 1916, pp. 541-6, 569-75.
- 2 Sparrow, E. M., and Gregg, J. L., "A Boundary-Layer Treatment of Laminar-Film Condensation," *JOURNAL OF HEAT TRANSFER*, TRANS. ASME, Series C, Vol. 81, No. 1, Feb. 1959, pp. 13-18.
- 3 Dhir, V. K., and Lienhard, J. H., "Laminar Film Condensation on Plane and Axisymmetric Bodies in Non-Uniform Gravity," *JOURNAL OF HEAT TRANSFER*, TRANS. ASME, Series C, Vol. 93, No. 1, Feb. 1971, pp. 97-100.
- 4 Gerstmann, J., and Griffith, P., "The Effects of Surface Instabilities on Laminar Film Condensation," Technical Report No. 5050-36, MIT, Cambridge 39, Mass., Sept. 30, 1965.
- 5 Lienhard, J. H., "On the Commonality of Equations for Natural Convection From Immersed Bodies," *International Journal of Heat and Mass Transfer*, Vol. 16, No. 11, 1973, pp. 2121-2123.

## Note on Forced Heat Transfer Over Thin Needles

Chang-yu Liu<sup>1</sup> and Liang-jy Leu<sup>1</sup>

Narain and Uberoi [1]<sup>2</sup> presented a note on forced heat transfer over thin needles with constant wall temperature and neglecting the dissipation term in the thermal energy equation. In this note it is found that if the wall temperature is of the form

$$T_w - T_\infty = NX^m \quad (1)$$

and if the dissipation term is retained

<sup>1</sup> National Taiwan University, Taipan, Taiwan.

<sup>2</sup> Numbers in brackets designate References at end of technical brief.

Contributed by the Heat Transfer Division of THE AMERICAN SOCIETY OF MECHANICAL ENGINEERS. Manuscript received by the Heat Transfer Division, April 8, 1974.

$$u \frac{\partial T}{\partial x} + v \frac{\partial T}{\partial y} = \frac{k}{\Gamma} \frac{\partial T}{\partial y} \Gamma \frac{\partial T}{\partial y} + \frac{\nu}{c_p} \left( \frac{\partial u}{\partial y} \right)^2 \quad (2)$$

a similarity transformation can also be obtained, where  $x$  and  $r$  are, respectively, the coordinates parallel and normal to the axis of the needle,  $u$  and  $v$  are their corresponding velocity components,  $k$ ,  $\nu$ , and  $c_p$  are standard notations of fluid properties, and  $N$  is a constant.

Defining the dimensionless stream function and temperature distribution in the form

$$\psi = \nu x \phi(z) \\ \theta(z) = \frac{T - T_\infty}{T_w - T_\infty}$$

where

$$z = \frac{Ur^2}{\nu x}$$

We can transform equation (2) into

$$(z\theta')' + \frac{1}{2} P_r (\phi\theta' - m\phi'\theta) + 4P_r E z \phi'^2 = 0 \quad (3)$$

For the case of constant wall temperature ( $m = 0$ ), equation (3) becomes

$$(z\theta')' + \frac{1}{2} P_r \phi\theta' = -4P_r E z \phi'^2 \quad (4)$$

By using a similar procedure as discussed by Schlichting [2] for the case of the flat plate, we assume that the general solution of equation (4) is composed of two functions of the form

$$\theta = C_1 \theta_1 + \frac{1}{2} E \theta_2 \quad (5)$$

where  $\theta_1$  denotes the general solution of the homogeneous equation with a prescribed temperature difference between the wall and free-stream,  $\theta_2$  denotes a particular solution of the nonhomogeneous equation with an adiabatic wall condition, and  $C_1$  is a constant to be determined later. Thus  $\theta_1$  and  $\theta_2$  satisfy the following equations

$$z\theta_1'' + \left(1 + \frac{1}{2} P_r \phi\right) \theta_1' = 0, \quad \theta_1(a) = 1, \quad \theta_1(\infty) = 0 \quad (6)$$

and

$$z\theta_2'' + \left(1 + \frac{1}{2} P_r \phi\right) \theta_2' = -8P_r z \phi'^2, \quad \theta_2'(a) = 0, \quad \theta_2(\infty) = 0 \quad (7)$$

With the boundary conditions at the wall, equation (5) can be written as

$$\theta = \left[1 - \frac{1}{2} E \theta_2(a)\right] \theta_1 + \frac{1}{2} E \theta_2 \quad (8)$$

Narain and Uberoi [1] have shown that  $\phi$  can be written as

$$\phi = \frac{-(z\phi'')'}{\phi'''} \quad (9)$$

Thus, the solution of equations (6) and (7) take the forms

$$\phi_1 = \frac{\int_a^\infty \frac{(z\phi''')^{Pr}}{z} dz}{\int_a^\infty \frac{(z\phi''')^{Pr}}{z} dz} \quad (10)$$

$$\theta_2 = 8P_r \int_a^\infty z^{Pr-1} \phi''^{Pr} \left( \int_a^\eta z^{1-Pr} \phi''^{2-Pr} dz \right) dz \quad (11)$$

For the particular case of  $Pr = 1$ , we have

$$\theta_1 = 1 - \phi'(z) = 1 - \frac{u}{U} \quad (12)$$

$$\theta_2 = 4 - \phi'^2 \quad (13)$$

Equation (12) assumes that the temperature distribution  $\theta_1$  is

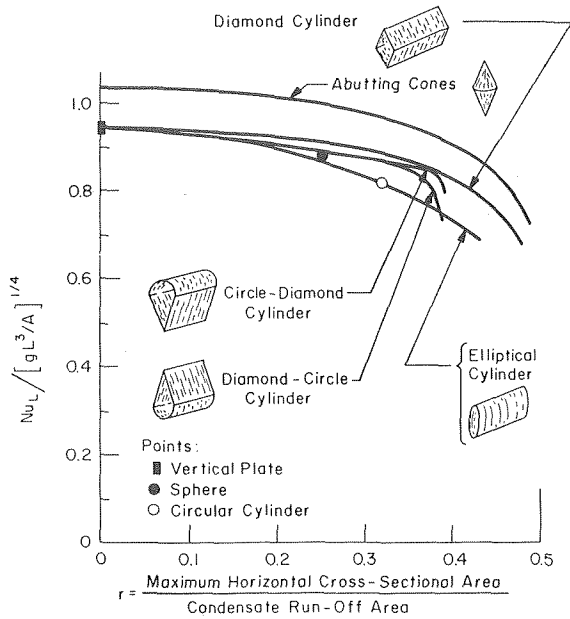


Fig. 1 Average Nusselt number for laminar film condensation on submerged isothermal bodies

tion has been made for natural convection heat transfer from submerged bodies [5].

## References

- 1 Nusselt, W., "Die Oberflächenkondensation des Wasserdampfes," *Z. Ver. Deutsch. Ing.*, Vol. 60, 1916, pp. 541-6, 569-75.
- 2 Sparrow, E. M., and Gregg, J. L., "A Boundary-Layer Treatment of Laminar-Film Condensation," *JOURNAL OF HEAT TRANSFER*, TRANS. ASME, Series C, Vol. 81, No. 1, Feb. 1959, pp. 13-18.
- 3 Dhir, V. K., and Lienhard, J. H., "Laminar Film Condensation on Plane and Axisymmetric Bodies in Non-Uniform Gravity," *JOURNAL OF HEAT TRANSFER*, TRANS. ASME, Series C, Vol. 93, No. 1, Feb. 1971, pp. 97-100.
- 4 Gerstmann, J., and Griffith, P., "The Effects of Surface Instabilities on Laminar Film Condensation," Technical Report No. 5050-36, MIT, Cambridge 39, Mass., Sept. 30, 1965.
- 5 Lienhard, J. H., "On the Commonality of Equations for Natural Convection From Immersed Bodies," *International Journal of Heat and Mass Transfer*, Vol. 16, No. 11, 1973, pp. 2121-2123.

## Note on Forced Heat Transfer Over Thin Needles

Chang-yu Liu<sup>1</sup> and Liang-jy Leu<sup>1</sup>

Narain and Uberoi [1]<sup>2</sup> presented a note on forced heat transfer over thin needles with constant wall temperature and neglecting the dissipation term in the thermal energy equation. In this note it is found that if the wall temperature is of the form

$$T_w - T_\infty = NX^m \quad (1)$$

and if the dissipation term is retained

<sup>1</sup> National Taiwan University, Taipan, Taiwan.

<sup>2</sup> Numbers in brackets designate References at end of technical brief.

Contributed by the Heat Transfer Division of THE AMERICAN SOCIETY OF MECHANICAL ENGINEERS. Manuscript received by the Heat Transfer Division, April 8, 1974.

$$u \frac{\partial T}{\partial x} + v \frac{\partial T}{\partial y} = \frac{k}{\Gamma} \frac{\partial T}{\partial y} \Gamma \frac{\partial T}{\partial y} + \frac{\nu}{c_p} \left( \frac{\partial u}{\partial y} \right)^2 \quad (2)$$

a similarity transformation can also be obtained, where  $x$  and  $r$  are, respectively, the coordinates parallel and normal to the axis of the needle,  $u$  and  $v$  are their corresponding velocity components,  $k$ ,  $\nu$ , and  $c_p$  are standard notations of fluid properties, and  $N$  is a constant.

Defining the dimensionless stream function and temperature distribution in the form

$$\psi = \nu x \phi(z) \\ \theta(z) = \frac{T - T_\infty}{T_w - T_\infty}$$

where

$$z = \frac{Ur^2}{\nu x}$$

We can transform equation (2) into

$$(z\theta')' + \frac{1}{2} P_r (\phi\theta' - m\phi'\theta) + 4P_r E z \phi'^2 = 0 \quad (3)$$

For the case of constant wall temperature ( $m = 0$ ), equation (3) becomes

$$(z\theta')' + \frac{1}{2} P_r \phi\theta' = -4P_r E z \phi'^2 \quad (4)$$

By using a similar procedure as discussed by Schlichting [2] for the case of the flat plate, we assume that the general solution of equation (4) is composed of two functions of the form

$$\theta = C_1 \theta_1 + \frac{1}{2} E \theta_2 \quad (5)$$

where  $\theta_1$  denotes the general solution of the homogeneous equation with a prescribed temperature difference between the wall and free-stream,  $\theta_2$  denotes a particular solution of the nonhomogeneous equation with an adiabatic wall condition, and  $C_1$  is a constant to be determined later. Thus  $\theta_1$  and  $\theta_2$  satisfy the following equations

$$z\theta_1'' + \left(1 + \frac{1}{2} P_r \phi\right) \theta_1' = 0, \quad \theta_1(a) = 1, \quad \theta_1(\infty) = 0 \quad (6)$$

and

$$z\theta_2'' + \left(1 + \frac{1}{2} P_r \phi\right) \theta_2' = -8P_r z \phi'^2, \quad \theta_2'(a) = 0, \quad \theta_2(\infty) = 0 \quad (7)$$

With the boundary conditions at the wall, equation (5) can be written as

$$\theta = \left[1 - \frac{1}{2} E \theta_2(a)\right] \theta_1 + \frac{1}{2} E \theta_2 \quad (8)$$

Narain and Uberoi [1] have shown that  $\phi$  can be written as

$$\phi = \frac{-(z\phi'')'}{\phi'''} \quad (9)$$

Thus, the solution of equations (6) and (7) take the forms

$$\phi_1 = \frac{\int_a^\infty \frac{(z\phi'')^{Pr}}{z} dz}{\int_a^\infty \frac{(z\phi'')^{Pr}}{z} dz} \quad (10)$$

$$\theta_2 = 8P_r \int_a^\infty z^{Pr-1} \phi''^{Pr} \left( \int_a^\eta z^{1-Pr} \phi''^{2-Pr} dz \right) dz \quad (11)$$

For the particular case of  $P_r = 1$ , we have

$$\theta_1 = 1 - \phi'(z) = 1 - \frac{u}{U} \quad (12)$$

$$\theta_2 = 4 - \phi'^2 \quad (13)$$

Equation (12) assumes that the temperature distribution  $\theta_1$  is

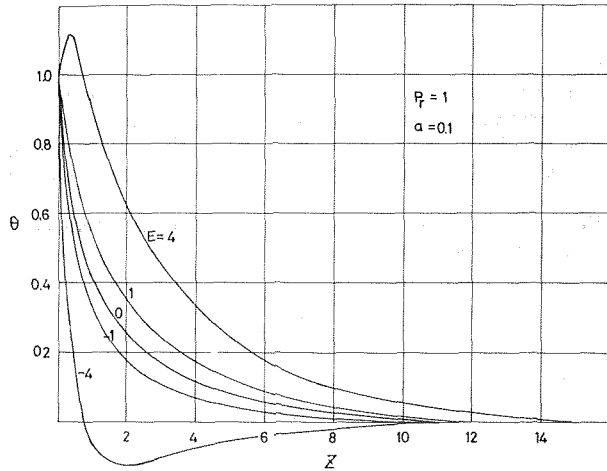


Fig. 1 Temperature profiles  $m = 0$

analogous with the velocity profile. Both equations (12) and (13) have a similar form as that presented by Schlichting [2].

Substituting equations (10) and (11) into equation (8), finally we get the solution

$$\theta = \left[1 - \frac{1}{2}E\theta_2(a)\right] \frac{\int_{\eta}^{\infty} \frac{(z\phi''')^{Pr}}{z} dz}{\int_a^{\infty} \frac{(z\phi''')^{Pr}}{z} dz} + 4PrE \int_a^{\eta} z^{Pr-1} \phi''^{Pr} \left( \int_a^{\eta} z^{1-Pr} \phi''^{2-Pr} dz \right) dz \quad (14)$$

Equation (14) reveals that if  $\phi''(z)$  can be calculated from momentum equation, then  $\theta$  can also be calculated for various combination of  $Pr$ ,  $E$ , and  $a$ . Fig. 1 shows the temperature profiles. For large positive value of  $E$  the boundary layer near the wall is warmer than the wall itself owing to the generation of friction heat which is consistent with the case of flat plate.

If the Nusselt number is defined as

$$Nu_x = \frac{-k\left(\frac{\partial T}{\partial r}\right)}{T_w - T_{\infty}} \quad (15)$$

the following relation can be obtained

$$Nu_x Re_x^{-1/2} = -2\sqrt{a}\theta_1'(a)\left[1 - \frac{1}{2}E\theta_2(a)\right] \quad (16)$$

Fig. 2 shows  $Nu_x Re_x^{-1/2}$  for various values of  $Pr$ ,  $a$ , and  $E$ . For constant values of  $Pr$  and  $a$ ,  $Nu_x Re_x^{-1/2}$  is linear variation with  $E$ .

If the Nusselt number is defined as

$$Nu_x = \frac{-k\left(\frac{\partial T}{\partial r}\right)_a}{T_w - T_r} \quad (17)$$

where  $T_r$  is the adiabatic wall temperature, we have

$$Nu_x Re_x^{-1/2} = -2\sqrt{a}\theta_1'(a) \quad (18)$$

For the case of  $E = 0$  and  $m \neq 0$ , the exact solution of the temperature profile can not be found, but can be calculated by computer. For this case the Nusselt number is usually defined by equation (15). Fig. 3 shows  $Nu_x Re_x^{-1/2}$  for various values of  $Pr$ ,  $a$ , and  $m$ . This figure has a similar shape as presented by Kundsén and Katz [3] for the case of flat plate. It can be seen that for  $m > -1$  heat transfer is from the surface to the stream. For the case of  $m = -1$ , there is no heat flux between the surrounding fluid and the needle surface. The decrease in temperature due to heat transfer from the fluid near the surface to the outer edge of the stream is just balanced by the decrease in wall temperature.

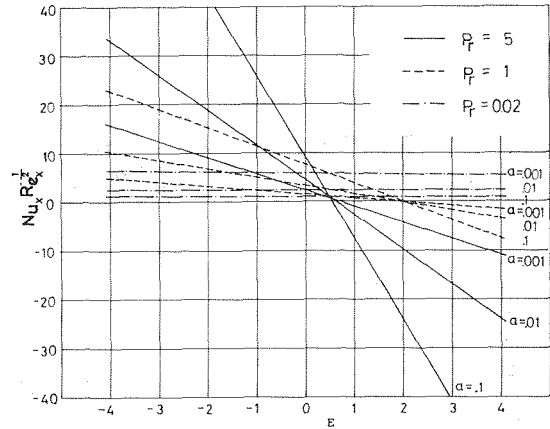


Fig. 2 Relation between  $Nu_x Re_x^{-1/2}$  and  $E$ ,  $Pr$ , and  $a$

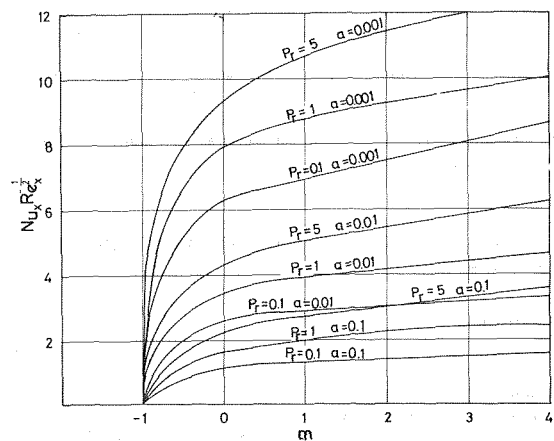


Fig. 3 Relation between  $Nu_x Re_x^{-1/2}$  and  $m$ ,  $Pr$ , and  $a$  ( $E = 0$ )

## References

- 1 Narian, J. P., and Uberoi, M., "Forced Heat Transfer Over Thin Needles," *JOURNAL OF HEAT TRANSFER*, TRANS. ASME, Series C, Vol. 94, No. 2, May 1972, pp. 240-242.
- 2 Schlichting, H., *Boundary Layer Theory*, McGraw Hill, New York, Sixth ed., 1968, pp. 252-300.
- 3 Kundsén, J. G., and Katz, D. L., *Fluid Dynamics and Heat Transfer*, McGraw Hill, New York, 1958, pp. 493-496.

## Bounding Effects on the Heat Loss by Free Convection From Spheres and Cylinders

R. E. Powe<sup>1</sup>

One difficulty frequently encountered in employing empirical heat transfer correlations for natural convection from a body to an enclosed fluid involves determining the range of relative gap

<sup>1</sup> Assist. Professor, Mechanical Engineering Department, Montana State University, Bozeman, Mont. Member ASME.

Contributed by the Heat Transfer Division of THE AMERICAN SOCIETY OF MECHANICAL ENGINEERS. Manuscript received by the Heat Transfer Division, February 4, 1974.

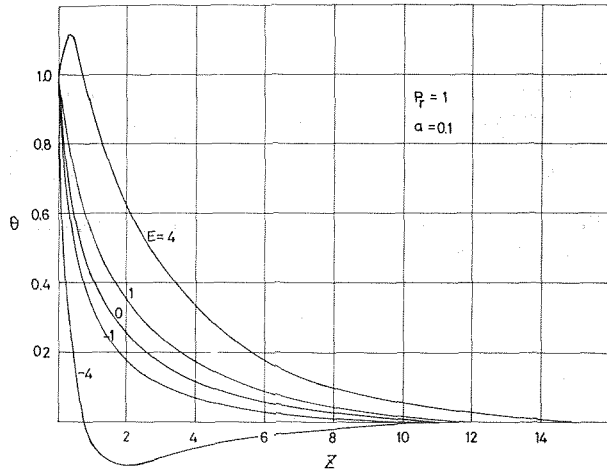


Fig. 1 Temperature profiles  $m = 0$

analogous with the velocity profile. Both equations (12) and (13) have a similar form as that presented by Schlichting [2].

Substituting equations (10) and (11) into equation (8), finally we get the solution

$$\theta = \left[1 - \frac{1}{2}E\theta_2(a)\right] \frac{\int_{\eta}^{\infty} \frac{(z\phi'')^{Pr}}{z} dz}{\int_a^{\infty} \frac{(z\phi'')^{Pr}}{z} dz} + 4PrE \int_a^{\eta} z^{Pr-1} \phi''^{Pr} \left( \int_a^{\eta} z^{1-Pr} \phi''^{2-Pr} dz \right) dz \quad (14)$$

Equation (14) reveals that if  $\phi''(z)$  can be calculated from momentum equation, then  $\theta$  can also be calculated for various combination of  $Pr$ ,  $E$ , and  $a$ . Fig. 1 shows the temperature profiles. For large positive value of  $E$  the boundary layer near the wall is warmer than the wall itself owing to the generation of friction heat which is consistent with the case of flat plate.

If the Nusselt number is defined as

$$Nu_x = \frac{-k \left( \frac{\partial T}{\partial r} \right)}{T_w - T_{\infty}} \quad (15)$$

the following relation can be obtained

$$Nu_x Re_x^{-1/2} = -2\sqrt{a}\theta_1'(a) \left[1 - \frac{1}{2}E\theta_2(a)\right] \quad (16)$$

Fig. 2 shows  $Nu_x Re_x^{-1/2}$  for various values of  $Pr$ ,  $a$ , and  $E$ . For constant values of  $Pr$  and  $a$ ,  $Nu_x Re_x^{-1/2}$  is linear variation with  $E$ .

If the Nusselt number is defined as

$$Nu_x = \frac{-k \left( \frac{\partial T}{\partial r} \right)_a}{T_w - T_r} \quad (17)$$

where  $T_r$  is the adiabatic wall temperature, we have

$$Nu_x Re_x^{-1/2} = -2\sqrt{a}\theta_1'(a) \quad (18)$$

For the case of  $E = 0$  and  $m \neq 0$ , the exact solution of the temperature profile can not be found, but can be calculated by computer. For this case the Nusselt number is usually defined by equation (15). Fig. 3 shows  $Nu_x Re_x^{-1/2}$  for various values of  $Pr$ ,  $a$ , and  $m$ . This figure has a similar shape as presented by Kundsens and Katz [3] for the case of flat plate. It can be seen that for  $m > -1$  heat transfer is from the surface to the stream. For the case of  $m = -1$ , there is no heat flux between the surrounding fluid and the needle surface. The decrease in temperature due to heat transfer from the fluid near the surface to the outer edge of the stream is just balanced by the decrease in wall temperature.

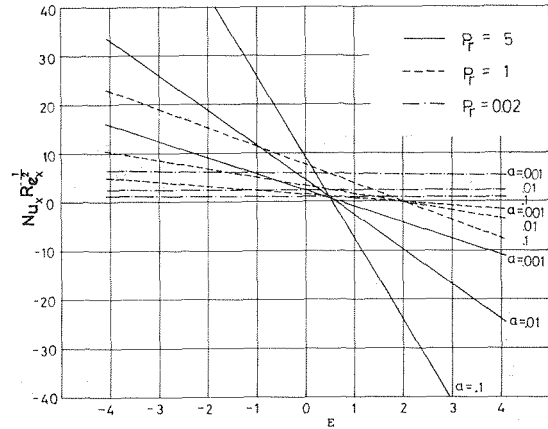


Fig. 2 Relation between  $Nu_x Re_x^{-1/2}$  and  $E$ ,  $Pr$ , and  $a$

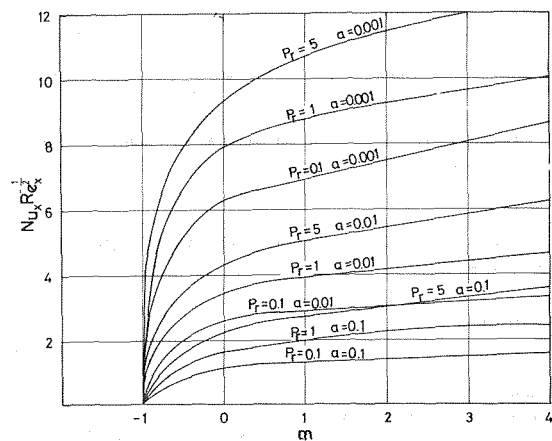


Fig. 3 Relation between  $Nu_x Re_x^{-1/2}$  and  $m$ ,  $Pr$ , and  $a$  ( $E = 0$ )

## References

- 1 Narian, J. P., and Uberoi, M., "Forced Heat Transfer Over Thin Needles," *JOURNAL OF HEAT TRANSFER*, TRANS. ASME, Series C, Vol. 94, No. 2, May 1972, pp. 240-242.
- 2 Schlichting, H., *Boundary Layer Theory*, McGraw Hill, New York, Sixth ed., 1968, pp. 252-300.
- 3 Kundsens, J. G., and Katz, D. L., *Fluid Dynamics and Heat Transfer*, McGraw Hill, New York, 1958, pp. 493-496.

## Bounding Effects on the Heat Loss by Free Convection From Spheres and Cylinders

R. E. Powe<sup>1</sup>

One difficulty frequently encountered in employing empirical heat transfer correlations for natural convection from a body to an enclosed fluid involves determining the range of relative gap

<sup>1</sup> Assist. Professor, Mechanical Engineering Department, Montana State University, Bozeman, Mont. Member ASME.

Contributed by the Heat Transfer Division of THE AMERICAN SOCIETY OF MECHANICAL ENGINEERS. Manuscript received by the Heat Transfer Division, February 4, 1974.

widths for which such correlations are applicable. This topic is pursued in the current note.

For natural convection from an isothermal sphere to water, the correlation equation given by Amato and Tien [1]<sup>2</sup> is

$$Nu_D = 2.0 + 0.5(Ra_D)^{0.25}, \quad (1)$$

while for water contained between isothermal concentric spheres, Scanlan, Bishop, and Powe [2] have correlated natural convection heat transfer rates with the equation

$$Nu_D = 0.0874(Ra_D)^{0.279}(1 + L/r_i)(L/r_i)^{-0.008}. \quad (2)$$

Examining equation (2), it may be observed that the Nusselt number,  $Nu_D$ , predicted is unbounded for very large relative gap widths,  $L/r_i$ . However, in the physical system it is known that this Nusselt number must actually be bounded. Thus, it is hypothesized that the limiting value of the Nusselt number for large relative gap widths will be that value predicted by equation (1) for heat transfer to an infinite atmosphere. Equating Nusselt numbers in equations (1) and (2), therefore, results in an expression for  $L/r_i$ , and this value of  $L/r_i$  is the largest for which the relation developed for concentric spheres should be employed.

In the other extreme, as the relative gap width becomes very small, the heat transfer would be expected to occur by pure conduction. In terms of the Nusselt number, the conduction solution may be expressed as

$$Nu_D = 2 + 2(L/r_i)^{-1}. \quad (3)$$

By comparing values of the Nusselt number predicted from equations (2) for a typical Rayleigh number with those predicted by equation (3), it is observed that, as the relative gap width is decreased from some large value, a point is eventually reached where the Nusselt number predicted for free convection becomes smaller than that predicted for conduction. However, this is certainly not in agreement with physical expectations. Therefore, the limiting relative gap width for which the pure conduction solution should be employed is taken to be that at which the Nusselt numbers predicted by equations (2) and (3) become equal.

A typical plot of the Nusselt number as a function of the relative gap width for a Rayleigh number of  $10^9$  is shown in Fig. 1. This plot indicates that the conduction solution should be utilized for relative gap widths less than about 0.07 and that the inner sphere should be taken as transferring heat to an atmosphere of infinite extent for relative gap widths greater than about 2.25. For relative gap widths between 0.07 and 2.25, the heat transfer must be evaluated using enclosure results. One hazard in using this scheme is evidenced by the discontinuities in slope indicated in Fig. 1. Certainly such discontinuities would not be expected, but in the absence of additional experimental information this scheme may be used to obtain an estimate of the ranges of validity of the various equations.

By repeating the calculations yielding the curves shown in Fig. 1 for various Rayleigh numbers, a band of values of limiting relative gap widths can be determined. The results of such a series of calculations are shown in Fig. 2. Also included in this figure are results for air obtained using the equation given by Yuge [3],

$$Nu_D = 2.0 + 0.428(Ra_D)^{0.25}, \quad (4)$$

for an atmosphere of infinite extent and the equation given by Scanlan, Bishop, and Powe [2],

$$Nu_D = 0.1917(Ra_D)^{0.252}(1 + L/r_i)(L/r_i)^{-0.185}, \quad (5)$$

for concentric spheres.

When employing these results, the range of available experimental data for enclosures shown in the figure should certainly be noted. In applying these results to Rayleigh numbers and relative gap widths outside this range, considerable uncertainty may be

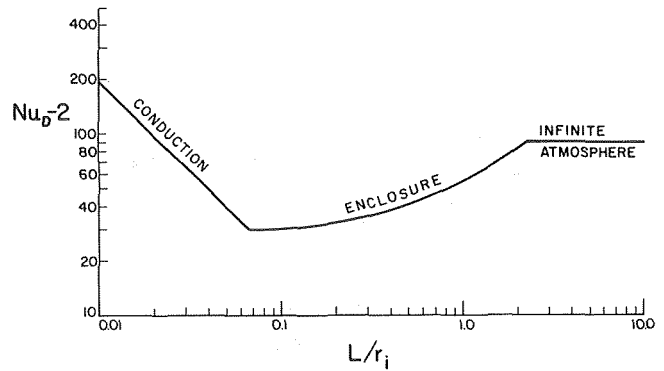


Fig. 1 Variation of Nusselt number with relative gap width for heat loss from a sphere to water,  $Ra_D = 10^9$

involved, but it is felt that this currently represents the best scheme available for predicting the heat transfer in these regions.

For cylindrical configurations, many more empirical equations are available for both confined and unconfined fluids than in the case of spheres. For natural convection from an isothermal cylinder to a fluid of infinite extent, the expressions presented by Holman [4] can be used to predict the heat transfer rates for a wide range of Rayleigh numbers and Prandtl numbers. Even though slightly better accuracy could be obtained through use of the data of Gebhart, Audunson, and Pera [5], Holman's expressions will be used for convenience. It is indicated that these relations are accurate to within about  $\pm 15$  percent. Since these results are readily available they will not be reproduced here. For natural convection between long, horizontal, isothermal, concentric cylinders Liu, Mueller, and Landis [6] indicate that heat transfer rates are given by the equation

$$Nu_D = \frac{0.1513}{\ln(1 + L/r_i)} \left[ \frac{Pr}{1.36 + Pr} \right]^{0.278} (Ra_D)^{0.278} (L/r_i)^{0.834}. \quad (6)$$

For pure conduction between concentric cylinders, the heat transfer is given by

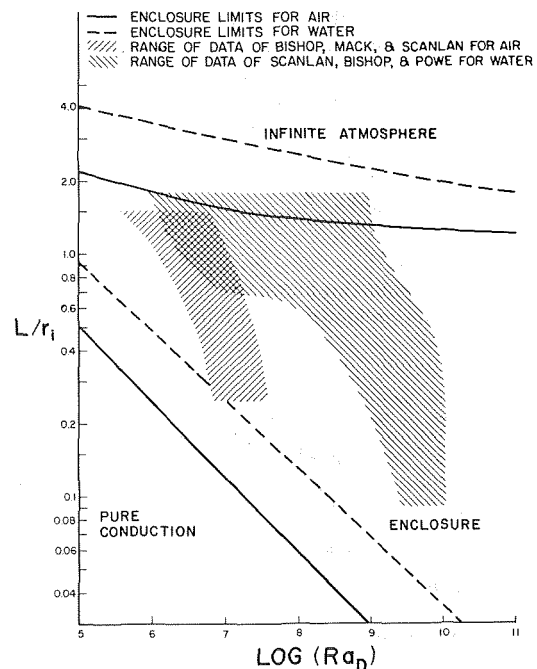


Fig. 2 Limits of applicability of various correlation equations for natural convection from a sphere

<sup>2</sup> Numbers in brackets designate References at end of technical brief.

# Laminar Heat Transfer in the Entrance Region of Concentric Annuli With Rotating Inner Walls.

J. E. R. Coney<sup>1</sup> and M. A. I. El-Shaarawi<sup>2</sup>

## Nomenclature

The following are added to the nomenclature used in [1]

- $D_h$  = hydraulic diameter of annulus,  $2(r_2 - r_1)$
- $h$  = local heat transfer coefficient based on area of heated surface
- $t$  = fluid temperature at any point
- $t_m$  = temperature over any cross section
- $t_0$  = fluid temperature at annulus entry
- $t_w$  = isothermal wall temperature
- $N$  = annulus radius ratio,  $r_1/r_2$
- $Nu_l$  = local Nusselt number,  $hD_h/k$
- $Pr$  = Prandtl number,  $\mu c_p/k$
- $Re$  = Reynolds number,  $\rho D_h \bar{v}_z/\mu$
- $Ta$  = Taylor number,  $2\Omega^2 r_1^2 b^3/\nu^2(r_1 + r_2)$
- $z$  = axial coordinate
- $\epsilon$  = dimensionless axial coordinate,  $2z(1 - N)/r_2 Re$
- $\theta$  = dimensionless temperature,  $(t - t_0)/(t_w - t_0)$
- $\theta_m$  = dimensionless mixing cup temperature,  $(t_m - t_0)/(t_w - t_0)$

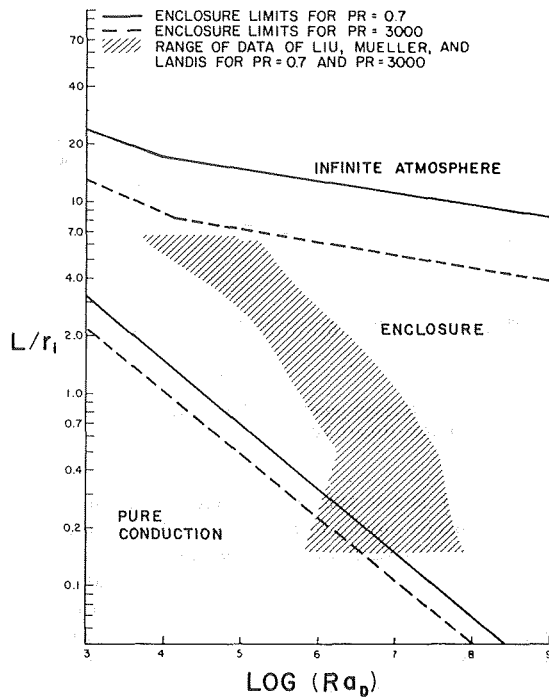


Fig. 3 Limits of applicability of various correlation equations for natural convection from a cylinder

$$Nu_D = 2/\ln(1 + L/r_1). \quad (7)$$

As in the case of the spherical configuration a band of values of limiting relative gap width may be determined, and these are shown in Fig. 3 for Prandtl numbers of 0.7 and 3000. Again, caution should be exercised in applying the results outside the range of available experimental data.

In conclusion, a systematic investigation of the limits of relative gap width for which available correlation equations for natural convection heat transfer in enclosures are applicable is presented. Specifically, existing results for long, horizontal, isothermal, concentric cylinders and for isothermal, concentric spheres are studied. Heat transfer rates for large relative gap widths are shown to be limited by those obtained for free convection to a fluid of infinite extent, and this criteria is used to calculate a maximum relative gap width for which the enclosure equations are applicable. A minimum relative gap width for applicability of the enclosure equations is determined by the pure conduction limit. It is observed that substantial errors in the heat transfer rate may be incurred if proper consideration is not given to these limiting relative gap widths.

## Acknowledgment

The work reported in this paper was supported by the National Science Foundation under grant GK-31908.

## References

- 1 Amato, W. S., and Tien, C., "Free Convection Heat Transfer From Isothermal Spheres in Water," *International Journal of Heat and Mass Transfer*, Vol. 15, 327-339, 1972, pp. 327-339.
- 2 Scanlan, J. A., Bishop, E. H., and Powe, R. E., "Natural Convection Heat Transfer Between Concentric Spheres," *International Journal of Heat and Mass Transfer*, Vol. 13, 1970, pp. 1857-1872.
- 3 Yuge, T., "Experiments on Heat Transfer From Spheres Including Natural and Forced Convection," *JOURNAL OF HEAT TRANSFER*, TRANS. ASME, Series C, Vol. 82, 1960, pp. 214-220.
- 4 Holman, J. P., *Heat Transfer*, Third ed., McGraw-Hill, New York, 1972.
- 5 Gebhart, B., Audunson, T., and Pera, L., *Proceedings of the Fourth International Heat Transfer Conference*, Paris, 1970.
- 6 Liu, C. Y., Mueller, W. K., and Landis, F., "Natural Convection Heat Transfer in Long Horizontal Cylindrical Annuli," *International Developments in Heat Transfer*, Paper No. 117, Boulder, Colo., 1961, pp. 976-984.

## Introduction

In a recent publication, [1]<sup>3</sup> the authors obtained a numerical solution of the boundary-layer equations representing laminar flow with constant physical properties in the entrance region of concentric annuli with rotating inner walls. The main aims of this technical brief are: (1) To show the extent to which the rotation of the inner cylinder affects the entrance-region laminar flow heat transfer when the speeds of rotation of the inner cylinder are lower than the critical speeds at which Taylor-vortices are generated. (2) To discuss the limitations on the values of  $Re^2/Ta$  in order that laminar solutions may be available over the entire development length.

## Problem Formulation, Simplifying Assumptions, and Method of Solution

The equations of conservation of momentum and mass can be solved to determine the hydrodynamic characteristics of the entry-length (see [1]), after which the energy equation can be solved using the velocity profiles previously obtained from the hydrodynamic calculations. Under the assumptions of [1], the energy equation, for an axisymmetric flow in the entry region of an annulus with a rotating inner cylinder, is

$$v_r \frac{\partial t}{\partial r} + v_z \frac{\partial t}{\partial z} = \alpha \left[ \frac{1}{r} \frac{\partial}{\partial r} \left( r \frac{\partial t}{\partial r} \right) \right] \quad (1)$$

in which the axial diffusion is neglected. The following two thermal boundary conditions have been considered in this investigation.

Case (a): The outer wall is isothermal while the inner wall is adiabatic i.e.,

<sup>1</sup> Mechanical Engineering Department, the University of Leeds, Leeds, England.

<sup>2</sup> Mechanical Engineering Department, the University of Leeds, Leeds, England; on leave from Alazhar University, Cairo.

<sup>3</sup> Numbers in brackets designate References at end of technical brief.

Contributed by the Heat Transfer Division of THE AMERICAN SOCIETY OF MECHANICAL ENGINEERS. Manuscript received by the Heat Transfer Division March 14, 1974.



# Laminar Heat Transfer in the Entrance Region of Concentric Annuli With Rotating Inner Walls.

J. E. R. Coney<sup>1</sup> and M. A. I. El-Shaarawi<sup>2</sup>

## Nomenclature

The following are added to the nomenclature used in [1]

- $D_h$  = hydraulic diameter of annulus,  $2(r_2 - r_1)$
- $h$  = local heat transfer coefficient based on area of heated surface
- $t$  = fluid temperature at any point
- $t_m$  = temperature over any cross section
- $t_0$  = fluid temperature at annulus entry
- $t_w$  = isothermal wall temperature
- $N$  = annulus radius ratio,  $r_1/r_2$
- $Nu_l$  = local Nusselt number,  $hD_h/k$
- $Pr$  = Prandtl number,  $\mu c_p/k$
- $Re$  = Reynolds number,  $\rho D_h \bar{v}_z/\mu$
- $Ta$  = Taylor number,  $2\Omega^2 r_1^2 b^3/\nu^2(r_1 + r_2)$
- $z$  = axial coordinate
- $\epsilon$  = dimensionless axial coordinate,  $2z(1 - N)/r_2 Re$
- $\theta$  = dimensionless temperature,  $(t - t_0)/(t_w - t_0)$
- $\theta_m$  = dimensionless mixing cup temperature,  $(t_m - t_0)/(t_w - t_0)$

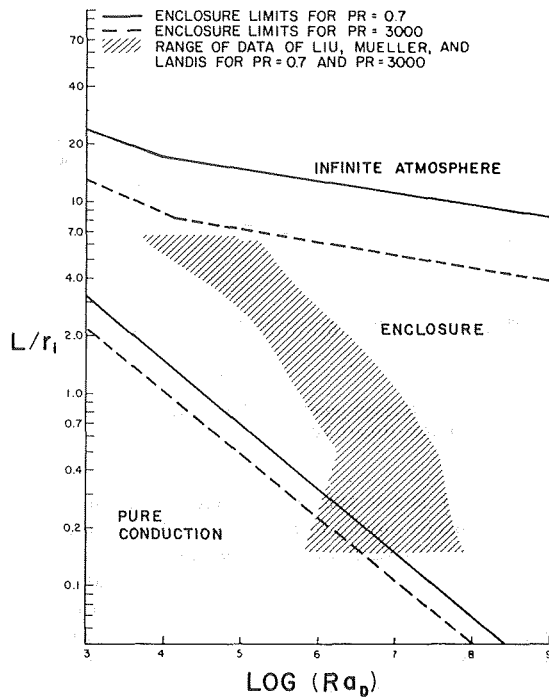


Fig. 3 Limits of applicability of various correlation equations for natural convection from a cylinder

$$Nu_D = 2/\ln(1 + L/r_1). \quad (7)$$

As in the case of the spherical configuration a band of values of limiting relative gap width may be determined, and these are shown in Fig. 3 for Prandtl numbers of 0.7 and 3000. Again, caution should be exercised in applying the results outside the range of available experimental data.

In conclusion, a systematic investigation of the limits of relative gap width for which available correlation equations for natural convection heat transfer in enclosures are applicable is presented. Specifically, existing results for long, horizontal, isothermal, concentric cylinders and for isothermal, concentric spheres are studied. Heat transfer rates for large relative gap widths are shown to be limited by those obtained for free convection to a fluid of infinite extent, and this criteria is used to calculate a maximum relative gap width for which the enclosure equations are applicable. A minimum relative gap width for applicability of the enclosure equations is determined by the pure conduction limit. It is observed that substantial errors in the heat transfer rate may be incurred if proper consideration is not given to these limiting relative gap widths.

## Acknowledgment

The work reported in this paper was supported by the National Science Foundation under grant GK-31908.

## References

- 1 Amato, W. S., and Tien, C., "Free Convection Heat Transfer From Isothermal Spheres in Water," *International Journal of Heat and Mass Transfer*, Vol. 15, 327-339, 1972, pp. 327-339.
- 2 Scanlan, J. A., Bishop, E. H., and Powe, R. E., "Natural Convection Heat Transfer Between Concentric Spheres," *International Journal of Heat and Mass Transfer*, Vol. 13, 1970, pp. 1857-1872.
- 3 Yuge, T., "Experiments on Heat Transfer From Spheres Including Natural and Forced Convection," *JOURNAL OF HEAT TRANSFER*, TRANS. ASME, Series C, Vol. 82, 1960, pp. 214-220.
- 4 Holman, J. P., *Heat Transfer*, Third ed., McGraw-Hill, New York, 1972.
- 5 Gebhart, B., Audunson, T., and Pera, L., *Proceedings of the Fourth International Heat Transfer Conference*, Paris, 1970.
- 6 Liu, C. Y., Mueller, W. K., and Landis, F., "Natural Convection Heat Transfer in Long Horizontal Cylindrical Annuli," *International Developments in Heat Transfer*, Paper No. 117, Boulder, Colo., 1961, pp. 976-984.

## Introduction

In a recent publication, [1]<sup>3</sup> the authors obtained a numerical solution of the boundary-layer equations representing laminar flow with constant physical properties in the entrance region of concentric annuli with rotating inner walls. The main aims of this technical brief are: (1) To show the extent to which the rotation of the inner cylinder affects the entrance-region laminar flow heat transfer when the speeds of rotation of the inner cylinder are lower than the critical speeds at which Taylor-vortices are generated. (2) To discuss the limitations on the values of  $Re^2/Ta$  in order that laminar solutions may be available over the entire development length.

## Problem Formulation, Simplifying Assumptions, and Method of Solution

The equations of conservation of momentum and mass can be solved to determine the hydrodynamic characteristics of the entry-length (see [1]), after which the energy equation can be solved using the velocity profiles previously obtained from the hydrodynamic calculations. Under the assumptions of [1], the energy equation, for an axisymmetric flow in the entry region of an annulus with a rotating inner cylinder, is

$$v_r \frac{\partial t}{\partial r} + v_z \frac{\partial t}{\partial z} = \alpha \left[ \frac{1}{r} \frac{\partial}{\partial r} \left( r \frac{\partial t}{\partial r} \right) \right] \quad (1)$$

in which the axial diffusion is neglected. The following two thermal boundary conditions have been considered in this investigation.

Case (a): The outer wall is isothermal while the inner wall is adiabatic i.e.,

<sup>1</sup> Mechanical Engineering Department, the University of Leeds, Leeds, England.

<sup>2</sup> Mechanical Engineering Department, the University of Leeds, Leeds, England; on leave from Alazhar University, Cairo.

<sup>3</sup> Numbers in brackets designate References at end of technical brief.

Contributed by the Heat Transfer Division of THE AMERICAN SOCIETY OF MECHANICAL ENGINEERS. Manuscript received by the Heat Transfer Division March 14, 1974.

$$\begin{aligned}
&\text{for } z \geq 0 \quad \text{and} \quad r = r_2, \quad t = t_w \\
&\text{for } z \geq 0 \quad \text{and} \quad r = r_1, \quad \frac{\partial t}{\partial r} = 0 \\
&\text{for } z = 0 \quad \text{and} \quad r_1 < r < r_2, \quad t = t_0
\end{aligned} \tag{2}$$

Case (b): The inner cylinder is isothermal while the outer cylinder is adiabatic i.e.,

$$\begin{aligned}
&\text{for } z \geq 0 \quad \text{and} \quad r = r_1, \quad t = t_w \\
&\text{for } z \geq 0 \quad \text{and} \quad r = r_2, \quad \frac{\partial t}{\partial r} = 0 \\
&\text{for } z = 0 \quad \text{and} \quad r_1 < r < r_2, \quad t = t_0
\end{aligned} \tag{3}$$

These thermal boundary conditions (a) and (b) correspond to the fundamental solution of the third kind according to the four fundamental solutions classified by Reynolds, et al. [3].

Now, using the previously determined axial and radial velocity profiles [1-2], the energy equation (1), associated with (2) or (3), has been solved by means of a simple implicit finite difference scheme [2].

### Results

A complete set of results is given in [2], of which a sample will be presented here.

Tables 1 and 2 give the local Nusselt number and the mixing cup temperature for  $Pr = 0.7$ , at various axial positions from the entrance for an annulus of radius ratio 0.85. The results are presented for  $Re^2/Ta = 0.5, 1$  and  $\infty$  (the stationary walls case). These were obtained using the same axial and radial mesh sizes in the numerical calculations so that the order of error magnitude would be the same at all values of  $Re^2/Ta$ . They show that decreasing  $Re^2/Ta$  causes a slight increase in the local heat transfer coefficient and the mixing cup temperature, if the inner wall is the heated boundary and vice versa if the outer wall is the heated boundary.

### Discussion

Although the above effects are slight, they can be attributed to the following significant reason. The effect of inner cylinder rotation on the laminar heat transfer characteristics ( $Nu_i$  and  $\theta_m$ ) in an annulus derives from the effect of the rotating core on the de-

velopment of both the axial and radial velocity components. These are the components responsible for transferring thermal energy from the heated boundary to the fluid and, therefore, are the only two components appearing in the energy equation.

Since a reduced effect of a rotating core on the development of both the axial and radial velocity components is expected as  $Re^2/Ta$  attains high values [1], it has been found that the difference between the heat transfer characteristics for the stationary walls case ( $Re^2/Ta = \infty$ ) and for  $Re^2/Ta = 10$  is very slight (maximum value of about 0.2 percent for radii ratios  $0.3 \leq N \leq 0.955$ ). However, with lower values of  $Re^2/Ta$ , the effect of a rotating core on the development of the axial and radial velocity components and hence on the heat transfer parameters becomes increasingly significant due to the effect of inner wall rotation on the pressure distribution. This effect causes the axial velocity profiles to be skewed inward as  $Re^2/Ta$  decreases [1, 4]. Hence, in the entrance region, the inner cylinder rotation causes the axial velocity boundary layer developing on the outer wall to be thickened while the inner wall axial velocity boundary layer diminishes. The increase in the outer wall and the decrease in the inner wall velocity boundary layer thicknesses derives from the fact that the inner cylinder rotation causes the axial pressure gradients in the outer and inner wall boundary layers to be decreased and increased, respectively. As the resistance to heat transfer between a heated boundary and a fluid is mainly due to the boundary layer, the effects of inner cylinder rotation on these two boundary layers cause a reduction in heat transfer if the outer wall is heated and vice versa. Thus, the heat transfer characteristics in the entrance region will be affected by the inner cylinder rotation differently from when the flow is hydrodynamically and thermally fully developed in an annulus of the same radius ratio. In the latter case, it is expected that, at core speeds insufficient to generate Taylor vortices, the local heat transfer coefficient,  $Nu_i$ , will remain constant at its fully developed value.

Finally, it should be noted that the solution for  $Re^2/Ta = 0.5$  in the tables is available up to a certain axial point in the entrance region, after which it starts to diverge from the laminar solution. This divergence appears as the radial velocity component starts to increase instead of decaying as in the laminar flow solution. This effect has been found for all values of  $Re^2/Ta < 1$ , but the point at which the solution starts to diverge always moves toward the entrance as the value of  $Re^2/Ta$  decreases. The finite difference scheme used in the analysis [1] has been checked in [2] by means of the available numerical stability theories summarized in [5] and

**Table 1 Local Nusselt number at various axial positions for an annulus of  $N = 0.85$  with various values of  $Re^2/Ta$**

$\epsilon \times 10^3$	Case (a)			Case (b)		
	$Re^2/Ta = 0.5$	$Re^2/Ta = 1$	$Re^2/Ta = \infty$	$Re^2/Ta = 0.5$	$Re^2/Ta = 1$	$Re^2/Ta = \infty$
0.025	16.690	16.730	16.777	21.115	20.813	20.469
0.125	9.837	9.888	9.946	10.960	10.754	10.524
0.250	7.728	7.797	7.856	8.798	8.401	8.232
1.000		5.340	5.399		5.769	5.692
4.000		4.704	4.748		5.057	5.017
16.000		4.736	4.737		5.006	5.006

**Table 2 Mixing cup temperature at various axial positions for an annulus of  $N = 0.85$  with various values of  $Re^2/Ta$**

$\epsilon \times 10^3$	Case (a)			Case (b)		
	$Re^2/Ta = 0.5$	$Re^2/Ta = 1$	$Re^2/Ta = \infty$	$Re^2/Ta = 0.5$	$Re^2/Ta = 1$	$Re^2/Ta = \infty$
0.050	0.04938	0.04944	0.04950	0.04067	0.04032	0.03989
0.125	0.07657	0.07674	0.07693	0.06716	0.06635	0.06543
0.250	0.10970	0.11035	0.11076	0.09977	0.09773	0.09623
1.000		0.23968	0.24115		0.21915	0.21602
4.000		0.53739	0.54090		0.50594	0.50166
16.000		0.93368	0.93450		0.91499	0.91393

shown to be stable for all mesh sizes and any values of  $Re^2/Ta$ , as long as the downstream axial velocity is non-negative. The following points may confirm that the phenomenon of a nonexistent laminar solution, which occurs after a certain axial length, at low values of  $Re^2/Ta$ , is not linked with a numerical instability but rather it may be a physical instability.

1 Astill and Chung [4], using a velocity ratio  $\Omega r_1/\bar{v}_z$  as a parameter, found the same effect in a recent momentum analysis, which predicts solutions up to the closing point of the two axial boundary layers.

It should be noted that even though the momentum integral analysis of [4] employs a Runge-Kutta integration procedure of ordinary differential equations, which is different from the finite-difference approximations of partial differential equations used in this investigation, the same conclusion appears.

2 Schlichting [6], investigating laminar flow around a rotating body of revolution in an axial air stream, included a velocity ratio (tangential to axial) as a parameter in an integral-momentum analysis; a similar result (which was attributed to a boundary layer separation due to high centrifugal forces at high values of the tangential to axial velocity ratio) was obtained i.e., laminar solutions are available for values of tangential to axial velocity ratio lower than certain critical values.

3 Since the boundary layer equations [1] merely represent a mathematical model describing laminar flow conditions at reasonably large Reynolds numbers, the previous discussion implies that,

at values of  $Re^2/Ta < 1$ , the laminar flow represented by these equations will not exist over the entire development length and that a type of flow which cannot be represented mathematically with the same differential equations will occur before the flow reaches full development. Since the parameter  $Re^2/Ta$ , which is included in the present analysis, has a physically significant meaning in that it represents the ratio between the inertia and centrifugal forces, this discussion indicates that, if the centrifugal forces are greater than the inertia forces, a laminar solution will not exist over the entire development length.

## References

- 1 Coney, J. E. R., and El-Shaarawi, M. A. I., "A Contribution to the Numerical Solution of Developing Laminar Flow in the Entrance Region of Concentric Annuli With Rotating Inner Walls," ASME Paper No. 74-FE-28.
- 2 El-Shaarawi, M. A. I., "Heat Transfer and Hydrodynamics in the Entrance Region of Concentric Annuli With Stationary and Rotating Inner Walls," PhD thesis, The University of Leeds, Leeds, England, 1974.
- 3 Reynolds, W. C., Lundberg, R. E., and McCuen, P. A., "Heat Transfer in Annular Passages. General Formulation of the Problem for Arbitrarily Prescribed Wall Temperatures and Heat Fluxes," *International Journal of Heat and Mass Transfer*, Vol. 6, 1963, pp. 483-493.
- 4 Chung, K., "The Momentum Integral Solution of the Developing Flow in the Entrance of an Annulus With a Rotating Inner Cylinder," MSc thesis, Tufts University, U.S.A., Mar. 1973.
- 5 Carnahan, B., Luther, H. A., and Wilkes, J. O., *Applied Numerical Methods*, J. Wiley, New York, 1969, pp. 242.
- 6 Schlichting, H., "Laminar Flow About a Rotating Body of Revolution in an Axial Airstream," NACA, TM 1415, 1956.

## A Compact Design of Shell and Tube Heat Exchangers

R. Rajasekaran<sup>1</sup> and P. A. Lytle<sup>1</sup>

### Introduction

Shell and tube type heat exchangers have long been used in several applications. Sizes of heat exchangers commonly used vary from fairly small to very large depending on the application. A common application of a shell and tube heat exchanger is for cooling lubricating oil in diesel engines. A reduction in oil cooler size is advantageous for the application of diesel engines in trucks. A typical oil cooler for diesel engines has the cooling water flowing through the tubes with the lubricating oil flowing on the shell side. Usually there are several baffles on the shell side to provide a circuitous path for the oil. Considerable work has already been done in analyzing and testing the shell and tube heat exchangers. Correlations for the shell side and tube side heat transfer coefficients, analytical techniques to predict the heat transfer and pressure drop characteristics of shell and tube heat exchangers, etc., are available in the literature. Good examples will be found in the references [1, 2, 3].<sup>2</sup>

Heat exchanger manufacturers try to reduce the size of the oil cooler without increasing cost or reducing effectiveness. Plate type oil coolers and fin and tube oil coolers are two examples of attempts to obtain a compact lubricating oil cooler for diesel engine applications. Most of these new oil coolers have higher oil pressure drop or higher costs of both when compared to the conventional shell and tube type oil coolers. The design of a shell and tube oil cooler which gives about 50% increase in heat transfer rate without any increase in pressure drop is described here.

### New Oil Cooler Design Compared to The Conventional Design

Conventional oil coolers have water tubes which pass through the holes in the baffles and which are soldered to the end plates. This cooler bundle is then assembled in a housing which is the "shell." In a given bundle volume, the heat transfer rate can be increased by increasing the surface area. This could be achieved by:

- 1 using larger diameter tubes;
- 2 increasing the number of tubes;
- 3 using fins on the oil side.

All of these methods of increasing the oil side heat transfer area involve inherent penalties. Some examples are:

- 1 using larger diameter tubes requires larger holes in baffles and end plates which weaken these components;
- 2 using more tubes or fins
  - (a) increases the number of solder joints in the cooler;
  - (b) increases the oil pressure drop; and
  - (c) possibly increases the cost.

The new design provides a method of using larger outside diameter tubes without any of these problems.

The details of the tube used in the new design are shown in Fig. 1 and described in Table 1.

The standard oil cooler has 172 water tubes made of 0.25 in. OD copper tubes. The new cooler has 185 tubes made of 0.320 in. OD copper tubes. To avoid making larger holes, and thus weakening the end plates, the tubes in the new design are necked down in the ends to about 0.24 in. dia. No transverse baffles are used in the new design on the oil side. Large diameter tubes reduce the oil side flow area and an increase in oil pressure drop results. To overcome this difficulty, most of the tubes are dimpled which increases the oil flow area. The pressure drop is further kept to a minimum by decreasing the number of passes on the oil side. Two passes are made in the new cooler compared to six in the conventional cooler. Two center rows have plain tubes with a nominal clearance of 0.005 in. between them for about 75 percent of the depth. This tube arrangement acts as a longitudinal baffle for oil flow. Oil enters the heat exchanger on one side of the "baffle" arrangement along the entire length of the cooler and leaves

<sup>1</sup> Senior Engineer, Cummins Engine Co., Columbus, Ind.

<sup>2</sup> Numbers in brackets designate References at end of technical brief.

Contributed by the Heat Transfer Division of THE AMERICAN SOCIETY OF MECHANICAL ENGINEERS. Manuscript received by the Heat Transfer Division, April 12, 1974.

shown to be stable for all mesh sizes and any values of  $Re^2/Ta$ , as long as the downstream axial velocity is non-negative. The following points may confirm that the phenomenon of a nonexistent laminar solution, which occurs after a certain axial length, at low values of  $Re^2/Ta$ , is not linked with a numerical instability but rather it may be a physical instability.

1 Astill and Chung [4], using a velocity ratio  $\Omega r_1/\bar{v}_z$  as a parameter, found the same effect in a recent momentum analysis, which predicts solutions up to the closing point of the two axial boundary layers.

It should be noted that even though the momentum integral analysis of [4] employs a Runge-Kutta integration procedure of ordinary differential equations, which is different from the finite-difference approximations of partial differential equations used in this investigation, the same conclusion appears.

2 Schlichting [6], investigating laminar flow around a rotating body of revolution in an axial air stream, included a velocity ratio (tangential to axial) as a parameter in an integral-momentum analysis; a similar result (which was attributed to a boundary layer separation due to high centrifugal forces at high values of the tangential to axial velocity ratio) was obtained i.e., laminar solutions are available for values of tangential to axial velocity ratio lower than certain critical values.

3 Since the boundary layer equations [1] merely represent a mathematical model describing laminar flow conditions at reasonably large Reynolds numbers, the previous discussion implies that,

at values of  $Re^2/Ta < 1$ , the laminar flow represented by these equations will not exist over the entire development length and that a type of flow which cannot be represented mathematically with the same differential equations will occur before the flow reaches full development. Since the parameter  $Re^2/Ta$ , which is included in the present analysis, has a physically significant meaning in that it represents the ratio between the inertia and centrifugal forces, this discussion indicates that, if the centrifugal forces are greater than the inertia forces, a laminar solution will not exist over the entire development length.

## References

- 1 Coney, J. E. R., and El-Shaarawi, M. A. I., "A Contribution to the Numerical Solution of Developing Laminar Flow in the Entrance Region of Concentric Annuli With Rotating Inner Walls," ASME Paper No. 74-FE-28.
- 2 El-Shaarawi, M. A. I., "Heat Transfer and Hydrodynamics in the Entrance Region of Concentric Annuli With Stationary and Rotating Inner Walls," PhD thesis, The University of Leeds, Leeds, England, 1974.
- 3 Reynolds, W. C., Lundberg, R. E., and McCuen, P. A., "Heat Transfer in Annular Passages. General Formulation of the Problem for Arbitrarily Prescribed Wall Temperatures and Heat Fluxes," *International Journal of Heat and Mass Transfer*, Vol. 6, 1963, pp. 483-493.
- 4 Chung, K., "The Momentum Integral Solution of the Developing Flow in the Entrance of an Annulus With a Rotating Inner Cylinder," MSc thesis, Tufts University, U.S.A., Mar. 1973.
- 5 Carnahan, B., Luther, H. A., and Wilkes, J. O., *Applied Numerical Methods*, J. Wiley, New York, 1969, pp. 242.
- 6 Schlichting, H., "Laminar Flow About a Rotating Body of Revolution in an Axial Airstream," NACA, TM 1415, 1956.

## A Compact Design of Shell and Tube Heat Exchangers

R. Rajasekaran<sup>1</sup> and P. A. Lytle<sup>1</sup>

### Introduction

Shell and tube type heat exchangers have long been used in several applications. Sizes of heat exchangers commonly used vary from fairly small to very large depending on the application. A common application of a shell and tube heat exchanger is for cooling lubricating oil in diesel engines. A reduction in oil cooler size is advantageous for the application of diesel engines in trucks. A typical oil cooler for diesel engines has the cooling water flowing through the tubes with the lubricating oil flowing on the shell side. Usually there are several baffles on the shell side to provide a circuitous path for the oil. Considerable work has already been done in analyzing and testing the shell and tube heat exchangers. Correlations for the shell side and tube side heat transfer coefficients, analytical techniques to predict the heat transfer and pressure drop characteristics of shell and tube heat exchangers, etc., are available in the literature. Good examples will be found in the references [1, 2, 3].<sup>2</sup>

Heat exchanger manufacturers try to reduce the size of the oil cooler without increasing cost or reducing effectiveness. Plate type oil coolers and fin and tube oil coolers are two examples of attempts to obtain a compact lubricating oil cooler for diesel engine applications. Most of these new oil coolers have higher oil pressure drop or higher costs of both when compared to the conventional shell and tube type oil coolers. The design of a shell and tube oil cooler which gives about 50% increase in heat transfer rate without any increase in pressure drop is described here.

### New Oil Cooler Design Compared to The Conventional Design

Conventional oil coolers have water tubes which pass through the holes in the baffles and which are soldered to the end plates. This cooler bundle is then assembled in a housing which is the "shell." In a given bundle volume, the heat transfer rate can be increased by increasing the surface area. This could be achieved by:

- 1 using larger diameter tubes;
- 2 increasing the number of tubes;
- 3 using fins on the oil side.

All of these methods of increasing the oil side heat transfer area involve inherent penalties. Some examples are:

- 1 using larger diameter tubes requires larger holes in baffles and end plates which weaken these components;
- 2 using more tubes or fins
  - (a) increases the number of solder joints in the cooler;
  - (b) increases the oil pressure drop; and
  - (c) possibly increases the cost.

The new design provides a method of using larger outside diameter tubes without any of these problems.

The details of the tube used in the new design are shown in Fig. 1 and described in Table 1.

The standard oil cooler has 172 water tubes made of 0.25 in. OD copper tubes. The new cooler has 185 tubes made of 0.320 in. OD copper tubes. To avoid making larger holes, and thus weakening the end plates, the tubes in the new design are necked down in the ends to about 0.24 in. dia. No transverse baffles are used in the new design on the oil side. Large diameter tubes reduce the oil side flow area and an increase in oil pressure drop results. To overcome this difficulty, most of the tubes are dimpled which increases the oil flow area. The pressure drop is further kept to a minimum by decreasing the number of passes on the oil side. Two passes are made in the new cooler compared to six in the conventional cooler. Two center rows have plain tubes with a nominal clearance of 0.005 in. between them for about 75 percent of the depth. This tube arrangement acts as a longitudinal baffle for oil flow. Oil enters the heat exchanger on one side of the "baffle" arrangement along the entire length of the cooler and leaves

<sup>1</sup> Senior Engineer, Cummins Engine Co., Columbus, Ind.

<sup>2</sup> Numbers in brackets designate References at end of technical brief.

Contributed by the Heat Transfer Division of THE AMERICAN SOCIETY OF MECHANICAL ENGINEERS. Manuscript received by the Heat Transfer Division, April 12, 1974.

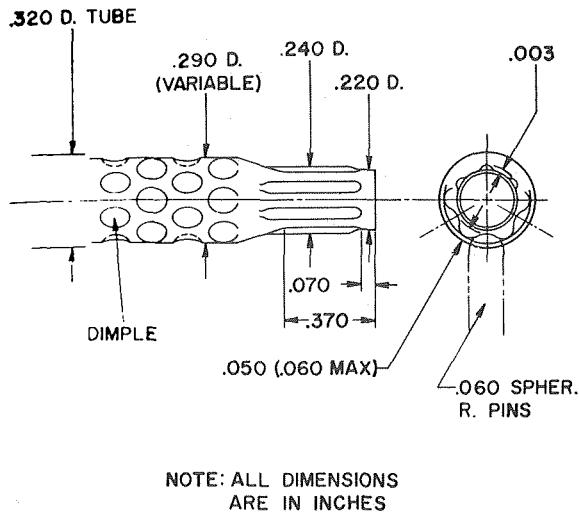


Fig. 1 Detail of the tube used in the new shell and tube type oil cooler design

on the other side as shown in Fig. 2. The new oil cooler has considerably more heat transfer area in the same bundle volume.

Due to the nature of the oil flow in the cooler, a new housing was designed and machined. Slots are provided along the length of the housing in order to facilitate oil entry and exit. Manifolds are provided to facilitate the oil flow through long narrow slots in the housing. These manifolds and slots in the housing for entry and exit provide uniform oil flow distribution through the bundle.

### Test Results

The oil cooler test bench consisted of an oil loop, a water loop, an oil heater, and the necessary instrumentation to measure the heat transfer rates and the pressure drops. The tests were conducted at three oil flow rates and three water flow rates. SAE 20 lubricating oil was used in all the tests. Comparative heat transfer and oil side pressure drop data are contained in Fig. 3. The waterside pressure drop is essentially the same in both the coolers. The heat transfer rate observed in the new cooler is higher by 47 percent at the lowest flow rates and by 55 percent at the highest flow rates compared to the conventional cooler. The new cooler shows slightly lower oil pressure drop than the conventional cooler. The increased heat transfer rate is attributed to the increased heat transfer area built into the new design and to the possible increase in turbulence on both the oil and water sides caused by the dimples in the tubes. This increase in heat transfer is achieved without any penalty in the form of increased pressure drop.

The clearance between tubes in the conventional cooler is 0.056 in. The nominal clearance between tubes in the new design is 0.005 in. excluding the clearance provided by the dimples. It is clear that the oil velocity in the new cooler will be higher if dimples are not provided, even though the number of passes in the

Table 1 Comparison of the geometrical features of the new oil cooler core and the conventional oil cooler core

	New design shell and tube oil cooler	Conventional shell and tube oil cooler
Tube bundle diameter	4.985 in.	4.985 in.
Tube bundle length	8.0 in.	8.0 in.
Tube outside diameter	0.320 in.	0.25 in.
Number of tubes	185	172
Heat transfer area	1488 in. <sup>2</sup>	1080 in. <sup>2</sup>
Number of baffles	Zero	Five

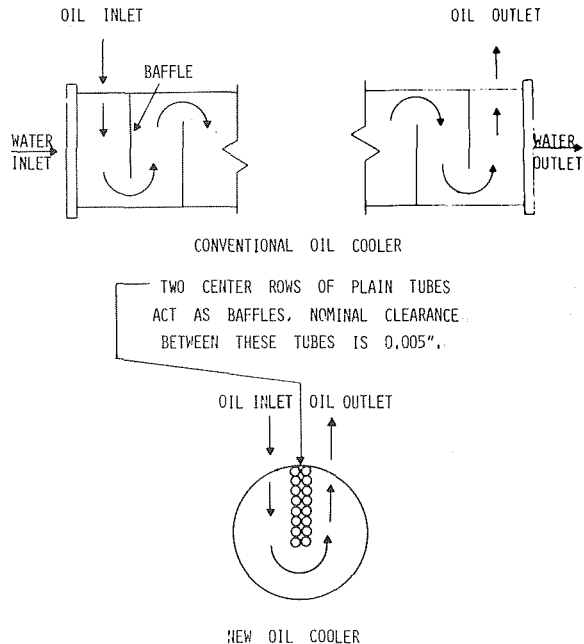


Fig. 2 Oil flow paths in the conventional and the new oil coolers

new cooler is two compared to six in the conventional cooler. The depth of the dimples can be varied as desired until the oil velocity is reduced to a level where the oil pressure drop is the same as in the conventional cooler.

The bench test data obtained on the new oil cooler were used to obtain a correlation. Essentially the new cooler has two passes on the oil side, each pass being a cross flow heat exchanger. Correlations available in the literature [3] were used to calculate the waterside heat transfer coefficient. The dimples in the tubes could

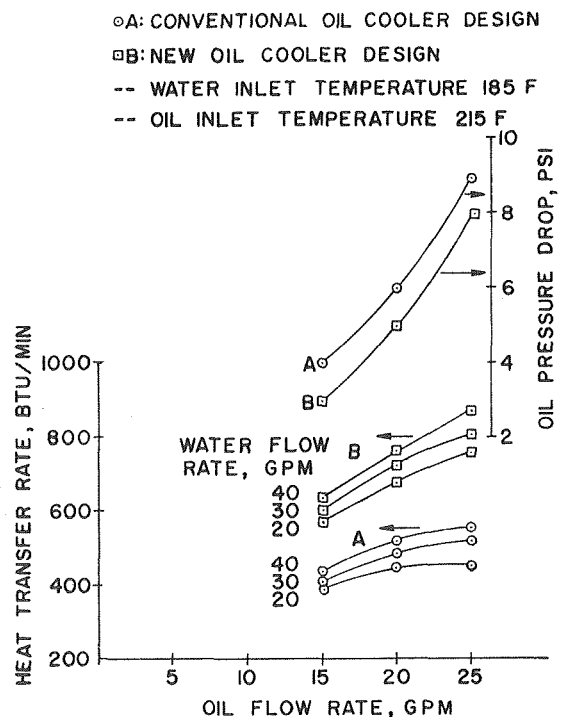


Fig. 3 Comparison of performances of identical size oil coolers of conventional design and new design

affect the waterside heat transfer coefficient as well as the oil side heat transfer coefficient. Since the performance of the oil cooler is usually limited by the oil side, the effect of dimples on the waterside heat transfer coefficient was neglected. The bench test data were used to obtain a correlation for the oil side heat transfer coefficient. The well known form of convective heat transfer correlations is:

$$Nu = c Re^n Pr^m$$

where

Nu = oil side Nusselt number based on the nominal outside diameter of the tube

Re = oil Reynold's number based on the nominal outside diameter of the tube

Pr = oil Prandtl number

$c, n, m$  = constants to be chosen to match the experimental data

It was found that the values of 0.4224, 0.6360, and 0.3333 for  $c$ ,  $n$ , and  $m$ , respectively, give a correlation with the bench test data within  $\pm 5$  percent.

## Conclusions

Necking the tube in the ends permits the use of larger diameter tubes in the same core volume. This gives a higher heat transfer area/core volume ratio for the shell and tube heat exchanger. Dimples in the tubes can be made to required depth to keep the shell side fluid pressure drop within allowable limits while the increased number of tubes helps to keep the tubeside pressure drop within allowable limits.

## Acknowledgment

The authors wish to thank the management of Cummins Engine Company for the permission given to publish this work and Mr. K. M. Hostetler for several useful suggestions.

## References

- 1 Lord, R. C., Minton, P. E., and Slusser, R. P., "Design of Heat Exchangers," *Chemical Engineering*, Jan. 26, 1970, pp. 96-118.
- 2 Kreith, F., *Principles of Heat Transfer*, Second ed., International Text Book Company.
- 3 Kays, W. M., and London, A. L., *Compact Heat Exchangers*, Second ed., McGraw-Hill, New York.
- 4 Rajasekaran, R., and Lytle, P. A., "A Compact Design of Shell and Tube Heat Exchangers," ASME Paper No. 73-HT-17.



## A Mathematical Model for Transient Subchannel Analysis of Rod-Bundle Nuclear Fuel Elements<sup>1</sup>

P. Buettiker.<sup>2,3</sup> The objective of the paper by Rowe, as stated in the Introduction, is timely and worthy of support. In the execution of this objective, however, so many fundamental errors are made that its physical meaning becomes questionable.

First, consider his assumptions. The treatment of the two-phase flow is apparently based on a homogeneous flow model, which is indicated by the use of one-phase equations. This contradicts assumption 1, where two-phase flow is specified. The errors introduced by doing this are not mentioned. The assumption of slip flow in a rod bundle cannot be made because a mix of solid and free fluid boundaries define subchannels. Slip flow, because of the absence of lateral gradients, would not permit radial momentum transfer. Rowe's second assumption specifies the subchannel density as a function of dependent and independent variables, violating thermodynamic principles. Basic assumption 3 fixes the coupling of adjacent subchannels by means of two types of lateral mixing mechanisms. Since the flow is basically in the axial direction one should expect that adjacent subchannels are coupled by the boundary conditions at the subchannel boundaries, involving the axial velocity and its derivatives. In the absence of the knowledge of the lateral velocity distribution and its derivatives, because of assumption 1, one should think that information to link subchannels must come from detailed experimental investigations.

Assumption 4 contradicts assumption 1, because it implies existence of transverse velocities. The application of the assumptions just discussed to the three conservation equations leads to more surprises.

Starting with the continuity equation for one-phase flow, one has

$$\frac{\partial \rho}{\partial t} + \frac{\partial}{\partial x} (\rho u) + \frac{\partial}{\partial y} (\rho v) + \frac{\partial}{\partial z} (\rho w) = 0 \quad (1)$$

To obtain a term

$$A_i \frac{\partial \rho_i}{\partial t} \quad (2)$$

as Rowe does in his equation (1), one must require that

$$\rho \neq f(y, z) \quad \text{and} \quad u \neq f(y, z) \quad (3)$$

such that

$$\int \int_{A_i} \frac{\partial \rho(x, t)}{\partial t} dy dz = A_i \frac{\partial \rho_i}{\partial t} \quad (4)$$

and

$$\int \int_{A_i} \frac{\partial \rho_i(x, t) u_i(x, t)}{\partial x} dy dz = A_i \frac{\partial (\rho u_i)}{\partial x} = \frac{\partial \dot{m}_i}{\partial x} \quad (5)$$

where Rowe apparently defines

$$\dot{m}_i = \rho_i A_i u_i \quad (6)$$

The continuity equation then becomes

$$A_i \frac{\partial \rho_i}{\partial t} + \frac{\partial \dot{m}_i}{\partial x} = 0 \quad (7)$$

Contrary to my equation (3) and his assumption 1, Rowe assumes  $w_{ij}$  is not zero. Furthermore, the dimension of  $w_{ij}$ , a mass flow per unit length, has no physical meaning. On purely mathematical grounds, one has to object to replacing the lateral components of the divergence of the velocity vector by  $w_{ij}$ . Doing this means that the simultaneous satisfaction of all boundary conditions relevant to the continuity equation is not possible and that, therefore, the solutions of the equation simplified by  $w_{ij}$  have no physical meaning.

A look at Rowe's energy and momentum equations reveals a host of other wrong manipulations with differential equations. As an example, the order of both differential equations for conservation of energy and momentum is reduced. Thus, the necessary boundary conditions cannot be satisfied and solutions of Rowe's equations (2) and (3) are physically meaningless. If integral functions, such as Nikuradse's friction equation, or Dittus-Boelter's Nusselt number relationship, are to be used, they can only be introduced within the framework of integral equations over the whole flow region. In fact, this is what Rowe is really trying to do—write balances over finite control volumes and account for exchange of momentum and energy between subchannels from experiment. He has lost all means of predicting such exchanges by averaging the Navier-Stokes equations over the finite control volumes. In view of all the errors and wrong mathematical manipulations one should ask: What does the numerical output of the COBRA III computer code, which is based on the erroneous equations in the paper under discussion, then mean?

### Author's Closure

Dr. Buettiker has interpreted the assumptions of the paper in a way that leads him to erroneous conclusions.

Consider the general integral form of the continuity equation [13]<sup>4</sup> for one-phase flow

$$\frac{\partial}{\partial t} \iiint \rho dV + \iint \rho \vec{v} \cdot \vec{n} dA = 0 \quad (1)$$

where  $dV$  is a differential volume,  $dA$  is the differential surface area,  $\rho$  is the local density,  $\vec{v}$  is the local velocity vector, and  $\vec{n}$  is the outward pointing normal to the surface. Integrate over the control volume as shown in Fig. 1. Consider flow through the top, bottom, and through only one lateral surface (rod gap) for now. The result is

$$\frac{\partial}{\partial t} \iiint \rho dA_i dx - \iint \rho u dA_i \Big|_x + \iint \rho u dA_i \Big|_{x+\Delta x} + \iint \rho v ds dx \quad (2)$$

where  $u$  and  $v$  are the axial and lateral velocities, respectively, through the control surfaces.

Define

$$\rho_i = \frac{1}{A_i \Delta x} \iiint \rho dA_i dx \quad (3)$$

$$\dot{m}_i = \iint \rho u dA_i \quad (4)$$

<sup>1</sup> By D. S. Rowe, published in the May 1973 issue of the JOURNAL OF HEAT TRANSFER, TRANS. ASME, Series C, Vol. 95, No. 2, pp. 211-217.

<sup>2</sup> Senior R&D engineer, Swiss Federal Institute for Reactor Research 5300 Würenlingen, Switzerland. Mem. ASME.

<sup>3</sup> The opinions expressed here are solely those of the author.

<sup>4</sup> Numbers in brackets designate Additional References at end of discussion.

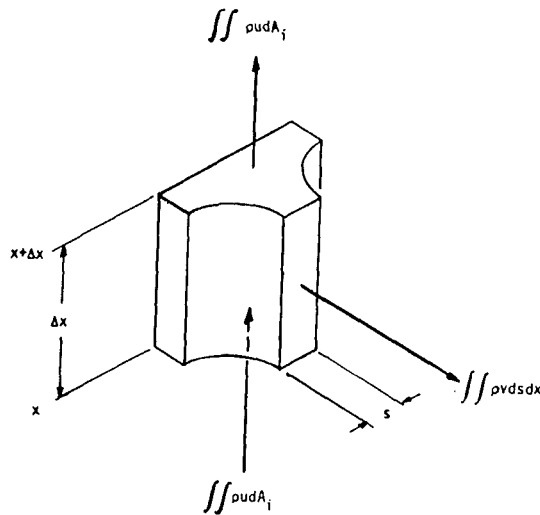


Fig. 1 Subchannel control volume for continuity

and

$$w_{ij} = \frac{1}{\Delta x} \iint \rho v ds dx \quad (5)$$

where  $\rho_i$  is the subchannel average density,  $m_i$  is the flow rate, and  $w_{ij}$  is the average crossflow per unit length from subchannel  $i$  to subchannel  $j$ . Substituting the integrals into equation (2), dividing by  $\Delta x$  and in the limit as  $\Delta x \rightarrow 0$ , the result is the equation

$$A_i \frac{\partial \rho_i}{\partial t} + \frac{\partial m_i}{\partial x} + w_{ij} = 0 \quad (6)$$

This is the equation of continuity given by equation (1) of the paper. Applying the same method to a differential cube of volume  $\Delta x \Delta y \Delta z$  for three-dimensional flow gives the classical form of the continuity equation presented by Buettiker as equation (1). The mass flux  $m_i/A_i$  can be interpreted as the one-dimensional or average mass flux for simple channels. This does not deny the existence of lateral gradients in density or velocity. Contrary to Buettiker's allegation, the crossflow per unit length is physically meaningful and represents the average lateral mass flux through the area  $s\Delta x$ . Equation (6) is generalized in the paper to consider additional lateral flow connections by using the [S]<sup>T</sup> matrix. This matrix is equivalent to a lateral finite difference operator. It provides the necessary lateral coupling and lateral boundary specification. This generalization also applies to the energy and axial momentum equation and, after introduction of the continuity equation, yields the equations presented in the paper.

Contrary to Buettiker's claim of wrong manipulations, the equations are treated correctly within the "lumped parameter" or integral equation concept. Microscopic details are considered by using integral relationships for friction factors, lateral mixing coefficients, etc. As Buettiker points out, these can only be introduced within the framework of integral equations over finite control volumes. This is in fact what was done in the paper. The finite difference forms of the equations are macroscopic control volume equations.

The use of the simplified transverse momentum equation can be justified for flow moving primarily in the axial direction. This is a good assumption for many rod bundle problems and is similar to the assumption used to develop the boundary layer equations. Only where the crossflow is changing rapidly with position does the assumption break down and this is often only a local phenomenon. Crossflow inertial effects can be included through the use of a semiempirical crossflow resistance function [14]. Development of more complete transverse momentum equations for subchannel analysis is the subject of ongoing work.

The two-phase flow model used in the paper is adapted from that of Meyer [6]. It allows the averaged equations of a two-phase

flow mixture to be written as a variable density fluid with an equation of the same form as for one-phase flow. For the continuity example presented previously, the definitions (3) through (5) can be replaced by

$$\rho_i = \frac{1}{A_i \Delta x} \iint \{ \rho_g \alpha + \rho_f (1 - \alpha) \} dA_i dx \quad (7)$$

$$m_i = \iint \{ \rho_g u_x \alpha + \rho_f u_x (1 - \alpha) \} dA_i \quad (8)$$

and

$$w_{ij} = \frac{1}{\Delta x} \iint \{ \rho_g v_x \alpha + \rho_f v_x (1 - \alpha) \} ds dx \quad (9)$$

where  $\rho_g$  is the vapor density,  $\rho_f$  is the fluid density, and  $\alpha$  is the local, time average, void fraction.

These definitions admit slip flow, density gradients and velocity gradients; however, their local values are not determinable because of the averaging. Local values to specify transport through subchannel interfaces must come from assumption or experiment.

The definition for density is the same as that used for pipe flow and, contrary to violating thermodynamic principles, it admits the existence of thermal nonequilibrium. While it is true that density is function of enthalpy only at a reference pressure for Meyer's model, mathematical models for nonequilibrium effects such as subcooled voids [15] can introduce the independent variables  $x$  and  $t$  in addition to other dependent variables.

Channel average definitions can also be made for the energy and momentum equations. The use of Meyer's equations allows for slip flow through the use of "effective densities" for energy and momentum transport.

The subchannel analysis concept is in wide use [1, 3, 4, 16, 17, 18, 19, 23]. Comparisons between calculations and experiments are in good agreement for single-phase flow [7, 8, 9, 18, 19, 20, 22], thus giving confidence to the subchannel approach. The same principles apply to two-phase flow where the equations can be written as a variable density fluid. Experimental evidence shows that this is a reasonable approach, especially for high pressure when the departure from homogeneity is small. Areas of disagreement have pointed out how two-phase flow and mixing models could be improved [7, 9, 20, 21, 22, 23] rather than discrediting the basic approach. For the near future it would seem that subchannel models will continue to be used for rod bundle analysis. As more detailed knowledge is obtained from experiments, two-phase flow models will be improved and empirical data will be developed to allow a wider range of application. In the future it may be possible to develop a more microscopic model, thus reduce the requirements for assumptions and empirical data.

### Additional References

- 13 Shapiro, Ascher H., *The Dynamics and Thermodynamics of Compressible Fluid Flow*, Ronald Press, New York, Vol. 1, 1953, p. 15.
- 14 Khan, E. U., Kim, K., and Lindstrom, G. E., "Crossflow Resistance and Diversion Crossflow Mixing Between Rod Bundles," *ANS Transactions* Vol. 14, No. 1, 1971, pp. 249-250.
- 15 Levy, S., "Forced Convection Subcooled Boiling Prediction of Vapor Volumetric Fraction," GEAP-5157, Apr. 1966.
- 16 Fajeau, Maurice, "Programme FLICA Etude Thermodynamique d'un Reacteur ou d'une Boucle d'Essai," CEA-R-3716, 1969.
- 17 "TEMP-Thermal Enthalpy Mixing Program," Babcock and Wilcox Co., BAW-10021, Apr. 1970.
- 18 Esposito, Vincent J., and Spencer, Arthur C., "Can Macro-Micro-Type Flow Computation Schemes be Reactor Engineering Tools?" Topical Meeting on Water Reactor Safety, Conf-730304, Mar. 1973, pp. 501-515.
- 19 Chelemer, H., Chu, P. T., and Hochreiter, L. E., "THINC-IV—An Improved Program for Thermal-Hydraulic Analysis of Rod Bundle Cores," WCAP-7956, June 1973.
- 20 Castellana, Frank S., and Casterline, Joseph E., "Subchannel Flow and Enthalpy Distributions at the Exit of a Typical Nuclear Fuel Core Geometry," *Nuclear Engineering and Design*, Vol. 22, 1972, pp. 3-18.
- 21 Bowering, R. W., and Levy, J., "Freon 7-Rod Cluster Subchannel Mixing Experiments," AEEW-M906, 1969.
- 22 Lahey, R. T., Jr., Shiralkar, B. S., Radcliffe, D. W., and Palomik, E. E., "Out-of-Pile Subchannel Measurements in a Nine-Rod Bundle for Water at 1000 psia," International Symposium on Two-Phase Systems, Haifa, Israel, Paper 3-1, 1971.
- 23 Forti, G., and Gonzalez-Santalo, J. M., "A Model for Subchannel Analysis of BWR Rod Bundles in Steady State and Transient," ANS International Meeting on Reactor Heat Transfer, Karlsruhe, Germany, 1973.